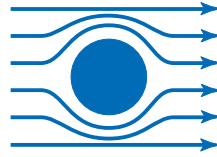




TECHNISCHE
UNIVERSITÄT
MÜNCHEN



WALTHER - MEISSNER -
INSTITUT FÜR TIEF -
TEMPERATURFORSCHUNG



BAYERISCHE
AKADEMIE DER
WISSENSCHAFTEN

Spin-transport-phenomena in metals, semiconductors, and insulators

Dissertation
von
Matthias Klaus Althammer

Betreuer: Prof. Dr. Rudolf Gross
München, Mai 2012

Abstract

Assuming that one could deterministically inject, transport, manipulate, store and detect spin information in solid state devices, the well-established concepts of charge-based electronics could be transferred to the spin realm. This thesis explores the injection, transport, manipulation and storage of spin information in metallic conductors, semiconductors, as well as electrical insulators.

On the one hand, we explore the spin-dependent properties of semiconducting zinc oxide thin films deposited via laser-molecular beam epitaxy (laser-MBE). After demonstrating that the zinc oxide films fabricated during this thesis have excellent structural, electrical, and optical properties, we investigate the spin-related properties by optical pump/probe, electrical injection/optical detection, and all electrical spin valve-based experiments. The two key results from these experiments are: (i) Long-lived spin states with spin dephasing times of 10 ns at 10 K related to donor bound excitons can be optically addressed. (ii) The spin dephasing times relevant for electrical transport-based experiments are ≤ 2 ns at 10 K and are correlated with structural quality.

On the other hand we focus on two topics of current scientific interest: the comparison of the magnetoresistance to the magnetothermopower of conducting ferromagnets, and the investigation of pure spin currents generated in ferromagnetic insulator/normal metal hybrid structures. We investigate the magnetoresistance and magnetothermopower of gallium manganese arsenide and Heusler thin films as a function of external magnetic field orientation. Using a series expansion of the resistivity and Seebeck tensors and the inherent symmetry of the sample's crystal structure, we show that a full quantitative extraction of the transport tensors from such experiments is possible. Regarding the spin currents in ferromagnetic insulator/normal metal hybrid structures we studied the spin mixing conductance in yttrium iron garnet/platinum heterostructures using two independent experiments based on the spin pumping effect. The yttrium iron garnet thin films were again deposited via laser-MBE and are state-of-the-art. Our results establish ferromagnetic insulator/normal metal structures as efficient spin current sources. Finally, we show that a new magnetoresistance effect due to spin currents is present in these ferromagnetic insulator/normal metal hybrids. This magnetoresistance effect in particular provides a simple means to establish spin current flow across the interface.

Kurzfassung

Diese Dissertation behandelt die Injektion, den Transport, die Manipulation und die Speicherung von Spininformation sowohl in metallischen Leitern und Halbleitern, als auch in elektrischen Isolatoren. Dadurch wird die Grundlage für die vollständige, deterministische Kontrolle des Spinfreiheitsgrades in festkörperbasierten Systemen geschaffen und somit die Übertragung der bereits etablierten Konzepte der ladungsbasierten Elektronik auf den Bereich des Spins ermöglicht.

Im ersten Teil betrachten wir die spinabhängigen Eigenschaften von halbleitenden Zinkoxid-Dünnschichten, welche durch Laser-Molekularstrahlepitaxie (laser-MBE) hergestellt wurden. Nachdem gezeigt wird, dass die Zinkoxid-Dünnschichten, die im Rahmen dieser Arbeit hergestellt wurden, exzellente strukturelle, elektrische und optische Eigenschaften besitzen, untersuchen wir im weiteren die spinabhängigen Eigenschaften mit Hilfe von rein optischer Anregung/Detektion, elektrischer Injektion/optischer Detektion und rein elektrischen, auf Spinventilen basierenden Experimenten. Die zwei Schlüsselergebnisse dieser Experimente sind: (i) Es ist möglich langlebige Spinzustände, die mit Donatorgebundenen Exzitonen verknüpft sind, mit einer Spindephasierungszeit von 10 ns bei 10 K optisch anzusprechen. (ii) Die Spindephasierungszeiten, die für elektrische Transportexperimente relevant sind, betragen ≤ 2 ns bei 10 K und korrelieren mit der strukturellen Qualität der Proben.

Im zweiten Teil konzentrieren wir uns auf den Vergleich des Magnetwiderstands mit der Magnetothermokrafft elektrisch leitender Ferromagnete und die Untersuchung von Spinströmen, die in ferromagnetischen Isolator-/Normalmetall-Hybridstrukturen erzeugt werden. Wir untersuchen den Magnetwiderstand und die Magnetothermokrafft von Gallium-Mangan-Arsenid- und Heusler-Dünnschichten in Abhängigkeit von der Orientierung des äußeren Magnetfeldes. Aus solchen Messungen lassen sich die vollständigen Tensoren der Transportkoeffizienten quantitativ mit Hilfe einer Reihenentwicklung der Widerstands- und Seebeck-Tensoren und unter Berücksichtigung der inhärenten Symmetrie der Kristallstruktur der Probe gewinnen. Aus Experimenten zu Spinströmen in ferromagnetischen Isolator/Metall-Hybridstrukturen, die auf dem Spinpump-Effekt basieren, haben wir die Spinmischleitfähigkeit in Yttrium-Eisen-Granat-/Platin-Heterostrukturen bestimmt. Die Yttrium-Eisen-Granat-Dünnschichten wurden ebenfalls mittels laser-MBE hergestellt und entsprechen in ihren strukturellen und magnetischen Eigenschaften dem aktuellen Stand der Forschung. Unsere Ergebnisse etablieren ferromagnetische Isolator-/Normalmetall-Hybridstrukturen als effiziente Quelle von Spinströmen. Abschließend zeigen wir, dass in diesen ferromagnetischen Isolator-/Normalmetall-Hybridstrukturen ein neuer Magnetwiderstandseffekt aufgrund der Spinströme existiert. Er erlaubt es, nur mit Hilfe eines Ladungsstroms Spinströme über die Grenzfläche der Hybridstruktur fließen zu lassen.

Contents

	Page
1 Introduction	1
2 Spin electronics in epitaxial zinc oxide thin films	5
2.1 Introduction into zinc oxide	6
2.2 Optimization of the laser-MBE growth of ZnO films	7
2.2.1 Structural optimization with buffer layer	8
2.2.2 Characteristics of optimized ZnO thin films	15
2.2.2.1 HRXRD results	15
2.2.2.2 Electronic transport measurements	22
2.2.2.3 TEM analysis of ZnO thin films with buffer layer	29
2.2.2.4 Photoluminescence of ZnO layers	30
2.3 Optical orientation experiments in ZnO thin films	34
2.4 Electrical injection and optical detection of spin-polarized charge carriers	39
2.5 All-electrical injection and detection of spin transport in ZnO	46
2.5.1 Introduction into giant magnetoresistance	46
2.5.2 Theory of giant magnetoresistance	48
2.5.3 Experimental	57
2.5.3.1 Growth and structural characterization of multilayer spin valve system	57
2.5.3.2 Electrical measurements with ZnO based spin valve structures	63
2.5.3.3 Extraction of spin transport parameters from the measurements	70
2.6 Spin electronics in epitaxial zinc oxide thin films: A summary	75
3 Spin caloritronics	79
3.1 Introduction into spin caloritronics	80
3.2 Materials for spin caloritronics grown via laser-MBE	81
3.2.1 Laser-MBE growth of Heusler compound thin films	81
3.2.1.1 Heusler compounds: a short introduction	82
3.2.1.2 Laser-MBE growth of the Heusler compound Co_2MnSi	83
3.2.2 Laser-MBE growth of yttrium iron garnets	87
3.2.2.1 An introduction into rare-earth iron garnets	88
3.2.2.2 Properties of target material and substrates	89
3.2.2.3 Structural and static magnetic properties of YIG thin films on GGG and YAG substrates	92

3.2.2.4	Dynamic magnetic properties of laser-MBE grown YIG films on GGG and YAG	102
3.2.2.5	Laser-MBE growth of YIG thin films: a summary	103
3.3	Anisotropic magnetothermopower and anisotropic magnetoresistance	104
3.3.1	Theory of magneto-galvanic effects	105
3.3.1.1	Calculation of the resistivity and Seebeck tensor in cubic symmetry	109
3.3.1.2	Calculation of the resistivity and Seebeck tensor in tetragonal symmetry	110
3.3.1.3	Projections of the resistivity and Seebeck tensor	113
3.3.1.4	Application of the model to experiment	127
3.3.1.5	Determination of longitudinal and transverse resistivity and thermopower	128
3.3.1.6	Experimental procedure for and analysis of AMDR and ADMTP experiments	130
3.3.2	Magnetothermopower and magnetoresistance in (Ga,Mn)As	132
3.3.2.1	Sample preparation and on-chip thermometry	133
3.3.2.2	ADMR and ADMTP for (001)-oriented (Ga,Mn)As	135
3.3.2.3	ADMR and ADMTP for (113)-oriented (Ga,Mn)As	140
3.3.3	Magnetoresistance in Heusler compound thin films	145
3.4	Spin currents in magnetic insulators	152
3.4.1	Spin current generation via spin pumping in YIG/Pt bilayers	152
3.4.2	Spin magnetoresistance in YIG/Pt thin films	158
3.5	Spin caloritronics: a summary	167
4	Conclusions and outlook	171
4.1	Summary	171
4.2	Outlook	172
A	Upgrade of the laser-MBE system	179
A.1	New lens system "Brenninger"	180
A.2	LabVIEW based control system	183
A.2.1	Basic Motor Control	183
A.2.2	Pressure Control	187
A.2.3	Excimer Laser Control	188
A.2.4	LASCON Control	190
A.2.5	Data Window	192
A.2.6	Target Control	194
A.2.7	Script Control	195
A.3	Basic operation of laser-MBE	196
A.4	Operation of the RF atom source	198
B	Extraction and simulation of temperature dependent Hall data	199
C	Calculation results and source code for GMR calculations	203
D	Expansion coefficients in cubic and tetragonal symmetry	211

List of publications	217
Bibliography	219
Acknowledgements	235

List of Figures

2.1	Orientation of ZnO on sapphire	8
2.2	Results optimization energy density	10
2.3	Results optimization temperature	11
2.4	Results optimization buffer layer	13
2.5	Results optimization pressure with buffer layer	15
2.6	Phi scan for in-plane orientation	16
2.7	RSM of various ZnO thin films	18
2.8	XRD scans for ZnO thin films grown on different oriented sapphire substrates	21
2.9	Hall measurement results for different purity target materials	23
2.10	Simulation results for two different ZnO films	24
2.11	Temperature dependent Hall results for ZnO+buffer	25
2.12	Temperature dependent Hall results for a (Mg,Zn)O buffer layer	26
2.13	Simulation results for two different ZnO films	28
2.14	TEM results for a ZnO thin film with buffer layer	30
2.15	Temperature dependent PL for ZnO thin films	31
2.16	PL fit results comparison	33
2.17	Delaytime scans for two different ZnO samples	35
2.18	Wavelength dependence for buffered ZnO sample	36
2.19	Temperature dependence	37
2.20	Results for electrical injection optical detection	40
2.21	Results for electrical injection optical detection wavelength dependence .	42
2.22	Comparison Hanle MOKE and TRFR at low temperatures	43
2.23	Temperature dependence of Hanle MOKE signal and extracted parameters	45
2.24	Graphical illustration spin valve effect	47
2.25	Schematic View of GMR structure	49
2.26	GMR theory plot of Parameters	54
2.27	GMR theory plot of MR	56
2.28	Structural characterization of spin valve Multilayer	59
2.29	In-plane orientation of spin valve Multilayer	60
2.30	Reflectometry of spin valve multilayer	61
2.31	SQUID Magnetometer measurements on spin valve multilayerstructure .	62
2.32	Fabrication of the GMR Devices	63
2.33	Electrical characterization GMR devices	64
2.34	MR as a function of current and field orientation	67
2.35	Comparison $R(H)$ and ADMR	68
2.36	Temperature dependence MR of spin valve	69
2.37	Fitting MR and extracted parameters	71
2.38	Determination of the spin dephasing time in spin valve devices	72

3.1	Introduction into Cobalt-based Heusler compounds	82
3.2	Structural comparison Co ₂ MnSi thin films on MgO (001)	85
3.3	SQUID magnetometry on a CMS film	86
3.4	Illustration of the YIG crystal structure	88
3.5	XRD diffraction data for bare GGG and YAG substrates	89
3.6	SQUID magnetometry data for bare GGG and YAG substrates	91
3.7	HRXRD results for a YIG layer on a GGG substrate	93
3.8	HRXRD results for a YIG layer on a YAG substrate	95
3.9	HRXRD results for a YIG/Pt bilayer on a GGG substrate	97
3.10	HRXRD results for a YIG/Pt bilayer on a YAG substrate	99
3.11	SQUID magnetometry data for a YIG layers on GGG and YAG substrates	100
3.12	Ferromagnetic resonance data for YIG layers on GGG and YAG substrates	102
3.13	Different rotation planes for ADMR and ADTP measurements	114
3.14	Simulation results for different magnetization rotation in cubic symmetry	115
3.15	Simulation results for different magnetization rotation in cubic symmetry for the thermopower	116
3.16	Definition of polarity for ADMR and ADMTP experiments	129
3.17	ADMR and ADMTP simulation software	130
3.18	On chip thermometry on a (Ga,Mn)As Hall bar	134
3.19	ADMR and ADMTP measurements on (001)-oriented (Ga,Mn)As	137
3.20	ADMR and ADMTP measurements on (113)-oriented (Ga,Mn)As	142
3.21	ADMR measurements on (001)-oriented Co ₂ FeAl	148
3.22	Extracted parameters from ADMR experiments on (001)-oriented Co ₂ FeAl	150
3.23	Spin pumping experiments for YIG/Pt hybrid structures	154
3.24	Frequency dependent ferromagnetic resonance data for a bare YIG layer and a YIG/Pt heterostructure on GGG	156
3.25	Illustration of ordinary Hall effect and spin Hall effect	159
3.26	Illustration of the spin reflection magnetoresistance for YIG/Pt heterostruc- tures	160
3.27	Spin reflection magnetoresistance for YIG/Pt heterostructures evaluated in various ADMR rotation planes	163
3.28	Extracted field dependence of ρ_2 and temperature dependence of SMR signal	165
3.29	Spin reflection magnetoresistance for YIG/NM/Pt heterostructures	166
4.1	New experiments with ZnO	173
4.2	Improvements for Caloritronix setup	175
4.3	SMR effect in different ferromagnetic insulators	176
4.4	SMR effects in novel structures	177
A.1	Introduction laser-MBE	179
A.2	Illustration new lens system	181
A.3	Screenshot laser-MBE control software	184
A.4	Screenshot Motor Control	185
A.5	Screenshot Pressure Control	188
A.6	Screenshot Excimer Control	189
A.7	Screenshot LASCON Control	191
A.8	Screenshot LASCON Control2	193

A.9 Screenshot Data Window	194
A.10 Screenshot Target Window	194
A.11 Screenshot Data Window	195
B.1 Illustration Van-der-Pauw geometry	199

Chapter 1

Introduction

”Non est ad astra mollis e terris via.”

”There is no easy way from earth to the stars.”

This quotation taken from the tragedy ”Hercules furens” written by Seneca (4 BC - 65 AD) has been widely used in science to describe the hardship it takes to reach great and unbelievable achievements. It inspired for example the expression ”Per aspera ad astra” used by the National Aeronautics and Space Administration (NASA), which attributes for the tough challenges and disasters mankind had to master for the still ongoing exploration of outer space. In a more general view, science would not be where it is today without the countless humans that were able to accomplish new breakthroughs in their field of research while mastering frustrating obstacles. Starting with the invention of fire, language and the wheel in the early beginnings of mankind, going over the foundations of mathematics, philosophy and written poetry in ancient Greek and Rome, the industrialization (e.g. the steam engine and electricity) in the 18th and 19th century and ending in the great advancements of the 20th century, among them the theory of relativity, nuclear fission, modern ways of communication and miniaturization.¹

In the field of miniaturization of the late 20th century the fastest progress has been achieved by semiconductor based electronics. The rapid development of semiconductor devices started with the invention of the transistor by Shockley, Bardeen, and Brattain in 1947, which awarded them the Nobel Prize in Physics in 1956 ”for their researches on semiconductors and their discovery of the transistor effect”. Over a period of three decades the miniaturization of semiconductor devices allowed the development of integrated circuits, which are nowadays based on complimentary metal-oxide-semiconductors (CMOS). These integrated circuits are the foundation of modern information technology utilizing the charge of an electron to store digital information. While this technology approaches in a fast pace the fundamental physical limits, it still produces even faster transistors, like the development of a 100 GHz graphene transistor [1]. Unfortunately, the accompanied Joule heating of charge currents becomes ultimately the limiting factor for a downscaling of these devices.

For future advances in modern information technology new ways of storing and processing information are currently investigated. Among them is the field of spin electronics (”spintronics”) exploiting the spin degree of freedom of an electron. Spintronics

¹The author admits to be unable to cover and remember all important inventions of mankind in this thesis. Therefore this is just a short compilation of examples for the accomplishments of mankind.

has already proven its relevance via the success story of giant magnetoresistance effect discovered by Albert Fert and Peter Grünberg in 1988 [2, 3], which awarded them the Nobel prize in physics in 2007. Until now, commercially available spintronic devices are used for the nonvolatile storage of information using the magnetization orientation of ferromagnets, such as hard disks and magnetic random access memories. The control of magnetization orientation in these devices is mainly achieved by the external magnetic field generated by an electrical current. Thus, when scaling down such devices power consumption and heat dissipation are still relevant problems. Novel concepts utilizing pure spin currents, which is the flow of angular momentum without the net transport of charge, might be a way to solve this issue, as pure spin currents are predicted to be dissipationless [4]. Therefore, the search for pure spin current sources is one hot topic in the field of spintronics. The generation of a pure spin current is driven by a non-equilibrium condition of the magnetic degrees of freedom in a ferromagnet, such as the relaxation of collectively excited magnetic moments [5–16] (“spin pumping”) or a thermal gradient [17–30] (“spin Seebeck effect”).

Besides the search for pure spin current sources, the transport of spin information across long length scales and an efficient way of manipulating the spin information are additional key ingredients for novel spintronic devices. To allow an easy integration of these devices into standard CMOS production technologies a large part of current spintronic research focuses on the transport and manipulation of spin information in semiconductors. A major obstacle in this field is the efficient injection and extraction of a spin current in and from a semiconductor, due to the conductivity mismatch problem [31]. A remedy for these problems may be provided by the use of pure spin current sources, tunnel junctions or ferromagnetic semiconductors.

In summary, novel spin electronic devices rely on the efficient transport and manipulation of spin information over large length scales and on short timescales. These requirements could make spin based information processing competitive to the already established charge based information processing.

The main topic of this thesis is the study of spin transport-phenomena in a variety of materials covering the whole range of electrical conductivity from metals, over semiconductors to insulators. It is structured as follows:

After this introduction, Chapter 2 deals with the investigation of spin related properties of the wide band gap semiconductor zinc oxide. After a short introduction into zinc oxide, we first present the excellent results obtained for the structural, electrical and optical properties of zinc oxide layers grown on sapphire via the laser-MBE (Molecular Beam Epitaxy) setup, after carrying out a careful growth optimization.

We then use these zinc oxide thin films to demonstrate in all-optical time-resolved Faraday rotation experiments the successful, long-lived (≥ 10 ns) storage of spin information on donor bound exciton states at liquid helium temperatures. Advancing a step further we show that it is possible to electrically address these states by injecting a spin polarized current from a ferromagnet into zinc oxide using a combination of electrical injection and optical detection.

For a comparison to the spin properties obtained by optical means, we extract the spin diffusion length in ZnO from all-electrical measurements in ZnO-based spin valve heterostructures. The temperature dependence of the spin dephasing time extracted from

all-electrical measurements reveals that there are two different regimes. At low temperatures ($T \leq 25$ K) the spin dephasing time is dominated by the Dzyaloshinsky-Moriya while at elevated temperatures ($T \geq 25$ K) the dominating spin dephasing mechanism is D'yakonov-Perel'. Moreover, this temperature dependence qualitatively agrees to the one obtained by all-optical measurements demonstrating that both experimental techniques observe the same spin dephasing mechanisms and that the spin dephasing time is sensitive to the structural quality of the sample.

In Chapter 3, we first report on the structural and magnetic properties of cobalt-based Heusler compounds and yttrium iron garnet thin films grown via laser-MBE. The state-of-the-art properties of these thin films are the foundation for the further experiments presented in the rest of Chapter 3, which is divided into two main parts.

In the remaining first part we establish a theoretical model to allow the full quantitative extraction of the resistivity and Seebeck tensors of a ferromagnetic material from magnetotransport experiments. As a proof of principle, we then investigate experimentally the validity of our theoretical model by evaluating the magnetoresistance and magnetothermopower in thin films of the ferromagnetic semiconductor gallium manganese arsenide and cobalt-based Heusler compounds. These first experiments show that it is in principle possible to extract quantitatively full magnetotransport tensor properties for single crystalline thin films of cubic and tetragonal symmetry.

In the second part we investigate pure spin currents in ferromagnetic insulator/normal metal hybrid structures based on yttrium iron garnet as the ferromagnetic insulator. In a set of two independent experiments we proof that the injection of a pure spin current from yttrium iron garnet via the spin pumping effect is as effective as from a conducting ferromagnet. This establishes ferromagnetic insulators as a convenient and effective spin current source. In addition, we investigate using conventional magnetotransport techniques a new magnetoresistance effect in ferromagnetic insulator/normal metal hybrid structures, that is based on the spin Hall effect in normal metals and the selective spin current sink generated by the ferromagnetic insulators. These first experiments pave the way for future applications of this effect.

Finally, the obtained experimental results are summarized in Chapter 4. In this chapter we also give an outlook on possible future experiments based on the results of this thesis, which highlight the relevance of this thesis.

In Appendix A we introduce the extensions and upgrades added to the laser-MBE setup during the work of this thesis.

In the end, let me make a personal statement: Working on this PhD was sometimes frustrating and not always easy, but in some unique moments I felt like I could reach the stars.

Chapter 2

Spin electronics in epitaxial zinc oxide thin films

Abstract

In this chapter we demonstrate how epitaxial ZnO thin films with excellent crystalline quality (full width at half maximum (FWHM) of the ZnO (0002) rocking curve $< 0.03^\circ$) can be grown by pulsed laser deposition (PLD) after a careful growth optimization. The optical properties of these films are also state-of-the-art: photoluminescence spectra show well pronounced donor bound exciton peaks at I_6 (aluminum donor bound exciton) and I_3 (ionized donor bound exciton). Optical pump and probe experiments (time-resolved Faraday rotation (TRFR) measurements) performed in collaboration with the group of B. Beschoten at the RWTH Aachen reveal a strong dependence of the exciton spin dephasing times on the wavelength of the pump and probe beams. In particular, the TRFR data demonstrate that long spin coherence times in excess of 10 ns at liquid He temperatures can be achieved using laser wavelengths appropriate to selectively excite particular donor bound excitons. Our results thus establish that spin information can be stored in ZnO by taking advantage of donor bound excitons. Going a step further, we demonstrate that the donor bound excitons can be spin-polarized by electrically injecting a current via a ferromagnetic cobalt electrode into the ZnO thin film. This enables an electrical addressing of excitonic spin states. Last but not least we compare the optically measured exciton spin decoherence times with all-electrical measurements of the spin diffusion length in ZnO-based spin valve heterostructures. The temperature dependence of the spin dephasing time extracted from these measurements agrees qualitatively with the one extracted from TRFR. This temperature dependence of the spin dephasing time exhibits two different regimes: at low temperatures the temperature independent Dzyaloshinsky-Moriya mechanism dominates, while at high temperatures the temperature dependent D'yakonov-Perel' mechanism is dominating.

2.1 Introduction into zinc oxide

The direct band gap semiconductor zinc oxide (ZnO) is a very versatile material for device applications [32–37]. For example, the direct and wide band gap of 3.44 eV at low temperatures and 3.37 eV at room temperature in the near-UV spectral region [38–42] makes ZnO an interesting candidate for future optoelectronic applications. Moreover, the excitonic emission processes in ZnO persist even at or above room temperature [43, 44], due to a large free exciton binding energy (60 meV) [39–42]. ZnO crystallizes in the polar wurtzite structure ($a = 0.32496$ nm, $c = 0.52042$ nm [45]) and is already available as large bulk single crystals [44, 46].

Over the past decade the quality of bulk and thin film single crystalline ZnO has been greatly improved [32–37] and has led to a revival of device concepts based on the semiconductor ZnO. The progress in deposition of epitaxial crystalline ZnO thin films is demonstrated in the increase of mobility [47] and realization of a 2 dimensional electron gas (2DEG) [48–52], leading to the observation of the quantum Hall effect [53, 54] and fractional quantum Hall effect [55, 56] in ZnO. These results prove that ZnO is still a promising material for device applications and will play an important role in oxide based electronics.

Despite the study of the electronic and optical properties of ZnO since the beginning of semiconductor physics [57], a reproducible bipolar control and tunability of the electrical conductivity in ZnO could not be achieved, posing a major obstacle for the use of ZnO in semiconductor device applications. Almost all ZnO crystals show n-type conduction, while p-type ZnO is elusive. The origin of this phenomenon has been a matter of extensive debate and research [32–37]. The problem in controlling the conductivity in ZnO arises from the fact that even relatively small concentrations of native point defects and impurities can significantly affect the electrical and optical properties of semiconductors [58, 59]. In the case of ZnO for a long time it has been postulated that the unintentional n-type doping is caused by the presence of oxygen vacancies or zinc interstitials [60–63]. Recent optically detected electron paramagnetic resonance on high quality ZnO crystals and theory calculations have shown that oxygen vacancies are actually deep donors and cannot contribute to n-type conduction [64–67]. Instead the unintentional incorporation of impurities, acting as shallow donors, such as interstitial and substitutional hydrogen [68], or substitutional aluminum, gallium and indium [69], might explain the origin of the n-type conduction in ZnO. The presence of such impurities depends on the growth conditions, methods and base materials used, and might explain the strongly varying carrier concentration reported in literature. The achievement of a stable p-type conductivity in ZnO is still a very difficult task [32–37]. Despite a number of reports on successful p-type doping of ZnO [70–80], there are no reports on reproducible p-n junctions raising questions about the reliability of the observations and the reproducibility and stability of the p-type doping. The most promising candidate for achieving a stable p-type conduction in ZnO is the substitution of oxygen by nitrogen [81], but only a few reports on a successful application are available [70, 73]. An additional problem for determining the type of conduction arises from the difficulties in interpreting Hall effect measurements due to surface conduction channels and inhomogeneities in ZnO [82–86]. Nevertheless, the reproducible and stable control of carrier type and concentration is a key element for future device applications.

The observation of possible room temperature ferromagnetism in transition metal

doped ZnO [45, 87–94] has fueled the interest in ZnO for spintronic applications, because ferromagnetic semiconductors are an efficient means of generating spin polarized currents in semiconducting materials. Unfortunately, the origin of the observed ferromagnetism is not an intrinsic feature of transition metal doped ZnO, but is generated by a secondary phase of transition metal clusters formed during deposition in the ZnO thin films [95, 96].

In contrast to the hassle in obtaining ferromagnetic ZnO, the small spin-orbit coupling [40] and interesting optical properties [32–37] make ZnO still an versatile candidate for spin electronic devices. Only very few publications have investigated quantitatively the spin dependent properties of ZnO [97–99] or shown a successful realization of spin injection into ZnO [100–103]. A fundamental understanding of the spin injection efficiency and the underlying spin dephasing mechanisms in ZnO are an important mile stone for a successful implementation of ZnO into spintronic devices.

In the following sections we present the results obtained with our optimized epitaxial ZnO thin films on sapphire substrates regarding their structural, electrical and optical properties. We then investigate their spin dependent properties using time-resolved Faraday/Kerr rotation and all-electrical transport experiments. In section 2.2 we first report on the optimization of the ZnO films grown on c-plane sapphire and present the characteristic results for these optimized films obtained from high resolution x-ray diffraction (HRXRD), temperature dependent Hall effect (TDH), high resolution transmission electron microscopy (HRTEM), and temperature dependent photoluminescence (PL) experiments. Section 2.3 then summarizes the information on the spin dephasing times, their temperature and characteristic excitation wavelength dependence in our optimized ZnO thin films extracted from time-resolved Faraday rotation (TRFR) experiments. In addition, we discuss the role of donor bound excitons for the long spin life-time in ZnO. Results and a discussion on electrical injection and optical detection via Kerr rotation (KR) are presented in section 2.4. Moreover, we show in this section that it is possible to spin polarize donor bound excitons by the injection of a spin polarized current into ZnO. Finally, section 2.5 summarizes all-electrical spin injection experiments utilizing a spin valve structure based on ZnO. The fit of the experimental data to a giant magnetoresistance (GMR) model enables us to extract quantitative data on the spin dependent transport properties. In the final section 2.6 we summarize the key results obtained with ZnO thin films in this thesis.

2.2 Optimization of the laser-MBE growth of ZnO films

A first crucial step in obtaining reproducible and trustworthy results for a material system grown via laser assisted molecular beam epitaxy (laser-MBE) onto a single crystalline substrate is the careful investigation of the influence of deposition parameters on characteristic material parameters. For the oxide semiconductor ZnO, we have analyzed the growth of (0001) ZnO thin films on (0001)-oriented sapphire (Al_2O_3) substrates. In the following we first present a study of the influence of the deposition parameters on the structural quality of the ZnO thin films, which leads in the end to the optimization of our laser-MBE grown samples. After this careful optimization we look into the typical properties of these films using HRXRD, TDH, HRTEM, and PL measurements. The results obtained from these measurements indicate that the optimized ZnO thin films on

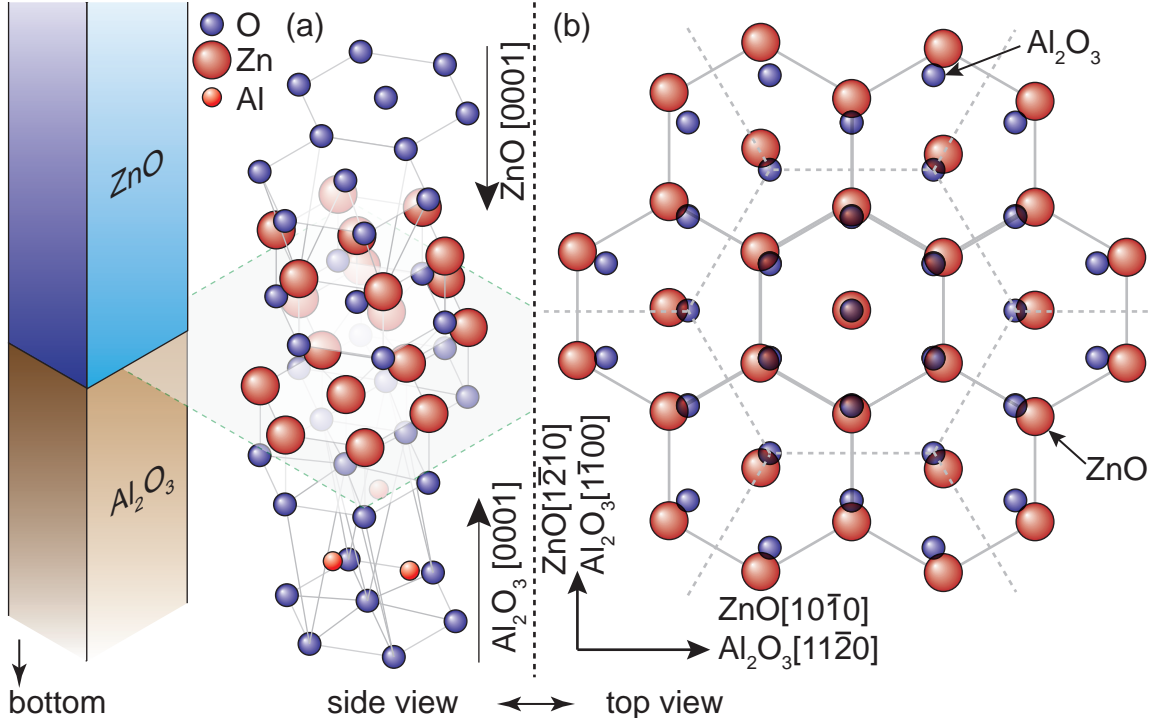


Figure 2.1: (a) Graphical illustration of the structural alignment between the (0001) sapphire substrate and the (0001) ZnO thin film. The wurtzite ZnO consists of two interpenetrating hcp lattices for Zn and O, respectively. (b) At the oxygen terminated substrate the Zn atoms will align with respect to the hexagonal O-sublattice of the Al₂O₃. This leads to an O-termination of the film and the epitaxial in-plane relations between substrate and ZnO: Al₂O₃(0001)[11 $\bar{2}$ 0] || ZnO(0001)[10 $\bar{1}$ 0].

sapphire are state-of-the-art, exhibiting excellent structural, electrical and optical properties. In addition, we finally propose further ways of optimizing the growth of ZnO on sapphire, which might lead to an improvement in the mobility of the charge carriers in our thin films.

2.2.1 Structural optimization with buffer layer

Zinc oxide thin films have already been deposited on many different substrate materials with varying results regarding their structural, electrical and optical quality [42, 47, 104–109]. For the studies in this work, we focused on the deposition on sapphire substrates, where a successful growth of single crystalline thin films by various growth techniques is already reported [42, 52, 109, 110]. In contrast to homoepitaxial growth, this heteroepitaxial approach enables us to clearly separate film and substrate physical properties in our measurements. One of the main disadvantages of this approach is the formation of dislocations in the zinc oxide due to the large lattice mismatch between sapphire and ZnO. In the following we focus on the growth of (0001)-oriented ZnO on (0001)Al₂O₃ substrates in our laser-MBE system. More details can be found in Appendix A. The structural analysis via x-ray diffraction(XRD) has been carried out at room temperature using a Bruker Discover 4-circle diffractometer.

The c-plane of sapphire consists of alternating layers of oxygen (sixfold symmetry) and

aluminum (threefold symmetry). In contrast, the wurtzite structure in ZnO results in a sixfold symmetry for both Zn and O along the c-axis. Under the assumption of an oxygen terminated sapphire substrate the Zn sublattice of the zinc oxide will align itself to the O sublattice of sapphire [42, 111]. This is illustrated in Fig. 2.1 and leads to the following epitaxial relationship between substrate and thin film: $\text{Al}_2\text{O}_3(0001)[11\bar{2}0] \parallel \text{ZnO}(0001)[10\bar{1}0]$. This 30° rotation between the a-axes of sapphire and zinc oxide lead to an effective reduction of the lattice mismatch to 18.4%, which is still an extremely large value. The large misfit and the resulting high dislocation density will dominate the physical properties of the ZnO thin film. One should also note that due to the bulk inversion asymmetry of the wurtzite structure (i.e. the $[0001]$ and $[000\bar{1}]$ direction are not equivalent), the alignment of the Zn sublattice of ZnO to the O-sublattice of Al_2O_3 leads to the orientation of the $[0001]$ -direction pointing towards the substrate, implying that the polarization in ZnO points toward the film surface [49]. One of the major goals during this thesis was to optimize the growth of ZnO on (0001) sapphire, which should in the end lead to a reduction of structural disorder and improvement of electrical and optical properties of the zinc oxide layer.

The improvements of the laser-MBE system (Appendix A) implemented in the course of this thesis, i.e. the installation of a new optical lens system and a new software control, enables us to monitor and control all important growth parameters with high precision and reproducibility during each stage of growth in our deposition chamber. The most important parameters for the pulsed laser deposition (PLD) process are substrate temperature T_{sub} , energy density ϱ_{ED} at the target and repetition rate of the ablating excimer laser, pressure p , type of background gas, and target-to-substrate distance. During the optimization process we kept the target-to-substrate distance at a constant value of 60 mm and varied systematically the other deposition parameters.

The first step towards high quality ZnO thin films on sapphire was the determination of optimal ϱ_{ED} . Therefore we studied the structural properties of ZnO layers grown at $T_{\text{sub}} = 600^\circ\text{C}$, $p_{\text{O}_2} = 1 \mu\text{bar}$, 2 Hz repetition rate, and a constant value of 2000 laser pulses with different ϱ_{ED} ranging from $\varrho_{\text{ED}} = 0.75 \text{ J/cm}^2$ up to $\varrho_{\text{ED}} = 1.5 \text{ J/cm}^2$. The goal of this study was to determine a ϱ_{ED} where we achieve an optimum in all of the following properties: high structural quality, maximum growth rate and low film roughness. The experimental results are summarized in Fig. 2.2(a)-(e). From the $2\theta - \omega$ scans in the vicinity of the ZnO (0002) reflection ("film peak") depicted in Fig. 2.2(a), we find that the film peak has its maximum in intensity and narrowest line width indicating a high growth rate with good structural properties for $\varrho_{\text{ED}} = 1 \text{ J/cm}^2$ and $\varrho_{\text{ED}} = 1.125 \text{ J/cm}^2$. All (0002) film reflections are close to the 2θ bulk value of $\approx 34.44^\circ$ pointing to a relaxed growth of the film on the substrate. This relaxed growth is due to the large lattice mismatch and has been observed for all films grown. Moreover, the optimum ϱ_{ED} lying between 1 J/cm^2 and 1.125 J/cm^2 is also supported by the minimum in the 2θ full-width at half maximum (FWHM) of the ZnO (0002) reflection as shown in Fig. 2.2(c) at exact the same ϱ_{ED} values, indicating a smaller in-plane mosaic spread. An additional indicator for superior structural quality at $\varrho_{\text{ED}} = 1 \text{ J/cm}^2$ and $\varrho_{\text{ED}} = 1.125 \text{ J/cm}^2$ is the minimum in FWHM for the ZnO(0002) rocking curve plotted in Fig. 2.2(d). Regarding the surface roughness and growth rate we investigated the obtained reflectometry data in Fig. 2.2(b) and extracted the corresponding film thicknesses and surfaces roughnesses by fitting the experimental data with a simulation via LEPTOS [112]. The results for t_{ZnO} are shown in Fig. 2.2(e). From the reflectometry data in Fig. 2.2(b) we can clearly see that the

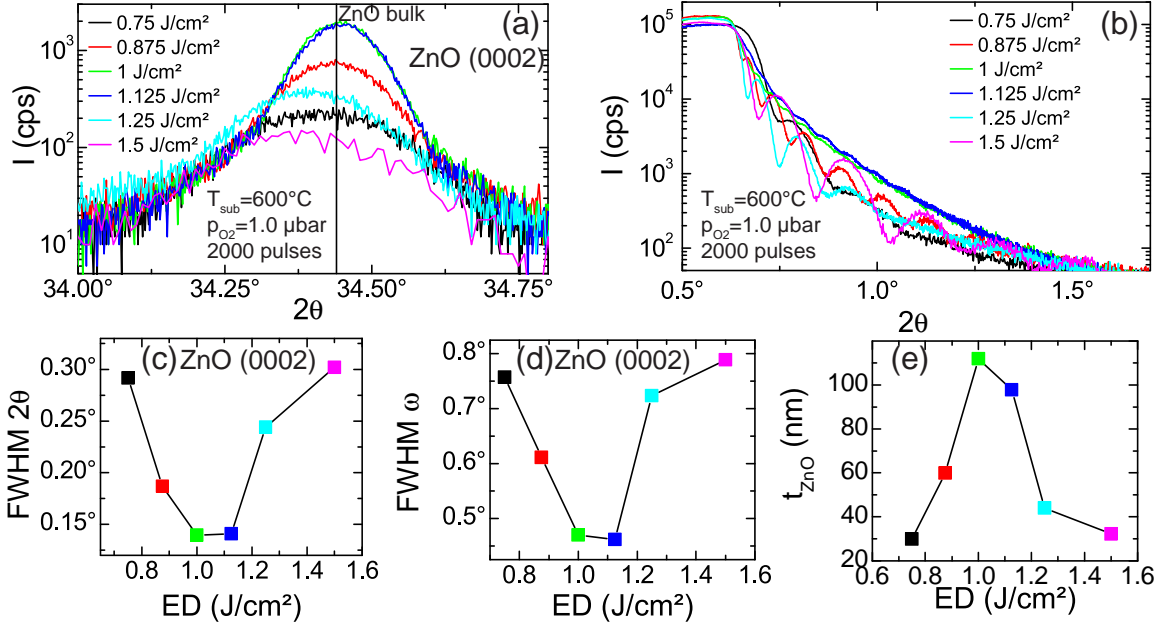


Figure 2.2: XRD results of the laser-MBE energy density optimization: (a) $2\theta - \omega$ scans around the ZnO(0002) reflection for ZnO films deposited on (0001) Al_2O_3 at $T_{\text{sub}} = 600^\circ\text{C}$, $p_{\text{O}_2} = 1 \mu\text{bar}$, $\rho_{\text{ED}} = 0.75 \text{ J/cm}^2$ (black line), $\rho_{\text{ED}} = 0.875 \text{ J/cm}^2$ (red line), $\rho_{\text{ED}} = 1 \text{ J/cm}^2$ (green line), $\rho_{\text{ED}} = 1.125 \text{ J/cm}^2$ (blue line), $\rho_{\text{ED}} = 1.25 \text{ J/cm}^2$ (cyan line), and $\rho_{\text{ED}} = 1.5 \text{ J/cm}^2$ (magenta line). (b) Obtained reflectometry data for the very same films as in (a) (same color code). (c) Extracted 2θ -FWHM of the ZnO (0002) as a function of energy density from (a). (d) Dependency of the FWHM of the ZnO(0002) rocking curve on ρ_{ED} . (e) Calculated t_{ZnO} from the reflectometry measurements for different energy densities. All the results obtained show that the optimum ρ_{ED} lies between 1 J/cm^2 and 1.125 J/cm^2 .

exponential decay, which is an indicator for the film surface roughness, is lowest for $\rho_{\text{ED}} = 1 \text{ J/cm}^2$ and $\rho_{\text{ED}} = 1.125 \text{ J/cm}^2$. In addition, the oscillation period of the beating pattern modulating the exponential drop is highest for these energy densities, indicating a thicker ZnO thin film at these values. This is supported by the film thickness dependence on ρ_{ED} in Fig. 2.2(e), where we find maximum growth rate for $\rho_{\text{ED}} = 1 \text{ J/cm}^2$. For smaller ρ_{ED} the kinetic energy of the plasma plume is lower and less target material arrives at the substrate reducing the growth rate. If $\rho_{\text{ED}} > 1 \text{ J/cm}^2$ the kinetic energy of the target material is further increased, at the substrate the particles may then destroy partly the already deposited film and this leads to a reduction of the growth rate. In summary, this energy density optimization yielded a value of 1 J/cm^2 for the growth of zinc oxide thin films with a high growth rate and good structural properties.

The epitaxial in-plane relationship between sapphire and ZnO depends on the relative alignment of the oxygen sublattice of Al_2O_3 and the zinc sublattice of ZnO. In recent publications it has been proven that an additional substrate annealing step at elevated temperatures $T > 800^\circ\text{C}$ in oxygen atmosphere leads to an improvement of the substrate surface and epitaxial quality of the ZnO thin film [113, 114]. We carried out an experimental study on the effect of substrate annealing on the structural quality and found a large improvement by annealing the substrate at $T_{\text{sub}} = 850^\circ\text{C}$ for 1 hour in an oxygen

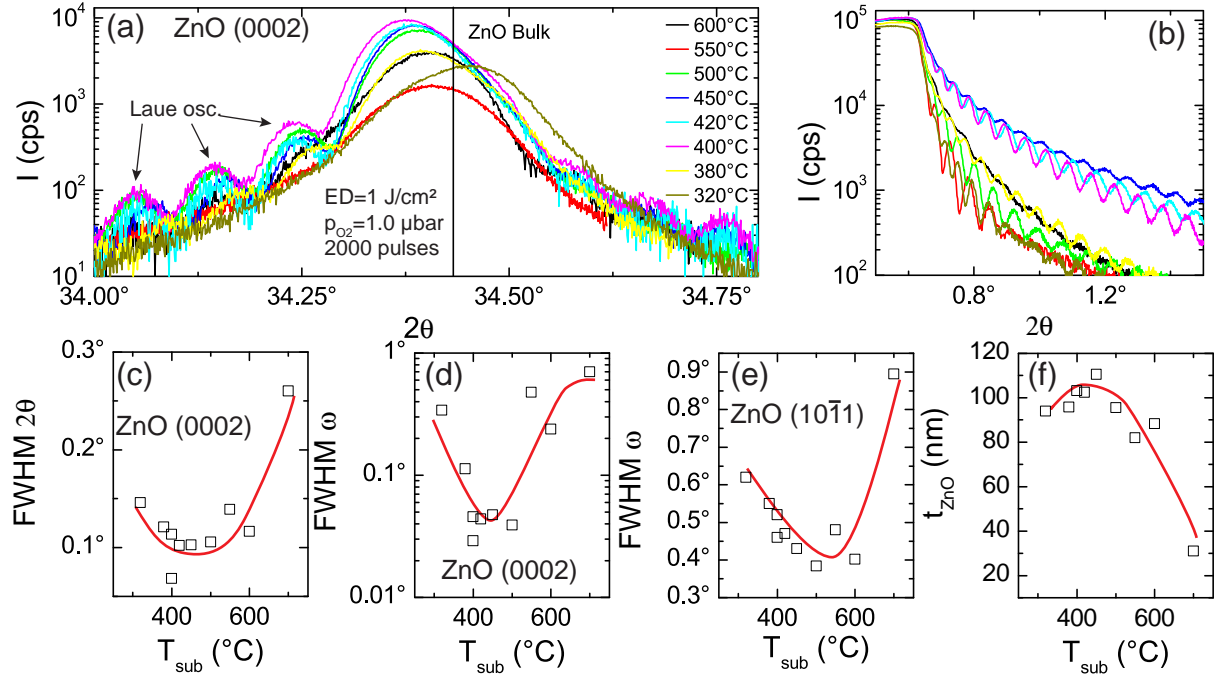


Figure 2.3: Structural characterization of ZnO(0001) thin films on (0001)Al₂O₃ for a systematic variation of substrate temperature, while keeping $\rho_{ED} = 1 \text{ J/cm}^2$ and $p_{O_2} = 1 \mu\text{bar}$ constant. (a) Development of the $2\theta - \omega$ scans around the ZnO(0002) reflection for $T_{\text{sub}} = 600^\circ\text{C}$ (black line), $T_{\text{sub}} = 550^\circ\text{C}$ (red line), $T_{\text{sub}} = 500^\circ\text{C}$ (green line), $T_{\text{sub}} = 450^\circ\text{C}$ (blue line), $T_{\text{sub}} = 420^\circ\text{C}$ (cyan line), $T_{\text{sub}} = 400^\circ\text{C}$ (magenta line), $T_{\text{sub}} = 380^\circ\text{C}$ (yellow line), and $T_{\text{sub}} = 320^\circ\text{C}$ (dark yellow line). (b) Evolution of the reflectometry for different substrate temperatures during growth (same color code as in (a)). (c) FWHM of the 2θ for the ZnO as a function of T_{sub} . T_{sub} dependent trend of the FWHM of the ZnO(0002)(d) and (10 $\bar{1}$ 0)(e) rocking curve. (f) Extracted t_{ZnO} for different T_{sub} from reflectometry measurements. The red lines in (c)-(f) are guides to the eye.

atmosphere of $p_{O_2} = 1 \mu\text{bar}$. In the following, we annealed the substrate in situ prior to deposition in $p_{O_2} = 1 \mu\text{bar}$ at $T_{\text{sub}} = 850^\circ\text{C}$ for one hour to obtain an oxygen terminated sapphire surface improving the quality of the ZnO thin film. To achieve such high substrate temperatures we have deposited a 180 nm thick Pt layer on the back side of the sapphire substrate to increase the absorption of the infrared laser heater (cf. App. A).

Another important parameter that influences the epitaxial quality of the ZnO thin film is the substrate temperature T_{sub} during deposition. To study the influence of T_{sub} we deposited ZnO thin films on in situ annealed Al₂O₃ substrates at various deposition temperatures, while keeping $\rho_{ED} = 1 \text{ J/cm}^2$, $p_{O_2} = 1 \mu\text{bar}$, repetition rate at 2 Hz and the number of laser pulses at 2000. The quality of the ZnO layer was then examined by HRXRD, the results obtained are depicted in Fig. 2.3(a)-(f). If we look at the curves for the $2\theta - \omega$ scans around the ZnO(0002) reflection in Fig. 2.3(a), we can clearly see that for deposition temperatures between 380°C and 500°C satellites due to Laue oscillations are visible, reflecting a coherent growth in the out-of-plane direction. Moreover, when we compare the 2θ FWHM values of the ZnO(0002) reflection in Fig. 2.3(c) for the different deposition temperatures, the values are as low as 0.1° for $400^\circ\text{C} \leq T_{\text{sub}} \leq 500^\circ\text{C}$.

In addition, the FWHM of the x-ray rocking curve (XRC) for the symmetric (0002) diffraction in Fig. 2.3(d), implying the tilt component of the in-plane mosaic misorientation [115], has its lowest value of 0.04° for $400^\circ\text{C} \leq T_{\text{sub}} \leq 500^\circ\text{C}$. The FWHM of XRC of the asymmetric ZnO(10 $\bar{1}$ 0) reflection in Fig. 2.3(e), reflecting both the twist component of the in-plane mosaic misorientation, which strongly influences the mobility of charge carriers [115] in ZnO on sapphire, and tilt component, has the lowest value of 0.4° at $T_{\text{sub}} = 500^\circ\text{C}$. To further narrow down the optimum growth temperature we now look at the XRD reflectometry data for the various films in Fig. 2.3(b), where all curves exhibit oscillations allowing a determination of the film thickness. In addition the reflectometry data show, that the exponential drop is smallest for a deposition temperature between 400°C and 450°C . From the film thickness versus growth temperature it is evident, that the final film thickness nearly stays constant at 100 nm for $T_{\text{sub}} < 500^\circ\text{C}$ and then slowly drops for higher deposition temperatures. This decrease in growth rate also explains the reduction in structural quality at high temperatures ($T_{\text{sub}} > 500^\circ\text{C}$). From these results we conclude that the optimum deposition temperature lies at $T_{\text{sub}} = 400^\circ\text{C}$. For this decision we have also considered, that a lower substrate temperature is desirable because it will allow the growth of sharp interfaces and lowers interdiffusion. The reduction of interdiffusion of Al from the substrate to the ZnO film is important to reduce the residual carrier concentration in ZnO because Al forms a shallow donor in ZnO [69]. The good structural quality verifies that the previous carried out optimization of ϱ_{ED} at $T_{\text{sub}} \leq 600^\circ\text{C}$ remains still valid for the lower substrate temperature. This is also further supported by a rough energy density optimization with two additional samples, not shown here.

A further increase in thin film quality can be achieved by introducing a buffer layer between the substrate and the thin film, which reduces the lattice mismatch. Several groups reported on an improvement of structural and electrical quality by using different complex buffer layer systems including an annealed ZnO buffer layer [105, 110, 116], a (Mg,Zn)O buffer with different Mg content [109, 117], and a double buffer layer of ZnO/MgO [47, 115]. But the introduction of a buffer layer will also complicate the analysis of the measurement of physical properties, because the origin of observed effects can be both, the thin film on top or the buffer layer below. In order to reduce the complexity of the buffer layer system we first investigated the influence of a high temperature annealed ZnO buffer layer onto the structural properties of a ZnO layer grown on top.

In Fig. 2.4(a)-(f) we have collected all information from growth and HRXRD for the optimum deposition conditions of buffer layer and film. The time dependent substrate temperature evolution for the whole growth process in the laser-MBE chamber is summarized in Fig. 2.4(a): First the sapphire substrate is heated up to 850°C and annealed for one hour in $p_{\text{O}_2} = 1 \mu\text{bar}$, the inset in Fig. 2.4(a) shows corresponding in situ reflection high-energy electron diffraction (RHEED) patterns for characteristic stages of growth. During the substrate anneal additional diffraction peaks appear in the RHEED pattern and the sharpness of the pattern increases indicating the surface reconstruction with an oxygen termination. T_{sub} is then lowered to 400°C , where the ZnO buffer layer with a thickness of 15 nm is grown at $\varrho_{\text{ED}} = 1 \text{ J/cm}^2$, $p_{\text{O}_2} = 1 \mu\text{bar}$, and a repetition rate of 2Hz. After the growth of the buffer layer the RHEED pattern has changed to a spotty pattern indicating a rough surface and the spacing between the streaks has increased. The buffer layer is then annealed at $T_{\text{sub}} = 600^\circ\text{C}$ for 30 min and $p_{\text{O}_2} = 1 \mu\text{bar}$. The buffer anneal changes the observed the RHEED pattern into a streaky one arising from the increased

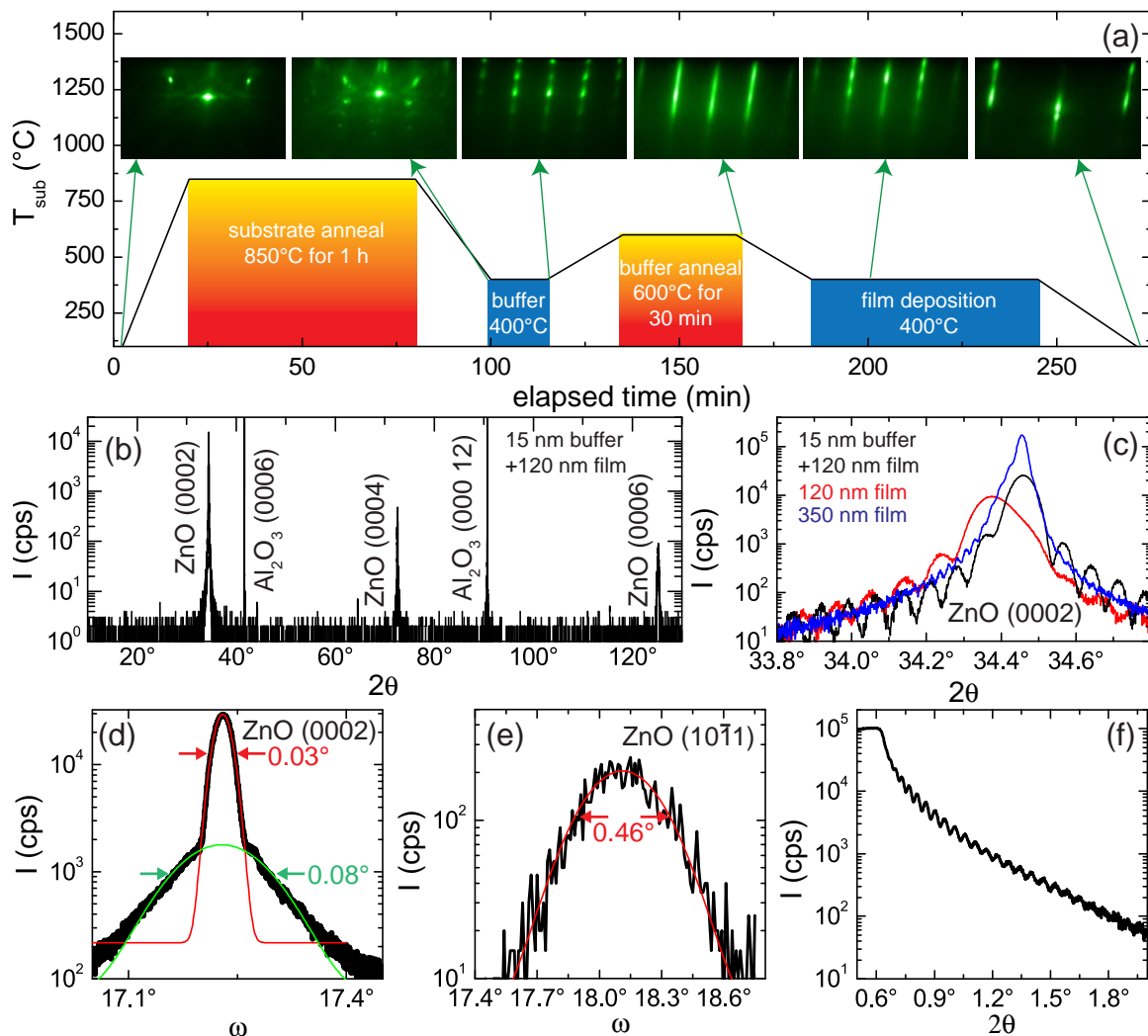


Figure 2.4: Results obtained for buffer layer optimization: (a) Time dependent evolution of the substrate temperature during growth of a ZnO thin film on a ZnO buffer layer. The insets show typical RHEED patterns at different stages during growth, the relation to the corresponding stage of growth is indicated by the green arrows. (b) $2\theta - \omega$ scan for a 120 nm ZnO thin film on a 15 nm ZnO buffer layer. Only reflections of the (0001)-oriented ZnO and the substrate are visible. Comparison of the $2\theta - \omega$ scans around the ZnO(0002) reflection for different ZnO thin films on (0001) sapphire substrates: 120 nm ZnO on 15 nm ZnO buffer (black), 120 nm ZnO thin film (red), and 350 nm ZnO thin film (blue). (d) ω rocking curve of the ZnO(0002) reflection for a 120 nm ZnO film on a 15 nm ZnO buffer layer. The red and green lines represent two Gaussian fits to the data. (e) Corresponding rocking curve of the ZnO(10 $\bar{1}$ 0) reflection with a FWHM of 0.46° obtained from a Gaussian fit (red line). (f) XRD reflectometry data for the very same film as in (d) and (e).

smoothness of the surface. Now the substrate temperature is again lowered at a rate of 10 K/min to 400 °C and the final 120 nm thick ZnO film is deposited at the same conditions as the buffer layer. After a few pulses the streaks in the RHEED pattern are overlaid by spots, representing a 3d growth on the buffer layer. After the deposition the

substrate is cooled down to room temperature at a rate of 10 K/min and $p_{\text{O}_2} = 1 \mu\text{bar}$. At the end of cool down the RHEED pattern remains a streaky one with super imposed spots, showing an increase in surface roughness.

The corresponding $2\theta - \omega$ scan of this buffered ZnO thin film is depicted in Fig. 2.4(b). The occurrence of peaks that can either be attributed to the (0001)-oriented substrate or the (0001)-oriented film evidently negate the existence of any secondary phases present in the sample. A magnification in the vicinity of the ZnO(0002) diffraction can be found in Fig. 2.4(c), where we also compare the buffered film with two ZnO films with different thicknesses and without buffer layer deposited on c-plane sapphire under the same optimum conditions reported above. Laue oscillations are observed in all 3 samples, but for the thinner buffer-less ZnO film the (0002) reflection is slightly asymmetric, which is an indicator for a strain gradient in the sample. In contrast, the 120 nm thick ZnO with buffer shows a symmetric peak comparable to or even better than a 300 nm thick ZnO film without buffer. This result shows that the introduction of an annealed buffer layer significantly reduces the strain in the ZnO layer grown on top of it. The curve in Fig. 2.4(d) represents the XRC of the ZnO(0002) reflection for the buffered ZnO film. On the logarithmic scale it is evident that the peak has two components, a broader peak with a low intensity and a narrow one with high intensity. We used a Gaussian fit to the data to extract the FWHM for both peaks and obtained 0.08° for the broad and 0.04° for the narrow one. We attribute the broad peak to the ZnO buffer, which has a slightly higher mosaic spread than the narrow ZnO top layer. Both values are excellent and indicate only a small tilt component of the buffer and the top ZnO film. This result also suggests that the mosaic spread of the ZnO layer is reduced with increasing film thickness. In contrast, the XRC of the asymmetric $(10\bar{1}1)$ reflection indicates a large twist component as the data in Fig. 2.4(e) suggests. Again from a Gaussian fit to the data we extracted the value of the FWHM of 0.46° . Compared with results from other groups both FWHM values of the XRC for the symmetric and asymmetric reflection are on par or exceed already published data [105, 109, 115, 116] for the growth of ZnO on c-plane sapphire. Last but not least we extracted from the XRD reflectometry measurement shown in Fig. 2.4(f) the total film thickness of 135 nm and a surface roughness < 0.5 nm for the ZnO layer. These results are clear evidence, that the introduction of a buffer layer in our samples lead to an improvement in structural quality of our samples with a low interface and surface roughness.

Triggered by recent reports on the influence of oxygen pressure on the growth mode and electrical and optical properties of ZnO thin films [118, 119] we also investigated the influence of different p_{O_2} on our buffered ZnO thin films. For a first analysis we have grown three different samples: One grown under the very same conditions as described in the last paragraph, one sample grown at $p_{\text{O}_2} = 0.4 \mu\text{bar}$ during deposition of buffer and ZnO layer and another one grown at $p_{\text{O}_2} = 5 \mu\text{bar}$. For each sample the number of pulses for the buffer and the film were identical (300 and 2000 respectively) and the other deposition parameters remained unchanged ($T_{\text{sub}} = 400^\circ\text{C}$, $q_{\text{ED}} = 1 \text{ J/cm}^2$, 2 Hz repetition rate). The annealing of the sapphire substrate was always carried out at $p_{\text{O}_2} = 1 \mu\text{bar}$ for all three samples. The data obtained from HRXRD are summarized in Fig. 2.5(a)-(c). From the peak position for the three samples in the $2\theta - \omega$ scan in Fig. 2.5(a), a systematical shift to higher 2θ values is observed for increasing p_{O_2} . Moreover, a higher asymmetry and less pronounced Laue oscillations are visible for the sample grown at $p_{\text{O}_2} = 5 \mu\text{bar}$. From the HRXRD reflectometry measurements in Fig. 2.5(b), an increase

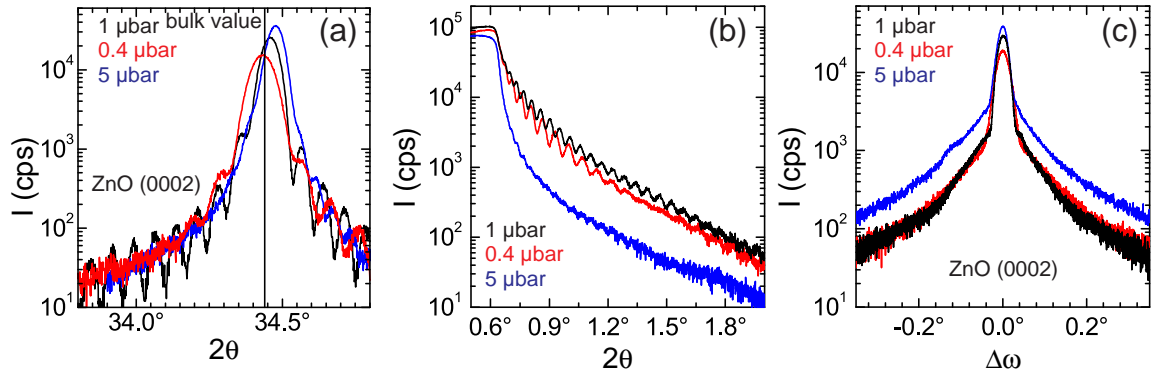


Figure 2.5: Structural evolution of the ZnO buffer layer system for different oxygen pressures during growth: (a) $2\theta - \omega$ scan around the ZnO(0002) reflection for $p_{\text{O}_2} = 1 \mu\text{bar}$ (black), $p_{\text{O}_2} = 0.4 \mu\text{bar}$ (red), and $p_{\text{O}_2} = 5 \mu\text{bar}$ (blue). (b) HRXRD reflectometry measurements for the three very same films as in (a) (identical color code). (c) XRC of the ZnO (0002) diffraction for all 3 films.

in surface roughness for $p_{\text{O}_2} = 5 \mu\text{bar}$ is indicated by the much steeper drop in intensity. In addition, the oscillation frequency has its highest value for $p_{\text{O}_2} = 1 \mu\text{bar}$. The XRC for the ZnO(0002) reflection for each sample are shown in Fig. 2.5(c). Each sample exhibits the already described double peak structure with a broad low intensity and a narrow high intensity peak. The width of the narrow peak does not depend on p_{O_2} , but the broader peak increases in width with increasing pressure. Combining all these results, the used p_{O_2} of $1 \mu\text{bar}$ seems to give the samples the highest structural quality, but it might be possible that a further reduction of p_{O_2} below $0.4 \mu\text{bar}$ leads to a further increase in sample quality. Unfortunately, due to technical limitations it is currently not possible to stabilize pressures below $0.4 \mu\text{bar}$ in a highly reproducible way. This makes a reliable further pressure related study impossible.

Summing up the results, the growth optimization yields high quality samples for the following deposition parameters: $p_{\text{O}_2} = 1 \mu\text{bar}$, $\rho_{\text{ED}} = 1 \text{ J/cm}^2$, $T_{\text{sub}} = 400^\circ\text{C}$. Prior to thin film deposition it is crucial to first anneal the sapphire substrate at $T_{\text{sub}} = 850^\circ\text{C}$ for 1 h in an oxygen atmosphere of $p_{\text{O}_2} = 1 \mu\text{bar}$. To further increase the quality of ZnO films with thicknesses below 300 nm the introduction of a ZnO buffer layer leads to a significant increase in structural quality.

2.2.2 Characteristics of optimized ZnO thin films

After the successful growth optimization we present below the typical physical properties obtained for our samples grown under the optimized conditions from HRXRD, TDH, TEM and PL experiments.

2.2.2.1 HRXRD results

In many ZnO films grown on *c*-plane Al_2O_3 via various deposition techniques the existence of rotational domains has been reported [42, 111]. These rotational domains have a negative influence on structural, electrical and optical properties [42]. In order to study the presence of rotational domains in our samples and the in-plane epitaxial relationship

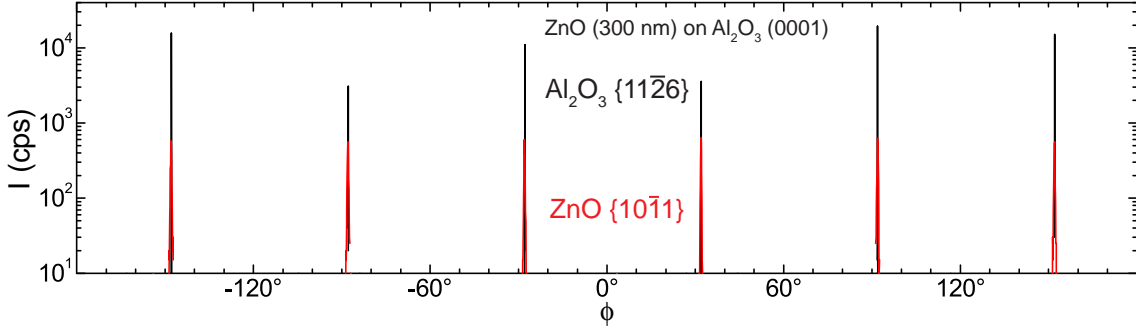


Figure 2.6: ϕ -scans for the Al_2O_3 $\{11\bar{2}6\}$ and $\text{ZnO}\{10\bar{1}1\}$ reflections for a 300 nm thick ZnO layer without buffer. The reflections from the substrate and the thin film coincide perfectly, exhibiting a sixfold symmetry and indicating a successful realization of the following epitaxial relationship: $\text{Al}_2\text{O}_3(0001)[11\bar{2}0] \parallel \text{ZnO}(0001)[10\bar{1}0]$. The absence of any additional reflections in the ϕ -scan of the ZnO provide clear evidence for the existence of only one rotational domain.

between substrate and film, we conducted ϕ -scans for the Al_2O_3 $\{11\bar{2}6\}$ and $\text{ZnO}\{10\bar{1}1\}$ diffraction peaks for all samples grown under the optimized deposition conditions with and without buffer layer. The data from a sample grown at $p_{\text{O}_2} = 1 \mu\text{bar}$, $\rho_{\text{ED}} = 1 \text{ J/cm}^2$, $T_{\text{sub}} = 400^\circ\text{C}$ and a thickness of 300 nm are shown in Fig. 2.6 and reflect the typical results obtained for all of our samples. Both ϕ -scans exhibit a sixfold symmetry and no additional reflexes in the ZnO $\{10\bar{1}1\}$ scan can be found. From this we conclude that no additional rotational domains in our ZnO thin films are present. The reflections from the substrate and film coincide at the same ϕ values, which is due to the parallel alignment of the oxygen sublattice of sapphire and the zinc sublattice of zinc oxide. This finally leads to the already expected in-plane epitaxial relationship of $\text{Al}_2\text{O}_3(0001)[11\bar{2}0] \parallel \text{ZnO}(0001)[10\bar{1}0]$. One should remember that this epitaxial relationship also implies that the $[0001]$ direction in ZnO points to the substrate. These results are also obtained for ZnO films grown on either ZnO or (Mg,Zn)O (maximum Mg content 10%) buffer layers, if the optimized deposition parameters are used. The HRTEM images presented in Sect. 2.2.2.3 support this finding (Fig. 2.14).

For a deeper insight into the epitaxial quality and an extraction of in-plane and out-of-plane lattice constants we have carried out reciprocal space mappings (RSM) for various ZnO thin films grown on (0001) oriented sapphire. The results are outlined in Fig. 2.7(a)-(f), while the relevant structural quality and lattice parameters for each film presented in Fig. 2.7(a)-(f) are summarized in Table 2.1. We first focus on the results obtained for ZnO layers of different thickness as grown on an oxygen annealed substrate. From the position of the $(\bar{1}014)$ reflection in Fig. 2.7(a) we extracted the lattice parameters for a 300 nm thick ZnO film $a_{\text{ZnO}} = 0.3250 \text{ nm}$ and $c_{\text{ZnO}} = 0.5205 \text{ nm}$. For the 1000 nm thick ZnO layer in Fig. 2.7(b) we obtained $a_{\text{ZnO}} = 0.3248 \text{ nm}$ and $c_{\text{ZnO}} = 0.5205 \text{ nm}$. Both sets of lattice parameters are very close to the bulk values of ZnO ($a_{\text{ZnO}} = 0.32496 \text{ nm}$, $c_{\text{ZnO}} = 0.52042 \text{ nm}$ [45]) attesting a relaxed growth of ZnO on the c-plane sapphire. In addition, both diffraction peaks exhibit an elliptical shape stemming from the difference in the FWHM of the tilt and twist components of the peak. With increasing film thickness the $(\bar{1}014)$ ZnO diffraction peak increases in sharpness. To further quantify this, we

also conducted ω -XRC around the (0002) and (10 $\bar{1}$ 1) reflection of ZnO and extracted the FWHM. For the 300 nm film we obtained $\text{FWHM}_{(0002)} = 0.02^\circ$ and $\text{FWHM}_{(10\bar{1}1)} = 0.4^\circ$, whereas in the case of a 1000 nm thick film we extracted $\text{FWHM}_{(0002)} = 0.02^\circ$ and $\text{FWHM}_{(10\bar{1}1)} = 0.27^\circ$. This shows that the width of the symmetric reflection stays constant, which means that the tilt component of the in-plane mosaic misorientation does not decrease. But the width of the asymmetric peak, which is dominated by the twist component, decreases with increasing thickness, indicating a reduction of the twist component for the in-plane mosaic misorientation.

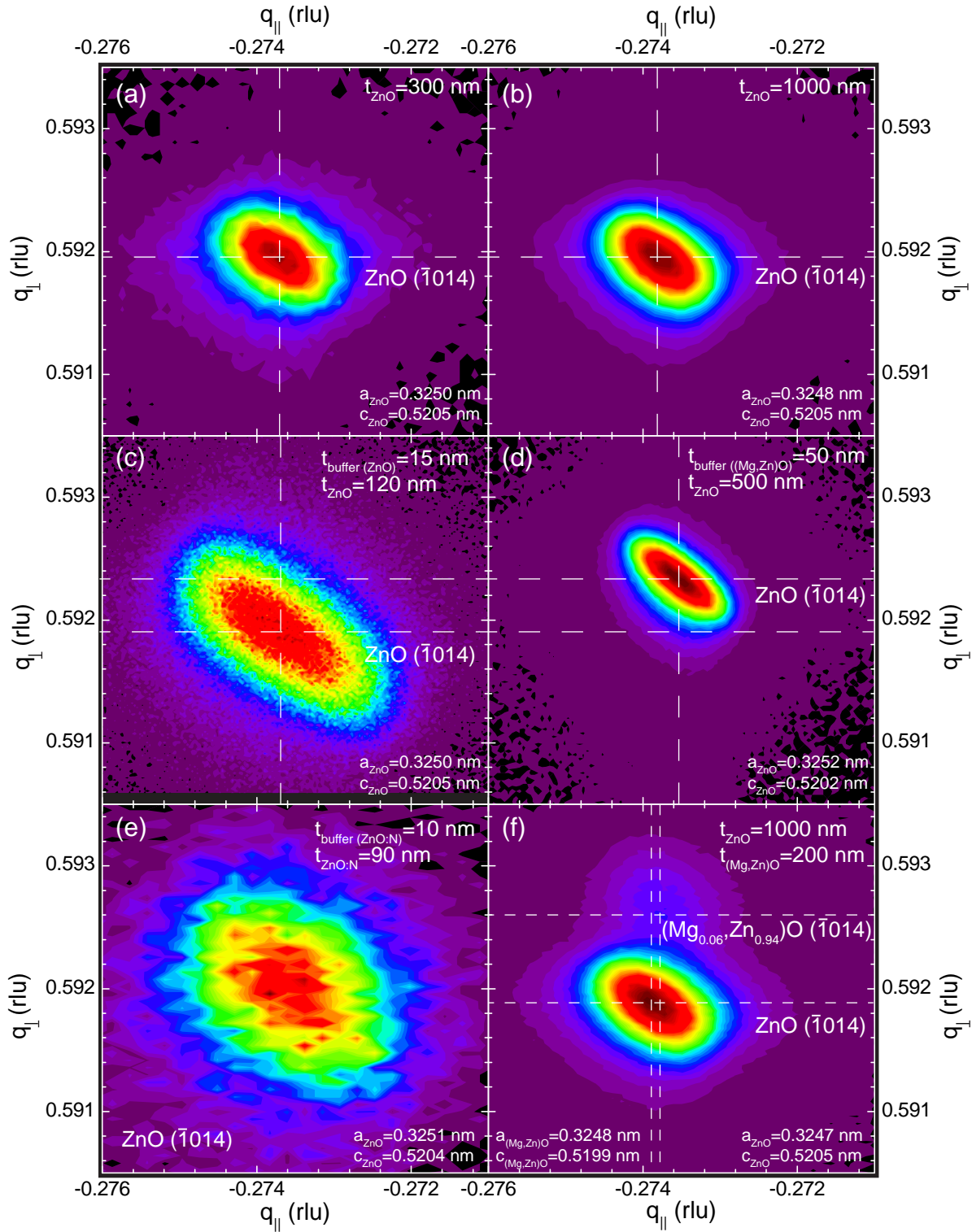


Figure 2.7: RSM of the ZnO ($\bar{1}014$) diffraction for different ZnO thin films grown using the optimized deposition parameters for our laser-MBE setup: (a) ($\bar{1}014$) RSM for a buffer-free 300 nm thick ZnO thin film. (b) ($\bar{1}014$) RSM for a 1000 nm thick film without buffer layer. (c) ($\bar{1}014$) RSM for a 120 nm thick ZnO film on a 15 nm ZnO buffer layer. (d) ($\bar{1}014$) RSM for a 500 nm thick ZnO film on a 50 nm $(\text{Mg}_{0.06}, \text{Zn}_{0.94})\text{O}$ buffer layer. (e) ($\bar{1}014$) RSM for a 80 nm thick ZnO film on a 10 nm ZnO buffer layer grown in nitrogen atmosphere $p_{\text{N}_2} = 0.8 \mu\text{bar}$ under irradiation by the nitrogen atom source ($P_{\text{rf}} = 400 \text{ W}$). (f) ($\bar{1}014$) RSM for a 200 nm thick $(\text{Mg}_{0.06}, \text{Zn}_{0.94})\text{O}$ film on a 1000 nm ZnO layer. In each panel, the dashed lines indicate the position of maximum intensity.

This reduction in the twist component might originate from the mutual annihilation of dislocations with increasing film thickness [120].

When we compare the results obtained for ZnO films grown on different buffer systems in Fig. 2.7(c)-(e), we first see a shift in the position of the ZnO diffraction peak depending on the used buffer layer. For a standard 15 nm ZnO buffer the position remains unchanged compared to the films without buffer layer, indicating no change in lattice parameters. For the thicker 50 nm ($\text{Mg}_{0.06}, \text{Zn}_{0.94}$)O buffer layer the lattice parameter changes to an increased a-lattice and a slightly decreased c-lattice constant. For the 10 nm ZnO:N buffer small deviations from the standard values are visible. When comparing the structural quality of the ZnO films on a buffer with those without a buffer (cf. Table 2.1), it is evident that comparable FWHM in the XRC are obtained for thinner ZnO samples if a buffer layer is used. We note that the use of a 50 nm ($\text{Mg}_{0.06}, \text{Zn}_{0.94}$)O buffer results in an improvement of crystalline quality of the samples. This is also supported by the results of the TDH measurements, presented below (cf. Sect.2.2.2.2). We also investigated the influence of nitrogen incorporation on the structural properties of buffered ZnO thin films. The buffered sample has been grown on an annealed sapphire substrate, using the optimized deposition parameters ($\varrho_{\text{ED}} = 1 \text{ J/cm}^2$, $T_{\text{sub}} = 400^\circ\text{C}$), in a nitrogen growth atmosphere of $p_{\text{N}_2} = 1 \mu\text{bar}$. To increase the efficiency of N incorporation into ZnO we used the installed radio frequency (RF-) atom source, which was running at a RF-power of 400 W during deposition of buffer and film, and a buffer anneal at $T_{\text{sub}} = 600^\circ\text{C}$ for 30 min. The RSM of this sample is shown in Fig. 2.7(e). The reduced sample quality for a nitrogen doped ZnO buffer might originate from the difficulty of stabilizing the deposition conditions, while the RF-atom source is running (cf. Appendix A).

The structural analysis attests an improvement in ZnO film quality if a buffer layer is used. This is due to the reduction of lattice mismatch by the buffer layer, but we expect a buffer layer with a high density of dislocations as the lattice mismatch is accommodated in the buffer itself. This will become important for the measurement of integral properties, where a separation of contributions from buffer layer and the film on top might be difficult to achieve. A viable way of reducing the lattice mismatch in the buffer layer is the use of a more advanced buffer system consisting of a (Zn,Mg)O buffer grown on a MgO buffer [115]. The lattice parameters of MgO range in between the ones of sapphire and zinc oxide, thus effectively reducing the lattice mismatch.

In proof-of-principle experiments, we looked also into the growth of heterostructures of ZnO and (Mg, Zn)O. In Fig. 2.7(f) we show the RSM of a sample with a 200 nm ($\text{Mg}_{0.06}, \text{Zn}_{0.94}$)O film grown on a 1000 nm thick ZnO layer, deposited on c-plane sapphire under the optimized deposition conditions. In the RSM a weak intensity peak of the ($\text{Mg}_{0.06}, \text{Zn}_{0.94}$)O layer and a strong ZnO diffraction are visible. This is a first evidence, that our optimized growth parameters allow the growth of more complicated heterostructures such as single quantum wells or multiple quantum wells [47, 52]. These quantum well structures might allow the investigation of 2DEGs and the quantum Hall effect in ZnO in our laser-MBE grown samples [54, 56]. Nevertheless, prior to such experiments a further improvement in sample quality needs to be achieved.

In another set of test experiments, we fabricated three different samples grown on differently oriented sapphire substrates and analyzed the structural quality via HRXRD measurements to demonstrate the versatility of the optimized growth parameters. All the samples were grown without a buffer layer but with a preceding substrate annealing step in O_2 at 850°C . The first sample investigated is a 300 nm thick (0001)-oriented

RSM in	FWHM $_{2\theta_{(0002)}}$	FWHM $_{\omega_{(0002)}}$	FWHM $_{\omega_{(10\bar{1}1)}}$	a_{ZnO} [nm]	c_{ZnO} [nm]
Fig. 2.7(a)	0.04°	0.02°	0.4°	0.3250	0.5205
Fig. 2.7(b)	0.06°	0.02°	0.27°	0.3248	0.5205
Fig. 2.7(c)	0.07°	0.03°	0.46°	0.3250	0.5205
Fig. 2.7(d)	0.03°	0.01°	0.28°	0.3252	0.5202
Fig. 2.7(e)	0.08°	0.03°	0.48°	0.3251	0.5204
Fig. 2.7(f)	0.07°	0.06°	0.27°	0.3247	0.5205

Table 2.1: Collection of all relevant properties of differently grown ZnO films with and without buffer layer on c-plane sapphire.

ZnO layer grown on c-plane sapphire ((0001)-orientation of the substrate) as a reference sample. The x-ray diffraction results for this sample are summarized in Fig. 2.8(a)-(c). As a second sample we have chosen a 300 nm thick (0001)-oriented ZnO layer on a-plane sapphire ((11 $\bar{2}$ 0)-orientation of the substrate), where recent reports indicated a uniaxially locked epitaxy due to the nearly multiple integer match of the ZnO a-lattice and the c-lattice parameter of Al₂O₃ [121, 122]. This uniaxial locked epitaxy should lead to a reduction of rotational domains and thus increase the quality of the ZnO thin film. The HRXRD results for this sample are shown in Fig. 2.8(d)-(f). To achieve an in-plane orientated c-axis of ZnO we have also grown a 750 nm (11 $\bar{2}$ 0)-oriented ZnO layer on r-plane sapphire ((1 $\bar{1}$ 02)-orientation of the substrate).

For the ZnO grown on (0001)-oriented sapphire, the Laue oscillations visible in the $2\theta - \omega$ scan (Fig. 2.8(a)) indicate a nice coherent growth of ZnO parallel to the out-of-plane direction. We further find again the double peak type XRC for the (0002) reflection in Fig. 2.8(b), which might be attributed to a splitting of the ZnO layers into two phases with different in-plane mosaic spread. The FWHM of 0.02° for the narrow peak attest a high structural quality. The twist component of the in-plane mosaic misorientation can be evaluated by the XRC of the (10 $\bar{1}$ 1) displayed in Fig. 2.8(c). The FWHM of 0.40° is an excellent value for a buffer-free ZnO layer on c-plane sapphire. The obtained results clearly show how our very well tuned deposition parameters lead to a formation of excellent quality ZnO thin films on c-plane sapphire.

We turn now to the sample grown on (11 $\bar{2}$ 0) sapphire (a-plane). First, the absence of Laue oscillations in the $2\theta - \omega$ scan in Fig. 2.8(d) is an indicator for a ZnO film with reduced structural quality as the one on c-plane sapphire grown under identical conditions. Moreover, we only observe a single peak in the ZnO(0002) XRC, with a broad FWHM of 0.28°, which is one order of magnitude larger than for the sample on c-plane sapphire. Interestingly, the FWHM of the (10 $\bar{1}$ 1) XRC remains unchanged at 0.4°. This implies that the twist component of the in-plane misorientation remains unchanged by going from c-plane to a-plane sapphire, but the tilt component is increased. The origin might be related to the fact, that the growth has not been optimized for a-plane sapphire. Nevertheless, the deposition parameters allow the growth of (0001) oriented ZnO on a-plane Al₂O₃.

We also investigated the growth of (11 $\bar{2}$ 0)-oriented ZnO on (1 $\bar{1}$ 02)-oriented Al₂O₃ (r-plane). The thin film obtained is highly (11 $\bar{2}$ 0) oriented, only a low intensity ZnO(0002) diffraction peak (intensity below 10 cps) has been found. Fig. 2.8(g) displays a $2\theta - \omega$ scan for the (11 $\bar{2}$ 0) diffraction of ZnO. The peak is broader than the ones for a-plane and c-plane sapphire and no Laue oscillations are visible, indicating a low coherence in

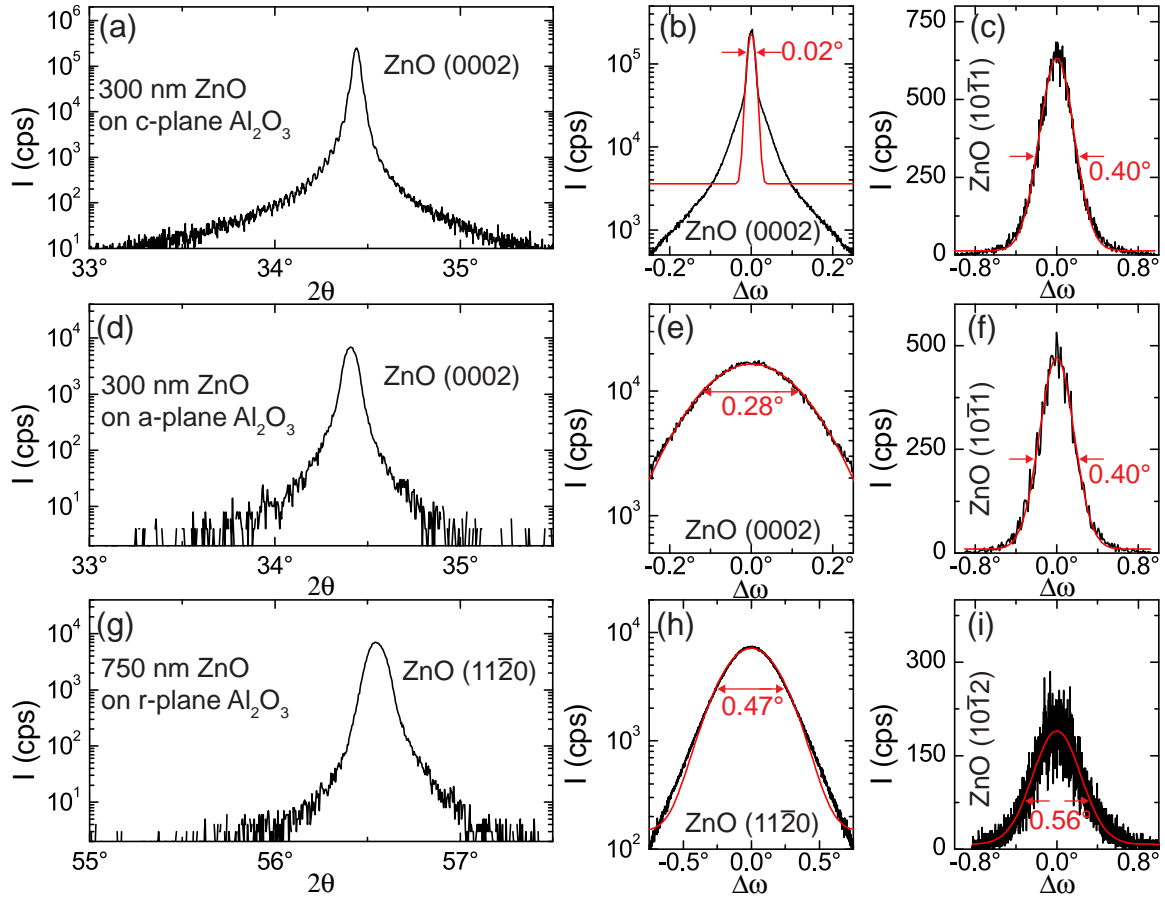


Figure 2.8: XRD data obtained for ZnO thin films grown under the optimized laser-MBE deposition conditions on differently oriented sapphire substrates: (a) $2\theta - \omega$ scan around the ZnO(0002) diffraction for a 300 nm thin ZnO layer on c-plane sapphire (0001), Laue oscillations are clearly visible. (b) Corresponding ω -XRC for the ZnO film in (a) of the (0002) reflection. The form of the peak indicates the existence of two layers with different mosaic tilt spread. (c) ω -XRC of the zinc oxide (10 $\bar{1}$ 1) reflection, with a FWHM of 0.4°. (d) $2\theta - \omega$ scan recorded in the vicinity of the ZnO(0002) diffraction for a 300 nm thin film on a-plane Al₂O₃ (11 $\bar{2}$ 0). Corresponding (0002) (e) and (10 $\bar{1}$ 1) (f) XRC of the very same sample as in (d). (g) $2\theta - \omega$ scan of the ZnO(11 $\bar{2}$ 0) reflection for a 750 nm thick ZnO layer grown on r-plane sapphire(1 $\bar{1}$ 02). In (h) and (i) the corresponding (11 $\bar{2}$ 0) and (10 $\bar{1}$ 2) ω -XRC are shown, respectively. Red lines in the XRC curves represent a Gaussian fit to the data.

the out-of-plane direction. Furthermore, the XRC of the (11 $\bar{2}$ 0) in Fig. 2.8(h) has a FWHM of 0.47°, which is a relatively large value but comparable to already reported values [123, 124]. For the asymmetric (10 $\bar{1}$ 2) XRC (Fig. 2.8(i)) we extracted a FWHM of 0.56°. These numbers prove that there is still room for further optimization of the growth of ZnO on (1 $\bar{1}$ 02)-oriented Al₂O₃ and that a high (11 $\bar{2}$ 0) orientation of the thin film can be achieved using c-plane optimized deposition parameters.

From the results obtained from the HRXRD measurements on samples grown with the optimized laser-MBE parameters, it is safe to say that the achieved structural quality is on par to results that other groups have obtained [105, 109, 115, 116].

We expect a further increase in structural quality by employing a double buffer layer of MgO and (Mg,Zn)O on sapphire, which should primarily reduce the still large FWHM of the XRC for the ZnO(10 $\bar{1}$ 1) reflection. By overcoming this obstacle the electrical and optical properties of ZnO thin films on sapphire will be further improved. The other route to increase the epitaxial quality of ZnO thin films, would be the use of lattice matched substrates, such as homoepitaxy on ZnO and growth on ScAlMgO₄.

2.2.2.2 Electronic transport measurements

A high structural quality verified by HRXRD is only the first step towards ZnO thin films with excellent physical properties. A tunability of carrier concentration and mobility is a desirable goal for the development of more complicated structures and for applications involving ZnO. In order to extract quantitative values we have conducted temperature dependent Hall effect measurements in Van-der-Pauw geometry with the external magnetic field perpendicular to and the electrical current in the film plane. The samples have been placed in an Oxford Spectromag 4000 magnet cryostat system ($\mu_0 H \leq 7$ T, 1.8 K $\leq T \leq 350$ K) after contacting them with aluminium wires via wedge bonding. Lab-view programs were used to record the magnetic field dependent resistance at different, stabilized sample temperatures. From the resistance values we calculated the longitudinal and transverse resistivity using the Van-der-Pauw formula [125]. We further increased the accuracy of our measurement by taking advantage of the symmetry or respectively antisymmetry of the longitudinal and transverse signal by only further evaluating the symmetric or antisymmetric part of the signal (for more details see Appendix B). From these measurements we extracted the Hall resistance R_H and the longitudinal resistivity ρ_{long} at $\mu_0 H = 0$. Using these two values and the film thickness t_{film} one can calculate the carrier concentration n_{Hall} and mobility μ_{Hall} of the thin film (assuming single band transport [126])

$$n_{\text{Hall}} = \frac{1}{R_H t_{\text{film}} e}$$

$$\mu_{\text{Hall}} = \frac{1}{\rho_{\text{long}} n_{\text{Hall}} e},$$

with e representing the elementary electron charge. Various deposition parameters will influence n_{Hall} and μ_{Hall} . In the following, we present some selected dependencies found for our optimized laser-MBE grown ZnO thin films. The results presented here have all been obtained for ZnO on c-plane sapphire. The use of a buffer layer will be explicitly mentioned in the text; if a buffer is not mentioned no buffer layer has been used for the growth of the samples.

One might expect that the purity of the target material plays an important role for the values of carrier concentration and mobility of the thin film. For a quantitative investigation, we have grown two samples from ZnO target material with 99.99%(4N) and 99.9995%(5N5) purity. Both ZnO films had a total thickness of 300 nm grown under the same, optimized deposition conditions. The comparison of the temperature dependence of n_{Hall} and μ_{Hall} are depicted in Fig. 2.9(a) and (b) respectively. For the 4N thin film, we obtain $\mu_{\text{Hall}} = 3.8$ cm²V⁻¹s⁻¹ and $n_{\text{Hall}} = 1.8 \times 10^{17}$ cm⁻³ at room temperature, in contrast for the 5N5 ZnO film we extracted $\mu_{\text{Hall}} = 11.3$ cm²V⁻¹s⁻¹ and $n_{\text{Hall}} = 1.3 \times 10^{17}$ cm⁻³. The use of 5N5 target material leads to an increase in Hall mobility by a factor of 3 and a

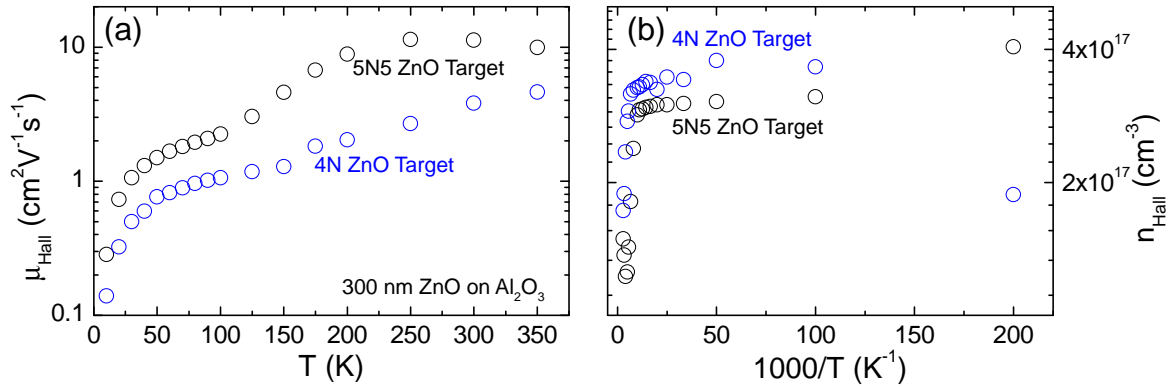


Figure 2.9: TDH measurement results for two 300 nm thick ZnO films on c-plane Al_2O_3 grown from target material with 4N and 5N5 purity. In (a) the extracted temperature dependence of μ_{Hall} is shown. For the sample with higher purity material the mobility is increased by at least a factor of 2 over the whole temperature range. The temperature dependent carrier concentration n_{Hall} is depicted in (b).

decrease in measured carrier concentration by 28%. This illustrates that it is beneficial to use high purity materials. But the increase in mobility and decrease in carrier concentration by less than one order of magnitude is a strong indicator that we are not limited by the purity of the target material to obtain ZnO films with low carrier concentration and high mobility. Other factors must dominate the observed mobility and carrier concentration. During growth it is possible that an interdiffusion of aluminum from the Al_2O_3 substrate into the zinc oxide thin film occurs. Al forms a shallow donor when substituted on a Zn site, effectively influencing the residual carrier concentration and the mobility due to scattering on ionized and neutral impurities. Still the contribution from ionized and neutral impurity scattering can not explain the low mobility values obtained [115]. Another major factor limiting the mobility is the existence of edge type dislocations due to the large lattice mismatch between substrate and film. These dislocations allow the thin film to relax the misfit strain from the substrate. An indicator for the density of dislocation sites is the FWHM of the $\text{ZnO}(10\bar{1}1)$ XRC [115]. For our two films we extracted a FWHM of 0.40° for the 4N and 0.43° for the 5N5 film. These values should be compared to the FWHM of 0.01° for a single crystalline ZnO substrate measured in the very same diffractometer¹. The thin film values exceed the bulk ones by a factor of 40, which explains the low mobility values and enables us to use structural data for a first qualitative estimation of electrical properties. Moreover, the target material is not influencing the number of dislocation sites, other parameters during growth limit the reduction of dislocations. By means of a buffer layer the strain transferred into the thin ZnO film can be significantly reduced lowering the density of dislocations in the ZnO thin film.

An interesting point is also the non-intuitive temperature dependence of Hall mobility and carrier concentration observed. The mobility for both films in Fig. 2.9(a) first increases with increasing temperature, as it is expected for a mobility limited by impurities and defects in the material, and then seems first to saturate at $T = 100$ K but

¹Typical values for a bulk hydrothermal grown ZnO crystal are $n_{\text{Hall}} = 7 \times 10^{13} \text{ cm}^{-3}$, $\mu_{\text{Hall}} = 200 \text{ cm}^2\text{V}^{-1}\text{s}^{-1}$ [127]

by further increasing the temperature the mobility again increases reaching a maximum of $11.4 \text{ cm}^2 \text{ V}^{-1} \text{ s}^{-1}$ at 250 K for the 5N5 film, whereas the 4N film increases its mobility value up to the maximum temperature measured. In contrast, the carrier concentration in Fig. 2.9(b) is nearly constant at low temperatures for both type of films, and starts to decrease for $T > 100 \text{ K}$, this occurs at the same temperature where we saw the surprisingly mobility increase with temperature. This drop in carrier concentration continues for the 4N sample up to the highest temperature measured, for the 5N5 sample the concentration reaches its minimum value of $1.2 \times 10^{17} \text{ cm}^{-3}$ at $T = 250 \text{ K}$, the temperature where the mobility reaches its maximum. All these findings are a strong indicator that the (at first sight) single ZnO layer consists of two parallel conducting channels with different mobilities and carrier concentrations. In the Hall measurements we extract values which are a combination of both conducting channels. This will be investigated in more detail in the following.

It has been already reported [120, 128] that the observed temperature dependence of mobility and carrier concentration in the ZnO thin films on Al_2O_3 can be understood in the picture of a two layer model, where a highly degenerate layer at the interface between substrate and film with a high dislocation density is formed due to the relaxation of misfit strain and a relaxed semiconducting film with lesser defects on top. We have grown two ZnO thin films on c-plane sapphire with different thicknesses of 300 nm and 1000 nm to verify, that this is also the case for our laser-MBE grown thin films. For the thicker sample the influence of the semiconducting layer on the Hall properties should be stronger than for the thinner one. The extracted temperature dependent Hall mobility and carrier concentration can be found in Fig. 2.10(a) and (b), respectively.

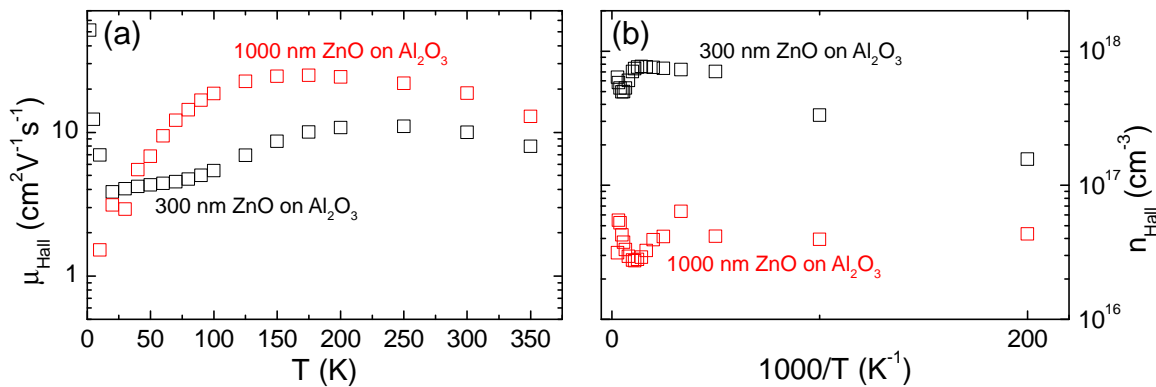


Figure 2.10: TDH measurement results for two ZnO films on c-plane Al_2O_3 grown from 5N5 target material with a thickness of 300 nm and 1000 nm. In (a) the extracted temperature dependence of μ_{Hall} is shown. For the sample with larger thickness the mobility is increased by at least a factor of 2 over the whole temperature range. The temperature dependent carrier concentration n_{Hall} is depicted in (b).

We first focus on the temperature dependence of the carrier mobility in Fig. 2.10(a). The increase in thickness also increases the measured mobility over the whole temperature range. Moreover, when looking at the position of maximum mobility for both films we clearly see that it is shifted from $T = 250 \text{ K}$ for the thinner to $T = 175 \text{ K}$ for the thicker sample. Looking now at the temperature dependence of n_{Hall} in Fig. 2.10(b), a reduction in carrier concentration by about one order of magnitude for the thicker sample is clearly

visible. Moreover, the minimum in carrier concentration at elevated temperatures shifts from $T = 250$ K for the thinner to $T = 175$ K for the thicker sample. In addition, we see that at low temperatures the carrier concentration for the thick sample is temperature independent, which is typical for a degenerate system. Therefore, we conclude that at low temperatures the Hall characteristics are dominated by the degenerate layer, and with increasing temperature the contribution from the semiconducting layer becomes more important.

The thickness related change in temperature dependence and absolute values for Hall mobility and carrier concentration irrefutably confirms, that our laser-MBE grown ZnO films on Al_2O_3 also suffer from the contribution of a low mobility degenerate layer formed at the interface of substrate and thin film. A more quantitative evaluation by fitting the Hall data with a theoretical model will be conducted at the end of this section.

Up to now, we have only investigated ZnO films without a buffer layer, which show a temperature dependency, that is reminiscent of a two layer system. For the buffered ZnO thin films, we already expect a two layer character in TDH measurements, since both the buffer and the film on top are electrically conducting and will both contribute to the integral measured Hall mobility and carrier concentration. To confirm this assumption and also investigate the influence of the repetition rate of the excimer laser, we have grown 3 samples with a 15 nm $(\text{Mg}_{0.06}, \text{Zn}_{0.94})\text{O}$ buffer layer annealed at 600°C and a 300 nm 4N ZnO layer on top with a repetition rate of 2 Hz, 5 Hz and 10 Hz. The extracted values of μ_{Hall} and n_{Hall} from TDH measurements are summarized in Fig. 2.11(a) and (b), respectively.

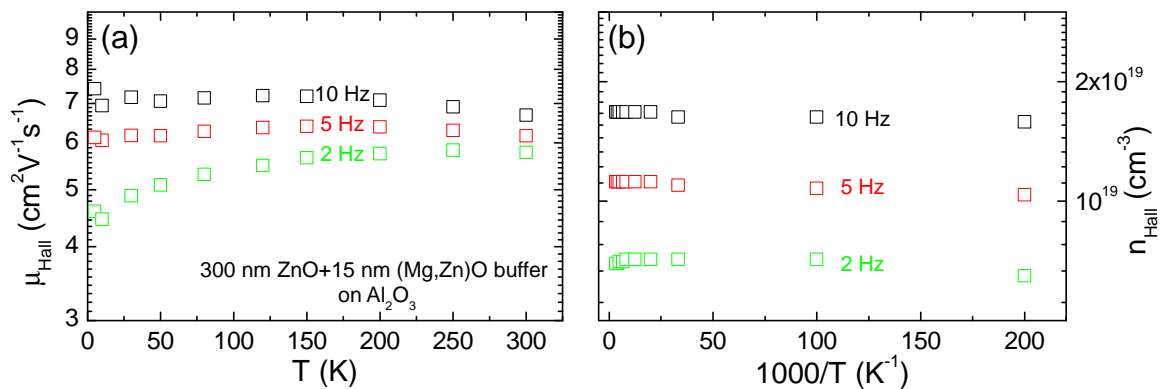


Figure 2.11: Extracted temperature dependent Hall mobility (a) and carrier concentration (b) for three samples consisting of a 300 nm 4N ZnO layer on a 15 nm $(\text{Mg}_{0.06}, \text{Zn}_{0.94})\text{O}$ buffer layer grown with a repetition rate of 2 Hz (green), 5 Hz (red) and 10 Hz (black).

For all 3 samples with buffer layer, we observe that the Hall mobility remains nearly constant over the whole temperature range. Only for the sample with 2 Hz repetition rate the mobility drops for temperatures below 150 K. For a repetition rate of 10 Hz we obtain a mobility of $\approx 7 \text{ cm}^2\text{V}^{-1}\text{s}^{-1}$ which is slightly higher than the value of $5 \text{ cm}^2\text{V}^{-1}\text{s}^{-1}$ obtained for the buffer free sample in Fig 2.10(a). More interestingly, the carrier concentration for the samples with buffer layer has increased by almost two orders of magnitude compared to the buffer free sample in Fig. 2.9(b). We attribute this significant change in carrier concentration to the annealing process of the buffer layer and the related strong

exponential increase of Al diffusion from the substrate into the buffer at the elevated annealing temperature of 600 °C. This leads in the end to a degenerate buffer layer with a low mobility, which dominates the Hall measurements.

This fact is supported by the TDH results of an annealed 15 nm (Mg_{0.06},Zn_{0.94})O buffer layer shown in Fig. 2.12(a) and (b). The carrier concentration of the buffer layer in

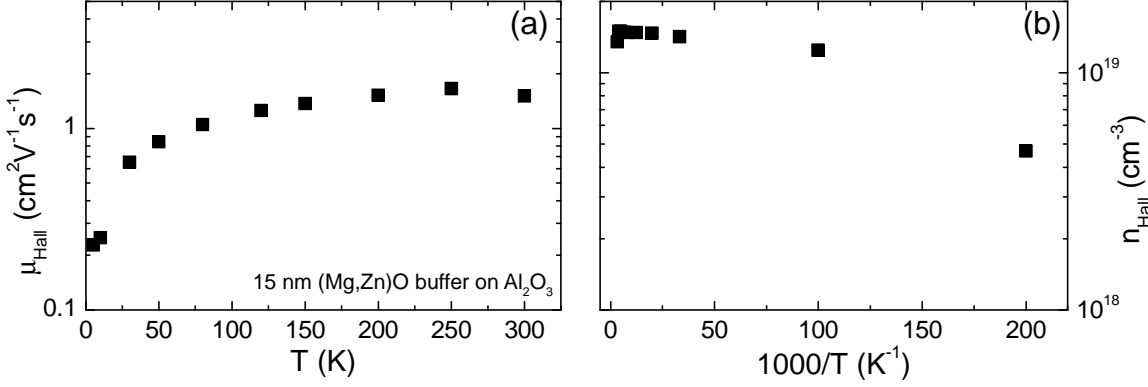


Figure 2.12: Temperature dependence of Hall mobility (a) and carrier concentration (b) for a 15 nm (Mg_{0.06},Zn_{0.94})O buffer layer extracted from TDH measurements.

Fig. 2.12(b) is independent of temperature for $T \geq 10$ K and remains at $1.5 \times 10^{19} \text{ cm}^{-3}$, which is greater than the Mott criterion of $2 \times 10^{18} \text{ cm}^{-3}$ for degenerate conduction in ZnO. In contrast to the temperature independent mobility of a combination of buffer layer and ZnO, the mobility of the buffer alone drops for decreasing temperatures by almost an order of magnitude. This difference in behavior might be explained by assuming the formation of a low mobility 2DEG at the interface between (Mg,Zn)O buffer and ZnO layer [47]. The formation of the 2DEG arises from the difference in band gap and polarization in (Mg,Zn)O and ZnO.

For an extraction of quantitative data regarding doping level, density of dislocations and activation energies, we follow the approach described in recent reports [115, 120, 128, 129]. Following this approach the measured temperature dependent Hall mobility and carrier concentration is fitted by using a theoretical description of a two layer system. The two layer system has different thicknesses t_1 of a degenerate layer 1 and t_2 of a semiconducting layer 2. This leads to a weighted average of the total measured $\mu_{\text{Hall}}(T)$ and $n_{\text{Hall}}(T)$ [129]:

$$\mu_{\text{Hall}}(T) = \frac{t_1 \mu_1^2(T) n_1(T) + t_2 \mu_2(T) \mu_{2,\text{Hall}}(T) n_2(T)}{t_1 \mu_1(T) n_1(T) + t_2 \mu_2(T) n_2(T)} \quad (2.1)$$

$$n_{\text{Hall}}(T) = \frac{(t_1 \mu_1(T) n_1(T) + t_2 \mu_2(T) n_2(T))^2}{(t_1 + t_2)(t_1 \mu_1^2(T) n_1(T) + t_2 \mu_2(T) \mu_{2,\text{Hall}}(T) n_2(T))}. \quad (2.2)$$

Here $\mu_1(T)$ and $\mu_2(T)$ are the drift mobility of layer 1 and layer 2, respectively. While $\mu_{2,\text{Hall}}(T)$ stands for the Hall mobility of layer 2.² Here the carrier concentration of the degenerate layer 1 is temperature independent and determined by the donor $N_{\text{d},1}$ and

²For the degenerate layer Hall and drift mobility are identical, while for the semiconducting layer the two mobilities need to be calculated separately from the average scattering time (See Appendix B and [129]).

acceptor $N_{a,1}$ concentrations $n_1(T) = N_{d,1} - N_{a,1}$. The temperature dependency of layer 2 is modeled by:

$$n_2(T) = \frac{1}{2}(\Phi(T) + N_{a,2}) \left(\sqrt{1 + \frac{4\Phi(T)(N_{d,2} - N_{a,2})}{(\Phi(T) + N_{a,2})}} - 1 \right), \quad (2.3)$$

where $\Phi(T) = (2(2\pi m_0 k_B T)^{\frac{3}{2}}/h^3)(g_0/g_1)(m_n/m_0)^{\frac{3}{2}} \exp(-E_{d,2}/k_B T)$ describes the activation of a hydrogen like donor. The degeneracy (g_0/g_1) is set to $1/2$, $E_{d,2}$ is the activation energy of the donor, k_B the Boltzmann constant, m_0 the mass of a free electron, m_n density-of-states effective mass and h the Planck constant. The description of $\mu_1(T)$, $\mu_{2,Hall}(T)$, and $\mu_2(T)$ is achieved by taking into account different scattering mechanism, including scattering on ionized and neutral impurities, scattering at dislocations (these three contributions dominate at low temperatures), scattering by acoustic, piezoelectric, and polar optical phonons (phonon scattering dominates at high temperatures). The effective scattering time is obtained from Mathiessen's Rule, more details can be found in [120, 129]. The Mathematica syntax used for the simulation can be found in Appendix B. The input parameters were manually optimized until a satisfying agreement between simulation and experimental data was achieved. In the following, we present the obtained simulation curves in comparison to the experimental data for two samples: First for a 1000 nm thin ZnO film grown directly on c-plane sapphire with the optimized deposition parameters in Fig. 2.13(a) for mobility and Fig. 2.13(c) for carrier concentration, and second a 500 nm ZnO film on a 50 nm ($\text{Mg}_{0.06}, \text{Zn}_{0.94}$)O buffer layer grown on (0001)Al₂O₃ in Fig. 2.13(b) and (d). The fit via the simulation allows for a quantitative understanding of the transport phenomena in the buffer free ZnO layer leading to the observed temperature dependence of μ_{Hall} and n_{Hall} . The thickness value for the degenerate layer is $t_1 = 60$ nm. For $T < 70$ K the integral Hall mobility and carrier concentration is dominated by the degenerate layer 1 as there is only a vanishing number of free electrons in layer 2 contributing to the Hall effect. By increasing the temperature above 70 K an increasing number of free electrons is thermally activated in layer 2, increasing its contribution to the total μ_{Hall} and n_{Hall} . For temperatures above 100 K, the total mobility and carrier concentration is dominated by the semiconducting layer 2. The extracted activation energy of 55 meV corresponds nicely with the one reported for aluminium donors in [130, 131]. Moreover, the extracted values for the donor concentration are by one order of magnitude lower than the ones in [120] and equal to the ones in [128]. This indicates that our samples have a low residual carrier concentration. In contrast, the mobility values obtained for our films are at least one order of magnitude lower than the ones reported in [120, 128]. This is mainly due to the high density of dislocations present in our samples limiting the maximum μ_{Hall} . The dislocation density in our samples are more than two orders of magnitude higher than the ones in [120]. But one should note that these lower values were obtained by using a high temperature MgO buffer layer on sapphire.

For the simulation of the ZnO film on the (Mg,Zn)O buffer layer, we assumed a thickness of $t_1 = 50$ nm and $t_2 = 500$ nm. For the buffer layer, we have used the measurements on the buffer alone as a reference. As it is evident from Fig. 2.13(b), the total theoretical approach underestimates the measured mobility by a factor of 3 for $T > 150$ K. This originates from the fact that the donor concentration $N_{d,1} = 4.5 \times 10^{19} \text{ cm}^{-3}$ in

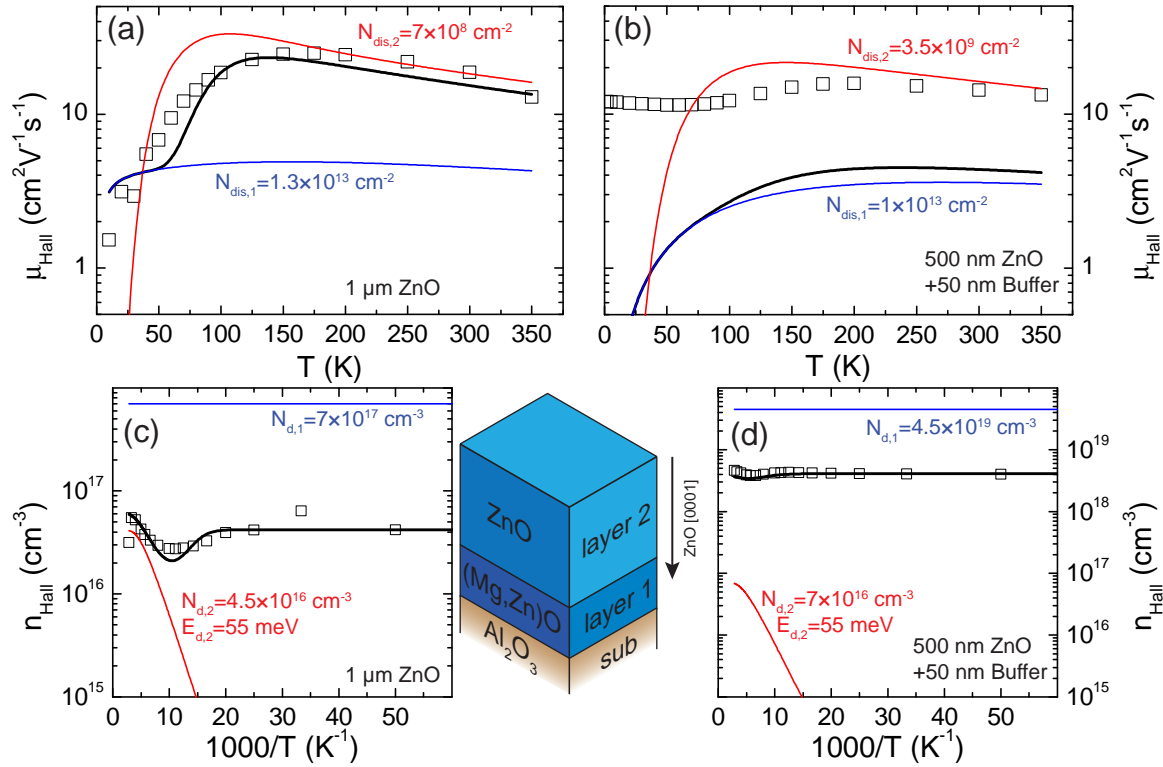


Figure 2.13: Application of the two layer Hall simulation model for the extraction of quantitative data for the density of dislocations $N_{\text{dis},1}$, $N_{\text{dis},2}$, density of donors $N_{\text{d},1}$, $N_{\text{d},2}$, and the corresponding activation energy $E_{\text{d},2}$. In all graphs simulations are indicated by differently colored lines: black represents a simulation for the whole system, blue layer 1 alone and red layer 2 alone. Data points are displayed as black open symbols. The temperature dependence of the mobility (a) and carrier concentration (c) in experiment and simulation for a 1000 nm thick ZnO film on sapphire show an excellent agreement between theory and experiment. The results obtained for the mobility and carrier concentration of a 500 nm thick ZnO film on a 50 nm thin (Mg_{0.06},Zn_{0.94})O buffer on c-plane sapphire are shown in panels (b) and (d), respectively. The sample sketch explains the orientation of the ZnO [0001] direction in our buffer sample, which allows the formation of a polarization induced 2DEG at the interface between (Mg,Zn)O and ZnO in the ZnO layer.

the degenerate buffer layer leads to a domination of the mobility by ionized impurities. But at such high impurity concentration the formation of an impurity band is possible, making an application of the used theoretical model impossible. In addition, the high number of free electrons in the buffer dominates the measured Hall mobilities and carrier concentration in the total system. Unfortunately, this dominating buffer layer makes the extracted quantities of the semiconducting ZnO layer highly questionable. Nevertheless, the low residual carrier concentration that has already been found in the buffer free layer, remains unchanged by the growth on a buffer layer with an activation energy pointing to aluminium as the main impurity in our samples.

At temperatures below 100 K, there exists a huge difference between the measured and theoretical mobility of our buffer sample. One should also remember that we saw a decrease in mobility also for the degenerate buffer layer alone, which is clearly not the

case when combining a (Mg,Zn)O buffer with a ZnO layer. This indicates the formation of a low mobility 2DEG at the interface between ZnO and (Mg,Zn)O, which is related to the difference in band gap and polarization of ZnO and (Mg,Zn)O forming a triangular-potential at the interface. More details and a more elaborate description can be found in [54]. Still the Hall mobility is rather small when compared to the values of several $100 \text{ cm}^2 \text{ V}^{-1} \text{ s}^{-1}$ in [52]. This is related with the still high number of dislocations in the ZnO which will drastically reduce the mobility of the 2DEG.

Summing up the results obtained from TDH measurements, the experimental data can be understood in the model of a two layer system, with a degenerate and a semi-conducting layer. Our samples show a low residual carrier concentration caused by the small interdiffusion of aluminium from the substrate into the film and the purity of our target material. The carrier concentration measured is comparable to results obtained by other groups. In contrast, our extracted mobility values are rather poor regardless if a (Mg,Zn)O buffer layer has been used or not, when compared to results from other groups.

This issue could be addressed by analyzing the influence of a MgO buffer layer on the one hand and optimizing the ZnO growth parameters on a buffer layer on the other hand. The use of a MgO buffer layer has two advantages over our used (Mg,Zn)O buffer system, as the lattice mismatch to sapphire is smaller the dislocation density at the substrate-buffer interface should be greatly reduced. Moreover, it might be possible to reduce influence of the interdiffused aluminium depending on the donor activation energy of Al in MgO, which might allow the growth of an insulating buffer layer. The introduction of an additional (Mg,Zn)O buffer (without an annealing step) between the MgO buffer and the ZnO layer could lead to a further optimization of the quality of our ZnO films. From the still high number of dislocations present in the ZnO even with a (Mg,Zn)O buffer when compared to results from other groups, we clearly need to optimize the growth of ZnO on the buffer layer. The aim of this optimization should be a significant reduction in the FWHM of the $(10\bar{1}1)$ XRC by at least a factor of 3, while still remaining the narrow FWHM for the (0002) XRC, indicating a reduction of dislocations in the ZnO.

The need for an optimized buffer layer growth is supported by the following results obtained from HRTEM measurements.

2.2.2.3 TEM analysis of ZnO thin films with buffer layer

HRTEM images of a 120 nm thick ZnO layer on a 15 nm thick ZnO buffer layer on c-plane sapphire, were measured in the group of W. Mader at the university of Bonn by Sven-Martin Hühne. The results obtained are collected in Fig. 2.14(a)-(e).

From the two TEM micrographs in Fig. 2.14(a) and (b), we conclude that we were able to grow a buffer layer with a sharp interface to the substrate. Interestingly no interface between buffer and ZnO layer is visible in 2.14(b).

The diffraction pattern in Fig. 2.14(c) confirms our HRXRD measurements. ZnO grows relaxed on sapphire with the epitaxial relationship of $\text{Al}_2\text{O}_3(0001)[11\bar{2}0] \parallel \text{ZnO}(0001)[10\bar{1}0]$. This proves that at the start of the growth the Zn sublattice of ZnO orients parallel to the O sublattice of sapphire.

The bright field and dark field micrographs in Fig. 2.14(d) and (e) allow us to investigate the density of dislocations. The red arrow in each figure indicates the same sample position. Within the ZnO buffer layer we can estimate a dislocation density of

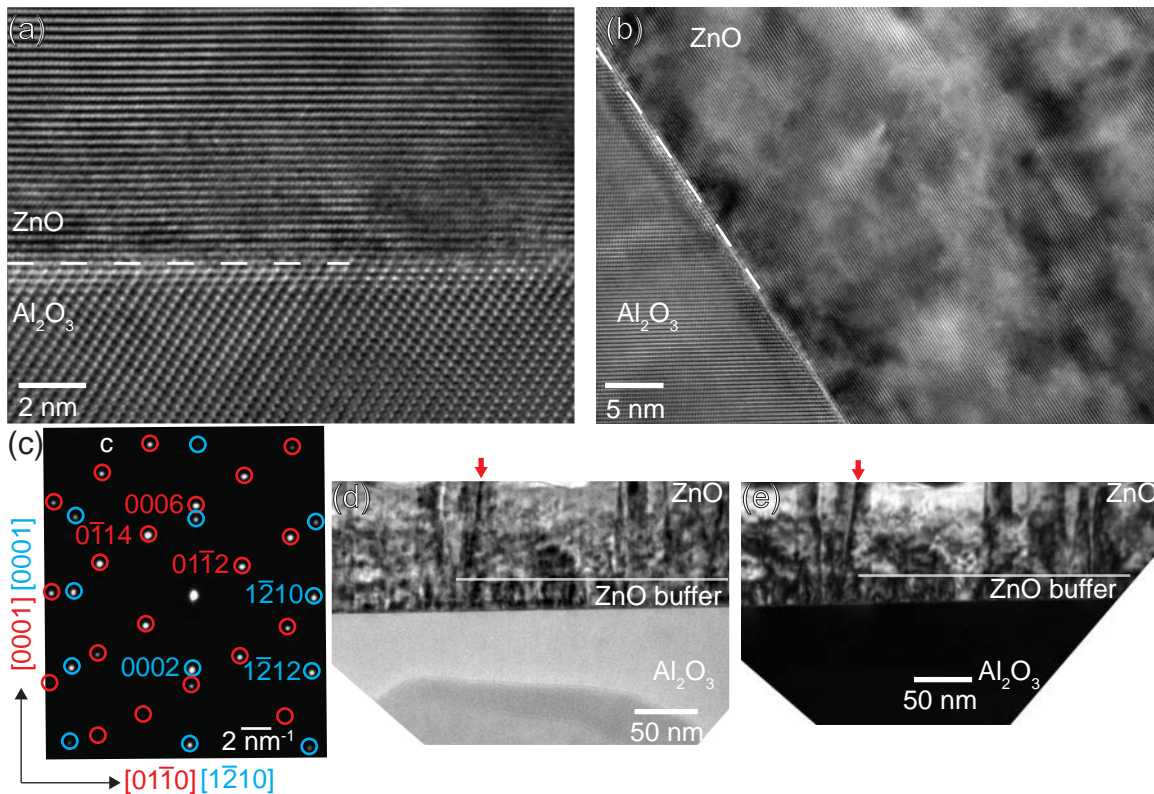


Figure 2.14: High resolution TEM images of a 120 nm thick ZnO film on a 15 nm thin ZnO buffer layer. (a) Cross-sectional TEM image at the interface between substrate and thin film, with a nice abrupt and smooth interface, indicated by the dashed line. (b) Large area TEM image of the same sample. An abrupt change at the interface of buffer and film is not visible. (c) TEM diffraction image. Diffraction peaks of sapphire are marked and labeled in red, the ones of zinc oxide in blue. The diffraction image confirms the epitaxial relations from XRD (indicated by arrows with corresponding crystal directions): $\text{Al}_2\text{O}_3(0001)[11\bar{2}0] \parallel \text{ZnO}(0001)[10\bar{1}0]$. (d) Bright field and (e) dark field micrograph, making the present dislocations and stacking faults visible.

$1 \times 10^{13} \text{ cm}^{-2}$. Interestingly, the density of dislocations is not significantly reduced in the ZnO layer on the buffer. Moreover, the ZnO layer shows no correlation of dislocations from the buffer and even forms new ones. The obtained bright field and dark field images show the same ZnO quality as the ones presented in [120] for a buffer free ZnO layer on sapphire.

Again these results encourage a further optimization of the buffer layer system and the growth of ZnO on the buffer. In [120] the introduction of a high temperature grown 3 nm thin MgO buffer has significantly reduced the number of dislocations in the ZnO grown on top and might be a possible way for improving our samples.

2.2.2.4 Photoluminescence of ZnO layers

To investigate the optical properties of our samples we have conducted temperature dependent PL measurements. These experiments have been carried out in the group of

B. Beschoten at the RWTH Aachen by Christoph Schwark and Christian Weier. In the following we compare the results obtained for a 300 nm thick ZnO film directly grown on (0001)-oriented sapphire and a 100 nm thick ZnO film on a 15 nm thin ZnO buffer layer on (0001)-oriented Al_2O_3 . For the temperature dependent PL experiments, the samples were mounted in an Oxford Spectromag 4000 magnet cryostat system (sample temperature 10 K – 300 K), excited via a HeCd laser (3.815 eV) and the luminescence light was detected by an Acton SpectraPro 500i spectrometer with a liquid nitrogen cooled CCD-sensor. The temperature dependent PL is summarized in Fig. 2.15(a) for the buffered and in Fig. 2.15(b) for the thick unbuffered ZnO layer.

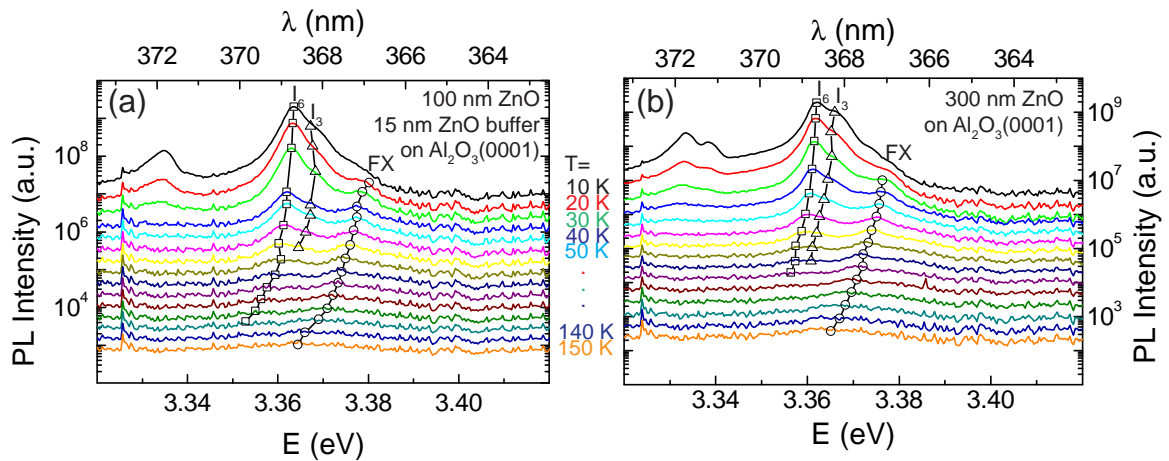


Figure 2.15: Evolution of the photoluminescence with temperature for two different ZnO samples: (a) PL for a 100 nm thick ZnO film on a 15 nm thin ZnO buffer and (b) PL for a 300 nm thick ZnO film on c-plane sapphire. For clarity, the PL curves at each temperature are colored differently and have been shifted with respect to each other. The corresponding temperature is summarized in the legend positioned between the two graphs. The square symbols represent the fitted position of the I_6 line, triangles the position of the I_3 and circles the position of the free exciton (FX) emission line. The lines connecting the symbols are guides to the eye.

For the buffered film in Fig. 2.15(a) the PL at 10 K, going from higher two lower energies, first shows a broad high intensity peak between 3.35 eV and 3.38 eV and a second one with lower intensity located between 3.33 eV and 3.34 eV, all below the band gap (3.44 eV [38]) of ZnO. Taking a closer look at the high intensity peak we find that the broad peak actually consists of a main high intensity peak located at 3.364 eV and the tail towards higher energies shows two shoulders located at 3.367 eV and 3.378 eV. All these excitations are below the band gap energy of ZnO, such that they must be related to excitonic excitations, which have been extensively studied in literature. Using the nomenclature of [130, 131] we can attribute the high intensity peak at 3.364 eV to the I_6 line, which is an exciton bound to a neutral aluminium donor. The shoulder at 3.367 eV is related to the I_3 line, an exciton bound to an ionized donor. And finally the low intensity shoulder at 3.378 eV corresponds to a free exciton (FX). The second peak at energies below 3.34 eV is the two electron satellite (TES) of the donor bound excitons. More details of these excitonic transitions can be found in [32, 131]. The

existence of aluminium donors in our samples arises due to the aluminium impurities, which are the main impurities in high purity ZnO material [132] in the target, and diffusion of aluminium from the substrate. Moreover, these findings prove that Al is the main impurity in our samples, which supports our results from TDH measurements.

With increasing temperature the intensities of the I_6 and I_3 lines decrease, while the intensity of the free exciton emission line stays constant and becomes more visible with increasing temperatures. For temperatures above 60 K the donor bound exciton peaks vanish, due to a thermal dissociation of donor and exciton, as the donor exciton binding energy has a value of several meV. For the free exciton emission, the increase in temperature leads to a broadening of the peak, due to thermal fluctuations. A thermal dissociation occurs at much higher temperatures than for the donor bound excitons, as the free exciton binding energy is one order of magnitude larger.

A comparison between the temperature dependent PL data of the buffered (Fig. 2.15(a)) and unbuffered (Fig. 2.15(b)) ZnO film shows that for the thicker unbuffered sample the donor bound exciton and free exciton lines become more pronounced and for $T = 10$ K the TES peaks are clearly separated. But nevertheless, the by a factor of 3 thinner buffer ZnO sample exhibits the same features as the unbuffered one, indicating that the optical properties of our samples remain unchanged by introducing a buffer layer in the system.

For a more quantitative analysis we extracted peak position, FWHM and peak area as a function of temperature for each sample from the PL data by fitting a multiline function (3 Lorentzian shaped peaks) to the broad high energy peak. This allows us to monitor separately the evolution of the I_6 , I_3 and FX line with temperature. The results for both samples are shown in Fig. 2.16(a)-(f)

From Fig. 2.16(a) and (b) we see that the position of the donor bound excitons and free excitons shift to lower energies for increasing temperatures. Both samples show in principle the same peak position evolution with temperature. One should note that the difference in the absolute position comes from a different wavelength calibration applied to each data set. When we compare the extracted FWHM for the two different samples, we find that both have the narrowest value for the I_6 excitation at $T = 10$ K of 3.8 meV for the buffered and 3.5 meV for the thick unbuffered ZnO layer. Both values are nearly identical and show the improvements achieved by the application of a buffer layer for thin ZnO films. Compared to reported values of the FWHM for the dominant bound exciton transition in literature of 3 meV [42] for ZnO on sapphire, our values for both samples are nearly on par to this value, indicating the high optical quality of our samples.

For the temperature dependence of the peak area, we observe a sharp decrease in peak area for the I_6 , I_3 lines for increasing temperatures, because of the already mentioned thermal dissociation of donor and exciton. For the I_6 line the reported localization energy is 15.1 meV and for I_3 9.4 meV [131]. This temperature dependence can be found in both samples indicating the same origin of these donor bound excitons. The peak area of the free excitonic transition is constant for temperatures above 40 K and increases for temperatures below.

Summarizing the results obtained for the temperature dependent PL our samples exhibit 3 excitonic emission lines, two of them are related to donor bound excitons (I_6, I_3) and one representing the free exciton emission (FX). The assigned origin of our dominant donor bound exciton I_6 line are aluminium impurities, which act as shallow donors in ZnO and are in accordance to our TDH measurements. Moreover, the extracted narrow FWHM of the dominating emission line proves the high optical quality of our samples

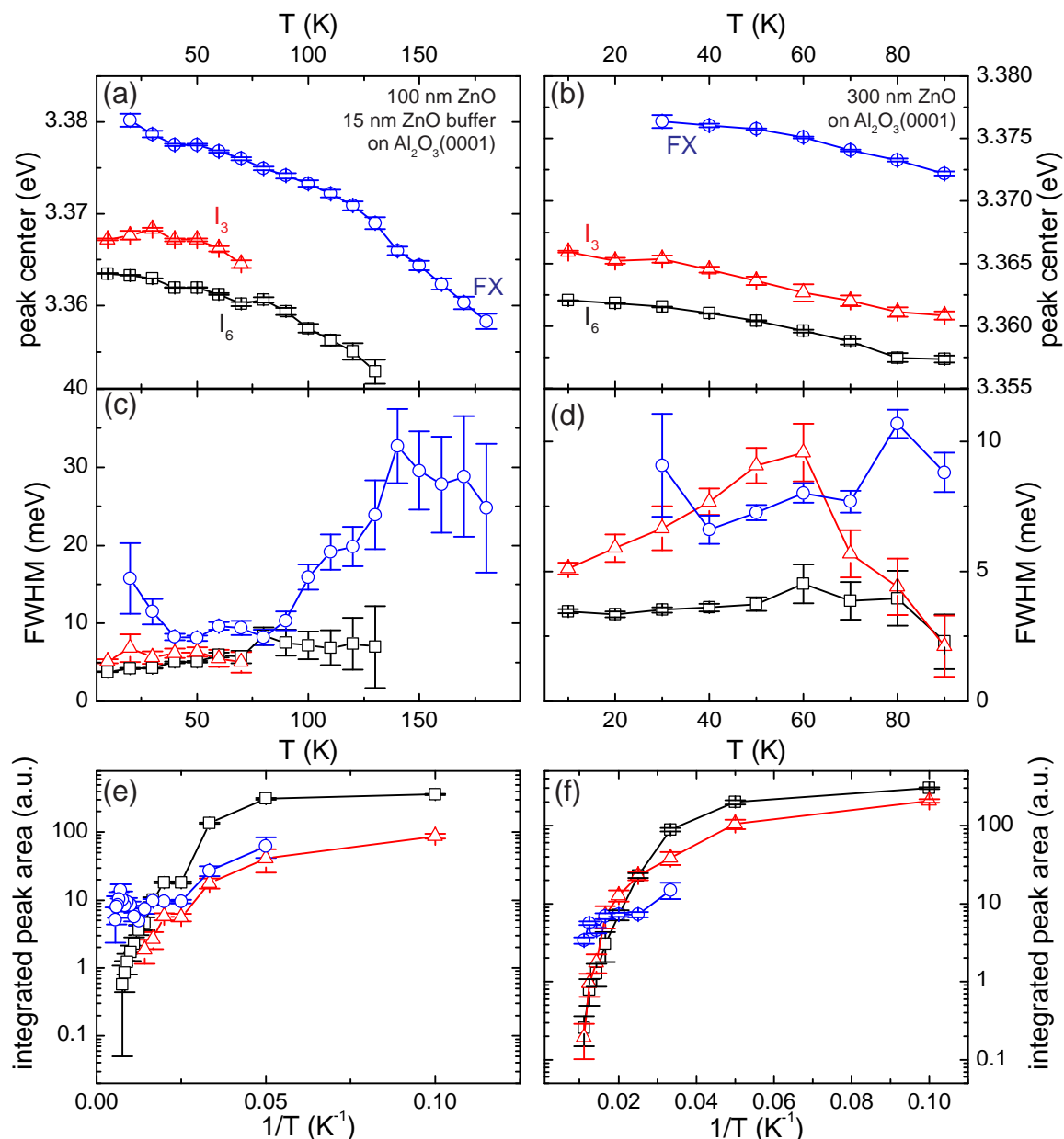


Figure 2.16: Extracted peak parameters from a multipeak fit to the temperature dependent PL in Fig.2.15. In all graphs black squares represent results for the I₆ line, red triangles results for the I₃ line, and blue circles results for the free exciton emission line (FX). Temperature dependence of the peak positions of each line determined from the multipeak fit for (a) the buffered sample and (b) the unbuffered thicker zinc oxide thin film. FWHM values of the Lorentzian fit extracted for each peak for (c) the buffered and (d) the unbuffered layer system. Evolution of the area of the fitted peaks with temperature is illustrated for the buffered and unbuffered sample in panel (e) and (f), respectively. The drastic decrease in area for the donor bound exciton lines I₆ and I₃ correspond to the thermal quenching of these excitations for temperatures above 60 K

compared to literature.

2.3 Optical orientation experiments in ZnO thin films

In the following section we report on the results obtained from time-resolved Faraday rotation (TRFR) experiments on our high quality ZnO thin films on sapphire substrates. All the data presented in this section have been measured in the group of B. Beschoten at the RWTH Aachen by Christoph Schwark, Christian Weier, and Vera Klinke.

The principle setup for TRFR measurements is illustrated in Fig. 2.17(a). The ps laser pulses of a Ti:sapphire-laser (12.5 ns duty cycle) are first frequency doubled (which allows to scan the laser frequency in the spectral region between 300 nm and 550 nm wavelength) by a second harmonic generation (SHG) crystal. After SHG, the beam is split into two propagating beams: A high intensity circularly polarized pump and a low intensity linearly polarized probe beam. The beams propagate along different optical beam paths, but are focused onto the same spot on the sample, which is mounted in a Oxford Spectromag 4000 magnet cryostat system (sample temperature 10 K – 300 K, magnetic fields $\mu_0 H \leq 7$ T). By using a mechanical delay line in the optical path of the probe beam, it is possible to systematically vary the time delay ($t_{\text{delay}} \leq 3.3$ ns) between pump and probe light pulse at the sample. In the following $t_{\text{delay}} = 0$ describes simultaneous arrival of the pump and probe pulses at the sample. The sample is oriented in such a way, that the probe laser beam is parallel to the surface normal and the magnetic field is applied in the film plane (Fig. 2.17(a)). When the wavelength λ of the circularly polarized pump beam ranges in the region of the band gap of zinc oxide, the optical selection rules for ZnO [133] lead to the generation of spin polarized electrons in the film. The generated spins are aligned parallel to the propagation direction of the pump pulse, i.e. a large part is parallel to the surface normal of the sample corresponding to an effective magnetization. Due to the applied external magnetic field $\mu_0 H$ oriented in-plane the electron spins start to precess around the magnetic field direction. The frequency of this precession is connected to the g-factor of the electrons. To monitor the time evolution of this precession the Faraday rotation of the linearly polarized probe beam is measured in transmission with a diode array and LockIn technique. As the magnitude of the Faraday rotation is sensitive to the effective magnetization of the spin polarized electrons parallel to the surface normal, we expect an oscillation of the Faraday rotation angle θ_F in time due to the precessing spins in ZnO. In a typical TRFR measurement, θ_F is recorded while changing the time delay between pump and probe beam, such that $\theta_F(t)$ can be reconstructed. In addition, the effective magnetization due to the spin polarized electrons decays over time, because the initial coherent ensemble of spin polarized electrons is destroyed by various dephasing mechanisms. This effectively leads to an exponential reduction of the amplitude of the oscillating θ_F signal. By fitting the exponential decay of the amplitude, one can then extract the spin dephasing time T_2^* from a TRFR measurement.

For the TRFR measurements we have grown two different samples on c-plane Al_2O_3 , a 100 nm thick ZnO film on a 15 nm thin ZnO buffer and a 300 nm thick zinc oxide film without buffer layer using the optimized deposition conditions described in section 2.2. After the growth of the samples via laser-MBE the backside of the substrates was mechanically polished to optimize optical transmission through the sample. In Fig. 2.17 (b) and (c) the TRFR signal is displayed at $T = 10$ K and $\mu_0 H = 500$ mT for the buffered sample at $\lambda = 368.90$ nm and the unbuffered sample at $\lambda = 368.80$ nm respectively. The coherent precession of spins is observed over the full laser repetition interval of 12.5 ns, as evident from the oscillations at negative delay which originate from the excited spin

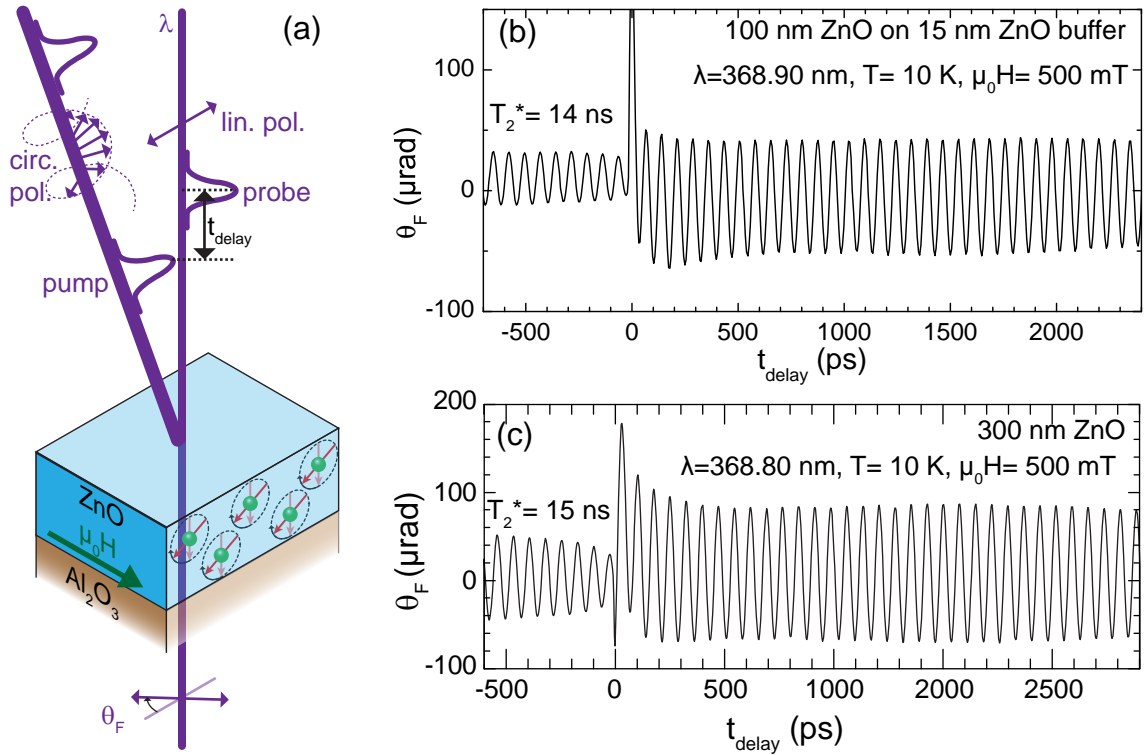


Figure 2.17: (a) Illustration of the principle configuration for TRFR measurements. The circular polarized pump beam generates a coherent spin packet, which precesses around the in-plane applied magnetic field. By varying the time delay of the linearly polarized probe beam with respect to the pump beam, one can monitor the precession and dephasing of the spin ensemble by measuring the Faraday angle θ_F . TRFR data measured for (b) a 100 nm thick (0001)ZnO film on a 15 nm ZnO buffer layer and (c) a 300 nm thick ZnO film, both grown by laser-MBE with the optimized growth parameters on c-plane sapphire. Both TRFR curves consist of a fast decaying contribution (excitonic recombination) and a slow one, which is still visible after the laser repetition interval of 12.5 ns (negative delay). The decay time T_2^* given for each sample is extracted from the long-lived contribution to the Faraday signal.

packet of the previous pump pulse. The estimated T_2^* from the exponential decay of the oscillating θ_F is of the order of 15 ns, which is nearly one order of magnitude larger than previously reported values of 2 ns for ZnO thin films on sapphire [97]. In addition, there is nearly no difference in T_2^* for both samples. Interestingly, these long spin dephasing times are observed at excitation wavelengths corresponding to energies well below the band gap of ZnO. This demonstrates that the coherent electron spins are either bound to unintentional dopants or originate from optically excited excitons. Using time-resolved transmission experiments not shown here, an excitonic recombination time of ≈ 100 ps has been determined. This recombination time is also visible in the TRFR experiments as an initial fast reduction of the oscillation amplitude after excitation of the spin packet at zero delay. As the measured T_2^* exceeds the measured exciton radiative lifetime by two orders of magnitude, we conclude that the initially generated spin polarization is transferred to other electron states.

To further explore the origin of the long spin dephasing times we carried out TRFR measurements at different excitation wavelengths and compared the spectra to the PL measurements. Fig.2.18(a)-(c) summarizes the results obtained at $T = 10$ K and $\mu_0 H = 500$ mT for our buffered 100 nm thick ZnO film on sapphire.

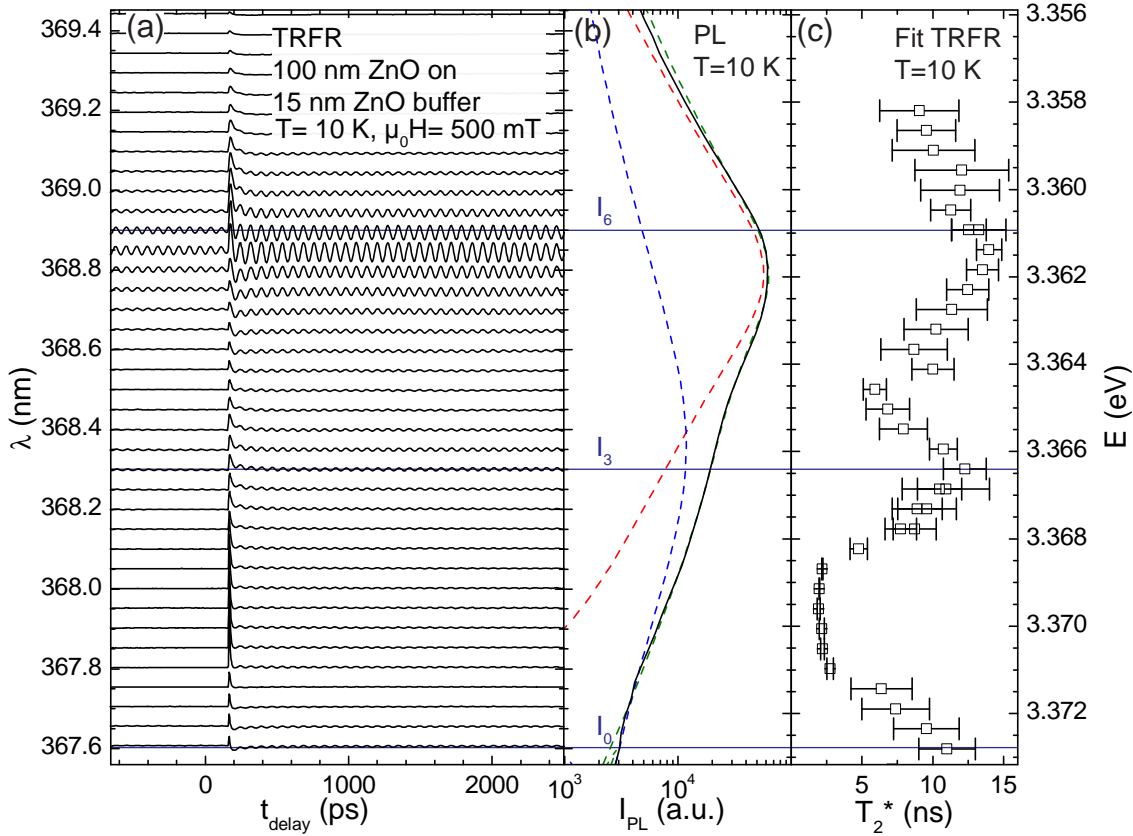


Figure 2.18: (a) Evolution of the TRFR Signal with excitation wavelength for a 100 nm ZnO film on a 15nm ZnO buffer layer at $T = 10$ K and $\mu_0 H = 500$ mT. (b) PL signal at $T = 10$ K for the very same sample (black line), the dashed green line indicates a fit to the PL data by the addition of two Lorentzian curves (dashed red and blue lines). (c) Extracted T_2^* from the wavelength dependent TRFR measurements in (a). The reported energy positions [131] for the I_6 , I_3 and I_0 donor bound excitons are indicated by blue lines. For excitation energies near donor bound excitons the observed oscillation amplitude is greatly enhanced and maxima in T_2^* occur.

The range of the excitation wavelength for the TRFR measurements in Fig. 2.18(a) covers the spectral region of the donor bound excitons in zinc oxide [131]. At energies corresponding to the I_6 , I_3 and I_0 donor bound exciton lines indicated by blue lines, the TRFR signal amplitude is strongly increased and vanishes for wavelengths lying between these excitation energies. The largest signal is observed for excitation energies near I_6 , which corresponds to an exciton bound to a neutral aluminum donor. The energy dependence of the TRFR signal amplitude corresponds nicely with the PL spectrum in Fig.2.18(b) measured at the very same temperature. At the energy near I_6 corresponding to the maximum in PL we also observe a maximum in the TRFR signal amplitude. We note that the position of the maximum in PL and TRFR signal amplitude deviates from

the reported position of the I_6 line. This might be attributed to the influence of growth parameters on the position of the donor bound exciton lines [131]. Moreover, the TRFR signal amplitude is strongly increased when the excitation energy approaches 3.367 eV (I_6), where the PL spectra shows a shoulder feature. This provides further evidence that a correlation between the resonant excitation of donor bound excitons and long spin dephasing times must exist. The resonant amplification is also evident from the energy dependence of T_2^* extracted from TRFR in Fig. 2.18(c). T_2^* is longest right at the energies corresponding to the excitation energies of donor bound excitons I_6, I_3 and I_0 and drops sharply to a short dephasing time for energies in between. The obtained spin dephasing times for all 3 donor bound exciton lines are well above 10 ns providing an efficient way of storing spin information on long time scales. As the physical origin of the I_3 and I_0 donor bound excitons is still under controversial discussion, we focus on the excitonic I_6 state, i.e. the exciton bound to Al.

Under the assumption, that the observed long spin dephasing times are correlated to excitons bound to donors, we also expect a reduction of T_2^* with increasing temperatures due to the thermal dissociation of donor bound excitons. In Fig. 2.19(a) we show a comparison between the temperature dependence of the PL intensity of the I_6 line and the extracted T_2^* from temperature dependent TRFR measurements conducted at the excitation wavelength of I_6 . All measurements have been carried out on the buffered 100 nm thick ZnO sample. The PL intensity of the I_6 line is nearly constant for $T \leq 20$ K

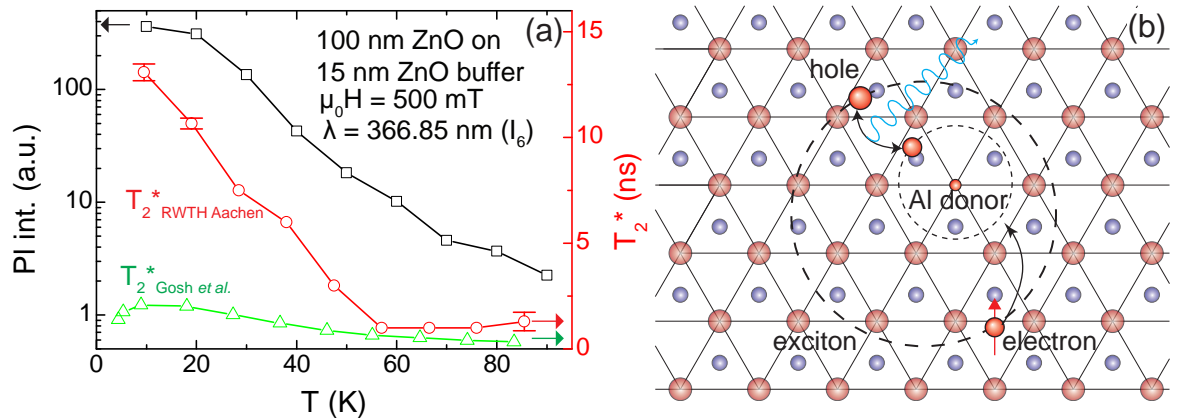


Figure 2.19: (a) Temperature dependence of the PL intensity (black squares, left axis) and the corresponding T_2^* (red circles, right axis) extracted from TRFR for excitons bound to an aluminium donor (I_6). Both, the PL intensity and the spin dephasing time, show about the same temperature dependence, for $T > 60$ K the spin dephasing time remains nearly constant at 1 ns. Our spin dephasing times exceed the values reported by Gosh *et al.* [97] for a 100 nm thick ZnO film (carrier concentration $n = 1.9 \times 10^{19} \text{ cm}^{-3}$) grown by pulsed laser deposition on c-plane sapphire (green triangles). But the temperature dependence nicely agrees with our observation. (b) Illustration of spin transfer mechanism. By the recombination of the exciton hole and the donor bound electron it is possible to store the spin polarized electron of the exciton on the aluminium donor.

and then starts to rapidly drop by two orders of magnitude for temperatures above 20 K. This temperature dependence is also reflected in T_2^* : Increasing T from 10 K to 60 K the spin dephasing time is reduced from 15 ns to 1 ns. For temperatures above 60 K, T_2^*

remains at 1 ns. Moreover the spin dephasing time is independent of the photon energy for $T \geq 70$ K. The two different regimes in temperature indicate that the TRFR probes two different spin states depending on the temperature. For low temperatures, donor bound excitons allow the storage of spin information on long time scales. At elevated temperatures, the excitons are thermally decoupled from the donor and an itinerant state, storing the spin information, dominates. Compared to the temperature dependence of T_2^* reported by Gosh *et al.* [97] for a 100 nm thick ZnO film (carrier concentration $n = 1.9 \times 10^{19} \text{ cm}^{-3}$) grown by pulsed laser deposition on c-plane sapphire (indicated as green triangles in Fig. 2.19(a)) we can deduce two things. On the one hand, the T_2^* of our films exceed the reported values by a factor of 5. On the other hand, the temperature dependence of the spin dephasing time is qualitatively identical. This suggests that the spin dephasing mechanisms are identical for both types of samples. We will discuss these mechanisms in more detail in Section 2.5.3.3.

A possible explanation for the long spin dephasing times at temperatures below 60 K is illustrated in Fig. 2.19(b). The donor bound exciton with a spin polarized electron (the spin polarization of the hole dephases on ps time scales) is generated by the circularly polarized pump beam. The recombination of the exciton hole with the donor bound electron allows the transfer of the spin polarized electron from the excitonic state into the localized donor state. Thus, the long T_2^* stems from localized electron states bound to donors. As the probability for this mechanism depends on the trapping of an exciton near a donor, the effect is enhanced at temperatures where donor bound excitons exist ($T \leq 60$ K) and is ineffective at higher temperatures, at which free excitons dominate the excitations below band gap. Localized electronic states and itinerant electronic states are subject to different spin dephasing mechanisms [99], which explains the different regimes in the temperature dependence of T_2^* .

For the I_3 and I_0 lines it is highly debatable if the same mechanism might explain the long spin dephasing times at low temperatures as they have a completely different ground state than I_6 . Nevertheless, all these excitonic excitations have in common that they represent excitons bound to a donor and exhibit long T_2^* at $T = 10$ K.

Summarizing these results, our samples show long spin dephasing times above 10 ns at $T = 10$ K. The excitation energy and temperature dependence suggest, that a long-lived spin information storage is possible by the transfer of the spin polarized electron from the donor bound exciton to the donor state. At temperatures above 60 K the excitons are dissociated from the donors and we observe $T_2^* = 1$ ns, which is independent of temperature and excitation wavelength.

The localized spin information storage at spectrally separated states provides the opportunity to investigate the coupling strength between these states by using two color TRFR experiments. Here, two pulsed lasers tuned to different excitation energies, corresponding to different localized states, are used. We can then generate a spin polarization in one localized state with a pump pulse by one laser and then monitor the influence of this spin packet on a second spin packet pumped by the other laser. A sufficient coupling between those localized states would allow the use of donor bound excitons in the framework of quantum information processing (QIP) and thus combine an optical control and solid state based storage of quantum information in one system. At the moment, corresponding experiments are conducted at the RWTH Aachen, which hopefully will yield a deeper insight into the efficiency of coupling between localized states and the possible application in QIP.

2.4 Electrical injection and optical detection of spin-polarized charge carriers

The promising results obtained from TRFR experiments on our high quality laser-MBE grown ZnO films, with long spin dephasing times related to localized donor bound excitons, raised the interesting question if it is possible to convert an electrically injected spin polarization, carried by delocalized electron states, to a spin polarization in localized states. To answer this question we have grown ferromagnet (FM)/ZnO heterostructures on (0001)-oriented sapphire in our thin film deposition facility. First we deposited a 15 nm thin ZnO buffer layer by laser-MBE on an annealed Al₂O₃ substrate using the optimized deposition parameters ($\varrho_{\text{ED}} = 1 \text{ J/cm}^2$, 2 Hz repetition rate, $p_{\text{O}_2} = 1 \mu\text{bar}$, $T_{\text{sub}} = 400 \text{ }^\circ\text{C}$) and annealed the buffer at $p_{\text{O}_2} = 1 \mu\text{bar}$ and $T_{\text{sub}} = 600 \text{ }^\circ\text{C}$ for 30 min. After the buffer annealing we have grown a 150 nm thick ZnO layer using the following deposition parameters: $\varrho_{\text{ED}} = 1 \text{ J/cm}^2$, 2 Hz repetition rate, $p_{\text{O}_2} = 10 \mu\text{bar}$, $T_{\text{sub}} = 500 \text{ }^\circ\text{C}$. After the laser-MBE deposition process, the sample was cooled down to room temperature with $p_{\text{O}_2} = 10 \mu\text{bar}$. Afterwards the laser-MBE chamber was evacuated to its base pressure $\approx 1 \times 10^{-8} \text{ mbar}$ and the sample in-situ transferred to an electron beam evaporation (EVAP) chamber. There we deposited a 30 nm thick cobalt layer on top of the sample. Using photolithography and argon ion milling we defined a disc-shaped Co electrode on the ZnO film with 400 μm diameter. With an additional photolithography step, we patterned gold contacts by DC-sputtering and lift-off. An optical micrograph of the final spin injection structure is shown in Fig. 2.20(a). From a structural characterization (not shown here) carried out by HRXRD we obtained a FWHM of the XRC of the ZnO(0002) reflection of 0.03° , demonstrating the excellent quality of the sample.

For further characterization we conducted electrical injection/optical detection experiments using Hanle magneto-optical Kerr effect (Hanle MOKE) [134, 135] measurements. These measurements have been carried out in the group of Bernd Beschoten at the RWTH Aachen by Christoph Schwark and Christian Weier. For the experiments the sample was mounted in an Oxford Spectromag 4000 magnet cryostat system (sample temperature 10 K – 300 K, magnetic fields $\mu_0 H \leq 7 \text{ T}$).

A graphical illustration of the principle of spin injection/detection is shown in Fig. 2.20 (b). By applying a dc bias voltage V_{bias} between the ring shaped gold contact and the cobalt electrode we can inject a spin polarized current from Co into ZnO (curved green arrows). The application of an external magnetic field, leads to a precession of the injected spins in ZnO (red arrows), which is possible due to the non vanishing angle between magnetization \mathbf{m}_{Co} and external magnetic field $\mu_0 \mathbf{H}$. The spot of a linearly polarized picosecond laserpulse, emitted by a frequency doubled Ti:Sa laser with tuneable wavelength λ , is positioned right on top of the cobalt electrode and allows for the detection of the spin polarization by measuring the rotation angle θ_K of the linear polarization of the reflected laser beam. By increasing the applied magnetic field, the spin polarization gets destroyed by the Hanle [136] effect. This loss of spin polarization can be detected by measuring θ_K as a function of the external applied field H . One should note that we require a finite angle between magnetization of the ferromagnet and external magnetic field for the precession of spins in ZnO. As the deposited Co layer exhibits no in-plane magnetic anisotropy, we have aligned the sample in a configuration, where the field includes an angle of 45° with the surface normal of the sample as illustrated in Fig. 2.20(c).

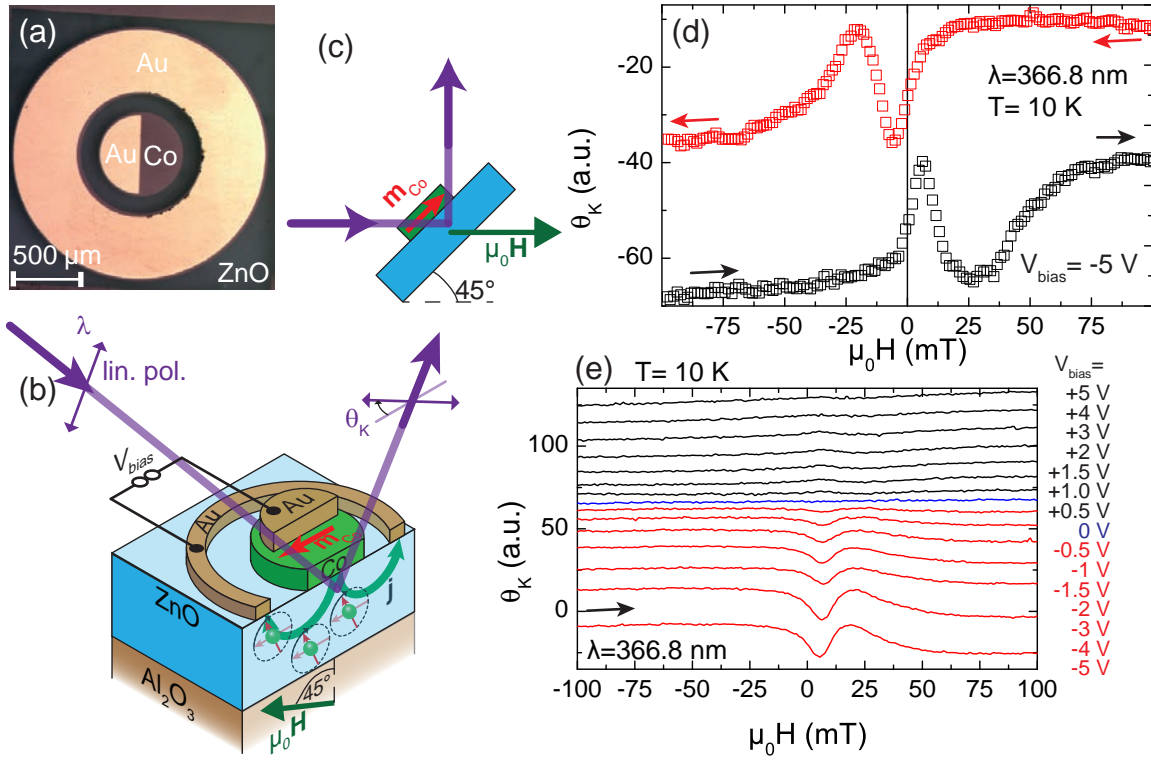


Figure 2.20: (a) Optical micrograph of the final mesa structure for electrical injection/optical detection experiments. (b) Illustration of the setup for Hanle MOKE measurements. By applying a bias voltage V_{bias} to the contact, a spin-polarized current j is injected into ZnO. Due to a non vanishing angle between external magnetic field and magnetization, the injected spins start to precess and dephase on shorter timescales for larger field values. The spin polarization is detected optically via the rotation of polarization direction of a reflected ps laser pulse. (c) Orientation of magnetization and external field in an oblique configuration. (d) Hanle MOKE signal for the upsweep (black squares) and downsweep (red squares) at $T = 10$ K, $\lambda = 366.8$ nm, and $V_{\text{bias}} = -5$ V. The sweep direction is indicated by black and red arrows. For both sweep directions the typical peak-dip structure is visible, which indicates successful spin injection into ZnO. (e) Bias dependence of the observed Hanle MOKE signal at $T = 10$ K, $\lambda = 366.8$ nm. The respective V_{bias} is given right of the graph. For positive V_{bias} the signal is very weak and vanishes completely for $V_{\text{bias}} = 0$ V. The signal increases in amplitude when going to negative bias voltages.

Due to the magnetic shape anisotropy of the thin film, the magnetization of the cobalt electrode will remain in the film plane, for $\mu_0 H \leq 300$ mT. This allows the decomposition of the magnetization into one component parallel (longitudinal) and one perpendicular (polar) to the external field. Only the polar component of the injected spins will precess and therefore dephase in ZnO, while the longitudinal component remains unaffected by the external field. The detection by MOKE will be sensitive to both spin components, but only the polar component is sensitive to the field magnitude, as long as the magnetization remains oriented in the same direction.

Experimental Hanle MOKE data obtained for our sample at $T = 10$ K, $\lambda = 366.8$ nm

and $V_{\text{bias}} = -5 \text{ V}$ are depicted in Fig. 2.20(d). The black symbols represent the data obtained when increasing the external magnetic field from -100 mT to 100 mT (upsweep) and the red symbols when decreasing the field from 100 mT to -100 mT (downsweep). Following the upsweep we observe a peak located at $\mu_0 H = 6.2 \text{ mT}$ followed by a dip at higher positive fields $\mu_0 H = 26.0 \text{ mT}$. For the downsweep we observe first a dip located at $\mu_0 H = -6.2 \text{ mT}$ and then a peak at $\mu_0 H = -20.3 \text{ mT}$. Comparing upsweep and downsweep, we note that the dip-peak structure is reversed. The origin of this reversal is due to different orientations of magnetization for up- and downsweep around $\mu_0 H = 0 \text{ mT}$, which leads to an inversion in the polar projection of the magnetization for the two sweep directions.

The observed peak in the upsweep and dip in the downsweep can be explained by the depolarization of the polar spins by the Hanle effect. By fitting a Lorentzian function to the peak, one can extract the FWHM ΔH of the peak/dip and calculate the spin dephasing time by:

$$T_2^* = \frac{2\hbar}{g\mu_B\Delta H}, \quad (2.4)$$

with $\hbar = h/(2\pi)$ the Planck constant, $g = 1.942$ the effective g-factor of the electrons, and μ_B Bohr magneton. From our experiment we extracted $T_2^* = 1 \text{ ns}$ [137].

The dip/peak for the up-/downsweep after the Hanle peak/dip originates from the reorientation of the magnetization at the coercive field $\mu_0 H_c = 16.3 \text{ mT}$. The coercive field has been determined by taking the average of the position for up- and downsweep and calculating the in-plane projection of this field for the given field configuration. The coercive field value is about a factor of 6 larger than values measured for the unstructured sample from in-plane SQUID magnetometry at $T = 10 \text{ K}$ (cf. Section 2.5.3). The reason for this increased coercive field value is currently unknown.

Interestingly, the maximum signal in the Hanle MOKE experiment has been obtained for $\lambda = 366.8 \text{ nm}$, which is not energetically related to any donor bound or free excitonic excitation in ZnO. A possible explanation will be discussed below, when we look at the wavelength dependence of the Hanle MOKE signal.

To prove that the observed Hanle MOKE signal is due to the injection of a spin-polarized current from the cobalt electrode into zinc oxide, we varied V_{bias} from -5 V to $+5 \text{ V}$, negative V_{bias} values represent an injection of spin-polarized electrons from Co into ZnO, positive values an extraction of spin-polarized electrons. The results are summarized in Fig.2.20(e) at $T = 10 \text{ K}$ and $\lambda = 366.8 \text{ nm}$, each line represents a different applied bias voltage measured for the upsweep. At $V_{\text{bias}} = 0 \text{ V}$ no field dependent signal is visible, which strongly suggests that the signal for non zero bias voltage is due to the injection/extraction of spin-polarized electrons in/from the zinc oxide. For negative V_{bias} the magnitude of the signal increases linearly, which is directly related to the increase in the number of spin-polarized electrons injected due to the higher electrical current flowing through the device. In case of positive V_{bias} , we see only a very weak signal, which is independent of the applied bias voltage. This clearly demonstrates that the extraction of spin polarized electrons is highly inefficient compared to the injection from the Co electrode into the ZnO.

From the TRFR measurements we already know that different excitonic states are reflected in the wavelength dependence of the TRFR signal. For a basic understanding of the underlying physics, it is therefore important to check, whether we can spin polarize these excitonic states via injecting a spin polarized current into the ZnO. For this we

conducted wavelength dependent Hanle MOKE measurements in oblique geometry at $T = 10$ K and $V_{\text{bias}} = -5$ V, a collection of the obtained data is shown in Fig. 2.21(a) for the magnetic field downsweep and (b) for the upsweep.

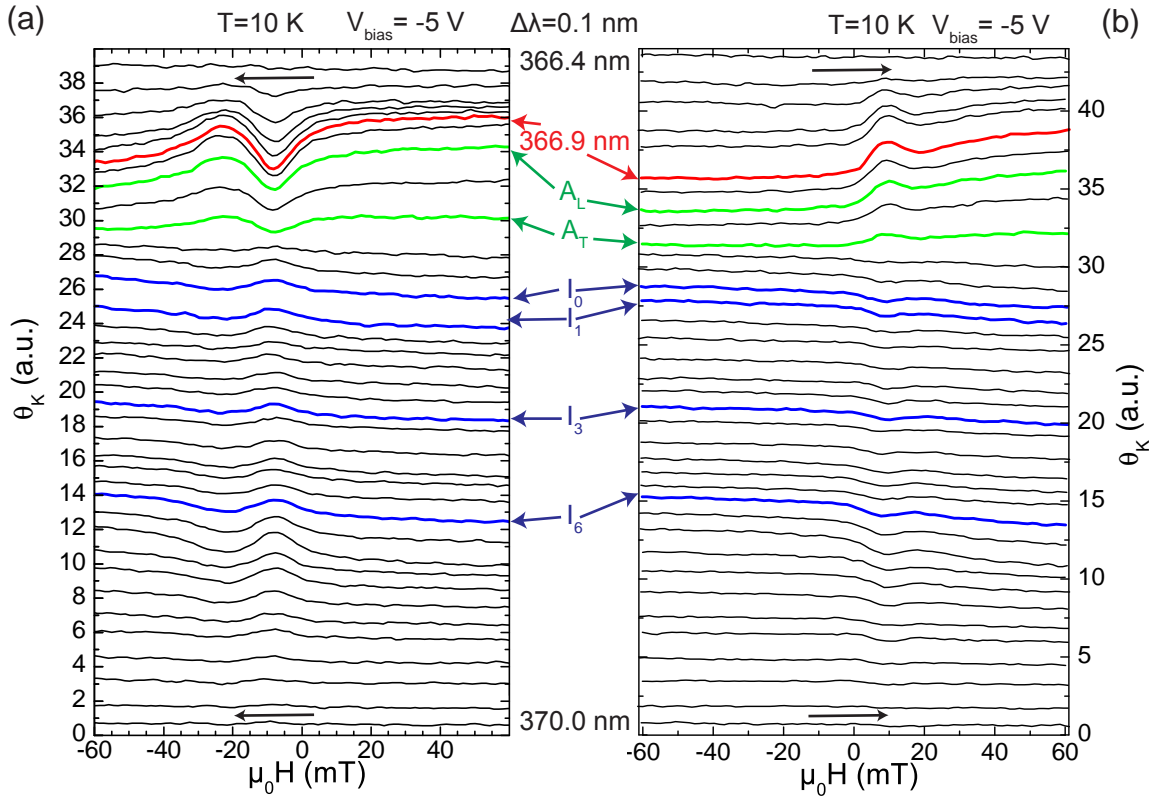


Figure 2.21: Wavelength dependence of the Hanle MOKE signal at $T = 10$ K for the downsweep (a) and upsweep (b) (sweep direction indicated by black arrows in the graph). Each line represents one detection wavelength going from 366.4 nm (top) to 370.0 nm (bottom) in 0.1 nm steps. The curves highlighted in blue and green represent detection wavelengths corresponding to excitation energies of donor bound and free excitons, labeled according to [131]. The red curves show the maximum Hanle MOKE signal at 366.9 nm (3.38 eV).

In each graph we highlighted the signal curves which probe donor bound excitons by coloring the line in blue, free excitons in green, and an energy of 3.38 eV in red. In both sweep directions, we can clearly see, that the signal is enhanced when the detection energy corresponds to an actual excitonic state or the high energy of 3.38 eV (see also Fig. 2.22(a)). This demonstrates that the spin-polarization injected by the ferromagnetic electrode is also transferred into the excitonic states of the zinc oxide. In other words, the spin information of the mobile electrons contributing to the electrical transport can be transferred to the localized excitonic states. A possible explanation is the trapping of conduction electrons in localized states. We have already shown in Fig. 2.19(b), that the long-lived spin storage has to be related to localized donor states. Another interesting feature is the inversion of the signal when lowering the detection wavelength below 368.6 nm. A possible explanation will be given below, when we discuss the quantitative wavelength dependence.

For each wavelength measured in Fig. 2.21(a),(b) we have extracted the amplitude $\Delta\theta_K$ of the Lorentzian peak/dip and calculated T_2^* from the FWHM. More precisely, the average of the values for up- and downsweep at each wavelength has been calculated. In addition, we measured for the very same sample TRFR as a function of wavelength at $T = 10$ K and $\mu_0 H = 500$ mT and extracted the amplitude $\Delta\theta_F$ and T_2^* from these measurements. The results are depicted in Fig. 2.22(a) and (b) respectively. The extracted T_2^* for Hanle MOKE is displayed in Fig. 2.22(c) and for TRFR in Fig. 2.22(d).

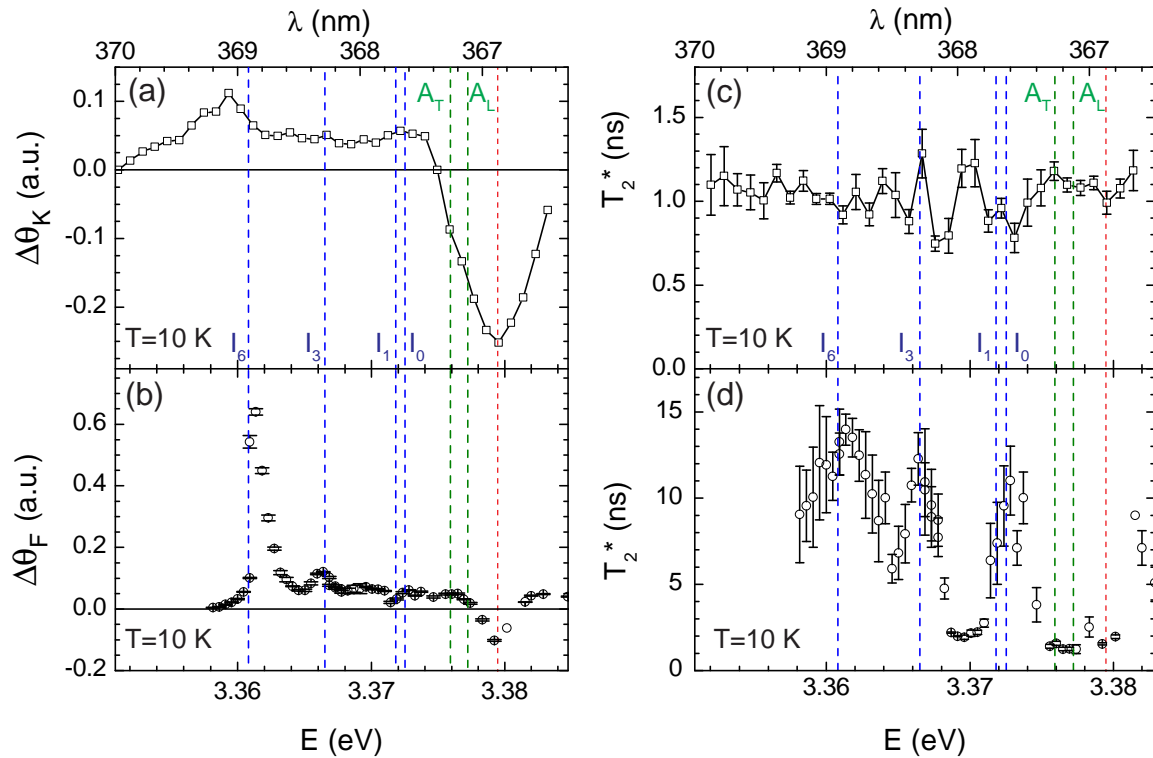


Figure 2.22: Comparison of the extracted wavelength dependence of (a) θ_K by Hanle MOKE and (b) θ_F by TRFR measured in the electrical spininjection sample at $T = 10$ K. The amplitude of both signals shows clear maxima at certain detection energies corresponding to the excitation of donor bound and free excitons. An additional maximum is visible at $E = 3.38$ meV which energetically corresponds to the Al donor level (binding energy 55 ± 5 meV). Evolution of the spin dephasing time extracted from Hanle MOKE (c) and TRFR (d) experiments. For the electrical injected spin polarization, T_2^* is independent of excitation energy. In contrast, the TRFR signal shows distinct maxima at energies corresponding to the excitation of donor bound and free excitons. Moreover, around $E = 3.38$ meV a maximum of T_2^* is visible in the TRFR experiments.

For the TRFR amplitude $\Delta\theta_F$ we observe the same behavior already found in zinc oxide alone, near excitation energies of donor bound excitons the amplitude assumes a maximum. (The corresponding states of donor bound excitons are indicated by blue dashed lines, those of free excitons by dashed green lines.) We have also increased the excitation energies to higher values and find a new increase in absolute amplitude near 366.8 nm (3.38 eV) indicated by the red dashed line, with a sign reversal. For the Hanle MOKE amplitude $\Delta\theta_K$ we also find a slight increase in amplitude at detection wave-

lengths correlated to donor bound excitons, but the feature is not as pronounced as in the TRFR data. But the increase in absolute amplitude at 366.8 nm and sign reversal is clearly visible. The corresponding excitation energy of 3.38 eV is about 50 meV below the band gap, which nicely corresponds to the donor binding energy of aluminium, and the separation to the I_6 related maxima is about 20 meV, which is nearly the value of the localization energy of 15.1 meV [131]. This leads us to the impression that the delocalized spin polarized electrons in the conduction band get partly trapped in localized Al donor states, which can then be detected by Hanle MOKE. In addition, the spin-polarization of the donor states influence the selection rules of the spin states of the donor bound exciton, which leads in the end to an antiparallel alignment of the trapped electron spin and the electron spin of the exciton, which might explain the change in the sign of the amplitude.

Interestingly the spin dephasing time from Hanle MOKE is constant over the whole wavelength interval measured. In contrast, we clearly observe maxima in spin dephasing time for the TRFR data, when resonantly exciting donor bound excitons. For a resonant excitation of the aluminium donor state at 3.38 eV we extract from TRFR experiments a low spin dephasing time of 1 ns (red dashed line in Fig. 2.22(d)). This value corresponds to the wavelength independent dephasing time of 1 ns for Hanle MOKE experiments. This strongly supports our assumption, that the mobile spin polarized electrons become trapped in localized, unoccupied Al donor states and influence then the excitons bound to an Al donor. This gives us the possibility to electrically address the Al donor related local storage of spin information by injection of a spin-polarized current into zinc oxide. Unfortunately, these results also show that our simple picture for the transfer of spin polarization from excitonic states to donor states in our TRFR experiments (see Fig. 2.19(b)) is not correct, as we find no enhancement in spin dephasing time for the electron donor state located at 3.38 eV. To this end we are unable to explain this enhancement in spin dephasing time indicated by our TRFR experiments. Hopefully, a deeper understanding of the underlying physics and a theoretical model will be obtained in the future. Nevertheless, the trapping of delocalized spin polarized electrons into donor states explains the observed wavelength dependence of the Hanle MOKE signal.

We expect that the trapping of conduction electrons must be temperature dependent, as on the one hand the time for the electron being trapped in the localized state will be reduced by increasing the thermal energy. On the other hand the existence of a higher number of ionized donors with increasing temperature leads to an increase in possible trapping sites. The competition between these two effects should lead to an optimum temperature at which the mechanism of transferring spin information from free conduction electrons into localized states is most efficient. To confirm this assumption we have carried out Hanle MOKE measurements as a function of temperature. In Fig. 2.23(a) the obtained signal is shown for the upswing at a detection wavelength of 366.8 nm. The extracted Kerr amplitude and T_2^* from these curves is shown in Fig. 2.23(b) and (c) respectively.

From the Hanle MOKE signal and the extracted θ_K we can deduce a maximum in signal amplitude for $T = 15$ K. Unfortunately, we could collect only one additional data set at lower temperatures, which makes the existence of the maximum in amplitude highly debatable. For temperatures above 30 K we could not detect any Hanle MOKE signal, which might either be attributed to the temperature related destruction of the transfer of spin information from mobile into localized states or the shift of the corresponding energy

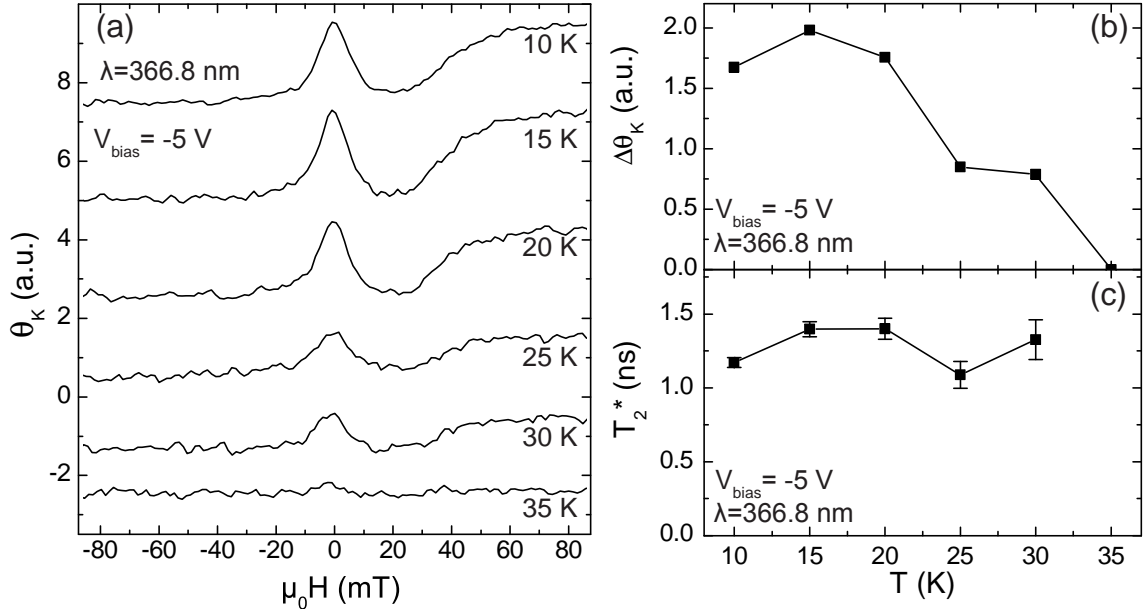


Figure 2.23: (a) Temperature dependent evolution of the upswEEP Hanle MOKE signal at $\lambda = 366.8$ nm. Each line represents a different temperature (curves have been offset for clarity). Extracted θ_K (b) and T_2^* (c) from these temperature dependent measurements for $\lambda = 366.8$ nm. The amplitude assumes a maximum at $T = 15$ K and then decreases for higher temperatures. The extracted spin dephasing time is independent of temperature.

of the donor states with temperature. Moreover, we find a constant spin dephasing time, which indicates under the assumption of the temperature dependence of the localization mechanism, that the spin dephasing time is not limited by the lifetime of the electron in the localized states but other spin dephasing mechanisms must dominate. By a deeper investigation of the dominating dephasing mechanism it might be possible to increase T_2^* up to the life time of the trapped electronic state.

In summary, our detection wavelength dependent Hanle MOKE experiments showed that by electrically injecting spin polarized mobile electrons into ZnO we can transfer spin information from mobile states into localized states. This mechanism might be explained in the picture of a trapping of mobile charge carriers in unoccupied localized donor states. This mechanism can explain the observed wavelength dependence and sign reversal of the Kerr amplitude. Further this localization of spin information is only efficient at low temperatures and is thermally destroyed at $T > 30$ K. A possible way of improving the temperature dependence is the use of deep acceptor states (for example lithium in ZnO [138]) to trap the mobile charge carriers by a first optical depletion of these states and then localizing the spin information. This mechanism is efficient at elevated temperatures and might allow the electrical, localized storage of spin information at even higher temperatures. Moreover, a time-resolved investigation of this localization mechanism by pulsed electrical injection and variable delayed optical detection might allow a deeper insight into the mechanisms involved.

2.5 All-electrical injection and detection of spin transport in ZnO

From the results of section 2.4 we already know that it is possible to electrically inject spin-polarized carriers via a ferromagnetic cobalt electrode into ZnO. But our results from TRFR and Hanle MOKE experiments using an optical detection scheme also suggest that we investigate the spin dephasing times of localized electron states, rather than the spin dephasing times of the delocalized conduction electrons. Thus we will put our focus in this chapter on an all electrical injection and detection scheme based on a vertical spin valve trilayer exhibiting a giant magnetoresistance (GMR) effect, which enables us to directly investigate the spin dephasing of the conduction electrons in ZnO. The trilayer consists of two ferromagnetic electrodes (cobalt and nickel) separated by a ZnO spacer layer (cf. Fig. 2.25). By measuring the magnetoresistance (MR) as a function of the ZnO thickness and fitting the obtained data with the Valet-Fert model [139] it is possible to extract the spin diffusion length of the ZnO thin film. In the following, we will first present the theoretical model to describe the observed giant magnetoresistance effect, then present the experimental transport data and corresponding fits to the model. In the end the obtained parameters for spin dependent transport in ZnO will be compared to the data obtained from the optical TRFR measurements.

2.5.1 Introduction into giant magnetoresistance

The giant magnetoresistance (GMR) effect³ and its application are one of the most prominent success stories in the field of spinelectronics, which in the end led to the Nobel prize in 2007 for Albert Fert and Peter Grünberg. Only a decade after the discovery of GMR in 1988 [2, 3] devices based on this phenomenon were commercially available, such as hard disk read-heads, magnetic field sensors and magnetic memory chips. This seminal achievement would have been impossible without a fundamental understanding of the GMR effect and its underlying physics based on spin-dependent transport in magnetic structures. The discovery of GMR was linked to the huge progress in thin film fabrication in the late 1980s, which made it possible to grow multilayer systems of different materials with a high precision in thickness. A typical sample for GMR consists of two ferromagnetic layers separated by a non-magnetic, metallic layer.

For the observation of GMR one has to provide a possibility to reorient the magnetic moments of the ferromagnetic layers with respect to one another. This can be achieved for example by introducing different coercivities of the ferromagnetic layers as illustrated in Fig. 2.24(a) for the simple case of two ferromagnetic layers sandwiching a non-magnetic layer. As it is evident from the magnetization versus applied magnetic field ($M(H)$) curve in the figure, the two ferromagnets possess two different coercive fields $H_{c1} < H_{c2}$. If one follows the orientation of the two magnetizations from large positive fields to large negative fields (down sweep), the two magnetizations $\mathbf{M}_1, \mathbf{M}_2$ (each depicted by one of the red arrows) of the ferromagnetic layers will first be aligned parallel for a large external magnetic field H ($H_{c2} \ll H$). When one sweeps the field to negative values

³In principle the GMR effect is only observed in ferromagnetic layers that are coupled antiferromagnetically to each other and with a normal metal sandwiched between these two FMs. In the following, we will investigate spin valve structures (decoupled FM layers), but will equivalently use the term GMR for these structures.

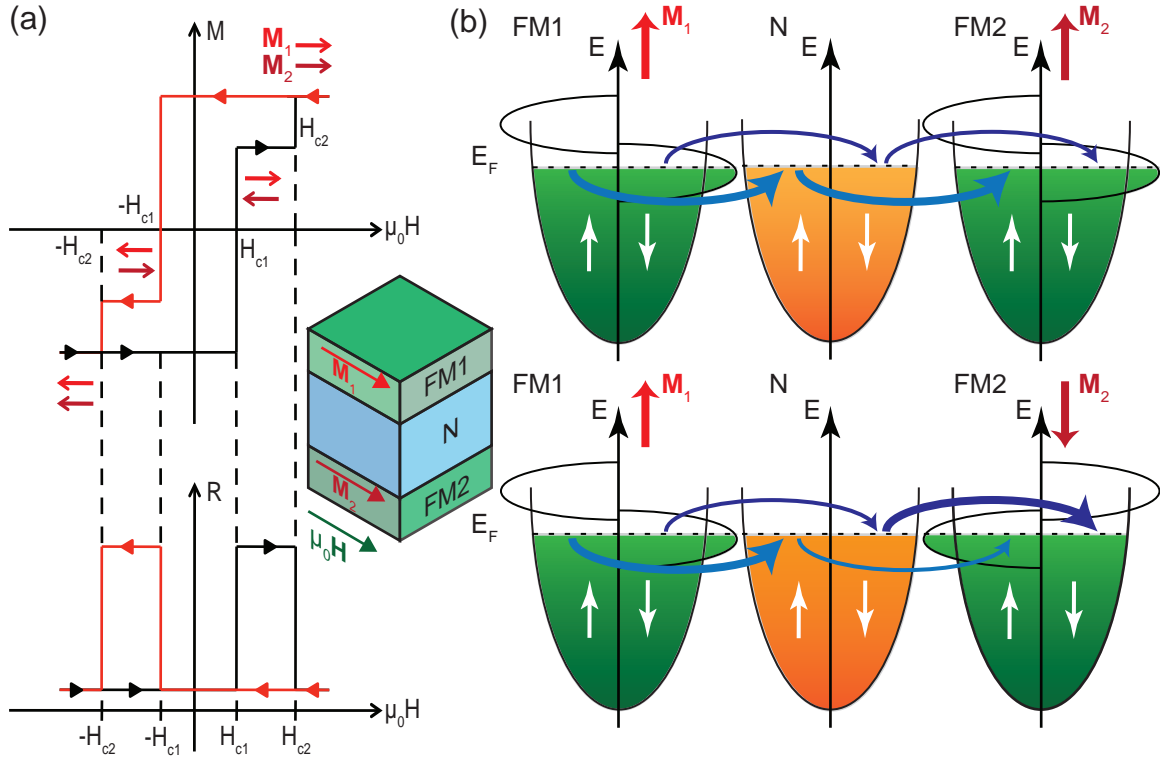


Figure 2.24: Illustration of the spin valve effect. (a) $M(H)$ loop of a spin valve system. The two ferromagnetic layers switch magnetization direction (red arrows) at different external magnetic fields. For fields in the range of $H_{c1} \leq H \leq H_{c2}$ and $-H_{c2} \leq H \leq -H_{c1}$ the two magnetizations are aligned in an antiparallel configuration. The resulting $R(H)$ curve exhibits a sharp increase in resistance, when the magnetization are aligned antiparallel. (b) Illustration of the origin of the increased resistance for antiparallel magnetization alignment in a two spin current model. Due to the increased density of states at the Fermi energy for one spin species, the scattering rate is increased leading to a lower current. The thick arrows connecting the density of states indicate a high conductivity (low scattering rate) for the spin species. Accordingly, the thin arrows indicate a low conductivity (high scattering rate).

$-H_{c2} < H < -H_{c1}$, \mathbf{M}_1 will change its direction and the two magnetizations are aligned antiparallel. For larger negative fields $-H_{c2} \gg H$, \mathbf{M}_2 will also be reoriented parallel to the applied field leading again to a parallel alignment of the magnetizations. If one then reverses the sweep direction of the external magnetic field, an antiparallel alignment can be achieved for $\mu_0 H_{c1} < \mu_0 H < \mu_0 H_{c2}$.

The two different relative orientations of the magnetizations (parallel or antiparallel) are also evident in resistance versus applied magnetic field ($R(H)$) measurements. One observes a high resistance state for an antiparallel alignment of \mathbf{M}_1 and \mathbf{M}_2 , and a low resistance state for parallel alignment. The resistance change ΔR is of the order of 10...100% of R [2, 3]. ΔR is at least one order of magnitude larger than the few percent change expected from anisotropic magnetoresistance. This giant change in resistance as a function of applied magnetic field coined the term GMR.

The two different resistance states depending on the relative orientation of the two mag-

netizations can most easily be understood within a two-current spin dependent transport formalism already proposed by Mott [140]. In this model, one divides the current transported through the structure into two spin channels, one for spin up and one for spin down electrons. Spin-flip processes are neglected, such that each spin channel can be treated individually. In addition, for ferromagnetic metals, the scattering rates of spin up and spin down electrons are quite different. One explanation for this phenomenon is the role of the d-bands as additional final states for scattered electrons carrying the electrical current. In ferromagnetic metals the d-bands are exchange split leading to a different density of states at the Fermi energy for spin up and spin down electrons as depicted in Fig. 2.24(b).

We first consider the case for parallel alignment of the ferromagnetic electrodes. The illustration shows that the spin-up electrons are scattered strongly (thin curved arrows) while the spin-down electrons are only scattered weakly (thick curved arrows). Since the two spin channels can be considered as a parallel resistor network, the highly conducting spin-down channel leads to a low total resistance of the device. In contrast, if we consider the antiparallel case, both spin species will be scattered strongly in one of the ferromagnetic layers leading to a high total resistance of the multilayer.

The investigation of GMR started with metal-based multilayer systems. In later studies the non-magnetic spacer layer has been replaced by semiconducting materials [141–144], with the aim to integrate GMR devices into established semiconductor fabrication techniques and to provide an effective mechanism for spin injection into semiconductors for novel devices such as the spin transistor or spin-light emitting diode. Different semiconductor materials have been successfully used as the spacer layer in GMR based devices, among them ZnO [100–103]. Although these publications all prove that it is possible to transport a spin polarized current through the ZnO layer even at room temperature [101–103], only little quantitative information on the spin dependent transport parameters, e.g. the spin diffusion length λ_{sf} , is to be found in those publications. This is mainly due to the limited ZnO layer thickness range ($1.3 \text{ nm} \leq t \leq 10 \text{ nm}$) of the ZnO layer studied, prohibiting a systematical evaluation of the measured MR data. An important goal of this thesis thus was to fabricate epitaxial ferromagnet/semiconductor spin valve systems based on cobalt, zinc oxide, and nickel with different ZnO thicknesses and to extract quantitative information on the spin dependent transport in these structures.

For the data analysis, we rely on a full quantitative model based solely on material parameters for GMR in ferromagnet/semiconductor heterostructures, described in the following.

2.5.2 Theory of giant magnetoresistance

After the discovery of the GMR effects in metallic multilayers [2, 3] many different theoretical models have been proposed to describe quantitatively the experimental data obtained for current flowing in the plane of the layers (CIP) [145, 146] and also for current perpendicular to the plane (CPP) [139, 147–150]. We will use the approach of Valet and Fert [139]. In this macroscopic model the spin diffusion in a multilayer stack of materials is characterized by spin diffusion equations. We here consider interfaces parallel to the xy plane and a current density J parallel to the z axis (see Fig. 2.25). The spin diffusion in this multilayer structure is driven by differences in electrochemical potentials $\Delta\mu = (\mu_{\uparrow} - \mu_{\downarrow})/2$ for charge carriers with spin $+1/2$ and $-1/2$. The subscripts used

here refer to the carriers with spins up and down, respectively. Thus the spin diffusion equation can be written as:

$$\frac{\partial^2 \Delta\mu}{\partial z^2} = \frac{\Delta\mu}{\lambda_{sf}^2}. \quad (2.5)$$

The parameter λ_{sf} is called the spin diffusion length and is related to the spin relaxation time τ_{sf} and the density of carriers for nondegenerate semiconductors as follows [151, 152]:

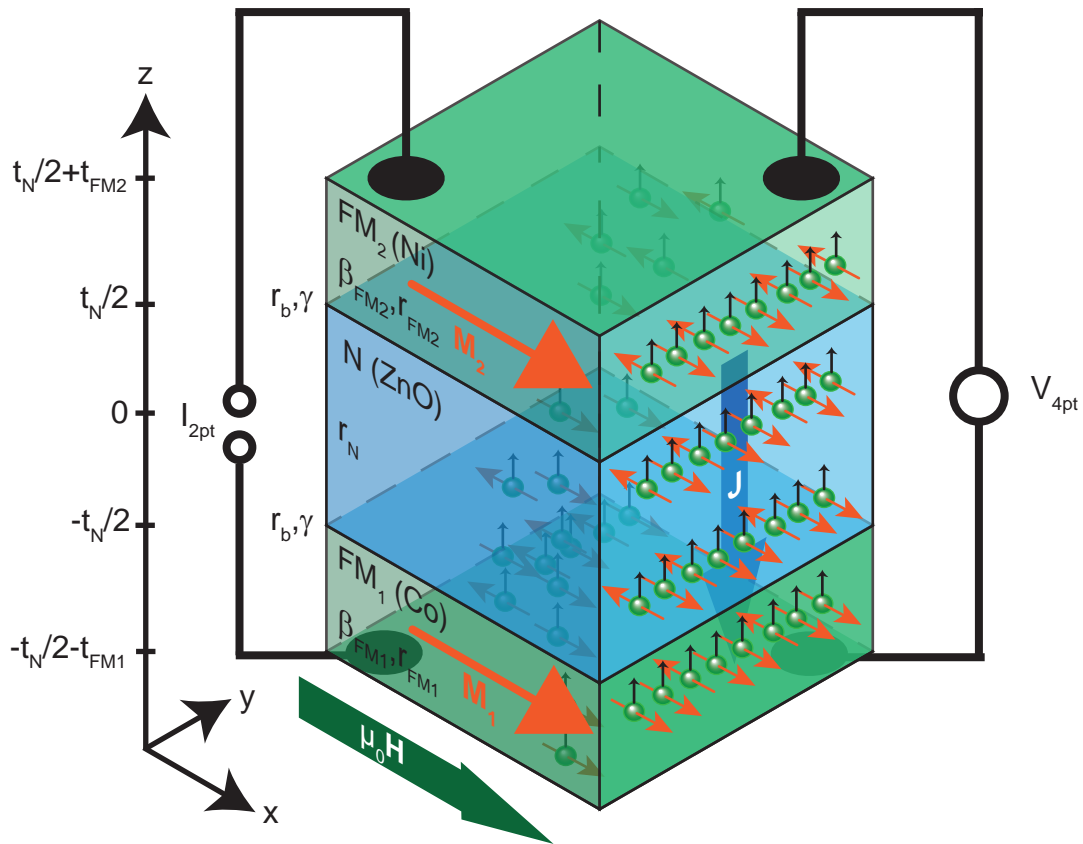


Figure 2.25: Schematic drawing of the structure of a trilayer for the observation of the GMR effect. The trilayer consists of two ferromagnetic layers separated by a non-ferromagnetic spacer layer. Using electrical contacts at the top and bottom of the structure one can drive an electrical current perpendicular to the layers along the z direction (cpp-geometry). The measured resistance is a function of the orientation of the magnetizations of two ferromagnetic layers. The spin dependent transport through the structure depends on the material parameters of the ferromagnetic layers, the non-ferromagnetic spacer layer and the interface between them. Large red arrows represent the magnetization of each ferromagnetic layer M_1 , M_2 . The green spheres represent electrons with spin direction (red arrows) and direction of movement (black arrows). For an explanation of the parameters see text.

$$\lambda_{\text{sf}} = \sqrt{\frac{\ell \ell_{\text{sf}}}{6}} = \sqrt{\frac{k_{\text{B}} T \tau_{\text{sf}}}{2n e^2 \rho}}, \quad (2.6)$$

The spin diffusion length is determined by the transport mean free path $\ell = \sqrt{\langle v^2 \rangle} \tau$ and the spin-flip length $\ell_{\text{sf}} = \sqrt{\langle v^2 \rangle} \tau_{\text{sf}}$, where τ is the mean free time between collisions, which can be derived from ρ using the simple Drude relation $\tau = \frac{m^*}{n e^2 \rho}$ and $\langle v^2 \rangle$ is the mean square velocity of the charge carriers, which can be calculated for a nondegenerate semiconductor using the thermal energy $\langle v^2 \rangle = 3k_{\text{B}}T/m^*$. Here k_{B} is the Boltzmann constant, T is the absolute temperature, e the elementary charge, n the carrier concentration and ρ the resistivity of the material⁴. Note that the additional factor of 1/2 in Eq.(2.6) is due to the two spin species considered (cf. [152]).

In addition to the spin diffusion equation, current continuity is also maintained in the trilayer:

$$\frac{\partial(J_{\uparrow} - J_{\downarrow})}{\partial z} = \frac{\partial^2(\sigma_{\uparrow}\mu_{\uparrow} + \sigma_{\downarrow}\mu_{\downarrow})}{\partial z^2} = 0, \quad (2.7)$$

with σ_{\uparrow} and σ_{\downarrow} being the conductivities for carriers with spins up and down respectively. The spin dependent conductivities can be expressed in terms of a spin dependent parameter β (This parameter is related to the spin polarization of the ferromagnet) and a resistivity parameter ρ :

$$\frac{1}{\sigma_{\uparrow(\downarrow)}} = 2\rho[1 - (+)\beta] = \rho_{\uparrow(\downarrow)}. \quad (2.8)$$

With the general solutions for the spin diffusion equation and current continuity provided in [139] we can now describe the spin dependent electrochemical potential $\mu_{\uparrow(\downarrow)}$ by

$$\begin{aligned} \mu_{\uparrow(\downarrow)}^{\text{FM1}}(z) &= [1 - \beta_{\text{FM1}}]^2 e \rho_{\text{FM1}} J[z - z_{\text{FM1}}] + K_1^{\text{FM1}} + (-)[1 + (-)\beta_{\text{FM1}}] \times \\ &\times \left[K_2^{\text{FM1}} \exp\left\{\frac{z - z_{\text{FM1}}}{\lambda_{\text{sf}}^{\text{FM1}}}\right\} + K_3^{\text{FM1}} \exp\left\{-\frac{z - z_{\text{FM1}}}{\lambda_{\text{sf}}^{\text{FM1}}}\right\} \right], \end{aligned} \quad (2.9)$$

while the current density $J_{\uparrow(\downarrow)}$ is given by

$$\begin{aligned} J_{\uparrow(\downarrow)}^{\text{FM1}}(z) &= [1 - (+)\beta_{\text{FM1}}] \frac{J}{2} + (-) \frac{1}{2e\rho_{\text{FM1}}\lambda_{\text{sf}}^{\text{FM1}}} \times \\ &\times \left[K_2^{\text{FM1}} \exp\left\{\frac{z - z_{\text{FM1}}}{\lambda_{\text{sf}}^{\text{FM1}}}\right\} - K_3^{\text{FM1}} \exp\left\{-\frac{z - z_{\text{FM1}}}{\lambda_{\text{sf}}^{\text{FM1}}}\right\} \right], \end{aligned} \quad (2.10)$$

and the difference in spin dependent electrochemical potential reads

$$\begin{aligned} \Delta\mu^{\text{FM1}}(z) &= \frac{1}{2}[\mu_{\uparrow}^{\text{FM1}}(z) - \mu_{\downarrow}^{\text{FM1}}(z)] = \\ &= \left[K_2^{\text{FM1}} \exp\left\{\frac{z - z_{\text{FM1}}}{\lambda_{\text{sf}}^{\text{FM1}}}\right\} + K_3^{\text{FM1}} \exp\left\{-\frac{z - z_{\text{FM1}}}{\lambda_{\text{sf}}^{\text{FM1}}}\right\} \right], \end{aligned} \quad (2.11)$$

⁴Using this formula and the parameters obtained from TDH and TRFR experiments ($T = 10$ K, $n = 3 \times 10^{17} \text{ cm}^{-3}$, $\rho = 0.027 \Omega\text{m}$) we calculate a spin diffusion length of 27 nm for our laser-MBE ZnO thin films. This value is relative small compared to $3 \mu\text{m}$ for Si [153] ($T = 10$ K, $n = 5 \times 10^{19} \text{ cm}^{-3}$ at room temperature) and $11 \mu\text{m}$ for GaAs [135] ($T = 4$ K, $n = 2 \times 10^{16} \text{ cm}^{-3}$ at room temperature). This lower value for ZnO is mainly due to the low electron mobility of our samples.

for the first ferromagnetic layer. Here $z_{\text{FM1}} = (-t_{\text{N}} - t_{\text{FM1}})/2$ is the middle of the first ferromagnetic layer in z direction, where t_{N} and t_{FM1} are the thicknesses of the N layer and the FM1 layer, respectively. K_1^{FM1} , K_2^{FM1} , and K_3^{FM1} are constants, which will be calculated from the boundary conditions, i.e., the continuity conditions to the next layer. The parameters β_{FM1} , ρ_{FM1} , and $\lambda_{\text{sf}}^{\text{FM1}}$ are the material constants of the FM1 layer.

Following the same scheme for the non ferromagnetic layer N we obtain:

$$\begin{aligned} \mu_{\uparrow(\downarrow)}^{\text{N}}(z) &= e\rho_{\text{N}}J[z - z_{\text{N}}] + K_1^{\text{N}} + (-)1 \times \\ &\times \left[K_2^{\text{N}} \exp\left\{\frac{z - z_{\text{N}}}{\lambda_{\text{sf}}^{\text{N}}}\right\} + K_3^{\text{N}} \exp\left\{-\frac{z - z_{\text{N}}}{\lambda_{\text{sf}}^{\text{N}}}\right\} \right] \end{aligned} \quad (2.12)$$

$$\begin{aligned} J_{\uparrow(\downarrow)}^{\text{N}}(z) &= \frac{J}{2} + (-)\frac{1}{2e\rho_{\text{N}}\lambda_{\text{sf}}^{\text{N}}} \times \\ &\times \left[K_2^{\text{N}} \exp\left\{\frac{z - z_{\text{N}}}{\lambda_{\text{sf}}^{\text{N}}}\right\} - K_3^{\text{N}} \exp\left\{-\frac{z - z_{\text{N}}}{\lambda_{\text{sf}}^{\text{N}}}\right\} \right] \end{aligned} \quad (2.13)$$

$$\Delta\mu^{\text{N}}(z) = \left[K_2^{\text{N}} \exp\left\{\frac{z - z_{\text{N}}}{\lambda_{\text{sf}}^{\text{N}}}\right\} + K_3^{\text{N}} \exp\left\{-\frac{z - z_{\text{N}}}{\lambda_{\text{sf}}^{\text{N}}}\right\} \right]. \quad (2.14)$$

For the N layer $z_{\text{N}} = 0$, according to our chosen coordinate system (cf. Fig. 2.25). In addition the constants K_1^{N} , K_2^{N} , and K_3^{N} can be later calculated from the set of equations describing the boundary conditions of the trilayer system. The two material parameters ρ_{N} and $\lambda_{\text{sf}}^{\text{N}}$ will depend on the material used for the N layer.

In the end, we obtain for the second ferromagnetic layer FM2 for the electrochemical potential and the current density:

$$\begin{aligned} \mu_{\uparrow(\downarrow)}^{\text{FM2}}(z) &= [1 - \beta_{\text{FM2}}]^2 e\rho_{\text{FM2}}J[z - z_{\text{FM2}}] + K_1^{\text{FM2}} + (-)[1 + (-)\beta_{\text{FM2}}] \times \\ &\times \left[K_2^{\text{FM2}} \exp\left\{\frac{z - z_{\text{FM2}}}{\lambda_{\text{sf}}^{\text{FM2}}}\right\} + K_3^{\text{FM2}} \exp\left\{-\frac{z - z_{\text{FM2}}}{\lambda_{\text{sf}}^{\text{FM2}}}\right\} \right] \end{aligned} \quad (2.15)$$

$$\begin{aligned} J_{\uparrow(\downarrow)}^{\text{FM2}}(z) &= [1 - (+)\beta_{\text{FM2}}] \frac{J}{2} + (-)\frac{1}{2e\rho_{\text{FM2}}\lambda_{\text{sf}}^{\text{FM2}}} \times \\ &\times \left[K_2^{\text{FM2}} \exp\left\{\frac{z - z_{\text{FM2}}}{\lambda_{\text{sf}}^{\text{FM2}}}\right\} - K_3^{\text{FM2}} \exp\left\{-\frac{z - z_{\text{FM2}}}{\lambda_{\text{sf}}^{\text{FM2}}}\right\} \right] \end{aligned} \quad (2.16)$$

$$\Delta\mu^{\text{FM2}}(z) = \left[K_2^{\text{FM2}} \exp\left\{\frac{z - z_{\text{FM2}}}{\lambda_{\text{sf}}^{\text{FM2}}}\right\} + K_3^{\text{FM2}} \exp\left\{-\frac{z - z_{\text{FM2}}}{\lambda_{\text{sf}}^{\text{FM2}}}\right\} \right]. \quad (2.17)$$

Here $z_{\text{FM2}} = (t_{\text{N}} + t_{\text{FM2}})/2$ and the other parameters K_1^{FM2} , K_2^{FM2} , K_3^{FM2} , β_{FM2} , ρ_{FM2} , and $\lambda_{\text{sf}}^{\text{FM2}}$ are analogous to the FM1 layer. All equations hold for a parallel alignment of the two ferromagnetic layers FM1 and FM2, for an antiparallel alignment one has to simply exchange $\mu_{\uparrow}^{\text{FM2}}$ with $\mu_{\downarrow}^{\text{FM2}}$ and vice versa (Same applies for $J_{\uparrow}^{\text{FM2}}$ and $J_{\downarrow}^{\text{FM2}}$).

As already pointed out in the paragraphs before, the constants K_1^{i} , K_2^{i} , and K_3^{i} (i ∈ {FM1, N, FM2}) need to be calculated from a set of equations describing the boundary conditions. For parallel alignment of the two ferromagnetic electrodes we obtain the following set of equations assuming current continuity and an electrochemical potential

difference proportional to the interface resistance parameters r_b and γ :

$$\begin{aligned}
K_1^{\text{FM1}} &= 0 \\
K_3^{\text{FM1}} &= 0 \\
K_2^{\text{FM2}} &= 0 \\
\mu_{\uparrow}^{\text{N}}(-\frac{t_{\text{N}}}{2}) - \mu_{\uparrow}^{\text{FM1}}(-\frac{t_{\text{N}}}{2}) &= 2er_b(1 - \gamma)J_{\uparrow}^{\text{FM1}}(-\frac{t_{\text{N}}}{2}) \\
\mu_{\downarrow}^{\text{N}}(-\frac{t_{\text{N}}}{2}) - \mu_{\downarrow}^{\text{FM1}}(-\frac{t_{\text{N}}}{2}) &= 2er_b(1 + \gamma)J_{\downarrow}^{\text{FM1}}(-\frac{t_{\text{N}}}{2}) \\
J_{\uparrow}^{\text{N}}(-\frac{t_{\text{N}}}{2}) - J_{\downarrow}^{\text{N}}(-\frac{t_{\text{N}}}{2}) &= J_{\uparrow}^{\text{FM1}}(-\frac{t_{\text{N}}}{2}) - J_{\downarrow}^{\text{FM1}}(-\frac{t_{\text{N}}}{2}) \\
\mu_{\uparrow}^{\text{FM2}}(\frac{t_{\text{N}}}{2}) - \mu_{\uparrow}^{\text{N}}(\frac{t_{\text{N}}}{2}) &= 2er_b(1 - \gamma)J_{\uparrow}^{\text{N}}(\frac{t_{\text{N}}}{2}) \\
\mu_{\downarrow}^{\text{FM2}}(\frac{t_{\text{N}}}{2}) - \mu_{\downarrow}^{\text{N}}(\frac{t_{\text{N}}}{2}) &= 2er_b(1 + \gamma)J_{\downarrow}^{\text{N}}(\frac{t_{\text{N}}}{2}) \\
J_{\uparrow}^{\text{FM2}}(\frac{t_{\text{N}}}{2}) - J_{\downarrow}^{\text{FM2}}(\frac{t_{\text{N}}}{2}) &= J_{\uparrow}^{\text{N}}(\frac{t_{\text{N}}}{2}) - J_{\downarrow}^{\text{N}}(\frac{t_{\text{N}}}{2}).
\end{aligned} \tag{2.18}$$

The conditions for K_3^{FM1} and K_2^{FM2} are obtained for a semi infinite ferromagnetic layer where $\Delta\mu$ vanishes for $z \rightarrow \pm\infty$. $K_1^{\text{FM1}} = 0$ can be used without loss of generality. The interface resistance area product r_b and the spin selectivity parameter γ describe a spin dependent scattering at the interface between two adjacent layers and lead to a discontinuity in the electrochemical potentials. These parameters are defined in analogy to Eq.(2.8) and for $\gamma = 0$ the discontinuity is identical for spin-up and spin-down electrochemical potential. We will show later that these spin dependent discontinuities will lead to an enhancement of the measured MR and the spin polarized current density in the N layer, for a trilayer with large conductivity mismatch ($\rho_{\text{N}}\lambda_{\text{sf}}^{\text{N}} \gg \rho_{\text{FM}}\lambda_{\text{sf}}^{\text{FM}}$) [31] as it is the case for a trilayer consisting of ferromagnetic metals and a semiconductor spacer layer. For an antiparallel alignment of the two ferromagnetic layers the first 6 equations remain unchanged, while the last 3 change to:

$$\begin{aligned}
K_1^{\text{FM1}} &= 0 \\
K_3^{\text{FM1}} &= 0 \\
K_2^{\text{FM2}} &= 0 \\
\mu_{\uparrow}^{\text{N}}(-\frac{t_{\text{N}}}{2}) - \mu_{\uparrow}^{\text{FM1}}(-\frac{t_{\text{N}}}{2}) &= 2er_b(1 - \gamma)J_{\uparrow}^{\text{FM1}}(-\frac{t_{\text{N}}}{2}) \\
\mu_{\downarrow}^{\text{N}}(-\frac{t_{\text{N}}}{2}) - \mu_{\downarrow}^{\text{FM1}}(-\frac{t_{\text{N}}}{2}) &= 2er_b(1 + \gamma)J_{\downarrow}^{\text{FM1}}(-\frac{t_{\text{N}}}{2}) \\
J_{\uparrow}^{\text{N}}(-\frac{t_{\text{N}}}{2}) - J_{\downarrow}^{\text{N}}(-\frac{t_{\text{N}}}{2}) &= J_{\uparrow}^{\text{FM1}}(-\frac{t_{\text{N}}}{2}) - J_{\downarrow}^{\text{FM1}}(-\frac{t_{\text{N}}}{2}) \\
\mu_{\downarrow}^{\text{FM2}}(\frac{t_{\text{N}}}{2}) - \mu_{\uparrow}^{\text{N}}(\frac{t_{\text{N}}}{2}) &= 2er_b(1 + \gamma)J_{\uparrow}^{\text{N}}(\frac{t_{\text{N}}}{2}) \\
\mu_{\uparrow}^{\text{FM2}}(\frac{t_{\text{N}}}{2}) - \mu_{\downarrow}^{\text{N}}(\frac{t_{\text{N}}}{2}) &= 2er_b(1 - \gamma)J_{\downarrow}^{\text{N}}(\frac{t_{\text{N}}}{2}) \\
J_{\downarrow}^{\text{FM2}}(\frac{t_{\text{N}}}{2}) - J_{\uparrow}^{\text{FM2}}(\frac{t_{\text{N}}}{2}) &= J_{\uparrow}^{\text{N}}(\frac{t_{\text{N}}}{2}) - J_{\downarrow}^{\text{N}}(\frac{t_{\text{N}}}{2}).
\end{aligned} \tag{2.19}$$

With those two sets of equations it is possible to calculate the parameters K_1^i , K_2^i , and K_3^i in each layer for both parallel and antiparallel alignment of the ferromagnetic electrodes. The mathematica source code used for this calculation can be found in Appendix C. For a more complex layer structure, it is possible to use a transfer matrix formalism to describe the connection conditions between each layer [154]. After solving the boundary conditions Eq.(2.18) and (2.19), the spin dependent chemical potentials and current densities only depend on material parameters.

In Fig. 2.26(a)-(d) we have plotted the corresponding chemical potentials and current densities as a function of z , for the material parameters given in the caption. For parallel alignment of the magnetizations of the ferromagnetic layers the calculated electrochemical potentials μ_\uparrow (black line) and μ_\downarrow (red dashed line) in Fig. 2.26(a) have a crossing point at $z = 0$ nm for $r_b = 2.5$ n Ω m². This results in a change of sign for $\Delta\mu$, which leads to a minimum for the spin polarization at $z = 0$ nm as can be seen in Fig. 2.26(c). Moreover, the discontinuity at the interface due the interface resistance parameter and interface selectivity parameter are evident from the graph. Note that the changes at the two interfaces are identical for μ_\uparrow and also for μ_\downarrow . Moreover, due to the linear scale and domination of the spacer layer the change in electrochemical potentials for spin-up and spin-down in the two ferromagnetic layers is not visible in the graph.

For $r_b = 0$ the influence of the large conductivity mismatch ($\rho_N \lambda_{sf}^N \gg \rho_{FM} \lambda_{sf}^{FM}$) of the used parameters can be seen in the identical evolution of μ_\uparrow (grey line) and μ_\downarrow (green dashed line) in Fig. 2.26(a). Thus the difference in spin dependent electrochemical potentials is zero for $r_b = 0$ and the current spin polarization in the N-layer is zero (cf. Fig. 2.26(c) grey curve.) This shows how important the interface parameters are for the observation of a GMR effect in a trilayer structure with a large conductivity mismatch.

Looking now at the spin dependent electrochemical potentials for antiparallel alignment of the ferromagnetic electrodes the difference in electrochemical potentials is nearly constant through the whole N-layer (Fig. 2.26(b)). This is due to the fact that the discontinuity in potential at the two interfaces interchanges between μ_\uparrow (black line) and μ_\downarrow (dashed red line). The current spin polarization for antiparallel arrangement is depicted in Fig. 2.26(d) (black curve), and shows a sign change at the middle of the N-layer.

Using the solutions obtained it is now possible to calculate the magnetoresistance of the trilayer structure. From the electrochemical potentials we can define a corresponding electric field $F(z)$:

$$F(z) = \frac{1}{e} \frac{\partial(\mu_\uparrow + \mu_\downarrow)/2}{\partial z}, \quad (2.20)$$

Applying this expression to the equations of the electrochemical potentials for the trilayer

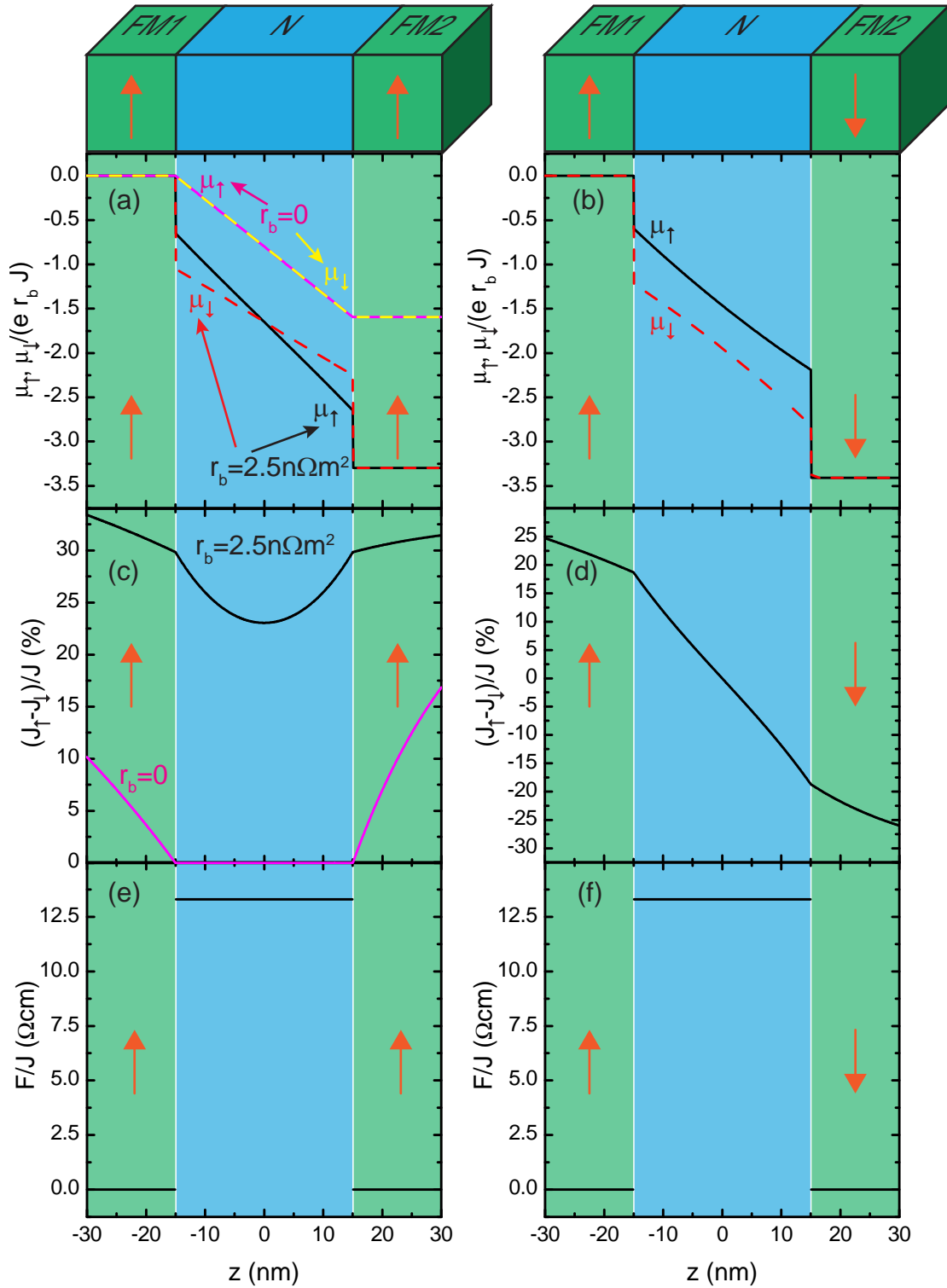


Figure 2.26: Calculated and normalized spin dependent electrochemical potentials μ_{\uparrow} , μ_{\downarrow} for (a) parallel and (b) antiparallel alignment of the FM electrodes along the z direction. Panels (c) and (d) show then the spinpolarization of the electrical current through the structure for parallel (c) and antiparallel (d) alignment calculated from the Valet-Fert-model. For $r_b = 0$ the spinpolarization in the N layer vanishes. Panels (e) and (f) show the corresponding electrical field for parallel (e) and antiparallel (f) magnetization alignment of FM1 and FM2. For the calculation we have used: $t_N = 30$ nm, $t_{\text{FM1}} = t_{\text{FM2}} = 15$ nm, $\rho_{\text{FM1}} = 75$ n Ωm , $\beta_{\text{FM1}} = -0.46$, $\lambda_{\text{sf}}^{\text{FM1}} = 60$ nm, $\rho_{\text{FM2}} = 59$ n Ωm , $\beta_{\text{FM2}} = -0.33$, $\lambda_{\text{sf}}^{\text{FM2}} = 21$ nm [139], $\rho_N = 0.133$ Ωm , $\lambda_{\text{sf}}^N = 20$ nm, $\gamma = 0.5$, $r_b = 2.5$ n Ωm^2 ; (For the ferromagnets we used the parameters of Co and Ni and for the N-layer the values we determined for ZnO from TDH and TRFR experiments.)

system we obtain the following expressions for the electric field in each layer:

$$\begin{aligned}
F^{\text{FM1}}(z) &= (1 - \beta_{\text{FM1}}^2)\rho_{\text{FM1}}J + \frac{\beta_{\text{FM1}}}{e\lambda_{\text{sf}}^{\text{FM1}}} \times \\
&\quad \times \left[K_2^{\text{FM1}} \exp\left\{\frac{z - z_{\text{FM1}}}{\lambda_{\text{sf}}^{\text{FM1}}}\right\} - K_3^{\text{FM1}} \exp\left\{-\frac{z - z_{\text{FM1}}}{\lambda_{\text{sf}}^{\text{FM1}}}\right\} \right] \\
F^{\text{N}}(z) &= \rho_{\text{N}}J \\
F^{\text{FM2}}(z) &= (1 - \beta_{\text{FM2}}^2)\rho_{\text{FM2}}J + \frac{\beta_{\text{FM2}}}{e\lambda_{\text{sf}}^{\text{FM2}}} \times \\
&\quad \times \left[K_2^{\text{FM2}} \exp\left\{\frac{z - z_{\text{FM2}}}{\lambda_{\text{sf}}^{\text{FM2}}}\right\} - K_3^{\text{FM2}} \exp\left\{-\frac{z - z_{\text{FM2}}}{\lambda_{\text{sf}}^{\text{FM2}}}\right\} \right].
\end{aligned}$$

With the electric fields defined in each layer one can calculate the resistance area product $R \times A$ of the whole structure by simply integrating along z over the whole structure:

$$\begin{aligned}
R \times A &= \frac{1}{J} \int_{-t_{\text{FM1}} - t_{\text{N}}/2}^{t_{\text{FM2}} + t_{\text{N}}/2} F(z) dz = \\
&= \frac{1}{J} \int_{-t_{\text{FM1}} - t_{\text{N}}/2}^{-t_{\text{N}}/2} F^{\text{FM1}}(z) dz + r_{\text{b}} \left(1 - \frac{\gamma}{J} (J_{\uparrow}^{\text{FM1}}(-\frac{t_{\text{N}}}{2}) - J_{\downarrow}^{\text{FM1}}(-\frac{t_{\text{N}}}{2}))\right) + \\
&\quad + \frac{1}{J} \int_{-t_{\text{N}}/2}^{t_{\text{N}}/2} F^{\text{N}}(z) dz + r_{\text{b}} \left(1 - \frac{\gamma}{J} (J_{\uparrow}^{\text{FM2}}(\frac{t_{\text{N}}}{2}) - J_{\downarrow}^{\text{FM2}}(\frac{t_{\text{N}}}{2}))\right) + \\
&\quad + \frac{1}{J} \int_{t_{\text{N}}/2}^{t_{\text{N}}/2 + t_{\text{FM2}}} F^{\text{FM2}}(z) dz.
\end{aligned} \tag{2.21}$$

One should note that the additional terms with r_{b} arise due to the discontinuities of the electrical field at the interfaces. Carrying out the integration of the single layers, one can simplify this expression into:

$$\begin{aligned}
R \times A &= (1 - \beta_{\text{FM1}}^2)\rho_{\text{FM1}}t_{\text{FM1}} + \rho_{\text{N}}t_{\text{N}} + (1 - \beta_{\text{FM2}}^2)\rho_{\text{FM2}}t_{\text{FM2}} \\
&\quad + r_{\text{b}} \left(1 - \frac{\gamma}{J} (J_{\uparrow}^{\text{FM1}}(-\frac{t_{\text{N}}}{2}) - J_{\downarrow}^{\text{FM1}}(-\frac{t_{\text{N}}}{2}))\right) + r_{\text{b}} \left(1 - \frac{\gamma}{J} (J_{\uparrow}^{\text{FM2}}(\frac{t_{\text{N}}}{2}) - J_{\downarrow}^{\text{FM2}}(\frac{t_{\text{N}}}{2}))\right) + \\
&\quad + \frac{2\beta_{\text{FM1}}}{eJ} (K_2^{\text{FM1}} - K_3^{\text{FM1}}) \sinh\left(\frac{t_{\text{FM1}}}{2\lambda_{\text{sf}}^{\text{FM1}}}\right) + \frac{2\beta_{\text{FM2}}}{eJ} (K_2^{\text{FM2}} - K_3^{\text{FM2}}) \sinh\left(\frac{t_{\text{FM2}}}{2\lambda_{\text{sf}}^{\text{FM2}}}\right).
\end{aligned} \tag{2.22}$$

We can now use the obtained solutions of K_1^i , K_2^i , and K_3^i in each layer to calculate the resistance area product $(R \times A)_{\text{parallel}}$ for parallel alignment of the ferromagnetic electrodes and $(R \times A)_{\text{antiparallel}}$ for antiparallel alignment. The MR of the structure can then be determined via:

$$MR = \frac{(R \times A)_{\text{antiparallel}} - (R \times A)_{\text{parallel}}}{(R \times A)_{\text{parallel}}} = \frac{N_{R \times A}}{D_{R \times A}}. \tag{2.23}$$

If we now substitute the set of solutions obtained from the boundary conditions for parallel and antiparallel alignment we obtain the lengthy but exact solution for the nominator $N_{R \times A}$ and denominator $D_{R \times A}$, which are given in Appendix C. With these expressions it is possible to investigate the evolution of the MR by varying one parameter and keeping

the others fixed. To obtain a deeper insight for our Co/ZnO/Ni spin valve structure we have chosen for these calculations typical material parameters for Co [155] and Ni [156] as the two ferromagnetic electrodes and for the N-layer material parameters of ZnO obtained from TDH and TRFR experiments on our laser-MBE grown samples (cf. Sect. 2.2 and 2.3). Figure 2.27(a) shows the dependency of the MR on the interface resistance parameter r_b for different fixed N-layer thicknesses t_N . All curves exhibit maximum MR in a certain range of r_b . In the case of the 2 nm (black line) thick N-layer the range for maximum MR stretches about one decade in values of the interface resistance indicated by the black arrows. For thicker N-layers this window gets smaller, for the 30 nm (green line) thick spacer layer the range for maximum MR is only a quarter of a decade indicated by the green arrows. If the interface resistance lies below or above this window the MR is greatly reduced. This shows that the measured GMR effect is strongly influenced and can be tuned by the interface resistance parameter r_b [151]. In addition, one can see in Fig. 2.27(a), that the maximum of the MR shifts to larger r_b values for increasing N-layer thickness due to the asymmetry of the two ferromagnetic electrodes. If one uses the identical material parameters for FM1 and FM2, this shift in the position of the maximum is not observed (cf. [151]). In figure 2.27(b) we have plotted the MR as a function of t_N ,

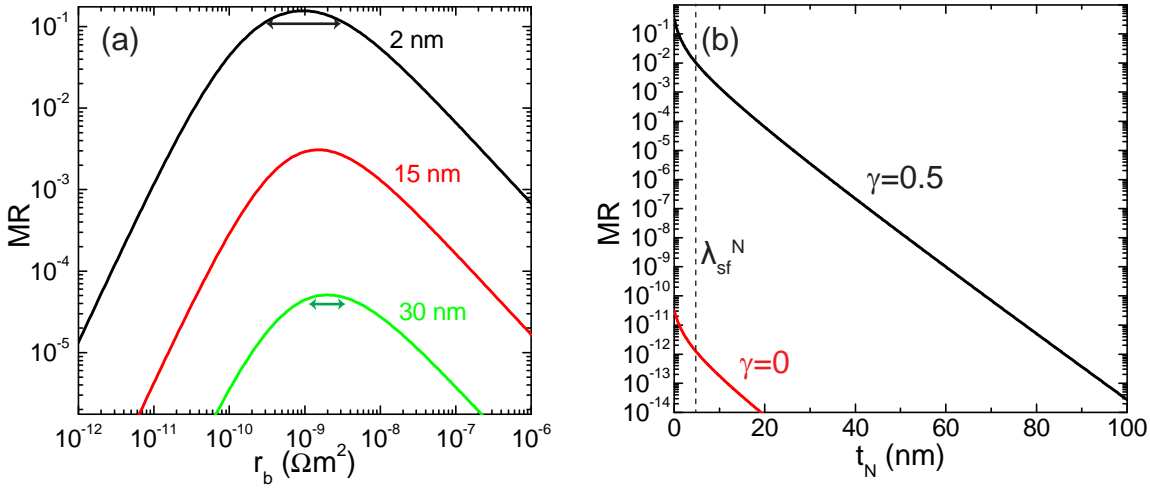


Figure 2.27: (a) Calculated dependency of the MR on the interface resistance r_b (a) for $t_N = 2$ nm (black line), $t_N = 15$ nm (red line) and $t_N = 30$ nm (green line). (b) MR as a function of the spacer layer thickness t_N for $\gamma = 0.5$ (black) and $\gamma = 0$ (red). For the calculations the following parameters were used: $t_{FM1} = t_{FM2} = 15$ nm, $\rho_{FM1} = 75$ n Ω m, $\beta_{FM1} = -0.46$, $\lambda_{sf}^{FM1} = 60$ nm, $\rho_{FM2} = 59$ n Ω m, $\beta_{FM2} = -0.33$, $\lambda_{sf}^{FM2} = 21$ nm, $\rho_N = 0.133$ Ω m, $\lambda_{sf}^N = 4$ nm, $\gamma = 0.5$, $r_b = 0.1$ n Ω m².

the interface resistance parameter has been chosen to be slightly away from the optimal value for maximum MR. For $\gamma = 0.5$ (black) the curve has two distinctive regimes. On the one hand for $t_N \gg \lambda_{sf}^N$, the MR is dominated by the exponential drop due to the spin diffusion in the non ferromagnetic layer ($\propto \exp(-t_N/\lambda_{sf}^N)$). On the other hand for $t_N \ll \lambda_{sf}^N$, we observe a sharp increase of the giant magnetoresistance, which is in this regime dominated by the interface spin selectivity parameter γ . For small enough t_N and

for semi infinite FM layers the MR will reach the maximum value given by

$$MR = \frac{\gamma^2}{1 - \gamma^2}. \quad (2.24)$$

It is obvious that for $\gamma = 1$ the MR will have its maximum value. Moreover, for $\gamma = 0$ (spin independent interface scattering) it is evident from the red line in Fig. 2.27(b) that the MR becomes drastically decreased by several orders of magnitude. This emphasizes the importance of the spin dependent interface scattering to increase the MR to detectable values.

In this theory part we have used the macroscopic model of diffusive spin transport to develop the equation of the MR as a function of material and geometrical parameters of the trilayer system. In the next section we will use this expression to fit the obtained experimental data and extract quantitative values of the spin diffusion length in the ZnO thin films.

2.5.3 Experimental

We will now focus on the actual measurement results obtained from our spin valve devices based on a Co/ZnO/Ni trilayer system.

2.5.3.1 Growth and structural characterization of multilayer spin valve system

The investigated samples were grown on one side epipolished (0001)-oriented sapphire (Al_2O_3) substrates in an ultra-high vacuum (UHV) (base pressure $p \approx 10^{-8}$ mbar) thin film deposition system equipped with chambers for laser-MBE and electron beam evaporation (EVAP). Prior to growth a 180 nm thick platinum layer was deposited on the backside of the sapphire substrates via DC-sputtering for a better absorption of the infrared laser light used later for substrate heating during the laser-MBE process. A transfer chamber allows an in-situ transfer between the two different deposition chambers. The multilayer system deposited on the Al_2O_3 substrates consists from bottom to top of a titanium nitride (TiN) layer (bottom electrode, 12 nm thick), a ferromagnetic Co layer (11 nm), a zinc oxide (ZnO) layer with thicknesses varying from 15 nm to 100 nm, a ferromagnetic Ni layer (11 nm) and a Au capping layer (24 nm). The multilayer deposition started by growing the TiN thin film via laser-MBE by ablating a polycrystalline, stoichiometric TiN target (99.99% purity) with a pulsed KrF excimer laser at a wavelength of 248 nm (More details on the system can be found in Appendix A). The deposition was carried out at a substrate temperature of $T_{\text{sub}} = 600$ °C, a laser fluence of $\rho_{\text{ED}} = 2$ J/cm² in an Ar atmosphere of $p_{\text{Ar}} = 7 \times 10^{-4}$ mbar and a repetition rate of $f = 10$ Hz⁵. After deposition of the TiN, the sample was cooled down to room temperature. Then the process chamber was evacuated to its base pressure. Afterwards the sample was transferred in-situ into the EVAP chamber. There a 11 nm thick cobalt layer was deposited at room temperature by evaporating a metallic cobalt target via electron beam heating. A deposition controller monitored the deposition process via crystal balance and automatically opened or closed a mechanical shutter for exact thickness control.

⁵These parameters were obtained from a growth optimization for single TiN thin films on sapphire substrates.

The pressure during deposition did not exceed 5×10^{-7} mbar. After the growth of the cobalt layer the sample was again moved in-situ to the laser-MBE chamber and a ZnO layer was grown on top under the following conditions: $T_{\text{sub}} = 400$ °C, $q_{\text{ED}} = 1$ J/cm², $p_{\text{Ar}} = 1 \times 10^{-3}$ mbar, $f = 10$ Hz (cf. Sect. 2.2). The purity of the target material was 99.99%. An argon atmosphere has been used to prevent oxidation of the Co layer. After cooldown and evacuation the sample was transported in-situ to the EVAP chamber for the final deposition steps. First a 11 nm thick Ni film was evaporated onto the sample, followed by a 24 nm thick Au capping layer, under the same deposition conditions as for the Co thin film.

After growth the spin valve multilayer systems were first characterized by high resolution X-ray diffraction (HR-XRD) in a 4-circle diffractometer (Bruker Discover) with monochromatic ($\lambda = 0.1540562$ nm) X-rays at room temperature. In addition, magnetization measurements were performed in a SQUID-magnetometer (Quantum Design MPMS) in a temperature range of 2 K – 350 K and an external magnetic field $\mu_0 H$ of up to 7 T.

Fig. 2.28(a) shows a typical 2θ - ω scan for a spin valve multilayer system with a ZnO layer thickness of 80 nm. The strong and sharp Al₂O₃ substrate (0003), (0006), (0009), (000 12) reflections can be clearly identified in the scan. The occurrence of the weak and normally forbidden (0003)- and (0009)-reflections could point to some lattice imperfections in the substrate, but have only negligible influence on the quality of the samples. The additional reflections that can be seen in the scan stem from the epilayers grown on the substrate. Using the bulk lattice values of the materials we can easily assign all of them to reflections of one of the deposited layers. From the 2θ - ω scan we rule out the existence of secondary phases. The inset in Fig. 2.28(a) shows a high resolution 2θ - ω scan around the sapphire (0006) reflection, where we find additional evidence for the high structural quality of our samples. Satellites around the TiN(111) reflection ($2\theta = 36.60^\circ$), the Au(111) reflection ($2\theta = 38.17^\circ$), and the Co(0002)/Ni(111) reflection ($2\theta = 44.50^\circ$) due to Laue oscillations are clearly visible, an indicator for coherent growth of the multilayer system. A separation of the Co(0002)/Ni(111) reflection is not possible due to the broad main peak, but note that the epitaxial quality of the cobalt layer should be higher due to the deposition on the high quality TiN layer. We also note that it is not possible to clearly distinguish between hcp and fcc structure for Co from the 2θ - ω scan. From the out-of-plane reflections we calculated the corresponding lattice constants for each layer: $c_{\text{ZnO}} = 0.521$ nm, $a_{\text{TiN}} = 0.425$ nm, $a_{\text{Au}} = 0.408$ nm, $c_{\text{Co}} = 0.407$ nm, $a_{\text{Ni}} = 0.352$ nm. All calculated values are relatively close (relative change below 10^{-3}) to their bulk values, indicating a relaxed growth of each epilayer on each other and an unstrained multilayer system.

To obtain further information on the structural quality we also performed ω rocking curves at each layer reflection in the inset, the results are shown in Figs. 2.28(b)-(e). The rocking curve of the ZnO (0002) reflection (Fig. 2.28(b)) is relatively broad with a full width at half maximum (FWHM) of 0.62° . But one should keep in mind that the ZnO has to grow on top of the Co layer leading to a larger in-plane lattice mismatch ($> 25\%$) than a direct growth on sapphire substrate making the achieved value still exceptionally good. The FWHM value of 0.03° for the TiN (111) reflection (Fig. 2.28(c)) shows the extremely good structural quality of the first grown layer, a prerequisite for the good epitaxial quality of the samples, and pointing to well tuned deposition parameters. For the rocking curve of the Au(111) reflection (Fig. 2.28(d)) we obtained a large FWHM of

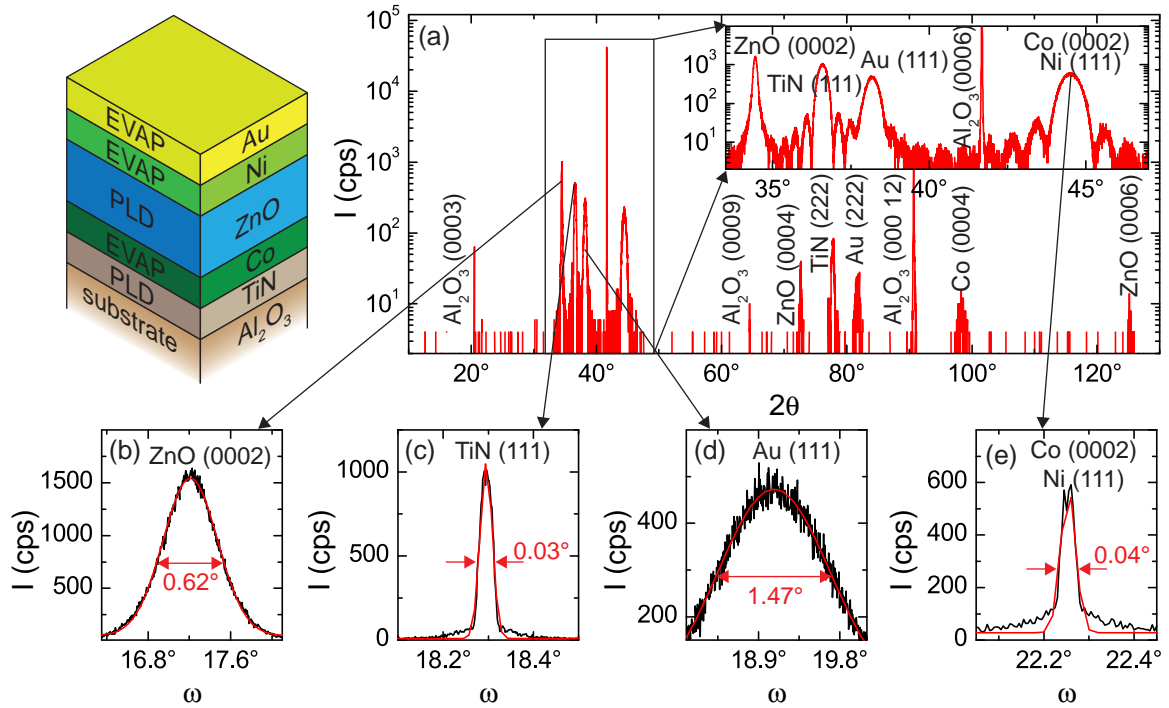


Figure 2.28: XRD data from the multilayer system grown on a (0001) oriented sapphire substrate. The multilayer consists of a TiN (12 nm) bottom electrode, Co (11 nm) as the first ferromagnetic layer, a ZnO (15 nm – 100 nm) spacer layer, Ni (11 nm) as the second ferromagnetic layer and a Au (24 nm) capping layer. (a) 2θ - ω scan of a multilayer structure with a 80 nm thick ZnO layer. All observed peaks can be correlated to the materials used in the multilayer, no secondary phases are visible. The inset shows the selected area around the (0006) Al_2O_3 for a better separation of the reflections of the multilayer system. (b) ω rocking curve of the ZnO(0002) reflection for the same structure as in (a), the FWHM is 0.62° . (c) ω rocking curve for the TiN (111) reflection in (a), the FWHM of 0.03° approve the high structural quality of the layer. (d) ω rocking curve for the Au (111) reflection in (a), the FWHM of 1.47° points to the full epitaxial relationship of all layers. (e) ω rocking curve for the Co (0002)/ Ni(111) reflection in (a), the FWHM of 0.04° approves the high structural quality of the ferromagnetic layers. The red lines in (b)-(e) indicate a Gaussian fit to the data, for the extraction of FWHM.

1.47° . For the rocking curve around the Co(0002)/Ni(111) reflection (Fig. 2.28(e)) we achieved a FWHM of only 0.04° , attesting a high structural quality of the cobalt layer. An additional broad curve is visible in (Fig. 2.28(e)) which might be attributed to the Ni layer with a FWHM of 0.28° . From this analysis it can be seen that the FWHM of the rocking curves increases with each successive layer deposited for this multilayer structure. Nevertheless, we obtained spin valve multilayer samples with good epitaxial quality.

The structural quality of the ZnO layer is relatively poor compared to the excellent results obtained for our optimized laser-MBE grown ZnO thin films in Sect. 2.2. For example we achieved a FWHM of 0.03° for the XRC of the ZnO (0002) reflection in our optimized thin films. The decrease in ZnO quality can be attributed to the TiN/Co template on which the ZnO film for the spin valve system has been grown and the use of

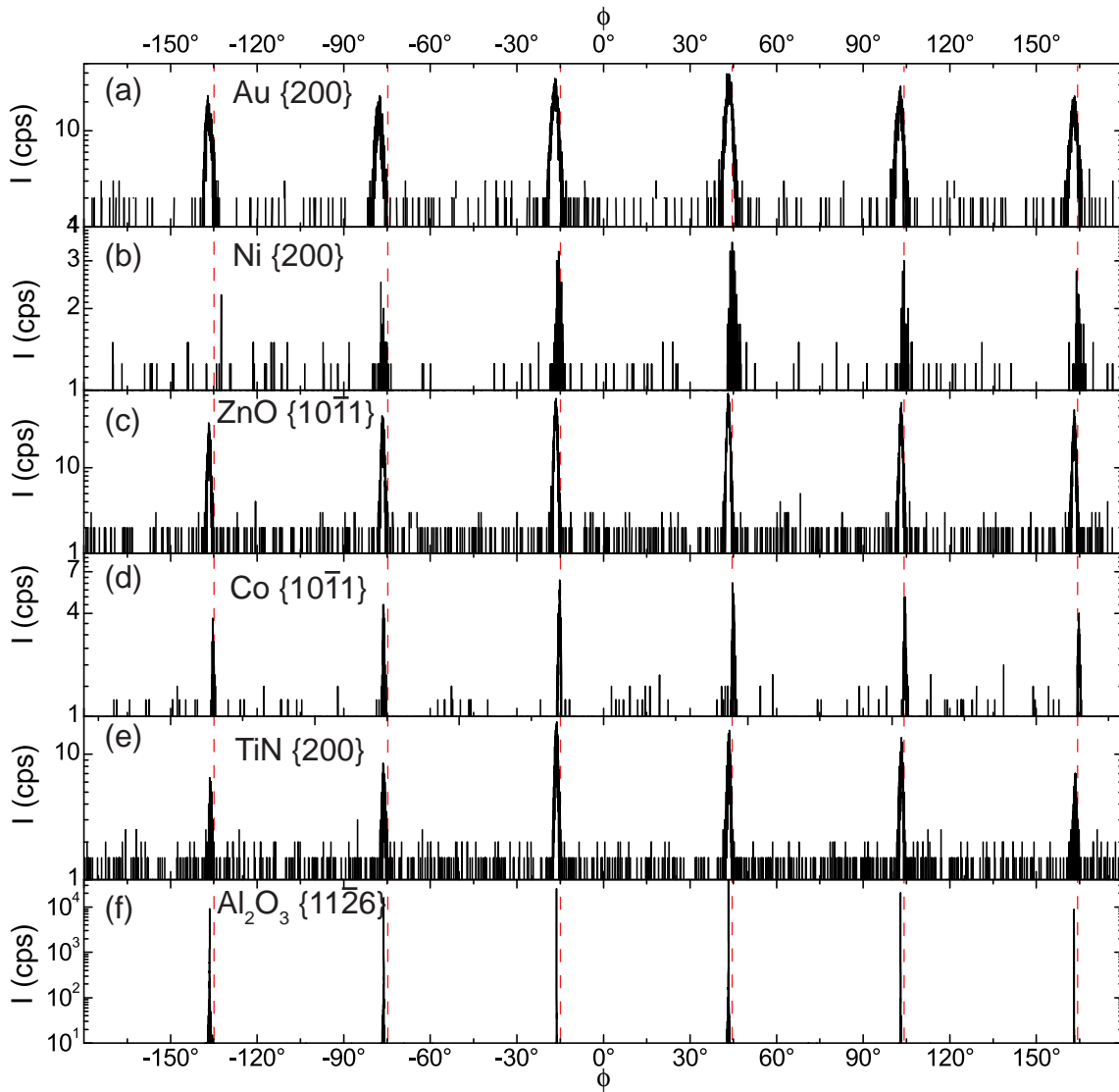


Figure 2.29: Phi(ϕ) scans of the Au (200) (a), Ni (200) (b), ZnO ($10\bar{1}1$) (c), Co ($10\bar{1}1$) (d), TiN (200) (e), and Al_2O_3 ($11\bar{2}6$) (f) reflections. All 6 curves exhibit 6 peaks, which line up at identical ϕ values illustrated by the vertical red dashed lines. This indicates a well formed epitaxial in-plane orientation of all deposited layers and leads to the following orientation relations: $\text{Au}(111) [2\bar{1}\bar{1}] \parallel \text{Ni}(111) [2\bar{1}\bar{1}] \parallel \text{ZnO}(0001) [10\bar{1}0] \parallel \text{Co}(0001) [10\bar{1}0] \parallel \text{TiN}(111) [2\bar{1}\bar{1}] \parallel \text{Al}_2\text{O}_3(0001) [11\bar{2}0]$.

an Ar atmosphere during ZnO growth.

In order to get a deeper knowledge of the in-plane epitaxial relationships between each successive layer, we performed phi(ϕ) scans for asymmetric layer and substrate reflections. Typical results are depicted in Fig. 2.29(a)-(f) and have been obtained from a spin valve multilayer with 80 nm thick ZnO. The ϕ -scans carried out for each reflection show six distinctive peaks at $\phi = -137^\circ$, $\phi = -77^\circ$, $\phi = -17^\circ$, $\phi = 43^\circ$, $\phi = 103^\circ$, and $\phi = 163^\circ$. Therefore we can now assume the following in-plane epitaxial relationships for the layers: $\text{Au}(111) [2\bar{1}\bar{1}] \parallel \text{Ni}(111) [2\bar{1}\bar{1}] \parallel \text{ZnO}(0001) [10\bar{1}0] \parallel \text{Co}(0001) [10\bar{1}0] \parallel \text{TiN}(111) [2\bar{1}\bar{1}] \parallel \text{Al}_2\text{O}_3(0001) [11\bar{2}0]$. As the chosen sapphire $\{11\bar{2}6\}$ reflection directly reflects

the orientation of the oxygen sublattice, it is evident, that each layer is aligned to this sublattice. This alignment has been already observed for TiN (111) [157, 158], Co(0001) [159], ZnO(0001) [42], and Au(111) [160] thin films all directly grown on (0001)-oriented Al_2O_3 substrates. Our results suggest that the previously reported in-plane orientations of the single layers are preserved with excellent quality when growing the layers on top of each other. This might explain why we were able to fabricate multilayers with relaxed layer growth but still exceptionally good crystalline quality.

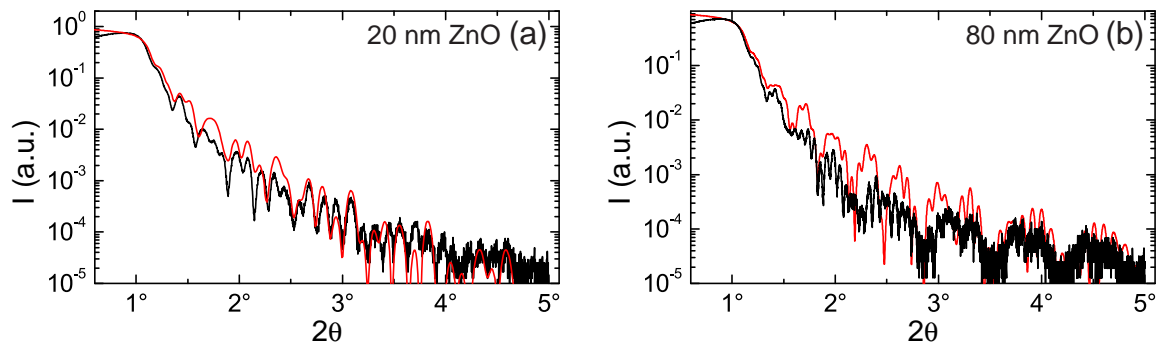


Figure 2.30: HRXRD reflectometry scan of a spin valve multilayer structure with (a) a 20 nm and (b) 80 nm thick ZnO spacer layer. The black curve represents the measured intensity and the red curve a simulation with the following parameters: $t_{\text{TiN}} = 12$ nm, $t_{\text{Co}} = 11$ nm, $t_{\text{Ni}} = 11$ nm, $t_{\text{Au}} = 24$ nm, and $t_{\text{ZnO}} = 20$ nm for (a) and $t_{\text{ZnO}} = 80$ nm for (b). Despite the complicated structure of the multilayer, simulation and experimental data fit nicely together.

To further analyze the surface roughness and interface sharpness we also measured HR-XRD reflectometry curves for each sample. Two curves for a sample with 20 nm and 80 nm ZnO thickness are shown in Fig. 2.30(a) and (b), respectively, as black lines. Both curves show clearly visible oscillations even for 2θ angles above 3° . This supports the fact, that we have fabricated multilayers with low surface roughness and sharp interfaces. For comparison we have simulated the reflectometry of the corresponding multilayer using the Bruker LEPTOS software, by directly plugging in the previously mentioned thickness values of each layer. The results are displayed as red curves in each graph. Although there is no 100% agreement between simulation and measurement, some beating patterns and oscillation periods are clearly identical in both curves. One should note that a direct determination of the thicknesses of each layer is nearly impossible due to the complex structure of the multilayer system.

After the structural characterization we further analyzed our spin-valve multilayers by SQUID magnetometry. In Fig. 2.31(a) we show typical in-plane hysteresis loops at $T = 25$ K obtained from a multilayer structure with a ZnO thickness of 15 nm. The two ferromagnets switch independently of each other at different coercive fields $\mu_0 H_C$, as evident from the two step shape of the measured hysteresis loop. From additional measurements with a multilayer structure without the nickel layer (not shown here), we could verify that the sharp first switching step in the up-sweep represents the reorientation of the magnetization of the cobalt layer. The second more rounded one is attributed to the switching of the magnetization of the nickel thin film. From the measurements at 25 K we extracted the following coercive fields (by extraction of the average field value at

which the switching step was halfway completed in magnitude for up- and downsweep) and saturation magnetizations: $\mu_0 H_C^{\text{Co}} = 1.5 \text{ mT}$, $\mu_0 H_C^{\text{Ni}} = 8.5 \text{ mT}$, $M_{\text{sat}}^{\text{Co}} = 1230 \text{ kA/m}$, and $M_{\text{sat}}^{\text{Ni}} = 430 \text{ kA/m}$. The saturation magnetizations for our thin films are 15% smaller than the bulk values reported in literature ($M_{\text{sat}}^{\text{Co}} = 1440 \text{ kA/m}$, $M_{\text{sat}}^{\text{Ni}} = 485 \text{ kA/m}$ [161]). These deviations from the bulk values can be accounted for by the relative error ($\approx 10\%$) for the determination of the volume of each layer and additional thin film effects. The occurrence of this independent, separate switching of the two ferromagnetic layers allows the realization of spin valve devices with our multilayers.

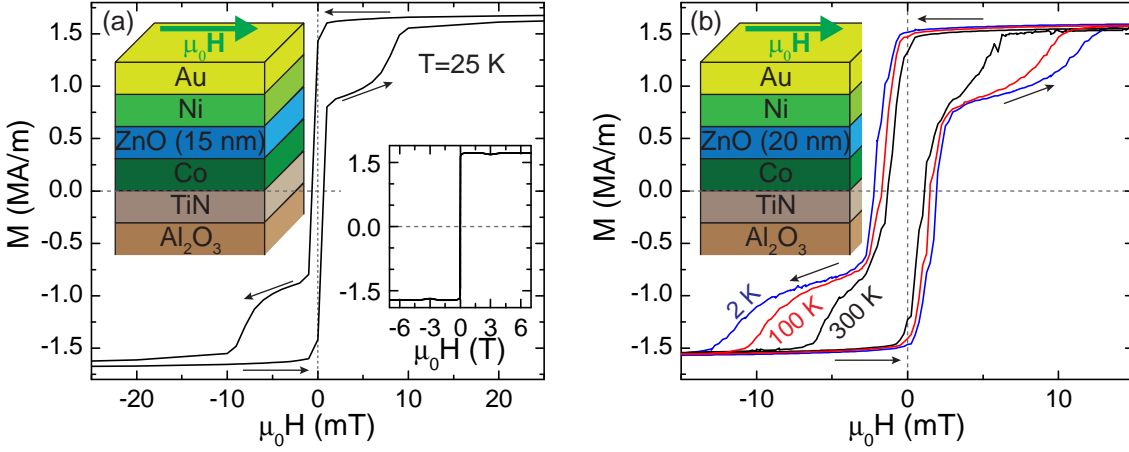


Figure 2.31: In plane magnetization loops (a) measured for a multilayer thin film sample with a ZnO layer thickness of 15 nm at $T = 25 \text{ K}$. The separate switching of the two ferromagnetic layers is clearly visible. The first abrupt change at $\mu_0 H_C^{\text{Co}} = 1.5 \text{ mT}$ is attributed to the cobalt layer with a saturation magnetization $M_{\text{sat}}^{\text{Co}} = 1230 \text{ kA/m}$, the second broad switching at $\mu_0 H_C^{\text{Ni}} = 8.5 \text{ mT}$ to the nickel thin film $M_{\text{sat}}^{\text{Ni}} = 430 \text{ kA/m}$. The inset shows the magnetization loop for $-7 \text{ T} \leq \mu_0 H \leq 7 \text{ T}$ after a diamagnetic background subtraction, with a total saturation magnetization $M_{\text{sat}} = 1660 \text{ kA/m}$. (b) Temperature dependence of the ip magnetization loops for $T = 300 \text{ K}$ (black), $T = 100 \text{ K}$ (red), $T = 2 \text{ K}$ (blue). The saturation magnetization is constant and the coercive fields change for Co from $\mu_0 H_C^{\text{Co}}(300 \text{ K}) = 1 \text{ mT}$ to $\mu_0 H_C^{\text{Co}}(2 \text{ K}) = 1.8 \text{ mT}$ and for Ni from $\mu_0 H_C^{\text{Ni}}(300 \text{ K}) = 5.2 \text{ mT}$ to $\mu_0 H_C^{\text{Ni}}(2 \text{ K}) = 10.7 \text{ mT}$. For the determination of M we normalized the magnetic moment to the total volume of the ferromagnetic layers.

Moreover, we investigated the temperature dependence of the in-plane hysteresis loops. In Fig 2.31(b) hysteresis loops at $T = 2 \text{ K}$, $T = 100 \text{ K}$, $T = 300 \text{ K}$ are depicted for a spin valve multilayer with a 20 nm thick ZnO spacer layer. With decreasing temperature the coercive fields of the ferromagnets increase, and the two step switching process of the two ferromagnetic layers becomes more pronounced.

All the samples investigated show a separate switching of the two ferromagnetic layers, a magnetic coupling between the two layers could not be observed. In summary, we could verify by in-plane hysteresis loops that for every sample, with a ZnO thickness ranging between 15 nm and 100 nm, the two ferromagnetic layers have two different coercive fields, which is a key requirement for a successful realization of spin valve devices based on our multilayers.

2.5.3.2 Electrical measurements with ZnO based spin valve structures

For the electrical characterization we first fabricated vertical mesa structures from the spin valve multilayer samples, which allow a transport measurement in the cpp geometry. The fabrication of the spin valve devices was carried out in 3 steps using standard photolithography. First we defined the contacts to the bottom TiN electrode using argon ion beam milling. In a second step the vertical mesa structure is established by first etching the mesa with Ar ion beam milling and then RF-sputtering a SiO_2 insulating layer around the mesa using lift-off technique. In the final step the top contact to the spin valve is formed by sputter deposition of 5 nm Cr and 50 nm Au and lift-off. A

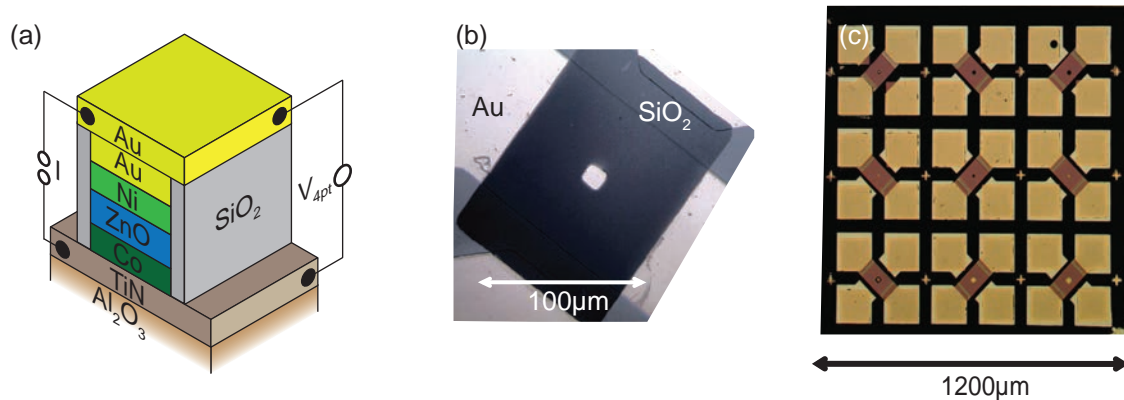


Figure 2.32: Fabrication process of the spin valve devices for cpp geometry. (a) Schematic illustration of the designed spin valve structure. The multilayer is first patterned into square mesas. Using insulating SiO_2 a separate electrical connection to the top Au and the bottom TiN layer is realized, allowing a four point resistance measurement of the spin valve device with the current perpendicular to the layers. (b) Microscope image of a nominal $100\mu\text{m}^2$ large spin valve contact after the etching process and the SiO_2 sputter deposition. (c) Picture of the final structure after the gold lift off with 9 contacts of different sizes.

schematical drawing of the fabricated mesa can be found in Fig. 2.32(a). Two Al wedge bond contacts to the top and bottom electrode allow a current bias 4 point voltage measurement. Figure 2.32(b) shows a $10 \times 10\mu\text{m}^2$ vertical mesa structure after the etching and SiO_2 lift-off. The structure is well defined with slightly rounded edges. The final sample can be seen in Fig. 2.32(c), it consists of a total of 9 spin valve structures with three different sizes: $10 \times 10\mu\text{m}^2$, $15 \times 15\mu\text{m}^2$, $20 \times 20\mu\text{m}^2$. After the mesa structure and electrical contacts were defined, the sample was mounted on our chip carrier system and contacted via Al wire wedge-bonding. The chip carrier with the mounted sample was then placed onto a dipstick in an Oxford Spectromag 4000 magnet cryostat system, which allowed electrical measurements in external magnetic fields $\mu_0 H \leq 7\text{T}$ and at temperatures $1.8\text{K} \leq T \leq 350\text{K}$. A stepper motor rotated the dipstick inside the cryostat, which enables us to freely orient the field direction in the film plane. All electrical measurements were carried out by applying a constant current flowing from the bottom electrode to the top electrode and measuring the voltage drop between top and bottom electrode (cf. Fig. 2.32(a)). Current bias was applied using a Keithley 2400 Sourceme-ter, and voltage measurements were carried out using a Keithley 2010 Multimeter or a

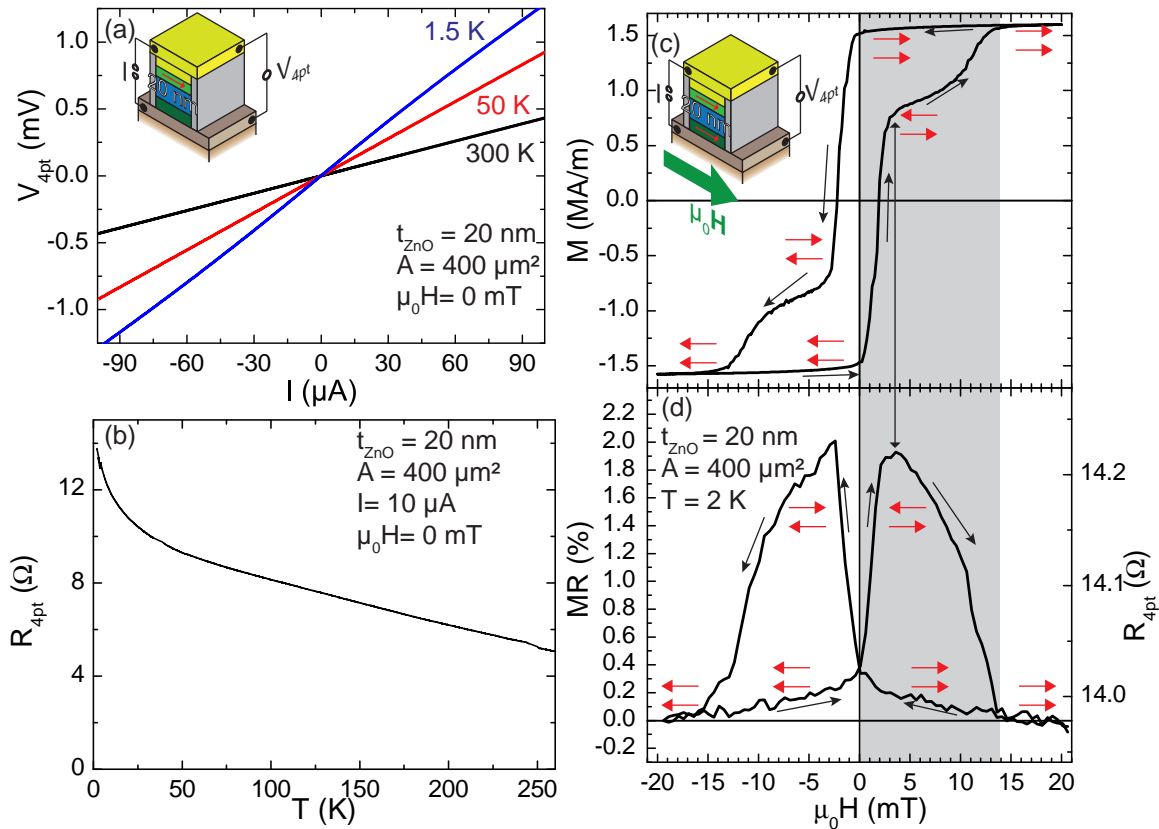


Figure 2.33: Electrical characteristics of two spin valve multilayer structures. (a) I-V curve for a Co/ZnO/Ni spin valve contact (area $400 \mu\text{m}^2$, $t_{\text{ZnO}} = 20 \text{ nm}$) at 300 K (black), 50 K (red) and 1.5 K (blue). The curves for $T > 1.5 \text{ K}$ show a linear Ohmic behavior and the resistance increases for lower temperatures. (b) Temperature dependent 4pt resistance of the same contact. The measured resistance increases by one order of magnitude over the whole temperature range, pointing to the fact that the resistance of the contact is dominated by the ZnO layer. Panels (c) and (d) show a comparison of the SQUID magnetometry data (c) and the magnetoresistance (d) for a $400 \mu\text{m}^2$ contact with $t_{\text{ZnO}} = 20 \text{ nm}$ at $T = 2 \text{ K}$. It is evident that the MR effect observed is correlated to the switching fields observed in magnetometry. The maximum of the $MR = 1.93 \%$ is located at $\mu_0 H = 3.6 \text{ mT}$, where the magnetization of Co and Ni electrodes are aligned antiparallel. Black arrows in (c) and (d) indicate magnetic field sweep direction and red arrows the orientation of the magnetizations of Co and Ni. The grey shaded area represents the part of the graph described in the text.

Keithley 2182 Nanovoltmeter.

A first electrical characterization via current-voltage (I-V) curves at three different temperatures $T = 300 \text{ K}$, 50 K , 1.5 K is presented in Fig. 2.33(a). The contact investigated had an area of $A = 20 \times 20 \mu\text{m}^2$ and a ZnO thickness of $t_{\text{ZnO}} = 20 \text{ nm}$. The I-V curves measured at 300 K and 50 K exhibit a linear behavior for currents of up to 1 mA (not depicted in the graph). As it can be seen from the three measured curves, the resistance of the contact increases with decreasing temperature. Current-induced heating results in a deviation from linearity as can be seen at $T = 1.5 \text{ K}$ for $I \geq 25 \mu\text{A}$. All the samples

investigated display ohmic behavior. This indicates that the carrier concentration in the ZnO layer is very high ($n_{\text{ZnO}} \geq 5 \times 10^{17} \text{ cm}^{-3}$) so that there is no Schottky contact effect. The current bias in all the presented data has always been chosen to be within the linear regime of the I-V curve, to avoid heating of the investigated contacts. We therefore can directly calculate the 4pt resistance of such a device from Ohm's law:

$$R_{4\text{pt}} = \frac{V_{4\text{pt}}}{I}. \quad (2.25)$$

A resistance versus temperature curve ($R(T)$) for the very same contact can be seen in the graph of Fig. 2.33(b). The resistance of the contact increases by a factor of 5 when decreasing the temperature from 300 K to 10 K. From this observation we conclude, that the resistance is dominated by the ZnO layer, because all other layers should show a metallic type of conduction leading to a decrease of resistance with decreasing temperature. Moreover, the resistivities of Co ($\rho_{\text{Co}}(300 \text{ K}) = 56.0 \text{ n}\Omega\text{m}$), Au ($\rho_{\text{Au}}(300 \text{ K}) = 20.5 \text{ n}\Omega\text{m}$), Ni ($\rho_{\text{Ni}}(300 \text{ K}) = 59.0 \text{ n}\Omega\text{m}$), and TiN ($\rho_{\text{TiN}}(300 \text{ K}) = 21.7 \mu\Omega\text{m}$) are more than 4 orders of magnitude lower than for ZnO ($\rho_{\text{ZnO}}(300 \text{ K}) = 0.133 \Omega\text{m}$) [162], such that the observed $R_{4\text{pt}}(300 \text{ K}) = 5.1 \Omega \approx \rho_{\text{ZnO}}(300 \text{ K})t_{\text{ZnO}}/A_{\text{ZnO}} = 6.65 \Omega$ is clearly dominated by the resistance of ZnO. All investigated samples exhibit this semiconductor like $R(T)$ evolution. However, the rather small change (by one order of magnitude) between room temperature and liquid Helium temperature supports the assumption of a nearly degenerately doped ZnO, leading to a nearly constant carrier concentration over the whole temperature range. Under the assumption of a constant carrier concentration $n_{\text{ZnO}} = 5 \times 10^{17} \text{ cm}^{-3}$ one can calculate the mobility of the carriers in ZnO

$$\mu_{\text{ZnO}} = \frac{t_{\text{ZnO}}}{R_{4\text{pt}} A n_{\text{ZnO}} e}. \quad (2.26)$$

The mobility of the carriers in our ZnO layer is quite low $\mu_{\text{ZnO}} \leq 1 \text{ cm}^2\text{V}^{-1}\text{s}^{-1}$ and varies as $\mu \propto T^{3/2}$ with temperature. This proves that the mobility of the ZnO layer is dominated by scattering from ionized defects (e.g.: charged donators, dislocations), as it would be expected because of the crystalline quality of our samples. In summary the measured I-V and $R(T)$ curves point to a domination of the resistance by a degenerately doped, low mobility ZnO layer.

For further electrical characterization we also measured the dependence of $R_{4\text{pt}}$ on the external applied magnetic field ($R_{4\text{pt}}(H)$) and extracted from these measurements the magnetoresistance $MR(H)$ as follows⁶:

$$MR(H) = \frac{R_{4\text{pt}}(H) - R_{4\text{pt}}(-200 \text{ mT})}{R_{4\text{pt}}(-200 \text{ mT})}. \quad (2.27)$$

In Fig. 2.33(d) we have plotted the $MR(H)$ for a spin valve contact with $A = 20 \times 20 \mu\text{m}^2$ and $t_{\text{ZnO}} = 20 \text{ nm}$ at $T = 2 \text{ K}$. The curve exhibits a hysteretic behavior, where the $MR(H)$ is different for up- and down-sweep. A high resistance state occurs at two field ranges, one at $0 \text{ mT} \leq \mu_0 H \leq 14 \text{ mT}$ (up-sweep) and another one at $-15 \text{ mT} \leq \mu_0 H \leq 0 \text{ mT}$ (down-sweep). The $MR(H)$ is axially symmetric with respect to $\mu_0 H = 0 \text{ mT}$ and

⁶We have chosen 200 mT as the reference value as at those magnetic field values both ferromagnets are in saturation (cf. Fig. 2.31(a)).

has a maximum value of 1.98% for negative fields at $\mu_0 H = -3.8$ mT and a maximum of 1.93% for positive field values at $\mu_0 H = 3.6$ mT. This observation can be explained by a GMR, where the measured resistance depends on the relative orientation of the magnetizations of the two ferromagnetic layers. It is crucial for a later quantitative analysis of the spin diffusion length in ZnO to exclude anisotropic magnetoresistance (AMR) or also a tunneling magnetoresistance (TMR) as a possible origin of the observed MR. Another possible explanation would be a combination of the AMR of both ferromagnetic layers resulting in the observed $MR(H)$ curve. The reported AMR ratio is 1.9% ($T = 300$ K) for Co [163] and 2.2% ($T = 4.2$ K) for Ni [164], which is in the range of the observed effect. However, we already know from the $R(T)$ behavior, that the resistance of the device is dominated by the ZnO layer. As the total resistance of the mesa structure could be represented by a series connection of resistors, one would expect that the total measured AMR is greatly reduced due to the large non hysteretic contribution of the ZnO layer. Comparing the magnetization data from SQUID magnetometry with the $MR(H)$ data as shown in Fig. 2.33(c) and (d) rather points to the presence of a GMR effect in our vertical mesa structure. For a direct comparison we take a closer look at the up-sweep of both data sets, the sweep direction is illustrated by black arrows in both graphs. In addition a pair of red arrows indicate the orientation of the magnetizations of the Co (lower arrow) and Ni (upper arrow) in certain field ranges. For large enough negative fields we know from the magnetometry data, that the two magnetizations of Co and Ni are aligned parallel to each other. In the $MR(H)$ we get a sharp increase of the MR from $\mu_0 H = 0$ mT to $\mu_0 H = 2.5$ mT, within the same field range the magnetization data also shows a sharp switching which was attributed to the reorientation of the Co layer, changing the relative orientation of the two magnetizations. The $MR(H)$ curve then reaches its maximum of 1.93% at $\mu_0 H = 3.6$ mT, at this field value the magnetization curve changes its slope and points to an antiparallel alignment of the Co and Ni magnetizations. For an antiparallel alignment of the magnetizations we expect the maximum GMR value, which is observed in our experiments. After the maximum the $MR(H)$ curve at $\mu_0 H = 3.6$ mT decreases slowly and reaches 0% at $\mu_0 H = 14.8$ mT. For the magnetization data we observe in this field range the reorientation of the Ni layer, such that the magnetizations of cobalt and nickel are again aligned parallel, which would result in $MR = 0$ according to the GMR model. Therefore it is possible to explain the observed $MR(H)$ within the model of a spin valve (GMR) using the magnetometry data and the information on the alignment of the magnetizations of Co and Ni. This strongly supports, that the observed MR is a GMR.

In addition, we have also investigated the electrical current bias dependence of the contacts. $MR(H)$ data obtained for $t_{\text{ZnO}} = 20$ nm, $A = 20 \times 20 \mu\text{m}^2$ and $T = 1.5$ K is represented in Fig. 2.34(a) for a current bias of $5 \mu\text{A}$ (black), $20 \mu\text{A}$ (red) and $100 \mu\text{A}$ (blue). The measured $MR(H)$ is nearly independent of the current bias. Only for the $100 \mu\text{A}$ curve we see a slight decrease in the maximum MR, which is related to the Joule heating of the contact as can be seen from the I-V characteristics of the contacts (cf. Fig. 2.33(a)). The temperature dependence of the MR will be discussed below. We have investigated this current bias dependence for all samples and found a similar current dependence of the MR for all other samples. These findings in combination with the Ohmic I-V curves clearly rule out a TMR as a possible source of the observed MR.

A further important characteristic for a discrimination between the different MR effects is the dependence of the $MR(H)$ on the orientation of the external applied magnetic field.

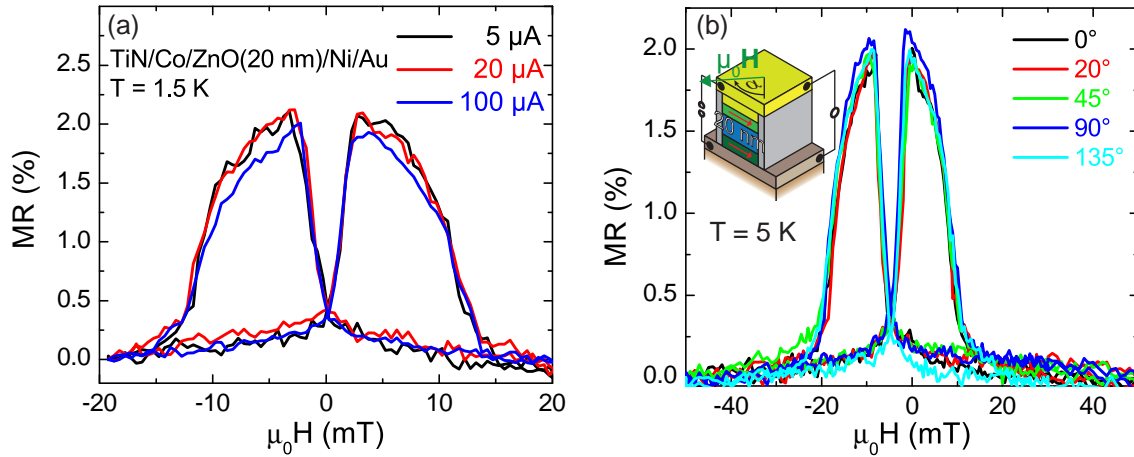


Figure 2.34: (a) $MR(H)$ as a function of the applied electrical current: $I = 5 \mu\text{A}$ (black), $I = 20 \mu\text{A}$ (red) and $I = 100 \mu\text{A}$ (blue). (b) $MR(H)$ for different in-plane orientations of the external magnetic field: $\alpha = 0^\circ$ (black), $\alpha = 20^\circ$ (red), $\alpha = 45^\circ$ (green), $\alpha = 90^\circ$ (blue) and $\alpha = 135^\circ$ (cyan). The $MR(H)$ is independent of the external field orientation. Both findings indicate that the origin of the observed MR is GMR.

We have conducted several $MR(H)$ for different angles α between external in-plane field and one diagonal of the square contacts. For $t_{\text{ZnO}} = 20 \text{ nm}$, $A = 20 \times 20 \mu\text{m}^2$ and $T = 5 \text{ K}$ the obtained $MR(H)$ are shown in Fig. 2.34(b) for $\alpha = 0^\circ$ (black), $\alpha = 20^\circ$ (red), $\alpha = 45^\circ$ (green), $\alpha = 90^\circ$ (blue), and $\alpha = 135^\circ$ (cyan). The drawing in the graph illustrates the definition of α for the description of the field orientation. We clearly observe a $MR(H)$ loop that is independent of the orientation α . This indicates that only the relative orientation of the magnetizations in the Co and Ni layer is important for the observed $MR(H)$ curves, which is the case for GMR. For an AMR type of effect one expects a clear dependence on the orientation of the external applied field with respect to the electrical current direction [165]. As we have measured in the cpp geometry, we would only expect a dependence on the in-plane orientation α , if the electrical current path has sections within the film plane. In addition, for the observation of an AMR effect in our cpp geometry the magnetizations of Co or Ni should have an in-plane field range, where the magnetization has an out-of-plane (oop) component, which is highly unlikely as the oop-direction represents a hard axis. In this context the orientation dependence of the $MR(H)$ is an evidence for the cause of the MR being GMR.

To further clarify the origin of the MR we have carried out additional angle dependent measurements. The experimental procedure was as follows: At a fixed in-plane orientation $\alpha = -20^\circ$ we applied a positive magnetic field $\mu_0 H = 500 \text{ mT}$ large enough to align both magnetizations along the field direction and parallel to each other. After this initialization process we reduced this positive field to the value H_{rot} . The magnitude of the external magnetic field was then kept constant at H_{rot} and the relative in-plane orientation α between sample and external magnetic field was stepwise changed while measuring the 4pt resistance of the contact (ADMR). A definition of the angle α describing the orientation of field and sample can be found in Fig. 2.35(a), together with the magnetization \mathbf{m}_{Co} of the cobalt layer and the magnetization \mathbf{m}_{Ni} of the nickel layer.

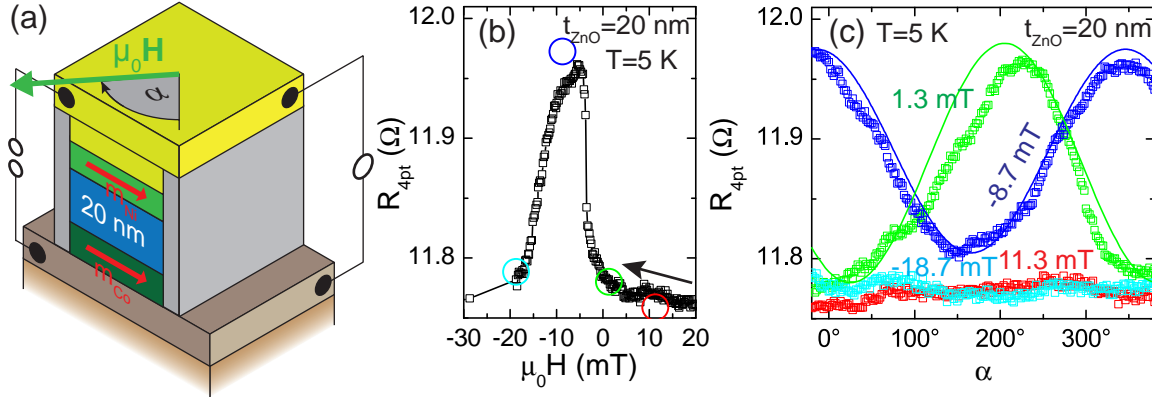


Figure 2.35: Comparison of resistance measurements on a spin valve device with 20 nm ZnO spacer layer and an area of $400 \mu\text{m}^2$. (a) Definition of the coordinate system. The angle α describes the orientation of the external magnetic field in the film plane. (b) Measured 4pt resistance of the device as a function of external magnetic field (black symbols) at $\alpha = -20^\circ$ and $T = 5$ K. The additional round open symbols (red, green, blue and cyan) depict the start value for the angle dependent magnetoresistance measurements at fixed external magnetic field. (c) ADMR measurements at $\mu_0 H_{\text{rot}} = 11.3$ mT (red symbols), 1.3 mT (green), -8.7 mT (blue) and -18.7 mT (cyan). For an external magnetic field of 1.3 mT and -8.7 mT, a fit with a cosine function is depicted by the green and blue lines.

For a contact with $t_{\text{ZnO}} = 20$ nm, $A = 20 \times 20 \mu\text{m}^2$ and $T = 5$ K, we recorded first the 4pt resistance as a function of the external magnetic field for $\alpha = -20^\circ$ starting at positive and going to negative fields ($R_{4pt}(H)$). The corresponding data is shown in Fig. 2.35(b) as open black squares. We here observe a characteristic first sharp switching at $\mu_0 H = -2.5$ mT, which corresponds to the reorientation of \mathbf{m}_{Co} and results in an antiparallel alignment of \mathbf{m}_{Co} and \mathbf{m}_{Ni} . After this first measurement we carried out ADMR measurements for $\mu_0 H_{\text{rot}} = 11.3$ mT (red symbols), $\mu_0 H_{\text{rot}} = 1.3$ mT (green symbols), $\mu_0 H_{\text{rot}} = 8.7$ mT (blue symbols), and $\mu_0 H_{\text{rot}} = -18.7$ mT (cyan symbols), which are represented in Fig. 2.35(c). The start values for $\alpha = -20^\circ$ are also displayed as a circle of the corresponding color in Fig. 2.35(b). This comparison shows only a small deviation (relative change at fixed field $< 10^{-4}$) between ADMR and $R_{4pt}(H)$ measurements. These deviation are caused by different magnetic domain states of the ferromagnetic electrodes for the ADMR and $R_{4pt}(H)$ measurements, originating from the different magnetic field sweep rates for these two measurements (1 T/min for ADMR and 0.05 T/min for $R_{4pt}(H)$).

If we compare the 4 measured ADMR curves we clearly see that for $\mu_0 H_{\text{rot}} = 11.3$ mT and $\mu_0 H_{\text{rot}} = -18.7$ mT the measured resistance is independent of α . But for $\mu_0 H_{\text{rot}} = 1.3$ mT and $\mu_0 H_{\text{rot}} = -8.7$ mT we observe a clear cosine and inverted cosine dependence of R_{4pt} on α respectively. This behavior can only be understood in the picture of a spin valve, as discussed in the next paragraph.

We first take a look at the ADMR data measured for $\mu_0 H_{\text{rot}} = 1.3$ mT. From the $R_{4pt}(H)$ we know that $\mathbf{m}_{\text{Co}} \parallel \mathbf{m}_{\text{Ni}}$ is the initial situation before we start changing the orientation of the external magnetic field. The chosen field value $\mu_0 H_{\text{rot}} = 1.3$ mT is only large enough to influence the orientation of \mathbf{m}_{Co} , for simplicity we neglect any

magnetic anisotropy and assume that \mathbf{m}_{Co} is always parallel to the external magnetic field and \mathbf{m}_{Ni} will remain aligned along $\alpha = -20^\circ$ for the whole field rotation. If we now start to rotate the magnetic field in the film plane, \mathbf{m}_{Co} directly follows this orientation effectively changing the relative angle φ between \mathbf{m}_{Co} and \mathbf{m}_{Ni} . In a simple model, the GMR changes $R_{4\text{pt}}$ as a function of relative orientation of the two magnetizations. This change is proportional to $\cos(\varphi)$. This expected cosine behavior is perfectly reproduced by our measured data. At $\alpha = 180^\circ$ the curve reaches its maximum corresponding to an antiparallel alignment of \mathbf{m}_{Co} and \mathbf{m}_{Ni} . If we now further increase α above 180° we observe the reversal from antiparallel to parallel alignment reducing $R_{4\text{pt}}$. For the ADMR measurement at $\mu_0 H = -8.7 \text{ mT}$ the case is reversed to $\mu_0 H = 1.3 \text{ mT}$. We first start at an antiparallel alignment of \mathbf{m}_{Co} and \mathbf{m}_{Ni} to a parallel configuration at $\alpha = 160^\circ$ (minimal value of $R_{4\text{pt}}$) and back to antiparallel. For further clarification we included a cosine fit to the data represented by the green and blue line in Fig. 2.35(c). In the case of $\mu_0 H = -18.7 \text{ mT}$ and $\mu_0 H = 11.3 \text{ mT}$ both magnetizations \mathbf{m}_{Co} and \mathbf{m}_{Ni} remain parallel to the external magnetic field resulting in a fixed orientation between the two magnetizations ($\varphi = 0^\circ$), which ultimately produces no change in $R_{4\text{pt}}$ for all field orientations. The measured ADMR evolution is a key evidence, that the observed MR is GMR, because the observed orientation dependence can only be understood in the model of GMR, where the relative orientation of the two magnetizations determines the resistance of the structure. From all the experimental results obtained from $MR(H)$ and ADMR, we unambiguously conclude that the observed MR is due to GMR.

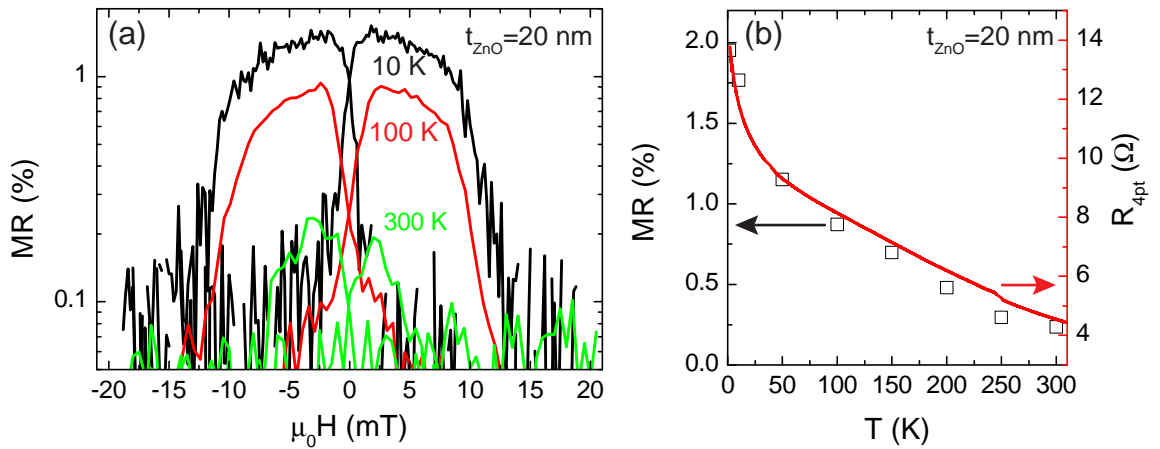


Figure 2.36: (a) MR as a function of the in-plane external magnetic field at $T = 10 \text{ K}$ (black), $T = 100 \text{ K}$ (red), and $T = 300 \text{ K}$ (green) for a spin valve device with $t_{\text{ZnO}} = 20 \text{ nm}$ and $A = 400 \mu\text{m}^2$. The MR decreases with increasing temperature, but even at 300 K , a maximum MR effect of 0.2% is obtained. (b) Temperature dependence of the maximum MR for the same device as in (a) depicted by the open black squares (left scale) and temperature dependence of the 4pt resistance (red line, right scale). The change in maximum MR follows the change in resistance with temperature.

For further systematic investigations we have conducted $MR(H)$ measurements at various temperatures. Experimental results for the $MR(H)$ for a spin valve device with $t_{\text{ZnO}} = 20 \text{ nm}$, $A = 20 \times 20 \mu\text{m}^2$ are depicted in Fig. 2.36(a) at $T = 10 \text{ K}$ (black),

$T = 100$ K (red), and $T = 300$ K (green). The maximum value of the MR decreases from 1.68% at 10 K down to 0.2% at 300 K. But even at 300 K a finite MR signal is still obtained, indicating an electrical injection, transport and detection of spin polarized carriers through 20 nm of ZnO at room temperature, exceeding the length scale of 10 nm reported in [102]. In Fig. 2.36(b), we have plotted the extracted maximum $MR(H)$ for positive field values as a function of temperature for the very same spin valve device as open black squares. The drop in maximum MR for increasing temperature is evident from the graph. Interestingly, the decrease in MR has the same temperature dependence as the 4pt resistance. This is a first hint that the spin dephasing time is somehow correlated to the transport properties. As already discussed above, the temperature dependence of the resistance is dominated by the carrier mobility in the ZnO determined from the mean scattering time of the charge carriers.

In summary, our experimental results on the electrical characteristics of our spin valve device with variable ZnO thickness show characteristic $MR(H)$ curves. The features in the curves are related to the relative magnetization orientation of the cobalt and the nickel layer. Moreover, ADMR measurements prove that the observed MR is indeed a GMR. In addition, our results give evidence for the injection, transport and detection of spin information over length scales larger than all values reported in the literature so far [102].

2.5.3.3 Extraction of spin transport parameters from the measurements

For a further quantitative analysis of the measured GMR in our spin valve devices we now extract the maximum MR at positive magnetic fields for different ZnO thicknesses $t_{\text{ZnO}} \in \{15 \text{ nm}, 20 \text{ nm}, 30 \text{ nm}, 50 \text{ nm}, 80 \text{ nm}\}$, at various temperatures $1.8 \text{ K} \leq T \leq 200 \text{ K}$ and the same contact sizes $A = 20 \times 20 \mu\text{m}^2$. In Fig. 2.37(a)-(d) we exemplarily display the values obtained at $T = 1.8$ K (a), $T = 50$ K (b), $T = 100$ K (c), and $T = 200$ K (d) as open black squares. The model presented in Sect. 2.5.2 is then used to extract the temperature dependence of $\lambda_{\text{sf}}^{\text{ZnO}}$, r_{b} , and γ by fitting the thickness dependence of the maximum MR. For the fit we have used the following values for the material parameters: $\rho_{\text{Co}} = 56 \text{ n}\Omega\text{m}$ [166], $\lambda_{\text{sf}}^{\text{Co}} = 59 \text{ nm}$ [167], $\beta_{\text{Co}} = -0.46$ [152], $t_{\text{Co}} = 11 \text{ nm}$, $\rho_{\text{Ni}} = 59 \text{ n}\Omega\text{m}$ [166], $\lambda_{\text{sf}}^{\text{Ni}} = 21 \text{ nm}$ [168], $\beta_{\text{Ni}} = -0.14$ [168], $t_{\text{Ni}} = 11 \text{ nm}$. As these parameters have only small influence on the MR we assume for simplicity that they are independent of temperature. The only temperature dependent input parameter for the fitting process is ρ_{ZnO} . To determine the temperature dependence we have fabricated a TiN/ZnO/Au reference sample, patterned in the same way as all the spin valve systems, without the two ferromagnetic layers. We then extracted from $R(T)$ measurements the temperature dependence of ρ_{ZnO} for $A = 20 \times 20 \mu\text{m}^2$, and determined values of ρ_{ZnO} at the temperatures investigated by using an exponential fit to the data. The ρ_{ZnO} values obtained with this procedure are illustrated in Fig. 2.37(e) as black solid squares. With all the needed input parameters at hand we can now fit the experimental MR data, to extract $\lambda_{\text{sf}}^{\text{ZnO}}$, r_{b} , and γ . The fitting curves obtained are depicted in Fig. 2.37(a)-(d) as red lines. The curves clearly reproduce the measured data, reflecting a perfect agreement between model and experiment. With the fit we could extract the temperature dependence of the spin diffusion length, the interface resistance and spin selectivity. The results are displayed in Fig. 2.37(e) for $\lambda_{\text{sf}}^{\text{ZnO}}$, (red circles) and in Fig. 2.37(f) for r_{b} (green up triangles), and γ (blue down triangles). The maximum value of $(11.6 \pm 1.0) \text{ nm}$ for

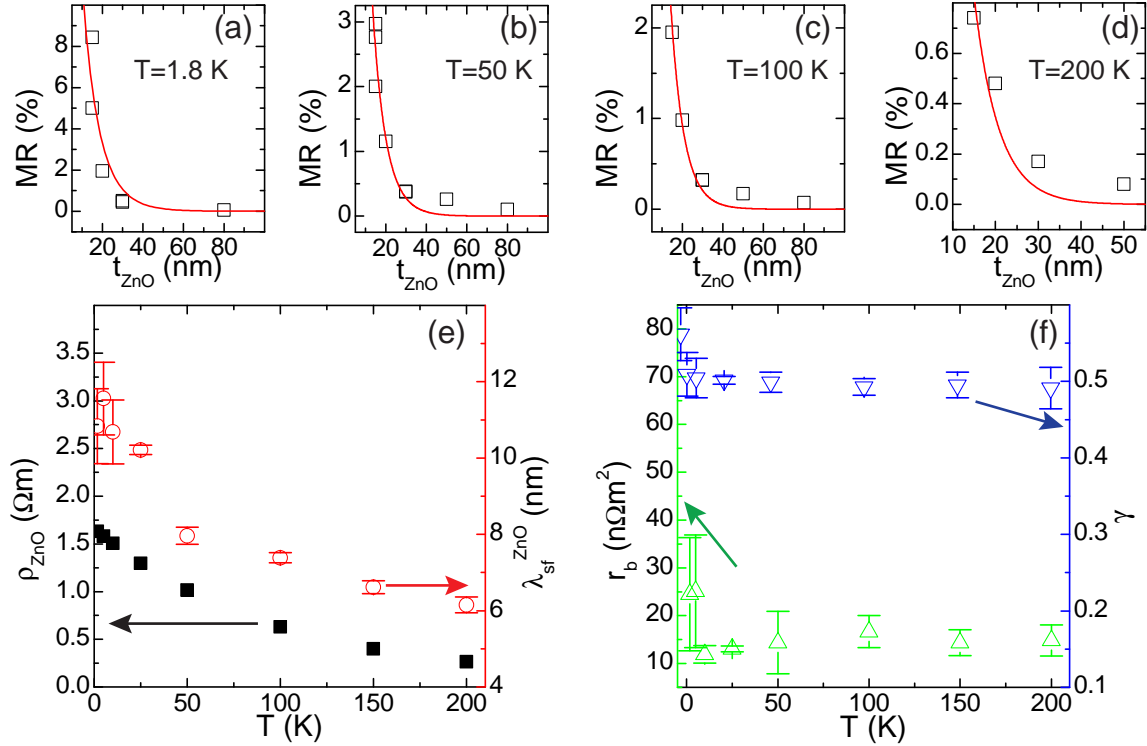


Figure 2.37: Dependence of the maximum MR on t_{ZnO} at $T = 1.8$ K (a), $T = 50$ K (b), $T = 100$ K (c), and $T = 100$ K (d). The open black symbols depict the data obtained for spin valve devices with an area of $400 \mu\text{m}^2$, the red lines are fits with the Valet-Fert model (Eq.(2.23)), which perfectly reproduce the data. (e) Calculated temperature dependent resistivity (closed black symbols, left scale) of the ZnO layer from a exponential fit to the data of a TiN/ZnO/Au reference sample, which is used as a parameter in the simulation, and obtained temperature dependence of the spin diffusion length in ZnO $\lambda_{\text{sf}}^{\text{ZnO}}$ (red circles, right scale) from the fit. (f) Interface resistance r_b (green up triangles) and spin selectivity γ (blue down triangles) as a function of temperature.

$\lambda_{\text{sf}}^{\text{ZnO}}$ is obtained at $T = 5$ K, the spin diffusion length then drops to (10.7 ± 0.8) nm at $T = 10$ K and then gradually decreases to (6.2 ± 0.2) nm at $T = 200$ K. To our knowledge these are the first quantitative values of the spin diffusion length in ZnO using an all electrical detection scheme. In contrast r_b and γ are nearly temperature independent. For $T \geq 10$ K the interface resistance parameter reaches a value around $11 \text{ n}\Omega\text{m}^2$, due to the large error bars at lower temperatures our data are not good enough to support the fact that r_b increases its value for $T < 10$ K. Regarding the spin selectivity parameter γ we obtain a temperature independent value of 0.5. By plugging in the parameters obtained by fitting our thickness dependent MR we calculated maximum MR values for $t_{\text{ZnO}} = 3$ nm and $t_{\text{ZnO}} = 10$ nm at $T = 100$ K and obtained 12% and 3.7% respectively. These values exceed the ones reported in [102] of 1.3% for 3 nm and 1.1% for 10 nm, demonstrating the excellent quality of our samples.

To further analyze the spin dependent transport in ZnO we calculated the corresponding spin dephasing time from the fitted spin diffusion length $\lambda_{\text{sf}}^{\text{ZnO}}$. Under the assumption of a nearly temperature independent carrier concentration $n_{\text{ZnO}} = 5 \times 10^{17} \text{ cm}^{-3}$ we

can calculate the Fermi temperature using $T_F = \frac{\hbar^2}{2m^*} (2\pi n_{\text{ZnO}})^{2/3}$ with an effective mass $m^* = 0.3m_0$ (cf. section 2.2.2.2) and obtain $T_F = 88.9$ K. The Fermi temperature lies within our investigated temperature range and thus we have to consider for the evaluation of the spin diffusion process the crossover from a degenerate Fermi gas at low temperatures to a thermal electron gas at high temperatures. In Eq.(2.6) we defined the spin diffusion length $\lambda_{\text{sf}} = \sqrt{\frac{\ell \ell_{\text{sf}}}{6}}$ as the product of the transport mean free path $\ell = \sqrt{\langle v^2 \rangle} \tau$ and the spin-flip length $\ell_{\text{sf}} = \sqrt{\langle v^2 \rangle} \tau_{\text{sf}}$. Where τ_{sf} is the spin dephasing time and τ is the mean free time between collisions, which can be calculated using the Drude relation $\tau = \frac{m^*}{ne^2\rho}$. For the mean square velocity we now have to use $\langle v^2 \rangle = \langle v_{\text{th}}^2 \rangle + \langle v_{\text{F}}^2 \rangle$ taking into account the crossover between Fermi electron gas and thermal electron gas. Using $\langle v_{\text{th}}^2 \rangle = 3k_{\text{B}}T/m^*$ and $\langle v_{\text{F}}^2 \rangle = 2k_{\text{B}}T_F/m^*$ we finally obtain for the temperature dependence of the spin dephasing time $\tau_{\text{sf}}^{\text{ZnO}}(T)$:

$$\tau_{\text{sf}}^{\text{ZnO}}(T) = \frac{2(\lambda_{\text{sf}}^{\text{ZnO}}(T))^2 n_{\text{ZnO}} \rho_{\text{ZnO}}(T) e^2}{k_{\text{B}}(T + \frac{2}{3}T_F)}. \quad (2.28)$$

The obtained values of $\tau_{\text{sf}}^{\text{ZnO}}$ are plotted as black squares in Fig. 2.38(a) as a function

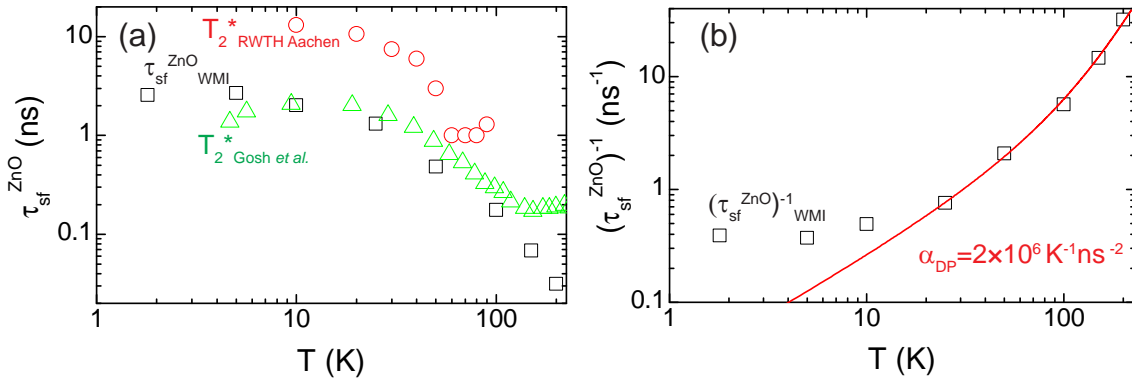


Figure 2.38: (a) Calculated spin dephasing time $\tau_{\text{sf}}^{\text{ZnO}}$ (open black squares) from Eq.(2.28) for $n_{\text{ZnO}} = 5 \times 10^{17} \text{ cm}^{-3}$. $\tau_{\text{sf}}^{\text{ZnO}}$ decreases with increasing temperature and saturates for $T \leq 10$ K; a maximum value of 2.6 ns is obtained at $T = 1.8$ K. The panel also includes TRFR data from RWTH Aachen (red circles) measured on our optimized laser-MBE grown, buffered ZnO layer on c-plane Al_2O_3 (cf. Fig. 2.19) and TRFR data reported by Gosh *et al.* (green triangles) [97] for a PLD grown 100 nm ZnO layer on c-plane sapphire. For $10 \text{ K} \leq T \leq 60 \text{ K}$ all three data sets exhibit qualitatively the same temperature dependence. (b) Temperature dependence of the ZnO spin dephasing rate (open black symbols) and a fit to the data ($T \geq 25 \text{ K}$) with a model solely based on a linear in k D'yakonov-Perel' mechanism (Eq.(2.29)). The material parameter $\alpha_{\text{DP}} = 2 \times 10^6 \text{ K}^{-1} \text{ ns}^{-2}$ seems unreasonably high compared to the theoretical value of $34.6 \text{ K}^{-1} \text{ ns}^{-2}$ reported in [99].

of temperature. For $T > 10$ K the spin dephasing time exponentially increases with decreasing temperature. For lower temperatures $\tau_{\text{sf}}^{\text{ZnO}}$ saturates and reaches a maximum value of 2.6 ns. This temperature dependence agrees well with the already published data in [97] for a 100 nm thick ZnO film grown by PLD on c-plane sapphire with a carrier concentration of $n_{\text{ZnO}} = 1.9 \times 10^{19} \text{ cm}^{-3}$, which is included in Fig. 2.38(a) as green

triangles, where the spin dephasing time for ZnO remains constant for low temperatures and only starts to decrease for $T \geq 50$ K. Interestingly our all electrical data even quantitatively coincides with these all optical measured data for $10 \text{ K} \leq T \leq 100 \text{ K}$, which suggests that the spin dephasing mechanism for both samples have to be identical. Moreover, the very same temperature dependence has been extracted from the TRFR experiments on our high quality ZnO thin films in Sect. 2.3, included as red circles in Fig. 2.38(a), which further substantiates that the mechanisms of spin dephasing have to be identical for all these ZnO thin films. The T_2^* measured for our optimized ZnO layer by TRFR exceed by a factor of 5 both the already published optical TRFR data by Gosh *et al.* and our all electrical spin valve data. As the structural quality of our ZnO layer in the all electrical spin valve experiments has a lower structural quality (FWHM of the ZnO (0002) XRC 0.62° cf. Fig. 2.28) than the samples we have used for the optical TRFR experiments (FWHM of the ZnO (0002) XRC 0.03° cf. Fig. 2.4), this increase in spin dephasing time shows that the structural quality also plays an important role for $\tau_{\text{sf}}^{\text{ZnO}}$. Taken together, this evaluation of the temperature dependence of the spin dephasing time evaluated by different experimental techniques suggests, that the spin dephasing mechanisms are identical for all the different ZnO samples independent of structural quality.

To further clarify this we followed the analysis and theoretical description of spin dephasing in ZnO described in [99]. In this publication different spin dephasing mechanisms were discussed to theoretically explain the data obtained in [97]. Two main mechanisms were needed to completely explain the data of the TRFR experiments: The Dzyaloshinsky-Moriya (DM) mechanism due to an anisotropic exchange between the localized electronic states and the D'yakonov-Perel'(DP) mechanism due to the reflection asymmetry of the ZnO along the c-axis and the bulk inversion asymmetry of the wurtzite crystal. In the theoretical description the authors have found the following temperature dependence: For $T < 50$ K the spin dephasing is dominated by the DM mechanism, because most of the charge carriers are bound to shallow and deep states within the band gap. At $T \geq 50$ K the DP mechanism dominates because it arises from scattering of delocalized charge carriers and the related change in effective magnetic field due to spin-orbit interaction. The DP mechanism in wurtzite crystals can be explained by two terms: One is linear in \mathbf{k} and one is cubic in \mathbf{k} . From the calculations presented in [99] it is evident, that for ZnO the linear in \mathbf{k} term dominates the DP mechanism. The temperature dependence of the DP mechanism can then be described by

$$\tau_{\text{DP}}^{-1} = \alpha_{\text{DP}} \tau(T) T, \quad (2.29)$$

τ_{DP} is the spin dephasing time arising due to the DP mechanism, α_{DP} describes the efficiency of this mechanism, $\tau(T)$ is again the mean free time between collisions and can be calculated from the mobility $\mu(T)$ of the system: $\tau(T) = \mu(T) m^* / e$. m^* is the effective mass of the free charge carriers.

At elevated temperatures we would expect that the dominating spin dephasing mechanism is DP. In order to confirm this expectation we further analyzed our obtained spin dephasing times. Figure 2.38(b) shows a double logarithmic representation of the spin dephasing rate $(\tau_{\text{sf}}^{\text{ZnO}})^{-1}$ versus temperature (open black squares) of our all electrical spin valve data. The red line represents a fit to the data for $T \geq 25$ K using Eq.(2.29), where we have calculated $\tau(T)$ from resistance dependent data of the reference sample

again using a constant carrier concentration of $n_{\text{ZnO}} = 5 \times 10^{17} \text{ cm}^{-3}$. The calculated values of $\tau(T)$ are in the range of 10 as, which is a very small value and is attributed to a dominant impurity/defect scattering. From the fit to our data we also obtained $\alpha_{\text{DP}} = 2 \times 10^6 \text{ K}^{-1} \text{ ns}^{-2}$, which is more than 5 orders of magnitude larger than the theoretically calculated $\alpha_{\text{DP}} = 34.6 \text{ K}^{-1} \text{ ns}^{-2}$ [99, 169]. This result might indicate that the used theoretical approach is not appropriate to explain the observed spin dephasing times and the influence of impurity concentration on α_{DP} has to be taken into account. However, interestingly, the simple assumption of a DP dominated spin dephasing still reproduces the temperature dependence $T \geq 25 \text{ K}$ of $\tau_{\text{sf}}^{\text{ZnO}}$ very well. For lower temperatures the spin dephasing rate is dominated by the temperature independent the Dzyaloshinsky-Moriya (DM) mechanism, which explains the saturation of $(\tau_{\text{sf}}^{\text{ZnO}})^{-1}$. Thus the temperature evolution of the spin relaxation rate extracted from our spin valve experiments is consistent with the theoretical description using a spin dephasing, which is dominated by two different mechanisms depending on the temperature, for $T \leq 25 \text{ K}$ the temperature independent Dzyaloshinsky-Moriya (DM) mechanism dominates and for $T \geq 25 \text{ K}$ the temperature dependent D'yakonov-Perel'(DP) mechanism dominates

In summary, we have demonstrated with our experiments on epitaxial spin valve structures with a ZnO spacer layer, that it is not only possible to inject, transport and detect spin polarized currents in ZnO up to room temperature and over length scales larger than 80 nm at low temperatures, but that a quantitative extraction of the relevant spin transport parameters $\lambda_{\text{sf}}^{\text{ZnO}}$, r_{b} , γ from our data is possible. The values obtained are the first set of data extracted via an all electrical injection and detection scheme in ZnO. The temperature dependence of $\lambda_{\text{sf}}^{\text{ZnO}}$ and accordingly $\tau_{\text{sf}}^{\text{ZnO}}$ exhibits two different regimes: at low temperatures $T \leq 25 \text{ K}$ $\tau_{\text{sf}}^{\text{ZnO}}$ saturates for higher temperatures $T \geq 25 \text{ K}$ $\tau_{\text{sf}}^{\text{ZnO}}$ decreases with increasing temperature. The qualitatively identical temperature dependence has been observed in our TRFR experiments and can be understood in terms of a DP mechanism linear in \mathbf{k} dominating $\tau_{\text{sf}}^{\text{ZnO}}$ at high temperatures and a temperature independent Dzyaloshinsky-Moriya (DM) mechanism dominating $\tau_{\text{sf}}^{\text{ZnO}}$ at low temperatures.

Our results show that it is of fundamental interest to further study the influence of impurities and defects in ZnO on the spin relaxation. A possible all electrical experiment could be carried out with lateral spin valve structures in a non local geometry using the high quality thin films obtained in Sect. 2.2. Due to the short length scales $\leq 100 \text{ nm}$ required in this geometry this will result in some challenges for the fabrication of such structures. In addition, these non local detection scheme could be carried out on differently oriented ZnO thin films, probing the influence of the relative orientation of spin transport direction and the c-axis in ZnO, which is responsible for the bulk asymmetry. Moreover, the introduction of a tunneling barrier between the ferromagnets and ZnO would allow a tunability of the interface resistance parameter r_{b} and the interface spin selectivity γ . This will open up further ways to influence the spin dependent transport in ZnO. The multiple possibilities arising from our spin valve experiments prove, that the spin dependent transport in ZnO is of fundamental interest for future spin electronics.

2.6 Spin electronics in epitaxial zinc oxide thin films: A summary

In this chapter we presented different physical properties of ZnO thin films grown on sapphire. The main focus of this study was the quantitative determination of spin related parameters. This was possible by employing all optical TRFR experiments in plain ZnO films, a combination of electrical injection and optical detection by Hanle MOKE experiments in FM/ZnO heterostructures, and all electrical injection and detection experiments in ZnO-based spin valve structures.

The first crucial step for the successful experiments was the optimization of laser-MBE grown ZnO films on Al₂O₃ (Sec. 2.2). By carefully tuning the growth parameters we were able to fabricate ZnO layers with a high quality in structural, electrical, and optical properties. Important for the growth of high quality samples is the annealing of the sapphire substrate prior to growth and the use of optimum deposition parameters ($\varrho_{ED} = 1 \text{ J/cm}^2$, $T_{\text{sub}} = 400^\circ\text{C}$, $p_{\text{O}_2} = 1 \mu\text{bar}$). The quality of zinc oxide thin films could be further improved by the introduction of a ZnO or (Mg,Zn)O buffer layer. The structural characterization of our thin films showed, that they grow with lattice parameters close to the bulk values. Laue oscillations in the $2\theta - \omega$ scans and the narrow FWHM of the ZnO (0002) XRC of 0.02° indicate a coherent growth along the out-of-plane direction. For the FWHM of the ZnO (10 $\bar{1}$ 1) XRC we achieved a value of 0.27° for a $1 \mu\text{m}$ thick ZnO layer which is comparable to recently published data [105, 109, 115, 116]. Moreover, the in-plane epitaxial relationship for c-plane sapphire was: Al₂O₃(0001)[11 $\bar{2}$ 0] || ZnO(0001)[10 $\bar{1}$ 0]. The analysis of TDH measurements suggested that in our unbuffered as well as in the buffered ZnO films, two different layers contribute to the Hall properties: A degenerate layer located at the interface between substrate and film and a semiconducting layer on top. The extracted residual carrier concentration of our n-type ZnO at room temperature was as low as $n = 4.5 \times 10^{16} \text{ cm}^{-3}$ caused by unintentional Al doping and is on par to other reported values [128]. In contrast, the Hall mobility in our samples is by one order of magnitude lower than the values reported by other groups. We could pin point the high density of dislocations in our samples as the source for the low mobility and suggest to reduce the density of dislocations by the introduction of a MgO buffer layer in the future. The HRTEM images from a buffered sample confirm the existence of a high number of dislocations. In addition, these HRTEM micrographs exhibit sharp interfaces and cross-sectional diffraction confirms the epitaxial in-plane relation between the oxygen sublattice of sapphire and the Zn sublattice of ZnO. Temperature dependent PL experiments confirmed the existence of donor bound and free excitons in our samples. The donor bound excitons are related to aluminum donors and verified Al as the main impurity in our samples. Moreover, the FWHM of the donor bound exciton line I₆ is as low as 3.5 meV in our samples, which is equal to already reported values [42]. The results obtained by HRXRD, TDH, HRTEM, and PL measurements in our samples again prove the high quality of the ZnO layers.

The long spin dephasing times of 14 ns obtained by time-resolved Faraday rotation experiments (Sec. 2.3) in our growth optimized samples exceed values reported so far for thin films by nearly one order of magnitude [97]. By wavelength dependent TRFR measurements we could show that this long-lived spin information storage is due to the resonant excitation of Al donor bound excitons. Moreover, the temperature dependence

showed that the underlying mechanism is only effective at low temperatures because of the thermal dissociation of donor bound excitons at $T > 60$ K. Interestingly, the spin dephasing times extracted from our TRFR measurements exceed the lifetime of a donor bound exciton by two orders of magnitude. We attribute this to the transfer of the spin polarized electron from the exciton into the donor state, by a recombination of the exciton hole with the donor electron and an occupation of the free donor level by the spin polarized excitonic electron. This mechanism allows a localized storage of spin information in the Al donor level increasing the spin dephasing times of the generated spin polarization. Moreover, as a storage of spin information on donor levels is possible at different excitation wavelengths, two color experiments should allow the manipulation and readout of the spin information in the donor state. This enables a combination of optical manipulation and solid state based storage for quantum information processing.

Subsequently, the storage of spin information in localized excitonic states has been investigated by Hanle MOKE experiments by sending a spin polarized electrical current from a ferromagnet through ZnO (Sec. 2.4). The voltage bias dependence of the Hanle MOKE signal unambiguously proves that the origin of the observed Hanle MOKE signal is the spin polarized current injected from the cobalt electrode. Moreover, the signal amplitude varied systematically with the detection wavelength of the linearly polarized laser beam, and the observed signal amplitude maxima occurred at energies corresponding to the excitation of donor bound excitons. The highest maximum in absolute signal amplitude was observed at 3.38 eV detection energy, corresponding to the aluminium donor level. These observations suggest the transfer of spin polarization from the mobile conduction electrons to the localized donor states. We model our data in terms of trapping of conduction electrons in localized donor levels, and our measurements show that this transfer mechanism is most effective at $T = 15$ K and vanishes for $T > 30$ K. The experimental results pave the way for an efficient, electrical storage and optical addressing of spin information on localized states in a semiconductor.

Finally, we were able to extract quantitative information on the spin transport properties in ZnO using spin valve systems with zinc oxide as a spacer layer and Co and Ni as ferromagnetic electrodes (Sec. 2.5). The structural characterization again demonstrated the high quality of our multilayer samples with only one in-plane orientation, which is preserved in all layers grown with laser-MBE and electron beam evaporation: Au(111) $[2\bar{1}\bar{1}] \parallel$ Ni(111) $[2\bar{1}\bar{1}] \parallel$ ZnO(0001) $[10\bar{1}0] \parallel$ Co(0001) $[10\bar{1}0] \parallel$ TiN(111) $[2\bar{1}\bar{1}] \parallel$ Al₂O₃(0001) $[11\bar{2}0]$. SQUID magnetometry data proved an individual magnetization reversal of the two electrodes, and a saturation magnetization close to the bulk value for our samples. Our spin valve contacts exhibit Ohmic behavior over the whole temperature range investigated. In addition, we were able to verify, that the observed MR is indeed a GMR effect by taking into account the agreement between SQUID magnetometry, magnetic field orientation dependence of MR, and ADMR experiments. Moreover, it was possible to successfully inject and detect spin polarized carriers at room temperature across a 20 nm thick ZnO layer. The fact that the temperature dependence of the MR and the resistance are identical in our samples indicates that the limitation in spin diffusion length is connected to the free electron path/mobility.

For the quantitative analysis of our data, we applied a Valet-Fert model to fit our MR as a function of ZnO thickness at various temperatures. The extracted temperature dependent spin diffusion length in our samples increased up to 11.6 nm with decreasing temperature. To our knowledge, our experiments are the first all-electrical spin injection

and detection in ZnO providing quantitative data. The interface resistance parameter r_b and spin selectivity γ are constant over the whole temperature range. Interestingly, we could show that the spin dephasing time in ZnO contributing to the GMR exhibits two different temperature regimes: at low temperatures the spin dephasing time is constant and is dominated by the temperature independent Dzyaloshinsky-Moriya mechanism, at higher temperatures the spin dephasing time decreases with increasing temperature and is dominated by the D'yakonov-Perel' mechanism linear in \mathbf{k} . Moreover, the temperature dependence agrees qualitatively with the results obtained in [97] and our own TRFR experiments indicating that the spin dephasing mechanisms are identical for all these ZnO samples. A direct quantitative comparison of the our TRFR data and the spin valve data shows that the structural quality of the ZnO layer plays a crucial role for the spin dephasing time. Thus our results indicate, that higher spin dephasing times and longer spin diffusion lengths can be achieved in ZnO thin films by further optimizing the structural and electrical properties.

To summarize, we extensively studied the spin related properties of our optimized laser-MBE grown ZnO thin films by TRFR, Hanle MOKE and spin valve experiments. In our optical experiments the existence of localized states with long spin lifetimes allows the storage of spin information on ns timescales. Moreover, these localized states can be electrically addressed by the trapping of injected, mobile spin polarized electrons. The spin valve multilayers with ZnO as the N-layer allowed us to quantify spin diffusion length, interface resistance and spin selectivity in our ZnO films by an all electrical measurement. In addition, the DP dominated spin dephasing time shows that by increasing the mobility of the charge carriers the spin diffusion length in ZnO will also increase.

An outlook on further possible experiments with spins in ZnO based on the results of this thesis is given in Chapter 4.

Chapter 3

Spin caloritronics

Abstract

In the second part of this thesis we address spin-related transport phenomena and pure spin currents in ferromagnetic metals and insulators. As a first step we investigate the structural and magnetic quality of Co_2MnSi and yttrium iron garnet thin films grown via laser-MBE. For the Cobalt-based Heusler compounds we find from a comparison to a reference sample that our laser-MBE grown thin films exhibit state-of-the-art structural and magnetic properties. Our epitaxial YIG films on GGG(111) substrates show state-of-the-art crystalline (FWHM YIG-(444) rocking curve $< 0.04^\circ$) and magnetic properties (saturation magnetization $> 110 \text{ kA/m}$, FMR linewidth at 10 GHz $< 1 \text{ mT}$). Moreover, we show that the in-situ deposition of a platinum layer on top of YIG does not influence the structural and magnetic quality of the YIG film.

In the second part, we quantitatively study magneto-galvanic potentials arising due to thermal gradients, e.g., anisotropic magnetothermopower and the spin Seebeck effect. We compare the magnetothermopower and magnetoresistance tensors and experimentally observe additional contributions in the magnetothermopower. By applying a theoretical model to fit our experimental magnetothermopower and magnetoresistance data we extract quantitatively resistivity and Seebeck coefficients and magnetic anisotropy parameters from the measurements. We test this approach with the model system $(\text{Ga},\text{Mn})\text{As}$ and prove that in principle it is possible to extract the full resistivity and Seebeck tensor from angle resolved experiments. The excellent agreement between simulation and experiment for the angle dependent magnetoresistance of metallic Heusler compound Co_2FeAl thin films confirms the universality of the model.

Finally, we use laser-MBE grown thin films of the ferromagnetic insulator yttrium iron garnet for pure spin current experiments. We demonstrate by spin pumping experiments in YIG/Pt bilayers that YIG thin films are an excellent source for pure spin currents and the spin mixing conductance of YIG/Pt heterostructures is comparable to conductive ferromagnet/Pt heterostructures. In addition, we observe a new type of magnetoresistance effect in our YIG/Pt samples. The origin of this effect is related to the conversion of charge currents to spin currents via the spin Hall effect and vice versa via the inverse spin Hall effect in combination with the absorption of spin currents at the YIG/Pt interface, which can be controlled by the magnetization orientation of the YIG.

3.1 Introduction into spin caloritronics

Pure spin currents - which transport only spin (angular momentum) and no electrical charge - build a new paradigm for spin transport and spin electronics. The search for pure spin current sources thus is a key issue for spin electronics. In the last few years two new methods to generate a spin current have evolved from theory to experiment: the spin Seebeck effect [17–30] and the spin pumping effect [5–16]. Both methods involve ferromagnet (FM)/nonferromagnet (NFM) hybrid structures to generate and detect the spin currents. Furthermore, to generate the spin current the FM is driven out-of-equilibrium in both approaches.

In case of the spin Seebeck effect this non-equilibrium condition in the FM [18, 19, 21] is achieved by applying a thermal gradient across the hybrid structure. Due to the boundary conditions at the FM/NFM interface the effective temperature of magnons and phonons are different. This difference leads to the flow of a spin current from the FM into the NFM. Interestingly, this effect is observed for different types of ferromagnets: electrical conductors [20, 24], semiconductors [25, 27], and insulators [17, 22, 23, 26, 30]. In addition, this spin current can flow from the FM into different nonferromagnetic materials such as normal metals [20, 24, 25, 27, 30] or semiconductors [28, 29], which makes this effect interesting for spintronic applications. This is supported by the fact that the spin current is not obstructed by tunnel barriers [28]. In case of electrically conductive FM/NFM heterostructures, the application of a thermal gradient leads not only to the spin Seebeck effect, but also to "conventional" magneto-thermo-galvanic effects such as the anisotropic magnetothermopower or the anomalous Nernst effect. To separate these different caloritronic effects from one another it is imperative to first obtain a deeper knowledge of the non spin Seebeck related, "conventional" thermopower signals, which is one main part of this chapter.

In the case of the spin pumping effect it is possible to generate a pure spin current flowing from the ferromagnet into the nonmagnetic material by driving a precessional motion of the magnetization utilizing ferromagnetic resonance [16]. In analogy to the spin Seebeck effect the spin pumping effect is not limited to electrically conductive materials [5, 6, 10, 11, 13, 15], but one can also use ferromagnetic insulators [14, 170, 171] and semiconductors [13] to generate a spin current. Moreover, it has already been shown that it is possible to inject a spin current from a ferromagnet into a semiconductor [8, 12] using spin pumping while elegantly bypassing the conductivity mismatch problem, which broadens the range of possible spintronic applications of this effect.

This chapter is divided into three main parts. In the first part the structural and magnetic properties of two new material classes we have successfully grown via laser-MBE are investigated: metallic Heusler compounds and insulating garnets. For the Heusler compounds (Sect. 3.2.1), we present a direct comparison of the structural and magnetic properties of Co_2MnSi thin films grown on MgO substrates via laser-MBE and via RF-sputtering technique. In case of the garnet material class, we demonstrate in section 3.2.2 that our laser-MBE grown yttrium iron garnet (YIG) layers exhibit excellent structural and magnetic properties and that the properties remain unchanged when a thin normal metal layer is deposited in-situ on top of the YIG.

In the second part we deal with the magnetothermopower and magnetoresistance of electrically conductive ferromagnets. In Sect. 3.3.1 we first introduce a theoretical model to describe the resistivity and Seebeck tensor of ferromagnetic materials as a series ex-

pansion of the magnetization direction. This theoretical model is then used in proof-of-principle experiments to demonstrate the quantitative extraction of the full resistivity and Seebeck tensors from magnetotransport measurements as a function of external magnetic field orientation. The validity of our model is tested by demonstrating the quantitative agreement between theoretical modeling and experimental data for two totally different types of ferromagnetic conductors: First we start with the prototype ferromagnetic semiconductor (Ga,Mn)As in Sect. 3.3.2 and second we study the magnetoresistance of Cobalt-based Heusler compounds in Sect. 3.3.3.

In the last part of this chapter we examine the generation and detection of pure spin currents utilizing the ferromagnetic insulator yttrium iron garnet. As a first important step we take advantage of the excellent physical properties of our YIG layer and determine the spin mixing conductance of the YIG/NM interface in Sect. 3.4.1 by means of two independent set of experiments based on spin pumping. Last but not least, we introduce in section 3.4.2 theoretically and experimentally a novel type of magnetoresistance effect, which only occurs in ferromagnetic insulator/normal metal hybrid structures. This effect is based on the reflection/absorption of a spin current induced via the spin Hall effect from a charge current flowing through the normal metal.

We close this chapter by a summary of the relevant results in Sect. 3.5.

3.2 Materials for spin caloritronics grown via laser-MBE

In this section we introduce two types of materials that have been successfully grown in state-of-the-art quality via laser-MBE during the work of this thesis using carefully optimized deposition parameters.

In Sect. 3.2.1 we investigate the successful laser-MBE growth of Co_2MnSi on (001)-oriented MgO and compare the structural and magnetic properties of these thin films to literature and a reference sample grown via RF-sputtering technique. The results of this comparison show that our laser-MBE films exhibit excellent structural and magnetic properties and are well suited for further spin caloritronic experiments. Unfortunately, due to time restrictions they could not be carried out during the work of this thesis.

In the second part of this section we present the excellent, state-of-the-art structural and magnetic properties of our laser-MBE grown YIG thin films and YIG/Pt hybrid structures grown on gadolinium gallium garnet (GGG) and yttrium aluminium garnet (YAG) substrates. The films have been investigated by HRXRD, SQUID magnetometry and ferromagnetic resonance (FMR) (Sect. 3.2.2).

3.2.1 Laser-MBE growth of Heusler compound thin films

This section deals with the investigation of the structural and magnetic quality of Co_2MnSi thin films probed via HRXRD and SQUID magnetometry. We start in Sect. 3.2.1.1 with a short introduction into Heusler compounds. Section 3.2.1.2 then presents the results obtained for our laser-MBE grown Co_2MnSi thin films and compares these results to literature and a reference sample grown via RF-sputtering technique at the Universität Bielefeld.

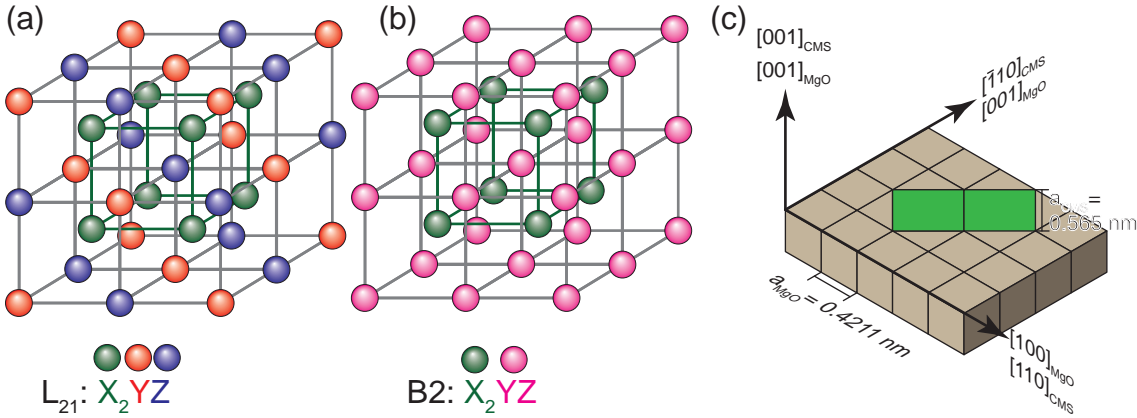


Figure 3.1: (a) Illustration of the crystal structure of full Heusler compounds X_2YZ in the highly ordered L_{21} phase. The crystal inherits 4 interpenetrating fcc lattices, evenly placed along the body diagonal of a cube. (b) Crystal structure of the B2 phase of a full Heusler compound. In contrast to the highly ordered L_{21} phase the Y and Z atoms are randomly distributed on the 2 corresponding fcc sublattice sites. (c) The epitaxial relationship for growth of Cobalt-based Heusler thin films on (001)-oriented MgO substrates is illustrated with Co_2MnSi (CMS) as an example. To reduce the lattice mismatch to 5%, the cubic unit cell of the Heusler compound is rotated by 45° leading to the epitaxial relationship $\text{MgO}(001)[100] \parallel \text{Co}_2\text{MnSi}(001)[110]$.

3.2.1.1 Heusler compounds: a short introduction

The discovery of Heusler compounds with the chemical structure X_2YZ , where X and Y are transition metals and Z is a main group element, dates back into 1903, when Friedrich Heusler discovered that Cu_2MnAl was ferromagnetic even though the constituents for themselves are not [172]. This discovery started a series of investigations to clarify the chemical and ferromagnetic ordering in these ternary compounds [173–176]. From these studies two different classes of Heusler compounds were discovered, the half-Heusler compounds with the chemical structure XYZ and the full-Heusler-compounds with X_2YZ . The variety of possible combination of materials allows to tune the physical properties of Heusler compounds from metallic to semiconducting [177, 178], or even superconducting [179–181].

The crystal structure of a full-Heusler compound X_2YZ is the cubic L_{21} structure ($Fm\bar{3}m$ space group). It consists of 4 interpenetrating face centered cubic (fcc) sublattices, two are occupied by the X atoms and the other two by the Y and Z atoms, as illustrated in Fig. 3.1(a). The two X sublattices are positioned at the 8c Wyckoff positions $(\frac{1}{4}, \frac{1}{4}, \frac{1}{4})$, $(\frac{3}{4}, \frac{3}{4}, \frac{3}{4})$ of the cubic unit cell, while the Y and Z atoms occupy the 4a (0,0,0) and 4b $(\frac{1}{2}, \frac{1}{2}, \frac{1}{2})$ positions, respectively. The L_{21} phase represents the most ordered phase of the full Heusler compounds. Interchange of atoms between the sublattices lead to different degrees of disorder. If the combined (0,0,0), $(\frac{1}{2}, \frac{1}{2}, \frac{1}{2})$ sites are randomly occupied by Y and Z atoms, the structure is referred to as the B2 structure (Fig. 3.1(b)).

For our growth experiments we focused on the ferromagnetic Cobalt-based Heusler compound Co_2MnSi (CMS) with a Curie temperature well above room temperature [182], which according to theoretical calculations [183] has a band gap for the minority spin species at the Fermi level. This leads to a half metallic conduction, where the conduction

type depends on the spin orientation of the charge carrier: metallic for the majority spin carriers and insulating for the minority spin carriers. As a direct result, the electrical current in this material is in theory 100% spin polarized. This predicted half metallicity has put this material into the focus of spin electronics. Moreover, the lattice parameter $a_{\text{CMS}} = 0.5654 \text{ nm}$ [184] of CMS is close to the one of GaAs $a_{\text{GaAs}} = 0.5653 \text{ nm}$ [182], which opens the possible use of CMS as a spin-injector and/or -detector in GaAs based spin electronic applications due to the small lattice mismatch of -0.02%. Moreover, the predicted high spin polarization makes CMS a promising candidate for magnetic tunnel junctions (MTJs). The state-of-the-art insulator for such MTJs is currently MgO. Unfortunately, the lattice constant $a_{\text{MgO}} = 0.4211 \text{ nm}$ of MgO is significantly smaller than the one of CMS, which would result in an enormously large lattice mismatch (-26%). For (001)-oriented MgO substrates the lattice mismatch is considerably reduced to 5%, if the cubic unit cell of CMS is rotated by 45° in the plane with respect to the cubic unit cell of MgO. This leads to the epitaxial relationship of $\text{MgO}(001)[100] \parallel \text{Co}_2\text{MnSi}(001)[110]$ as illustrated in Fig. 3.1(c).

3.2.1.2 Laser-MBE growth of the Heusler compound Co_2MnSi

In order to obtain higher quality thin films and more control over the growth parameters, we investigated the possibility of growing Cobalt-based Heusler compound thin films with our laser-MBE system. The use of pulsed laser deposition for the growth of metallic systems results in some obstacles, that need to be resolved. In particular, the generation of a plasma plume from a metallic target requires a high energy density ϱ_{ED} at the target, due to the weak absorption of the UV excimer pulses and the high melting point of the material. Moreover and as always, the incorporation of impurities into the thin film or the target material need to be prevented by achieving a low base pressure in the deposition chamber. Despite these obstacles the successful growth of Cobalt-based Heusler compounds on various substrates has been already reported [185–191]. In the following we present the results for the growth of Co_2MnSi (CMS) thin films on (001)-oriented MgO using our laser-MBE setup.

Prior to growth, the fabrication of a stoichiometric target with high purity is a prerequisite towards high quality thin films. The polycrystalline Co_2MnSi target was synthesized by melting high purity (99.95%) Co, Mn, Si slugs in a RF-induction furnace in cooperation with Andreas Bauer from the group of Christian Pfeleiderer (E21) at the TU München. The slugs were cleaned by chemical etching and individual melting to remove oxides. Afterwards the elements were weighed into the stoichiometric 2:1:1 relation and placed into the RF furnace. In an Ar atmosphere of 2 bar the material was melted several times and cooled to obtain a polycrystalline Co_2MnSi rod. From this rod a disc with a thickness of 0.5 cm and a diameter of 2 cm was cut by spark erosion, which was then used as the target for the laser-MBE process. A more detailed description of the fabrication can be found in [192].

We checked the stoichiometry of the target via energy dispersive X-ray spectroscopy. The obtained concentrations of Co, Mn, and Si are within 1% to the desired 2:1:1 composition. Locally resolved measurements yielded no noteworthy deviations from the desired composition. These results verify that we have fabricated polycrystals with good stoichiometry, which can be used as target materials for laser-MBE.

From this Co_2MnSi target, we have grown a set of thin films with different deposition

parameters (substrate temperature, energy density at the target, growth atmosphere) on (001)-oriented MgO substrates. For a better absorption of the infrared laser substrate heater, we sputtered a 150 nm thick Pt layer on the backside of the substrate. The structural quality of the films was investigated in HRXRD experiments [192]. We determined an optimum set of growth parameters for Co₂MnSi thin films with our laser-MBE system: 60 mm target to substrate distance, 400 °C substrate temperature, 3 J/cm² energy density at the target, 10 Hz repetition rate, and deposition at the base pressure of 3×10^{-8} mbar. Using these optimized parameters we have grown a 21 nm (100000 pulses) thick Co₂MnSi thin film on a (001)-oriented MgO substrate. We compare the structural and magnetic properties of our film to a state-of-the-art reference sample, which is a 20 nm thick CMS film on (001)-oriented MgO grown via RF-sputtering at room temperature and annealing at 400 °C at the university of Bielefeld by Inga-Mareen Imort.

The results that we have obtained for both films are summarized in Fig. 3.2(a)-(d).

The $2\theta - \omega$ scans of both samples (Fig. 3.2(a)) only contain reflections that can be attributed to the CMS film or the MgO substrate. Moreover, both samples have highly (001)-oriented thin films, as we could not observe any other reflections in our scans. In comparison, the intensity and position of the (002) and (004) Co₂MnSi reflexes are different for the two growth techniques. For our laser-MBE grown sample, the 2θ positions are 31.36° for the (002) reflection and 65.39° for the (004) reflection. For the sputtered CMS film, they are 31.82° and 66.30°, respectively. From these values we calculated the out-of-plane lattice constant of the two CMS films using the Bragg equation and averaging over the two values. We obtained 0.5702 nm and 0.5627 nm for our laser-MBE and the sputtered thin film, respectively. The reported bulk lattice constant for Co₂MnSi is 0.5654 nm [184]. If we compare this value with the lattice constant of MgO (0.4211 nm) and include the 45° rotation of the CMS unit cell with respect to the MgO unit cell ($\sqrt{2} \times 0.4211 \text{ nm} = 0.5955 \text{ nm}$), we expect a tensile in-plane strain for the Co₂MnSi layer on the MgO substrate, which should lead to a smaller out-of-plane lattice constant compared to the bulk value. The sputtered sample is in agreement with this assumption, but the laser-MBE grown sample in contrast has a larger out-of-plane lattice constant. We attribute this difference to the annealing step carried out for the sputtered sample, which will change the strain relaxation in the film. Moreover, the intensity of the film reflections are different for the two samples, while for the (002) reflection the intensity for the sputtered film is higher than for our laser-MBE grown film, this observation is reversed for the (004) reflection. These different intensities can be explained with different atomic order on the 4 fcc sublattices for the two samples, due to the different growth techniques. The difference in intensity and position for the CMS (004) reflections is clearly visible in the enlargement in Fig. 3.2(b). For a fully ordered CMS crystal the relative intensities have been calculated in [193], from these calculations the ratio in intensities between the (002) and (004) reflections should be 4.67:16.46 ($\approx 1 : 3.5$). Comparing the ratios for our CMS film we obtain a ratio of roughly 1:4 and for the sputtered reference sample a ratio of 1:1. From this we conclude that the structural order in our sample is higher and closer to the ideal L₂₁ structure of the Heusler compounds.

Another important difference between the two samples is illustrated in the rocking curves obtained for the CMS (004) reflection in Fig. 3.2(c). Our laser-MBE grown sample has a much narrower rocking curve than the sputtered sample, which proves that our laser-MBE sample has a lower mosaic spread. To further quantify this difference we fitted a Gaussian function to both rocking curves and extracted the FWHM of these

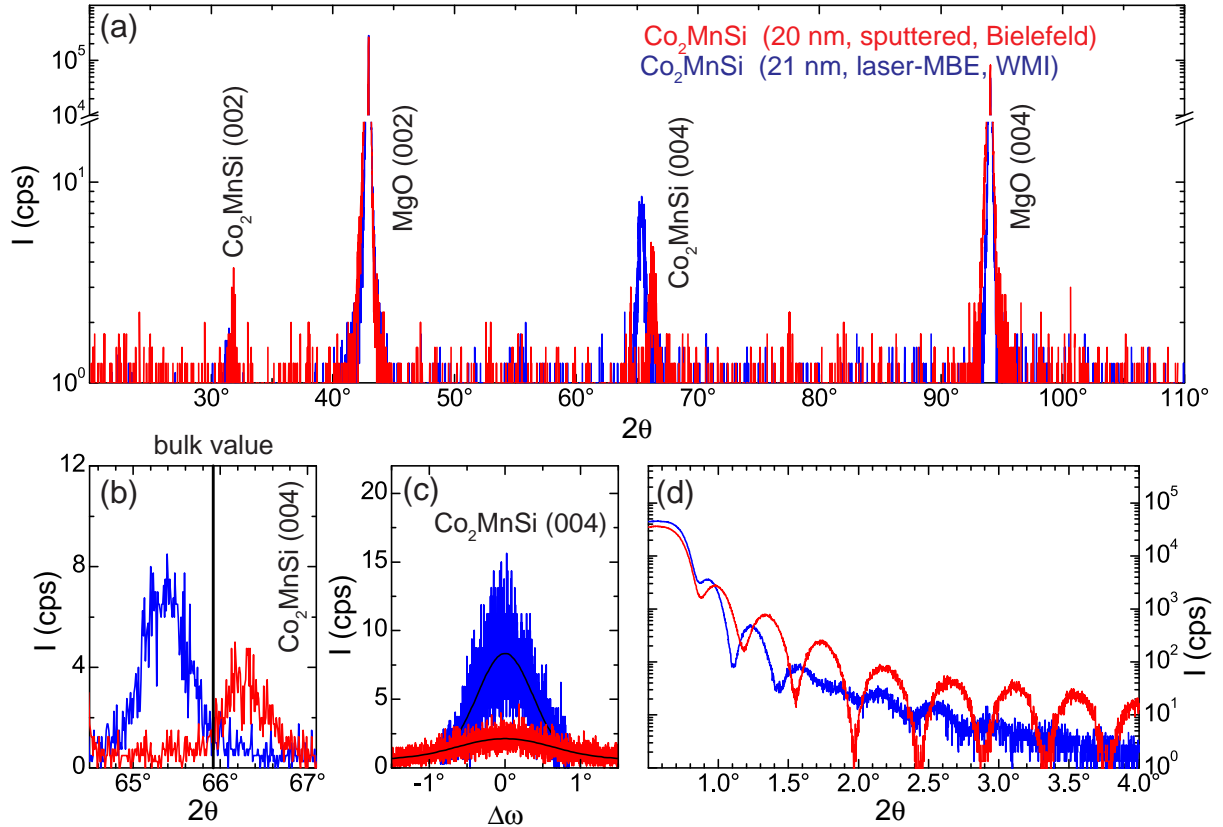


Figure 3.2: Comparison of the structural quality of a RF-sputtered, 20 nm thick (red) and our laser-MBE grown, 21 nm thick (blue) Co_2MnSi thin film. (a) Both $2\theta - \omega$ scans verify the high (001)-orientation of the thin films and no secondary phases. (b) Comparison of the $2\theta - \omega$ scan around the (004) Co_2MnSi reflection for both samples. For our laser-MBE grown thin film the intensity is twice as high as for the sputtered thin film. (c) ω rocking curve of the (004) Co_2MnSi reflection for both samples. The black lines indicate Gaussian fits to the data for the extraction of the FWHM. From these fits we obtained a FWHM of 0.86° for our laser-MBE film and a FWHM of 1.5° for the sputtered film. (d) Reflectometry curves for both samples. The oscillations are more pronounced for the sputtered sample, indicating a smoother surface.

fits. For our laser-MBE sample we obtained a FWHM of 0.86° and for the sputtered reference sample a FWHM of 1.5° . These results support that our laser-MBE sample has a superior out-of-plane coherence length and lower mosaic spread compared to the reference sample.

From the reflectometry data for both samples presented in Fig. 3.2(d) we can compare the surface quality for the two different growth techniques and extract the film thickness. The sputtered and annealed CMS film exhibits more pronounced oscillations than our laser-MBE film. This indicates that the reference sample has a smoother film surface and a sharper substrate to film interface than our laser-MBE sample.

From this structural comparison we can already state that we are able to grow CMS thin films via laser-MBE that are on par or even of better structural quality than the state-of-the-art reference sample. Only the roughness of the film surface needs improvement,

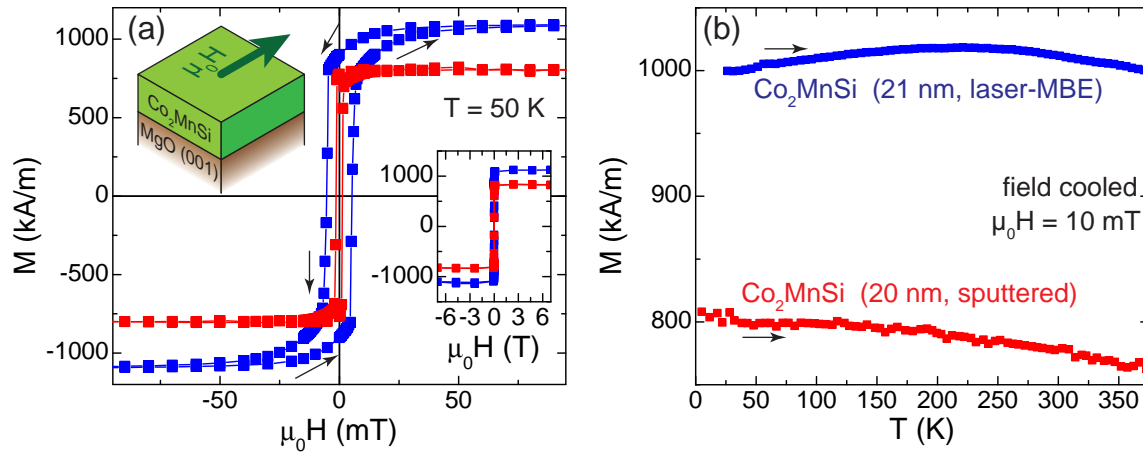


Figure 3.3: (a) $M(H)$ loop at $T = 50$ K for a 21 nm thick Co_2MnSi film grown by laser-MBE after subtraction of a diamagnetic background. Magnetic field sweep directions are indicated by black arrows. We extracted a coercive field of 5.7 mT and a saturation magnetization $M_S = 1120$ kA/m = $5.45 \mu_B/\text{f.u.}$ for our film, while the sputtered reference sample yields a coercive field of 1.7 mT and $M_S = 780$ kA/m = $3.80 \mu_B/\text{f.u.}$. The inset shows the evolution and saturation of the loop at large magnetic fields. The lines are guides to the eye. (b) Temperature dependent magnetization of the very same sample at $\mu_0 H = 10$ mT. Prior to the measurement the sample was cooled down in a magnetic field of 7 T.

which might be resolved by an additional in-situ annealing step after deposition.

The crystallographic structure is only one important quality factor for ferromagnetic thin films. We also need to consider the magnetic properties of our samples. To obtain information on the magnetic quality of our samples we have conducted SQUID magnetometry (Quantum Design MPMS) experiments on our laser-MBE grown, 21 nm thick Co_2MnSi film and the sputtered reference sample. The data are summarized in Fig.3.3.

We conducted $M(H)$ measurements at $T = 5$ K, $T = 15$ K, $T = 50$ K, $T = 300$ K with the external magnetic field in the film plane applied parallel to the MgO [100]-direction. In Fig. 3.3(a) we show the $M(H)$ loop for our laser-MBE grown sample (blue) and the sputtered Bielefeld sample (red) at $T = 50$ K, after subtraction of a diamagnetic background signal, which is caused by the MgO substrate, and normalization to the volume of the thin film. From this curve we extracted the saturation magnetization $M_S = 1120$ kA/m = $5.45 \mu_B/\text{f.u.}$ for our film and $M_S = 780$ kA/m = $3.80 \mu_B/\text{f.u.}$ for the sputtered sample. Compared to the bulk saturation magnetization $M_S = 1020$ kA/m = $4.96 \mu_B/\text{f.u.}$ [194] of Co_2MnSi our films have a slightly larger saturation magnetization, while the sputtered sample exhibits only 80% of the bulk saturation magnetization. In most reports a reduced saturation magnetization compared to the bulk values has been observed for Cobalt-based Heusler compound thin films [188, 189, 195]. An explanation for the observation of a higher saturation magnetization in our films might either be the uncertainty of the film volume determination (at least 5% relative error) or a different atomic ordering in the 4 fcc sublattices. This higher saturation magnetization has also been observed at other temperatures investigated [192]. The coercive field of 5.7 mT for our film and 1.7 mT for the sputtered film was extracted by averaging of up- and down-

sweep from Fig. 3.3(a). The difference in coercive fields is mainly due to the smoother surface of the sputtered sample. But nevertheless, both values are comparable to the reported values in [195]. It decreases with increasing temperature and reaches 2.7 mT for our sample and 0.7 mT for the sputtered sample at room temperature. This decrease in coercive field corresponds nicely with the decrease in magnetic anisotropy we extracted for the sputtered Co_2FeAl thin films in Sect. 3.3.3. This might be attributed to the strain in the thin film caused by the different thermal expansion coefficients of substrate and film.

For both samples we have carried out a $M(T)$ measurement at an external magnetic field of 10 mT after field cooling each sample down to $T = 5$ K in 7 T. The corresponding curves are shown in Fig. 3.3(b). The measured magnetic moment has been again normalized to the volume of the CMS film. The magnetization is for both samples nearly temperature independent, which demonstrates that the Curie temperature in both samples lies well above room temperature and thus agrees nicely to the reported bulk Curie temperature of 985 K [194]. Moreover, the magnetization of the sputtered film is only 80% of our laser-MBE film. The magnetic properties obtained from SQUID magnetometry prove that our laser-MBE grown samples are state-of-the-art exhibiting a saturation magnetization close to the bulk value and a Curie temperature well above room temperature.

In summary, the high structural quality and excellent magnetic properties of our laser-MBE grown sample obtained from HRXRD and SQUID magnetometry verify that we are capable to grow metallic Heusler compound thin films with state-of-the-art quality. These results establish laser-MBE as a growth technique for Heusler compound thin films and act as a starting point for growing high quality Heusler compounds for novel spin caloritronic experiments. Unfortunately, due to the short amount of time we could not conduct further experiments with these laser-MBE grown samples within the work of this thesis. In the future an improvement of the structural quality of laser-MBE grown samples could be achieved by using a lattice matched substrate like GaAs. By using CMS and CFA thin films grown on (113)-oriented GaAs substrates one could then apply the same procedure as for (Ga,Mn)As (cf. 3.3.2) and extract the full resistivity and Seebeck tensor from ADMR and ADMTP experiments. In addition, the use of ferromagnetic Heusler compounds with large Seebeck coefficients such as Fe_2VAl or Co_2VAl [196, 197] could provide a remedy for the highly demanding requirements for ADMTP experiments in Heusler compound thin films.

3.2.2 Laser-MBE growth of yttrium iron garnets

In this section we focus on the growth of insulating, ferromagnetic yttrium iron garnet thin films using our laser-MBE setup. Single crystals of YIG grown from the melt [198] are widely available and substitution with various elements to tailor the magnetic properties of YIG has been extensively studied in the last decades [199–203]. Thin film deposition of high quality YIG has been mainly achieved using liquid phase epitaxy [204, 205]¹, but there are also recent reports on the successful pulsed laser deposition (PLD) of YIG thin films [206–212]. Triggered by these successful reports, we investigated the growth of yttrium iron garnet thin films on gadolinium gallium garnet (GGG) and yttrium

¹LPE is the deposition of a few μm thick film on a substrate by placing the substrate in a melt of the material. For more details see [204, 205].

aluminium garnet (YAG) substrates in our improved laser-MBE setup (Appendix A).

We start this section with a short introduction into rare-earth garnets (Sect. 3.2.2.1). Afterwards we summarize in Section 3.2.2.2 the results obtained from the investigations of the magnetic properties of the laser-MBE target material and the single crystalline GGG and YAG substrates. In Section 3.2.2.3 we then present the structural and magnetic properties of our laser-MBE grown YIG thin films on GGG and YAG substrates, accomplished by a careful optimization of the deposition parameters. Moreover, we demonstrate in this section that the structural and magnetic properties of the YIG thin film remain unchanged, when we deposit in-situ a thin Pt layer on top of the YIG layer. Finally, in Section 3.2.2.4 we present the results for our laser-MBE grown YIG films on GGG and YAG substrates obtained from ferromagnetic resonance experiments (FMR). We conclude in Section 3.2.2.5 by summarizing the key results obtained for the laser-MBE growth of YIG on GGG and YAG substrates.

3.2.2.1 An introduction into rare-earth iron garnets

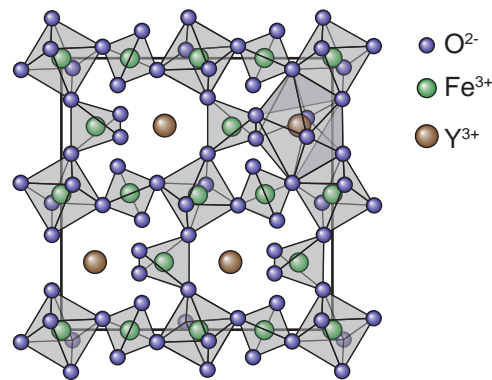


Figure 3.4: Illustration of the cubic $\text{Y}_3\text{Fe}_5\text{O}_{12}$ crystal structure. The three Y^{3+} ions are coordinated dodecahedrally, two Fe^{3+} ions octahedrally, and the remaining three Fe^{3+} ions tetrahedrally to the oxygen ions.

For our experiments we choose yttrium iron garnet ($\text{Y}_3\text{Fe}_5\text{O}_{12}$, or YIG for short). YIG is an artificial ferrimagnetic insulator with a Curie temperature well above room temperature ($T_C = 560$ K [213]). Since its first fabrication over 50 years ago [214, 215] YIG is widely used in microwave applications, for example as a tunable narrow bandpass filter or resonator [216], and in magneto-optical applications, for example as an optical insulator in optical fibre communications [198] or even for the ultra fast magneto-optic sampling of current pulses [217]. This broad application range is based on the excellent magnetic properties of YIG, such as very low magnetic damping and large Faraday rotation angles when doped with bismuth. In the cubic garnet structure (Ia3d) of YIG (lattice constant $a = 1.238$ nm) illustrated in Fig. 3.4 three Fe^{3+} ($S = 5/2$) ions are tetrahedrally coordinated (24d) by oxygen while the remaining two Fe^{3+} ions are coordinated octahedrally (16a) in one formula unit. This leads to the formation of two oppositely aligned ferroic sublattices with a net magnetization of $5 \mu_B/\text{f.u.}$ [218, 219]. Ga substitution of tetrahedral iron results in a compensation point due to the different temperature dependence of the two sublattices [201]. Other rare-earth iron garnets exhibit a compensation temperature due to the magnetic moment of the rare-earth element, which is either parallel

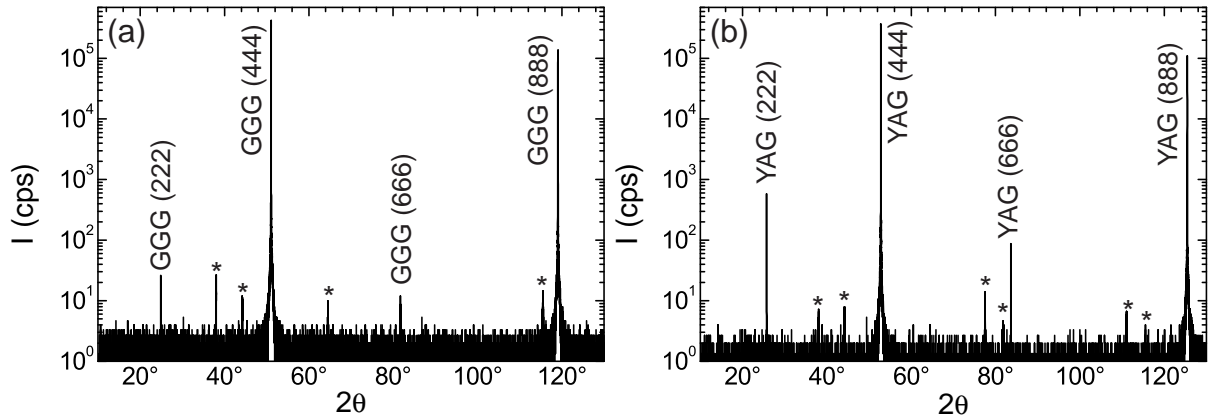


Figure 3.5: Comparison of the structural properties of a GGG (left panels) and a YAG (right panels) substrate determined by HRXRD at room temperature. Both 2θ - ω scans exhibit reflections that can not be attributed to the substrates themselves (marked with a \star). The origin of these secondary phases is presently unknown.

or antiparallel oriented to the net magnetization of the two iron sublattices [213]. All in all, rare-earth iron garnets are a very versatile magnetic material class and allow to tune their magnetic properties by doping with various elements. This versatility makes the insulating compound YIG an interesting candidate for spin current related experiments.

3.2.2.2 Properties of target material and substrates

We start this section with the investigation of the target material. The polycrystalline target used for our experiments has been obtained by pressing and sintering (oxygen atmosphere, 1400°C) a mixture with the right stoichiometric weights of Y_2O_3 and Fe_2O_3 (each with 99.99% purity). X-ray diffraction and SQUID magnetometry characterization of the target at room temperature confirm the high purity, i.e. no secondary phases present, and excellent magnetic properties (bulk like saturation magnetization $M_S = 141.65\text{ kA/m}$ and low coercivity $\leq 0.1\text{ mT}$) of our target material [220].

For the deposition of high quality thin films the lattice mismatch between substrate and film is an important parameter. The lattice constant of cubic (Ia3d) GGG ($a = 1.238\text{ nm}$) and the thermal expansion correspond nicely to the parameters of YIG [221], which leads to negligible lattice misfit (0.03%) and makes GGG single crystals a first class choice as substrates. However, one of the main disadvantages of GGG crystals as substrates is the paramagnetism induced by the Gd^{3+} ions, which generates a large background signal in magnetometry measurements and obstructs an easy separation of substrate and ferromagnetic thin film magnetic signal (see Fig. 3.5(a)). This magnetic problem is circumvented by the use of diamagnetic YAG substrates (see Fig. 3.5(b)), but the YAG lattice constant ($a = 1.200\text{ nm}$) [221] leads to a considerable lattice mismatch of -3% , which might in the end deteriorate the structural and magnetic properties of the YIG thin films on YAG.

We first start by investigating the structural properties of the two different substrates by HRXRD. The results of the $2\theta - \omega$ scans are summarized in Fig. 3.5(a) and (b) for a (111)-oriented GGG and YAG substrate, respectively.

For the GGG substrate we find besides the allowed (444) and (888) GGG reflections

the normally forbidden (222) and (666) reflections. The existence of these forbidden reflections is attributed to surface defects due to the polishing process of the substrate. Most surprisingly, the substrate also exhibits reflections that can not be assigned to substrate peaks (marked with a \star in the figure). The 2θ values and the corresponding d-spacing are collected in Table 3.1. The origin of these impurities is presently unknown.

In the very same fashion we find for the YAG substrate in Fig. 3.5(b), that besides the allowed (444), (888) and the forbidden (222), (666) substrate reflections additional reflections are visible (marked with a \star). The corresponding 2θ values and d-spacings for these impurity reflections are also summarized in Table 3.1.

2θ for GGG	d-spacing for GGG	2θ for YAG	d-spacing for YAG
38.04°	0.2364 nm	38.02°	0.2364 nm
44.20°	0.2047 nm	44.16°	0.2049 nm
64.50°	0.1444 nm	77.53°	0.123 nm
		81.93°	0.1175 nm
		111.04°	0.0934 nm
115.50°	0.0911 nm	115.52°	0.0911 nm

Table 3.1: Extracted 2θ and d-spacing values of the impurities in the GGG and YAG substrates.

If we compare the d-spacing of the impurity reflections in the GGG and YAG substrates, we see that some values are nearly equal, which provides evidence that some of the secondary phases in both substrates have the same origin. It might be possible that during the Czochralski growth of the single crystal for the substrates the crucible material (typically platinum or iridium) is introduced into the crystal. Unfortunately, calculations of the 2θ positions based on the bulk lattice constants for cubic Pt ($a = 0.39231$ nm [222]) and cubic Ir ($a = 0.38394$ nm [222]) yield no agreement to the observed impurity reflections (Pt (222): $2\theta = 85.80^\circ$, Ir (222): $2\theta = 88.14^\circ$). But it is also possible that the crucible material forms complex oxides within the single crystal. The existence of these secondary phases in the substrate need to be carefully considered when investigating the structural properties after the laser-MBE growth.

To investigate the magnetic properties of GGG and YAG substrates we used SQUID magnetometry and measured $M(H)$ and $M(T)$ curves for a (111)-oriented GGG and (111)-oriented YAG substrate. The calculation of the magnetization from the measured magnetic moment was carried out by determining the mass of each substrate and using the bulk density value of the material to obtain the volume of the substrate. The obtained experimental data are summarized in Fig. 3.6(a)-(d).

For the bare GGG substrate we expect a paramagnetic signal due to the Gd^{3+} ions ($J = 7/2$) present in the crystal. Indeed we observe a paramagnetic signal in our $M(H)$ measurements carried out at $T = 300$ K and $T = 3$ K in Fig. 3.6(a) (open symbols). At $T = 300$ K, the magnetization increases linearly with the applied magnetic field and does not saturate at the maximum magnetic field $\mu_0 H = 7$ T. At $T = 3$ K we observe the typical S-shaped curve of a paramagnet with localized magnetic moments, but again the maximum field of $\mu_0 H = 7$ T is not large enough to achieve a complete saturation. To further substantiate that the observed magnetization signal is purely paramagnetic we simulated the data using a Brillouin function with $J = 7/2$ and a saturation magnetization $M_S = 821$ kA/m calculated from the theoretical density of magnetic moments

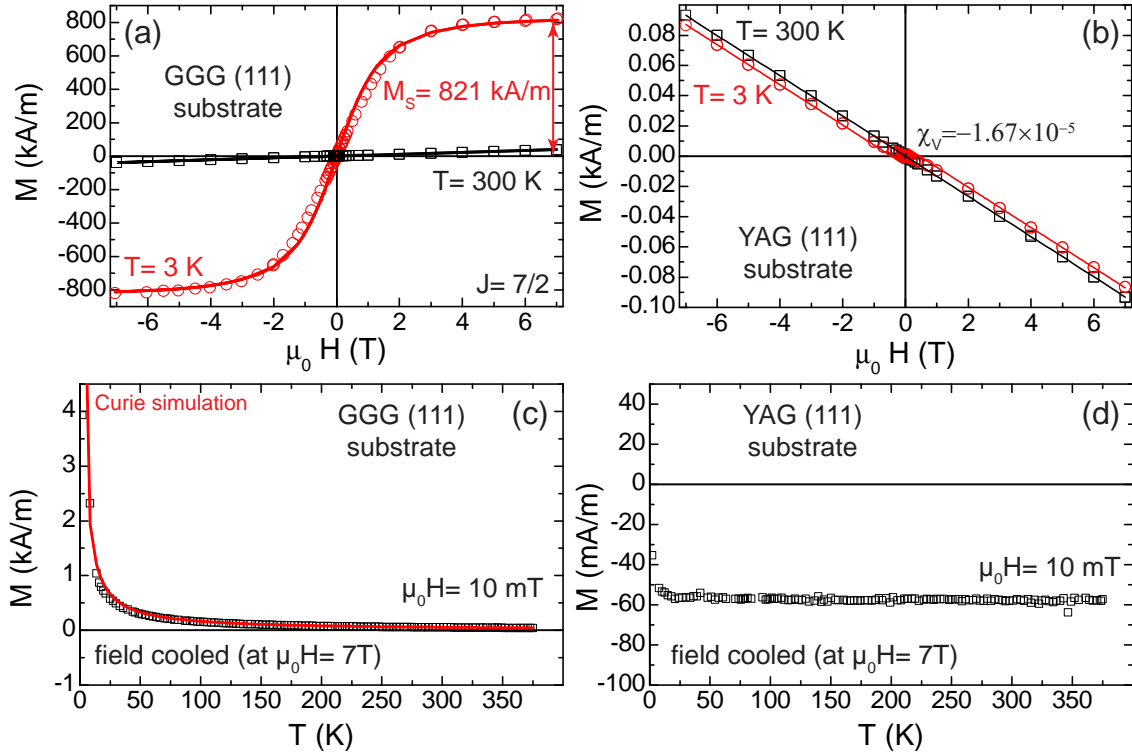


Figure 3.6: Comparison of the magnetic properties of a GGG (left panels) and a YAG (right panels) substrate determined by SQUID magnetometry. $M(H)$ curves at $T = 300$ K (black) and $T = 3$ K (red) for the (a) GGG and (b) YAG substrate. The lines represent a Brillouin simulation for the paramagnetic GGG with $J = 7/2$ (a) and a linear fit ($\chi_V = -1.67 \times 10^{-5}$) for the diamagnetic YAG substrate. $M(T)$ curves at $\mu_0 H = 10$ mT obtained for the (c) GGG and (d) YAG substrate after field cooling the sample at $\mu_0 H = 7$ T. The red line in (c) is a Curie simulation $J = 7/2$ to the data.

in GGG (For more details see [220]). These simulation curves are displayed as lines in Fig. 3.6(a) and reproduce the experimental data nicely.

We also expect that the temperature dependence of the magnetization in GGG follows the Curie law ($\propto 1/T$). To substantiate the paramagnetism in GGG we also measured a $M(T)$ curve at $\mu_0 H = 10$ mT after cooling the GGG substrate in a magnetic field of $\mu_0 H = 7$ T down to $T = 3$ K. The open symbols in Fig. 3.6(c) represent the obtained magnetization data, while the red line represents a Curie simulation with $J = 7/2$ to the data. The nice agreement between simulation and experimental data is an additional proof for the purely paramagnetic signal coming from localized Gd^{3+} moments of the GGG substrate. One should note that this paramagnetic signal represents an obstacle for the determination of the magnetic properties of the ferrimagnetic YIG film on GGG. At $T = 3$ K the saturation magnetization of bulk YIG $M_S = 196.7$ kA/m [201] is about a factor of 4 smaller than the saturation magnetization of the GGG substrate, but more importantly the volume of the YIG thin film $V_{\text{film}} = 5 \text{ mm} \times 5 \text{ mm} \times 50 \text{ nm} = 12.5 \times 10^{-4} \text{ mm}^3$ is 4 orders of magnitude smaller than the volume of the GGG substrate ($V_{\text{sub}} = 5 \text{ mm} \times 5 \text{ mm} \times 0.5 \text{ mm} = 12.5 \text{ mm}^3$). Thus, the total measured magnetic moment of substrate and film is always dominated by the paramagnetic moment of the substrate.

Moreover, the paramagnetic background signal will increase with decreasing temperature and thus complicate the evaluation of the low temperature data.

This makes YIG films on YAG substrates attractive because YAG is diamagnetic, as it does not contain any magnetic ions. From the $M(H)$ curves at $T = 300$ K and $T = 3$ K of a bare YAG substrate in Fig. 3.6(b) we can state that the diamagnetic contribution is nearly temperature independent, as one would expect for pure diamagnetism. The perfect linear evolution of the magnetic signal as indicated by the perfect agreement between linear fit ($\chi_V = -1.67 \times 10^{-5}$) and data further substantiates the pure diamagnetism of YAG. This allows an easy subtraction of the substrate signal for YIG films on YAG. Moreover, the magnetization of the YAG substrate at $T = 3$ K is 4 orders of magnitude smaller than the magnetization signal of a GGG substrate (Fig. 3.6(a)), which enables us to easily evaluate low temperature data of YIG on YAG substrates.

From the $M(T)$ curve obtained after cooling the bare YAG substrate down to $T = 3$ K in a magnetic field of $\mu_0 H = 7$ T in Fig. 3.6(d), we observe at low temperatures ($T \leq 10$ K) a deviation from the expected constant magnetization value. The origin of this deviation are paramagnetic impurities present in the YAG substrate. The origin of these paramagnetic impurities is still under discussion. Possible candidates are platinum and iridium impurities as these two materials are widely used as crucibles for the Czochralski growth of YAG single crystals.

From these results we conclude that YAG substrates provide a diamagnetic, nearly temperature independent signal. It can more easily be subtracted from SQUID magnetometry data to extract the magnetic properties of YIG films compared to the paramagnetic, strongly temperature dependent magnetic signal of GGG substrates which complicates a background subtraction.

3.2.2.3 Structural and static magnetic properties of YIG thin films on GGG and YAG substrates

After studying the structural and magnetic properties of target and substrates we carried out a careful growth optimization of YIG on (111)-oriented GGG substrates and found the following optimum deposition parameters [220]: 60 mm target to substrate distance, 550 °C substrate temperature, $\rho_{ED} = 2$ J/cm² energy density at the target, 10 Hz repetition rate, and deposition in oxygen atmosphere at $p_{O_2} = 25 \times 10^{-3}$ mbar. Using these optimized deposition parameters we have fabricated YIG thin films on (111)-oriented GGG and (111)-oriented YAG substrates to compare their structural and magnetic properties using HRXRD and SQUID magnetometry experiments. Prior to growth we sputtered a 180 nm thick Pt layer onto the backside of the substrate to allow a better absorption of the infrared substrate heating laser. For the fabrication of YIG/NM hybrid structures we deposited in-situ, without breaking the vacuum, NM thin films by electron beam evaporation after the laser-MBE growth of YIG and substrate cool down.

We start the comparison of the structural and magnetic quality by investigating the structural properties of a typical YIG layer with 67 nm thickness grown on a (111)-oriented GGG substrate. The obtained results are compiled in Fig. 3.7(a)-(d).

All reflections in the 2θ - ω scan displayed in Fig. 3.7(a) can be assigned to film or substrate reflections. Thus we find no secondary phases in our YIG/GGG samples, indicating a well optimized set of growth parameters. The occurrence of the normally forbidden GGG (222) reflection indicates some defects in the substrate, which might be

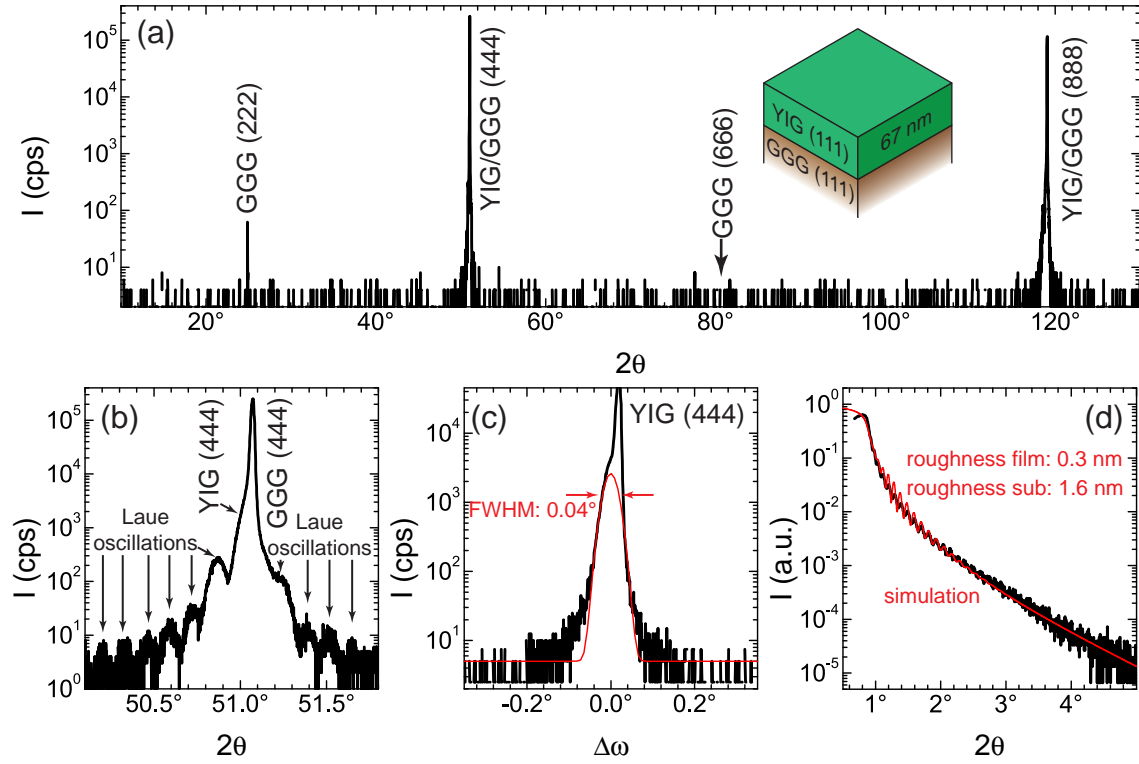


Figure 3.7: HRXRD results obtained for 67 nm thick YIG layer grown on a (111)-oriented GGG substrate. (a) 2θ - ω scan exhibits only reflections that are attributed to either the film or the substrate. (b) Magnification of the 2θ - ω scan around the GGG (444) reflection. The Laue oscillations verify the high structural quality of the sample. (c) XRC of the YIG (444) reflection yields a FWHM of 0.04° . The red line represents a Gaussian fit to the data (black) to extract the FWHM. (d) X-ray reflectometry carried out on the sample (black) and corresponding simulation (red). From the simulation we extract a large substrate roughness, which limits the surface quality of our YIG films on GGG.

generated during the polishing process. Interestingly, the 2θ - ω scan exhibits no forbidden GGG (666) reflection, this might be related to a small misalignment as these forbidden reflections are very sharp and the misalignment is more prominent at higher 2θ values. The polishing induced damages are also visible in the high surface roughness of the substrate extracted from the X-ray reflectometry measurements in Fig. 3.7(d)².

The Laue oscillations visible in the high resolution 2θ - ω scan around the GGG (444) reflection in Fig. 3.7(b) indicate a coherent, (111)-oriented growth of the YIG layer on the lattice matched GGG substrate. Moreover, the YIG (444) reflection is only weakly discernible from the high intensity substrate reflection indicated by the arrow in Fig. 3.7(b). From the position of this reflection we calculate an interplane spacing of $d_{444} = 0.1787$ nm from the Bragg equation. Assuming a still undistorted cubic lattice structure this leads to a lattice constant $a = 1.238$ nm, which is identical to the bulk value. From the lattice mismatch of substrate and film we expect a rhombohedral distortion of the YIG

²The substrate supplier Crystec GmbH states a root mean square (RMS) roughness below 0.5 nm for this set of substrates. Unfortunately, Crystec was unable to send us an atomic force microscopy (AFM) scan of these substrates to confirm these values.

crystalline lattice, which should in the end increase the lattice parameter. The position of the YIG (444) and YIG (888) reflections of our YIG films grown with the optimized set of laser-MBE parameters, which nearly coincide with the bulk values, are in stark contrast to already reported structural data on PLD grown YIG films in [206–209]. In these publications the YIG (444) and (888) reflections are at much smaller 2θ values as compared to our results. In [209, 223] this deviation from the bulk values is attributed to a large rhombohedral distortion of the YIG lattice due to a deficiency of iron ions in the YIG structure. According to the results in [223] the amount of iron deficiency can be tuned by varying the oxygen partial pressure during deposition. As our films exhibit no large deviation from the bulk YIG lattice parameters it is safe to assume that we have found a set of growth parameters, which allow the growth of highly stoichiometric YIG films from a stoichiometric polycrystalline target.

To evaluate the mosaic spread of our YIG films we carried out XRC of the YIG (444) reflection for our YIG film on GGG, the results are displayed in Fig. 3.7(c). As the YIG (444) reflection lies close to the high intensity GGG (444) substrate reflection we observe a double peak structure in our rocking curve. The narrow peak with a high intensity stems from the substrate itself, while the broader one is the film reflection. We have applied a Gaussian fit to the data to extract the FWHM of the film reflection indicated by the red line in Fig. 3.7(c). The obtained FWHM of 0.04° is an excellent value for laser-MBE grown thin films and confirms the high structural quality of our samples. Moreover, it exceeds the FWHM of 0.067° reported in [206, 207] and is nearly on par to the FWHM of 0.017° reported in [209], which has been obtained for a YIG film with a thickness of 220 nm. Note, however, that these values have been obtained for an iron deficient YIG film, while our films are stoichiometric.

For a deeper insight into the surface properties of substrate and film we performed X-ray reflectometry measurements on our sample as displayed in Fig. 3.7(d). Although the slow exponential decay indicates a smooth film surface, the oscillations are only weakly visible indicating a rough substrate surface. For a quantitative analysis we fitted the data with a simulation using LEPTOS, the obtained result is displayed as a red curve in Fig. 3.7(d). From this simulation we extracted a film roughness of 0.3 nm and a substrate roughness of 1.6 nm. The large substrate roughness lowers the quality of our films due to interface interactions. A possible way to smoother substrate surfaces might be the annealing of the substrate at elevated temperatures in oxygen atmosphere. This could even further improve the already excellent structural quality of our YIG films on GGG.

Despite the rough substrate surface, our YIG films on GGG display excellent structural quality indicated by a narrow XRC of the YIG (444) reflection and Laue oscillations visible in the vicinity of the GGG (444) reflection.

By an additional growth optimization of YIG on YAG substrates we could verify that the already mentioned growth parameters for YIG on GGG result in the best structural YIG film properties also on YAG. To demonstrate this we focus in the following on the structural properties of a 62 nm thick YIG film grown on a (111)-oriented YAG substrate obtained from HRXRD experiments. The results are summarized in Fig. 3.8(a)-(d).

In the 2θ - ω -scan displayed in Fig. 3.8(a) we observe apart from the reflections from (111)-oriented YAG and (111)-YIG additional reflections (marked with a \star) at $2\theta = 77.52^\circ$ and $2\theta = 115.46^\circ$. However, these reflections are also present in bare YAG substrate, so we can exclude the existence of any secondary phases in our YIG film. As already discussed in Sect. 3.2.2.2 complex oxides formed with Pt and Ir are possible

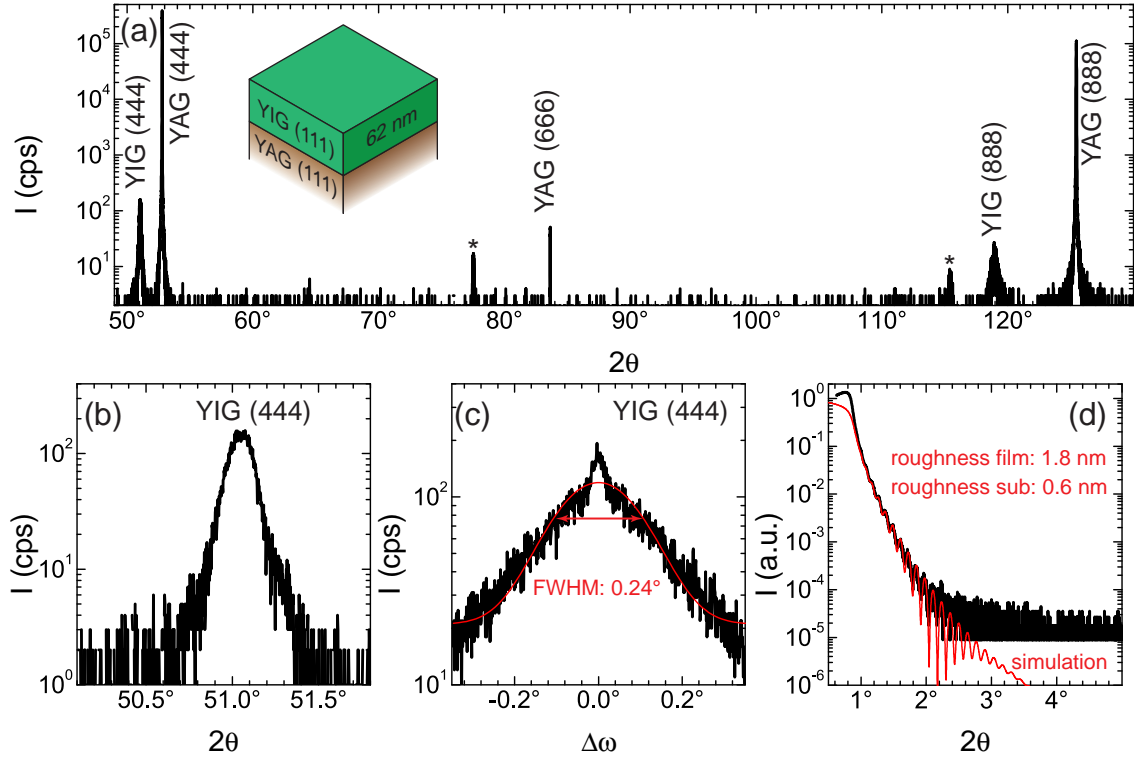


Figure 3.8: Structural characterization carried out for a 62 nm thick YIG film grown on a (111)-oriented YAG substrate. (a) The reflections observed in the 2θ - ω scan are all assigned to substrate or film reflexes and verify the (111)-oriented growth of YIG on the YAG substrate. (b) The magnification of the 2θ - ω scan around the YIG (444) reflection displays no Laue oscillations. (c) The XRC of the YIG (444) reflection results in a large FWHM of 0.24° . The red line indicates a Gaussian fit to the data for the extraction of the FWHM. Moreover, relaxation of lattice misfit is visible in the superimposed, narrow peak around $\Delta\omega = 0^\circ$. (d) X-ray reflectometry curve (black) obtained from the very same sample and corresponding simulation (red). Due to the large lattice mismatch we observed a large film roughness of 1.8 nm.

candidates for these impurities.

The YIG film grows relaxed in (111)-orientation on the (111)-oriented YAG substrate, because of the large lattice mismatch of -3% . In addition, the high resolution 2θ - ω -scan around the YIG (444) reflection in Fig. 3.8(b) exhibits a broad peak without any Laue oscillations, which indicates, that due to the larger lattice mismatch the structural quality of our relaxed YIG films on YAG substrates is lower than for our YIG films on GGG substrates. But from the 2θ position of the peak we can extract an interplane spacing $d_{444} = 0.1787$ nm which is identical to the one we observed in our YIG films on GGG substrates. Using this interplane spacing we can calculate the lattice constant of YIG as $a = 1.238$ nm under the assumption of a cubic YIG lattice structure. This value is the same as the one obtained from our YIG films on GGG substrates and confirms the relaxed growth on YAG. Thus, we conclude that the stoichiometry of our YIG films is maintained on both substrates. However, these results are in contrast to a recent publication [224], where the authors find a shift in the lattice constant of PLD-grown YIG films on YAG compared to films on GGG. The main cause for these different observations

could be the totally different deposition parameters used by Popova *et al.* [224]. (50 mm target to substrate distance, $T_S = 660^\circ\text{C}$ substrate temperature, $\rho_{\text{ED}} = 8\text{ J/cm}^2$ energy density at the target, 10 Hz repetition rate, and deposition in oxygen atmosphere at $p_{\text{O}_2} = 40 \times 10^{-3}\text{ mbar}$) compared to our optimized set of parameters.

We show the XRC of the YIG (444) reflection and the Gaussian fit to the data in Fig. 3.8(c) as black and red lines, respectively. From the fit we extract a FWHM of the rocking curve of 0.24° , which is a rather large value and indicates a high mosaic spread. We attribute this increase in rocking curve width compared to our YIG films on GGG to the large lattice mismatch. In order to reduce the stress in the film structural defects are produced, which broaden the rocking curve. A relaxation of the strain is visible in the rocking curve from the superimposed narrow peak centered around $\Delta\omega = 0^\circ$. This result shows that the relaxation of strain is already complete at film thicknesses below 60 nm. For XRC on thicker (up to 100 nm film thickness) YIG films on YAG we observe an increase in intensity for the narrow peak, which supports that the mosaic spread reduces with increasing film thickness. In addition, this relaxation process and the related reduction of the mosaic spread with increasing film thickness in our YIG films suggest that the introduction of a buffer layer between YAG substrate and YIG film might help to improve the structural quality of the YIG. A possible candidate for the buffer system may be Sc substituted YAG, where one can increase the lattice constant compared to YAG depending on the Sc concentration.

For the 62 nm thick YIG film on YAG we evaluated the surface properties using reflectometry measurements and a fit to the data via a simulation with LEPTOS. The obtained results are displayed in Fig. 3.8(d) as black (data) and red (simulation) lines. The 1.8 nm roughness of the film is larger than the 0.3 nm obtained for the YIG film on GGG in Fig. 3.7(d) with nearly the same thickness. This increase in film surface roughness is most likely due to the large lattice mismatch between substrate and film. Interestingly, the surface roughness of the substrate is a factor of 2 lower for the YIG film on YAG (Fig. 3.8(d)) than for the YIG film on GGG (Fig. 3.7(d)) indicating a higher surface quality of the YAG substrates. Future atomic force microscopy studies are mandatory to obtain a deeper insight into the surface properties of substrate and film.

In summary, our HRXRD results on YIG films grown on YAG substrates using our optimized set of laser-MBE parameters exhibit the identical 2θ position of the YIG (444) reflection as YIG films on GGG indicating the same stoichiometry. Moreover, the superimposed narrow peak in the XRC of the YIG (444) reflection indicates a relaxation of lattice misfit for film thicknesses $\geq 50\text{ nm}$. Thus, the insertion of a buffer layer lattice matched to YIG is expected to result in an increase of structural quality of our YIG films on YAG.

For the experiments presented in Sect. 3.4.1 and Sect. 3.4.2 we fabricate YIG/NM hybrid structures. To verify, that the structural quality of the YIG layer is not influenced by the deposition of a metallic Pt layer via electron beam evaporation, we employed HRXRD measurements on YIG/Pt bilayers grown on GGG and YAG substrates. The YIG films have been grown using laser-MBE and our optimized set of parameters. After the deposition of the YIG film and cool down of the substrate to room temperature we transferred the sample in-situ (without breaking the vacuum) to the electron beam evaporation chamber. In this chamber we deposited a Pt layer (typical thickness: 7 nm) onto the YIG at room temperature with an average deposition rate of 0.15 nm/s.

We first look into the structural properties of a YIG (21 nm)/ Pt (7 nm) multilayer on

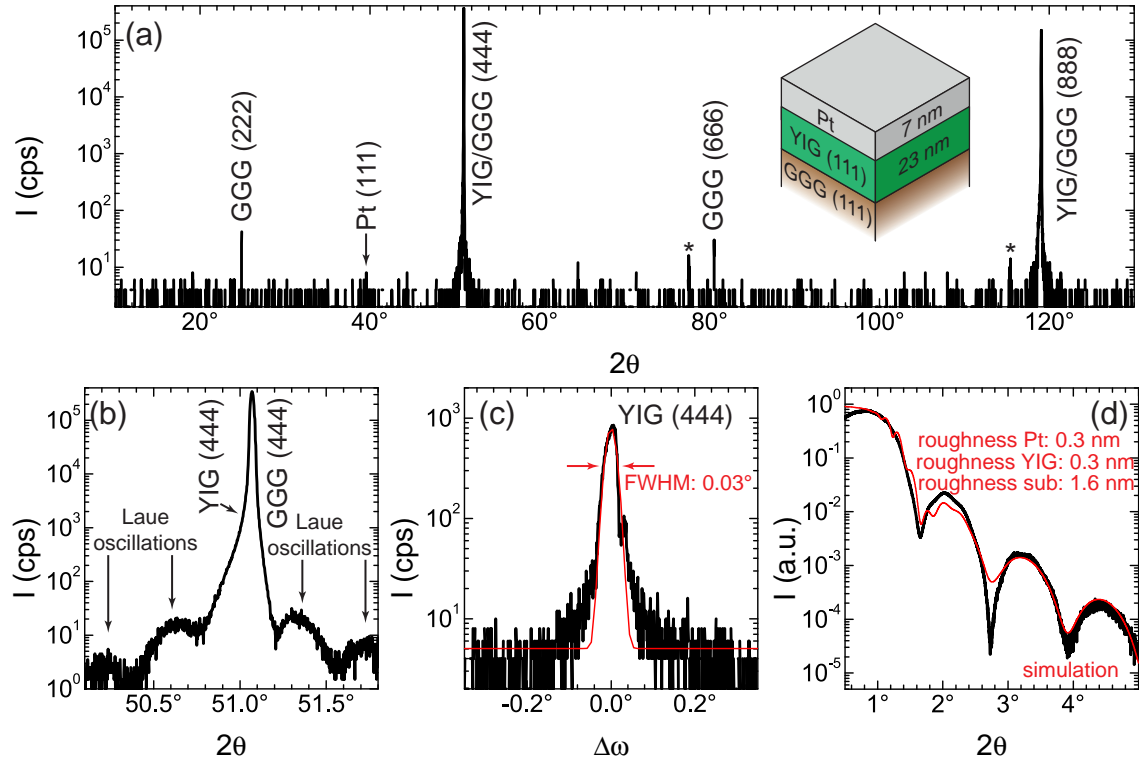


Figure 3.9: Analysis of the structural quality evaluated by HRXRD for a 21 nm thick YIG film on (111)-oriented GGG covered in-situ with a 7 nm Pt layer. (a) Full range 2θ - ω scan exhibits only reflections from the film layers or the substrate, thus no secondary phases are present. (b) High resolution 2θ - ω scan in vicinity of the GGG (444) reflection obtained for the hybrid structure. The clearly visible Laue oscillations indicate a high structural quality of the YIG film. (c) XRC of the YIG (444) reflection exhibits a FWHM of 0.03° . The red line represents a Gaussian fit to the data (black). (d) Reflectometry data (black) obtained for the Pt/YIG heterostructure and corresponding fit (red), which allows the determination of the surface roughness for each layer.

(111)-oriented GGG using HRXRD. We note that here a thinner YIG layer as before is investigated, but the results obtained are not influenced by this thickness change. The obtained results are collected in Fig. 3.9(a)-(d).

The structural quality of the YIG layer is not influenced by the additional deposition of a Pt film as evident from the still visible Laue oscillations in the 2θ - ω -scan in the vicinity of the GGG (444) reflection in Fig. 3.9(b). Note that due to the thinner YIG layer the oscillation period is different to the one in Fig. 3.7(b). Moreover, the FWHM of the YIG (444) rocking curve remains as narrow as 0.03° indicating a low mosaic spread of the YIG layer (cf. Fig. 3.9(c)). In the full range 2θ - ω -scan in Fig. 3.9(a) two additional reflections marked with a \star are visible compared to the scan of a bare YIG film on GGG in Fig. 3.7(a) located at $2\theta = 77.55^\circ$ and $2\theta = 115.45^\circ$. We attribute these two reflections to a background contribution from the substrate (cf. Sect.3.2.2.2). Thus, we can exclude the formation of any secondary phases due to the deposition of a Pt film. The in-situ deposition of a Pt layer on top of YIG thus does not impact its structural quality.

In the full range 2θ - ω -scan (Fig. 3.9(a)) the calculated 2θ position of the Pt (111)

reflection ($2\theta = 39.76^\circ$) is indicated by a black arrow. Around this position no peak is discernible from the background signal. This suggests that either the Pt layer grows polycrystalline without any texture onto the YIG layer or the intensity of the Pt (111) reflection is too low to resolve due to the only 7 nm thickness of the layer. Because of the large lattice mismatch $\approx 16\%$ (taking into account the 3 times larger unit cell of YIG) Pt should grow relaxed on YIG. We assume that due to the room temperature deposition Pt grows without any preferential texture on YIG.

From the X-ray reflectometry scan in Fig. 3.9(d) we can evaluate the interface quality of our layers by fitting the measured data (black) with a LEPTOS simulation (red). From the simulation we extract extremely low surface roughness for the Pt and YIG layer. Only the 1.6 nm surface roughness of the GGG substrate is large, which is consistent with our data obtained for a bare YIG film in Fig. 3.7(d). From these results it seems again beneficial for future growth experiments to improve the substrate surface roughness by an additional annealing step prior to thin film deposition.

In a second set of experiments we investigated the influence of the Pt layer on the structural quality of YIG grown on YAG substrates. Using HRXRD we evaluated the structural properties of a YIG (52 nm)/ Pt (7 nm) multilayer grown on (111)-oriented YAG. The obtained experimental results are summarized in Fig. 3.10(a)-(d).

We first evaluate the structural quality of the YIG layer. The high resolution 2θ - ω -scan of the YIG (444) reflection in Fig. 3.10(b) reveals that due to the unchanged 2θ position of the reflection the lattice parameter of our YIG films on YAG remain unchanged when we deposit a Pt layer on top of it. However, the FWHM of the XRC for the YIG (444) reflection (Fig. 3.10(c)) has increased to 0.39° compared to the 0.24° of a bare YIG film on YAG (cf. Fig. 3.8(c)). The observed broadening is attributed to the slightly thinner YIG layer (52 nm compared to 62 nm for the bare YIG film), such that the relaxation of film stress is not fully complete for the thinner YIG layer effectively broadening the rocking curve. The superimposed narrow peak remains visible in the XRC of the YIG (444) reflection. In total, the structural quality of our YIG films on (111)-oriented YAG substrates remains unchanged when depositing an additional Pt layer on top of it.

In the full range 2θ - ω -scan (Fig. 3.10(a)) we observe apart from the $\{111\}$ reflections of YIG and YAG three additional reflections located at $2\theta = 38.03^\circ$, $2\theta = 77.59^\circ$, and $2\theta = 81.72^\circ$ marked with a \star . The cause for these three reflections could either be the (111)-texture of the thin Pt layer on top or an impurity phase present in the sample. As all three of these reflections are also visible in the bare YAG substrate (Fig. 3.5(b)) we assume that an impurity phase in the substrate is present and responsible for the observed additional reflections. From these results we find that the platinum layer grown at room temperature exhibits also no texture for YIG on YAG and is consistent with the results obtained from YIG/Pt hybrid structures on GGG substrates.

The reflectometry measurements in Fig. 3.10(d) show that our YIG/Pt hybrid structures on YAG exhibit a low surface roughness (≤ 1 nm). A further improvement of the surface quality may be achieved by introducing a buffer layer between YAG and YIG to reduce the initial lattice mismatch.

From this structural quality evaluation of YIG/Pt heterostructures grown on (111)-oriented GGG and YAG substrates we can conclude that the structural properties of our YIG films are not influenced by the deposition of an additional Pt layer and can be used in further experiments.

The high structural quality is a first indicator for perfect stoichiometry of our YIG films.

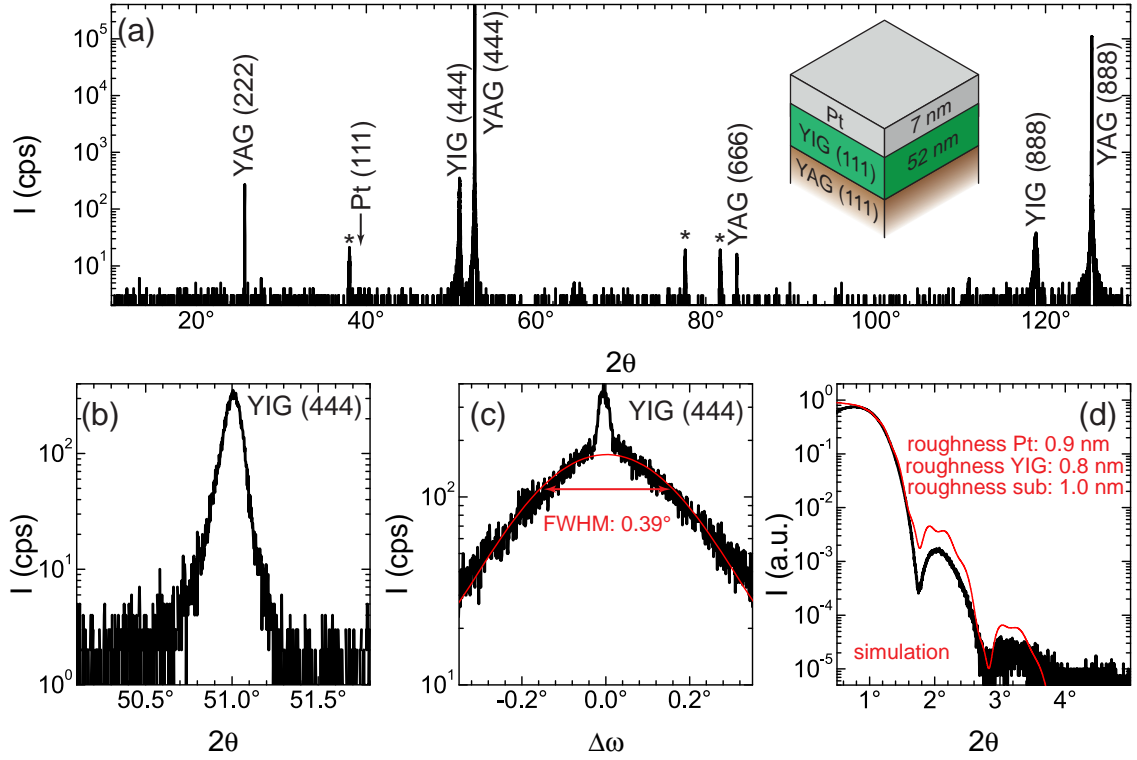


Figure 3.10: Evaluation of the structural quality of a YIG (52 nm)/Pt (7 nm) hybrid structure on a (111)-oriented YAG substrate determined from HRXRD. (a) 2θ - ω scan over a large 2θ range obtained from the heterostructure. No secondary phases are visible. (b) 2θ - ω -scan in close vicinity of the YIG (444) reflection displays identical properties as in Fig. 3.8(b). (c) XRC of the YIG (444) reflection displays a large mosaic spread of the YIG film indicated by the FWHM of 0.31° from the Gaussian fit (red) to the data (black). (d) X-ray reflectometry measured for our YIG/Pt heterostructure (black) and corresponding simulation (red).

For a deeper insight into the quality of our YIG films we analyzed the magnetic properties using SQUID magnetometry. In the following we will compare these measurements and quantities extracted thereof to values obtained for bulk YIG. We hereby focus on a 43 nm thick YIG film on (111)-oriented GGG, in comparison to a 62 nm thick YIG film on (111)-oriented YAG. We have grown both films by laser-MBE using the optimized set of deposition parameters. A collection of the relevant data is provided in Fig. 3.11(a) and (b) for YIG on GGG and YIG on YAG, respectively, with the external magnetic field applied in the film plane. For both films we subtracted the magnetic background signal of the corresponding substrate (paramagnetic contribution for GGG and diamagnetic for YAG) and normalized the remaining magnetic moment signal to the volume of the YIG layer to obtain the magnetization of the YIG film.

For the YIG film on GGG substrate the $M(H)$ hysteresis curve at $T = 300$ K in Fig. 3.11(a) exhibits a low coercive field $\mu_0 H_c = 3$ mT and reaches a saturation magnetization $M_S = 129$ kA/m, which is approximately 90% of the reported bulk value $M_S = 141.65$ kA/m [201] of YIG. We note that due to the large paramagnetic background signal the error for the determination of the saturation magnetization is extremely large (at least 10%) and thus alone could account for the measured difference to the bulk value

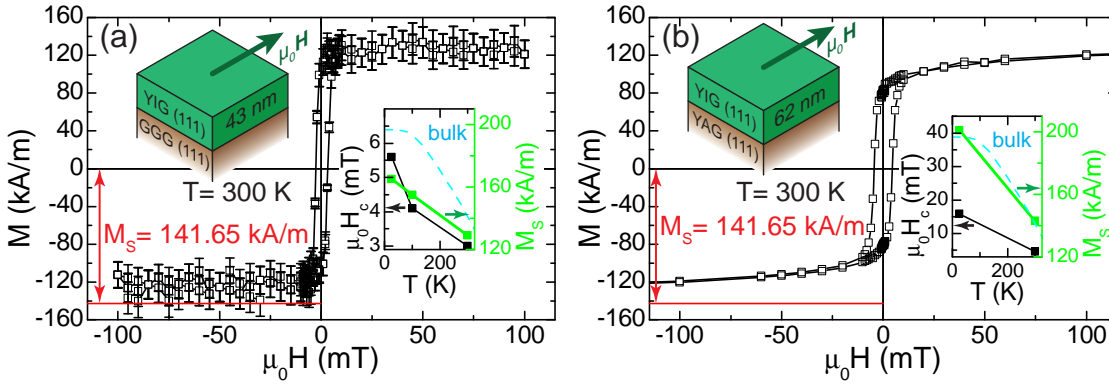


Figure 3.11: Comparison of the magnetic properties of a 43 nm thick YIG layer on a (111)-oriented GGG substrate and a 62 nm thick YIG film on a (111)-oriented YAG substrate extracted from SQUID magnetometry with the external magnetic field applied in the film plane. (a) $M(H)$ loop obtained from the YIG film on a GGG substrate at $T = 300$ K. The inset shows the temperature dependence of the extracted coercive field H_c and saturation magnetization M_S . (b) $M(H)$ loop measured for the YIG film on YAG substrate at $T = 300$ K. The inset shows the temperature dependence of the extracted coercive field H_c and saturation magnetization M_S . The dashed cyan line in both insets displays the temperature dependence of a bulk YIG sample from [201]. Connecting lines between data symbols are guides to the eye.

(cf. error bars in Fig. 3.11(a)). Compared to the results on saturation magnetization of PLD grown YIG reported by other groups [206–209, 211] we can confirm that the saturation magnetization of YIG thin films on GGG substrates is close to the bulk value. But the reported coercive fields in [208, 209, 211] at $T = 300$ K are much lower (below 1 mT) than the one we observe in our YIG films. On the other hand the films grown in [206, 207] exhibit coercive fields as large as 15 mT. From these huge fluctuations of literature values for coercive fields and keeping in mind that H_c sensitively depends on the domain configuration, one can conclude that growth conditions greatly influence this quantity. We attribute the difference in coercive field to the high surface roughness of our GGG substrates extracted from X-ray reflectometry (see Fig. 3.7(d)). Moreover, the SQUID-magnetometry results in [206–209] were obtained for YIG films with iron vacancies (indicated by the large YIG film lattice constant), while our films according to HRXRD experiments are close to ideal stoichiometry and thus exhibit different coercive fields.

The inset in Fig. 3.11(a) shows the temperature evolution of the coercive field (black) and the saturation magnetization (blue) extracted from $M(H)$ measurements at $T = 300$ K, $T = 100$ K, and $T = 25$ K. For a better comparison, the temperature evolution of the saturation magnetization for bulk YIG [201] is indicated as a cyan dashed line in the inset. The coercive field increases with decreasing temperatures and reaches 5.6 mT at $T = 25$ K. The saturation magnetization also increases with decreasing temperatures and reaches 165 kA/m at $T = 25$ K. A comparison with the temperature evolution of bulk YIG yields a deviation of the saturation magnetization at low temperatures of 15%. Again we attribute this difference to the error connected to the large paramagnetic substrate contribution, which increases with decreasing temperature. Thus, the determination of

the saturation magnetization for our films should be taken with caution. Only in [207] a temperature dependence of the saturation magnetization is evaluated by means of $M(T)$ curves, which follows nicely the reported temperature evolution of bulk YIG. Using thicker YIG films (≥ 150 nm) we might be able to obtain a more precise result for the saturation magnetization, due to the increase in magnetic moment for the film. The increase of the coercive field with decreasing temperature is consistent with literature [206–209, 211].

In summary, the magnetic properties evaluated by SQUID magnetometry of our laser-MBE grown YIG films on GGG substrates are equal to already reported values with a close to bulk values saturation magnetization and low coercive fields $\mu_0 H_c \geq 3$ mT. We expect to obtain films with lower coercivity by annealing the substrate prior to the YIG growth leading to a smoother surface.

For the YIG films grown on YAG an analysis of the SQUID magnetometry data is more easily achieved because the diamagnetic substrate contribution allows to easily separate substrate and film magnetic contributions. From the $M(H)$ curve at $T = 300$ K (Fig. 3.11(b)) we extract a coercive field of 4.5 mT which is larger than the one obtained for the YIG film on GGG. Interestingly, the magnetization of the YIG layer increases after hysteresis closure and reaches a near bulk saturation magnetization of 143.2 kA/m for an external magnetic field exceeding 2 T. In [224] a similar behavior is observed for a 62 nm thick YIG film on YAG. In this publication this behavior is explained by the presence of two ferromagnetic phases: a magnetically soft phase ($\text{Y}_3\text{Fe}_5\text{O}_{12}$) and a magnetically hard phase ($\text{Y}_3\text{Fe}_{5-x}\text{Al}_x\text{O}_{12}$). The $\text{Y}_3\text{Fe}_{5-x}\text{Al}_x\text{O}_{12}$ phase is generated by the diffusion of Al from the substrate into the YIG film during growth at elevated temperatures. A comparison of the magnetization hysteresis loop in [224] with the one obtained from our YIG film on YAG leads to the impression that the diffusion process in our samples is not as pronounced as in the samples in [224] due to the hysteresis closure at lower magnetic fields. This is related to the lower substrate temperature during deposition of our films. Moreover, we also observe an exchange coupling at $T = 2$ K with an exchange field of $\mu_0 H_{\text{ex}} = 7$ mT (not shown here), which is due to the pinning of the YIG phase by the $\text{Y}_3\text{Fe}_{5-x}\text{Al}_x\text{O}_{12}$ phase. A more detailed description is given in [224]. The coercive field increases with decreasing temperature up to 15.9 mT at $T = 25$ K (at $T = 25$ K no exchange coupling is visible in our films). The saturation magnetization increases with decreasing temperature and reaches $M_S = 201$ kA/m at $T = 25$ K which is close to the bulk value $M_S = 199$ kA/m [201].

From the SQUID results on our YIG films grown on YAG we conclude that our films in agreement to [224] also have a thin Al substituted YIG layer at the substrate/film interface due to the diffusion of Al from the YAG substrate into the YIG film during growth. The introduction of a buffer layer might help to resolve this issue by acting as a diffusion barrier between substrate and YIG film and in addition improves the structural quality of the YIG films.

For YIG/Pt hybrid structures the obtained SQUID magnetometry results of the magnetic properties of the YIG layer remain qualitatively and quantitatively unchanged and thus are not shown here.

3.2.2.4 Dynamic magnetic properties of laser-MBE grown YIG films on GGG and YAG

The FMR linewidth of YIG is very sensitive to off-stoichiometry, defects and surface roughness and thus can be used as a measure of film quality. For the analysis of our YIG films we conducted FMR measurements at room temperature with a microwave frequency of 10.3 GHz in our custom built FMR setup [225]. Due to the Lock-In detection the FMR signal has the form of the derivative of a Lorentzian function (Fig. 3.12(a)). The inflection point of this curve yields the ferromagnetic resonance field H_{res} , while the peak to peak separation gives the linewidth ΔH_{pp} . In our experiments we investigated the evolution of this FMR signal by a stepwise change of the orientation of the external magnetic field from in-plane to out-of-plane for two different types of YIG layers: a 25 nm thick YIG film on a (111)-oriented GGG substrate and a 62 nm thick YIG film grown on a (111)-oriented YAG substrate. The obtained results are summarized in Fig.3.12(a)-(f). For the extraction of the resonance field and the linewidth we fitted a Lorentzian derivative to our data indicated as blue lines in Fig.3.12(a)-(d).

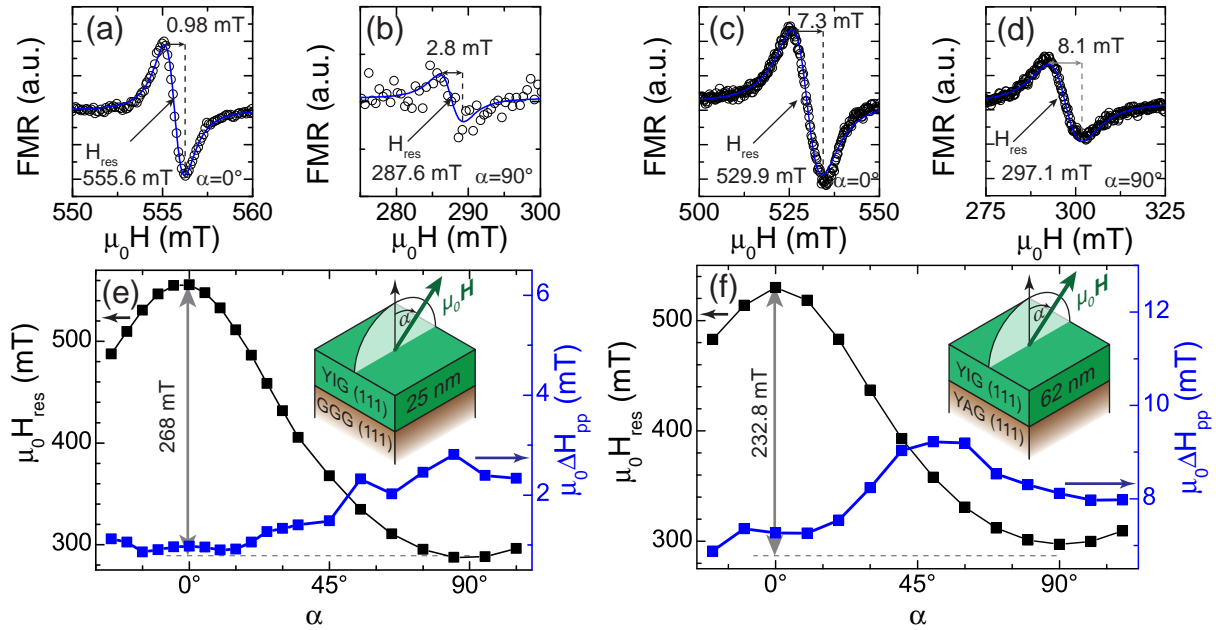


Figure 3.12: Experimental data collected from FMR measurements on a 25 nm thick YIG layer on GGG and a 62 nm thick YIG film on YAG. (a) Out-of-plane and (b) in-plane FMR signal (symbols) recorded for the YIG on GGG sample. The corresponding out-of-plane and in-plane FMR signal for the YIG on YAG sample is shown in (c) and (d) respectively. The blue lines represent a Lorentzian derivative fit to the data for the extraction of ferromagnetic resonance field and FMR linewidth. Extracted resonance field and linewidth for (e) our YIG film on GGG and (f) our YIG film on YAG. The inset in (e) and (f) defines the rotation angle α .

We first focus on the results obtained for YIG on GGG. The FMR signals for the external magnetic field applied oop and ip are shown in Fig. 3.12(a) and (b), respectively. From these FMR signals we extract $\mu_0 H_{\text{res}} = 555.6$ mT for oop and $\mu_0 H_{\text{res}} = 287.6$ mT for ip magnetic field orientation. From these values we can calculate the effective uniaxial

anisotropy [212] $|B_u^*|$ and obtain $|B_u^*| = 184.4 \text{ mT}$ [220] which is close to the reported value $|B_u^*| = 179 \text{ mT}$ for stoichiometric YIG films in [209]. It is mainly caused by the shape anisotropy (expected anisotropy field due to shape anisotropy: $|B_u^*| = 178.0 \text{ mT}$ [209]). These results confirm, that our YIG films on GGG exhibit excellent stoichiometry.

The out-of-plane FMR linewidth in our film $\mu_0\Delta H_{\text{pp}} = 0.98 \text{ mT}$ nearly reaches the best reported value $\mu_0\Delta H_{\text{pp}} = 0.8 \text{ mT}$ in [209] for stoichiometric YIG films. For bulk YIG spheres a FMR line width of 0.02 mT at 3.33 GHz has been reported [226]. This would result in a FMR linewidth of 0.06 mT at 10.3 GHz assuming Gilbert-type (viscous) damping. Manuilov *et al.* [209] achieve a narrowing of the oop linewidth for films with iron vacancies reaching $\mu_0\Delta H_{\text{pp}} = 0.09 \text{ mT}$. But this iron deficiency is not a desirable solution as it destroys the stoichiometry of YIG. Thus, the only way for even narrower FMR linewidths appears to be a smoother substrate surface, which reduces the inhomogeneities due to the stray field in the sample. Nevertheless, the FMR linewidth achieved is nearly equal to stoichiometric YIG films on GGG in [209].

The angular evolution of $\mu_0 H_{\text{res}}$ and $\mu_0\Delta H_{\text{pp}}$ is shown in Fig.3.12(e) where α defines the angle between surface normal and external magnetic field (see inset). The resonance field decreases from $\alpha = 0^\circ$ to $\alpha = 90^\circ$ which is due to the uniaxial out-of-plane magnetic anisotropy field caused by the shape anisotropy. The linewidth of our films only slightly increases for $\alpha = 0^\circ$ to $\alpha = 90^\circ$ as also observed in [212].

For our YIG films on YAG we observe a change in resonance field from $\mu_0 H_{\text{res}} = 529.9 \text{ mT}$ for oop to $\mu_0 H_{\text{res}} = 297.1 \text{ mT}$ for ip magnetic field orientation (see Fig. 3.12(c) and (d), respectively). From these values we extract an uniaxial anisotropy field $|B_u^*| = 159.6 \text{ mT}$, which is significantly smaller than the expected bulk value $|B_u^*| = 178.0 \text{ mT}$. The deviation can be either attributed to an additional anisotropy contribution or the Al substitution at the substrate/film interface. Interestingly, we do not observe the double resonance structure described in [224] for the magnetic field applied in the film plane, which might be due to the larger film thickness of our sample. Thus higher intensity of the FMR signal from the thicker YIG phase overshadows the FMR signal of the $\text{Y}_3\text{Fe}_{5-x}\text{Al}_x\text{O}_{12}$ phase.

The out-of-plane FMR linewidth in our film on YAG $\mu_0\Delta H_{\text{pp}} = 7.3 \text{ mT}$ (Fig. 3.12(c)) is also much larger than the linewidth obtained for our YIG film on GGG, but smaller than $\mu_0\Delta H_{\text{pp}} = 25 \text{ mT}$ obtained for a 22 nm thick YIG film on YAG in [224].

The angular dependence of the ferromagnetic resonance field and linewidth are shown in Fig. 3.12(f) for our YIG film on YAG. Both evolutions qualitatively agree with the results obtained for our YIG layer on GGG. But the absolute change in H_{res} and the absolute values of ΔH_{pp} indicate that our YIG films on YAG have a lower magnetic quality compared to our YIG films on GGG.

3.2.2.5 Laser-MBE growth of YIG thin films: a summary

In summary, we investigated the structural and magnetic properties of YIG films grown on (111)-oriented GGG and YAG substrates using optimized deposition parameters by means of HRXRD, SQUID magnetometry and FMR. For the growth on lattice matched GGG substrates our YIG films exhibit a lattice parameter $a = 1.238 \text{ nm}$ close to the bulk value and a low mosaic spread (FWHM of the XRC for the YIG (444) reflection $\leq 0.04^\circ$), a coercive field $\mu_0 H_c = 3 \text{ mT}$ and a close to bulk saturation magnetization $M_S = 129 \text{ kA/m}$ at $T = 300 \text{ K}$. Moreover, the 10.3 GHz FMR signal of these films

has a narrow linewidth of up $\mu_0\Delta H_{pp} = 0.98$ mT along the [111]-direction. These results support that we are able to grow high-quality stoichiometric epitaxial YIG films on GGG. A further improvement in sample quality may be achieved by smoothing the substrate surface using an annealing procedure prior to YIG film deposition.

For our YIG films grown on YAG substrates, we find that the YIG films grow relaxed with a close to bulk lattice parameter onto the substrate. But the structural quality is substantially reduced due to the large lattice mismatch with a large mosaic spread (FWHM of the XRC for the YIG (444) reflection $\geq 0.24^\circ$). Moreover, the magnetic properties of the YIG films are influenced by the Al diffusion from the substrate into the film during growth. This leads to the generation of two separate, exchange coupled magnetic phases: a YIG phase on top and a Al:YIG phase at the substrate interface. The structural and magnetic characterization show that our YIG films on YAG substrates can be still improved, which might be mainly achieved by introducing a buffer layer and lowering the Al interdiffusion at the substrate/film interface.

3.3 Anisotropic magnetothermopower and anisotropic magnetoresistance

In this section we discuss the anisotropic magnetothermopower (AMTP) and anisotropic magnetoresistance (AMR) in two different classes of ferromagnetic materials, namely the prototype ferromagnetic semiconductor (Ga,Mn)As and Cobalt-based Heusler compounds as metallic ferromagnets. In the beginning of this section we introduce a theoretical model to describe AMTP and AMR using a series expansion of the resistivity and Seebeck tensor in powers of the magnetization orientation \mathbf{m} (Sect. 3.3.1). We then discuss the application of this model to angle dependent³ magnetothermopower (ADMTP) and angle dependent magnetoresistance (ADMR) experiments to extract the full resistivity and Seebeck tensors for cubic and tetragonal symmetry of the ferromagnet investigated. This full tensor extraction can then be used to obtain further information on the shape of the Fermi surface via the Mott relation. After this introduction into the theoretical model we discuss first proof-of-principle experiments on (Ga,Mn)As in Sect. 3.3.2. The results of these experiments show that our model is well suited to describe the ADMTP and ADMR experiments for tetragonal (001)- and (113)-oriented (Ga,Mn)As and enables us to extract components of the resistivity and Seebeck tensors and even quantitative information on the magnetic anisotropy of the sample from angle dependent measurements. Please note that a full extraction of all tensor components is not achieved. Moreover, we apply our model to the Cobalt-based Heusler compound Co_2FeAl in Sect. 3.3.3 and find an excellent agreement between theory and experiment for ADMR experiments (Due to the limitations imposed by the signal-to-noise ratio of our measurement setup an investigation of the ADMTP in Co_2FeAl was not possible). This further demonstrates the versatility of our model, which is thus not restricted to one class of ferromagnetic materials.

³In the following we use the phrase "angle dependent" synonymously for "as a function of external magnetic field orientation".

3.3.1 Theory of magneto-galvanic effects

In the past 40 years the influence of crystal symmetry on transport tensor properties of magnetically ordered crystals has been discussed by many authors with quite controversial results [227–230]. We here outline an already well established model for the resistivity and conductivity tensor and expand this model to also include the Seebeck and Peltier tensor. We start with the assumption, that in a magnetic crystal the electric and thermal currents, \mathbf{j} and \mathbf{h} , depend linearly on the electric $F_{\mathbf{E}} = q\mathbf{E}$ and thermal forces $F_{\text{th}} = -S_t\nabla T$, with the electric field $\mathbf{E} = -\nabla(\bar{\varphi})$, the charge q and the transport entropy S_t (linear response). We thus do not consider any deviation from Ohm's law in its generalized form. This leads us in cartesian coordinates to [226, 231]⁴

$$\mathbf{j}_i = \sigma_{ik}(\mathbf{B})\mathbf{E}_k - \beta'_{ik}(\mathbf{B})T^{-1}(\nabla T)_k, \quad (3.1)$$

$$\mathbf{h}_i = -\beta''_{ik}(\mathbf{B})\mathbf{E}_k - \gamma_{ik}(\mathbf{B})T^{-1}(\nabla T)_k, \quad (3.2)$$

where we used the temperature T , electrochemical potential $\bar{\varphi} = \varphi - \mu/e$, with φ the electrical, μ the chemical potential, e the negative electrical charge, $\mathbf{B} = \mu_0(\mathbf{H} + \mathbf{M})$ the magnetic induction, with \mathbf{H} the external magnetic field and \mathbf{M} the magnetization of the crystal, and the summation convention over cartesian coordinates. The cartesian tensors $\sigma_{ik}(\mathbf{B})$, $\beta'_{ik}(\mathbf{B})$, $\beta''_{ik}(\mathbf{B})$, $\gamma_{ik}(\mathbf{B})$ connecting the electric and thermal currents with the corresponding forces depend on the strength and direction of the magnetization \mathbf{M} and external magnetic field \mathbf{H} . For a more convenient description in experiments, where the independent variables are \mathbf{j} and ∇T , because it is easier to electrically insulate the system ($\mathbf{j} = 0$) and keep the boundaries at constant temperature ($\nabla T = 0$), we reformulate Eqs.(3.1),(3.2) into

$$\mathbf{E}_i = \rho_{ik}(\mathbf{B})\mathbf{j}_k + \Sigma'_{ik}(\mathbf{B})(\nabla T)_k, \quad (3.3)$$

$$\mathbf{h}_i = T\Sigma''_{ik}(\mathbf{B})\mathbf{j}_k - \kappa_{ik}(\mathbf{B})(\nabla T)_k. \quad (3.4)$$

Here $\rho_{ik}(\mathbf{B})$ represents the resistivity tensor, $\Sigma'_{ik}(\mathbf{B})$ the Seebeck tensor, $\Sigma''_{ik}(\mathbf{B})$ the Peltier tensor, and $\kappa_{ik}(\mathbf{B})$ the thermal conductivity tensor. These 4 tensors are connected to the 4 tensors above via:

$$\rho_{ik}(\mathbf{B}) = (\sigma)_{ik}^{-1}(\mathbf{B}) \quad (3.5)$$

$$\kappa_{ik}(\mathbf{B}) = -T^{-1}(\beta''_{ij}\rho_{jl}\beta'_{lk}(\mathbf{B}) - \gamma_{ik}(\mathbf{B})) \quad (3.6)$$

$$\Sigma'_{ik}(\mathbf{B}) = T^{-1}\rho_{ij}\beta'_{kj}(\mathbf{B}) \quad (3.7)$$

$$\Sigma''_{ik}(\mathbf{B}) = T^{-1}\beta''_{ij}\rho_{jk}(\mathbf{B}) \quad (3.8)$$

We can reformulate this in terms of the 6×6 matrix of generalized transport coefficients \mathbf{L}_{ij} :

$$\mathbf{L}(\mathbf{B}) = \begin{pmatrix} \rho(\mathbf{B}) & \Sigma'(\mathbf{B}) \\ \Sigma''(\mathbf{B}) & \kappa(\mathbf{B}) \end{pmatrix}. \quad (3.9)$$

For this tensor the Onsager relation for a magnetic crystal yields

$$\mathbf{L}_{ij}(\mathbf{B}) = \mathbf{L}_{ji}(-\mathbf{B}), \quad (3.10)$$

⁴The following introduction into transport coefficients and linearized Boltzmann transport is inspired by the description given by Ziman in [231].

which implies that the transposition of \mathbf{L}_{ij} can only be equal to itself if the magnetic field and magnetization are also reversed. The off-diagonal elements must be an odd function of \mathbf{B} . This further introduces the following relations for the resistivity, Seebeck, Peltier, and thermal conductivity tensors

$$\rho_{ij}(\mathbf{B}) = \rho_{ji}(-\mathbf{B}), \quad (3.11)$$

$$\kappa_{ij}(\mathbf{B}) = \kappa_{ji}(-\mathbf{B}), \quad (3.12)$$

$$\Sigma'_{ij}(\mathbf{B}) = \Sigma''_{ji}(-\mathbf{B}). \quad (3.13)$$

We note that due to the Onsager relation the number of independent terms is reduced from 36 to 21 for the 4 3×3 transport tensors. Moreover, each of those terms is either an odd or even function of \mathbf{B} , depending on whether it is an off-diagonal or diagonal element of the tensor.

We can formulate the electrical current (j) in terms of a linearized Boltzmann transport equation with relaxation time τ [231]

$$\mathbf{j} = \int e \mathbf{v}_{\mathbf{k}} (1 + \Omega)^{-1} \left[\tau \mathbf{v}_{\mathbf{k}} \left(-e \mathbf{E} + \frac{E_{\mathbf{k}} - \mu}{T} \nabla T \right) \frac{\partial f_{\mathbf{k}}^0}{\partial E_{\mathbf{k}}} \right] d\mathbf{k}. \quad (3.14)$$

In this equation we define $E_{\mathbf{k}}$ as the electron energy, $\mathbf{v}_{\mathbf{k}} = \nabla_{\mathbf{k}} E_{\mathbf{k}}$ as the electron group velocity, $\Omega = e\tau/\hbar \mathbf{v}_{\mathbf{k}} \times \mathbf{B} \circ \nabla_{\mathbf{k}}$ as the magnetic differential operator, E_{F} the Fermi energy of the system, and $f_{\mathbf{k}}^0$ the Fermi-Dirac distribution function. In the same way we can write down the heat current

$$\mathbf{h} = \int (E_{\mathbf{k}} - \mu) (1 + \Omega)^{-1} \left[\tau \mathbf{v}_{\mathbf{k}} \left(-e \mathbf{E} + \frac{E_{\mathbf{k}} - \mu}{T} \nabla T \right) \frac{\partial f_{\mathbf{k}}^0}{\partial E_{\mathbf{k}}} \right] d\mathbf{k}. \quad (3.15)$$

These two equations (3.14) and (3.15) are equivalent to Eqs. (3.1) and 3.2. \mathbf{E} and ∇T are multiplied by tensor quantities defined by certain integrals over the electron distribution. The important point is, that the operator $(1 + \Omega)^{-1}$, in which the whole magnetic effect is concealed, only acts on $\tau \mathbf{v}_{\mathbf{k}}$ and not at all on functions, which are constant upon an energy surface, such as $E_{\mathbf{k}} - E_{\text{F}}$ and $\partial f_{\mathbf{k}}^0 / \partial E_{\mathbf{k}}$. By carrying out the integration over energy independently of the other operation and using the pseudo-delta properties of the function $\partial f_{\mathbf{k}}^0 / \partial E_{\mathbf{k}}$, we can identify the following relationship between the 4 different tensors [231]:

$$\Sigma'_{ik} \sigma_{kl}(\mathbf{B}) = \frac{\pi^2 k_{\text{B}}^2 T}{3 e} \left[\frac{\partial}{\partial E} \sigma_{il}(\mathbf{B}) \right]_{E=E_{\text{F}}}, \quad (3.16)$$

$$\gamma_{ik}(\mathbf{B}) = \frac{\pi^2 k_{\text{B}}^2}{3 e^2} \sigma_{ik}(\mathbf{B}), \quad (3.17)$$

here $k_{\text{B}} = 1.38065 \times 10^{-23}$ J/K is the Boltzmann constant. The first of these equations (3.16) is the generalized Mott relation, which connects the derivative of conductivity with respect to the Fermi level to the Seebeck tensor. The second equation (3.17) is a generalized Wiedemann-Franz law. These two equations hold, when the electron scattering is effectively elastic. Moreover, this set of equations allows the calculation of the thermomagnetic coefficients from a theory only treating the galvanomagnetic effects [232, 233].

A direct calculation of the thermomagnetic tensors is possible if Ω is small compared to

unity (i.e., $|\mathbf{B}|e\tau/m = \omega_c\tau \ll 1$, where ω_c is the electron cyclotron frequency, which means that the scattering rate is much higher than the precession frequency of the electrons in the magnetic field), because we can then expand the operator $(1 + \Omega)^{-1}$ in powers of Ω [234]:

$$(1 + \Omega)^{-1} = 1 - \Omega + \Omega^2 - \Omega^3 + \dots \quad (3.18)$$

This is equivalent to the construction of successive approximations in powers of \mathbf{B} . The general term assumes the form

$$(-\Omega)^n = \left[-\frac{e\tau}{\hbar} \mathbf{v}_{\mathbf{k}} \times \mathbf{B} \circ \nabla_{\mathbf{k}} \right] \left[-\frac{e\tau}{\hbar} \mathbf{v}_{\mathbf{k}} \times \mathbf{B} \circ \nabla_{\mathbf{k}} \right] \dots \quad (3.19)$$

We can calculate now the electrical and heat current as in Eqs.(3.14,3.15) and identify the coefficients of the tensor components. For example the conductivity may be expanded up to the second order of \mathbf{B} in the following way (with the summation convention over the indices of the cartesian components)

$$\mathbf{j}_i = \sigma_{ij} \mathbf{E}_j + \sigma_{ijk}^{(I)} \mathbf{E}_j \mathbf{B}_k + \sigma_{ijkl}^{(II)} \mathbf{E}_j \mathbf{B}_k \mathbf{B}_l + \dots \quad (3.20)$$

Here the terms linear in \mathbf{B} describe the Hall effect and terms quadratic in \mathbf{B} the magnetoresistance. The tensor components can be expressed as integrals

$$\sigma_{ij} = \int e^2 \tau \frac{\partial f_{\mathbf{k}}^0}{\partial E_{\mathbf{k}}} \mathbf{v}_{\mathbf{k}_i} \mathbf{v}_{\mathbf{k}_j} d\mathbf{k}, \quad (3.21)$$

$$\sigma_{ijk}^{(I)} = \epsilon_{klm} \int e^3 \tau^2 \frac{\partial f_{\mathbf{k}}^0}{\partial E_{\mathbf{k}}} \mathbf{v}_{\mathbf{k}_i} \mathbf{v}_{\mathbf{k}_m} \mathbf{M}_{jl}^{-1} d\mathbf{k}, \quad (3.22)$$

$$\sigma_{ijkl}^{(II)} = \epsilon_{pk\sigma} \epsilon_{nlm} \int e^4 \tau^3 \frac{\partial f_{\mathbf{k}}^0}{\partial E_{\mathbf{k}}} \mathbf{v}_{\mathbf{k}_i} \mathbf{v}_{\mathbf{k}_p} \left[\mathbf{M}_{mj}^{-1} \mathbf{M}_{no}^{-1} + \mathbf{v}_{\mathbf{k}_n} \frac{\partial}{\partial \mathbf{k}_j} (\mathbf{M}_{mo}^{-1}) \right] d\mathbf{k}. \quad (3.23)$$

ϵ_{klm} are the totally antisymmetric tensor components introduced by the vector products, \mathbf{M}_{ij}^{-1} are the components of the inverse effective mass tensor:

$$\mathbf{M}_{ij}^{-1} = \frac{1}{\hbar^2} \frac{\partial^2 E_{\mathbf{k}}}{\partial \mathbf{k}_i \partial \mathbf{k}_j} \quad (3.24)$$

The calculation of higher order terms becomes more complex as even higher derivatives of the effective mass tensor are required. Nevertheless, these expressions allow to calculate an approximation of the conductivity tensor, if one has knowledge of the form of the Fermi surface of the crystal. This calculation becomes really difficult depending on the form of the surface. In addition, even the determination of the Fermi surface for more complex crystals from theory is nearly impossible to achieve.

For a ferromagnet we have neglected up to now, the influence of the spin polarized transport on the tensors. One possible way to include these effects, is the application of the two spin current model [140] and divide the electrical and heat current into two contributions, stemming from two different spin species (up and down) and describe the transport as linearized Boltzmann equations for each one separately. Unfortunately this general approach is rather complicated to achieve and will not be used in this thesis.

Rather, we use a phenomenological approach based on a series expansion of the transport tensors with respect to the magnetization direction [227] $\mathbf{m} = \mathbf{M}/M_{\text{sat}}$ to include

spin dependent transport. This enables us to provide a model to calculate magnetic effects in a ferromagnet using a fixed set of parameters. At first glance the number of independent parameters seems to be enormous (9 components for 0th, 27 for 1st, 81 for 2nd order in \mathbf{m}), but it can be greatly reduced by taking into account the Onsager relations and the symmetry of the crystal itself. The approach presented here has been already described in [227, 235–237]. In the following we outline the steps needed to reduce the number of independent variables for the resistivity tensor $\rho_{ij}(\mathbf{m})$ and the Seebeck tensor $\Sigma'_{ij}(\mathbf{m})$ for cubic and tetragonal symmetry of a ferromagnetic crystal. We can then express $\rho_{ij}(\mathbf{m})$, $\Sigma'_{ij}(\mathbf{m})$ as a series expansion of \mathbf{m}

$$\rho_{ij}(\mathbf{B}) = \rho_{ij}^{(0)} + \rho_{ijk}^{(1)}\mathbf{m}_k + \rho_{ijkl}^{(2)}\mathbf{m}_k\mathbf{m}_l + \rho_{ijklm}^{(3)}\mathbf{m}_k\mathbf{m}_l\mathbf{m}_m + \rho_{ijklmn}^{(4)}\mathbf{m}_k\mathbf{m}_l\mathbf{m}_m\mathbf{m}_n + \dots, \quad (3.25)$$

$$\Sigma'_{ij}(\mathbf{m}) = \Sigma_{ij}^{(0)} + \Sigma_{ijk}^{(1)}\mathbf{m}_k + \Sigma_{ijkl}^{(2)}\mathbf{m}_k\mathbf{m}_l + \Sigma_{ijklm}^{(3)}\mathbf{m}_k\mathbf{m}_l\mathbf{m}_m + \Sigma_{ijklmn}^{(4)}\mathbf{m}_k\mathbf{m}_l\mathbf{m}_m\mathbf{m}_n + \dots \quad (3.26)$$

Please note that this series expansion in direction cosines of the magnetization is different to the series expansion in \mathbf{B} in Eq.(3.20), the dependence of the coefficients on the magnetic field strength is here not taken into account. Due to the commutative multiplication of the magnetic field components $\mathbf{m}_k\mathbf{m}_l = \mathbf{m}_l\mathbf{m}_k$, we can already reduce the number of independent parameters for the 2nd, 3rd and 4th order of our expansion:

$$\rho_{ijkl}^{(2)} = \rho_{ijlk}^{(2)}, \quad (3.27)$$

$$\rho_{ijklm}^{(3)} = \rho_{ijkml}^{(3)} = \rho_{ijlkm}^{(3)} = \rho_{ijlmk}^{(3)} = \rho_{ijmkl}^{(3)} = \rho_{ijmlk}^{(3)}, \quad (3.28)$$

$$\rho_{ijklmn}^{(4)} = \rho_{ijklnm}^{(4)} = \rho_{ijlkmn}^{(4)} = \rho_{ijlknm}^{(4)} = \dots \quad (3.29)$$

The same holds for the Seebeck tensor series expansion coefficients. With the application of Neumann's principle the number of series expansion coefficients can be further reduced, as the crystal symmetry has to be also reflected in the physical property tensors themselves⁵. We here use a small set of generating matrixes \mathbf{S} for each crystal symmetry [227], which makes the calculations a lot easier. The generating matrixes will construct linear equations between expansion coefficients of the same order, reducing the number of independent coefficients:

$$\begin{aligned} \rho_{ij}^{(0)} &= S_{io}S_{jp}\rho_{op}^{(0)}, \\ \rho_{ijk}^{(1)} &= \det[S]S_{io}S_{jp}S_{kq}\rho_{opq}^{(1)}, \\ \rho_{ijkl}^{(2)} &= (\det[S])^2S_{io}S_{jp}S_{kq}S_{lr}\rho_{opqr}^{(2)}, \\ \rho_{ijklm}^{(3)} &= (\det[S])^3S_{io}S_{jp}S_{kq}S_{lr}S_{ms}\rho_{opqrs}^{(3)}, \\ \rho_{ijklmn}^{(4)} &= (\det[S])^4S_{io}S_{jp}S_{kq}S_{lr}S_{ms}S_{nt}\rho_{opqrst}^{(4)}. \end{aligned}$$

The very same equations can be constructed for the expansion of the Seebeck tensor. An additional restriction to the number of independent variables for the expansion of

⁵We defined in Eq.(3.5) the Seebeck tensor as a tensor product containing the resistivity tensor. Nevertheless, as the Seebeck tensor describes a physical property of the crystal it has to reflect the symmetry of the system.

the resistivity tensor arises from the Onsager relations (Eq.(3.11)). The expansion coefficients for an even number of \mathbf{m}_k have to be symmetric in ij and for an odd number antisymmetric in ij

$$\begin{aligned}\rho_{ij}^{(0)} &= \rho_{ji}^{(0)}, \\ \rho_{ijk}^{(1)} &= -\rho_{jik}^{(1)}, \\ \rho_{ijkl}^{(2)} &= \rho_{jikl}^{(2)}, \\ \rho_{ijklm}^{(3)} &= -\rho_{jiklm}^{(3)}, \\ \rho_{ijklmn}^{(4)} &= \rho_{jiklmn}^{(4)}.\end{aligned}$$

Note that these restrictions only apply for the expansion of the resistivity and not for the expansion of the Seebeck tensor, as the Onsager relations (Eq.(3.11)) imply for the Seebeck tensor $\Sigma'_{ij}(\mathbf{m})$ only a connection to the Peltier tensor $\Sigma''_{ij}(\mathbf{m})$.

3.3.1.1 Calculation of the resistivity and Seebeck tensor in cubic symmetry

With these general expressions at hand we can calculate the resistivity and Seebeck tensor expansion for cubic symmetry ($\bar{4}3m$) with the generating matrixes \mathbf{S}_8 and \mathbf{S}_9 [227, 235, 236]

$$\begin{aligned}\mathbf{S}_8 &= \begin{pmatrix} 0 & -1 & 0 \\ 1 & 0 & 0 \\ 0 & 0 & -1 \end{pmatrix}, \\ \mathbf{S}_9 &= \begin{pmatrix} 0 & 1 & 0 \\ 0 & 0 & 1 \\ 1 & 0 & 0 \end{pmatrix}.\end{aligned}$$

This leads us in the cubic case to the following expansion of the resistivity $\boldsymbol{\rho}_{\text{cubic}}$

$$\begin{aligned}\boldsymbol{\rho}_{\text{cubic}}(\mathbf{m}) &= (\rho^{(0)} + \rho^{(2,1)} + \rho^{(4,1)}) \begin{pmatrix} 1 & 0 & 0 \\ 0 & 1 & 0 \\ 0 & 0 & 1 \end{pmatrix} + (\rho^{(1)} + \rho^{(3,1)}) \begin{pmatrix} 0 & -\mathbf{m}_z & \mathbf{m}_y \\ \mathbf{m}_z & 0 & -\mathbf{m}_x \\ -\mathbf{m}_y & \mathbf{m}_x & 0 \end{pmatrix} \\ &+ (\rho^{(2,2)} + \rho^{(4,2)}) \begin{pmatrix} \mathbf{m}_x^2 & 0 & 0 \\ 0 & \mathbf{m}_y^2 & 0 \\ 0 & 0 & \mathbf{m}_z^2 \end{pmatrix} + (\rho^{(2,3)} + \rho^{(4,3)}) \begin{pmatrix} 0 & \mathbf{m}_x \mathbf{m}_y & \mathbf{m}_x \mathbf{m}_z \\ \mathbf{m}_x \mathbf{m}_y & 0 & \mathbf{m}_y \mathbf{m}_z \\ \mathbf{m}_x \mathbf{m}_z & \mathbf{m}_y \mathbf{m}_z & 0 \end{pmatrix} \\ &+ \rho^{(3,2)} \begin{pmatrix} 0 & -\mathbf{m}_z^3 & \mathbf{m}_y^3 \\ \mathbf{m}_z^3 & 0 & -\mathbf{m}_x^3 \\ -\mathbf{m}_y^3 & \mathbf{m}_x^3 & 0 \end{pmatrix} + \rho^{(4,4)} \begin{pmatrix} \mathbf{m}_x^4 & 0 & 0 \\ 0 & \mathbf{m}_y^4 & 0 \\ 0 & 0 & \mathbf{m}_z^4 \end{pmatrix} \\ &+ \rho^{(4,5)} \begin{pmatrix} \mathbf{m}_y^2 \mathbf{m}_z^2 & 0 & 0 \\ 0 & \mathbf{m}_x^2 \mathbf{m}_z^2 & 0 \\ 0 & 0 & \mathbf{m}_x^2 \mathbf{m}_y^2 \end{pmatrix} + \rho^{(4,6)} \begin{pmatrix} 0 & \mathbf{m}_x \mathbf{m}_y \mathbf{m}_z^2 & \mathbf{m}_x \mathbf{m}_y^2 \mathbf{m}_z \\ \mathbf{m}_x \mathbf{m}_y \mathbf{m}_z^2 & 0 & \mathbf{m}_x^2 \mathbf{m}_y \mathbf{m}_z \\ \mathbf{m}_x \mathbf{m}_y^2 \mathbf{m}_z & \mathbf{m}_x^2 \mathbf{m}_y \mathbf{m}_z & 0 \end{pmatrix}.\end{aligned}\tag{3.30}$$

Her we used the expressions $\mathbf{m}^2 = \mathbf{m}_x^2 + \mathbf{m}_y^2 + \mathbf{m}_z^2 = 1$ and $\mathbf{m}^4 = (\mathbf{m}^2)^2 = 1$. The parameters $\rho^{(i,j)}$ are linear combinations of the expansion coefficients, equations connecting these

two variables are presented in Appendix D. The number of independent parameters has been reduced to 1 for 0th, 1 for 1st, 3 for 2nd, 2 for 3rd, and 6 for 4th order respectively.

In the same way we can calculate the representation of the Seebeck tensor for cubic symmetry Σ_{cubic} :

$$\begin{aligned}
\Sigma_{\text{cubic}}(\mathbf{m}) = & (\Sigma^{(0)} + \Sigma^{(2,1)} + \Sigma^{(4,1)}) \begin{pmatrix} 1 & 0 & 0 \\ 0 & 1 & 0 \\ 0 & 0 & 1 \end{pmatrix} \\
& + (\Sigma^{(1)} + \Sigma^{(3,1)}) \begin{pmatrix} 0 & -\mathbf{m}_z & \mathbf{m}_y \\ \mathbf{m}_z & 0 & -\mathbf{m}_x \\ -\mathbf{m}_y & \mathbf{m}_x & 0 \end{pmatrix} + (\Sigma^{(2,2)} + \Sigma^{(4,2)}) \begin{pmatrix} \mathbf{m}_x^2 & 0 & 0 \\ 0 & \mathbf{m}_y^2 & 0 \\ 0 & 0 & \mathbf{m}_z^2 \end{pmatrix} \\
& + (\Sigma^{(2,3)} + \Sigma^{(4,3)}) \begin{pmatrix} 0 & \mathbf{m}_x\mathbf{m}_y & \mathbf{m}_x\mathbf{m}_z \\ \mathbf{m}_x\mathbf{m}_y & 0 & \mathbf{m}_y\mathbf{m}_z \\ \mathbf{m}_x\mathbf{m}_z & \mathbf{m}_y\mathbf{m}_z & 0 \end{pmatrix} + \Sigma^{(3,2)} \begin{pmatrix} 0 & -\mathbf{m}_z^3 & \mathbf{m}_y^3 \\ \mathbf{m}_z^3 & 0 & -\mathbf{m}_x^3 \\ -\mathbf{m}_y^3 & \mathbf{m}_x^3 & 0 \end{pmatrix} \\
& + \Sigma^{(3,3)} \begin{pmatrix} 0 & -\mathbf{m}_y^2\mathbf{m}_z & \mathbf{m}_y\mathbf{m}_z^2 \\ \mathbf{m}_x^2\mathbf{m}_z & 0 & -\mathbf{m}_x\mathbf{m}_z^2 \\ -\mathbf{m}_x^2\mathbf{m}_y & \mathbf{m}_x\mathbf{m}_y^2 & 0 \end{pmatrix} + \Sigma^{(4,4)} \begin{pmatrix} \mathbf{m}_x^4 & 0 & 0 \\ 0 & \mathbf{m}_y^4 & 0 \\ 0 & 0 & \mathbf{m}_z^4 \end{pmatrix} \\
& + \Sigma^{(4,5)} \begin{pmatrix} \mathbf{m}_y^2\mathbf{m}_z^2 & 0 & 0 \\ 0 & \mathbf{m}_x^2\mathbf{m}_z^2 & 0 \\ 0 & 0 & \mathbf{m}_x^2\mathbf{m}_y^2 \end{pmatrix} + \Sigma^{(4,6)} \begin{pmatrix} 0 & \mathbf{m}_x\mathbf{m}_y\mathbf{m}_z^2 & \mathbf{m}_x\mathbf{m}_y^2\mathbf{m}_z \\ \mathbf{m}_x\mathbf{m}_y\mathbf{m}_z^2 & 0 & \mathbf{m}_x^2\mathbf{m}_y\mathbf{m}_z \\ \mathbf{m}_x\mathbf{m}_y^2\mathbf{m}_z & \mathbf{m}_x^2\mathbf{m}_y\mathbf{m}_z & 0 \end{pmatrix} \\
& + \Sigma^{(4,7)} \begin{pmatrix} 0 & \mathbf{m}_x\mathbf{m}_y^3 & \mathbf{m}_x\mathbf{m}_z^3 \\ \mathbf{m}_x^3\mathbf{m}_y & 0 & \mathbf{m}_y\mathbf{m}_z^3 \\ \mathbf{m}_x^3\mathbf{m}_z & \mathbf{m}_y^3\mathbf{m}_z & 0 \end{pmatrix}.
\end{aligned} \tag{3.31}$$

We find that the number of independent parameters is 1 for 0th, 1 for 1st, 3 for 2nd, 3 for 3rd, and 7 for 4th order. A comparison between resistivity tensor and Seebeck tensor reveal two additional functional dependencies in the Seebeck tensor, described by $\Sigma^{(3,3)}$ and $\Sigma^{(4,7)}$. These additional terms in the Seebeck tensor arise from the non existent restriction from the Onsager relation, which increases the number of independent parameters for the 3rd and 4th order of the series expansion. These two expressions enable us to model the resistivity and Seebeck tensor up to the 4th order of \mathbf{m} with 13 and 15 parameters respectively.

3.3.1.2 Calculation of the resistivity and Seebeck tensor in tetragonal symmetry

In the case of a tetragonal symmetry ($\bar{4}2m$) of the crystal (the c-axis is oriented along the z-axis of our coordinate system), we can use the generating matrixes \mathbf{S}_8 from the cubic case and \mathbf{S}_2 [227, 235, 236]

$$\mathbf{S}_2 = \begin{pmatrix} -1 & 0 & 0 \\ 0 & 1 & 0 \\ 1 & 0 & -1 \end{pmatrix}$$

We first calculate the resistivity tensor $\boldsymbol{\rho}_{\text{tetra}}$ up to fourth order

$$\begin{aligned}
\boldsymbol{\rho}_{\text{tetra}}(\mathbf{m}) = & (\rho^{(0,a)} + \rho^{(2,1,a)} + \rho^{(4,1,a)}) \begin{pmatrix} 1 & 0 & 0 \\ 0 & 1 & 0 \\ 0 & 0 & 0 \end{pmatrix} + (\rho^{(0,c)} + \rho^{(2,1,c)} + \rho^{(4,1,c)}) \begin{pmatrix} 0 & 0 & 0 \\ 0 & 0 & 0 \\ 0 & 0 & 1 \end{pmatrix} \\
& + (\rho^{(1,a)} + \rho^{(3,1,a)}) \begin{pmatrix} 0 & -\mathbf{m}_z & 0 \\ \mathbf{m}_z & 0 & 0 \\ 0 & 0 & 0 \end{pmatrix} + (\rho^{(1,c)} + \rho^{(3,1,c)}) \begin{pmatrix} 0 & 0 & \mathbf{m}_y \\ 0 & 0 & -\mathbf{m}_x \\ -\mathbf{m}_y & \mathbf{m}_x & 0 \end{pmatrix} \\
& + (\rho^{(2,2,a)} + \rho^{(4,2,a)}) \begin{pmatrix} \mathbf{m}_x^2 & 0 & 0 \\ 0 & \mathbf{m}_y^2 & 0 \\ 0 & 0 & 0 \end{pmatrix} + (\rho^{(2,2,c)} + \rho^{(4,2,c)}) \begin{pmatrix} 0 & 0 & 0 \\ 0 & 0 & 0 \\ 0 & 0 & \mathbf{m}_z^2 \end{pmatrix} \\
& + (\rho^{(2,3,a)} + \rho^{(4,3,a)}) \begin{pmatrix} 0 & \mathbf{m}_x \mathbf{m}_y & 0 \\ \mathbf{m}_x \mathbf{m}_y & 0 & 0 \\ 0 & 0 & 0 \end{pmatrix} \\
& + (\rho^{(2,3,c)} + \rho^{(4,3,c)}) \begin{pmatrix} 0 & 0 & \mathbf{m}_x \mathbf{m}_z \\ 0 & 0 & \mathbf{m}_y \mathbf{m}_z \\ \mathbf{m}_x \mathbf{m}_z & \mathbf{m}_y \mathbf{m}_z & 0 \end{pmatrix} \\
& + (\rho^{(2,4,a)} + \rho^{(4,4,a)}) \begin{pmatrix} \mathbf{m}_z^2 & 0 & 0 \\ 0 & \mathbf{m}_z^2 & 0 \\ 0 & 0 & 0 \end{pmatrix} + \begin{pmatrix} 0 & -\rho^{(3,2,a)} \mathbf{m}_z^3 & \rho^{(3,2,c)} \mathbf{m}_y^3 \\ \rho^{(3,2,a)} \mathbf{m}_z^3 & 0 & -\rho^{(3,2,c)} \mathbf{m}_x^3 \\ -\rho^{(3,2,c)} \mathbf{m}_y^3 & \rho^{(3,2,c)} \mathbf{m}_x^3 & 0 \end{pmatrix} \\
& + \rho^{(3,3,c)} \begin{pmatrix} 0 & 0 & \mathbf{m}_y \mathbf{m}_z^2 \\ 0 & 0 & -\mathbf{m}_x \mathbf{m}_z^2 \\ -\mathbf{m}_y \mathbf{m}_z^2 & \mathbf{m}_x \mathbf{m}_z^2 & 0 \end{pmatrix} \\
& + \begin{pmatrix} \rho^{(4,5,a)} \mathbf{m}_x^4 & 0 & 0 \\ 0 & \rho^{(4,5,a)} \mathbf{m}_y^4 & 0 \\ 0 & 0 & \rho^{(4,5,c)} \mathbf{m}_z^4 \end{pmatrix} \\
& + \begin{pmatrix} \rho^{(4,6,a)} \mathbf{m}_y^2 \mathbf{m}_z^2 & 0 & 0 \\ 0 & \rho^{(4,6,a)} \mathbf{m}_x^2 \mathbf{m}_z^2 & 0 \\ 0 & 0 & \rho^{(4,6,c)} \mathbf{m}_x^2 \mathbf{m}_y^2 \end{pmatrix} \\
& + \begin{pmatrix} 0 & \rho^{(4,7,a)} \mathbf{m}_x \mathbf{m}_y \mathbf{m}_z^2 & \rho^{(4,7,c)} \mathbf{m}_x \mathbf{m}_y^2 \mathbf{m}_z \\ \rho^{(4,7,a)} \mathbf{m}_x \mathbf{m}_y \mathbf{m}_z^2 & 0 & \rho^{(4,7,c)} \mathbf{m}_x^2 \mathbf{m}_y \mathbf{m}_z \\ \rho^{(4,7,c)} \mathbf{m}_x \mathbf{m}_y^2 \mathbf{m}_z & \rho^{(4,7,c)} \mathbf{m}_x^2 \mathbf{m}_y \mathbf{m}_z & 0 \end{pmatrix} \\
& + \rho^{(4,8,a)} \begin{pmatrix} \mathbf{m}_z^4 & 0 & 0 \\ 0 & \mathbf{m}_z^4 & 0 \\ 0 & 0 & 0 \end{pmatrix} + \rho^{(4,9,c)} \begin{pmatrix} 0 & 0 & \mathbf{m}_x \mathbf{m}_z^3 \\ 0 & 0 & \mathbf{m}_y \mathbf{m}_z^3 \\ \mathbf{m}_x \mathbf{m}_z^3 & \mathbf{m}_y \mathbf{m}_z^3 & 0 \end{pmatrix}.
\end{aligned} \tag{3.32}$$

For tetragonal symmetry the number of independent parameters for the resistivity tensor are 2 for 0th, 2 for 1st, 7 for 2nd, 5 for 3rd, and 15 for 4th order. Compared to cubic symmetry the total number of independent variables has increased from 13 to 31.

In the same way we obtain the Seebeck tensor Σ_{tetra} in tetragonal symmetry:

$$\begin{aligned}
\Sigma_{\text{tetra}}(\mathbf{m}) = & (\Sigma^{(0,a)} + \Sigma^{(2,1,a)} + \Sigma^{(4,1,a)}) \begin{pmatrix} 1 & 0 & 0 \\ 0 & 1 & 0 \\ 0 & 0 & 0 \end{pmatrix} + (\Sigma^{(0,c)} + \Sigma^{(2,1,c)} + \Sigma^{(4,1,c)}) \begin{pmatrix} 0 & 0 & 0 \\ 0 & 0 & 0 \\ 0 & 0 & 1 \end{pmatrix} \\
& + (\Sigma^{(1,a)} + \Sigma^{(3,1,a)}) \begin{pmatrix} 0 & -\mathbf{m}_z & 0 \\ \mathbf{m}_z & 0 & 0 \\ 0 & 0 & 0 \end{pmatrix} \\
& + (\Sigma^{(1,c1)} + \Sigma^{(3,1,c1)}) \begin{pmatrix} 0 & 0 & \mathbf{m}_y \\ 0 & 0 & -\mathbf{m}_x \\ 0 & 0 & 0 \end{pmatrix} + (\Sigma^{(1,c2)} + \Sigma^{(3,1,c2)}) \begin{pmatrix} 0 & 0 & 0 \\ 0 & 0 & 0 \\ -\mathbf{m}_y & \mathbf{m}_x & 0 \end{pmatrix} \\
& + (\Sigma^{(2,2,a)} + \Sigma^{(4,2,a)}) \begin{pmatrix} \mathbf{m}_x^2 & 0 & 0 \\ 0 & \mathbf{m}_y^2 & 0 \\ 0 & 0 & 0 \end{pmatrix} + (\Sigma^{(2,2,c)} + \Sigma^{(4,2,c)}) \begin{pmatrix} 0 & 0 & 0 \\ 0 & 0 & 0 \\ 0 & 0 & \mathbf{m}_z^2 \end{pmatrix} \\
& + (\Sigma^{(2,3,a)} + \Sigma^{(4,3,a)}) \begin{pmatrix} 0 & \mathbf{m}_x \mathbf{m}_y & 0 \\ \mathbf{m}_x \mathbf{m}_y & 0 & 0 \\ 0 & 0 & 0 \end{pmatrix} + (\Sigma^{(2,3,c1)} + \Sigma^{(4,3,c1)}) \begin{pmatrix} 0 & 0 & \mathbf{m}_x \mathbf{m}_z \\ 0 & 0 & \mathbf{m}_y \mathbf{m}_z \\ 0 & 0 & 0 \end{pmatrix} \\
& + (\Sigma^{(2,3,c2)} + \Sigma^{(4,3,c2)}) \begin{pmatrix} 0 & 0 & 0 \\ 0 & 0 & 0 \\ \mathbf{m}_x \mathbf{m}_z & \mathbf{m}_y \mathbf{m}_z & 0 \end{pmatrix} \\
& + (\Sigma^{(2,4,a)} + \Sigma^{(4,4,a)}) \begin{pmatrix} \mathbf{m}_z^2 & 0 & 0 \\ 0 & \mathbf{m}_z^2 & 0 \\ 0 & 0 & 0 \end{pmatrix} \\
& + \begin{pmatrix} 0 & -\Sigma^{(3,2,a)} \mathbf{m}_z^3 & \Sigma^{(3,2,c1)} \mathbf{m}_y^3 \\ \Sigma^{(3,2,a)} \mathbf{m}_z^3 & 0 & -\Sigma^{(3,2,c1)} \mathbf{m}_x^3 \\ -\Sigma^{(3,2,c2)} \mathbf{m}_y^3 & \Sigma^{(3,2,c2)} \mathbf{m}_x^3 & 0 \end{pmatrix} \\
& + \begin{pmatrix} 0 & -\Sigma^{(3,3,a)} \mathbf{m}_y^2 \mathbf{m}_z & \Sigma^{(3,3,c1)} \mathbf{m}_y \mathbf{m}_z^2 \\ \Sigma^{(3,3,a)} \mathbf{m}_x^2 \mathbf{m}_z & 0 & -\Sigma^{(3,3,c1)} \mathbf{m}_x \mathbf{m}_z^2 \\ -\Sigma^{(3,3,c2)} \mathbf{m}_y \mathbf{m}_z^2 & \Sigma^{(3,3,c2)} \mathbf{m}_x \mathbf{m}_z^2 & 0 \end{pmatrix} \\
& + \Sigma^{(3,4,a)} \begin{pmatrix} -\mathbf{m}_x \mathbf{m}_y \mathbf{m}_z & 0 & 0 \\ 0 & \mathbf{m}_x \mathbf{m}_y \mathbf{m}_z & 0 \\ 0 & 0 & 0 \end{pmatrix} + \begin{pmatrix} \Sigma^{(4,5,a)} \mathbf{m}_x^4 & 0 & 0 \\ 0 & \Sigma^{(4,5,a)} \mathbf{m}_y^4 & 0 \\ 0 & 0 & \Sigma^{(4,5,c)} \mathbf{m}_z^4 \end{pmatrix} \\
& + \begin{pmatrix} \Sigma^{(4,6,a)} \mathbf{m}_y^2 \mathbf{m}_z^2 & 0 & 0 \\ 0 & \Sigma^{(4,6,a)} \mathbf{m}_x^2 \mathbf{m}_z^2 & 0 \\ 0 & 0 & \Sigma^{(4,6,c)} \mathbf{m}_x^2 \mathbf{m}_y^2 \end{pmatrix} \\
& + \begin{pmatrix} 0 & \Sigma^{(4,7,a)} \mathbf{m}_x \mathbf{m}_y \mathbf{m}_z^2 & \Sigma^{(4,7,c1)} \mathbf{m}_x \mathbf{m}_y^2 \mathbf{m}_z \\ \Sigma^{(4,7,a)} \mathbf{m}_x \mathbf{m}_y \mathbf{m}_z^2 & 0 & \Sigma^{(4,7,c1)} \mathbf{m}_x^2 \mathbf{m}_y \mathbf{m}_z \\ \Sigma^{(4,7,c2)} \mathbf{m}_x \mathbf{m}_y^2 \mathbf{m}_z & \Sigma^{(4,7,c2)} \mathbf{m}_x^2 \mathbf{m}_y \mathbf{m}_z & 0 \end{pmatrix} \\
& + \Sigma^{(4,8,a)} \begin{pmatrix} \mathbf{m}_z^4 & 0 & 0 \\ 0 & \mathbf{m}_z^4 & 0 \\ 0 & 0 & 0 \end{pmatrix} + \begin{pmatrix} 0 & \Sigma^{(4,9,a)} \mathbf{m}_x \mathbf{m}_y^3 & \Sigma^{(4,9,c1)} \mathbf{m}_x \mathbf{m}_z^3 \\ \Sigma^{(4,9,a)} \mathbf{m}_x^3 \mathbf{m}_y & 0 & \Sigma^{(4,9,c1)} \mathbf{m}_y \mathbf{m}_z^3 \\ \Sigma^{(4,9,c2)} \mathbf{m}_x \mathbf{m}_z^3 & \Sigma^{(4,9,c2)} \mathbf{m}_y \mathbf{m}_z^3 & 0 \end{pmatrix}.
\end{aligned} \tag{3.33}$$

The calculation yields 2 for the 0th, 3 for the 1st, 8 for the 2nd, 10 for the 3rd, and 19 for the 4th order as number of independent parameters. Compared to the resistivity tensor in tetragonal symmetry we obtain 3 additional terms with new dependency on \mathbf{m} connected to $\Sigma^{(3,3,a)}$, $\Sigma^{(3,4,a)}$, and $\Sigma^{(4,9,a)}$. We would like to stress that the above series expansions adopted from [227, 235–237] do not include a magnetic field dependence of the expansion coefficients. In the ADMR and ADMTP experiments the applied external magnetic field is usually small $\mu_0 H \leq 7$ T and thus the influence of magnetic field dependence is negligible. This model thus only includes effects dependent on the orientation of the magnetization.

3.3.1.3 Projections of the resistivity and Seebeck tensor

In our experiments on thin ferromagnetic films, we apply an electrical current \mathbf{j} (or a thermal gradient ∇T) along a certain crystallographic direction and measure the longitudinal ρ_{long} (Σ_{long}) and transverse ρ_{trans} (Σ_{trans}) resistivity (thermopower) in the film plane. For our model we need to define the unit vector $\hat{\mathbf{j}}$ pointing along the direction of the current (thermal gradient), the unit vector $\hat{\mathbf{n}}$ along the surface normal, and the transverse unit vector $\hat{\mathbf{t}} = \hat{\mathbf{n}} \times \hat{\mathbf{j}}$. With the above descriptions of the resistivity tensor $\boldsymbol{\rho}(\mathbf{m})$ and Seebeck tensor $\boldsymbol{\Sigma}(\mathbf{m})$, we can then calculate ρ_{long} and ρ_{trans} or Σ_{long} and Σ_{trans} respectively [227, 235, 236]:

$$\rho_{\text{long}} = \hat{\mathbf{j}} \boldsymbol{\rho}(\mathbf{m}) \hat{\mathbf{j}}, \quad (3.34)$$

$$\rho_{\text{trans}} = \hat{\mathbf{t}} \boldsymbol{\rho}(\mathbf{m}) \hat{\mathbf{j}}, \quad (3.35)$$

$$\Sigma_{\text{long}} = \hat{\mathbf{j}} \boldsymbol{\Sigma}(\mathbf{m}) \hat{\mathbf{j}}, \quad (3.36)$$

$$\Sigma_{\text{trans}} = \hat{\mathbf{t}} \boldsymbol{\Sigma}(\mathbf{m}) \hat{\mathbf{j}}. \quad (3.37)$$

These projections can then be used to describe the ordinary and anomalous Hall, Nernst, magnetoresistance and magnetothermopower effects. The three vectors $\hat{\mathbf{j}}$, $\hat{\mathbf{t}}$, and $\hat{\mathbf{n}}$ also describe a new coordinate system, and we can generate the projections of \mathbf{M} along the new axes of the coordinate system as the scalar product of \mathbf{m} with the unit vectors $m_{\hat{\mathbf{j}}} = \hat{\mathbf{j}} \circ \mathbf{m}$, $m_{\hat{\mathbf{t}}} = \hat{\mathbf{t}} \circ \mathbf{m}$, and $m_{\hat{\mathbf{n}}} = \hat{\mathbf{n}} \circ \mathbf{m}$. The projection of the tensors allows us to determine only selected tensor elements from the experiment. For an application of the general Mott relation (Eq.(3.16)) we need the full description of the resistivity and Seebeck tensors.

Cubic symmetry In the case of cubic symmetry we can determine all entries of the resistivity tensor by just measuring along one crystallographic direction, for example $\hat{\mathbf{j}}$ along the [100]-direction for a (001)-oriented film, and use the symmetry of the crystal to gain the full resistivity tensor. The inverse of this tensor will be the conductivity tensor. This is most evident when we carry out the projection of the cubic resistivity tensor for $\hat{\mathbf{j}} = (1,0,0)$, $\hat{\mathbf{t}} = (0,1,0)$, and $\hat{\mathbf{n}} = (0,0,1)$

$$\rho_{\text{long,cubic,100}} = \rho_0 + \rho_1 m_{\hat{\mathbf{j}}}^2 + \rho_2 m_{\hat{\mathbf{j}}}^4 + \rho_3 m_{\hat{\mathbf{t}}}^2 m_{\hat{\mathbf{n}}}^2, \quad (3.38)$$

$$\rho_{\text{trans,cubic,100}} = \rho_4 m_{\hat{\mathbf{n}}} + \rho_5 m_{\hat{\mathbf{j}}} m_{\hat{\mathbf{t}}} + \rho_6 m_{\hat{\mathbf{n}}}^3 + \rho_7 m_{\hat{\mathbf{j}}} m_{\hat{\mathbf{t}}} m_{\hat{\mathbf{n}}}^2. \quad (3.39)$$

Here we used $\rho_0 = \rho^{(0)} + \rho^{(2,1)} + \rho^{(4,1)}$, $\rho_1 = \rho^{(2,2)} + \rho^{(4,2)}$, $\rho_2 = \rho^{(4,4)}$, $\rho_3 = \rho^{(4,5)}$, $\rho_4 = -(\rho^{(1)} + \rho^{(3,1)})$, $\rho_5 = \rho^{(2,3)} + \rho^{(4,3)}$, $\rho_6 = -\rho^{(3,2)}$, and $\rho_7 = \rho^{(4,6)}$.

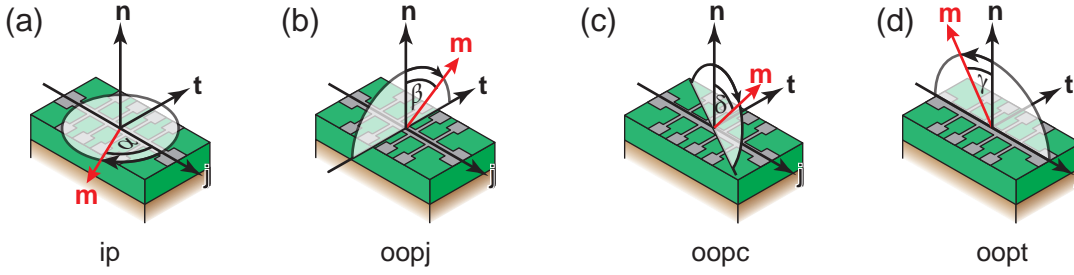


Figure 3.13: Illustration of the different rotation planes of the magnetization, in the coordinate system defined by the vectors \mathbf{j} , \mathbf{t} , \mathbf{n} : (a) in-plane rotation, (b) out-of-plane rotation perpendicular to \mathbf{j} , (c) out-of-plane rotation perpendicular to $\mathbf{j} + \mathbf{t}$, (d) out-of-plane rotation perpendicular to \mathbf{t} . The red arrow represents the magnetization direction \mathbf{m} and the positive rotation angle α is defined for each rotation plane as indicated by black arrows on the rotation circle.

To understand the extraction of the ρ_i parameters, we look at the theoretical evolution of $\rho_{\text{long,cubic,100}}$ and $\rho_{\text{trans,cubic,100}}$ for the rotation of \mathbf{m} in selected planes: in the film plane (ip), i.e. a rotation of \mathbf{m} in a plane perpendicular to $\hat{\mathbf{n}}$; out-of-plane rotation with the rotation plane of \mathbf{m} perpendicular to $\hat{\mathbf{j}}$ (oopj); and out-of-plane rotation with the rotation plane of \mathbf{m} perpendicular to the unit vector of the sum of $\hat{\mathbf{j}}$ and $\hat{\mathbf{t}}$ (oopc). These 3 rotation planes are illustrated in Fig. 3.13(a)-(c).

To familiarize one with the role of the different contributions to the longitudinal and transverse resistivity and to provide a basic understanding of how one can extract these parameters from an experiment, we present in the following the simulation results obtained from our model in cubic symmetry for a rotation of the magnetization in these different rotation planes. The simulation results are summarized in Fig. 3.14(a)-(c). Within these rotation planes, one of the projections of the magnetization m_i becomes zero, which allows to separate the contributions of the ρ_i . For the ip rotation we know that $m_{\hat{\mathbf{n}}} = 0$ and thus contributions in powers of $m_{\hat{\mathbf{n}}}$ vanish. The only parameters which can influence ρ_{long} and ρ_{trans} , are then ρ_0 , ρ_1 , ρ_2 , and ρ_5 . In Fig. 3.14(a) we show how each parameter influences the observed angular dependence on the ip magnetization orientation. ρ_0 just acts as a baseline in ρ_{long} , on which the parameters ρ_1 and ρ_2 add an oscillation with the orientation angle α . Depending on the sign with respect to each other the appearance of the angular dependency can drastically change. For $\rho_1 \neq 0$, $\rho_2 = 0$ (black line in the graph), we observe the typical \cos^2 dependence of the longitudinal resistivity reminiscent of the anisotropic magnetoresistance (AMR). If we now change to $\rho_1 = \rho_2 \neq 0$ (red curve in the graph), the maxima in the curve are more pronounced than in the black curve. If $\rho_1 = -\rho_2 \neq 0$ (blue curve) we observe a change in the maxima to a more flat shape. It is evident from these observations, that each parameter results in distinctive features in the orientation dependence of the longitudinal resistivity. For the transverse resistivity the in-plane rotation of the magnetization results in only one remaining parameter ρ_5 , which describes the planar Hall effect. In addition, if we now investigate the behavior for oopj rotations of the magnetization, where $m_{\hat{\mathbf{j}}} = 0$, we have two parameters for the longitudinal, ρ_0 and ρ_3 , and two parameters, ρ_4 and ρ_6 , for the transverse resistivity. The results of our simulation are depicted in Fig. 3.14(b). For ρ_{long} ρ_0 is again only a baseline and has no influence on the orientation dependence, here only ρ_3 will have an influence on

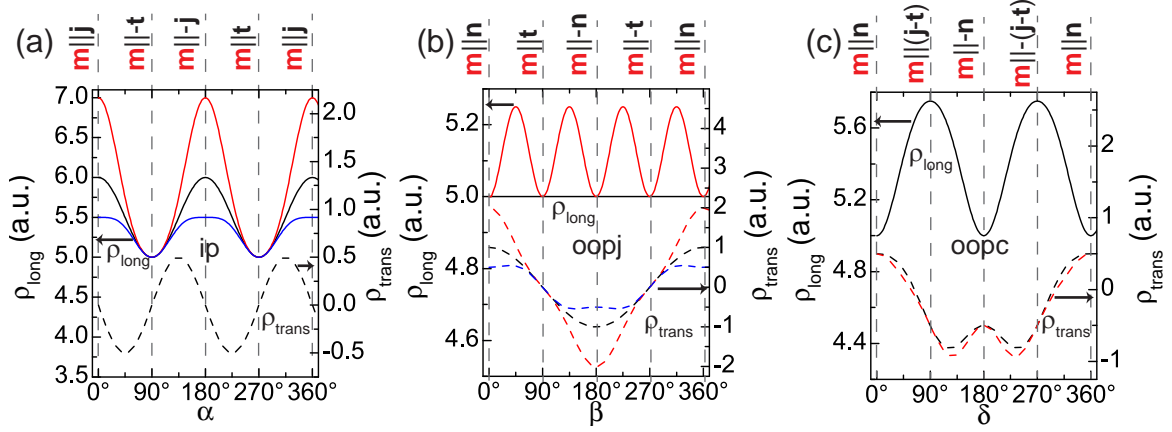


Figure 3.14: Results of a simulation based on our resistivity model for cubic symmetry in a (001)-oriented film and \mathbf{j} along the [100]-direction. Solid lines represent ρ_{long} , dotted lines ρ_{trans} . (a) Simulation results for the rotation of \mathbf{m} in the film plane. Parameters for the simulation are: $\rho_0 = 5$ and $\rho_5 = 1$ (constant), $\rho_1 = 1$ (black), $\rho_1 = \rho_2 = 1$ (red), $\rho_1 = -\rho_2 = 1$ (blue). (b) Simulated resistivity for a rotation of \mathbf{m} in the oopj rotation plane. Parameters for the simulation are: $\rho_0 = 5$, $\rho_1 = \rho_2 = \rho_5 = 1$ (constant), $\rho_3 = 0$, $\rho_4 = 1$ (black), $\rho_3 = \rho_4 = \rho_6 = 1$ (red), $\rho_4 = -2\rho_6 = 1$ (blue). (c) Results of the simulation for a rotation of the magnetization in oopc rotation plane. $\rho_0 = 5$, $\rho_5 = 1$, $\rho_1 = \rho_2 = \rho_5 = -2\rho_6 = 1$ (constant), $\rho_7 = 0$ (black), $\rho_7 = 1$ (red).

the oscillation amplitude. One should note that the oscillation is now four fold symmetric over the 360° rotation, in contrast to the two fold symmetry for an ip rotation. For the transverse resistivity we can distinguish between contributions from ρ_4 , which displays a $\cos(\beta)$ dependence (black dotted line), and ρ_6 , which has a $\cos^3(\beta)$ dependency. These two parameters describe the sum of the anomalous Hall (AHE) and normal Hall effect in a ferromagnet. The last remaining parameter for a full tensor description is ρ_7 , which can be extracted by using an oopc rotation of the magnetization. This parameter only influences the appearance of ρ_{trans} . As depicted in Fig. 3.14(c) the influence of ρ_7 is only small compared to the other parameters, which will be a major obstacle in obtaining the full resistivity tensor in an experiment. Moreover, as will be discussed below, it is not possible in an experiment to rotate the magnetization in a ferromagnet. One can only change an external control parameter influencing the orientation of the magnetization and measure the dependency of ρ_{long} and ρ_{trans} on this external control parameter.

For a deeper insight in the physical properties of a ferromagnetic system it is imperative to not only obtain the full resistivity but also the full Seebeck tensor. For the Seebeck tensor in cubic symmetry it is possible to determine the full tensor by also using just one crystallographic projection, for example $\hat{\mathbf{j}}$ along the [100]-direction for a (001)-oriented film. If we carry out the projection as described in Eqs.(3.36),(3.37), we obtain for the longitudinal and transverse thermopower

$$\Sigma_{\text{long,cubic,100}} = \Sigma_0 + \Sigma_1 m_{\hat{\mathbf{j}}}^2 + \Sigma_2 m_{\hat{\mathbf{j}}}^4 + \Sigma_3 m_{\hat{\mathbf{t}}}^2 m_{\hat{\mathbf{n}}}^2, \quad (3.40)$$

$$\Sigma_{\text{trans,cubic,100}} = \Sigma_4 m_{\hat{\mathbf{n}}} + \Sigma_5 m_{\hat{\mathbf{j}}} m_{\hat{\mathbf{t}}} + \Sigma_6 m_{\hat{\mathbf{n}}}^3 + \Sigma_7 m_{\hat{\mathbf{j}}} m_{\hat{\mathbf{t}}} m_{\hat{\mathbf{n}}}^2 + \Sigma_A m_{\hat{\mathbf{t}}}^2 m_{\hat{\mathbf{n}}} + \Sigma_B m_{\hat{\mathbf{j}}} m_{\hat{\mathbf{t}}}^3. \quad (3.41)$$

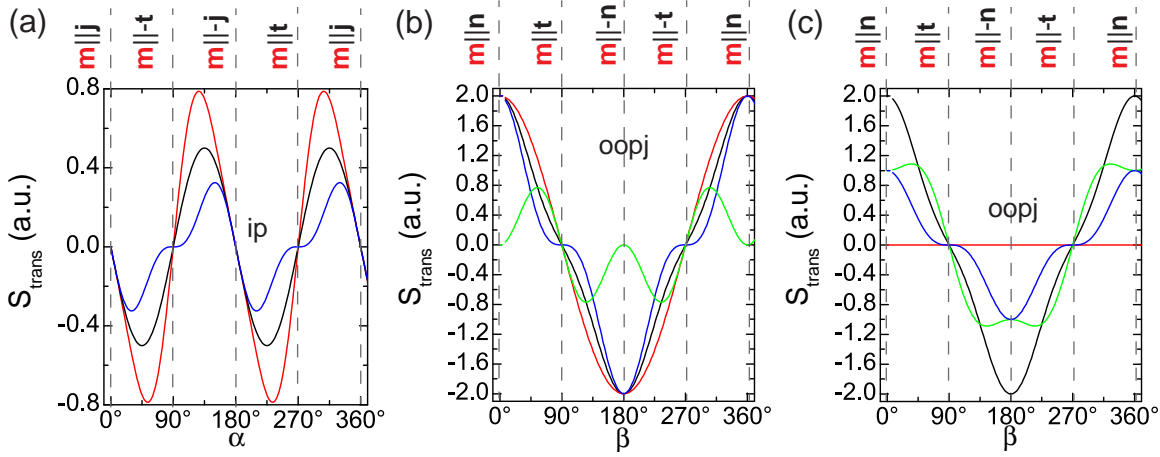


Figure 3.15: Results of a simulation based on our Seebeck model for cubic symmetry in a (001)-oriented film and $-\nabla T$ along the [100]-direction. (a) Simulation results for the rotation of \mathbf{m} in the film plane for Σ_{trans} . Parameters for the simulation are: $\Sigma_5 = 1, \Sigma_B = 0$ (black), $\Sigma_5 = \Sigma_B = 1$ (red), $\Sigma_5 = -\Sigma_B = 1$ (blue). (b) Simulated transverse thermopower for a rotation of \mathbf{m} in the oopj plane. Parameters for the simulation are: $\Sigma_4 = \Sigma_6 = 1, \Sigma_A = 0$ (black), $\Sigma_4 = \Sigma_6 = \Sigma_A = 1$ (red), $\Sigma_4 = \Sigma_6 = -\Sigma_A = 1$ (blue), $\Sigma_4 = -\Sigma_6 = \Sigma_A = 1$ (green). (c) Results of the simulation for a rotation of the magnetization in oopj rotation plane. $\Sigma_4 = \Sigma_6 = 1, \Sigma_A = 0$ (black), $\Sigma_4 = -\Sigma_6 = -\Sigma_A = 1$ (red), $\Sigma_4 = \Sigma_A = 1, \Sigma_6 = 0$ (blue), $\Sigma_4 = -\Sigma_A = 1, \Sigma_6 = 0$ (green).

Here we have defined $\Sigma_0 = \Sigma^{(0)} + \Sigma^{(2,1)} + \Sigma^{(4,1)}$, $\Sigma_1 = \Sigma^{(2,2)} + \Sigma^{(4,2)}$, $\Sigma_2 = \Sigma^{(4,4)}$, $\Sigma_3 = \Sigma^{(4,5)}$, $\Sigma_4 = -(\Sigma^{(1)} + \Sigma^{(3,1)})$, $\Sigma_5 = \Sigma^{(2,3)} + \Sigma^{(4,3)}$, $\Sigma_6 = -\Sigma^{(3,2)}$, $\Sigma_7 = \Sigma^{(4,6)}$, $\Sigma_A = -\Sigma^{(3,3)}$, and $\Sigma_B = \Sigma^{(4,7)}$. Compared to the projection of the resistivity tensor, we have now 2 additional contributions with new functional dependency on \mathbf{m} described by the parameters Σ_A and Σ_B . These two new contributions originate from the 2 additional independent parameters in the series expansion of the Seebeck tensor in cubic symmetry. One should note that these contributions are of 3rd and 4th order in \mathbf{m} . As already explained in the case of the resistivity tensor projection, we are able to determine each parameter in an experiment by choosing selected rotation planes for the magnetization, where one of the projections of \mathbf{m} vanishes. The first 8 parameters are identical to the resistivity case, the additional contributions from the new 2 parameters Σ_A and Σ_B are depicted in Fig. 3.15(a)-(c). For an in-plane rotation only the parameter Σ_B plays an additional role. As it is evident from Fig. 3.15(a) this additional contribution leads to characteristic changes in the orientation dependence. If the parameters Σ_5 and Σ_B are equal in sign (red), the transverse thermopower signal is tilted compared to the signal without the contribution Σ_B (black). On the other hand, if Σ_5 and Σ_B are opposite in sign, the signal develops plateaus at $\alpha = 90^\circ$ and $\alpha = 270^\circ$. For a rotation of \mathbf{m} in the oopj plane, the relevant additional parameter in $\Sigma_{\text{trans,cubic,100}}$ is Σ_A . Due to the two additional components Σ_4 and Σ_6 a multitude of sign combination arises, the results are summarized in Fig. 3.15(b)-(c). It is evident from these simulations, that each possible combination in sign of Σ_A , Σ_4 , and Σ_6 leads to characteristic features in the transverse thermopower signal. This enables us to extract the parameters from experimental data. A more detailed description on how the extraction of parameters from the experiment is

carried out follows in Sect. 3.3.1.4.

Tetragonal symmetry For tetragonal symmetry the problem becomes more complicated, as due to the lower symmetry of the crystal additional contributions to the resistivity and Seebeck tensors are generated. For the resistivity tensor we have in total 20 parameters describing the full matrix up to the fourth order of \mathbf{m} , and for the Seebeck tensor the total number of parameters for a full description up to the fourth order in \mathbf{m} is 29. We first take a look at the projections of the resistivity and Seebeck tensor for a (001)-oriented thin film and electrical current/thermal gradient along the [110]-direction, thus $\hat{\mathbf{j}}$ is parallel to the [110]-, $\hat{\mathbf{t}}$ to the $[\bar{1}10]$ -, and $\hat{\mathbf{n}}$ to the [001]-direction. If we carry out the projection for the resistivity tensor in tetragonal symmetry as described in Eqs.(3.34,3.35), we obtain up to the fourth order of \mathbf{m} , the following relations for the longitudinal $\rho_{\text{long,tetra},001}$ and transverse $\rho_{\text{trans,tetra},001}$ resistivity

$$\rho_{\text{long,tetra},001} = \rho_{0,110} + \rho_{1,110}m_{\hat{\mathbf{j}}}^2 + \rho_{2,110}m_{\hat{\mathbf{n}}}^2 + \rho_{3,110}m_{\hat{\mathbf{j}}}^4 + \rho_{4,110}m_{\hat{\mathbf{n}}}^4 + \rho_{5,110}m_{\hat{\mathbf{j}}}^2m_{\hat{\mathbf{n}}}^2, \quad (3.42)$$

$$\rho_{\text{trans,tetra},001} = \rho_{6,110}m_{\hat{\mathbf{n}}} + \rho_{7,110}m_{\hat{\mathbf{j}}}m_{\hat{\mathbf{i}}} + \rho_{8,110}m_{\hat{\mathbf{n}}}^3 + \rho_{9,110}m_{\hat{\mathbf{j}}}m_{\hat{\mathbf{i}}}m_{\hat{\mathbf{n}}}^2. \quad (3.43)$$

Here we defined the new parameters $\rho_{i,110}$ as linear combinations of the resistivity tensor parameters [235, 236]

$$\begin{aligned} \rho_{0,110} &= (\rho^{(0,a)} + \rho^{(2,1,a)} + \rho^{(4,1,a)}) + \frac{1}{2}(\rho^{(2,2,a)} + \rho^{(4,2,a)}) - \frac{1}{2}(\rho^{(2,3,a)} + \rho^{(4,3,a)}) + \frac{1}{4}\rho^{(4,5,a)}, \\ \rho_{1,110} &= (\rho^{(2,3,a)} + \rho^{(4,3,a)}) + \rho^{(4,5,a)}, \\ \rho_{2,110} &= -\frac{(\rho^{(2,2,a)} + \rho^{(4,2,a)})}{2} + \frac{(\rho^{(2,3,a)} + \rho^{(4,3,a)})}{2} + (\rho^{(2,4,a)} + \rho^{(4,4,a)}) - \frac{\rho^{(4,5,a)}}{2} + \\ &\quad + \frac{\rho^{(4,6,a)}}{2} - \frac{\rho^{(4,7,a)}}{2}, \\ \rho_{3,110} &= -\rho^{(4,5,a)}, \\ \rho_{4,110} &= \frac{\rho^{(4,5,a)}}{4} - \frac{\rho^{(4,6,a)}}{2} + \frac{\rho^{(4,7,a)}}{2} + \rho^{(4,8,a)}, \\ \rho_{5,110} &= -\rho^{(4,5,a)} + \rho^{(4,7,a)}, \\ \rho_{6,110} &= (\rho^{(1,a)} + \rho^{(3,1,a)}), \\ \rho_{7,110} &= (\rho^{(2,2,a)} + \rho^{(4,2,a)}) + \rho^{(4,5,a)}, \\ \rho_{8,110} &= \rho^{(3,2,a)}, \\ \rho_{9,110} &= -\rho^{(4,5,a)} - \rho^{(4,6,a)}. \end{aligned}$$

It is also possible in the tetragonal case to utilize the different magnetization rotation planes defined in Fig.3.13(a)-(d) to separate the different contributions from each other, which will allow an easier determination of these parameters from the experiment. If we now assume that we are able to determine these 10 parameters describing the functional dependence of $\rho_{\text{long,tetra},001}$ and $\rho_{\text{trans,tetra},001}$ on \mathbf{m} from the experiment, we are able to calculate 10 of the total 20 parameter components of the resistivity tensor $\boldsymbol{\rho}_{\text{tetra}}(\mathbf{m})$ using

the following set of equations

$$\begin{aligned}
(\rho^{(0,a)} + \rho^{(2,1,a)} + \rho^{(4,1,a)}) &= \frac{1}{4} (4\rho_{0,110} + 2\rho_{1,110} + \rho_{3,110} - 2\rho_{7,110}), \\
(\rho^{(1,a)} + \rho^{(3,1,a)}) &= \rho_{6,110}, \\
(\rho^{(2,2,a)} + \rho^{(4,2,a)}) &= \rho_{3,110} + \rho_{7,110}, \\
(\rho^{(2,3,a)} + \rho^{(4,3,a)}) &= \rho_{1,110} + \rho_{3,110}, \\
(\rho^{(2,4,a)} + \rho^{(4,4,a)}) &= \frac{1}{2} (-\rho_{1,110} + 2\rho_{2,110} - 3\rho_{3,110} + \rho_{5,110} + \rho_{7,110} + \rho_{9,110}), \\
\rho^{(3,2,a)} &= \rho_{8,110}, \\
\rho^{(4,5,a)} &= -\rho_{3,110}, \\
\rho^{(4,6,a)} &= \rho_{3,110} - \rho_{9,110}, \\
\rho^{(4,7,a)} &= -\rho_{3,110} + \rho_{5,110}, \\
\rho^{(4,8,a)} &= \frac{1}{4} (5\rho_{3,110} + 4\rho_{4,110} - 2\rho_{5,110} - 2\rho_{9,110}).
\end{aligned} \tag{3.44}$$

For a (001)-oriented film, we are not able to determine the full resistivity tensor. This also holds for the Seebeck tensor, if we carry out the projections according to Eqs.(3.36,3.37), we obtain

$$\begin{aligned}
\Sigma_{\text{long,tetra},001} &= \Sigma_{0,110} + \Sigma_{1,110}m_{\mathbf{j}}^2 + \Sigma_{2,110}m_{\mathbf{\hat{n}}}^2 + \Sigma_{3,110}m_{\mathbf{j}}^4 + \Sigma_{4,110}m_{\mathbf{\hat{n}}}^4 \\
&+ \Sigma_{5,110}m_{\mathbf{j}}^2m_{\mathbf{\hat{n}}}^2 + \Sigma_{\text{A},110}m_{\mathbf{j}}m_{\mathbf{\hat{t}}}m_{\mathbf{\hat{n}}},
\end{aligned} \tag{3.45}$$

$$\begin{aligned}
\Sigma_{\text{trans,tetra},001} &= \Sigma_{6,110}m_{\mathbf{\hat{n}}} + \Sigma_{7,110}m_{\mathbf{j}}m_{\mathbf{\hat{t}}} + \Sigma_{8,110}m_{\mathbf{\hat{n}}}^3 + \Sigma_{9,110}m_{\mathbf{j}}m_{\mathbf{\hat{t}}}m_{\mathbf{\hat{n}}}^2 \\
&+ \Sigma_{\text{B},110}m_{\mathbf{j}}^2m_{\mathbf{\hat{n}}} + \Sigma_{\text{C},110}m_{\mathbf{j}}^3m_{\mathbf{\hat{t}}}.
\end{aligned} \tag{3.46}$$

We here defined $\Sigma_{i,110}$ as linear combinations of our expansion coefficients for the Seebeck tensor

$$\begin{aligned}
\Sigma_{0,110} &= (\Sigma^{(0,a)} + \Sigma^{(2,1,a)} + \Sigma^{(4,1,a)}) + \frac{1}{2}(\Sigma^{(2,2,a)} + \Sigma^{(4,2,a)}) - \frac{1}{2}(\Sigma^{(2,3,a)} + \Sigma^{(4,3,a)}) \\
&\quad + \frac{1}{4}\Sigma^{(4,5,a)} - \frac{1}{4}\Sigma^{(4,9,a)}, \\
\Sigma_{1,110} &= (\Sigma^{(2,3,a)} + \Sigma^{(4,3,a)}) + \Sigma^{(4,5,a)} + \frac{1}{2}\Sigma^{(4,9,a)}, \\
\Sigma_{2,110} &= -\frac{(\Sigma^{(2,2,a)} + \Sigma^{(4,2,a)})}{2} + \frac{(\Sigma^{(2,3,a)} + \Sigma^{(4,3,a)})}{2} + (\Sigma^{(2,4,a)} + \Sigma^{(4,4,a)}) \\
&\quad - \frac{\Sigma^{(4,5,a)}}{2} + \frac{\Sigma^{(4,6,a)}}{2} - \frac{\Sigma^{(4,7,a)}}{2} + \frac{\Sigma^{(4,9,a)}}{2}, \\
\Sigma_{3,110} &= -\Sigma^{(4,5,a)}, \\
\Sigma_{4,110} &= \frac{\Sigma^{(4,5,a)}}{4} - \frac{\Sigma^{(4,6,a)}}{2} + \frac{\Sigma^{(4,7,a)}}{2} + \Sigma^{(4,8,a)} - \frac{\Sigma^{(4,9,a)}}{4}, \\
\Sigma_{5,110} &= -\Sigma^{(4,5,a)} + \Sigma^{(4,7,a)} - \frac{\Sigma^{(4,9,a)}}{2}, \\
\Sigma_{A,110} &= -\Sigma^{(3,3,a)} \\
\Sigma_{6,110} &= (\Sigma^{(1,a)} + \Sigma^{(3,1,a)}) + \frac{\Sigma^{(3,3,a)}}{2} - \frac{\Sigma^{(3,4,a)}}{2}, \\
\Sigma_{7,110} &= (\Sigma^{(2,2,a)} + \Sigma^{(4,2,a)}) + \Sigma^{(4,5,a)} + \frac{\Sigma^{(4,9,a)}}{2}, \\
\Sigma_{8,110} &= \Sigma^{(3,2,a)} - \frac{\Sigma^{(3,3,a)}}{2} + \frac{\Sigma^{(3,4,a)}}{2}, \\
\Sigma_{9,110} &= -\Sigma^{(4,5,a)} - \Sigma^{(4,6,a)} - \frac{\Sigma^{(4,9,a)}}{2}, \\
\Sigma_{B,110} &= \Sigma^{(3,4,a)}, \\
\Sigma_{C,110} &= -\Sigma^{(4,9,a)}.
\end{aligned}$$

These equations allow a direct calculation of 13 of the 29 parameters describing the full Seebeck tensor up to the 4th order of \mathbf{m} , by using the following set of equations:

$$\begin{aligned}
(\Sigma^{(0,a)} + \Sigma^{(2,1,a)} + \Sigma^{(4,1,a)}) &= \frac{1}{4} (4\Sigma_{0,110} + 2\Sigma_{1,110} + \Sigma_{3,110} - 2\Sigma_{7,110} - \Sigma_{C,110}), \\
(\Sigma^{(1,a)} + \Sigma^{(3,1,a)}) &= \frac{1}{2} (2\Sigma_{6,110} + \Sigma_{A,110} + \Sigma_{B,110}), \\
(\Sigma^{(2,2,a)} + \Sigma^{(4,2,a)}) &= \frac{1}{2} (2\Sigma_{3,110} + 2\Sigma_{7,110} + \Sigma_{C,110}), \\
(\Sigma^{(2,3,a)} + \Sigma^{(4,3,a)}) &= \frac{1}{2} (2\Sigma_{1,110} + 2\Sigma_{3,110} + \Sigma_{C,110}), \\
(\Sigma^{(2,4,a)} + \Sigma^{(4,4,a)}) &= \frac{1}{2} (-\Sigma_{1,110} + 2\Sigma_{2,110} - 3\Sigma_{3,110} + \Sigma_{5,110} + \Sigma_{7,110} + \Sigma_{9,110}), \\
\Sigma^{(3,2,a)} &= \frac{1}{2} (\Sigma_{8,110} - \Sigma_{A,110} - \Sigma_{B,110}), \\
\Sigma^{(3,3,a)} &= -\Sigma_{A,110}, \\
\Sigma^{(3,4,a)} &= \Sigma_{B,110}, \\
\Sigma^{(4,5,a)} &= -\Sigma_{3,110}, \\
\Sigma^{(4,6,a)} &= \Sigma_{3,110} - \Sigma_{9,110} + \frac{\Sigma_{C,110}}{2}, \\
\Sigma^{(4,7,a)} &= \frac{1}{2} (-2\Sigma_{3,110} + 2\Sigma_{5,110} - \Sigma_{C,110}), \\
\Sigma^{(4,8,a)} &= \frac{1}{4} (5\Sigma_{3,110} + 4\Sigma_{4,110} - 2\Sigma_{5,110} - 2\Sigma_{9,110} + \Sigma_{C,110}), \\
\Sigma^{(4,9,a)} &= -\Sigma_{C,110}.
\end{aligned} \tag{3.47}$$

Interestingly, the projection of the Seebeck tensor yields 3 additional parameters describing the longitudinal and transverse thermopower, as compared to the description of the longitudinal and transverse resistivity. These additional parameters depend to the 3rd or 4th order on \mathbf{m} , this fact leads to a highly demanding accuracy in the experiments, as will be discussed in Sect. 3.3.2.

From these projections of the resistivity and Seebeck tensors for a (001)-oriented thin film, we find that it is impossible to gain the full tensor description for the resistivity and the thermopower. A remedy for this problem is the use of other orientations of the tetragonal film. In the following we show, how one can determine the full resistivity and Seebeck tensors for a tetragonal symmetry using a (113)-oriented film⁶. In the following we only use the series expansion of $\boldsymbol{\rho}_{\text{tetra}}(\mathbf{m})$ and $\boldsymbol{\Sigma}_{\text{tetra}}(\mathbf{m})$ up to the 2nd order of \mathbf{m} , to reduce the length of the expressions. But in principle it is even possible to extract the full tensor for higher orders in \mathbf{m} for this orientation. For the extraction of the full magneto-galvanic tensors for a tetragonal (113)-oriented film we need the projections of the resistivity and Seebeck tensors for $\hat{\mathbf{j}}$ parallel the $[3\bar{3}2]$ - and $[\bar{1}10]$ -direction. We start with the projection of $\boldsymbol{\rho}_{\text{tetra}}(\mathbf{m})$ according to Eqs.(3.34,3.35) for $\hat{\mathbf{j}}$, $\hat{\mathbf{t}}$, and $\hat{\mathbf{n}}$ parallel to

⁶Please note that in principle the full extraction of the tensor would also be possible for a (111)-oriented film. Moreover, we here assume, that the tetragonal symmetry is not reduced due to strain effects by the (113)-oriented growth.

the $[3\bar{3}\bar{2}]$ -, $[\bar{1}10]$ -, and $[113]$ -direction respectively

$$\rho_{\text{long,tetra},3\bar{3}\bar{2},113} = \rho_{0,3\bar{3}\bar{2}} + \rho_{1,3\bar{3}\bar{2}}m_{\hat{j}}^2 + \rho_{2,3\bar{3}\bar{2}}m_{\hat{j}}m_{\hat{n}} + \rho_{3,3\bar{3}\bar{2}}m_{\hat{n}}^2, \quad (3.48)$$

$$\rho_{\text{trans,tetra},3\bar{3}\bar{2},113} = \rho_{4,3\bar{3}\bar{2}}m_{\hat{j}} + \rho_{5,3\bar{3}\bar{2}}m_{\hat{n}} + \rho_{6,3\bar{3}\bar{2}}m_{\hat{j}}m_{\hat{k}} + \rho_{7,3\bar{3}\bar{2}}m_{\hat{k}}m_{\hat{n}}. \quad (3.49)$$

The following set of equation relates the $\rho_{i,3\bar{3}\bar{2}}$ with the expansion coefficients

$$\begin{aligned} \rho_{0,3\bar{3}\bar{2}} &= \frac{9(\rho^{(0,a)} + \rho^{(2,1,a)})}{11} + \frac{2(\rho^{(0,c)} + \rho^{(2,1,c)})}{11} + \frac{9\rho^{(2,2,a)}}{22} - \frac{9\rho^{(2,3,a)}}{22}, \\ \rho_{1,3\bar{3}\bar{2}} &= -\frac{9\rho^{(2,2,a)}}{121} + \frac{4\rho^{(2,2,c)}}{121} + \frac{90\rho^{(2,3,a)}}{121} + \frac{36\rho^{(2,3,c)}}{121} + \frac{18\rho^{(2,4,a)}}{121}, \\ \rho_{2,3\bar{3}\bar{2}} &= \frac{27\sqrt{2}\rho^{(2,2,a)}}{121} - \frac{12\sqrt{2}\rho^{(2,2,c)}}{121} + \frac{27\sqrt{2}\rho^{(2,3,a)}}{121} - \frac{42\sqrt{2}\rho^{(2,3,c)}}{121} - \frac{54\sqrt{2}\rho^{(2,4,a)}}{121}, \\ \rho_{3,3\bar{3}\bar{2}} &= -\frac{81\rho^{(2,2,a)}}{242} + \frac{18\rho^{(2,2,c)}}{121} + \frac{117\rho^{(2,3,a)}}{242} - \frac{36\rho^{(2,3,c)}}{121} + \frac{81\rho^{(2,4,a)}}{121}, \\ \rho_{4,3\bar{3}\bar{2}} &= -\frac{3\sqrt{2}\rho^{(1,a)}}{11} + \frac{3\sqrt{2}\rho^{(1,c)}}{11}, \\ \rho_{5,3\bar{3}\bar{2}} &= \frac{9\rho^{(1,a)}}{11} + \frac{2\rho^{(1,c)}}{11}, \\ \rho_{6,3\bar{3}\bar{2}} &= \frac{9\rho^{(2,2,a)}}{11} + \frac{2\rho^{(2,3,c)}}{11}, \\ \rho_{7,3\bar{3}\bar{2}} &= \frac{3\sqrt{2}\rho^{(2,2,a)}}{11} - \frac{3\sqrt{2}\rho^{(2,3,c)}}{11} \end{aligned}$$

A determination from the experimental data is possible if we utilize the 4 rotation planes for the magnetization in Fig. 3.13(a)-(d). With the $\rho_{i,3\bar{3}\bar{2}}$ we can then calculate the full description of the resistivity tensor by using

$$\begin{aligned} (\rho^{(0,c)} + \rho^{(2,1,c)}) &= -\frac{9}{2}(\rho^{(0,a)} + \rho^{(2,1,a)}) + \frac{99}{216} \left(12\rho_{0,3\bar{3}\bar{2}} + 6\rho_{1,3\bar{3}\bar{2}} + \sqrt{2}\rho_{2,3\bar{3}\bar{2}} - 6\rho_{6,3\bar{3}\bar{2}} \right), \\ \rho^{(1,a)} &= \frac{1}{3} \left(-\sqrt{2}\rho_{4,3\bar{3}\bar{2}} + 3\rho_{5,3\bar{3}\bar{2}} \right), \\ \rho^{(1,c)} &= \frac{3\rho_{4,3\bar{3}\bar{2}} + \sqrt{2}\rho_{5,3\bar{3}\bar{2}}}{\sqrt{2}}, \\ \rho^{(2,2,c)} &= -\frac{9}{2}\rho^{(2,4,a)} + \frac{9}{108} \left(33\rho_{1,3\bar{3}\bar{2}} - 55\sqrt{2}\rho_{2,3\bar{3}\bar{2}} - 21\rho_{6,3\bar{3}\bar{2}} + 81\sqrt{2}\rho_{7,3\bar{3}\bar{2}} \right), \\ \rho^{(2,3,a)} &= \frac{1}{54} \left(66\rho_{1,3\bar{3}\bar{2}} + 11\sqrt{2}\rho_{2,3\bar{3}\bar{2}} - 12\rho_{6,3\bar{3}\bar{2}} + 18\sqrt{2}\rho_{7,3\bar{3}\bar{2}} \right), \\ \rho^{(2,3,c)} &= \rho_{6,3\bar{3}\bar{2}} - \frac{3\rho_{7,3\bar{3}\bar{2}}}{\sqrt{2}}, \\ \rho^{(2,2,a)} &= \frac{3\sqrt{2}\rho_{6,3\bar{3}\bar{2}} + 2\rho_{7,3\bar{3}\bar{2}}}{3\sqrt{2}}. \end{aligned} \quad (3.50)$$

From the 9 parameters needed to describe the full resistivity tensor, we can calculate 7 if we already know the value of $(\rho^{(0,a)} + \rho^{(2,1,a)})$ and $\rho^{(2,4,a)}$, which we will determine from

the second projection with $\hat{\mathbf{j}}$ along $[\bar{1}10]$. In addition we obtain the following restriction for the $\rho_{i,3\bar{3}2}$ from the linear equations

$$\frac{7\rho_{2,3\bar{3}2}}{6\sqrt{2}} + \rho_{3,3\bar{3}2} + \rho_{6,3\bar{3}2} = \rho_{1,3\bar{3}2} + \frac{3\rho_{7,3\bar{3}2}}{\sqrt{2}}. \quad (3.51)$$

The parameters determined from the experiment need to satisfy this equation to allow a calculation of the full resistivity tensor.

The second projection for $\hat{\mathbf{j}}$, $\hat{\mathbf{t}}$, and $\hat{\mathbf{n}}$ parallel to the $[\bar{1}10]$ -, $[\bar{3}\bar{3}2]$ -, and $[113]$ -direction respectively in accordance to Eqs.(3.34,3.35) leads to the following expressions for the longitudinal and transverse resistivity

$$\rho_{\text{long,tetra},\bar{1}10,113} = \rho_{0,\bar{1}10} + \rho_{1,\bar{1}10}m_{\hat{\mathbf{j}}}^2 + \rho_{2,\bar{1}10}m_{\hat{\mathbf{t}}}m_{\hat{\mathbf{n}}} + \rho_{3,\bar{1}10}m_{\hat{\mathbf{n}}}^2, \quad (3.52)$$

$$\rho_{\text{trans,tetra},\bar{1}10,113} = \rho_{4,\bar{1}10}m_{\hat{\mathbf{t}}} + \rho_{5,\bar{1}10}m_{\hat{\mathbf{n}}} + \rho_{6,\bar{1}10}m_{\hat{\mathbf{j}}}m_{\hat{\mathbf{t}}} + \rho_{7,\bar{1}10}m_{\hat{\mathbf{j}}}m_{\hat{\mathbf{n}}}. \quad (3.53)$$

A set of linear equations connects the $\rho_{i,\bar{1}10}$ with the expansion coefficients

$$\begin{aligned} \rho_{0,\bar{1}10} &= (\rho^{(0,a)} + \rho^{(2,1,a)}) + \frac{9\rho^{(2,2,a)}}{22} - \frac{9\rho^{(2,3,a)}}{22} + \frac{2\rho^{(2,4,a)}}{11}, \\ \rho_{1,\bar{1}10} &= \frac{\rho^{(2,2,a)}}{11} + \frac{10\rho^{(2,3,a)}}{11} - \frac{2\rho^{(2,4,a)}}{11}, \\ \rho_{2,\bar{1}10} &= -\frac{3\sqrt{2}\rho^{(2,2,a)}}{11} + \frac{3\sqrt{2}\rho^{(2,3,a)}}{11} + \frac{6\sqrt{2}\rho^{(2,4,a)}}{11}, \\ \rho_{3,\bar{1}10} &= -\frac{7\rho^{(2,2,a)}}{22} + \frac{7\rho^{(2,3,a)}}{22} + \frac{7\rho^{(2,4,a)}}{11}, \\ \rho_{4,\bar{1}10} &= +\frac{3\sqrt{2}\rho^{(1,a)}}{11} - \frac{3\sqrt{2}\rho^{(1,c)}}{11}, \\ \rho_{5,\bar{1}10} &= \frac{9\rho^{(1,a)}}{11} + \frac{2\rho^{(1,c)}}{11}, \\ \rho_{6,\bar{1}10} &= \frac{9\rho^{(2,2,a)}}{11} + \frac{2\rho^{(2,3,c)}}{11}, \\ \rho_{7,\bar{1}10} &= -\frac{3\sqrt{2}\rho^{(2,2,a)}}{11} + \frac{3\sqrt{2}\rho^{(2,3,c)}}{11}. \end{aligned}$$

Using these linear relations we can also express the expansion coefficients as a linear

combination of the $\rho_{i,\bar{1}10}$ parameter

$$\begin{aligned}
(\rho^{(0,a)} + \rho^{(2,1,a)}) &= \frac{1}{12} \left(12\rho_{0,\bar{1}10} + 6\rho_{1,\bar{1}10} - \sqrt{2}\rho_{2,\bar{1}10} - 6\rho_{6,\bar{1}10} + 2\sqrt{2}\rho_{7,\bar{1}10} \right), \\
\rho^{(1,a)} &= \frac{1}{3} \left(\sqrt{2}\rho_{4,\bar{1}10} + 3\rho_{5,\bar{1}10} \right), \\
\rho^{(1,c)} &= \frac{-3\rho_{4,\bar{1}10} + \sqrt{2}\rho_{5,\bar{1}10}}{\sqrt{2}}, \\
\rho^{(2,3,c)} &= \rho_{6,\bar{1}10} + \frac{3\rho_{7,\bar{1}10}}{\sqrt{2}}, \\
\rho^{(2,3,a)} &= \frac{1}{6} \left(6\rho_{1,\bar{1}10} + \sqrt{2}\rho_{2,\bar{1}10} \right), \\
\rho^{(2,2,a)} &= \frac{1}{3} \left(3\rho_{6,\bar{1}10} - \sqrt{2}\rho_{7,\bar{1}10} \right), \\
\rho^{(2,4,a)} &= -\frac{3\sqrt{2}\rho_{1,\bar{1}10} - 10\rho_{2,\bar{1}10} - 3\sqrt{2}\rho_{6,\bar{1}10} + 2\rho_{7,\bar{1}10}}{6\sqrt{2}}.
\end{aligned} \tag{3.54}$$

This set of equations allows us to determine $(\rho^{(0,a)} + \rho^{(2,1,a)})$, $\rho^{(2,4,a)}$ and enables us to calculate the full resistivity tensor up to the second order of \mathbf{m} . Moreover, these equations provide us the ability to compare experimental data from both projections. From the linear equations we also obtain the following restriction for the $\rho_{i,\bar{1}10}$ parameters

$$\rho_{3,\bar{1}10} = \frac{7\sqrt{2}}{12}\rho_{2,\bar{1}10}. \tag{3.55}$$

In the end the use of two different perpendicular current directions in a tetragonal (113)-oriented ferromagnet allows us to determine the full $\boldsymbol{\rho}_{\text{tetra}}(\mathbf{m})$ up to the second order of \mathbf{m} . In Sect. 3.3.1.4 we discuss how the model presented in this section can be used to extract the resistivity and Seebeck parameters from an experiment.

In case of the Seebeck tensor we can carry out the projection in analogous fashion. For the thermopower with the thermal gradient ∇T along the $[3\bar{3}\bar{2}]$ -direction, we find the following relations for longitudinal and transverse thermopower:

$$\Sigma_{\text{long,tetra},3\bar{3}\bar{2},113} = \Sigma_{0,3\bar{3}\bar{2}} + \Sigma_{1,3\bar{3}\bar{2}}m_{\mathbf{j}}^2 + \Sigma_{2,3\bar{3}\bar{2}}m_{\mathbf{j}}m_{\mathbf{\hat{n}}} + \Sigma_{3,3\bar{3}\bar{2}}m_{\mathbf{\hat{n}}}^2 + \Sigma_{A,3\bar{3}\bar{2}}m_{\mathbf{\hat{t}}}, \tag{3.56}$$

$$\Sigma_{\text{trans,tetra},3\bar{3}\bar{2},113} = \Sigma_{4,3\bar{3}\bar{2}}m_{\mathbf{j}} + \Sigma_{5,3\bar{3}\bar{2}}m_{\mathbf{\hat{n}}} + \Sigma_{6,3\bar{3}\bar{2}}m_{\mathbf{j}}m_{\mathbf{\hat{t}}} + \Sigma_{7,3\bar{3}\bar{2}}m_{\mathbf{\hat{t}}}m_{\mathbf{\hat{n}}}. \tag{3.57}$$

We defined the $\Sigma_{i,33\bar{2}}$ as linear combinations of the expansion coefficients

$$\begin{aligned}
\Sigma_{0,33\bar{2}} &= \frac{9(\Sigma^{(0,a)} + \Sigma^{(2,1,a)})}{11} + \frac{2(\Sigma^{(0,c)} + \Sigma^{(2,1,c)})}{11} + \frac{9\Sigma^{(2,2,a)}}{22} - \frac{9\Sigma^{(2,3,a)}}{22}, \\
\Sigma_{1,33\bar{2}} &= -\frac{9\Sigma^{(2,2,a)}}{121} + \frac{4\Sigma^{(2,2,c)}}{121} + \frac{90\Sigma^{(2,3,a)}}{121} + \frac{18\Sigma^{(2,3,c1)}}{121} + \frac{18\Sigma^{(2,3,c2)}}{121} + \frac{18\Sigma^{(2,4,a)}}{121}, \\
\Sigma_{2,33\bar{2}} &= \frac{27\sqrt{2}\Sigma^{(2,2,a)}}{121} - \frac{12\sqrt{2}\Sigma^{(2,2,c)}}{121} + \frac{27\sqrt{2}\Sigma^{(2,3,a)}}{121} - \frac{21\sqrt{2}\Sigma^{(2,3,c1)}}{121} \\
&\quad - \frac{21\sqrt{2}\Sigma^{(2,3,c2)}}{121} - \frac{54\sqrt{2}\Sigma^{(2,4,a)}}{121}, \\
\Sigma_{3,33\bar{2}} &= -\frac{81\Sigma^{(2,2,a)}}{242} + \frac{18\Sigma^{(2,2,c)}}{121} + \frac{117\Sigma^{(2,3,a)}}{242} - \frac{18\Sigma^{(2,3,c1)}}{121} - \frac{18\Sigma^{(2,3,c2)}}{121} + \frac{81\Sigma^{(2,4,a)}}{121}, \\
\Sigma_{A,33\bar{2}} &= -\frac{3\sqrt{2}\Sigma^{(1,c1)}}{11} + \frac{3\sqrt{2}\Sigma^{(1,c2)}}{11} \\
\Sigma_{4,33\bar{2}} &= -\frac{3\sqrt{2}\Sigma^{(1,a)}}{11} + \frac{3\sqrt{2}\Sigma^{(1,c1)}}{11}, \\
\Sigma_{5,33\bar{2}} &= \frac{9\Sigma^{(1,a)}}{11} + \frac{2\Sigma^{(1,c1)}}{11}, \\
\Sigma_{6,33\bar{2}} &= \frac{9\Sigma^{(2,2,a)}}{11} + \frac{2\Sigma^{(2,3,c1)}}{11}, \\
\Sigma_{7,33\bar{2}} &= \frac{3\sqrt{2}\Sigma^{(2,2,a)}}{11} - \frac{3\sqrt{2}\Sigma^{(2,3,c1)}}{11}
\end{aligned}$$

We note that compared to the projection of the resistivity tensor we now obtained an additional parameter $\Sigma_{A,33\bar{2}}$, which adds a new functional dependence on \mathbf{m} to the longitudinal thermopower. Using these linear relations we can formulate the following for the

expansion variables

$$\begin{aligned}
(\Sigma^{(0,c)} + \Sigma^{(2,1,c)}) &= -\frac{9}{2}(\Sigma^{(0,a)} + \Sigma^{(2,1,a)}) + \frac{1}{4}(22\Sigma_{0,33\bar{2}} + 9\Sigma_{1,33\bar{2}} + 3\sqrt{2}\Sigma_{2,33\bar{2}} + 2\Sigma_{3,33\bar{2}} \\
&\quad - 9\Sigma_{6,33\bar{2}} - 3\sqrt{2}\Sigma_{7,33\bar{2}}), \\
\Sigma^{(1,a)} &= \frac{1}{3} \left(-\sqrt{2}\Sigma_{4,33\bar{2}} + 3\Sigma_{5,33\bar{2}} \right), \\
\Sigma^{(1,c1)} &= \frac{3\Sigma_{4,33\bar{2}} + \sqrt{2}\Sigma_{5,33\bar{2}}}{\sqrt{2}}, \\
\Sigma^{(1,c2)} &= \frac{1}{6} \left(9\sqrt{2}\Sigma_{4,33\bar{2}} + 6\Sigma_{5,33\bar{2}} + 11\sqrt{2}\Sigma_{A,33\bar{2}} \right), \\
\Sigma^{(2,2,c)} &= -\frac{9}{2}\Sigma^{(2,4,a)} + \frac{1}{4} \left(-5\Sigma_{1,33\bar{2}} - 9\sqrt{2}\Sigma_{2,33\bar{2}} + 16\Sigma_{3,33\bar{2}} + 9\Sigma_{6,33\bar{2}} + 3\sqrt{2}\Sigma_{7,33\bar{2}} \right), \\
\Sigma^{(2,3,a)} &= \frac{9\sqrt{2}\Sigma_{1,33\bar{2}} + 6\Sigma_{2,33\bar{2}} + 2\sqrt{2}\Sigma_{3,33\bar{2}}}{9\sqrt{2}}, \\
\Sigma^{(2,3,c1)} &= \Sigma_{6,33\bar{2}} - \frac{3\Sigma_{7,33\bar{2}}}{\sqrt{2}}, \\
\Sigma^{(2,3,c2)} &= 2\Sigma_{1,33\bar{2}} - \frac{7\Sigma_{2,33\bar{2}}}{3\sqrt{2}} - 2\Sigma_{3,33\bar{2}} - \Sigma_{6,33\bar{2}} + \frac{3\Sigma_{7,33\bar{2}}}{\sqrt{2}}, \\
\Sigma^{(2,2,a)} &= \frac{3\sqrt{2}\Sigma_{6,33\bar{2}} + 2\Sigma_{7,33\bar{2}}}{3\sqrt{2}}.
\end{aligned} \tag{3.58}$$

In principle this set of equations allows us to determine 9 of the 11 parameters needed for the full tensor description, if we already know the remaining two components ($\Sigma^{(0,a)} + \Sigma^{(2,1,a)}$), and $\Sigma^{(2,4,a)}$. The remaining two parameters are obtainable by using a different projection of the tensor. For a thermal gradient along the $[\bar{1}10]$ -direction, we calculate the following dependencies for $\Sigma_{\text{long,tetra},\bar{1}10,113}$ and $\Sigma_{\text{trans,tetra},\bar{1}10,113}$

$$\Sigma_{\text{long,tetra},\bar{1}10,113} = \Sigma_{0,\bar{1}10} + \Sigma_{1,\bar{1}10}m_{\hat{j}}^2 + \Sigma_{2,\bar{1}10}m_{\hat{t}}m_{\hat{n}} + \Sigma_{3,\bar{1}10}m_{\hat{n}}^2, \tag{3.59}$$

$$\Sigma_{\text{trans,tetra},\bar{1}10,113} = \Sigma_{4,\bar{1}10}m_{\hat{t}} + \Sigma_{5,\bar{1}10}m_{\hat{n}} + \Sigma_{6,\bar{1}10}m_{\hat{j}}m_{\hat{t}} + \Sigma_{7,\bar{1}10}m_{\hat{j}}m_{\hat{n}}. \tag{3.60}$$

The $\Sigma_{i,\bar{1}10}$ parameters represent linear combinations of the expansion coefficients

$$\begin{aligned}
\Sigma_{0,\bar{1}10} &= (\Sigma^{(0,a)} + \Sigma^{(2,1,a)}) + \frac{9\Sigma^{(2,2,a)}}{22} - \frac{9\Sigma^{(2,3,a)}}{22} + \frac{2\Sigma^{(2,4,a)}}{11}, \\
\Sigma_{1,\bar{1}10} &= \frac{\Sigma^{(2,2,a)}}{11} + \frac{10\Sigma^{(2,3,a)}}{11} - \frac{2\Sigma^{(2,4,a)}}{11}, \\
\Sigma_{2,\bar{1}10} &= -\frac{3\sqrt{2}\Sigma^{(2,2,a)}}{11} + \frac{3\sqrt{2}\Sigma^{(2,3,a)}}{11} + \frac{6\sqrt{2}\Sigma^{(2,4,a)}}{11}, \\
\Sigma_{3,\bar{1}10} &= -\frac{7\Sigma^{(2,2,a)}}{22} + \frac{7\Sigma^{(2,3,a)}}{22} + \frac{7\Sigma^{(2,4,a)}}{11}, \\
\Sigma_{4,\bar{1}10} &= +\frac{3\sqrt{2}\Sigma^{(1,a)}}{11} - \frac{3\sqrt{2}\Sigma^{(1,c2)}}{11}, \\
\Sigma_{5,\bar{1}10} &= \frac{9\Sigma^{(1,a)}}{11} + \frac{2\Sigma^{(1,c2)}}{11}, \\
\Sigma_{6,\bar{1}10} &= \frac{9\Sigma^{(2,2,a)}}{11} + \frac{2\Sigma^{(2,3,c2)}}{11}, \\
\Sigma_{7,\bar{1}10} &= -\frac{3\sqrt{2}\Sigma^{(2,2,a)}}{11} + \frac{3\sqrt{2}\Sigma^{(2,3,c2)}}{11}.
\end{aligned}$$

Interestingly if we compare the functional dependence on \mathbf{m} for the longitudinal and transverse thermopower to the corresponding resistivity expressions we obtain no additional contributions. This is in clear contrast to the case of current/temperature gradient along the $[3\bar{3}\bar{2}]$ -direction, where we found a new functional dependency for the longitudinal thermopower. This is due to the tetragonal symmetry which compensates the additional contributions in the Seebeck tensor in this projection. Moreover, we can reverse the linear equations to calculate the expansion coefficients

$$\begin{aligned}
(\Sigma^{(0,a)} + \Sigma^{(2,1,a)}) &= \frac{1}{12} \left(12\Sigma_{0,\bar{1}10} + 6\Sigma_{1,\bar{1}10} - \sqrt{2}\Sigma_{2,\bar{1}10} - 6\Sigma_{6,\bar{1}10} + 2\sqrt{2}\Sigma_{7,\bar{1}10} \right), \\
\Sigma^{(1,a)} &= \frac{1}{3} \left(\sqrt{2}\Sigma_{4,\bar{1}10} + 3\Sigma_{5,\bar{1}10} \right), \\
\Sigma^{(1,c2)} &= \frac{-3\Sigma_{4,\bar{1}10} + \sqrt{2}\Sigma_{5,\bar{1}10}}{\sqrt{2}}, \\
\Sigma^{(2,3,c2)} &= \Sigma_{6,\bar{1}10} + \frac{3\Sigma_{7,\bar{1}10}}{\sqrt{2}}, \\
\Sigma^{(2,3,a)} &= \frac{1}{6} \left(6\Sigma_{1,\bar{1}10} + \sqrt{2}\Sigma_{2,\bar{1}10} \right), \\
\Sigma^{(2,2,a)} &= \frac{1}{3} \left(3\Sigma_{6,\bar{1}10} - \sqrt{2}\Sigma_{7,\bar{1}10} \right), \\
\Sigma^{(2,4,a)} &= -\frac{3\sqrt{2}\Sigma_{1,\bar{1}10} - 10\Sigma_{2,\bar{1}10} - 3\sqrt{2}\Sigma_{6,\bar{1}10} + 2\Sigma_{7,\bar{1}10}}{6\sqrt{2}}.
\end{aligned} \tag{3.61}$$

In addition the following relation between the $\Sigma_{i,\bar{1}10}$ must be full filled

$$\Sigma_{3,\bar{1}10} = \frac{7\sqrt{2}}{12}\Sigma_{2,\bar{1}10}. \tag{3.62}$$

These results prove that it is possible to determine the full Seebeck tensor if we use two different orientations of the thermal gradient in a (113)-oriented tetragonal thin film.

Polycrystalline limit We would like to emphasize that it is possible to calculate the polycrystalline limit from the single crystalline expression from above by averaging over all possible crystal orientations. This is accomplished by first calculating the projections for all current directions and then integrate over all these directions as explained in [227, 235, 236]. From these calculation one then obtains the following expressions for the longitudinal $\rho_{\text{long,poly}}$ and transverse $\rho_{\text{trans,poly}}$ resistivity describing the "conventional", polycrystalline AMR:

$$\rho_{\text{long,poly}} = \rho_{0,\text{poly}} + \rho_{1,\text{poly}} m_{\hat{\mathbf{j}}}^2, \quad (3.63)$$

$$\rho_{\text{trans,poly}} = \rho_{2,\text{poly}} m_{\hat{\mathbf{n}}} + \rho_{1,\text{poly}} m_{\hat{\mathbf{j}}} m_{\hat{\mathbf{t}}}. \quad (3.64)$$

Here we only have 3 parameters $\rho_{0,\text{poly}}$, $\rho_{1,\text{poly}}$, $\rho_{2,\text{poly}}$, which are complex sums of the tensor components. Three contributions to $\rho_{\text{long,poly}}$ and $\rho_{\text{trans,poly}}$ depend on the orientation of the magnetization. The orientation dependence described by $\rho_{1,\text{poly}}$ can be described with a \cos^2 in $\rho_{\text{long,poly}}$ with respect to the angle between current direction $\hat{\mathbf{j}}$ and magnetization orientation. Please note that the results of this calculation are independent of the symmetry of the single crystal [227, 235, 236].

3.3.1.4 Application of the model to experiment

In Sect. 3.3.1.3 we showed that by using differently oriented rotation planes for the magnetization we are able to separate the different contributions from the longitudinal and transverse resistivity and thermopower. Unfortunately, it is impossible in an experiment to directly manipulate the orientation of the magnetization. Rather, an external control parameter must be used. Normally, we apply an external magnetic field $\mu_0 \mathbf{H} = \mu_0 H \mathbf{h}$ to the sample to influence the orientation of the magnetization. But the external magnetic field is not the only parameter influencing the orientation of the magnetization, in addition the magnetic anisotropy defined by shape and crystal contributions plays an important role. In order to describe the dependency of the magnetization orientation on the magnetic anisotropy and external magnetic field we need to introduce the well established free enthalpy density approach [165, 235, 236]. Within this framework we assume that the magnetization of our sample can be described in the picture of single domain (macro spin) and the magnitude M of the magnetization is not changed during our experiments. This allows us to describe the influence of external magnetic field and magnetic anisotropy in an potential energy landscape G for the magnetization orientation. We use the following general expression of the normalized $G_M = G/M$ for a thin ferromagnetic film

$$G_M(\mathbf{m}) = -\mu_0 H(\mathbf{h} \circ \mathbf{m}) + B_{\hat{\mathbf{n}}}(\hat{\mathbf{n}} \circ \mathbf{m})^2 + B_{\hat{\mathbf{u}} \circ \mathbf{m}}(\hat{\mathbf{u}})^2 + B_{c,x} \mathbf{m}_x^4 + B_{c,y} \mathbf{m}_y^4 + B_{c,z} \mathbf{m}_z^4 + \dots \quad (3.65)$$

The first term describes the contribution from the external magnetic field (Zeeman contribution), m_i are the direction components of \mathbf{m} along the cubic axes, $B_{\hat{\mathbf{n}}}$ describes the anisotropy due to the shape of the film and anisotropy due to intrinsic effects along the surface normal, $B_{\hat{\mathbf{u}}}$ stands for an intrinsic uniaxial anisotropy along an arbitrary unit

vector $\hat{\mathbf{u}}$, $B_{c,i}$ parameters quantify the intrinsic cubic anisotropy of the thin film along the cubic directions. One should note that due to the normalization of the enthalpy to M the anisotropy constants are described in units of Tesla. Moreover, the sign of the anisotropy constant determines whether it characterizes an easy $B_i < 0$ or a hard $B_i > 0$ axis. The here presented general approach can be tailored to fit to the actual ferromagnet under investigation by adding appropriate additional uniaxial contributions, that may for example arise due to strain effects. Using this free enthalpy approach we can determine the orientation of the magnetization for a given set of anisotropy parameters and fixed field orientation and strength by minimizing the free enthalpy with respect to \mathbf{m} . Moreover, we see from this formulation that the orientation of the magnetization will be dominated by the external field contribution, if we apply magnetic fields larger than the magnetic anisotropy parameters.

From these observations we are able to simulate ADMR and ADMTP experiments in the following way: From $G_M(\mathbf{m})$ we determine the magnetization orientation \mathbf{m} by minimizing $G_M(\mathbf{m})$ for every orientation of the external magnetic field at fixed field strength in the 4 rotation planes described by Fig. 3.13(a)-(d). Substituting the obtained \mathbf{m} into the expressions for the projections of the resistivity and Seebeck tensors given in Sect. 3.3.1.3 we calculate the corresponding longitudinal and transverse resistivity/thermopower. Unfortunately, for a fit to the experimental data, the ρ_i , Σ_i , and B_i parameters are first all unknown. Making use of the fact that the Zeeman contribution dominates at large enough external magnetic fields, we first determine the ρ_i , Σ_i parameters. Then in a second step we use the high field determined ρ_i , Σ_i parameters at lower magnetic fields to determine the magnetic anisotropy parameters B_i . Thus the free enthalpy expression in combination with the series expansion model of the resistivity and Seebeck tensors enables us to quantitatively determine magnetic anisotropy and resistivity (Seebeck) parameters from ADMR and ADMTP experiments.

3.3.1.5 Determination of longitudinal and transverse resistivity and thermopower

So far we have only described how we determine longitudinal and transverse resistivity and thermopower in our model from a projection of the corresponding tensors. But we also need to extract these quantities from the experiment, as discussed in this section. For the determination of ρ_{long} , ρ_{trans} from our experiments we apply a fixed current I in a Hall bar structure and measure in 4pt-geometry the voltages V_{long} and V_{trans} as depicted in Fig. 3.16(a)

Starting from the definition of the resistivity tensor in Eq.(3.3) and our definition of the projection of the tensors Eqs.(3.34,3.35) we can identify $(\nabla T = 0)$ ⁷:

$$\rho_{\text{long}} = \frac{E_{\text{long}}}{J} = \frac{V_{\text{long}}}{I} \frac{w \times d}{l}, \quad (3.66)$$

$$\rho_{\text{trans}} = \frac{E_{\text{trans}}}{J} = \frac{V_{\text{trans}}}{I} d. \quad (3.67)$$

Here we used $E_{\text{long}} = V_{\text{long}}/l$, $J = I/(w \times d)$, $E_{\text{trans}} = V_{\text{trans}}/w$. In the experiment we only need to measure the voltages V_{long} , V_{trans} , and the current I applied to the Hall bar,

⁷Using Ohms law $\mathbf{E} = \rho \mathbf{j}$ we can establish the following definition of sign for ρ_{long} : if \mathbf{E}_{long} is parallel to \mathbf{j} then ρ_{long} is positive, if \mathbf{E}_{long} is antiparallel to \mathbf{j} then ρ_{long} is negative. In the very same way we can then define the sign of ρ_{trans} using $\mathbf{E}_{\text{trans}}$ and the reference direction \mathbf{t} .

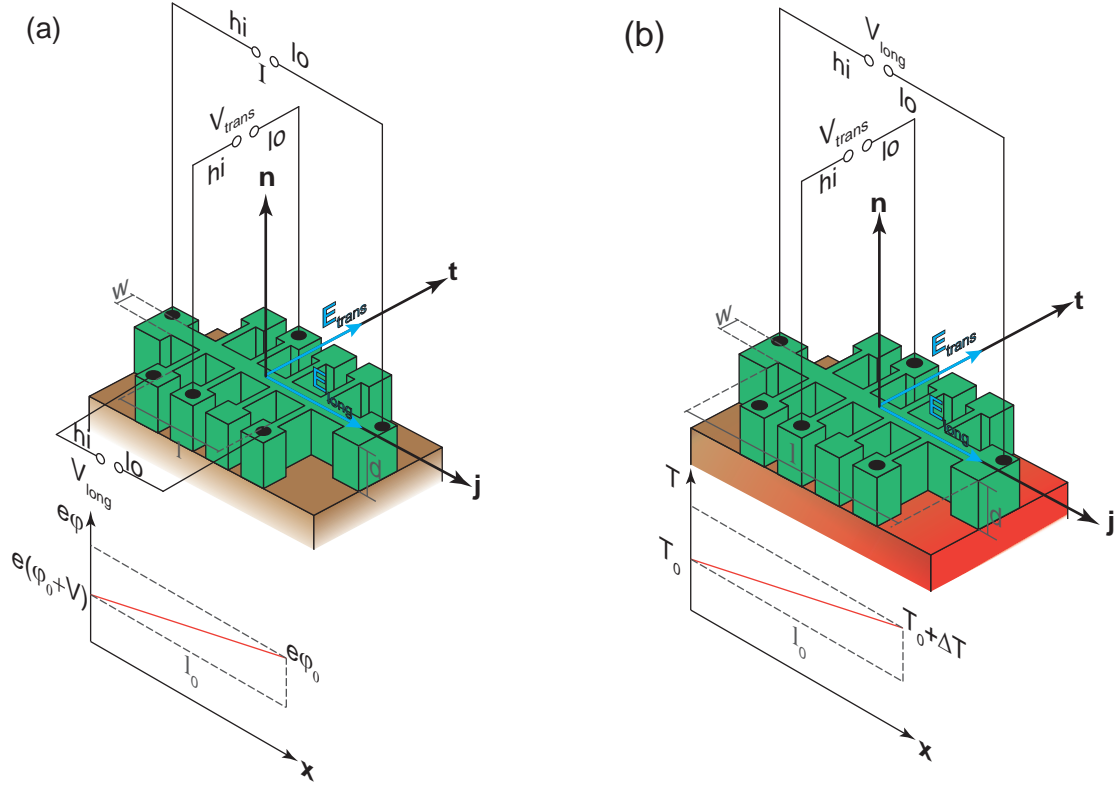


Figure 3.16: (a) Definition of the parameters and connection polarity for the determination of ρ_{long} , ρ_{trans} in Hall bar geometry. A constant current I is applied to a Hall bar with thickness d and width w . The longitudinal voltage V_{long} is measured across a distance l , together with the perpendicular voltage V_{trans} across w . (b) Definition of the parameters and connection polarity for the determination of Σ_{long} , Σ_{trans} in Hall bar geometry. A constant temperature difference ΔT is applied between the two ends of the Hall bar with a total length l_0 . The voltage drop V_{long} along the Hall bar is measured over a distance l , and a second perpendicular voltage V_{trans} , over the width of the Hall bar.

and calculate the resistivity using the geometrical data of the Hall bar mesa structure.

For the determination of the Seebeck parameters Σ_{long} , Σ_{trans} in an experiment, we apply a constant temperature difference ΔT across the whole structure over a length l_0 and measure the voltage difference longitudinal and transverse to the thermal gradient as depicted in Fig. 3.16(b). To calculate the Seebeck coefficients we use the definition in Eq.(3.3) and the projection of the tensors Eqs.(3.36,3.37) and find ($\mathbf{j} = 0$)

$$\Sigma_{\text{long}} = \frac{E_{\text{long}}}{\nabla T} = \frac{V_{\text{long}} l_0}{\Delta T l}, \quad (3.68)$$

$$\Sigma_{\text{trans}} = \frac{E_{\text{trans}}}{\nabla T} = \frac{V_{\text{trans}} l_0}{\Delta T w}. \quad (3.69)$$

Here we used $\nabla T = \Delta T/l_0$. These two equations are only correct, if the temperature increases linearly over the whole Hall bar (i.e. the magnitude of the temperature gradient is constant). Thus the extraction of Seebeck parameters is possible, if we know the

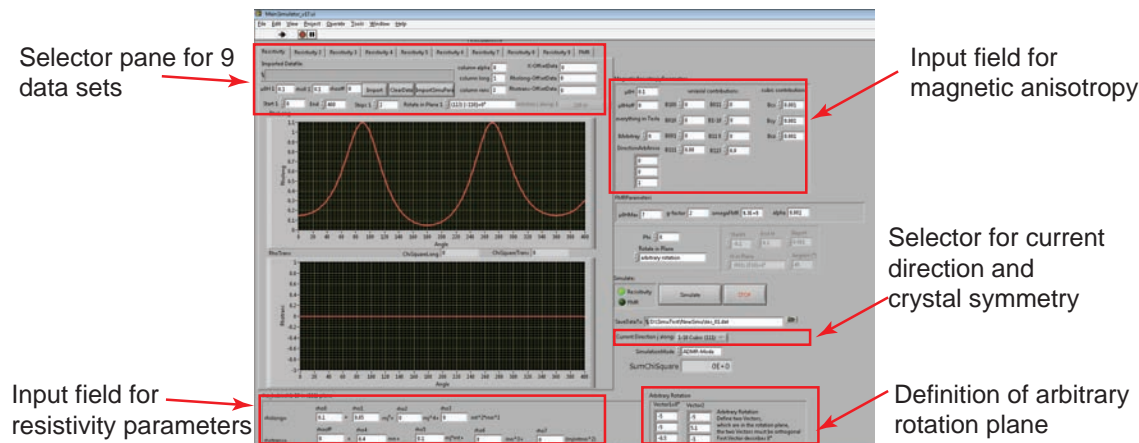


Figure 3.17: Screen shot and description of selected input fields for the final simulation software of ADMR and ADMTP experiments.

temperature difference between the two ends and the dimensions of the Hall bar and measure V_{long} , V_{trans} under a constant temperature difference.

3.3.1.6 Experimental procedure for and analysis of AMDR and ADMTP experiments

In the preceding section we showed how one extracts experimentally longitudinal and transverse resistivity and thermopower. In the following we explain in more detail the experimental procedure for ADMR and ADMTP experiments and give insight into the realization of a simulation algorithm written in LabVIEW to fit the data with our series expansion model.

In an ADMR (ADMTP) experiment the external magnetic field \mathbf{H} is rotated with fixed field magnitude $\mu_0 H_{\text{meas}}$ in one of the 4 rotation planes defined in Fig. 3.13(a)-(d), while the longitudinal and transverse resistivity (thermopower) are recorded as a function of external magnetic field orientation (α , β , γ , δ , depending on the selected rotation plane). To achieve an identical magnetic domain configuration prior to each measurement an initialization is carried out by sweeping the field at a fixed orientation from $\mu_0 H_{\text{init}}$ to $\mu_0 H_{\text{meas}}$. For a successful quantitative extraction these measurement have to be carried out at various $\mu_0 H_{\text{meas}}$ and in at least 3 rotation planes defined by Fig. 3.13(a)-(d).

For the analysis and quantitative extraction of the data a LabVIEW based software has been developed during the work of this thesis. The LabVIEW software allows to load 9 independent data sets for a simultaneous processing. Moreover, the code of the software includes 15 different rotation planes in cartesian coordinates and allows also the user a definition of individual rotation planes by the input of two orthogonal vectors in the rotation plane. The description of the free enthalpy in this software already contains 8 uniaxial, 3 cubic anisotropy parameters and allows the definition of one additional uniaxial anisotropy parameter. In addition, the software includes 17 different projections of the resistivity and Seebeck tensors in cubic and tetragonal symmetry. The modular framework allows the easy definition of new projections in the future.

For the simulation the software loops for each external field orientation through the following procedure: First the external magnetic orientation in cartesian coordinates

is determined from the field orientation angle. Next, based on the input parameters (external magnetic field strength, magnetic anisotropy parameters) the magnetization orientation is determined from a numerical minimization of the free enthalpy in spherical coordinates (to reduce the number of independent parameters from 3 (cartesian) to 2 (spherical)). This numerical minimization utilizes a "Quasi-Newton" method to find the global minimum of the free enthalpy with a gradient search. Finally, using the resistivity (Seebeck) input parameters and the determined magnetization orientation the longitudinal and transverse resistivity (Seebeck coefficient) are calculated. The software automatically generates for each data set a simulation file in a user specified folder. In this file all relevant input parameters and the simulation results are stored. An import routine allows to load old simulation parameters stored in these files into the program. In addition, the software allows to simulate the ferromagnetic resonance field as a function of external magnetic field orientations. This allows a seamless comparison of magnetotransport determined magnetic anisotropy to the anisotropy determined from ferromagnetic resonance experiments.

The following steps have to be carried out during a simulation process to obtain in the end an optimized set of magnetic anisotropy and resistivity (thermopower) parameters from ADMR (ADMTP) experiments: First we choose reasonable starting values for the magnetic anisotropy parameters using an educational guess (Or set them all to 0). This enables us to carry out the numerical global minimization of the free enthalpy in the software. We then start to optimize the resistivity (Seebeck) parameters for the projection of the tensor that fits our sample (Sect. 3.3.1.3). At a first glance the simulation seems to be rather tedious to carry out as we have to optimize many parameters. But one can utilize for a first guess of parameters that the magnetization follows directly the external magnetic field rotation for large magnetic fields. This enables us to neglect the influence of magnetic anisotropy at large magnetic fields. In addition, for any of the used rotation planes (Fig. 3.13(a)-(d)) not all $\rho_{i,110}$ ($\Sigma_{i,110}$) parameters contribute to the angular dependence of longitudinal and transverse resistivity (thermopower). For example for an ip rotation we can safely assume $m_{\hat{n}} = 0$, thus the number of parameters contributing to the resistivity (thermopower) are greatly reduced. The very same arguments can be used for the oopj ($m_{\hat{j}} = 0$) and oopt ($m_{\hat{k}} = 0$) rotation planes at large field values. This enables us to determine a first set of $\rho_{i,110}$ ($\Sigma_{i,110}$) from the experiment. We then tune the anisotropy parameters and $\rho_{i,110}$ ($\Sigma_{i,110}$) iteratively until an optimal agreement between simulation and experiment is achieved [235].

To conclude this whole section we summarize the results obtained. Starting with a linear response model of electrical and thermal currents we defined the resistivity and Seebeck tensors as tensors connecting an electrical field with a electrical current and a thermal gradient, respectively. Neglecting spin dependent scattering these quantities can be calculated from the Fermi surface of the material using the effective mass tensor. In case of a ferromagnetic system the calculation process becomes very complicated and we chose to describe the tensors in a phenomenological approach as a series expansion of the magnetization direction. We utilized the Onsager relations and Neumann's principle to reduce the number of parameters of the expansion for cubic and tetragonal symmetry. In an experiment on thin films it is only possible to measure projections of the tensor components and thus only selected expansion coefficients. This can be described in the right handed coordinate system defined by the unit vectors of the direction of electrical

current (thermal gradient), surface normal and transverse direction. In our model we project the resistivity and Seebeck tensor using this coordinate system and obtain linear relations between the parameters describing the longitudinal and transverse projection and the expansion coefficients. These relations enable us to calculate the full tensor description for cubic symmetry by using the results of measurements carried out along one crystallographic direction and rotations of the magnetization in three different planes (ip, oopj, oopc). In case of tetragonal symmetry the calculation of the full resistivity and Seebeck tensor is possible, if we use for example an (113)-oriented ferromagnetic film (c-axis along [001]-direction) and use experimental data obtained for the electrical current (thermal gradient) along two orthogonal directions ($[33\bar{2}]$ and $[\bar{1}10]$) for rotations of the magnetization in 3 different planes (ip, oopj, oopt). To take into account the competition of external \mathbf{H} field and magnetic anisotropy we use the free enthalpy approach, which allows us to determine the magnetization orientation by taking into account contributions from the external magnetic field and magnetic anisotropy of the sample. The series expansion and the free enthalpy formulation are the key ingredients for a full quantitative description of the magneto-galvanic properties and the magnetic anisotropy from the experiment. Moreover, we defined the polarity of the connection scheme for the measurements of the longitudinal and transverse resistivity and thermopower, which is crucial for the exact determination of the full tensor description of the galvanomagnetic effects.

3.3.2 Magnetothermopower and magnetoresistance in (Ga,Mn)As

In Sect. 3.3.1 we provided the framework for a full quantitative extraction of the resistivity and Seebeck tensors from ADMR and ADMTP experiments. In the following section we focus on the partly extraction of these tensor properties from ferromagnetic (Ga,Mn)As thin films grown on differently oriented GaAs substrates by low temperature MBE.

(Ga,Mn)As is the prototype of a ferromagnetic semiconductor with a Curie temperature below 170 K [238–240]. The compatibility of (Ga,Mn)As to GaAs makes it an interesting candidate for spintronic applications. The successful realization of novel spin-electronic devices has already been demonstrated in (Ga,Mn)As, such as the emission of circularly polarized light from a spin light emitting diode [241, 242], the tunneling anisotropic magnetoresistance in (Ga,Mn)As/insulator/normal metal structures [243], and nonvolatile memory device concepts [244–246]. The strong $p-d$ coupling between the delocalized holes and the localized electrons in the Mn d shell leads to large magneto resistive effects in (Ga,Mn)As [241, 247–250], which makes it an ideal test bed for the full quantitative extraction of the transport property tensors. Moreover, recent publications already verified that it is possible to apply the here presented resistivity model to ADMR experiments in (Ga,Mn)As and extract quantitative data for the resistivity and magnetic anisotropy [235, 236] and even quantify small changes in magnetic anisotropy induced by strain effects [251]. The few existing publications [252, 253] dealing with the anisotropic magnetothermopower and the Nernst effect in (Ga,Mn)As showed large magnetothermopower effects and a direct dependence on the orientation of the magnetization. These results are suggesting that it should be possible to extract the full quantitative description of the resistivity and Seebeck tensors, and gain a deeper understanding of the Fermi surface of (Ga,Mn)As using the Mott relation (Eq.(3.16)). In addition, recent experiments have revealed the spin-Seebeck effect in (Ga,Mn)As/Pt heterostructures [25, 27]. To separate spurious contributions from the spin-Seebeck signal a deeper understanding

of anisotropic magnetothermopower effects certainly is important.

In this following section we focus on experiments paving the way for the quantitative determination of both the resistivity and Seebeck tensors in (Ga,Mn)As. First a description of the sample and the experimental setup is provided. On-chip thermometry carried out on our samples allowed us to monitor the evolution of the temperature gradient as a function of position, directly by resistance measurements. In the end we present the experimental results obtained for (001)- and (113)-oriented (Ga,Mn)As thin films and compare the extracted components of the tensors quantitatively.

3.3.2.1 Sample preparation and on-chip thermometry

The samples investigated here are two 30 nm thick $(\text{Ga}_{1-x}\text{Mn}_x)\text{As}$ films, one ($x = 4\%$) grown on (001)- and the other ($x = 5\%$) on (113)-oriented GaAs via low temperature molecular beam epitaxy [235, 236] by W. Schoch in the group of W. Limmer at the university of Ulm. The samples have been cleaved into $2 \times 6 \text{ mm}^2$ rectangles, with the long side along the [110]- and $[\bar{3}3\bar{2}]$ -direction, respectively. Using optical lithography and wet chemical etching Hall bar mesa structures have been defined, with the current direction parallel to the long side of the sample. The width of the Hallbar was $250 \mu\text{m}$ and the separation between the contact pairs was $625 \mu\text{m}$. The samples were then mounted on a specially designed, home-built carrier, which allowed to couple one end of the sample to a thermally isolated resistive heater and the other end to a temperature bath via a copper block. An illustration is shown in Fig. 3.18(a). This setup enables us to control the temperature gradient in the sample by changing the power applied to the resistive heater. Two calibrated Cernox temperature sensors enabled us to monitor the temperature of the hot and cold end of the sample holder. To achieve a good thermal contact between carrier and sample we glued the sample using GE Varnish to the hot and cold end. Electrical contacts to the Hall bar were established by Al wedge-bonding. The sample carrier was then mounted onto a dipstick and placed in a superconducting magnet cryostat system ($\mu_0 H = 7 \text{ T}$, $1.8 \text{ K} \leq T \leq 350 \text{ K}$) equipped with a stepper motor, which allowed a rotation of the external magnetic field in different planes with respect to the sample. More details can be found in the Diploma thesis of S. Meyer, whom I supervised as a part of my PhD thesis [254].

As it is important for the exact determination of the thermopower to know the temperature evolution across the sample, we applied on chip thermometry. This is realized by measuring the resistance of different transverse contact pairs, labeled 1, 2, 3 in Fig. 3.18(a). The measured resistance is dominated by the narrow connections between bar and contact pads, thus representing a lateral, well-defined temperature sensor. To determine the relation between resistance and temperature we first carried out a calibration by slowly (10 K/h) increasing the dipstick temperature from 8 K to 75 K, without a current applied to the resistive heater. In order to exclude spurious signals, we measured each pair separately and repeated each measurement twice. The results obtained are summarized in Fig. 3.18 for the (001)-oriented sample. All resistance curves exhibit a distinct minimum around 15 K and a maximum at 65 K, and are highly reproducible. These calibration curves allow us to identify from the resistance of the transverse contact pair the temperature at the position of the pair on the sample. We established a dipstick temperature of 10 K, changed the electrical power applied to the resistor, and measured simultaneously the resistance of each contact pair. The graph in Fig. 3.18(c) displays

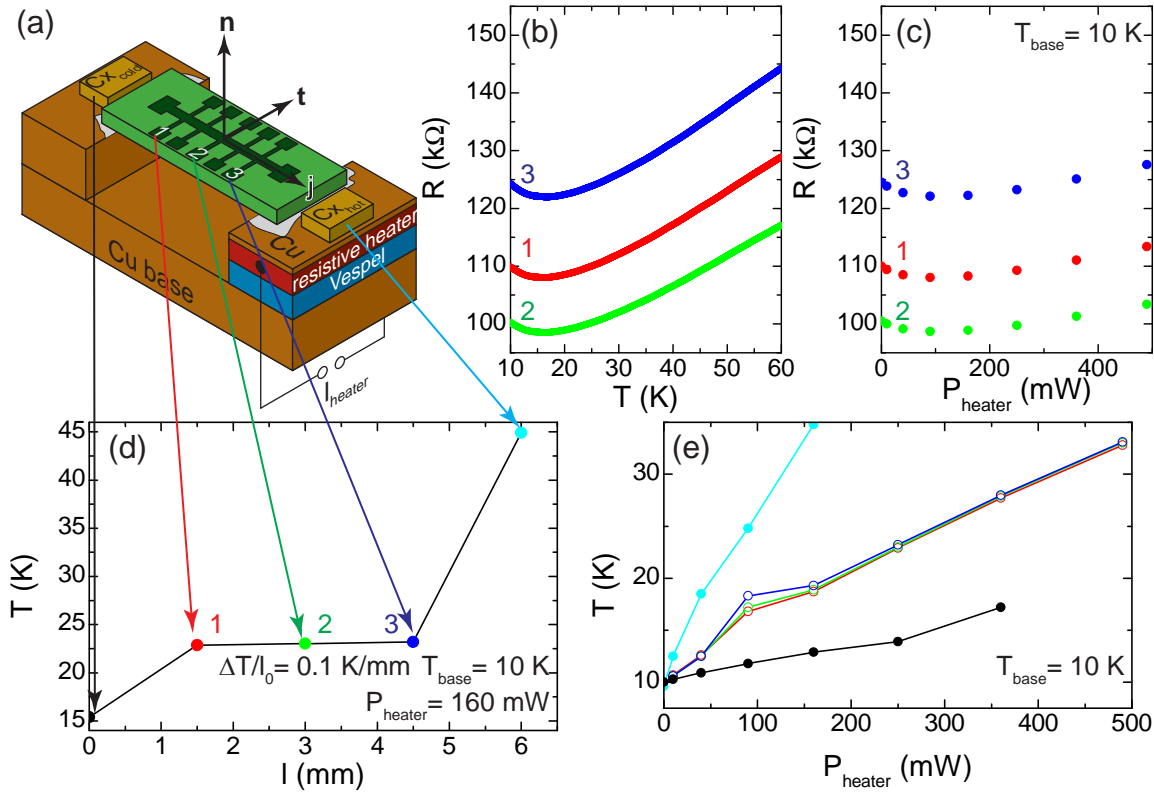


Figure 3.18: Results of the on chip thermometry for a 30 nm thick (001)-oriented $(\text{Ga}_{0.96},\text{Mn}_{0.04})\text{As}$ sample. (a) Illustration of the sample mounted to the temperature gradient holder, which is equipped with a resistive heater to control the temperature at the hot end of the sample. (b) Temperature calibration curves for the resistance of each transverse contact pair, establishing a direct connection between the resistance of each pair and the temperature at their respective position on the sample. (c) Change in resistance of each contact pair with increasing power applied to the heater at a base temperature of 10 K. (d) Extracted spatial evolution of the temperature for $P_{\text{heater}} = 160 \text{ mW}$, due to a bad thermal connection between sample and carrier we loose a large amount of the temperature gradient. (e) Calculated evolution of the local temperatures for different heater powers. The average sample temperature drastically increases while the temperature gradient on the sample experiences only minor changes. Drawn lines are only a guide to the eye.

the results obtained from these measurements. All three resistances show a distinct minimum at $P_{\text{heater}} = 100 \text{ mW}$ and increase with higher heater power. Using the calibration curves and the temperatures of the Cernox temperature sensors we calculated the evolution of temperature across the whole sample for different powers applied to the resistor. For $P_{\text{heater}} = 160 \text{ mW}$ we show in Fig. 3.18(d) the lateral evolution of the temperature. Although the temperature difference between the two Cernox sensors is 30 K, the temperature gradient measured between the transverse contact pairs is only 0.1 K/mm. We attribute this large decrease in thermal gradient to the bad thermal contact between cold and hot end of the sample holder and the sample itself. The power applied to the resistor not only induces a thermal gradient in the sample but also considerably changes the

average temperature T_{avg} of the sample itself. This effect becomes more visible if we look at the evolution of the temperature in Fig. 3.18(e). For $P_{\text{heater}} > 200$ mW the temperature gradient across the sample stays constant and only the average sample temperature increases with heater power. Moreover, the largest temperature gradient is established for $P_{\text{heater}} = 90$ mW. In order to take into account the increase in T_{avg} with P_{heater} we carried out the ADMR and ADMTP experiments under a constant P_{heater} for resistivity and thermopower measurements. Nevertheless, for future experiments it is important to reduce the loss in temperature gradient at the sample, which we plan to achieve by mechanical clamping the sample and carrying out the experiments in vacuum. Moreover, the expected larger tuning range of the temperature gradient allows to study in more detail the linear dependence of the longitudinal and transverse thermopower signal on the thermal gradient, while the average sample temperature remains nearly unchanged. In our current setup due to a constant increase of the sample temperature with increasing heater power an inspection of the linearity is impossible, but we assume in the following sections that the linearity is maintained in our setup.

3.3.2.2 ADMR and ADMTP for (001)-oriented (Ga,Mn)As

In the following we first present the results obtained for the (001)-oriented (Ga,Mn)As thin film and electrical current (thermal gradient) along the [110]-direction. In our ADMR and ADMTP experiments we applied a fixed current to the resistive heater ($P_{\text{heater}} = 250$ mW) of our setup, establishing a fixed average temperature $T_{\text{avg}} = 25.2$ K and gradient $\nabla T = 0.5$ K/mm determined from on-chip thermometry. For the experiments we used three distinct rotation planes for the external magnetic field: in-plane (ip, Fig. 3.19(a)), out-of-plane perpendicular to $\hat{\mathbf{j}}$ (oopj, Fig. 3.19(d)), and out-of-plane perpendicular to $\hat{\mathbf{t}}$ (oopt, Fig. 3.19(g)). Following the experimental procedure described in Sec. 3.3.1.6 we applied an external initialization field $\mu_0 H_{\text{init}} = 3$ T at a fixed field orientation ($\alpha = 0^\circ$ for ip and $\beta, \gamma = -90^\circ$ for oopj, oopt) before carrying out the ADMR and ADMTP ($\mathbf{j} = 0$) measurements at $\mu_0 H_{\text{meas}}$. The thermal gradient applied to the sample was identical for both types of experiments. Using Eqs.(3.66,3.67,3.68,3.69) we calculated then ρ_{long} , ρ_{trans} and Σ_{long} , Σ_{trans} . The transverse signals are offset corrected, such that the signal is symmetric to the y -axis. The offset in the transverse signals arises due to a lateral displacement (in our measurements $2 - 10$ μm) of the transverse contacts on the sample, which leads to a spurious longitudinal signal. For the offset correction we subtract a fraction (0.1-4%) of the longitudinal signal from the transverse signal. In Fig.3.19(a)-(i) we compare the results obtained for ADMR and ADMTP experiments at a constant magnetic field of 1 T and a fixed heater power of 250 mW.

The results obtained for the ip ADMR measurements reflect the anisotropic magnetoresistance (AMR) of (Ga,Mn)As and are represented in Fig. 3.19(b). At $\mu_0 H = 1$ T it is safe to assume that the magnetization follows directly the orientation of the external magnetic field. The ip ADMR measurement map the dependence of ρ_{long} and ρ_{trans} on the orientation of the magnetization direction. In classical AMR theory the important parameter defining the resistivity is the angle between current and magnetization direction (cf. Eqs.(3.63,3.64)). For ρ_{long} we observe that the resistivity for magnetization parallel to the current direction ρ_{\parallel} is smaller than for a perpendicular alignment ρ_{\perp} . This is in contrast to the observation for classical 3d ferromagnets, where one finds $\rho_{\parallel} > \rho_{\perp}$ [252], and is one characteristic feature of the ferromagnetic semiconductor (Ga,Mn)As. More-

over, the observed angular dependency of ρ_{long} clearly deviates from the expected \cos^2 dependency for a classical AMR theory Eq.(3.63), but can be explained within the series expansion model, outlined in Sect. 3.3.1.3 as discussed below. Another interesting feature, that can only be explained if we consider the crystal symmetry of the system is the difference in oscillation amplitude for ρ_{long} and ρ_{trans} : for the longitudinal resistivity we observe a change of $0.5 \mu\Omega\text{m}$, whereas the transverse resistivity changes by $6 \mu\Omega\text{m}$, which is a more than a magnitude larger. This effect is not expected for a classical AMR theory, where the change in resistivity for longitudinal and transverse resistivity is equal (cf. Eqs.(3.63,3.64)). We note that both ρ_{long} and ρ_{trans} exhibit a two fold symmetry for a full 360° field rotation, which reflects, that only contributions even in \mathbf{m} from our series expansion model influence the ip ADMR measurements.

For the ip ADMTP measurements in Fig. 3.19(c) we observe again a two fold symmetry over the whole 360° rotation in $\Sigma_{\text{long}}(\alpha)$ and $\Sigma_{\text{trans}}(\alpha)$, which represents the anisotropic thermopower. Interestingly, the angular ip evolution of Σ_{long} is inverted compared to ρ_{long} , the thermopower is largest for parallel alignment of \mathbf{m} and \mathbf{j} and smallest for perpendicular alignment, thus $\Sigma_{\parallel} > \Sigma_{\perp}$. This inversion has also been reported by Pu *et al.* [252]. In contrast $\Sigma_{\text{trans}}(\alpha)$ shows the same structure as $\rho_{\text{trans}}(\alpha)$ for the ip case, minima and maxima occur roughly at the same positions, only the signal to noise ratio is not as good for the transverse thermopower.

The angular dependence of ρ_{long} and ρ_{trans} for an external field rotation in the oopj plane for $\mu_0 H = 1 \text{ T}$ is depicted in Fig. 3.19(e). The applied external magnetic field is large enough that the magnetizations follows the field direction and only minor deflections from this behavior due to the demagnetizing field of the thin film are expected. The longitudinal resistivity exhibits a two fold symmetry and we identify a maximum for $\mathbf{h} \parallel \hat{\mathbf{n}}$ and a minimum for $\mathbf{h} \parallel \hat{\mathbf{t}}$. The angular dependence of $\rho_{\text{long}}(\beta)$ arises due to the out-of-plane AMR of (Ga,Mn)As and is in contrast to the angular dependence reported in [235], where $\rho_{\text{long}}(\beta)$ developed additional maxima and minima. These differences might be attributed to the different measurement temperatures, 25.2 K used here and 4.2 K in [235]. In this field rotation plane the transverse resistivity is dominated by the contributions from anomalous and normal Hall effect. For these contributions, we expect a maximum signal for $\mathbf{h} \parallel \hat{\mathbf{n}}$ and a minimum for $\mathbf{h} \parallel -\hat{\mathbf{n}}$ due to the p-type conductivity of the (Ga,Mn)As layer, which is also visible in our experimental data.

The angular dependence of $\Sigma_{\text{long}}(\beta)$ for an oopj rotation of the external magnetic field in Fig. 3.19(f) is identical to the one of $\rho_{\text{long}}(\beta)$ in Fig. 3.19(e). We observe minima in the longitudinal thermopower if the field is oriented in the film plane and maxima for \mathbf{h} parallel or antiparallel to $\hat{\mathbf{n}}$. In contrast the angular evolution of the transverse thermopower is inverted compared to $\rho_{\text{trans}}(\beta)$ in this rotation plane, with a minimum in $\Sigma_{\text{trans}}(\beta)$ for $\mathbf{h} \parallel \hat{\mathbf{n}}$ and a maximum for $\mathbf{h} \parallel -\hat{\mathbf{n}}$.

If we rotate the magnetic field in the oopt plane (Fig. 3.19(g)), the longitudinal resistivity in Fig. 3.19(h) exhibits again a two fold symmetry and shows the same characteristic evolution as for the oopj rotation plane. Maxima in $\rho_{\text{long}}(\gamma)$ occur for \mathbf{h} parallel or antiparallel to \mathbf{n} and minima for \mathbf{h} in the film plane. Moreover, the shape of $\rho_{\text{trans}}(\gamma)$ is dominated by the contributions due to the anomalous and normal Hall effect, leading to the characteristic cosine dependence.

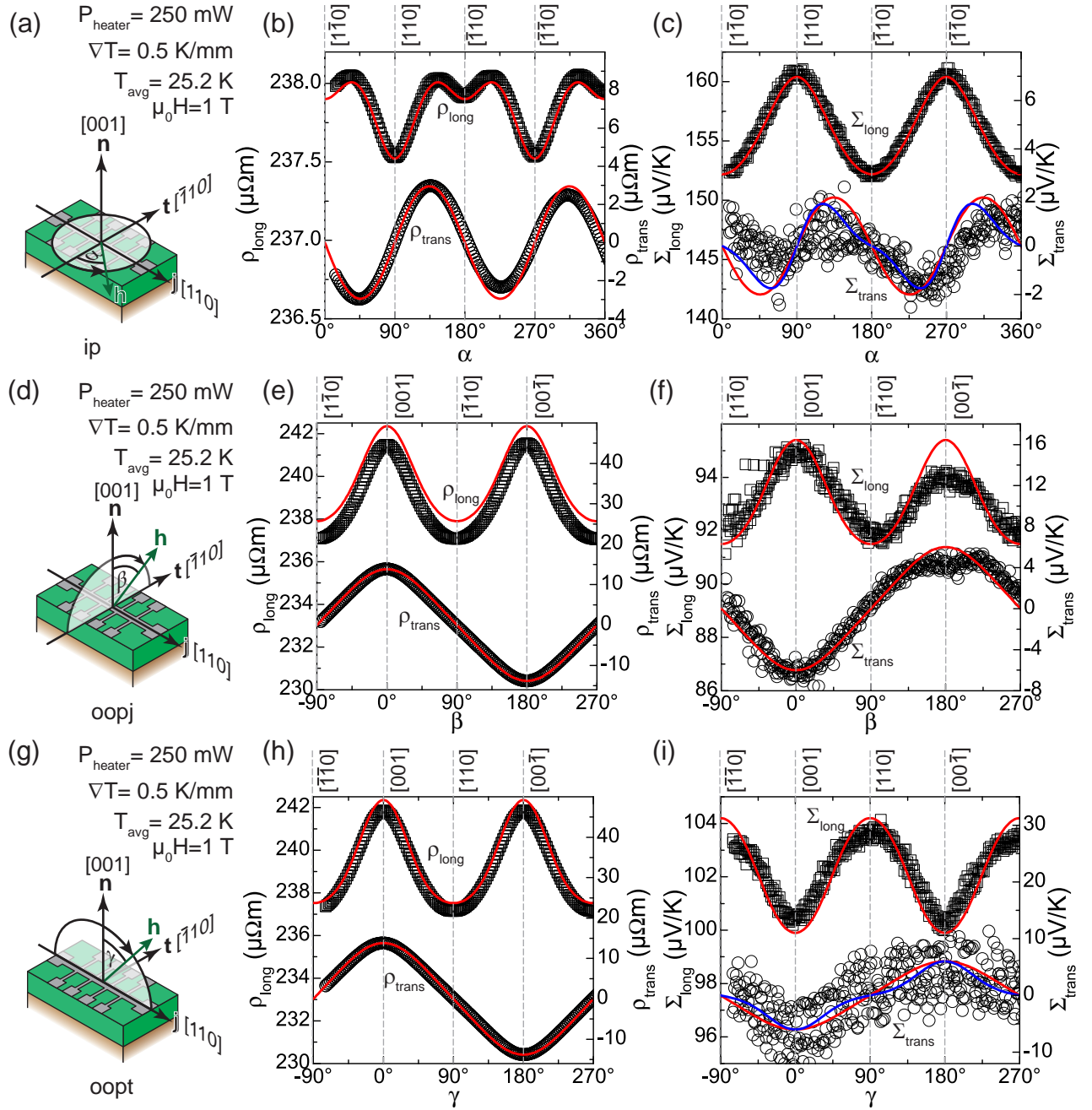


Figure 3.19: Results obtained from ADMR and ADMTP experiments on a 30 nm thick (001)-oriented $(\text{Ga}_{0.96}, \text{Mn}_{0.04})\text{As}$ sample at $T_{\text{avg}} = 25.2 \text{ K}$ and $\mu_0 H = 1 \text{ T}$. (a) Illustration of the ip rotation plane of the external field direction \mathbf{h} in the coordinate system defined by $\hat{\mathbf{j}}$, $\hat{\mathbf{t}}$, and $\hat{\mathbf{n}}$. The arrow indicates the direction for a positive rotation angle α . (b) Angular dependence of ρ_{long} and ρ_{trans} for an ip rotation of the external magnetic field. (c) Evolution of Σ_{long} and Σ_{trans} for an ip rotation. (d) Illustration of the oopj rotation plane and definition of positive rotation angle β . Oopj rotation results for ρ_{long} and ρ_{trans} (e) and Σ_{long} and Σ_{trans} (f). (g) Definition of the oopt rotation plane with positive rotation angle γ . (h) Angular dependence of ρ_{long} and ρ_{trans} for oopt rotation. (i) $\Sigma_{\text{long}}(\alpha)$ and $\Sigma_{\text{trans}}(\alpha)$ for an oopt rotation. Symbols represent experimental data and red lines fits via Eqs.(3.42,3.43) and Eqs.(3.45,3.46).

Surprisingly, the longitudinal thermopower shows an inverted trend in Fig. 3.19(i) compared to the angular evolution of $\rho_{\text{long}}(\gamma)$ in Fig. 3.19(h). $\Sigma_{\text{long}}(\gamma)$ has its lowest values for \mathbf{h} parallel or antiparallel to \mathbf{n} and its largest for \mathbf{h} oriented in the film plane. One should note that this inversion between the angular dependence of $\rho_{\text{long}}(\gamma)$ and $\Sigma_{\text{long}}(\gamma)$ could not be seen in the oopj rotation plane. In contrast, the angular dependence of $\Sigma_{\text{trans}}(\gamma)$ in the oopt rotation plane is, despite the decreased signal to noise ratio, similar to $\Sigma_{\text{trans}}(\beta)$ in the oopj rotation plane. This also includes, that $\rho_{\text{trans}}(\gamma)$ and $\Sigma_{\text{trans}}(\gamma)$ exhibit an inverted angular evolution. For a maximum in $\rho_{\text{trans}}(\gamma)$ we find a minimum in $\Sigma_{\text{trans}}(\gamma)$ and vice versa.

The aim of our measurements is to extract a quantitative description of the resistivity and Seebeck tensor including effects from the magnetization orientation. In order to investigate the influence of magnetic anisotropy, we have carried out measurements of the longitudinal and transverse resistivity (thermopower) at three distinct external magnetic fields $\mu_0 H_{\text{meas}} = 1 \text{ T}$, $\mu_0 H_{\text{meas}} = 0.5 \text{ T}$, and $\mu_0 H_{\text{meas}} = 0.1 \text{ T}$, the last two are not shown here. To reflect the magnetic anisotropy in our model we used the following description of the free enthalpy

$$G_{M,(001)}(\mathbf{m}) = -\mu_0 H(\mathbf{h} \circ \mathbf{m}) + B_{001}(\mathbf{m}_z)^2 + B_{110} \frac{1}{2}(\mathbf{m}_x + \mathbf{m}_y)^2 + B_{c,x} \mathbf{m}_x^4 + B_{c,y} \mathbf{m}_y^4 + B_{c,z} \mathbf{m}_z^4. \quad (3.70)$$

Following the process described in Sect. 3.3.1.6 and using the LabVIEW based simulation, we optimized the set of anisotropy (B_{001} , B_{110} , $B_{c,x}$, $B_{c,y}$, $B_{c,z}$), resistivity (Eqs.(3.42,3.43)) and Seebeck (Eqs.(3.45,3.46)) parameters until we achieved a satisfactory agreement between simulation and experiment [235]. During this optimization process we only allowed $\rho_{0,110}$ and $\Sigma_{0,110}$ to depend on the magnetic field strength.

For the thin film investigated here, we found for the magnetic anisotropy parameters $B_{001} = 83 \text{ mT}$, $B_{110} = 10 \text{ mT}$, and $B_{c,x} = B_{c,y} = B_{c,z} = -12 \text{ mT}$. The resistivity and Seebeck parameters are summarized for $\mu_0 H = 1 \text{ T}$ in Table 3.2. The red lines in Fig. 3.19(b),(c),(e),(f),(h),(i) represent the simulation results obtained with these parameters, which reproduce nicely the measured data. We note, that we are not able to determine $\rho_{9,110}$, $\Sigma_{9,110}$, and $\Sigma_{A,110}$, as they vanish for all 3 rotation planes used in the experiment [235].

From our series expansion of the resistivity and Seebeck tensor in powers of \mathbf{m} in Sect. 3.3.1 we found that we expect additional contributions in the thermopower due to the Onsager relation, which are described by the parameters $\Sigma_{A,110}$, $\Sigma_{B,110}$, and $\Sigma_{C,110}$ in Eqs. (3.45,3.46). With the 3 rotation planes used in our experiment we are unable to determine $\Sigma_{A,110}$. But for the ip rotation we expect from the theory an influence of $\Sigma_{C,110}$ on $\Sigma_{\text{trans}}(\alpha)$. Unfortunately the low signal to noise ratio makes a confident extraction impossible. This fact is illustrated by two fits to the data in red and blue in Fig. 3.19(c). The red one represents $\Sigma_{C,110} = 0 \mu\text{V/K}$ and the blue $\Sigma_{C,110} = 4.0 \mu\text{V/K}$. It is evident, that both curves describe the experimental results in a satisfactory way. From this we conclude, that our data provides no clear indicator for the existence of the additional parameter $\Sigma_{C,110}$ compared to the theoretical description of ρ_{trans} , such that we chose $\Sigma_{C,110} = 0$. In case of $\Sigma_{B,110}$ we expect only a contribution in $\Sigma_{\text{trans}}(\alpha)$ for the oopt rotation plane, unfortunately we again face the problem of a low signal to noise ratio, which makes a confident extraction impossible. This becomes visible from the two fits to the data in red $\Sigma_{B,110} = 0 \mu\text{V/K}$ and blue $\Sigma_{B,110} = 4.0 \mu\text{V/K}$ in Fig. 3.19(i). As it is

parameter ADMR		parameter ADMS	
$\rho_{0,110}$ ($\mu\Omega\text{m}$)	237.9	$\Sigma_{0,110}$ ($\mu\text{V}/\text{K}$)	152.2
$\rho_{1,110}/\rho_{0,110}$	2.8×10^{-3}	$\Sigma_{1,110}/\Sigma_{0,110}$	3.7×10^{-2}
$\rho_{2,110}/\rho_{0,110}$	1.4×10^{-2}	$\Sigma_{2,110}/\Sigma_{0,110}$	2.4×10^{-2}
$\rho_{3,110}/\rho_{0,110}$	-4.4×10^{-3}	$\Sigma_{3,110}/\Sigma_{0,110}$	1.6×10^{-2}
$\rho_{4,110}/\rho_{0,110}$	4.6×10^{-3}	$\Sigma_{4,110}/\Sigma_{0,110}$	2.0×10^{-3}
$\rho_{5,110}/\rho_{0,110}$	-8.4×10^{-3}	$\Sigma_{5,110}/\Sigma_{0,110}$	1.2×10^{-2}
$\rho_{6,110}/\rho_{0,110}$	5.8×10^{-2}	$\Sigma_{6,110}/\Sigma_{0,110}$	-3.9×10^{-2}
$\rho_{7,110}/\rho_{0,110}$	2.5×10^{-2}	$\Sigma_{7,110}/\Sigma_{0,110}$	2.6×10^{-2}
$\rho_{8,110}/\rho_{0,110}$	0.0	$\Sigma_{8,110}/\Sigma_{0,110}$	0.0
$\rho_{9,110}/\rho_{0,110}$	–	$\Sigma_{9,110}/\Sigma_{0,110}$	–
		$\Sigma_{A,110}$	–
		$\Sigma_{B,110}$	0
		$\Sigma_{C,110}$	0

Table 3.2: Extracted simulation parameters from ADMR and ADMTP measurements for the (001)-oriented (Ga,Mn)As thin film for $\mu_0 H = 1$ T and $T_{\text{avg}} = 25.2$ K

evident from these two curves the additional parameter reflects no increase in fit quality, we therefore chose $\Sigma_{B,110} = 0 \mu\text{V}/\text{K}$ for our simulation.

From the experimental data we already discussed the differences in angular dependency between resistivity and thermopower. These differences are visible in the set of $\rho_{i,110}$ and $\Sigma_{i,110}$ parameters in Table 3.2. The inverted ip angular evolution for ρ_{long} and Σ_{long} results in the opposite sign of $\rho_{3,110}$ compared to $\Sigma_{3,110}$. We also find a sign reversal for $\rho_{5,110}$ and $\Sigma_{5,110}$, which reflects the inverted angular dependence for the oopt rotation plane in Fig. 3.19(h)+(i). The third set of parameters with different sign for resistivity and thermopower are $\rho_{6,110}$ and $\Sigma_{6,110}$, which describe the anomalous and normal Hall/Nernst effect in our sample. This is due to the inverted evolution of ρ_{trans} compared to Σ_{trans} for the two out-of-plane rotation planes. These sign changes between selected parameters in the set of $\rho_{i,110}$ and $\Sigma_{i,110}$, also indicate that it is impossible to use a single scaling factor to transform each $\rho_{i,110}$ to the corresponding $\Sigma_{i,110}$ parameter. This is a direct result of the tensor formulation of the Mott relation in Eq.(3.16).

We can now use the extracted $\rho_{i,110}$ and $\Sigma_{i,110}$ to calculate a part of the tensor components for the resistivity and the Seebeck tensor with the set of equations (3.44) and (3.47). As already pointed out above, this enables us to calculate 10 out of 20 tensor components for the resistivity and 13 out of the 29 parameters for the Seebeck tensors. As our experimental data allows us not to determine $\rho_{9,110}$, $\Sigma_{9,110}$, and $\Sigma_{A,110}$, these numbers are further reduced to 7 for the resistivity and 7 for the Seebeck tensor. The obtained values for the tensor parameters are summarized in Table 3.3. From these calculations we find, that $(\rho^{(2,3,a)} + \rho^{(4,3,a)})$ has the opposite sign as $(\Sigma^{(2,3,a)} + \Sigma^{(4,3,a)})$. This sign reversal is also found in $\rho^{(4,5,a)}$ and $\Sigma^{(4,5,a)}$. As already discussed in Sect. 3.3.1.3 we are not able to determine all components of the tensors in the (001)-oriented (Ga,Mn)As thin film. Thus, we can not use the Mott relation (Eq.(3.16)) and invert the resistivity tensor to calculate the energy derivative of the conductivity at the Fermi energy for the (001)-oriented (Ga,Mn)As thin film. These limitations can be circumvented by carrying out the same experiments in (113)-oriented (Ga,Mn)As (cf. Sect. 3.3.1.3).

parameter resistivity	($\mu\Omega\text{m}$)	parameter Seebeck	($\mu\text{V}/\text{K}$)
$(\rho^{(0,a)} + \rho^{(2,1,a)} + \rho^{(4,1,a)})$	235.0	$(\Sigma^{(0,a)} + \Sigma^{(2,1,a)} + \Sigma^{(4,1,a)})$	150.8
$(\rho^{(1,a)} + \rho^{(3,1,a)})$	13.8	$(\Sigma^{(1,a)} + \Sigma^{(3,1,a)})$	–
$(\rho^{(2,2,a)} + \rho^{(4,2,a)})$	4.9	$(\Sigma^{(2,2,a)} + \Sigma^{(4,2,a)})$	6.5
$(\rho^{(2,3,a)} + \rho^{(4,3,a)})$	-0.4	$(\Sigma^{(2,3,a)} + \Sigma^{(4,3,a)})$	2.5
$(\rho^{(2,4,a)} + \rho^{(4,4,a)})$	–	$(\Sigma^{(2,4,a)} + \Sigma^{(4,4,a)})$	–
$\rho^{(3,2,a)}$	0	$\Sigma^{(3,2,a)}$	–
$\rho^{(4,5,a)}$	1.1	$\Sigma^{(4,5,a)}$	-2.5
$\rho^{(4,6,a)}$	–	$\Sigma^{(4,6,a)}$	–
$\rho^{(4,7,a)}$	-1.0	$\Sigma^{(4,7,a)}$	-0.7
$\rho^{(4,8,a)}$	–	$\Sigma^{(4,8,a)}$	–
		$\Sigma^{(3,3,a)}$	–
		$\Sigma^{(3,4,a)}$	0
		$\Sigma^{(4,9,a)}$	0

Table 3.3: Extracted tensor parameters from ADMR and ADMTP measurements for the (001)-oriented (Ga,Mn)As thin film for $\mu_0 H = 1$ T and $T_{\text{avg}} = 25.2$ K

3.3.2.3 ADMR and ADMTP for (113)-oriented (Ga,Mn)As

From the previous experiments on (001)-oriented (Ga,Mn)As thin films, we can state that our series expansion model is perfectly suited to describe the observed angular dependence of resistivity and thermopower. Unfortunately, we could not find substantial evidence for the additional parameters in the Seebeck tensor, which are created by the lower number of restrictions from the Onsager relations compared to the resistivity tensor. This was mainly caused by the low signal to noise ratio of our experimental thermopower signal. Moreover, the selected projection plane of (001)-oriented (Ga,Mn)As is not suited to extract the full resistivity and Seebeck tensor. Both problems can be solved by using (113)-oriented (Ga,Mn)As. For this orientation we already pointed out in Section 3.3.1, that it is in principle possible to extract the full tensor description by applying an electrical current/thermal gradient along two perpendicular directions.

As a first step towards the determination of the full tensor description, we carried out ADMR and ADMTP experiments on the (113)-oriented, 30 nm thick (Ga_{0.95}Mn_{0.05})As film grown via LT-MBE on a (113)A-oriented GaAs substrate in the same fashion as in Sect. 3.3.2.2. For the ADMR and ADMTP experiments we applied a fixed current to the resistive heater ($P_{\text{heater}} = 160$ mW) of our setup, establishing a fixed average temperature $T_{\text{avg}} = 25.0$ K and gradient $\nabla T = 0.6$ K/mm determined from on-chip thermometry. For the experiments we used the following three distinct rotation planes for the external magnetic field: in-plane (ip, Fig. 3.20(a)), out-of-plane perpendicular to $\hat{\mathbf{j}}$ (oopj, Fig. 3.20(d)), and out-of-plane perpendicular to $\hat{\mathbf{t}}$ (oopt, Fig. 3.20(g)). For the experiments we used $\mu_0 H_{\text{init}} = 3$ T) at a fixed field orientation ($\alpha = 0^\circ$ for ip and $\beta, \gamma = -90^\circ$ for oopj, oopt). The ADMR and ADMTP experiments were evaluated in analogy to Sect. 3.3.2.2. The results obtained for ADMR and ADMTP experiments at an external magnetic field of $\mu_0 H = 1$ T are summarized in Fig. 3.20(a)-(i)

In Fig. 3.20(b) we show the results of ip ADMR experiments. For the ip geometry it is safe to assume, that the magnetization directly follows the external field orientation. The origin of the observed angular dependence in ρ_{long} and ρ_{trans} is the AMR of the ferromag-

netic semiconductor. For the longitudinal resistivity we find a two fold symmetry and $\rho_{\parallel} < \rho_{\perp}$, which is consistent with the data obtained from the (001)-oriented (Ga,Mn)As film (Sect. 3.3.2.2) and with [236]. The transverse resistance shows no inherent symmetry over the full 360° rotation, this is evident from the different absolute values of the maxima and minima of the curve, which has been already reported in [236].

In comparison, the angular dependence of the longitudinal and transverse thermopower from the ip ADMTP measurements in Fig. 3.20(c) exhibits remarkable differences to the ADMR measurements. $\Sigma_{\text{long}}(\alpha)$ is not two fold symmetric as $\rho_{\text{long}}(\alpha)$, due to the different absolute values of the minima in $\Sigma_{\text{long}}(\alpha)$, as a direct result the longitudinal thermopower for $\mathbf{m} \parallel \mathbf{t}$ is larger than for $\mathbf{m} \parallel -\mathbf{t}$. This effect can be understood within our series expansion model and will be discussed below. Moreover, we find that $\Sigma_{\parallel} > \Sigma_{\perp}$, meaning that $\rho_{\text{long}}(\alpha)$ and $\Sigma_{\text{long}}(\alpha)$ are inverted in their angular dependence, a result that we have also obtained for the (001)-oriented sample in Sect. 3.3.2.2. In contrast, $\Sigma_{\text{trans}}(\alpha)$ is not inverted in the angular dependence compared to $\rho_{\text{trans}}(\alpha)$, but the asymmetry in absolute values is more pronounced for the transverse thermopower, such that the only visible maximum is around $\alpha = 135^{\circ}$ and visible minimum is around $\alpha = 225^{\circ}$, whereas the minimum at $\alpha = 45^{\circ}$ and maximum at $\alpha = 315^{\circ}$ in $\rho_{\text{trans}}(\alpha)$ have vanished into a plateau at $\alpha = 0^{\circ}$ for the transverse thermopower.

For the ADMR experiments in the oopj rotation plane in Fig. 3.20(e) $\rho_{\text{long}}(\beta)$ exhibits a two fold symmetry with minima at \mathbf{h} parallel or antiparallel to \mathbf{t} and maxima at \mathbf{h} parallel or antiparallel to \mathbf{n} . The evolution of $\rho_{\text{trans}}(\beta)$ follows a cosine dependence, with a maximum for $\mathbf{h} \parallel \mathbf{n}$ and a minimum for $\mathbf{h} \parallel -\mathbf{n}$. This angular dependence of ρ_{trans} indicates the domination of normal and anomalous Hall effect in (Ga,Mn)As.

We compare these ADMR measurements with the ADMTP experiments in oopj geometry (Fig. 3.20(f)). The longitudinal thermopower exhibits no symmetry for a full rotation, which is visible in the different absolute values of maxima and minima of $\Sigma_{\text{long}}(\beta)$. Interestingly, we observe no exchange of the position of maxima and minima when we compare $\Sigma_{\text{long}}(\beta)$ with $\rho_{\text{long}}(\beta)$, which is identical to the ADMR and ADMTP experiments on the (001)-oriented sample. The angular dependence of the transverse thermopower exhibits a minimum for $\beta = 10^{\circ}$ and a maximum for $\beta = 170^{\circ}$, this suggests that the position of maximum and minimum have shifted away from $\mathbf{h} \parallel \mathbf{n}$ and $\mathbf{h} \parallel -\mathbf{n}$ compared to $\rho_{\text{trans}}(\beta)$. Moreover, a plateau in $\Sigma_{\text{trans}}(\beta)$ is visible at $\beta = -90^{\circ}$, which is not the case for $\rho_{\text{trans}}(\beta)$. These differences between $\rho_{\text{trans}}(\beta)$ and $\Sigma_{\text{trans}}(\beta)$ are reflected in the modeling of the ADMR and ADMTP experiments, which we will further discuss below.

For the oopt rotation plane ADMR experiments in Fig. 3.20(h), we observe a two fold symmetry of $\rho_{\text{long}}(\gamma)$. The longitudinal resistivity shows maxima for $\gamma = -10^{\circ}$ and $\gamma = 170^{\circ}$, and minima for $\gamma = 80^{\circ}$ and $\gamma = 265^{\circ}$. One should note that these γ values no longer coincidence with any coordinate axes defined by \mathbf{j} , \mathbf{t} , and \mathbf{n} . For the transverse resistivity we find again a normal and anomalous Hall effect domination characterized by a cosine dependence. The ADMTP experiments in oopt geometry yield a angular dependence in Σ_{long} that is inverted compared to ρ_{long} , this behavior has been also observed in the ADMR and ADMTP experiments on the (001)-oriented sample presented in Sect.3.3.2.2. The minima of $\Sigma_{\text{long}}(\gamma)$ have different absolute values. For $\Sigma_{\text{trans}}(\gamma)$ the angular evolution is inverted compared to $\rho_{\text{trans}}(\gamma)$.

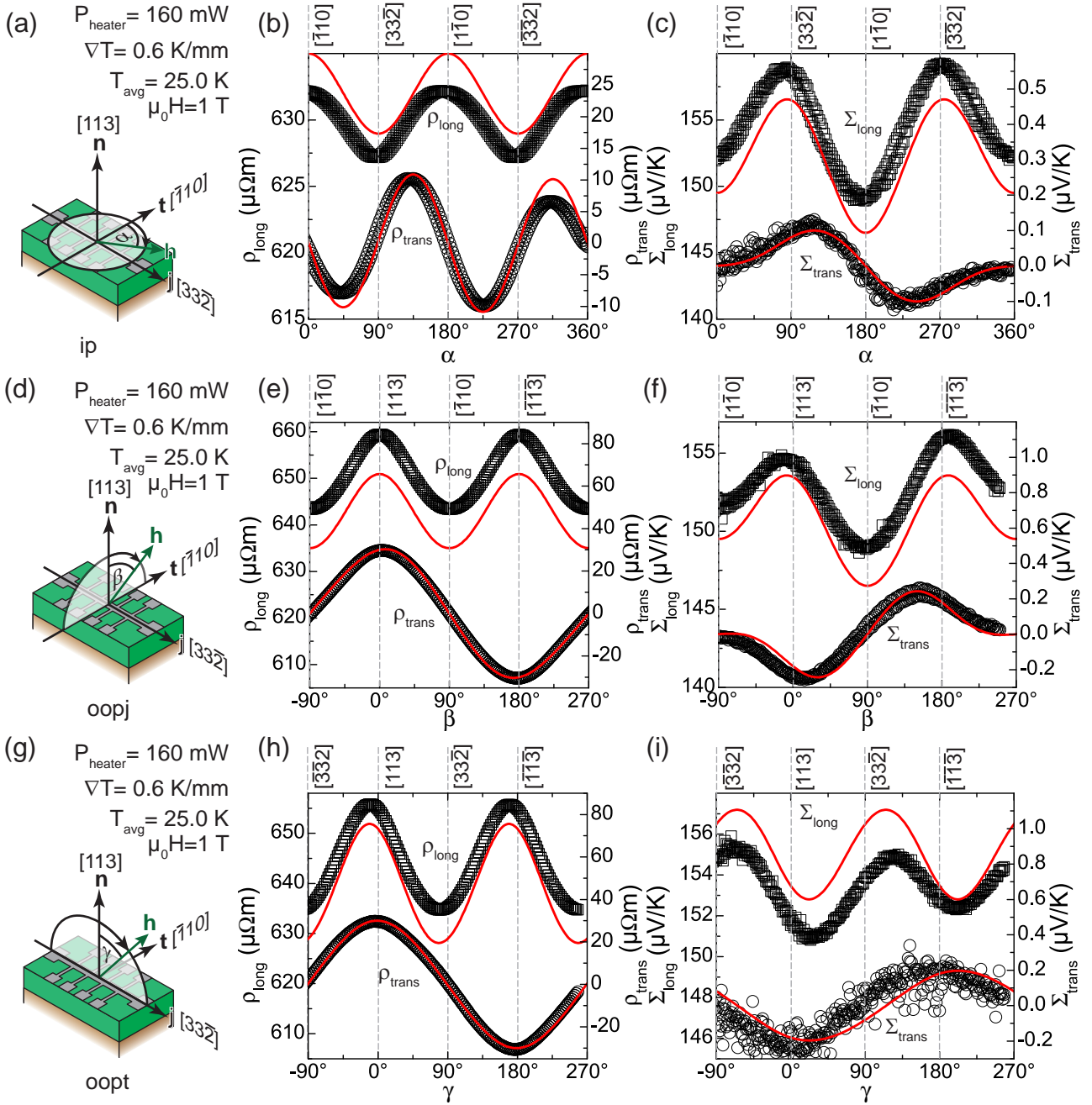


Figure 3.20: Results obtained from ADMR and ADMTP experiments on a 30 nm thick (113)-oriented $(\text{Ga}_{0.95}, \text{Mn}_{0.05})\text{As}$ sample at $T_{\text{avg}} = 25.0 \text{ K}$ and $\mu_0 H = 1 \text{ T}$. (a) Illustration of the ip rotation plane of the external field direction \mathbf{h} in the coordinate system defined by $\hat{\mathbf{j}}$, $\hat{\mathbf{t}}$, and $\hat{\mathbf{n}}$. The arrow indicates the direction for a positive rotation angle α . (b) Angular dependence of ρ_{long} and ρ_{trans} for an ip rotation of the external magnetic field. (c) Evolution of Σ_{long} and Σ_{trans} for an ip rotation. (d) Illustration of the oopj rotation plane and definition of positive rotation angle β . Oopj rotation results for ρ_{long} and ρ_{trans} (e) and Σ_{long} and Σ_{trans} (f). (g) Definition of the oopt rotation plane with positive rotation angle γ . (h) Angular dependence of ρ_{long} and ρ_{trans} for oopt rotation. (i) $\Sigma_{\text{long}}(\alpha)$ and $\Sigma_{\text{trans}}(\alpha)$ for an oopt rotation. Symbols represent experimental data and red lines fits via Eqs.(3.52,3.49) and Eqs.(3.56,3.57) with a single set of parameters.

Following the same procedure as for the (001)-oriented sample we used the following equation to describe the magnetic anisotropy within our free enthalpy formulation:

$$G_{M,(113)}(\mathbf{m}) = -\mu_0 H(\mathbf{h} \circ \mathbf{m}) + B_{001}(\mathbf{m}_z)^2 + B_{110} \frac{1}{2}(\mathbf{m}_x + \mathbf{m}_y)^2 + B_{113} \frac{1}{11}(\mathbf{m}_x + \mathbf{m}_y + 3\mathbf{m}_z)^2 + B_{c,x} \mathbf{m}_x^4 + B_{c,y} \mathbf{m}_y^4 + B_{c,z} \mathbf{m}_z^4. \quad (3.71)$$

Using the Eqs.(3.52,3.49) and Eqs.(3.56,3.57) and iteratively optimizing our set of parameters for $\mu_0 H = 1$ T, $\mu_0 H = 500$ mT, and $\mu_0 H = 100$ mT (Sect. 3.3.1.6. From this process we obtained the magnetic anisotropy parameters $B_{c,x} = B_{c,y} = -5$ mT, $B_{c,z} = -3$ mT, $B_{001} = -10$ mT, $B_{110} = -2$ mT, and $B_{113} = 35$ mT. The final $\rho_{i,33\bar{2}}$ and $\Sigma_{i,33\bar{2}}$ parameters are summarized in Table 3.4 and the results of our simulation are depicted as red lines in Fig. 3.20(b), (c), (e), (f), (h), (i). The red lines reproduce the measured data very well and are able to reflect the angular dependence found in the resistivity and thermopower. The observed offset between simulation curve and data in the longitudinal signals originates from small deviations of the sample temperature for the three different rotation planes, as for each rotation plane the sample has to be remounted onto the dipstick.

parameter ADMR		parameter ADMS	
$\rho_{0,33\bar{2}}$ ($\mu\Omega\text{m}$)	635.0	$\Sigma_{0,33\bar{2}}$ ($\mu\text{V}/\text{K}$)	148.0
$\rho_{1,33\bar{2}}/\rho_{0,33\bar{2}}$	-9.4×10^{-3}	$\Sigma_{1,33\bar{2}}/\Sigma_{0,33\bar{2}}$	5.7×10^{-2}
$\rho_{2,33\bar{2}}/\rho_{0,33\bar{2}}$	1.4×10^{-2}	$\Sigma_{2,33\bar{2}}/\Sigma_{0,33\bar{2}}$	2.2×10^{-2}
$\rho_{3,33\bar{2}}/\rho_{0,33\bar{2}}$	2.5×10^{-2}	$\Sigma_{3,33\bar{2}}/\Sigma_{0,33\bar{2}}$	3.7×10^{-2}
$\rho_{4,33\bar{2}}/\rho_{0,33\bar{2}}$	7.9×10^{-4}	$\Sigma_{4,33\bar{2}}/\Sigma_{0,33\bar{2}}$	5.4×10^{-4}
$\rho_{5,33\bar{2}}/\rho_{0,33\bar{2}}$	4.7×10^{-2}	$\Sigma_{5,33\bar{2}}/\Sigma_{0,33\bar{2}}$	-1.2×10^{-3}
$\rho_{6,33\bar{2}}/\rho_{0,33\bar{2}}$	-3.3×10^{-2}	$\Sigma_{6,33\bar{2}}/\Sigma_{0,33\bar{2}}$	-4.7×10^{-4}
$\rho_{7,33\bar{2}}/\rho_{0,33\bar{2}}$	6.3×10^{-3}	$\Sigma_{7,33\bar{2}}/\Sigma_{0,33\bar{2}}$	1.4×10^{-3}
		$\Sigma_{A,33\bar{2}}$	1.0×10^{-2}

Table 3.4: Extracted simulation parameters from ADMR and ADMTP measurements for the (113)-oriented (Ga,Mn)As thin film for $\mu_0 H = 1$ T and $T_{\text{avg}} = 25.0$ K

Comparing the $\rho_{i,33\bar{2}}$ with the $\Sigma_{i,33\bar{2}}$ parameters, we find a sign change in the following two parameter pairs: $\rho_{1,33\bar{2}}$ and $\Sigma_{1,33\bar{2}}$, $\rho_{5,33\bar{2}}$ and $\Sigma_{5,33\bar{2}}$. The sign change between $\rho_{1,33\bar{2}}$ and $\Sigma_{1,33\bar{2}}$ reflects the inversion between longitudinal resistivity and thermopower for the ip and oopt rotation planes. The observed inversion of angular dependence between transverse resistivity and thermopower is accounted by the sign change between $\rho_{5,33\bar{2}}$ and $\Sigma_{5,33\bar{2}}$. The additional parameter in the thermopower model $\Sigma_{A,33\bar{2}} = 1.5 \mu\text{V}/\text{K}$ is in contrast to the simulation results for the (001)-oriented sample an important parameter, that describes the different absolute values of the minima in the longitudinal thermopower for the ip (Fig. 3.20(c)) and oopj (Fig. 3.20(f)) rotation plane. These findings make it impossible to neglect this additional parameter in the thermopower simulation, thus our experimental data and the corresponding simulation approve that our assumptions for the development of the series expansion model are correct. Unfortunately the difference in absolute value found in the maxima of Σ_{long} for the ip, oopj and in the minima/maxima in the oopt rotation plane are not accounted by any of our parameters. We attribute these differences to an additional transverse thermopower signal superimposed onto the

longitudinal thermopower signal or a possible tilting of the rotation planes in the experiment.

Moreover, it is impossible to find a universal scaling constant that translates all $\rho_{i,33\bar{2}}$ to their corresponding $\Sigma_{i,33\bar{2}}$, which supports the assumption of a tensor Mott relation (Eq.(3.16)).

We calculate the components of the resistivity and Seebeck tensor using Eqs.(3.50) and Eqs.(3.58) respectively. The results of this calculation are summarized in Table 3.5. From the linear relation for the resistivity parameters we extracted a linear restriction for the $\rho_{i,33\bar{2}}$ parameters given by Eq.(3.51). If we use the parameters extracted from our experiment we obtain for the LHS $2.425 \mu\Omega\text{m}$ and for the RHS $2.421 \mu\Omega\text{m}$, the values differ only by 6×10^{-3} from each other. Thus we assume that our extracted parameters fulfill the imposed linear restriction, which further supports, that our underlying model is capable of describing the various effects found in ADMR and ADMTP experiments.

parameter resistivity	($\mu\Omega\text{m}$)	parameter Seebeck	($\mu\text{V}/\text{K}$)
$(\rho^{(0,a)} + \rho^{(2,1,a)})$	–	$(\Sigma^{(0,a)} + \Sigma^{(2,1,a)})$	–
$(\rho^{(0,c)} + \rho^{(2,1,c)})$	–	$(\Sigma^{(0,c)} + \Sigma^{(2,1,c)})$	–
$\rho^{(1,a)}$	29.8	$\Sigma^{(1,a)}$	-0.22
$\rho^{(1,c)}$	31.1	$\Sigma^{(1,c1)}$	-0.01
$\rho^{(2,2,a)}$	-19.1	$\Sigma^{(2,2,a)}$	0.02
$\rho^{(2,2,c)}$	–	$\Sigma^{(2,2,c)}$	–
$\rho^{(2,3,a)}$	1.8	$\Sigma^{(2,3,a)}$	11.2
$\rho^{(2,3,c)}$	-29.4	$\Sigma^{(2,3,c1)}$	-0.49
$\rho^{(2,4,a)}$	–	$\Sigma^{(2,4,a)}$	–
		$\Sigma^{(1,c2)}$	3.9
		$\Sigma^{(2,3,c2)}$	1.2

Table 3.5: Extracted tensor parameters from ADMR and ADMTP measurements for the (113)-oriented (Ga,Mn)As thin film for $\mu_0 H = 1 \text{ T}$ and $T_{\text{avg}} = 25.0 \text{ K}$

Our extracted $\rho_{i,33\bar{2}}$ and $\Sigma_{i,33\bar{2}}$ parameters, allow us to calculate 5 of a total of 9 and 7 of a total of 11 components of the resistivity and Seebeck tensor respectively. This represents the first successful step to a full description of the resistivity and Seebeck tensor for a (113)-oriented (Ga,Mn)As sample, under the assumption of a tetragonal symmetry. Due to the limited amount of available samples and time, we were unable to conduct further experiments with electrical current/thermal gradient along the $[\bar{1}10]$ -direction on an identical sample. In the future such experiments could be carried out after the improvement of the caloritronic measurement setup is finished [254]. Nevertheless, these calculations allow us to directly compare selected components of resistivity and Seebeck tensor with each other and even with the components obtained from the (001)-oriented sample.

A comparison of the tensor components for the (113)-oriented sample shows that $\rho^{(1,a)}$ and $\Sigma^{(1,a)}$ are different in sign. Moreover, for the calculated Seebeck components $\Sigma^{(2,3,a)}$ is the largest contribution, in contrast there are 3 components $\rho^{(1,a)}$, $\rho^{(1,c)}$, and $\rho^{(2,3,c)}$ that are largest in their absolute value. In addition, it is not possible to translate the resistivity tensor components into the corresponding Seebeck components using a single scaling factor, supporting our tensor description of the Mott relation Eq.(3.16).

A comparison between identical tensor components for the (001)- and (113)-oriented sample reveals that for example the value of the $\rho^{(1,a)}$ component changes from $13.8 \mu\Omega\text{m}$ for the (001)-oriented to $29.8 \mu\Omega\text{m}$ for the (113)-oriented sample. This holds also for other components for both the resistivity and Seebeck tensor. Whether this change in components can be attributed to the difference in Mn concentration, or in differences in strain states for the two different orientations, or a combination of both, is not possible to determine from these experiments on single samples. But the results emphasize, that it is important to use for the extraction of the full resistivity and Seebeck tensors a set of samples from the very same wafer from one growth run to exclude these influences.

In summary, our results obtained for (001)-oriented and (113)-oriented (Ga,Mn)As demonstrate, that the model proposed for the description of ADMR and ADMTP experiments is suited to reproduce the measured data. We would like to stress that while the ADMR series expansion model is already known in literature [236], the ADMTP series expansion is a new approach investigated by this thesis. Moreover, the results proof, that we are in principle able to extract the full tensor description of resistivity and thermopower from a (113)-oriented (Ga,Mn)As sample, if we use the two perpendicular in-plane directions, $[3\bar{3}2]$ and $[\bar{1}10]$, as directions for the applied electrical current and thermal gradient. We note that recent publications report the successful applications of the series expansion model to extract the resistivity parameters in (113)-oriented (Ga,Mn)As for an electrical current along the $[\bar{1}10]$ direction [255] and the $[3\bar{3}2]$ direction [236]. These reports pave the way for an extraction of the full resistivity and Seebeck tensors for a (113)-oriented (Ga,Mn)As.

The on-chip thermometry used to determine the thermal gradient on the sample, is an elegant way to directly quantify the local thermal evolution on the sample. The results from these experiments show, that the thermal coupling between cold/hot base and the sample itself needs improvement. In the future such an improvement of the setup could be achieved by introducing a new dip-stick system where the sample is placed in vacuum and not in the He gas flow [254]. Moreover, the the thermal coupling between base and sample could be increased by using a mechanical clamping technique.

3.3.3 Magnetoresistance in Heusler compound thin films

Our results obtained for (Ga,Mn)As thin films proved that our proposed resistivity and thermopower model is capable to describe the angular dependence observed in ADMR and ADMTP experiments. The assumptions used for the development of the model are universal and not limited to a particular material system. In the framework of the provided theory, we also carried out ADMR and ADMTP experiments on Cobalt-based Heusler compound thin films, as discussed in the following.

For our experiments we use the Cobalt-based Heusler compound Co_2FeAl (CFA) as up to now only a qualitative analysis of the magnetoresistance and magnetic anisotropy is available in literature [182, 256]. A more profound quantitative analysis of these effects allows to directly compare experimental results with theoretical calculations. Recent publications already verified an application of the series expansion model to the ADMR of Fe_3Si [237, 257–259]. Based on these promising results we focused in our experiments on the extraction of resistivity and magnetic anisotropy parameters of CFA thin films as a function of temperature.

The samples we have investigated were grown at the university of Bielefeld by Inga-

Mareen Imort. CFA thin films were deposited on (001)-oriented MgO substrates via magnetron sputtering at room temperature. The base pressure of the chamber was 1×10^{-7} mbar, during deposition an Ar atmosphere of 1.5×10^{-3} mbar was maintained. Prior to deposition of the CFA film a 5 nm thick MgO buffer layer was sputtered onto the substrate [260]. Then the CFA thin film was sputtered onto the buffer layer at room temperature. Afterwards the CFA thin films were annealed in-situ at 500 °C for 1 h, which leads to a single crystalline CFA thin film in the B2 structure. To protect the film from oxidation a 1.2 nm thick MgO layer was sputtered in-situ onto the sample as a capping layer. In the following, we present data obtained from a set of samples with different CFA film thicknesses: 20 nm, 50 nm, 80 nm, and 100 nm. Using optical lithography and argon ion beam milling, the films were patterned into Hall bar structures with the current path along the CFA [110]-direction for electrical characterization. Each sample was then mounted onto a custom built sample holder and electrically contacted via Al wire wedge bonding (More details can be found in the diploma thesis of A. Krupp [192]). The samples were then placed into an Oxford Spectromag 4000 magnet cryostat system equipped with a stepper motor to freely adjust the orientation between sample and external magnetic field. The sample holder in combination with the dip stick enabled us to rotate the external magnetic field in three different planes: ip (Fig. 3.21(a)), oopj (Fig. 3.21(d)), and oopt (Fig. 3.21(g)). In analogy to Section 3.3.2 we used ADMR experiments for the quantitative extraction of resistivity and magnetic anisotropy parameters. Here we used $\mu_0 H_{\text{init}} = 3$ T at $\alpha = 0^\circ$ (ip), $\beta, \gamma = 270^\circ$ (oopj and oopt).

In the following we present the ADMR data obtained for a 50 nm thick (001)-oriented Co_2FeAl film at $T = 10$ K, the results are collected in Fig. 3.21(a)-(i).

For an ip rotation (Fig. 3.21(a)) at $\mu_0 H = 1$ T the magnetization directly follows the rotation of the external field such that $\mathbf{m} \parallel \mathbf{h}$. The angular dependence of the longitudinal resistivity in Fig. 3.21(b) exhibits a $\cos^2(\alpha)$ dependence, which is reflected in the dumbbell shape in the polar plot of the ADMR data. Moreover, we find that $\rho_{\parallel} < \rho_{\perp}$ from the position of the maxima and minima. This has been already reported for the Heusler compound Fe_3Si [237] and we also found the same ip magnetization orientation dependence in our (Ga,Mn)As samples. But one should note that this dependence is in contrast to that of classical 3d-ferromagnets, where one finds $\rho_{\parallel} > \rho_{\perp}$ [163, 252]. For ρ_{trans} (Fig. 3.21(c)) at $\mu_0 H = 1$ T the curve exhibits also a dumbbell shape, but compared to ρ_{long} it is rotated by 45° . This is consistent with AMR theory, from which we expect a $\sin(2\alpha)$ dependence. Moreover, the ρ_{trans} curve is asymmetric, with a more pronounced maximum at $\alpha = 225^\circ$ and a less pronounced one at $\alpha = 45^\circ$. This originates from the combination of a non-perfectly oriented ip rotation, i.e. the external field has also an oop component, and the fact that ρ_{trans} is dominated by the AHE and Hall contributions, as will be discussed below. When we reduce the field to $\mu_0 H = 20$ mT the magnetization will not always stay parallel to the external magnetic field, due to the magnetic anisotropy in our sample. This is reflected in ρ_{long} (Fig. 3.21(b)) as abrupt changes located close to $\alpha = 45^\circ$, $\alpha = 135^\circ$, $\alpha = 225^\circ$, and $\alpha = 315^\circ$. These abrupt changes indicate a nearby magnetic hard axis, where the magnetization orientation drastically changes, which then leads to an abrupt change in ρ_{long} . Moreover, around $\alpha = 0^\circ$, $\alpha = 90^\circ$, $\alpha = 180^\circ$, and $\alpha = 270^\circ$ ρ_{long} nearly stays constant, which is equivalent to the fact that the magnetization stays at a fixed orientation. Thus these ranges indicate a nearby easy axis. From the experimental data, we can already extract the existence of two ip easy axes along the [110]- and $[\bar{1}10]$ -direction and two ip hard axes along the [100]- and [010]-direction. This qualitative

description of magnetic anisotropy is substantiated by the quantitative extraction of anisotropy parameters discussed below. In contrast, the influence of magnetic anisotropy is for ρ_{trans} (Fig. 3.21(c)) only weakly visible as abrupt changes at $\alpha = 45^\circ$, $\alpha = 135^\circ$, $\alpha = 225^\circ$, and $\alpha = 315^\circ$.

In case of the oopj rotation plane (Fig. 3.21(d)) we again observe a dumbbell shaped curve for ρ_{long} at $\mu_0 H = 3 \text{ T}$ in Fig. 3.21(e). The minima are located at $\beta = 0^\circ$ and $\beta = 180^\circ$, while the maxima are at $\beta = 90^\circ$ and $\beta = 270^\circ$. This means that ρ_{long} is larger for \mathbf{m} parallel or antiparallel to \mathbf{t} than for \mathbf{m} parallel or antiparallel to \mathbf{n} . Compared to our (001)-oriented (Ga,Mn)As sample (Fig. 3.19(e)) the angular dependence has been inverted. For ρ_{trans} and an external field of $\mu_0 H = 3 \text{ T}$ we observe a cosine dependence which is indicated by the heart shaped structure in Fig. 3.21(f). We attribute this angular evolution to the AHE and Hall effect of the sample. Moreover, one finds that $\rho_{\text{trans}} > 0$ for $\mathbf{m} \parallel \mathbf{n}$, compared to literature, where in Cobalt-based Heusler compounds both positive and negative values have been reported [185, 261, 262]. A quantitative comparison between the oscillation amplitude of ρ_{trans} for ip and oopj rotation yields $40 \text{ n}\Omega\text{cm}$ and $1100 \text{ n}\Omega\text{cm}$ respectively. This clearly indicates that the AHE and Hall contributions dominate ρ_{trans} , which explains the asymmetry of ρ_{trans} for the ip rotation due to an imperfect sample alignment⁸. By reducing the field to $\mu_0 H = 1 \text{ T}$ the influence of the large shape anisotropy due to the huge magnetic moment of CFA becomes clearly visible in our ADMR experiments. ρ_{long} and ρ_{trans} both stay at constant values for the large parts of the whole field rotation, only around $\beta = 0^\circ$ and $\beta = 180^\circ$ deviations are visible. This observation is explained by the fact that the magnetization stays for the constant part of the rotation at a fixed orientation in the film plane. At rotation angles near the oop direction, the projection of \mathbf{H} along \mathbf{n} is large enough to align the magnetization partly out-of-plane. These results indicate that the [001]-direction is a magnetic hard axis.

In the last oopt rotation configuration (Fig. 3.21(g)) we obtain for ρ_{long} at $\mu_0 H = 3 \text{ T}$ in Fig. 3.21(h) again a dumbbell shaped curve. But compared to the oopj rotation the curve is rotated by 90° and elongated with maxima located at $\gamma = 0^\circ$ and $\gamma = 180^\circ$. These inversion in angular dependence arises due to the difference in ip and oop AMR contributions to ρ_{long} and will become more visible when comparing the extracted resistivity parameters. For ρ_{trans} (Fig. 3.21(i)) the angular evolution does not change between oopj and oopt rotation, due to the dominance of the AHE and Hall contribution. At a reduced field of $\mu_0 H = 1 \text{ T}$ the influence of the shape anisotropy is clearly visible in ρ_{long} and ρ_{trans} .

⁸From our fit we extracted a tilt angle of 0.014° for the ip rotation axis with respect to the surface normal.

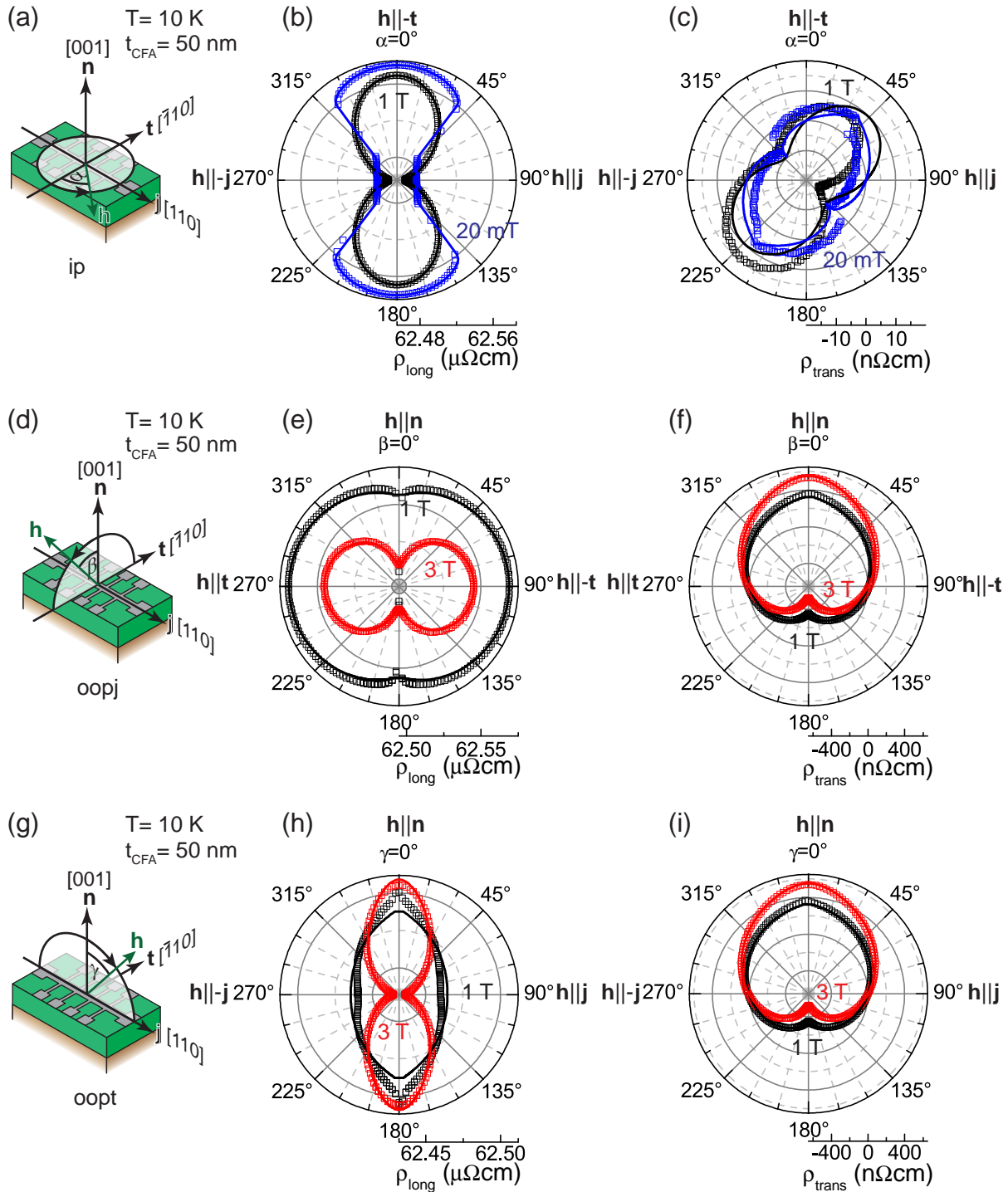


Figure 3.21: Results obtained from ADMR experiments on a 50 nm thick (001)-oriented Co_2FeAl sample at $T = 10$ K. (a) Illustration of the ip rotation plane of the external field direction \mathbf{h} in the coordinate system defined by \hat{j} , \hat{t} , and \hat{n} . The arrow indicates the direction for a positive rotation angle α . Angular dependence of ρ_{long} (b) and ρ_{trans} (c) obtained for an ip rotation of the external magnetic field at $\mu_0 H = 1$ T (black) and $\mu_0 H = 20$ mT (blue). (d) Schematic drawing to illustrate the oopj rotation plane and define the positive rotation angle β . ADMR results in oopj configuration for ρ_{long} (e) and ρ_{trans} (f) at $\mu_0 H = 1$ T (black) and $\mu_0 H = 3$ T (red). (g) Definition of the oopt rotation plane with positive rotation angle γ . Angular dependence of ρ_{long} (h) and ρ_{trans} (i) for a rotation executed in oopt orientation at $\mu_0 H = 1$ T (black) and $\mu_0 H = 3$ T (red). Symbols represent experimental data and lines corresponding fits via Eqs.(3.42) and (3.43).

For the quantitative extraction of resistivity and anisotropy parameters, we used the following expression for the free enthalpy:

$$G_{M,(001)CFA}(\mathbf{m}) = -\mu_0 H(\mathbf{h} \circ \mathbf{m}) + B_{001}(\mathbf{m}_z)^2 + B_{110} \frac{1}{2}(\mathbf{m}_x + \mathbf{m}_y)^2 + B_c(\mathbf{m}_x^4 + \mathbf{m}_y^4 + \mathbf{m}_z^4). \quad (3.72)$$

Here, B_{001} represents an oop uniaxial anisotropy, a combination of contributions from shape and intrinsic anisotropy, B_{110} an in-plane uniaxial anisotropy and B_c a cubic anisotropy. Due to the lattice mismatch between substrate and film, we expect that the intrinsic cubic symmetry of CFA is reduced to a tetragonal symmetry due to strain effects. We thus used Eqs.(3.42) and (3.43) to calculate ρ_{long} and ρ_{trans} from the magnetization orientation. In order to reduce the number of resistivity parameters we only included parameters up to the second order of \mathbf{m} , which reduces the set of parameters to $\{\rho_{0,110}, \rho_{1,110}, \rho_{2,110}, \rho_{6,110}, \rho_{7,110}\}$ ⁹. To fit the experimental data we optimized the set of parameters until a satisfactory agreement between simulation and experiment was achieved (cf. Sect. 3.3.1.6). The only field dependent parameter was ρ_0 , while all other parameters were kept constant for all field strengths. We note that the number of parameters is further reduced due to vanishing projections of \mathbf{m} for selected rotation planes. The obtained fits are represented as colored lines in Fig. 3.21(b), (c), (e), (f), (h), (i). The perfect agreement between simulation and experiment verifies the validity of our proposed model for the Cobalt-based Heusler compound CFA.

We have carried out ADMR experiments for all 4 CFA samples (20 nm, 50 nm, 80 nm, 100 nm) at various temperatures $T \in \{10 \text{ K}, 50 \text{ K}, 100 \text{ K}, 150 \text{ K}, 200 \text{ K}, 250 \text{ K}, 300 \text{ K}, 350 \text{ K}\}$. For all samples and temperatures we fitted the data with our model and extracted a set of anisotropy and resistivity parameters. The results of this procedure are summarized in Fig. 3.22.

For all thicknesses the resistivity parameter ρ_0 (Fig. 3.22(a)), which is the only contribution to ρ_{long} that is independent of magnetization orientation, reflects the typical temperature dependence for metallic conduction: with increasing temperature the resistivity increases and at low temperatures the resistivity approaches a residual value. This metallic temperature dependence has already been reported by other groups for Cobalt-based Heusler compounds [256]. Comparing the absolute values of ρ_0 for the different thicknesses, we find that the 20 nm and 50 nm thick CFA film resistivity parameter are identical, but the 80 nm and 100 nm thick films slightly deviate. These differences might be attributed to diverging relaxation of strain for the variable thicknesses. As already mentioned above, ρ_0 was the only field dependent resistivity parameter in our simulation. As an example we show ρ_0 as a function of the external magnetic field for the 50 nm thick sample at $T = 10 \text{ K}$ in Fig. 3.22(c). The resistivity parameter exhibits negative magnetoresistance as ρ_0 decreases with increasing field.

The remaining 4 \mathbf{m} dependent resistivity parameters are up to 3 orders of magnitude smaller than ρ_0 . For all thicknesses investigated the temperature dependence in each resistivity parameter is qualitatively identical, but they differ in their absolute values. The parameter ρ_1 , representing the in-plane AMR, is negative for all thicknesses and temperatures and thus reflects that the longitudinal resistance for $\mathbf{j} \parallel \mathbf{m}$ is smaller than for $\mathbf{j} \perp \mathbf{m}$. With increasing temperature the magnitude of this parameter decreases. The out-of-plane AMR parameter ρ_2 is also negative for all temperatures and thicknesses

⁹In the following we omit the 110 in the index of the resistivity parameters.

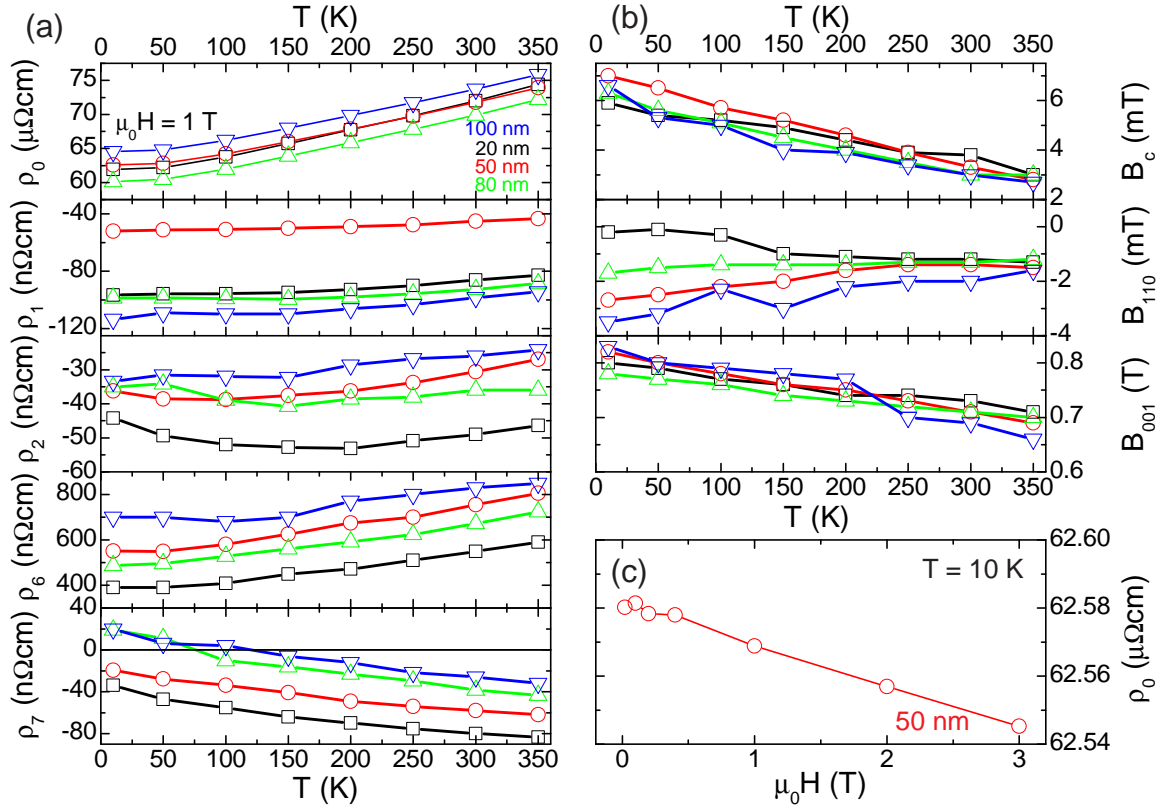


Figure 3.22: (a) Extracted resistivity parameters as a function of temperature for 4 CFA thin films with 20 nm (black), 50 nm (red), 80 nm (green), and 100 nm (blue) thickness. (b) Temperature dependence of the magnetic anisotropy parameters B_c , B_{110} , and B_{001} extracted from the ADMR experiments. (c) Field dependence of ρ_0 observed at $T = 10$ K for a 50 nm thick Co_2FeAl film. The lines are guides to the eye.

investigated and differs from ρ_1 , which is a result of the single crystalline structure of the samples. In addition, one can clearly see, that the anomalous Hall effect, represented by ρ_6 , is one order of magnitude larger than the other magnetization orientation dependent resistivity parameters, thus dominating the contributions to the transverse resistivity. Moreover, ρ_6 increases with higher temperatures. An interesting temperature dependence is observed for ρ_7 representing the planar Hall effect. For the 80 nm and 100 nm thick films the sign of this parameter changes between 100 K and 150 K. All other resistivity parameters, exhibit no characteristic features in this temperature range. At the moment we can not give any explanation for this behavior, but it might be connected to the strain relaxation with increasing film thickness. Moreover, due to the B2 structure the atomic order in our thin films might change with increasing thickness, which also influences the resistivity parameters.

The magnetic anisotropy parameters for the different film thicknesses and their temperature dependence are depicted in Fig. 3.22(b). The two contributions B_{110} and B_c influencing the in-plane magnetic anisotropy are rather small. The film thickness has no influence on the cubic contribution and B_c decreases with rising temperature. The positive value indicates that we have two easy axes in the film plane oriented parallel to the $[110]$ - and $[\bar{1}10]$ -direction. The additional negative uniaxial B_{110} contribution makes

the two easy axes unequal, such that the [110]-axis is more "easy" than the other and changes with film thickness. Unfortunately, the change is not systematic, which makes a determination of the origin rather difficult. A possible explanation might be the relaxation of misfit strain with increasing thickness. The in-plane magnetic anisotropy values we have obtained have the same order of magnitude than recently published values obtained for Co_2MnGe on (001)-oriented GaAs [263]. The large uniaxial contribution B_{001} shows for all 4 samples within the experimental error identical values, which linearly decrease with higher temperature. Thus B_{001} is thickness independent. Two effects contribute to this parameter, magnetic shape anisotropy and strain induced anisotropy. Using the saturation magnetization $M_S = 4.8 \mu_B/\text{f.u.}$ [183] we can calculate the shape anisotropy of a thin film via $B_{\text{shape}} = \frac{1}{2}\mu_0 M_S$ and obtain $B_{\text{shape}} = 614 \text{ mT}$. The difference between B_{shape} and B_{001} must be covered by the additional anisotropy originating from strain. Due to the high Curie temperature the saturation magnetization is nearly constant over the temperature range we have investigated, the temperature dependence of B_{001} can then be explained as a temperature dependent strain originating from the different thermal expansion coefficients of substrate and thin film.

As already mentioned, the \mathbf{m} dependent parameters $\rho_1, \rho_2, \rho_3, \rho_6, \rho_7$ are up to 3 orders of magnitude smaller than the independent parameter ρ_0 . From our experiments on (Ga,Mn)As we know that the ratios $\frac{\rho_i}{\rho_0}, \frac{\sum_i}{\sum_0}$ between the \mathbf{m} dependent and independent parameters are nearly identical (cf. Table 3.2 and Table 3.4). Due to the metallic nature of conduction, the reported Seebeck coefficient for the Cobalt-based Heusler compounds is only some $-10 \mu\text{V/K}$ [196]. This value is one order of magnitude smaller than for (Ga,Mn)As (see Table 3.2 and Table 3.4). For our ADMTP experiments on CFA thin films these low ratios and the small Seebeck coefficient lead to a highly demanding accuracy of the measured thermopower voltages. In a first series of experiments with our setup, we could not find any angular dependence of the longitudinal or transverse thermopower in ADMTP experiments [192]. Such that a direct comparison of ADMR and ADMTP for CFA thin films is currently not possible, but it may be possible to resolve these issues with an improved dipstick system [254], if we achieve an increase in signal-to-noise ratio by at least one order of magnitude.

The results presented in this section prove that it is possible to apply the series expansion model to Co_2FeAl thin films on (001)-oriented MgO and extract quantitative resistivity and magnetic anisotropy parameters from ADMR data. For the resistivity the magnetization dependent terms are dominated by the AHE/Hall contribution parameter ρ_6 . Moreover, we find that ρ_7 describing the planar Hall effect changes its sign with temperature for the 80 nm and 100 nm thick films. The magnetic anisotropy exhibits a large uniaxial oop anisotropy, 2/3 of this contribution can be attributed to the shape anisotropy of the thin film, the remaining part is related to magnetoelastic contributions, originating from the difference in thermal expansion for the substrate and the film.

These promising first results open up the opportunity to also extract the full resistivity and Seebeck tensors for a (113)-oriented Cobalt-based Heusler compound, following the approach described in Sect. 3.3.1. The knowledge of the full tensor descriptions can then be used to calculate the Fermi surface of this material and obtain a deeper insight into the underlying physics.

3.4 Spin currents in magnetic insulators

In the third part of this chapter we focus on pure spin currents in ferromagnetic insulators (FMI) and FMI/normal metal (NM) hybrid structures. A pure spin current corresponds to a flow of spin angular momentum only. Thus, a pure spin current can propagate not only in electrically conducting, but also electrically insulating materials. Spin currents thus are very different from charge currents, which only exist in electric conductors. As already discussed in Sect. 3.1 spin pumping and the spin Seebeck effect can be used to generate pure spin currents from a ferromagnet into a NM. In the following we investigate the application of ferromagnetic insulators as pure spin current sources and drains. We utilize the inverse spin Hall (ISHE) and spin Hall (SHE) effect in normal metals, which translates a spin current into a charge current and vice versa, to detect these spin currents in FMI/NM heterostructures.

For our experiments we choose yttrium iron garnet ($\text{Y}_3\text{Fe}_5\text{O}_{12}$) as the ferromagnetic insulator. YIG and rare-earth iron garnets are a very versatile ferromagnetic material class and allow to tune their magnetic properties by doping with various elements. This versatility makes YIG an interesting candidate for spin current related experiments. The YIG samples we use for the experiments have been grown during the work of this thesis via laser-MBE (Sect. 3.2.2).

Utilizing the spin pumping effect we determine the spin mixing conductance ($g_{\uparrow\downarrow}$) for our YIG/Pt hybrid samples as a function of YIG film thickness in Sect. 3.4.1 with two different sets of experiments: on the one hand, we extract $g_{\uparrow\downarrow}$ by measuring simultaneously the FMR signal and ISHE voltage in our hybrid structures. On the other hand, we calculate the spin mixing conductance from the difference in Gilbert damping for a single YIG thin film and a YIG/Pt heterostructure. Last but not least we introduce in Sect. 3.4.2 a new magnetoresistance effect in FMI/NM hybrid structures. Stemming from the combined action of the SHE and ISHE. The effect is observed in ADMR experiments on YIG/Pt hybrid structures, where Pt is used as a spin current generator and detector, while YIG serves as a selective spin current sink.

3.4.1 Spin current generation via spin pumping in YIG/Pt bilayers

As already discussed in Sect. 3.1 a well established way to generate pure spin currents is spin pumping: a precessing magnetization (with cone angle Θ) emits a pure spin current \mathbf{J}_s into an adjacent normal metal (NM). Inside the NM, the diffusing spin current generates a conventional charge current \mathbf{J}_c via the inverse spin Hall effect which can be detected via conventional electronics (see Fig. 3.23(a)) [6, 13, 264]. A great part of the experimental results presented here were obtained in close collaboration with Franz Czeschka and Johannes Lotze. A more detailed and in depth description of spin pumping experiments can be found in the PhD thesis of Franz Czeschka [265]. In his thesis Franz Czeschka has investigated the spin pumping effect in mostly metallic FM/NM heterostructures, within the work of this thesis the scope was extended to FMI.

A crucial parameter in spin pumping measurements is the spin mixing conductance $g_{\uparrow\downarrow}$. As detailed in the PhD thesis of F. Czeschka [265] and in Ref. [13], we could show that for conductive ferromagnets (FM), $g_{\uparrow\downarrow}$ indeed is essentially independent of the ferromagnet's properties as predicted by theory. However, whether the same also holds for magnetic insulators (FMI) is not clear up to now. As pointed out by Heinrich *et al.* [170],

$g_{\uparrow\downarrow}$ for FM/NM interfaces is determined by the sum of the transmission and reflection amplitudes at the interface, whereas $g_{\uparrow\downarrow}$ for FMI/NM interfaces also does not vanish but is determined by the phase of the reflection amplitude. Recent calculations predict a comparable magnitude of $g_{\uparrow\downarrow}$ for both types of interfaces [266]. However, so far no broad quantitative experimental data for FMI/NM interfaces exist to clarify this point.

In the fashion of the experiments in the PhD thesis of F. Czeschka [265] and in Ref. [13], we performed a quantitative analysis of the spin pumping data of Kajiwara *et al.* [171] who used YIG as FMI and Pt as NM. We found that $g_{\uparrow\downarrow}$ is several orders of magnitude smaller ($g_{\uparrow\downarrow}$ ranges from $6 \times 10^{15} \text{ m}^{-2}$ to $4 \times 10^{17} \text{ m}^{-2}$) than determined for F/N interfaces (typically $g_{\uparrow\downarrow} = 1 \times 10^{19} \text{ m}^{-2}$). Recently, Heinrich *et al.* [170] experimentally obtained $g_{\uparrow\downarrow} \approx 1.2 \times 10^{18} \text{ m}^{-2}$ for YIG/Au interfaces from a difference in the Gilbert damping between bare YIG and YIG/Au/Fe/Au films. This value is much larger than the one of Ref. [171]. For both of these experiments the NM layer was deposited ex-situ on the YIG layer, which will negatively influence the interface quality.

In the following, we use our excellent, laser-MBE grown YIG/Pt hybrid structures (Sect. 3.2.2) to perform spin pumping measurements on various in-situ fabricated YIG/Pt bilayers at various temperatures and find that for our samples, $g_{\uparrow\downarrow}$ of FMI/NM is comparable ($g_{\uparrow\downarrow}$ ranges from $3 \times 10^{18} \text{ m}^{-2}$ to $9 \times 10^{19} \text{ m}^{-2}$) to that of FM/NM interfaces. These experiments were performed at the Walter Schottky Institute in the group of Martin Brandt. In addition, we compare these results with $g_{\uparrow\downarrow}$ calculated from the difference in Gilbert damping between our bare YIG and YIG/Pt films determined from frequency dependent FMR experiments carried out in cooperation with the group of Georg Woltersdorf at the Universität Regensburg.

The opportunity to in-situ fabricate FMI/NM bilayers in our laser-MBE setup results in a clean YIG/Pt interface. For our spin pumping experiments we have grown stoichiometric YIG layers on (111)-oriented GGG with a thickness ranging between $10 \text{ nm} \leq t_{\text{YIG}} \leq 160 \text{ nm}$ as FMI and Pt with $t_{\text{Pt}} = 7 \text{ nm}$ as NM. The deposition parameters and the resulting structural and magnetic properties of these samples are identical to the values given in Sect. 3.2.2. The samples were then cut into rectangular bars (length $L = 3 \text{ mm}$ and width $w = 1 \text{ mm}$) and contacted via aluminum wire bonds for spin pumping measurements as indicated in Fig. 3.23(a).

We used a magnetic resonance spectrometer (Bruker ESP 300) in a temperature range $3 \text{ K} \leq T \leq 290 \text{ K}$ at a fixed microwave frequency of $\nu_{\text{MW}} = 9.3 \text{ GHz}$ and measured as a function of the external magnetic field \mathbf{H} for the spin pumping experiments. The samples were positioned at the center of the TE_{102} microwave cavity, at a node of the microwave electric field and an anti-node of the microwave magnetic field. In this way, it is possible to suppress microwave rectification voltages [13, 265]. The FMR signal was detected via lock-in technique, so that the microwave absorption at the FMR corresponds to a peak-dip structure in the signal, where the inflection point indicates the resonance field H_{res} . To allow for an unambiguous measurement of the dc voltage sign, the dc voltage V_{dc} was recorded via a nanovoltmeter [265].

Figure 3.23 shows (b) FMR and (c) V_{dc} traces measured on a YIG/Pt bilayer sample with $t_{\text{YIG}} = 10 \text{ nm}$ at a microwave power of $P_{\text{MW}} = 100 \text{ mW}$ for a series of temperatures between 3 K and 290 K. \mathbf{H} is oriented in the FMI film plane, parallel to the short side of the sample (Fig. 3.23(a)). The FMR signal (Fig. 3.23(b)) shows a single resonance line for each temperature. The simultaneously recorded V_{dc} (Fig. 3.23(c)) exhibits a maximum at the resonance field of the FMR. We attribute this extremum in V_{dc} to spin pumping

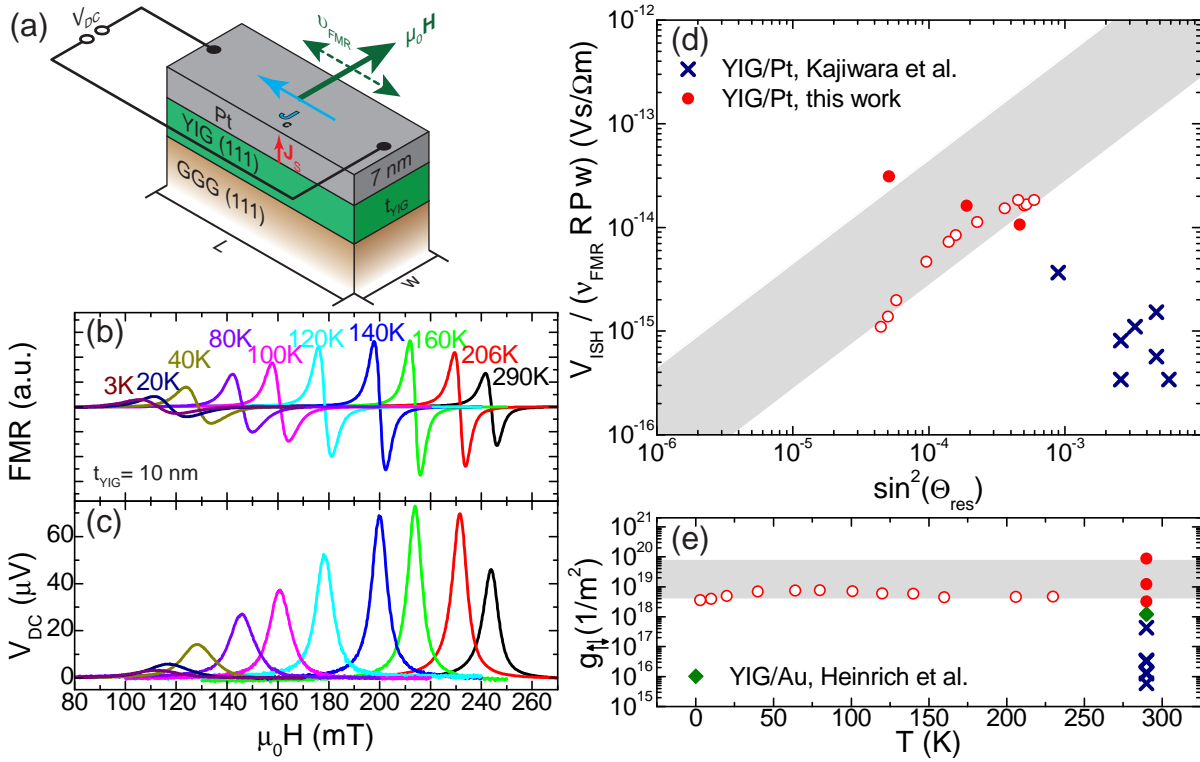


Figure 3.23: (a) Illustration of the spin pumping experiment in our YIG/Pt hybrid structures: A precession of the magnetization in the YIG layer is achieved by FMR using a static \mathbf{H} in the film plane and an additional microwave field with a characteristic frequency. The precessing magnetization emits a spin current \mathbf{J}_s into the Pt. In the Pt layer the inverse spin Hall effect transforms \mathbf{J}_s into a charge current \mathbf{J}_c , which can then be detected as a voltage drop V_{DC} between the two bondwires. Panels (b) and (c) show the temperature dependent evolution of the FMR (b) and V_{DC} (c) as a function of applied field obtained for a YIG/Pt hybrid structure with $t_{YIG} = 10$ nm. The resonance field and the maximum in V_{DC} coincide for all temperatures investigated. (d) Scaling behavior of our spin pumping signal evaluated via Eq. (3.73). Our data (red circles) lies well within the grey shaded area, which represents the scaling for conductive ferromagnets/Pt heterostructures [13]. For comparison we included the data of Kajiwara *et al.* as blue crosses [171]. (e) Temperature dependence of the spin mixing conductance determined from our experiment using Eq. (3.74) (circles) and spin mixing conductance at room temperature obtained by Heinrich *et al.* (squares) [170] and Kajiwara *et al.* (crosses) [171].

at the YIG/Pt interface in combination with the inverse spin Hall effect in Pt and thus identify $V_{ISH} = V_{dc}$ [6, 13, 16, 264, 267]. The sign of V_{dc} corresponds to the one obtained for the FM/NM bilayers in [13, 265].

With decreasing temperature, H_{res} shifts to lower fields as does the maximum in V_{dc} . This shift is related to the increase of the magnetization of YIG (cf. SQUID magnetometry data in the inset of Fig. 3.11(a)), which in the end leads to an increase of the shape anisotropy contribution effectively lowering the ip ferromagnetic resonance field.

The magnetization precession cone angle at resonance $\Theta_{res} = 2h_{MW}/(\sqrt{3}\Delta H_{pp})$ [268] can be extracted from the FMR peak-to-peak linewidth ΔH_{pp} , and the dc voltage $V_{dc,res}$

at H_{res} is used as a measure for $V_{\text{ISH}} = V_{\text{dc, res}}$.

Figure 3.23(d) shows $V_{\text{ISH}}/(\nu_{\text{MW}}PRw)$ versus $\sin^2 \Theta_{\text{res}}$ thus obtained as circles, where P represents the ellipticity correction factor as detailed in [269], w the width of the sample and R the 4-point resistance of the sample¹⁰. Full symbols indicate data obtained at room temperature, whereas open symbols represent data taken at lower T . For comparison, the data for YIG/Pt extracted from the spin waves spectrum of Ref. [171] are added as crosses. In our previous publication [13] we could confirm the scaling law

$$V_{\text{ISH}} = \frac{-e \alpha_{\text{SH}} \lambda_{\text{SD}} \tanh \frac{t_{\text{N}}}{2\lambda_{\text{SD}}}}{\sigma_{\text{F}} t_{\text{F}} + \sigma_{\text{N}} t_{\text{N}}} g_{\uparrow\downarrow} \nu_{\text{MW}} L P \sin^2 \Theta \quad (3.73)$$

derived by Mosendz *et al.* [270, 271] for the inverse spin Hall dc voltage V_{ISH} arising due to spin pumping in conductive FM/NM bilayers, assuming that the NM layer is an ideal spin current sink. Here, e is the electron charge, λ_{SD} the spin diffusion length in the NM, σ_{F} the conductivity of the FM, σ_{N} the conductivity of the NM, t_{F} the thickness of the FM, t_{N} the thickness of the NM, α_{SH} the spin Hall angle [272] of the NM, and $g_{\uparrow\downarrow}$ the effective spin mixing conductance [271]. From the experiments presented in [13, 265] we find that for the double logarithmic scaling plot of Fig. 3.23(d), all values of conductive ferromagnets lie within a certain region, indicated as a gray shaded area.

All measurements of our in-situ fabricated YIG/Pt bilayers are located within or close to the gray shaded region in contrast to the data extracted from Ref. [171] (blue crosses in Fig. 3.23(d)). These deviations indicate differences in interface quality between our samples and the YIG/Pt bilayers used by Kajiwara *et al.*

From Eq. (3.73), the spin mixing conductance

$$g_{\uparrow\downarrow} = -V_{\text{ISH}} / [\nu_{\text{MW}} P R w e C \sin^2 \Theta_{\text{res}}] \quad (3.74)$$

with $C \equiv \alpha_{\text{SH}} \lambda_{\text{SD}} \tanh(t_{\text{N}}/2\lambda_{\text{SD}})$ can be calculated using the experimental data as shown in Fig. 3.23(d), the room temperature values $\alpha_{\text{SH}} = 0.013$ and $\lambda_{\text{SD}} = 10$ nm for Pt [271, 273] and $P = 1.2$ calculated as detailed in Ref. [271]. Figure 3.23(e) shows the results versus temperature. Again, the gray shaded area indicates the values of $g_{\uparrow\downarrow}$ found in our previous publications [13] for conductive FM/NM heterostructures. Clearly, the here measured values for YIG/Pt interfaces lie within the gray area which suggests that $g_{\uparrow\downarrow}$ of magnetic insulator/Pt corresponds to that of ferromagnetic conductor/Pt interfaces. This correspondence thus confirms theoretical calculations [266] and the experimental results obtained by Heinrich *et al.* for YIG/Au interfaces [170]. Moreover, $g_{\uparrow\downarrow}$ only slightly depends on T confirming our observations for other FM/Pt bilayer samples [13].

For a better comparison, we added to Fig. 3.23(e) the value of $g_{\uparrow\downarrow}$ for a YIG/Au interface as determined by Heinrich *et al.* [170]. This value is slightly smaller than our values for YIG/Pt, which may indicate a difference in interface quality or a difference in the band structure of Au and Pt.

A potential reason why $g_{\uparrow\downarrow}$ extracted from Kajiwara *et al.* [171] are orders of magnitude smaller than ours of the FM/NM bilayers might be attributed to a difference in interface quality. This difference in interface quality originates from the ex-situ deposition of Pt by Kajiwara *et al.* [171]. Another reason might be the presence of spin wave excitations

¹⁰The 4-point resistance was measured using two additional contacts not shown in the illustration in Fig. 3.23(a).

in their samples, which complicate the evaluation of the spin mixing conductance [274].

In a second set of experiments in Regensburg, frequency dependent FMR experiments on a bare YIG sample ($t_{\text{YIG}} = 27 \text{ nm}$) and a YIG/Pt ($t_{\text{YIG}} = 27 \text{ nm}$, $t_{\text{Pt}} = 7 \text{ nm}$) hybrid structure both grown on (111)-oriented GGG substrates were conducted to determine the difference in the Gilbert damping parameter α arising from the Pt layer. These FMR experiments have been carried out in collaboration with the Universität Regensburg in the group of Georg Woltersdorf. In these experiments the external magnetic field was applied perpendicular to the film surface. For both samples FMR spectra were recorded at different frequencies ranging from 5 GHz to 20 GHz. From these spectra the ferromagnetic resonance field H_{res} and the linewidth ΔH_{pp} were extracted. One should note that in both samples the FMR signal exhibited a structure consisting of multiple Lorentzian lines. We used 3 Lorentzian curves to fit the data and extract H_{res} and ΔH_{pp} for each peak. The final results are depicted in Fig. 3.24(a) and (b) for the bare YIG and the YIG/Pt hybrid structure, respectively.

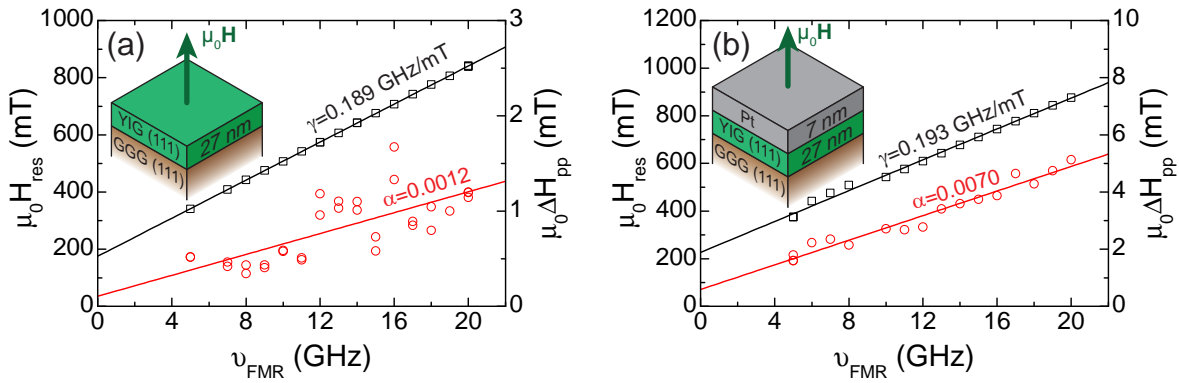


Figure 3.24: Frequency dependence of the resonance field H_{res} (black symbols) and the FMR signal line width ΔH_{pp} (red symbols) determined from FMR measurements at various microwave frequencies ν_{FMR} for (a) a bare YIG thin film and (b) a YIG/Pt heterostructure on (111)-oriented GGG substrates. Using linear fits (colored lines) to the data we extract the gyromagnetic ratio γ and the Gilbert damping α for both samples. The difference in Gilbert damping is then used to determine $g_{\uparrow\downarrow}$ via Eq.(3.75).

For the bare YIG sample in Fig. 3.24(a) the extracted H_{res} (black symbols) increases linearly with the microwave frequency ν_{FMR} as one would expect from the simple oop resonance formula $\mu_0 H_{\text{res}} = \gamma^{-1} 2\pi \nu_{\text{FMR}} + B_{\text{u}}$. Using a linear fit (black line) to the data we extract for the gyromagnetic ratio $\gamma_{\text{YIG}} = 0.189 \text{ GHz/mT}$ and the uniaxial anisotropy field $B_{\text{u}} = 175 \text{ mT}$. From γ we can then calculate the effective g-factor of the YIG layer using $\gamma = g\mu_{\text{B}}\hbar^{-1}$ and obtain $g = 2.14$. This value differs from the expected $g = 2$ of bulk YIG and may be attributed to the stress present in the YIG/substrate interface due to the lattice mismatch between substrate and film. Please note that within the experimental error the HRXRD measurements in Sect. 3.2.2 revealed no deviation from the bulk lattice value for YIG. The extracted anisotropy field $B_{\text{u}} = 175 \text{ mT}$ corresponds well to $B_{\text{u}} = 184 \text{ mT}$ obtained from measurements on another 25 nm thick YIG film on GGG in our FMR setup (cf. Fig. 3.12(a)) by comparing the out-of-plane and in-plane resonance fields.

The FMR linewidth (red symbols) for our bare YIG sample also increases linearly with microwave frequency as one would expect for pure Gilbert damping. The frequency dependence is described by $\mu_0\Delta H_{\text{pp}} = \gamma^{-1}\alpha 2\pi\nu_{\text{FMR}}$, and one expects a vanishing linewidth for $\nu_{\text{FMR}} = 0$. From a linear fit (red line in Fig. 3.24(a)) we extract from the slope $\alpha_{\text{YIG}} = 0.0012$. Interestingly the abscissae of our fit is nonzero (0.1 mT) indicating that the nature of damping is not only Gilbert but also magnon related. Compared to $\alpha_{\text{YIG}} = 0.0006$ obtained by Heinrich *et al.* [170] for a bare YIG film, our value is a factor of 2 larger. We mainly attribute this difference to the high surface roughness of our GGG substrates (cf. Sect. 3.2.2.4), which may be improved by annealing the substrate prior to the YIG deposition. Nevertheless the low Gilbert damping in our samples verifies the high quality of our stoichiometric YIG thin films.

For the Pt/YIG hybrid structure we expect an increased Gilbert damping and a negligible shift in resonance field due to the spin current generated at the YIG/Pt interface. This is supported by the frequency dependent FMR measurements shown in Fig. 3.24(b). From the position of H_{res} (black symbols) at various frequencies we determine $\gamma_{\text{YIG/Pt}} = 0.193 \text{ GHz/mT}$ and $B_{\text{u}} = 227 \text{ mT}$ from a linear fit to the data (black line). The gyromagnetic ratio only changes by 2% compared to the value we obtain for our bare YIG film. In contrast, the uniaxial anisotropy field has changed significantly by 52 mT (20%). The origin of this difference is not clear. In the future, further investigations in Pt/YIG hybrid structures with different thicknesses could resolve this issue.

The linewidth ΔH_{pp} depicted in Fig. 3.24(b) as red symbols increases linearly with increasing ν_{FMR} . Using a linear fit to the data, we extract $\alpha_{\text{YIG/Pt}} = 0.007$ using γ obtained from the frequency dependence of the resonance field. Comparing this value to our bare YIG we observe an increase in the Gilbert damping by a factor of 6 due to the spin current generation at the interface. We note that this increase in α is larger by a factor of 3 than the one reported in [170] for YIG/Au interfaces. We attribute this to the in-situ deposition of our films, which improves the interface quality, or a difference in the spin mixing conductance for YIG/Pt and YIG/Au interfaces.

We use now the difference in α between the bare YIG and the YIG/Pt heterostructure to determine the spin mixing conductance $g_{\uparrow\downarrow}$. According to the theory provided in [170, 275] we calculate $g_{\uparrow\downarrow}$ via

$$g_{\uparrow\downarrow} = \frac{(\alpha_{\text{YIG/Pt}} - \alpha_{\text{YIG}}) 4\pi M_S t_{\text{YIG}}}{g\mu_B}. \quad (3.75)$$

Here $\frac{M_S t_{\text{YIG}}}{g\mu_B}$ is proportional to the number of spins per unit area, accordingly $\alpha_{\text{YIG}} \frac{M_S t_{\text{YIG}}}{g\mu_B}$ is the number of lost spins per unit area due to damping and $\alpha_{\text{YIG/Pt}} \frac{M_S t_{\text{YIG}}}{g\mu_B}$ is the number of spins lost per unit area due to spin-pumping and damping. This equation holds only under the assumption that Pt acts as a perfect spin sink. Using the saturation magnetization $M_S = 129 \text{ kA/m}$ determined from SQUID-magnetometry measurements (cf. Fig. 3.11(a)) we obtain $g_{\uparrow\downarrow} = 1.4 \times 10^{19} \text{ m}^{-2}$ for our YIG/Pt hybrid structure. The determined spin mixing conductance agrees very well with the values we extracted from spin pumping experiments. Moreover, the calculated spin mixing conductance lies within the grey shaded area in Fig. 3.23(e) which confirms that our samples exhibit a $g_{\uparrow\downarrow}$ which is equal to conductive FM/Pt hybrid structures. Compared to $g_{\uparrow\downarrow} = 1.3 \times 10^{18} \text{ m}^{-2}$ determined by Heinrich *et al.* [170] for YIG/Au heterostructures, our spin mixing conductance exceeds this value by one order of magnitude. As stated above, we attribute this increase to

the improved interface quality due to the in-situ deposition of our hybrid structure, or an material specific difference in the spin mixing conductance of YIG/Pt and YIG/Au interfaces.

In conclusion, a pure spin current can be generated in the NM Pt by exciting a precessing motion of the magnetization in the FMI YIG using FMR. To determine the effectiveness of angular momentum transfer $g_{\uparrow\downarrow}$ we applied spin pumping and frequency dependent FMR experiments, which both yield that $1.0 \times 10^{18} \text{ m}^{-2} \leq g_{\uparrow\downarrow} \leq 1.0 \times 10^{20} \text{ m}^{-2}$. Most importantly, our data suggest that the effectiveness of angular momentum transfer from the FMI to the NM described by $g_{\uparrow\downarrow}$ is in our YIG/Pt hybrid structures equal to the values obtained for conductive ferromagnets. Thus our experiments establish YIG/Pt heterostructures as ideal spin current sources (YIG) and detectors (Pt) paving the way for new pure spin current based applications and experiments.

3.4.2 Spin magnetoresistance in YIG/Pt thin films

In the preceding section (Sect. 3.4.1) we investigated the generation of a spin current in YIG/Pt hybrid structures by spin pumping. From these experiments we know that our heterostructures are very efficient pure spin current sources and that these spin currents can be detected exploiting the inverse spin Hall effect (ISHE) in the Pt layer. In this section we investigate a magnetoresistance effect referred to as the spin current magnetoresistance (SMR), which occurs only in FMI/NM heterostructures. The SMR stems from a combination of the spin Hall effect (SHE), which transforms a charge current into a spin current, and the inverse spin Hall effect, which transforms a spin current into a charge current. The physical principles resulting in the SMR effect are schematically illustrated in the following using a phenomenological model. Please note that this phenomenological model has been derived after the experiments and is only capable of describing qualitatively the experiment, but is unable to produce exact quantities.

For the explanation of the SMR we first consider the ordinary Hall effect in the single band model as illustrated in Fig. 3.25(a). Due to the external magnetic field the charge carriers experience a Lorentz force. The normally assumed boundary condition is that the charge carriers can not escape on the sides transverse to the charge current \mathbf{J}_c (connecting a voltmeter between contacts A and B, contacts are open). Thus the charge accumulation leads to a compensating electrical field \mathbf{E}_{Hall} , which can be detected as a voltage drop between the contacts A and B. In the single band model we can write the equilibrium of forces accordingly $-q\mathbf{E}_{\text{Hall}} = q\mathbf{v} \times \mathbf{B}$. Within the single band model this boundary condition also yields that the longitudinal resistance is independent of \mathbf{B} . If we now change the boundary conditions and short $\mathbf{E}_{\text{Hall}} = 0$ (placing a short between the transverse contacts A and B) we allow a transverse current to flow. The current source driving the charge current has to compensate this transverse current flow such that \mathbf{J}_c stays constant. This leads to an effective increase of the longitudinal voltage applied to the sample. Thus, the longitudinal resistance is under this boundary condition even in the single band model dependent on the external magnetic field.

In the case of the spin Hall effect as illustrated in Fig. 3.25(b) we obtain a spin accumulation on the transverse sides to \mathbf{J}_c in the sample. If this spin accumulation cannot escape the sample, a gradient in the spin dependent electrochemical potential compensates the spin current generated by the spin Hall effect. The longitudinal resistance is independent of the spin Hall effect. But if the generated spin current can flow via the contacts A

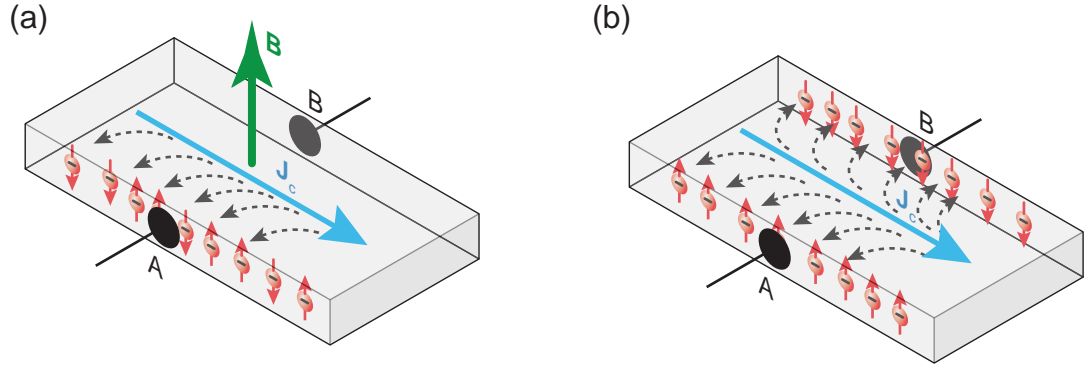


Figure 3.25: (a) Illustration of the ordinary Hall effect in the single band model. Due to the applied external magnetic field \mathbf{B} and the longitudinal charge current \mathbf{J}_c the charge carriers are accumulated on one side of the sample. If the contacts A and B are open, then a voltage drop between the transverse contacts can be detected. If we place a short between the two contacts, a transverse current will flow, leading to a change in the longitudinal current. (b) The very same argument holds for the spin accumulation generated by the spin Hall effect due to the charge current \mathbf{J}_c . If the contacts allow no flow of spin current, the spin accumulation generates a gradient in the spin dependent electrical potential. In contrast, if the spin current is allowed to pass through the transverse contacts, the longitudinal current is influenced and thus the longitudinal resistance changed.

and B (connecting a "spin current short") the current source driving the charge current has to compensate this transverse current flow, which again results in a increase in the longitudinal resistance.

In both cases, the longitudinal resistance either remains constant or changes depending on the boundary conditions. The observed SMR in FMI/NM heterostructures is thus strictly speaking no new magnetoresistance effect, but caused by the spin Hall effect in the NM and the possibility to continually change the boundary conditions by varying the orientation of the magnetization in the FMI. In the following we will discuss the change of boundary conditions and the spin current generation via the spin Hall effect in more detail.

For a more quantitative explanation of the SMR effect we consider first a charge current \mathbf{J}_c flowing through the NM (Pt) layer as indicated by the blue arrow in Fig. 3.26(a). This charge current induces a spin current due to the spin Hall effect in the NM layer, which flows across the NM/FMI interface, depicted as the magenta arrow in Fig. 3.26(a) and named \mathbf{J}_s . The spin orientation \mathbf{s} of \mathbf{J}_s is oriented perpendicular to \mathbf{J}_c and \mathbf{J}_c because of the SHE:

$$\mathbf{J}_s = \alpha_{\text{SH}} \left(-\frac{\hbar}{2e} \right) \mathbf{J}_c \times \mathbf{s}. \quad (3.76)$$

Here $\alpha_{\text{SH}} = \sigma_{\text{SH}}/\sigma$ is the spin Hall angle defined by the ratio of spin Hall conductivity σ_{SH} and the electric conductivity σ [272]. At the FMI (YIG)/NM (Pt) interface, this spin current can be absorbed by the ferromagnet if \mathbf{s} is perpendicular to the magnetization \mathbf{M} of the ferromagnet. This absorption can only occur in the perpendicular configuration, because only then it is possible to transfer the spin angular momentum of the spin

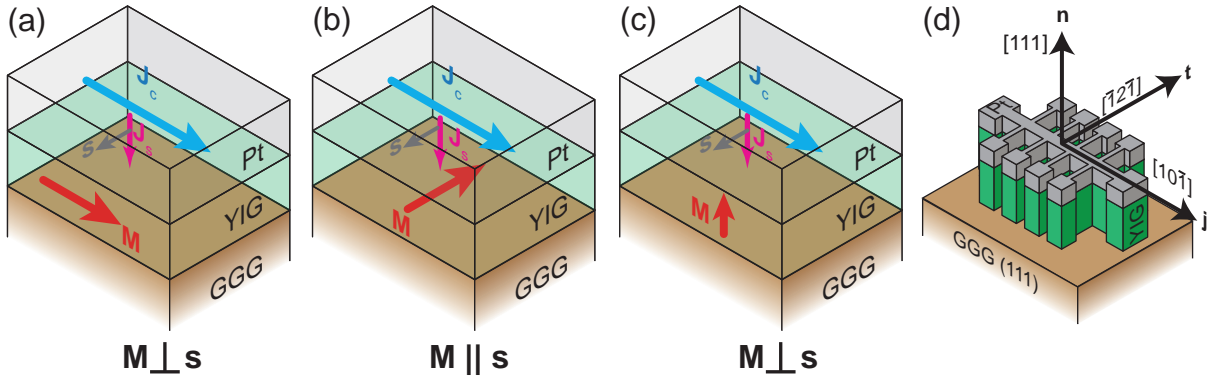


Figure 3.26: Graphical illustrations for the spin magnetoresistance effect exhibited by FMI/NM hybrid structures. A charge current \mathbf{J}_c (blue arrow) flowing in the NM (Pt) is converted via the spin Hall effect into a spin current \mathbf{J}_s (magenta arrow) oriented antiparallel to the surface normal. Due to the vector product for the conversion the spin orientation \mathbf{s} (grey arrow) is perpendicular to \mathbf{J}_c and \mathbf{J}_s . At the FMI/NM (here: YIG/Pt) interface the spin current is absorbed or reflected depending on the orientation of the magnetization \mathbf{M} (red arrow) to \mathbf{s} . The panels (a)-(c) show the basic three principle orientations and the resulting alignment of \mathbf{M} to \mathbf{s} . (d) Definition of the coordinate system defined by \mathbf{j} , \mathbf{t} , and \mathbf{n} in our YIG/Pt hybrid structures.

current in the NM to the magnetization of the FMI. In the cartesian coordinate system defined by \mathbf{j} , \mathbf{t} , and \mathbf{n} (see Fig. 3.26(d)) three different configurations are possible as illustrated by Fig. 3.26(a), (b), and (c). In Fig. 3.26(a) the magnetization is oriented along \mathbf{j} and thus perpendicular to the spin orientation of \mathbf{J}_s such that the spin current is absorbed. Figure 3.26(b) illustrates the case, when \mathbf{M} is oriented along \mathbf{t} and thus antiparallel to \mathbf{s} , the spin current is not absorbed at the interface. Last but not least in Fig. 3.26(c) the magnetization points along \mathbf{n} and is perpendicular to \mathbf{s} which allows again an absorption of the spin current in the insulating ferromagnet. From these three different magnetization orientations the ones in Fig. 3.26(a) and (c) are identical, because in both cases \mathbf{M} is perpendicular to \mathbf{s} , while in Fig. 3.26(b) \mathbf{M} is antiparallel to \mathbf{s} . In this simple picture we expect an higher resistance of the NM layer if the spin current is absorbed at the interface, effectively changing the boundary conditions, and a lower resistance if not, such that $R_{\mathbf{M} \perp \mathbf{s}} > R_{\mathbf{M} \parallel \mathbf{s}}$.

For a deeper understanding one has to consider the various vector products involved in the conversion of a charge current into a spin current, absorption and reflection of the spin current at the FMI/NM interface, and conversion of the reflected spin current into a charge current. We illustrate this phenomenological approach in the following and use the coordinate system defined by \mathbf{j} , \mathbf{t} , and \mathbf{n} in Fig. 3.26(d). We start by the conversion of the charge current \mathbf{J}_c oriented along \mathbf{j} into a spin current \mathbf{J}_s oriented along $-\mathbf{n}$. Due to the vector product nature of this conversion (Eq.(3.76)) we find that $\mathbf{s} \parallel -\mathbf{t}$. At the FMI/NM interface the part $1 - \mathbf{m} \circ \mathbf{s} = 1 + \mathbf{m} \circ \mathbf{t}$ of the spin current perpendicular to the magnetization direction \mathbf{m} gets absorbed. To reduce the lengthy expressions we now define $m_t = \mathbf{m} \circ \mathbf{t}$. The remaining part $\mathbf{m} \circ \mathbf{s} = -m_t$ of the spin current gets reflected at the interface. This reflected spin current $\mathbf{J}_{s,\text{back}}$ flows parallel to \mathbf{n} and the spin orientation \mathbf{s}_{back} is oriented along $-\mathbf{m}$ due to the projection of the spin orientation

onto the quantization axis of the magnetization in the FMI [276]. This reflected spin current is converted into a charge current $\mathbf{J}_{c,\text{back}}$ via the inverse spin Hall effect. This process can be described by

$$\mathbf{J}_{c,\text{back}} = \alpha_{\text{SH}} \left(-\frac{2e}{\hbar} \right) \mathbf{J}_{s,\text{back}} \times (-\mathbf{m}). \quad (3.77)$$

For the reflected spin current $\mathbf{J}_{s,\text{back}}$ we write:

$$\mathbf{J}_{s,\text{back}} = \alpha_{\text{SH}} \left(-\frac{\hbar}{2e} \right) (-m_t) |\mathbf{J}_c| (-\mathbf{j} \times (-\mathbf{t})). \quad (3.78)$$

We can now substitute Eq.(3.78) into Eq.(3.77) and obtain

$$\begin{aligned} \mathbf{J}_{c,\text{back}} &= \alpha_{\text{SH}}^2 (-m_t) |\mathbf{J}_c| (\mathbf{j} \times \mathbf{t}) \times (-\mathbf{m}) \\ &= \alpha_{\text{SH}}^2 m_t |\mathbf{J}_c| (\mathbf{n}) \times (\mathbf{m}) \\ &= -\alpha_{\text{SH}}^2 m_t |\mathbf{J}_c| (\mathbf{m} \times \mathbf{n}). \end{aligned} \quad (3.79)$$

The vector product $\mathbf{m} \times \mathbf{n}$ can be written in the coordinate system defined by \mathbf{j} , \mathbf{t} , \mathbf{n} in the following fashion:

$$\mathbf{m} \times \mathbf{n} = m_t \mathbf{j} - m_j \mathbf{t}. \quad (3.80)$$

Here we used the projections of the magnetization direction $m_j = \mathbf{m} \circ \mathbf{j}$, $m_t = \mathbf{m} \circ \mathbf{t}$, $m_n = \mathbf{m} \circ \mathbf{n}$ onto the coordinate system. Using the expression defined in Eq.(3.80) we rewrite once more Eq.(3.79) and obtain the final result:

$$\mathbf{J}_{c,\text{back}} = -\alpha_{\text{SH}}^2 m_t^2 |\mathbf{J}_c| \mathbf{j} + \alpha_{\text{SH}}^2 m_j m_t |\mathbf{J}_c| \mathbf{t} \quad (3.81)$$

In the end we find that the final charge current $\mathbf{J}_{c,\text{back}}$ is divided into two contributions: one along the initial current direction \mathbf{j} and a second part along the transverse direction \mathbf{t} . In figurative speech we may say that the initial charge current in the NM gets increased if the magnetization of the FMI is oriented parallel or antiparallel to \mathbf{t} , due to the m_t^2 term in Eq.(3.81). In addition, a perpendicular current along \mathbf{t} is generated, the magnitude of this current follows the product $m_j m_t$ which resembles the planar Hall effect present in conducting ferromagnets (cf. Eq.(3.64)).

This effect thus leads to a magnetoresistance effect in the NM, which is sensitive to the magnetization direction of the FMI. The relative magnitude of this effect is defined by α_{SH}^2 , which would result for Pt ($\alpha_{\text{SH}} = 0.012$ [271]) in a 10^{-4} relative resistance change. Moreover, this effect will only be visible if the thickness of the NM layer does not exceed the spin diffusion length in this material. A more quantitative description requires the analysis of the spin accumulation and diffusion in the NM, where the FMI/NM interface acts as a selective spin sink for the spin accumulation depending on the magnetization orientation in the FMI.

In analogy to the ADMR experiments in Sect. 3.3 and for a quantitative analysis of our data presented further below we introduce the longitudinal ρ_{long} and transverse ρ_{trans}

resistivity of the NM as a function of magnetization orientation \mathbf{m} of the FMI

$$\rho_{\text{long}} = \rho_0 + \rho_1 m_t^2, \quad (3.82)$$

$$\rho_{\text{trans}} = \rho_2 m_n + \rho_3 m_j m_t. \quad (3.83)$$

This magnetization orientation dependence described by ρ_1 and ρ_3 are based on our phenomenological approach (Eq.(3.81)). Thus, we expect $\rho_1 = -\rho_3$ from our calculations. Moreover, the ratios ρ_1/ρ_0 and ρ_3/ρ_0 should be of the order of 10^{-4} . For the description of ρ_{trans} we included an additional parameter ρ_2 to describe the normal Hall effect in the NM layer. Thus we expect ρ_2 to depend on the magnitude of the external magnetic field. Interestingly, if we compare Eq.(3.82) to the polycrystalline AMR description defined by Eq.(3.63) and think of it in the framework of ADMR experiments, we expect that the SMR is not discernible from the polycrystalline AMR of a ferromagnetic conductor for rotations of the magnetization in the film plane (i.e. the plane enclosed by \mathbf{j} and \mathbf{t}). But for the oop rotations we expect a different behavior: the magnetization orientation dependence of the SMR vanishes for a rotation of the magnetization in the oopt plane (plane enclosed by \mathbf{j} and \mathbf{n}) and depends on \mathbf{m} for a rotation of \mathbf{m} in the oopj plane (plane enclosed by \mathbf{t} and \mathbf{n}). In contrast, for the conventional AMR of a polycrystalline FM the situation is reversed: no \mathbf{m} dependence for the oopj rotation plane and a clear \mathbf{m} dependence for oopt rotation plane. The SMR thus is qualitatively different from a polycrystalline AMR.

To describe the magnetization orientation in the FMI we apply again the free enthalpy approach. To keep the discussion as simple as possible we use the expression

$$G_M(\mathbf{m}) = -\mu_0 H(\mathbf{h} \circ \mathbf{m}) + B_n m_n^2, \quad (3.84)$$

for the free enthalpy $G_M(\mathbf{m})$, which takes only the shape anisotropy contribution (B_n) and the Zeeman energy into account.

With these expressions at hand we now present the experimental results obtained for our YIG/Pt heterostructures. For these experiments we used YIG/NM and YIG/NM1/-NM2 heterostructures grown on (111)-oriented GGG substrates. For the NM we chose either Cu, Au, or Pt in these structures. The YIG layer for these samples was grown via laser-MBE using our optimized set of parameters described in Sect. 3.2.2. After the growth of the YIG we in-situ deposited the NM layers on top of the sample using electron beam evaporation, while the sample remained at room temperature. After the deposition process the structural properties were investigated using HRXRD confirming the excellent structural quality of our YIG layers as described in Sect. 3.2.2. As a next step we patterned Hall bar mesa structures out of the plain film using photolithography and argon ion beam milling as illustrated in Fig. 3.26(d). The width and length of the Hall bar were $80 \mu\text{m}$ and $800 \mu\text{m}$, respectively. The SMR effect was then analyzed using ADMR experiments. In an ADMR experiment we record ρ_{long} and ρ_{trans} as a function of the external magnetic field orientation, while rotating the external magnetic field at a fixed field strength H_{meas} in three distinct rotation planes: ip, oopj, oopt as defined in Sect. 3.3.1.4. Prior to the angular variation we initialize the magnetization by applying $\mu_0 H_{\text{init}} = 3 \text{ T}$ along $\alpha = 0^\circ$ (ip), $\beta = \gamma = -90^\circ$ (oopj, oopt). For the definition of α , β , and γ see the illustrations in Fig. 3.27(a),(b), and (c), respectively.

We begin the evaluation of the SMR with the analysis of the ADMR results obtained

for a YIG (20 nm)/Pt (7 nm) hybrid structure at $T = 300$ K. The obtained experimental results are summarized in Fig. 3.27(a)-(c).

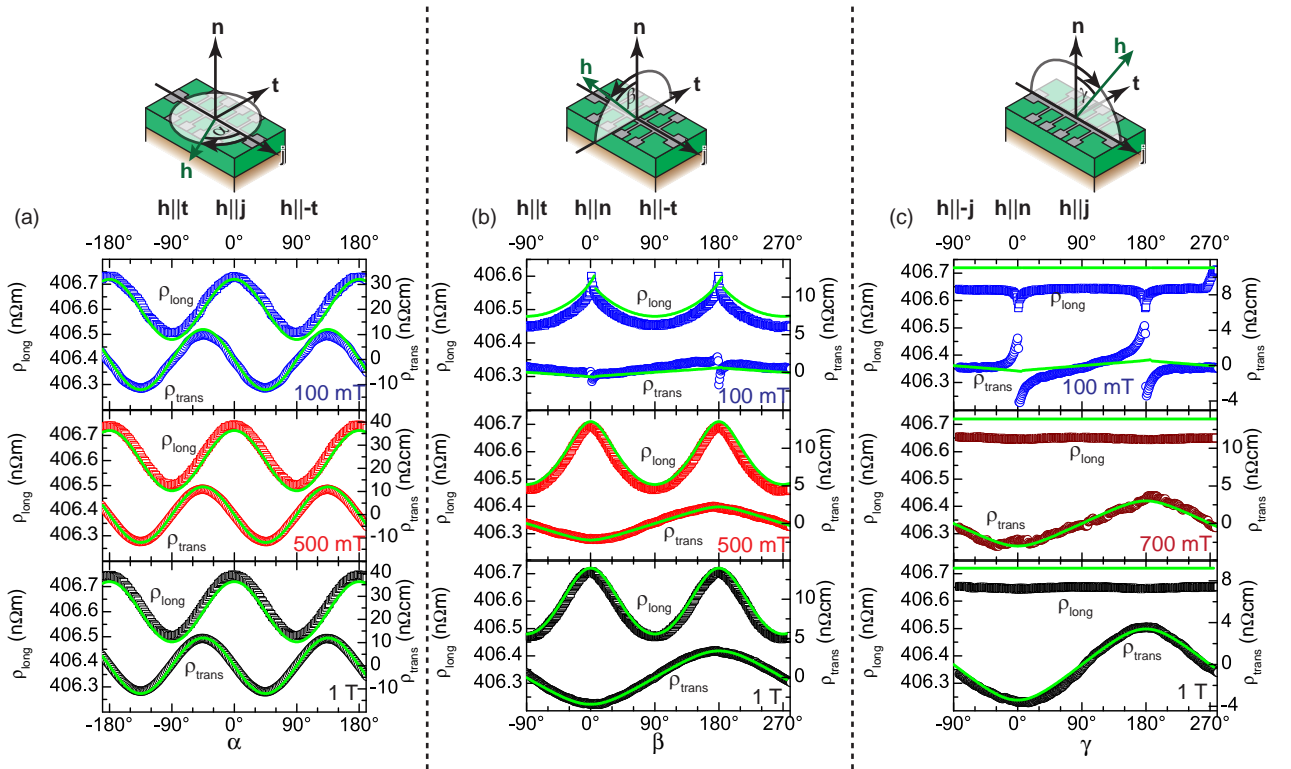


Figure 3.27: ADMR results obtained for a YIG (20 nm)/Pt (7 nm) hybrid structure on a (111)-oriented GGG substrate at $T = 300$ K. (a) Angular dependence of ρ_{long} (squares) and ρ_{trans} (circles) for an in-plane rotation of the external magnetic field at $\mu_0 H_{\text{meas}} = 1$ T (black), $\mu_0 H_{\text{meas}} = 500$ mT (red), and $\mu_0 H_{\text{meas}} = 100$ mT (blue). The ip angle α is defined in the illustration above the data panels (arrow indicates positive direction). (b) Dependence of ρ_{long} (squares) and ρ_{trans} (circles) on the oopj magnetic field angle β at $\mu_0 H_{\text{meas}} = 1$ T (black), $\mu_0 H_{\text{meas}} = 500$ mT (red), and $\mu_0 H_{\text{meas}} = 100$ mT (blue). The positive angle β is illustrated by the drawing above the data plots. (c) Angular evolution of ρ_{long} (squares) and ρ_{trans} (circles) for the oopt rotation plane at $\mu_0 H_{\text{meas}} = 1$ T (black), $\mu_0 H_{\text{meas}} = 700$ mT (wine red), and $\mu_0 H_{\text{meas}} = 100$ mT (blue). The oopt angle γ is defined in the illustration above the experimental data. The green lines in each panel represent a fit to the data using Eqs.(3.82,3.83). Interestingly, the angular dependence of ρ_{long} vanishes for the oopt rotation plane, which is not consistent with the conventional AMR of a polycrystalline FM, but indeed reproduces the behavior expected for SMR.

For the ADMR experiments for an ip magnetic field rotation $\mu_0 H_{\text{meas}} = 1$ T (black), $\mu_0 H_{\text{meas}} = 500$ mT (red), and $\mu_0 H_{\text{meas}} = 100$ mT (blue), depicted in Fig. 3.27(a), we observe a maximum in ρ_{long} for $\mathbf{h} = \mathbf{H}/H$ parallel ($\alpha = 0^\circ$) or antiparallel ($\alpha = 180^\circ$) to \mathbf{j} and a minimum for \mathbf{h} parallel ($\alpha = -90^\circ$) or antiparallel ($\alpha = 90^\circ$) to \mathbf{t} at every fixed H_{meas} . Due to the vanishing ip magnetic anisotropy of the YIG layer it is safe to assume that the magnetization of the YIG layer is always oriented parallel to the external magnetic field. Thus ρ_{long} is expected to follow a $\cos^2(\alpha)$ dependence in accordance to Eq.(3.82), which is nicely reproduced by our ADMR data. In addition, the transverse

resistance also exhibits a $\cos^2(\alpha)$ dependence shifted by -90° . We observe a maximum in ρ_{trans} at $\alpha = -45^\circ$ and $\alpha = 135^\circ$, while the minimum is located at $\alpha = 45^\circ$ and $\alpha = -135^\circ$. For both ρ_{long} and ρ_{trans} the amplitude of the angular dependence is not influenced by the external magnetic field strength.

In case of the oopj rotation plane we observe for ρ_{long} at $\mu_0 H_{\text{meas}} = 1 \text{ T}$ and $\mu_0 H_{\text{meas}} = 500 \text{ mT}$ maxima in resistivity located at $\beta = 0^\circ$ ($\mathbf{h} \parallel \mathbf{n}$) and $\beta = 180^\circ$ ($\mathbf{h} \parallel -\mathbf{n}$). The minima in ρ_{long} occur at $\beta = -90^\circ$ ($\mathbf{h} \parallel \mathbf{t}$) and $\beta = 90^\circ$ ($\mathbf{h} \parallel -\mathbf{t}$). At $\mu_0 H_{\text{meas}} = 1 \text{ T}$ the longitudinal resistivity again exhibits a $\cos^2(\beta)$ dependence. Upon reducing H_{meas} the shape anisotropy more and more influences the orientation of the magnetization in YIG and explains the deviations from the $\cos^2(\beta)$ dependence. For the transverse resistivity we now observe a completely different angular dependence as for ρ_{long} . ρ_{trans} has a minimum at $\beta = 0^\circ$ ($\mathbf{h} \parallel \mathbf{n}$) and a maximum at $\beta = 180^\circ$ ($\mathbf{h} \parallel -\mathbf{n}$). The amplitude of this $\cos(\beta)$ dependence of ρ_{trans} is strongly dependent on the external magnetic field strength (cf. Fig. 3.28(a)) and is mainly caused by the ordinary Hall effect of the Pt layer. The abrupt changes at $\mu_0 H_{\text{meas}} = 100 \text{ mT}$ visible in ρ_{long} and ρ_{trans} originate from the in-plane reorientation of the magnetization, if the field is rotated near $\beta = 0^\circ$ and 180° .

Interestingly, the angular dependence of ρ_{long} vanishes for the oopt rotation plane. This is in stark contrast to the expected angular dependence of a conventional AMR of a polycrystalline FM, but corresponds nicely to our qualitative model of the SMR. Thus, we exclude a conventional AMR as the source of the observed MR. For ρ_{trans} we again observe a $\cos(\gamma)$ angular dependence, which again stems from the ordinary Hall effect in Pt. The abrupt changes in ρ_{long} and ρ_{trans} visible at $\mu_0 H_{\text{meas}} = 100 \text{ mT}$ are explained within the abrupt in-plane reorientation of the magnetization, when the field orientation is continuously rotated near $\gamma = 0^\circ$, $\gamma = 180^\circ$.

For a more quantitative analysis we employ here the simulation technique we already successfully applied to (Ga,Mn)As in Sect.3.3.2 and Cobalt-based Heusler compounds in Sect. 3.3.3. First we choose a starting value for $B_{\mathbf{n}}$ and determine for every magnetic field orientation the magnetization direction \mathbf{m} by numerically minimizing the free enthalpy given by Eq.(3.84). Knowing \mathbf{m} for every field orientation we use a fixed set of ρ_i parameters to calculate ρ_{long} and ρ_{trans} using Eqs.(3.82,3.83). We then iteratively optimize $B_{\mathbf{n}}$ and the ρ_i parameters until we achieve a satisfactory agreement between experiment and simulation for all rotation planes and H_{meas} . For the simulation all ρ_i parameters except ρ_2 were chosen to be independent of the external magnetic field strength. The simulation curves finally obtained are drawn as green lines in Fig. 3.27(a)-(c) and reproduce the experimental data very well. From the simulation we find $B_{\mathbf{n}} = 75 \text{ mT}$. The corresponding ρ_i parameters are summarized in Table 3.6.

YIG (20 nm)/...	Pt (7 nm)	Au (7 nm)/Pt (7 nm)	Cu (9 nm)/Pt (7 nm)
ρ_0 [nΩm]	406.5	143.0	111.0
ρ_1/ρ_0	-5.9×10^{-4}	-2.4×10^{-4}	-0.9×10^{-4}
ρ_3/ρ_0	5.9×10^{-4}	2.4×10^{-4}	0.9×10^{-4}
$\rho_2(1 \text{ T})$ [nΩcm]	-3.4	-11	-8

Table 3.6: Results obtained for ρ_i from fits to the experimental data at $T = 300 \text{ K}$ for Pt/YIG, Pt/Au/YIG, and YIG/Cu/Pt heterostructures

From the extracted ρ_i parameters of our simulation we find that $\rho_1 = -\rho_3$. This

corroborates the prediction based on the qualitative description of the SMR effect, and makes the assumption of a spin current-related origin of the observed MR plausible.

We studied in more detail the field dependence of ρ_2 for $T = 300$ K and $T = 30$ K extracted from the fit of our ADMR data. In Fig. 3.28(a) ρ_2 increases linearly with increasing magnetic field as we would expect for an ordinary Hall effect. We applied a linear fit to the data to extract the Hall coefficient of our Pt and obtained $r_{\text{Hall}} = -2.5 \times 10^{-11} \text{ m}^3/\text{C}$ for both temperatures. This value is close to $-2.1 \times 10^{-11} \text{ m}^3/\text{C}$ reported in [277] for evaporated Pt films. Moreover, we find a non vanishing abscissa $\rho_{\text{AHE}} = -0.80 \text{ n}\Omega\text{cm}$ at $T = 300$ K and $\rho_{\text{AHE}} = -0.87 \text{ n}\Omega\text{cm}$ at $T = 30$ K. The origin of this effect can not be explained within our simple, qualitative model of the SMR. However, it is reminiscent of an anomalous Hall effect. Therefore we conclude that this effect may either be attributed to an additional effect in the SMR which can only be calculated from a full quantitative approach or indicates an induced ferromagnetism at the YIG/Pt interface [278–280]. However, this induced magnetism can not account for the characteristic angular dependence of our YIG/Pt hybrid structure as one then expects a polycrystalline AMR in the Pt. As this is not consistent with our data, we exclude the induction of magnetism in Pt as a source for the observed AHE type of signal in ρ_2 .

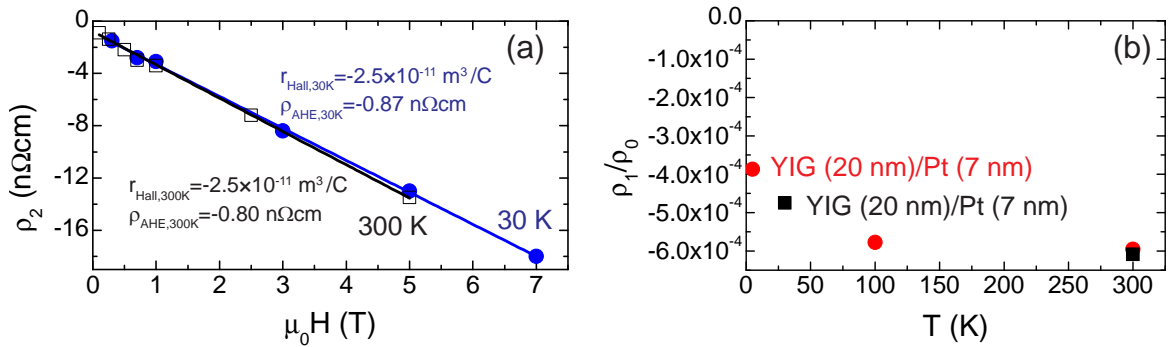


Figure 3.28: (a) Magnetic field dependence of ρ_2 extracted from the fit to the ADMR data at $T = 300$ K (black squares) and $T = 30$ K (blue circles). The black and blue lines represent linear fits to determine the Hall coefficients r_{Hall} and AHE contributions ρ_{AHE} for $T = 300$ K and $T = 30$ K, respectively. (b) Temperature dependence of ρ_1/ρ_0 determined for two different YIG (20 nm)/Pt (7 nm) samples (black, red) from our fit to the ADMR data. The observed SMR varies only slightly with temperature.

The SMR is based on the tunable absorption/reflection of spin currents at the FMI/NM interface, thus one would expect that the spin mixing conductance $g_{\uparrow\downarrow}$ plays a crucial role. From the spin pumping experiments on YIG/Pt hybrid structures in Sect. 3.4.1 we already know that $g_{\uparrow\downarrow}$ varies only weakly with temperature. In Fig. 3.28(b) we plotted the extracted ratio ρ_1/ρ_0 as a function of temperature for two different YIG (20 nm)/Pt (7 nm) samples. The ratio decreases slightly with decreasing temperature. At $T = 5$ K ρ_1/ρ_0 is reduced by 34% compared to $T = 300$ K. This observation agrees well with the temperature dependence of $g_{\uparrow\downarrow}$ in Sect. 3.4.1. However, a full quantitative analysis of the SMR effect would be necessary to account for the influence of the spin mixing conductance. Such an analysis is beyond the scope of this thesis.

While the magnetoresistive behavior observed in our YIG/Pt samples is not consistent

with an induced magnetization (magnetic proximity effect) at the interface, an experiment to rule out magnetic proximity as the origin of the SMR appears desirable. Following a suggestion by E. Saitoh in January 2012, we investigated the impact of a second NM layer between YIG and Pt on the SMR. In Fig. 3.29(a)-(f) we compare the ADMR signal of a YIG (20 nm)/Pt (7 nm) hybrid structure to a YIG (20 nm)/Au (7 nm)/Pt (7 nm) and a YIG (20 nm)/Cu (9 nm)/Pt (7 nm) heterostructure.

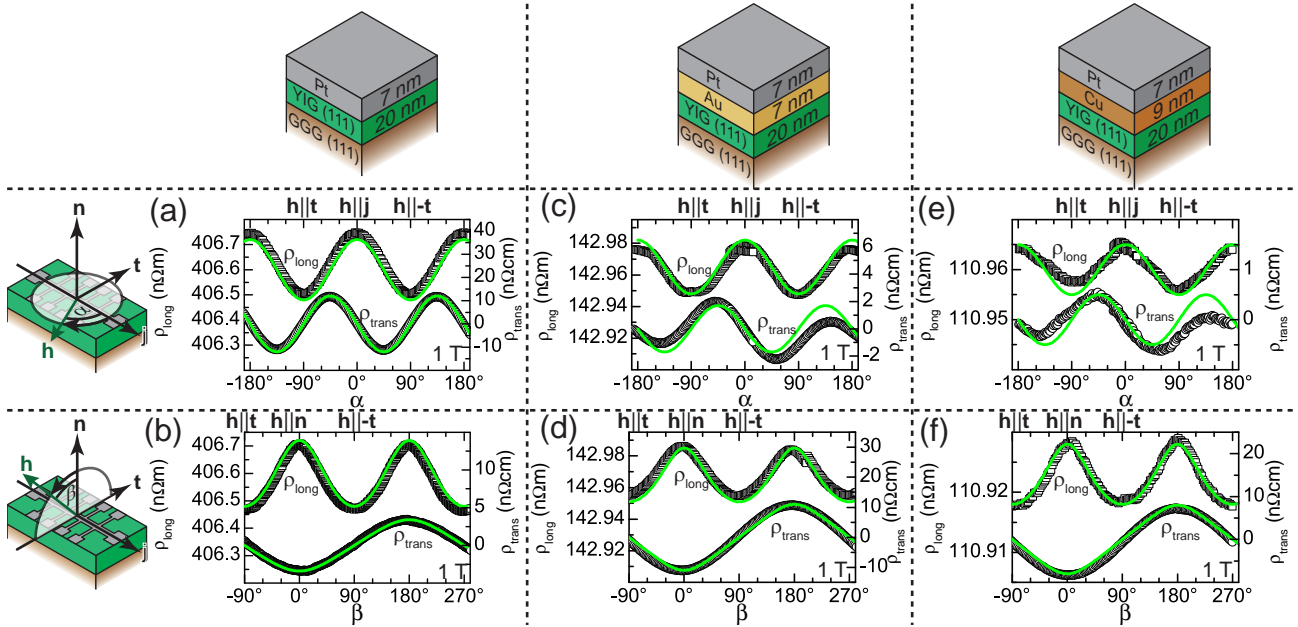


Figure 3.29: Magnetoresistance data (symbols) and corresponding fit (lines) for YIG (20 nm)/Pt (7 nm) (panels (a) and (b)), YIG (20 nm)/Au (7 nm)/Pt (7 nm) (panels (c) and (d)), and YIG (20 nm)/Cu (9 nm)/Pt (7 nm) (panels (e) and (f)) at $T = 300$ K and $\mu_0 H = 1$ T. The opt rotations (not shown here) exhibit for all 3 samples no angular dependence in ρ_{long} . The introduction of a second NM layer between YIG and Pt influences only the magnitude of the observed SMR. This clearly indicates that the SMR arises due to the spin current absorption at the YIG/NM interface and is not due to the MR behavior of an induced magnetic polarization in the Pt layer.

For the ip rotation in Fig. 3.29(a),(c) and (e) and the oopj rotation in Fig. 3.29(b),(d) and (f) we observe the same angular dependence of ρ_{long} and ρ_{trans} for all heterostructures. Moreover, we did not observe any ip angular dependence for a YIG (20 nm)/Au (7 nm) and a YIG (20 nm)/Cu (7 nm) heterostructure. With these results we can conclude that the observed SMR is an effect related to spin currents and not due to an induced ferromagnetism in the Pt layer. The extracted quantitative data for all heterostructures from the ADMR simulation are summarized in Table 3.6. ρ_0 decreases with increasing total NM layer thickness due to the higher conductivity of Au and Cu compared to Pt as in these double NM structure the two parallel conducting NM layers both contribute to the total resistivity. This fact is also supported by the increase in $\rho_2(1\text{T})$ for the trilayer system compared to the YIG/Pt hybrid structure, due to the larger absolute Hall constant of Cu and Au [281, 282]. The ratio ρ_1/ρ_0 decreases by a factor of 2.5 for the YIG/Au/Pt heterostructure compared to the reference of the YIG/Pt hybrid

structure. For the YIG/Cu/Pt heterostructure the ratio even decreases by a factor of 6.6. This decrease in SMR effect can be rationalized in terms of the exponential decay of the spin current determined by the spin diffusion length in the NM and the parallel conduction channel which NM2 represents. By measuring the SMR with varying Au or Cu thickness and employing a quantitative model of the SMR, it might thus even become possible to extract the spin diffusion length using simple ADMR experiments in the future.

In summary, we have investigated in this section a MR effect in FMI/NM heterostructures. The effect, that we call SMR, is based on the conversion of charge to spin currents via the spin Hall effect and vice versa via the inverse spin Hall effect. In addition, the effect also depends on the selective absorption of spin currents at the FMI/NM interface depending on the orientation of the magnetization. Thus this effect enables us to remotely sense the magnetization direction in the FMI by measuring just the resistance of the adjacent NM layer. The signature of SMR in ADMR experiments is qualitatively different from conventional AMR. As for the SMR the angular dependence in ρ_{long} for the opt rotation plane vanishes while for the conventional AMR we would observe an angular dependence. We note that in our experiments we only used YIG as the FMI. But the SMR is in principle not restricted to this one material. Other FMI, i.e. ferromagnets which have a several orders of magnitude higher resistance than the NM layer on top, should also exhibit this type of effect. Further examples using nickel ferrite and magnetite as FMI are given in the outlook of this thesis in Fig. 4.3. This simple method also makes the SMR a perfect tool for the precharacterization of FMI/NM heterostructures for other spin current related experiments. With a quantitative model for the effect at hand it may even be possible to extract the spin Hall angle α_{SH} from SMR experiments and determine the spin diffusion length of various NM. In the end, this observation of a novel, simple to measure magnetoresistance effect opens the way for new spin current related experiments in the future.

3.5 Spin caloritronics: a summary

In the preceding sections of this chapter we focused on two main topics of current scientific interest: on the one hand the comparison of the magnetoresistance to the magnetothermopower of conducting ferromagnets and on the other hand the investigation of pure spin currents generated in FMI/NM hybrid structures.

Prior to these successful experiments we presented in Section 3.2 the structural and magnetic quality of Co_2MnSi (CMS) and yttrium iron garnet (YIG) thin films grown via laser-MBE.

In section 3.2.1 we showed that, after an optimization of the growth parameters, the structural and magnetic quality of Co_2MnSi films on (001)-oriented MgO substrates is on par or even better than sputtered reference samples provided by the Universität Bielefeld. These results show that our laser-MBE setup is capable of growing metallic, ferromagnetic material systems with excellent structural and magnetic properties. These results are a first step towards the in-house production of thin films of the Heusler compounds tailored for future spincaloric experiments.

In a second series of experiments, we optimized the growth of YIG in our laser-MBE setup on (111)-oriented GGG and YAG substrates. The structural and magnetic charac-

terization in Sect. 3.2.2 of YIG films grown with the optimized set of parameters prove that our YIG films are state-of-the-art and qualify for further experiments. More specifically, the YIG films on GGG substrates grow epitaxially, with the perfect stoichiometry, in (111)-orientation with low mosaic spread (FWHM of the (444) YIG rocking curve $\leq 0.03^\circ$), exhibit low coercive fields (≤ 3 mT), a bulk-like saturation magnetization ($M_S \geq 129$ kA/m) and a narrow FMR linewidth ($\mu_0 \Delta H_{pp} \leq 1$ mT at 10.1 GHz) at room temperature. Due to the large lattice mismatch and the interdiffusion of Al, YIG films on YAG need further improvement, e.g.: the application of a buffer layer.

We furthermore studied the structural and magnetic properties of YIG/Pt hybrid structures, since these are routinely used for spin current related experiments. The experiments showed that the quality of the YIG layer is not influence by the in-situ deposition of a Pt layer on top.

As a first step in investigating the magnetoresistance and magnetothermopower of conducting ferromagnets we presented in Sect. 3.3 a theoretical model based on a series expansion in powers of the magnetization direction applied to the resistivity and Seebeck tensors and reduced the number of parameters by utilizing the crystal symmetry restrictions. Due to the Onsager relations these two magnetotransport tensors are not identical, such that we obtain for cubic and tetragonal symmetry additional magnetization dependent terms in the Seebeck tensor compared to the resistivity tensor. Moreover, our calculations show that it is in principle possible to quantitatively extract the full resistivity and Seebeck tensors in cubic and tetragonal symmetry by applying angle dependent magnetoresistance (ADMR) and magnetothermopower (ADMTP) measurements and a simulation based on our series expansion model. The simulation was realized in a LabVIEW based software during the work of this thesis. This versatile software allows to extract quantitatively the resistivity, Seebeck and magnetic anisotropy parameters from ADMR and ADMTP experiments. The knowledge of the full magnetotransport tensors would allow to determine the Fermi surface of the ferromagnetic material via the generalized Mott relation. As a side effect, we can also extract the magnetic anisotropy of the ferromagnet by investigating the field dependence of ADMR and ADMTP signals.

To demonstrate that our theory is capable of describing experimental data, we carried out ADMR and ADMTP experiments in two different conductive regimes: On the one hand, we used the dilute magnetic semiconductor (Ga,Mn)As in (001)- and (113)-orientation (Sect. 3.3.2) and, on the other hand, metallic Cobalt-based Heusler compounds (Sect. 3.3.3). These proof-of-principle experiments showed that we can simulate the experimental results with our model and extract quantitative numbers for magnetotransport tensor elements and the magnetic anisotropy for these two different regimes of conductivity. Moreover, our experiments showed that the additional functional terms in the Seebeck tensor due to the Onsager relations are indeed present. These first promising results confirm that ADMR in combination with ADMTP experiments are powerful tools to reveal the properties of the Fermi surface of ferromagnetic conductors.

In the second part of this chapter we investigated the generation of pure spin currents using ferromagnetic insulators (FMI). The usage of FMI allows to separate the flow of angular momentum (spin current) from the flow of charge carriers (charge currents). For our experiments we focused on the FMI yttrium iron garnet.

With excellent YIG layers on GGG substrates at hand we carried out spin pumping experiments as discussed in Sect. 3.4.1. For the determination of the crucial FMI/NM interface parameter $g_{\uparrow\downarrow}$ we applied two different types of experiments: in a first series

of experiments we extracted $g_{\uparrow\downarrow}$ by simultaneously measuring the FMR signal and the inverse spin Hall voltage signal, in the second set of experiments we calculated $g_{\uparrow\downarrow}$ from the difference in Gilbert damping from frequency dependent FMR measurements of a bare YIG film and a YIG/Pt hybrid structure. For our samples we obtain a spin mixing conductance ranging from $1 \times 10^{18} \text{ m}^{-2} \leq g_{\uparrow\downarrow} \leq 1 \times 10^{20} \text{ m}^{-2}$. These results show that the spin mixing conductance of YIG/Pt bilayers is comparable to the one of ferromagnetic conductor/Pt heterostructures. Moreover, our results corroborate theoretical calculations [266] and the experimental results of Heinrich *et al.* [170]. In the end, these results establish our YIG/Pt bilayers as perfectly suited pure spin current generators and detectors.

In Sect. 3.4.2 we investigated a magnetoresistance effect, the SMR, stemming from the conversion of charge currents to spin currents via the spin Hall effect and vice versa via the inverse spin Hall effect in combination with the selective absorption of spin currents at a FM/NM interface. Due to the nature and magnitude of this effect, it is only detectable in FMI/NM hybrid structures. In ADMR experiments on YIG/Pt bilayers, we established the existence of the SMR and its unique oop rotation plane signal signature (angle dependence of ρ_{long} vanishes for oopt rotation while for an oopj rotation the signal is angle dependent). By introducing a second NM layer between YIG and Pt we verified that the observed effect is not related to an induced ferromagnetism in the Pt layer. In the future, the SMR effect may be used to determine the spin Hall angle and spin diffusion length in NM layers using simple magnetoresistance measurements. Moreover, as this effect is sensitive to the magnetization orientation of the FMI one can remotely sense the orientation by measuring the resistance of the NM layer.

In summary, we studied the magnetoresistance and magnetothermopower of metallic and semiconducting ferromagnets using angle dependent measurement techniques and an advanced model for the quantitative extraction of the resistivity and Seebeck tensor. These results show that a combination of ADMR and ADMTP provides a powerful experimental toolbox to study transport properties of ferromagnetic conductors. In the second part of this chapter we looked into the properties of spin currents generated by a ferromagnetic insulators. Our results show that FMI can effectively be used as a spin current source (spin pumping) and drain (spin current magnetoresistance).

An outlook on further possible experiments dealing with spin-dependent transport in conductors and isolators based on the results of this thesis is given in Chapter 4.

Chapter 4

Conclusions and outlook

This thesis deals with the investigation of spin-related phenomena in metals, semiconductors, and insulators, in both plain epitaxial thin films as well as heterostructures.

This chapter concludes this thesis by summarizing the key results obtained. In order to highlight the importance and potential influence of these results, we in addition provide an outlook into future experiments.

4.1 Summary

State-of-the-art samples are a key requirement for the successful study of spin-related phenomena. A particular focus of this thesis thus was to fabricate thin film heterostructures with excellent structural and magnetic quality. This was achieved by the improvements of the laser-MBE setup carried out during this thesis (c.f. Appendix A). In a complementary approach, we established or intensified collaborations with other groups in order to get access to particular samples.

A specific achievement was the optimization of ZnO thin film growth by laser-MBE (Chapter 2). To this end, we used TRFR, Hanle MOKE and GMR experiments to study their spin-related properties. From the optical experiments, carried out in collaboration with RWTH Aachen, we find that localized states exist in ZnO with long spin lifetimes, which allow the storage of spin information on ns timescales. Moreover, these localized states can be electrically addressed by the trapping of injected, mobile spin polarized electrons. The all electrical approach using spin valve multilayers (FM/N/FM) with ZnO as the N-layer allowed us to quantitatively extract the spin diffusion length, interface resistance and spin selectivity in our ZnO films. Most interestingly, we could identify that the temperature dependence of the spin dephasing time exhibits two different regimes. At low temperatures ($T \leq 25$ K) the spin dephasing time saturates and the dominating spin dephasing mechanism is a temperature independent Dzyaloshinsky-Moriya mechanism. At higher temperatures ($T \geq 25$ K) the spin dephasing time decreases with increasing temperature and the spin dephasing is dominated by a temperature dependent D'yakonov-Perel' mechanism linear in \mathbf{k} . The comparison between the spin dephasing time determined by all electrical and all optical methods reveals that the temperature dependence is qualitatively identical. Moreover, our data suggest that the spin dephasing time in ZnO can be increased by increasing the structural quality.

The second main part of this thesis (Chapter 3) dealt with two newly emerging and interconnected fields of spin electronics: spin caloritronics and pure spin current sources.

On the one hand, we investigated the magnetoresistance and magnetothermopower of metallic and semiconducting ferromagnets using angle dependent measurement tech-

niques. Fitting the data to an advanced phenomenological model we were able to provide a proof of concept for the quantitative extraction of the resistivity and Seebeck tensors. These results show that using a combination of ADMR and ADMTP experiments one can study in great detail the transport properties of ferromagnetic conductors. In addition, we verified by the experimental results in this section that the Mott relation Eq.(3.16) is only valid in the tensor form for single crystalline samples.

On the other hand, in the second part of Chapter 3 we looked into the properties of spin currents generated and absorbed by ferromagnetic insulators (FMI). Our results show that FMI can effectively be used as a spin current source (spin pumping) and spin current drain (spin current magnetoresistance). Using these concepts we showed that the spin mixing conductance $g_{\uparrow\downarrow}$ determined from two independent experiments utilizing spin pumping in YIG/Pt bilayers is comparable to the one of ferromagnetic conductor/Pt heterostructures. These two types of experiments were: a quantitative evaluation of the DC voltage generated by the spin pumping (in collaboration with the Walter Schottky Institut) and the determination of the difference in Gilbert damping from frequency dependent FMR experiments (in collaboration with the Universität Regensburg). In addition, we discovered a new magnetoresistance effect in FMI/normal metal hybrids, stemming from the absorption of a pure spin current in the ferromagnetic insulator. Based on angle dependent magnetoresistance (ADMR) experiments we showed that the signature of this spin current magnetoresistance (SMR) effect in our YIG/Pt bilayers is qualitatively different from polycrystalline anisotropic magnetoresistance. These experiments benefited from collaborations with TU Delft (Netherlands) and IMR Tohoku (Japan).

A more detailed summary of the results is provided in Section 2.6 for Chapter 2 and in Section 3.5 for Chapter 3.

4.2 Outlook

The results obtained in this thesis pave the way for more advanced experiments, which in the end will provide a deeper understanding of spin dependent transport phenomena. A selection of possible experiments is discussed in the following.

Our results on ZnO thin film growth and study of their electrical properties show that our ZnO layers on sapphire can be further improved by optimizing the buffer layer. This may be achieved by using a combination of MgO and (Mg,Zn)O as a buffer system. In the end, the aims of a buffer optimization should be an increase of the Hall mobility in the ZnO layer and a low Al interdiffusion from the sapphire substrate, while the buffer itself should not significantly contribute to the electrical properties of the whole buffer/ZnO system.

The possibility to store spin information in localized excitonic states on timescales of several ns opens the way to further experiments in the field of spin based quantum information processing and allows to combine optical manipulation and read-out with solid-state based storage of quantum information. A first crucial step is the investigation of the coupling between the different excitonic states and a more profound theoretical model to explain the resonant enhancement of the spin dephasing times. Subsequent experiments should then be focused on the increase of spin dephasing time and the tunability of the coupling between different excitonic states. It is important to note that localized excitonic states are also present in various other semiconductors and thus

the experiments on ZnO can be also extended to other semiconductors, like for example GaN [283].

Based on recent experiments in our group [30] using a scannable laser to generate spatially resolved thermal gradients in thin films it should be possible to investigate the magnetothermopower of ZnO based spin valve structures and compare these measurements to the magnetoresistance of such a device. In Fig. 4.1(a) this experiment is illustrated in more detail. While the laser spot generates the thermal gradient perpendicular to the layer structure, the thermal voltage V_{th} caused by the thermal gradient is recorded as a function of the applied external magnetic field. As it is possible to laterally scan the laser with a few μm resolution, it thus is possible to investigate the evolution of the signal as a function of position. First experiments at room temperature using the very same setup as in [30] were unfortunately unsuccessful for a sample with a 20 nm thick ZnO spacer layer. Due to the increase in spin diffusion length with decreasing temperature we however expect that successful experiments should be possible at liquid He temperatures. In accordance with the experiments presented in [284], where Gravier *et al.* investigated the spin/charge transport under a thermal gradient in metallic multilayers, such experiments in ZnO spin valve structures would allow to extend these investigations to semiconductors.

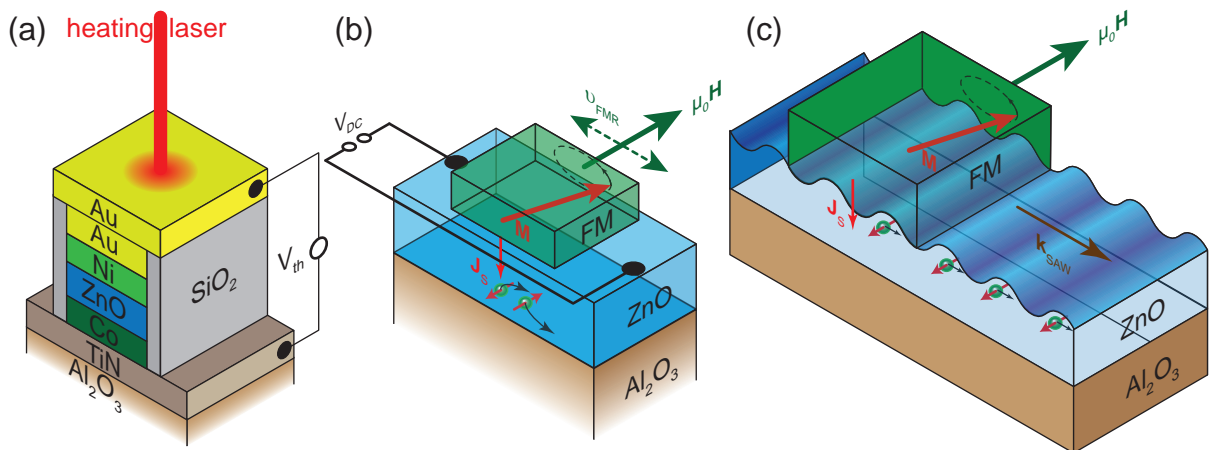


Figure 4.1: Novel types of experiments related to spin-dependent phenomena in ZnO. (a) Utilizing the thermal gradient generated by the absorption of a laser spot one can measure the magnetic field dependence of the thermopower of a ZnO based spin valve structure at low temperatures in a spatially resolved fashion. (b) A precessing motion of the magnetization in the ferromagnet on top of the ZnO layer leads to the pumping of a spin current into ZnO. Utilizing the inverse spin Hall effect in ZnO one can then detect these spins as a DC voltage between the two electrical contacts in the ZnO. (c) Taking the concept of spin current injection via spin-pumping a step further one may also inject spins into ZnO by first generating a surface acoustic wave in the ZnO layer that propagates through a ferromagnet. In the ferromagnet the elastically excited ferromagnetic resonance leads to the pumping of a spin current into the ZnO. The spins may then be transported by the surface acoustic wave in the ZnO.

Bypassing the problem of conductivity mismatch, an efficient injection of a spin (polarized) current into a semiconductor has been achieved by the spin pumping effect [8, 12]

in silicon and gallium arsenide. These experiments can be extended to ZnO as illustrated in Fig. 4.1(b). Here the magnetization of a ferromagnet (FM) is driven into a precessing motion by an external microwave field (ferromagnetic resonance). Due to the spin pumping effect a spin current is then injected into the ZnO layer underneath. Within the ZnO the spin current is transferred into a charge current via the inverse spin Hall effect and can then be detected as a DC voltage V_{DC} . In analogy to Saitoh *et al.* [8, 12] these measurements allow to simultaneously determine the spin dephasing time and the spin Hall angle in the semiconductor. Thus, such an experiment could yield more information on the spin dephasing and the spin-orbit coupling in ZnO. Moreover, the geometry of the experiment allows to use our high quality buffered ZnO thin films on sapphire and enables a direct comparison of optical- and spin pumping-determined spin dephasing times in one and the same sample. In more advanced experiments, utilizing coplanar wave guides and microwave pulses to excite the ferromagnetic resonance, even the time- and spatially resolved optical probing of the spin current injected via spin pumping might become accessible. Such time- and spatially resolved experiments allow to further investigate the physical mechanisms localizing the mobile spin carriers on donor states as proposed in this thesis.

Taking the concept of spin pumping a step further and inspired by the experiments of Mathias Weiler in our group [15, 285] it is also possible to excite a ferromagnetic resonance and then inject a spin current with surface acoustic waves (SAWs). Due to the electrical polarization along the c-axis present in the ZnO it should be possible to utilize this effect in ZnO/FM hybrid structures as illustrated in Fig. 4.1(c). A SAW is generated in a ZnO layer [286] and passes through a ferromagnet deposited on top of the ZnO. Due to the magnetoelastic coupling [285] a ferromagnetic resonance is excited in the ferromagnet. The spin pumping effect then leads to the injection of a spin current into the ZnO. As the spin information is carried by charge carriers and these charge carriers couple to the SAW it is then possible to transport spin information along the SAW \mathbf{k} -vector and later detect it via optical or electrical means. This novel device concept should enable the study of many different effects such as for example the spin injection efficiency with SAW spin pumping and the influence of the SAW on the spin dephasing time.

Regarding the results obtained in this thesis for the extraction of a full quantitative description of the resistivity and Seebeck tensors a first next experimental step consists in the improvement of the setup for the generation of the thermal gradient. To resolve the issue of insufficient thermal contact between hot and cold side of the sample holder we propose the following improvements to the existing setup. As illustrated in Fig. 4.2 the thermal contact from the sample to the cold reservoir is improved by clamping the sample using screws and a top cap pressing against the sample. To allow an electrical isolation between sample and clamp the use of sapphire might prove ideal. On the hot side the direct evaporation of a platinum meander structure as an on-chip heater solves the problem of low heat transfer from the heater to the sample and also allows to use the resistance of the Pt meander for on-chip thermometry. In addition experiments in vacuum amend problems arising due to the additional heat exchange by the He gas flow in the cryostat. Influences of the substrate itself may still have a negative impact on the measurements, but can be circumvented by free standing structures as inspired by Sultan *et al.* [287].

After a successful upgrade of the measurement setup further experiments on (113)-oriented (Ga,Mn)As allow a full extraction of resistivity and Seebeck tensor. Utilizing

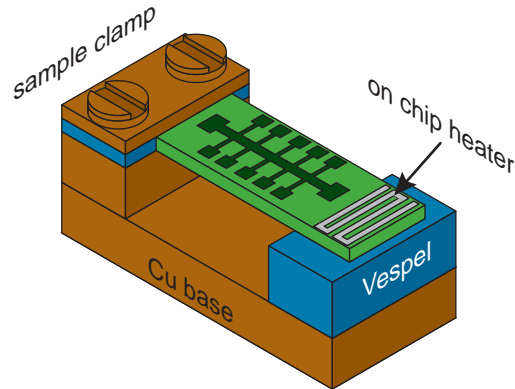


Figure 4.2: Illustration of possible improvements for the caloritronics setup. Based on the results obtained in this thesis a better thermal coupling between cold side and sample is desirable and may be achieved by clamping the sample to the cold base. In addition, the deposition of an electrically isolated Pt meander structure allows to generate heat directly on-chip improving the thermal contact to the hot reservoir.

the Mott relation one then could infer the Fermi surface of (Ga,Mn)As. A next step would be to focus on systems with a different symmetry. Here cubic or isotropic systems are preferred, as according to our theory an easy extraction of the resistivity and Seebeck tensors should be possible. The investigation of further materials by ADMR and ADMTP experiments would allow to test the limits of the phenomenological theory provided in this thesis.

The successful laser-MBE growth of Heusler compounds by laser-MBE established in Section 3.2.1 opens the way to either utilize the low lattice mismatch between GaAs and cobalt-based Heusler compounds to investigate the spin transport properties in Heusler compound/GaAs hybrid structures, or even grow Vanadium-based Heusler compounds with large Seebeck coefficients for future spincaloric experiments.

The spin magnetoresistance (SMR) effect found in YIG/Pt and YIG/NM/Pt heterostructures in Section 3.4.2 is not limited to the ferromagnetic insulator YIG alone according to the current phenomenological theory, but should also be present in other ferromagnets with a resistance that is several orders of magnitude larger than the resistance of the platinum layer. As a first set of experiments we also investigated the existence of the SMR effect by means of ADMR experiments in two samples with different ferromagnetic insulators. The first sample consists of a 20 nm thick, (001)-oriented Magnetite (Fe_3O_4) layer grown via laser-MBE on a (001)-oriented MgO substrate covered in situ by an electron beam evaporated, 7 nm thick, Pt film. The second sample consists of a 620 nm thick nickel ferrite (NiFe_2O_4) layer grown via chemical vapor deposition on (001)-oriented MgAl_2O_4 and a sputter deposited 10 nm thick Pt layer, which was deposited after cleaning the surface of the nickel ferrite by Ar ion beam milling.¹ Both samples have been structured into Hall bars using photolithography and Ar ion beam milling at WMI. We then conducted ADMR experiments in ip, oopj, and oopt geometry in the fashion of the experiments with YIG/Pt hybrid structures in Section 3.4.2. In Fig. 4.3(a)-(f) we compare the obtained results to the data obtained for the YIG (20 nm)/Pt (7 nm) al-

¹The NiFe_2O_4 layer was grown in the group of A. Gupta at the University of Alabama. The Pt layer was deposited later in the group of Günther Reiss at the Universität Bielefeld.

ready shown in Fig. 3.27(a)-(c). We also applied the same theoretical model to simulate the obtained data for the three different samples. In Fig. 4.3(a)-(f) the open symbols represent experimental data, while the green lines represent a fit to the data. We note that in case of the magnetite sample the data was recorded at $T = 5$ K, while all the other data were taken at $T = 300$ K.

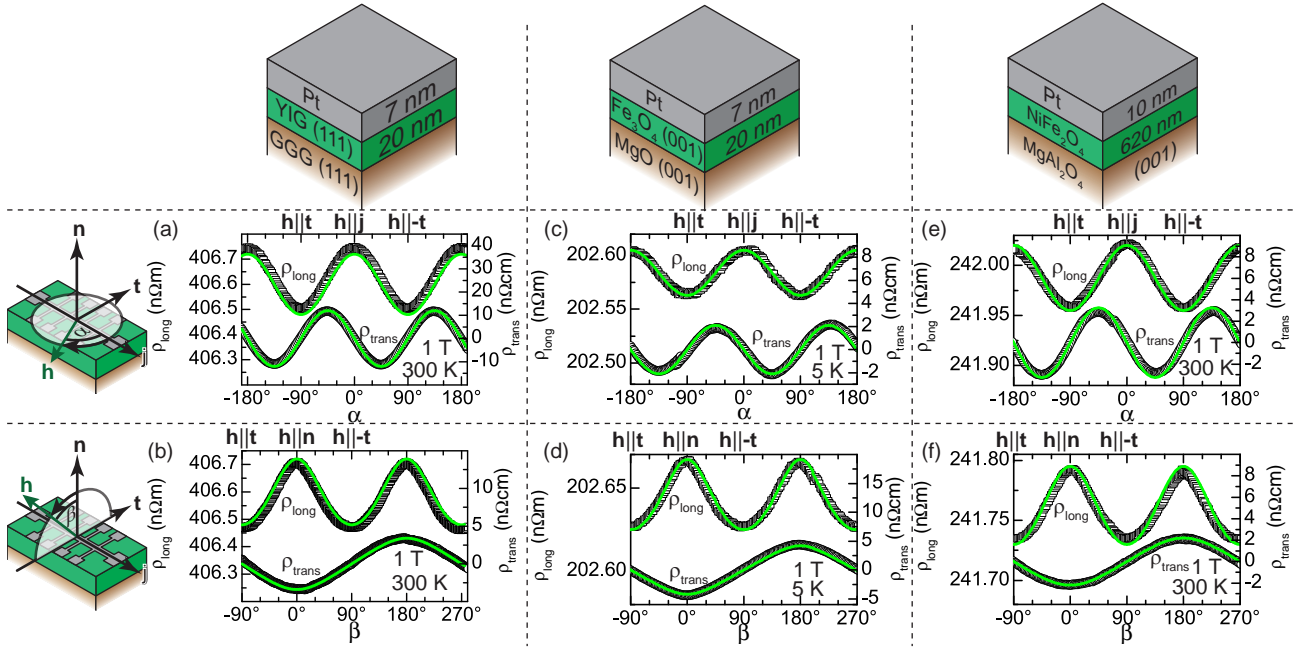


Figure 4.3: Magnetoconductance data (symbols) and corresponding fit (lines) for the YIG(20nm)/Pt (7 nm) (panels (a) and (b)), the Fe_3O_4 (20 nm)/Pt (7 nm) (panels (c) and (d)), and the NiFe_2O_4 (620 nm)/Pt (10 nm) (panels (e) and (f)) heterostructure at $\mu_0 H = 1$ T (For the YIG and NiFe_2O_4 sample, $T = 300$ K, and for the Fe_3O_4 sample, $T = 5$ K). The longitudinal resistance in the oopt rotation plane (not shown here) exhibited no angular dependence for all three samples. The angular dependence in all three samples corresponds to the one expected for the spin magnetoconductance. The ρ_1/ρ_0 ratio determined from the simulation is -5.9×10^{-4} for YIG/Pt, -2.1×10^{-4} for Fe_3O_4 /Pt, and -2.7×10^{-4} for NiFe_2O_4 /Pt. These results indicate that the spin magnetoconductance is an universal effect and is not limited to the use of YIG as the ferromagnetic insulator.

The parameters of the fit extracted from the experiments at $\mu_0 H = 1$ T are summarized in Table 4.1. In all cases the fit reproduces very well the angular evolution of the data and confirms our simple phenomenological model of the SMR effect.

The identical angular evolution for all 3 samples clearly demonstrates that the SMR effect is not limited to YIG as a ferromagnetic insulator, but is an universal effect that is detectable when the resistance of the normal metal is several orders of magnitude lower than the one of the ferromagnet.

Future experiments on the SMR effect should provide a deeper understanding of the underlying physics by investigating the SMR signal as a function of Pt layer thickness and the thickness of an additional NM layer (such as Au or Cu) between the platinum and the ferromagnetic insulator. Moreover, the spin mixing conductance and the spin Hall angle

	YIG/Pt (20 nm)/(7 nm)	Fe ₃ O ₄ /Pt (20 nm)/(7 nm)	NiFe ₂ O ₄ /Pt (620 nm)/(10 nm)
ρ_0 [n Ω m]	406.5	202.6	242.0
ρ_1/ρ_0	-5.9×10^{-4}	-2.1×10^{-4}	-2.7×10^{-4}
ρ_3/ρ_0	5.9×10^{-4}	2.1×10^{-4}	2.7×10^{-4}
$\rho_2(1 \text{ T})$ [n Ω cm]	-3.4	-4.2	-2.2

Table 4.1: results obtained for ρ_i from fit to the experimental data for a Pt/YIG ($T = 300 \text{ K}$), a Pt/Fe₃O₄ ($T = 5 \text{ K}$), and a Pt/NiFe₂O₄ ($T = 300 \text{ K}$) heterostructure

are parameters that influence the magnitude of the SMR signal. Thus a direct comparison of the SMR signal to the spin pumping signal in the very same heterostructures will supply further evidence for the physical origin of the SMR effect. In the very same line of argument a quantitative comparison of the SMR signal to the spin Seebeck effect (SSE) seen in spatially resolved thermal gradient experiments [30] involving Pt/YIG hybrid structures would be helpful to investigate a connection between these two effects in more detail. If the phenomenological description for the SMR effect given in this thesis is correct, we expect a universal scaling relation between SMR, spin pumping and spatially SSE signal magnitude, as all three effects will be influenced by the spin mixing conductance $g_{\uparrow\downarrow}$ and the spin Hall angle α_{SH} .

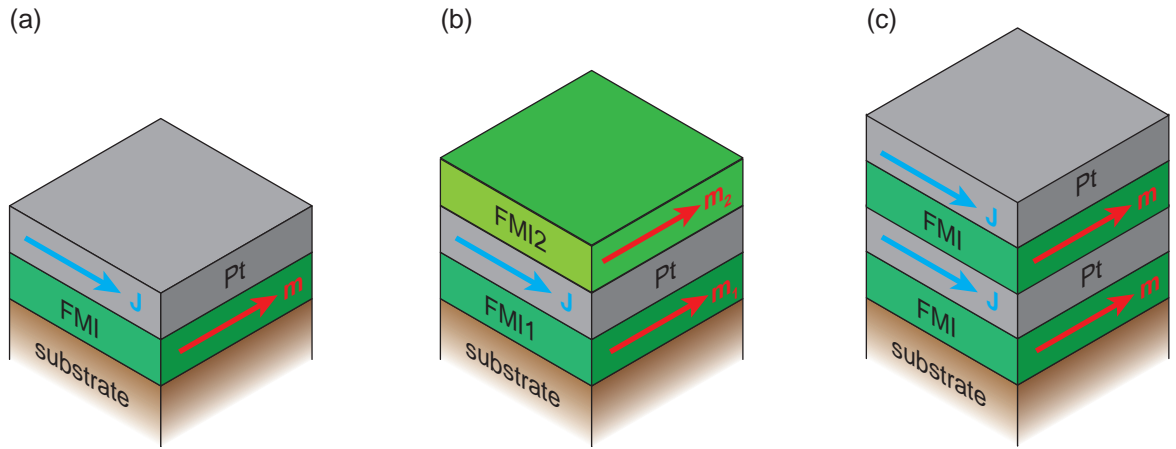


Figure 4.4: (a) Illustration of the conventional sample geometry for the observation of the SMR effect consisting of a Pt/FMI hybrid structure on a substrate. (b) More advanced structure using a platinum layer sandwiched between two different ferromagnetic insulating ferromagnets. (c) FMI/Pt multilayers allow to increase the signal of the SMR effect.

Inspired by the results obtained for the SMR effect one can think about more advanced heterostructures, which allow us to investigate the effect on a new level. In Fig. 4.4(a) we depicted the standard setup for the SMR effect consisting of a bilayer of FMI and NM (in this case Pt). If we add a second different FMI on top of the Pt layer as illustrated in Fig. 4.4(b), we introduce a second selective spin sink on top of the Pt. Assuming the two FMI have different coercive fields, or one of the magnetizations is

pinned by coupling it to an antiferromagnet, it should be possible to generate different relative orientations between the two magnetizations \mathbf{m}_1 and \mathbf{m}_2 of the two FMI by either sweeping the magnetic field or changing the external magnetic field orientation. This relative orientation then should influence the MR signal generated by the SMR if one passes a current \mathbf{J} through the Pt layer and measures the resistance of the NM layer.

If we continue to think about multilayer structures, the aim of increasing the SMR magnitude is achieved by a more complicated multilayer structure. In hindsight, we expect from our proposed model also an increase in $\Delta R/R$ if the NM is sandwiched between two FMI insulators with identical magnetic properties. This should increase the signal by a factor of 2. Taking the concept a step further, as illustrated in Fig. 4.4(c), one can stack repeatedly a combination of NM/FMI double layers on a FMI layer. It is then possible to investigate the propagation of the spin current through a FMI layer by passing an electrical current through one Pt layer and detecting the voltage drop generated by the propagating spin current due to the inverse spin Hall effect in the other Pt layer [288, 289]. These new heterostructures represent a challenge to the growth department, as it is necessary to obtain multilayers with high crystalline and magnetic quality, an alternative would be the use of lateral structures, as already reported by Chumak *et al.* [290]. Another interesting field is the fabrication of tunnel devices with a FMI as the tunnel barrier. This aim is simultaneously achieved by realizing the structure in Fig. 4.4(c) with very thin (below 2 nm) FMI layers. With these structures it might be possible to investigate the influence of the magnetization orientation on the tunnel current through the FMI barrier. It may be beneficial to use an all oxide epitaxial approach for the growth of such FMI/NM multilayers. Indium tin oxide (ITO) (cubic crystal structure, lattice constant $a = 1.01$ nm [291]) could be a possible candidate for such structures as successful spin pumping with YIG/ITO heterostructures has already been demonstrated [5].

As evident from the list of possible experiments inspired by the results of this thesis, a multitude of new physical questions arise related to spin transport. Clearly, interesting results are to be expected in the years to come.

Appendix A

Upgrade of the laser-MBE system

Laser-MBE is a physical vapor deposition technique that allows to grow epitaxial thin films on single crystalline substrates. The process uses high fluence UV excimer laser pulses to ablate a polycrystalline target (cf. Fig. A.1). This target usually consists of a polycrystalline material with the same stoichiometry as the film to be deposited and is mounted below the substrate. Due to the high energy density on the target surface, a plasma plume is generated directed towards the substrate, where the material is deposited. To optimize the growth conditions various parameters can be changed and controlled during the deposition process: laser energy fluence at the target ρ_{ED} , target-to-substrate distance, background gas type, pressure in the chamber, and substrate temperature.

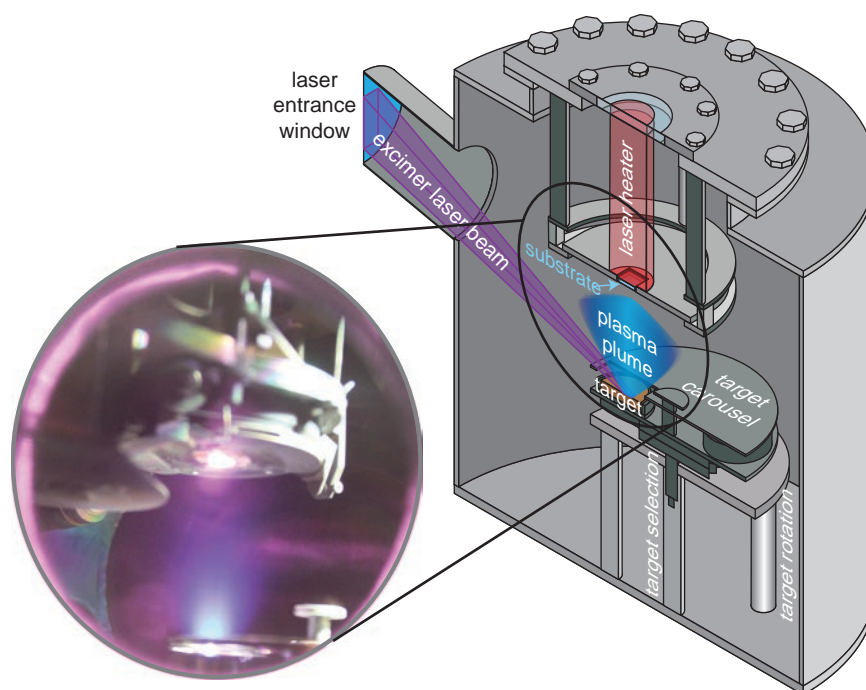


Figure A.1: Illustration of the laser-MBE process. A focused UV-excimer laser beam with a pulse duration of about 25 ns hits a polycrystalline target. Due to the high power density exceeding GW/cm^2 a plasma plume is generated and target material is moved towards the substrate mounted above the target. With a second continuous wave infrared laser it is possible to heat the substrate. The optical photograph on the left has been taken during a deposition process of a ZnO thin film on a sapphire substrate in our laser-MBE chamber.

During the work of this thesis we upgraded our laser-MBE system by adding various new components and optimizing the existing setup. The extensions to the system consisted of a new infrared laser heater system (Surface, LH 140), with integrated realtime, pyrometer-based temperature control, a new optical beam guide, lens system (both custom built in-house) and entrance window (PVD Products, PLD Intelligent window) for the excimer laser, a new RF-plasma single atom source unit (Oxford, HD25), and a new LabVIEW based control software allowing for an automated operation of the laser-MBE system. On the following pages, we will provide an introduction into these additions with a focus on the new lens system and the LabVIEW based control software.

A.1 New lens system "Brenninger"

The new optical beam guide for the excimer laser (Lambda Physik, COMPexPro201, wavelength 248 nm (KrF)), maximum pulse energy 700 mJ, pulse duration 25 ns, maximum repetition rate 10 Hz) installed during the work of this thesis¹ consists of two rectangular apertures and 4 dielectrically coated (reflection optimized for 248 nm) mirrors. It is mounted on a custom built optical track that shields the UV laser beam, guiding the excimer beam from the laser through the lens system (Fig. A.2(a)) into the laser entrance window (Fig. A.2(b)) of the laser-MBE chamber. The main part of the new optical train is a telescope system consisting of 5 lenses in total, cf. Fig. A.2(a). Lenses 1 to 5 are mounted on 4 motor-driven lens carriers allowing a vertical movement across a total height of 120 cm. The lens carriers are attached to 4 stepper motors (MAXON Motor, DC brushless motor with planetary gearhead (reduction 1539/65) and encoder (500 counts/2000 quad counts per turn), track pitch of 1.75 mm per revolution), each connected to a controller with a spatial resolution of less than 0.005 mm. They are controlled by a PC (MAXON Motor EPOS controller), thus allowing full automation of the lens system itself. The lenses are arranged such that they build up a classical telescope zoom optics, creating a sharp image of the excimer laser's rectangular aperture on the surface of the PLD target. Thereby, the positions of lenses 1 to 3 determine the size of the image, lenses 4 and 5 assure perfect focusing. For the lenses the following focal lengths were selected: 350 mm for lens 1 (plano-convex), -100 mm for lens 2 (plano-concave), -100 mm for lens 3 (plano-concave, installed inverted), 350 mm for lens 4 (plano-convex), and 750 mm for lens 5. Moreover, lens 2 and lens 3 are connected to each other and move together on the lens track. To reduce the number of parameters for the optimization of the focal point of the system, we kept the distance $l_3 = 120$ mm (distance between lens 2 and lens 3), $l_5 = 240$ mm (distance between lens 4 and lens 5), and $l_6 = 774$ mm (distance between lens 5 and the target in the laser-MBE chamber) fixed. A change of these 3 parameters influences the range of achievable spot area sizes on the target, determining the tuning range of ρ_{ED} . This leaves the parameters l_2 and l_4 for the optimization process. Note that l_1 is simply determined from the other 5 parameters as the total track length (4020 mm) from the excimer laser to the target is fixed.

The optimization of the lens distance parameters was carried out in the following way. For fixed l_4 values we varied l_2 and put for each value an ablation spot on a SrTiO₃ polycrystalline target to evaluate the sharpness of the spot. We then selected

¹A large part of the planning and installation process was carried out with the unlimited support of Stephan Geprägs and Thomas Brenninger.

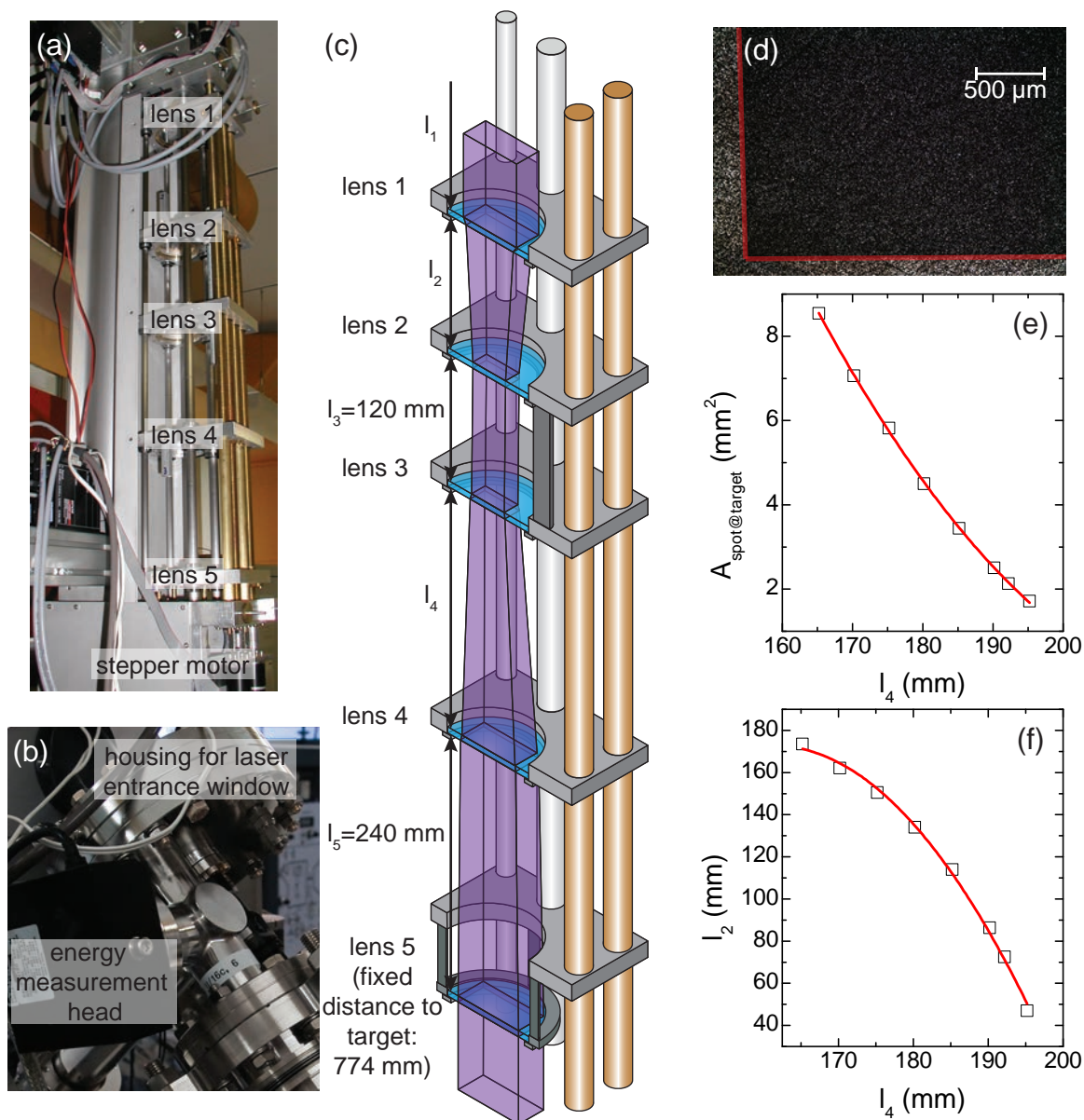


Figure A.2: (a) Photograph of the new lens system after installation. (b) Photograph of the intelligent window with energy monitor equipped. (c) Illustration of the new lens system consisting of 5 lenses. The 5 lenses have a focal length of 350 mm, 100 mm, 100 mm, 350 mm, 750 mm for lens 1, lens 2, lens 3, lens 4, lens 5, respectively. (d) Optical micrograph of the focal spot when firing one laser pulse onto a SrTiO₃ polycrystalline target after optimization of the lens system was finished. (e) Area of the spot size as a function of lens 3 to lens 4 distance l_4 determined from the experiment (symbols) and second order polynomial fit to the data (line). (f) Lens 1 to lens 2 distance l_2 as a function of l_4 obtained from an optimum focus determination experiment (symbols) and second order polynomial fit to the data (line).

the l_2 yielding the sharpest ablation spot. This optimization process was carried out for different l_4 values. An example for an ablation spot after optimization is shown in the

optical micrograph in Fig. A.2(d) (the edges are highlighted with red lines). The spot has a nice rectangular shape (only two edges are shown) and sharp edges. In Figure A.2(e) we plot the resulting area of the ablation spot $A_{\text{spot@target}}$ versus l_4 (symbols). The area decreases with increasing l_4 value as expected for a classical telescope zoom optics. The resulting dependence of l_2 on l_4 is depicted in Fig. A.2(f) as symbols. To allow for a direct calculation of l_4 and l_2 from the desired spot area we fitted both data sets with a second order polynomial. This yields the following two equations:

$$\begin{aligned} A_{\text{spot@target}}[\text{mm}^2] &= 0.00258 \times (l_4[\text{mm}])^2 - 1.15938 \times (l_4[\text{mm}]) + 129.62389, \\ l_2[\text{mm}] &= -0.10688 \times (l_4[\text{mm}])^2 + 34.49139 \times (l_4[\text{mm}]) - 2609.8966. \end{aligned}$$

Solving the first equation for l_4 gives us a direct way of calculating l_4 as a function of the desired spot size area and will be used in the LabVIEW control software to seamlessly change ρ_{ED} . The second equation then allows to determine l_2 from the calculated l_4 and used for this purpose in the software.

From this optimization process we obtain a lens system that allows to change the size of the rectangular excimer laser spot on the PLD target between 1.2 mm^2 and 12 mm^2 without losing sharpness of the spot itself. The corresponding on-target laser fluences are 0.5 J/cm^2 to 5.5 J/cm^2 corresponding to a power density of 20 MW/cm^2 to 0.2 GW/cm^2 at a pulse duration of about 25 ns. the maximum fluence is by 1.5 J/cm^2 higher as compared to the previously installed optics.

In addition, the UHV laser entrance port of the PLD chamber was replaced by an Intelligent Window (IW, PVD Products), combining two unique features. First, it is able to keep the optical beam path clean for extended periods of time. A high quality, anti-reflection coated window mates to the large flange using a Viton O-ring. Inside the large flange is a large diameter, UV grade fused silica disc. Between the disc and the PLD target is an aperture that limits to a small section the portion of the disc coated by ablated material from inside the deposition chamber. This disc ensures that the coated window is kept clean by intercepting the ablated plasma plume. Once the exposed section of the disc has become coated, the disc can be easily rotated exposing a new, optically clean surface, even during deposition. If the disc is fully coated a spare disc is inserted, and the coating of the old disc is removed via chemical-mechanical polishing². Second, an insertable mirror allows to determine the energy of the incoming excimer laser beam after the disc through a second installed window. For this purpose we use a pyroelectric detector head (OPHIR, PE50BF-SH-V2) with a resolution of $3 \mu\text{J}$. Knowing the absorption factor ($E_{\text{@target}} = 1.735 \times E_{\text{@monitor}}$), one can calculate the energy at the target. This IW helps to improve the deposition capability by accurately monitoring one of the most critical parameters in the process: ρ_{ED} . The properties of laser-MBE grown thin films depend strongly on this value, which may vary due to several factors in all PLD systems. Films continually build up on the inner surface of the PLD chamber's laser entrance port. Also, excimer laser output and beam brightness can vary significantly depending on the lifetime of the laser gas fill, output coupler, and electrodes. Furthermore, the components of the optical train degrade with time due to color centers and/or degradation of reflecting or coated surfaces. Monitoring and adjusting the energy that actually enters the chamber before each run, or during the growth process, results

²Normally, polishing is carried out by the crystal laboratory of the TU München.

in a constant on-target laser fluence and helps to yield reproducible film properties and deposition rates.

A.2 LabVIEW based control system

To use the full potential of this optical train, a new LabVIEW based application has been developed for the laser-MBE PC, which controls all the sensitive parameters of the laser-MBE system. To allow this all around control the PC is interfaced in the following way with the components: the stepper motors for the lens system and for target height, selection and rotation are connected to EPOS (MAXON Motor) controllers, one of these controllers (for the target height) is connected via serial communication (COM port 15) to the PC and relays via CAN Bus the communication to the other 6 controllers. The excimer laser is serially connected (COM port 7) to the PC and has 2 additional BNC cables connected to the trigger in and trigger out running to the output and input of a DAC card (Adlink, NuDAQ) in the PC, which allow to trigger the laser via the PC. The tunability of the pressure in the laser-MBE chamber is achieved by a VAT variable pressure controller connected to a motorized slab gate valve and a baratron pressure transducer (MKS, 1 mbar full scale equals an output voltage of 10 V), serial communication to the PC is established via COM port 9. The substrate temperature is stabilized by heating the back of the substrate via an infrared 140 W laser (wavelength 940 nm) coupled into the laser-MBE chamber via a lens system and an optical fibre. The output of this heating laser is controlled in real-time via the LASCON server (Linux based real-time control from the company Dr. Mergenthaler). This server monitors (10 kHz sampling rate) the substrate temperature via a two color pyrometer (lowest detectable temperature in single color mode: 300 °C) and adjusts the laser output to achieve a typical temperature stability below 0.1 °C. This server is connected to the PC via ethernet (IP of the LASCON server: 192.168.30.12, TCP Port: 9125).

The LabVIEW system is based on the query-state-machine concept. Each interfaced device is running in its own instanced loop. Command queues and events are used to establish ways of communication between the user interface and the connected devices. In the following we present in detail the different user interface parts of the laser-MBE control software. The main user interface is divided into 5 parts: "Basic Motor Control" contains simple controls for the stepper motors of the lens system and target height, rotation and selection. "Pressure Control" provides access to the variable pressure controller. Settings of the excimer laser, such as pulse energy, repetition rate, refill and gas line handling, are displayed and changed via the "Excimer Laser Control". The "LASCON Control" is an user interface that allows to change the basic settings of the LASCON server, i.e. temperature set point, laser heater output, script execution. The "Data Selection Panel" is a tab selector that provides access to in depth controls and information of the different devices.

In the following, each user interface control is explained in more detail.

A.2.1 Basic Motor Control

The motor control is realized via two user interface inputs: "Basic Motor Control" (Fig. A.4(a)) and the "EPOS Control" tab (Fig. A.4(b)) in the "Data Selection Panel".

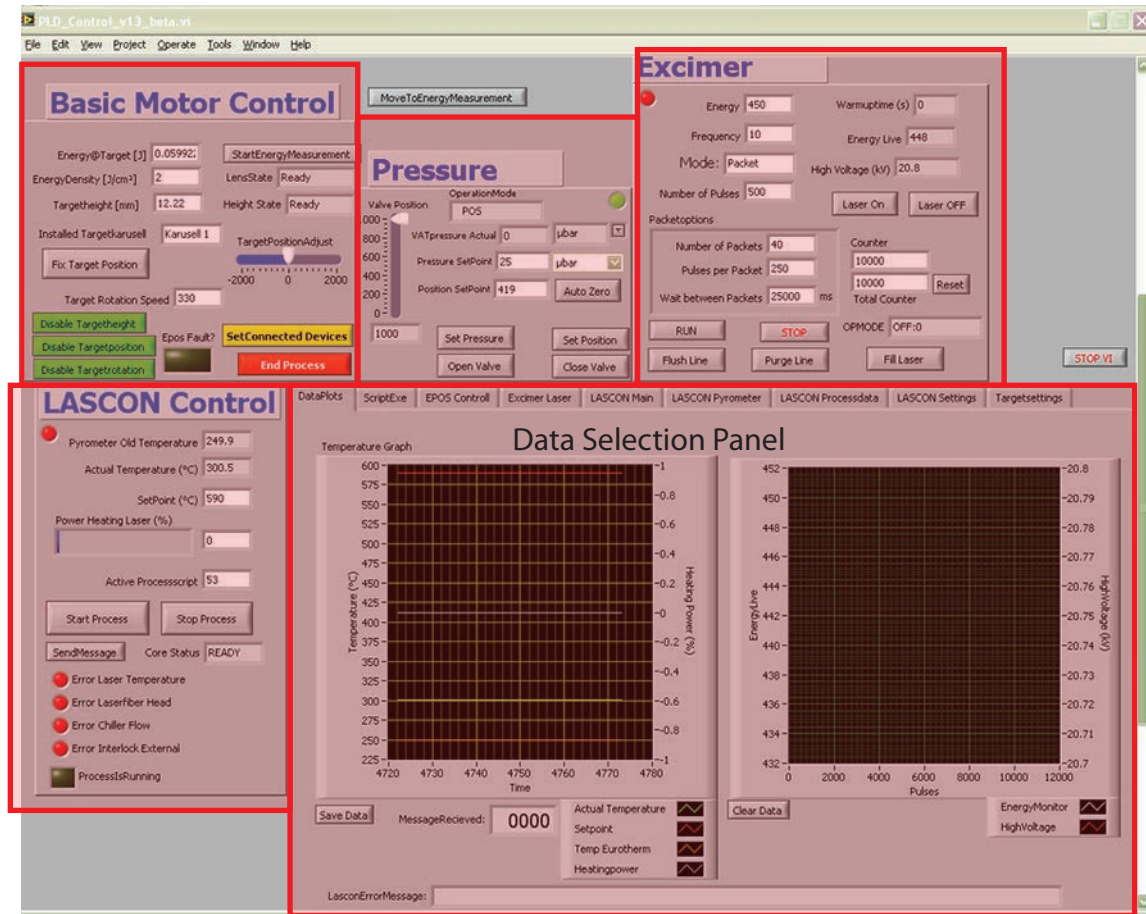


Figure A.3: Screenshot of the main user interface of the latest version of the LabVIEW based control software which has 5 substructures: "Basic Motor Control", "Pressure Control", "Excimer Laser Control", "LASCON Control" and "Data Selection Panel" with a tab selector.

The "Basic Motor Control" allows to change parameters that are normally relevant during a laser-MBE process. The "EPOS Control" tab allows to adjust in more detail parameters of the stepper motors.

Within the "Basic Motor Control", the "Energy@Target" textbox displays the energy of the excimer laser in Joule at the target calculated from the last energy measurement with the OPHIR pyroelectric measurement head. This value will be automatically updated after an energy measurement. Moreover, if the software is run after a shutdown the last stored value in the Log file is automatically loaded and displayed.

The textboxes "LensState" and "Height State" display the status of the lens system and the target height, respectively. For the "LensState" one of five different statuses will be displayed: "None" (system after a restart), "Lenses moving" (movement of lens positions is currently in progress), "Lenses moving (Energy)" (lens system moves into the energy measurement position, energy measurement in progress), "Ready" (lens system reached position for set energy density at target, ablation can begin). For the "Height State" of the target height one of three different statuses is selected: "Moving" (target height

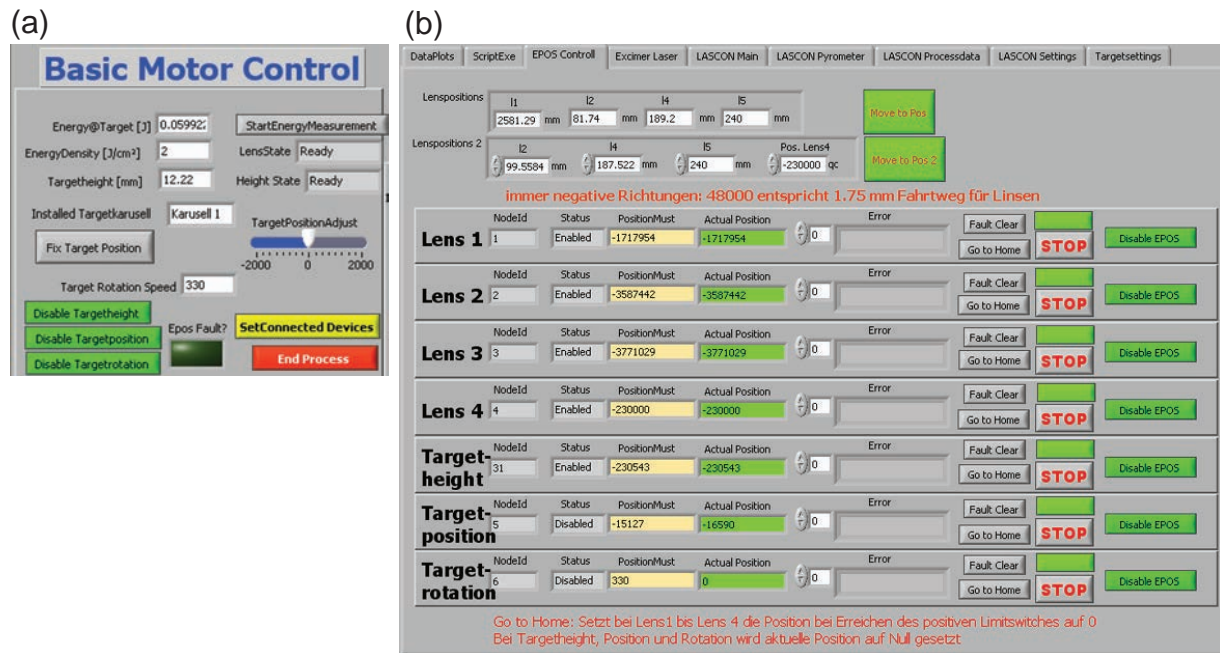


Figure A.4: (a) Basic Motor Control enables the user to easily access relevant tasks for the stepper motors. (b) The "Epos Control" tab provides in depth information on the status of each stepper motor and allows to home and clear errors for each stepper motor.

is adjusted), "Moving to 0" (target height is moving to home position), and "Ready" (selected target height is reached, ready for ablation).

An indicator "Epos Fault?" provides the user with information of any errors of any of the 7 stepper motors used for the lens movement or the target manipulation. If this indicator is colored red an error has occurred, and the user should check the "Epos Control" tab to see which stepper motor has an error and should immediately fix the cause of this error.

By clicking on one of the 3 green buttons "Disable Targetheight", "Disable Targetposition" and "Disable Targetrotation" the user disables the stepper motor controller of the respective target manipulation axis and can then carry out manual adjustments.

The button "End Process" sets first the target rotation to 0, then disables all 3 axes of the target manipulation. Thus this button can be used after a deposition process to set the target manipulation into an idle state.

The input field "Installed Targetkarusell" has three values "Karusell 1", "Karusell 2", and "Karusell 3". For a correct positioning of the target into the focal spot of the lens system the correct value for the installed target carousel must be selected (each carousel has different offset corrections stored in the software). For positioning the target in the focal spot it is crucial to have selected the right target carousel in the software.

The input field "Targetheight [mm]" allows to adjust the target height such that the top of the target sits in the focal spot of the lens system. The value to type in here is the distance from the top of the target to the base plate of the target carousel in mm. If this value is changed, the software calculates the correct position by taking into account the selected target carousel and the target height. Then it first moves the target height into

the 0 position ("Moving to 0") and then to the correct value ("Moving"). After reaching the final value the "Height State" will display "Ready".

Clicking the button "Fix Target Position" leads to a storage of the current position of the target selection as a setpoint into the EPOS controller and enables the position control of the target position. This button should be pressed after adjusting the target position, such that the excimer laser will hit the right spot on the target. The slider "TargetPositionAdjust" allows to fine tune the target position on the fly.

By changing the value in the input field "Target Rotation Speed", the target rotation is enabled and the target will start to rotate with the given value as quad counts per second (revolution of the target itself is about 0.25 Hz for a value of 300).

When clicking the button "StartEnergyMeasurement" the system will prepare and carry out an energy measurement of the excimer laser. *Please note that this button is only to be clicked on after the excimer laser has been switched on, warmed up and fired such that the energy of the pulses has stabilized.* After this button has been clicked the lens system first moves into the energy measurement position (during first tests we found that the measured energy is very sensitive to the lens positions), during this process the "LensState" displays "Lenses moving (Energy)". After the lens system has moved into this position the "LensState" displays "Energy measurement". A user dialog pops up prompting the user to open the shutter of the excimer laser and to move the mirror of the "Intelligent Window" into position. The user should only confirm the dialog after carrying out the required steps. After the user interaction the software automatically fires 40 laser pulses and measures for each pulse the energy using the pyroelectric measurement head. The first 10 results are discarded and the remaining 30 values are used to calculate the mean value. Using the conversion factor (1.735) this mean value is then converted into the energy at the target. Using this value and the value in the field "EnergyDensity [J/cm²]" the new values of the lens positions are calculated. The lens system then moves into these positions, while the "LensState" displays "Lenses moving". After reaching the correct positions the "LensState" changes to "Ready". For each energy measurement the software generates an ASCII encoded file that stores the measurement values located in the path "D:\User\Excimer_Energy\Logs\". Each filename has the prefix "run" and a combination of date and time affixed to it.

The input field "EnergyDensity [J/cm²]" allows the user to change the energy density at the target. The software uses this input value and the value of "Energy@Target [J]" to determine the corresponding spot area at the target and then uses the equations determined from the optimization process to calculate the lens positions. After changing the value a user dialogue appears asking the user if an energy measurement should be carried out. If this dialogue is closed with "No" the software uses the already present value in "Energy@Target [J]" for its calculation process.

Clicking the button "SetConnectedDevices" opens a new user dialog, where the connection of the software to the VAT pressure controller, the excimer laser, and the LASCON server can be switched on and off separately. *To warrant an optimal operation of the software it is important to disable first the connection of the software to one of these devices before switching the device off.* Please also note that the connection to the LASCON server can only safely be established by waiting 1 minute after switching on the laser heater, due to the boot time of the server.

More advanced settings for each stepper motor can be accessed in the software using the "EPOS Control" tab. Within this tab there are two sets of lens parameters that can

be used to adjust the lens positions manually (for a focal spot optimization). For each set of parameters the corresponding button will start the movement of the lenses to the desired positions. We note that the software moves the lenses always upwards towards the final position to minimize hysteresis effects. Moreover, before each move the software checks for possible lens crashes and accordingly corrects the set point values if necessary and displays a user warning.

In addition, the "EPOS Control" tab provides further information of each stepper motor controller. Each axis is displayed as a horizontal arrangement of buttons and textboxes. The "NodeId" is a read-only textbox displaying the NodeId of the corresponding axis. The "Status" textbox displays the current status of the axis: "enabled", "disabled", "Fault", and "blank". The input textbox "Position Must" allows to manually adjust the current position (displayed values are quadcounts). The green textboxes "ActualPosition" display the actual position of the axes. The grey "Error" textboxes contain entries describing the source of the error of the axes, if the axis is in the "Fault" state. The "Fault Clear" buttons allow to clear the "Fault" state of the axes. *The clearing of the "Fault" state should only be carried out by an experienced user and after the source of the error has been fixed!* The buttons "STOP" allow to halt any movement of the respective axis immediately. "Disable EPOS" disables the active feedback control of the corresponding axis via the stepper motor.

Clicking the button "Go to Home" has different results depending on the axis used. For "Lens 1", "Lens 2", "Lens 3", and "Lens 4" the axis moves into positive directions until the positive limit switch is reached and takes this position as the new zero-position. For the "Targetheight" the positive limit switch has to be enabled first by switching on the grey box underneath the laser-MBE chamber, before pressing the homing button. The axis moves after clicking the button into positive direction until the positive limit switch is closed. This position is then used as the new zero position. For the "Targetposition" and "Targetrotation" axes a click on the "Go to Home" button just sets the current position of the axis as the new zero position.

A.2.2 Pressure Control

The "Pressure Control" in Figure A.5 enables the user to directly change relevant parameters of the pressure stabilization. Note that if the LabVIEW software is connected to the pressure controller, the controller becomes remotely locked, no front panel operation is possible.

The LED indicator on the top right side signals the connection state of the software: green color means the software is connected to the pressure controller, red no connection.

Within this panel three textboxes inform the user of the current status of the variable pressure valve: "OperationMode", "VATpressure Actual" and "Valve Position". The textbox "OperationMode" has two values: "POS" indicating a direct position control of the gate valve and "PRES" indicating a PI-loop control of the gate valve position to stabilize a certain pressure. The actual pressure from the Baratron pressure gauge is shown in the textbox "VATpressure Actual", while the actual valve position is displayed in the "Valve Position" scrollbar.

The "Auto Zero" button can be used to set the zero value of the pressure reading, which compensates the voltage signal of the pressure gauge to 0. This button should be clicked if the actual pressure fluctuates around zero at the base pressure of the laser-MBE

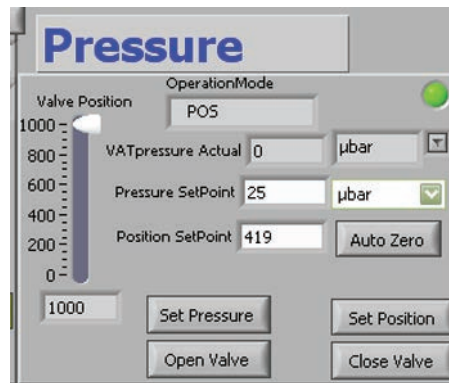


Figure A.5: The Pressure Control allows the user to adjust the pressure in the laser-MBE chamber.

chamber. An "Auto Zero" should only be carried out if the pressure in the laser-MBE chamber is at the base pressure.

The "Open Valve" and "Close Valve" buttons open and close, respectively, the gate valve completely ("Open" equals a position value of 1000, and "Closed" a position value of 0). Clicking these buttons sets the controller into the "POS" state. *The pressure controller should be in the "POS" state when a gas atmosphere is introduced or extracted from the laser-MBE chamber, i.e. opening or closing gas inlet valves and changing settings of the gas flow controllers.*

To directly control the valve position it is possible to input an integer value between 0 and 1000 in the "Position SetPoint" textbox and then click the "Set Position" button. This sets the controller into the "POS" state.

The direct pressure stabilization of the pressure control is activated by typing a pressure set point into the textbox "Pressure SetPoint" (note that you can change the pressure measurement unit with the dropdown box to the right) and clicking on the "Set Pressure" button. The software then calculates automatically the optimal values for the analog to digital conversion of the pressure gauge and activates the pressure control mode with the desired set point.

A.2.3 Excimer Laser Control

The excimer laser can be controlled in the software via the "Excimer" control (Fig. A.6(a)). All relevant information read out from the laser are collected in the "Excimer Laser" data tab (Fig. A.6(b)). The round LED indicator in the top left corner of the "Excimer" panel indicates the status of the connection to the laser: red no connection, green connection present.

There are 4 textboxes in the control panel that inform the user of the important parameters of the excimer laser: "OPMODE", "High Voltage (kV)", "Energy Live", and "Warmuptime (s)". "OPMODE" displays the current operation mode of the excimer laser. It should normally display "OFF:0" (laser is off without any errors) or "ON" (laser is switched on, ready to fire). If there are any errors indicated by the operation mode, the software will inform the user with a popup and more information on the error.

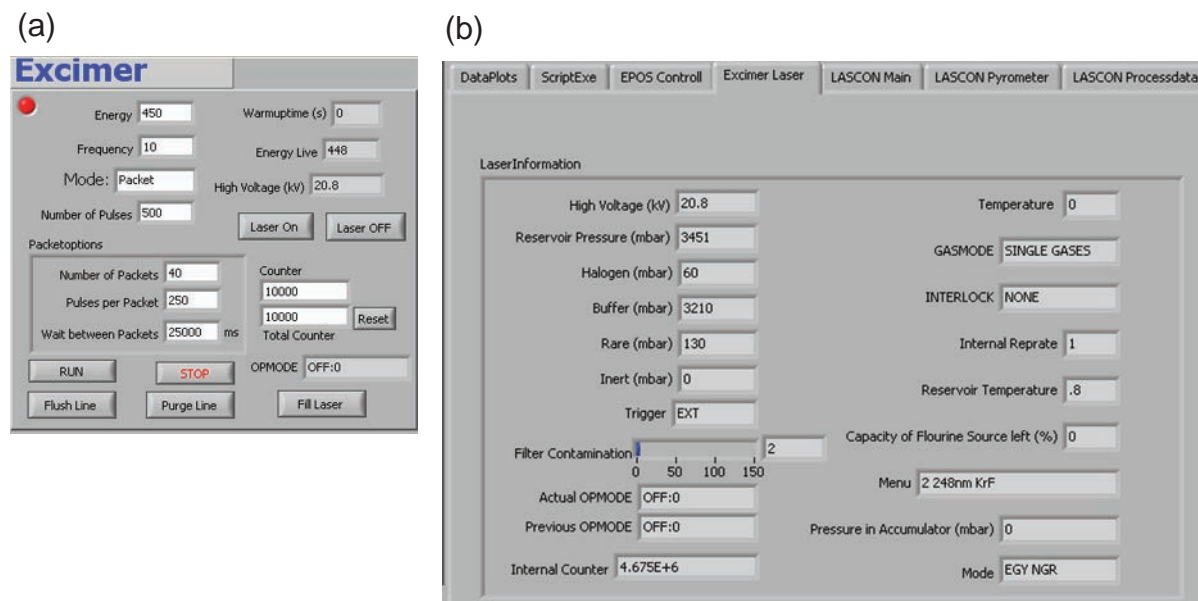


Figure A.6: (a) The main Excimer Control allows to fully control the excimer laser and the pulses fired by the laser. (b) In depth information on all the relevant excimer laser parameters are provided in the Excimer Laser data tab.

”Warmuptime (s)” displays the remaining time in seconds until the warm up process of the excimer is finished. (After the power of the laser is switched on, the thyratron in the excimer laser needs to warm up to protect it from damage.) ”High Voltage (kV)” displays the voltage of the discharge used to initiate the lasing process in kilovolts. ”Energy Live” shows the energy of the last laser pulse measured internally (a beam splitter inside the laser couples out a small fraction $< 1\%$ of the laser pulse to an energy monitor).

With the buttons ”Laser On” and ”Laser Off” the user can switch the excimer laser on (laser is ready to fire) or off (laser is in standby and not ready to fire).

Three buttons allow to manipulate the gas handling of the excimer laser ”Flush Line”, ”Purge Line” and ”Fill Laser”. A click on the button ”Flush Line” allows to pump out one of the gas lines which can be selected from a pop up window. ”Purge Line” pumps out the selected gas line and fills it with inert gas. A refill of the laser reservoir is carried out by clicking the ”Fill Laser” button. A series of pop up windows guides the user through this process and displays the progress. First all gas bottles need to be opened, the software then flushes each line twice to clean the gas lines. Then the laser reservoir is pumped out to a low pressure level (< 20 mbar). After the pump out a new fill is initiated, the laser automatically mixes the gas in the reservoir. After the fill is complete the user is prompted to close all gas bottles except the inert gas. The software then purges the halogen line two times to remove any remaining halogen gas in the line. Afterwards all gas bottles can be closed and the filling process is complete.

The energy of the laser pulses can be set by the input field ”Energy” in mJ. The excimer laser internally monitors the energy of each pulse and adjusts the voltage of the discharge to stabilize the desired energy set point (in most cases this value will be 450 mJ).

The control also allows to specify the pulses the laser should fire. ”Frequency” sets the repetition rate of the laser pulses in Hertz (a maximum of 10 Hz is possible). ”Mode”

allows the user to select from two pulse modes "Normal" and "Packet". In "Normal" mode, the laser will fire the number of pulses defined in "Number of Pulses" with a repetition rate defined by "Frequency". In the "Packet" mode the laser will fire a sequence of pulse packets as specified by the input fields "Number of Packets", "Pulses per Packet" and "Wait between packets" (time is in ms). Note that the excimer laser has to be in the "On" operation mode, which is established by clicking the "Laser On" button. A pulse series is started by clicking the "RUN" button and can be stopped immediately by clicking the "STOP" button. The laser is triggered externally via the digital out of the DAC card installed in the laser-MBE PC. The timing of each pulse is carried out in the LabVIEW software itself.

The "Counter" and "Total Counter" textboxes enable the user to monitor the number of pulses fired, clicking on the "Reset" button sets the total counter to 0. The "Total Counter" adds up each laser pulse fired while the software is running, while the "Counter" counts up for each pulse series initiated by pressing the "RUN" button.

More detailed information on the parameters of the laser are displayed in the "Excimer Laser" data tab. Most of the values are self explanatory. One important parameter is the "Reservoir Pressure (mbar)", which displays the pressure in mbar of the laser reservoir. This value is a good indicator for the age and quality of the laser fill: After a new laser fill this value is above 3400 mbar and decreases, the longer the filling remains in the reservoir. It is advisable to refill the laser at reservoir pressures below 3330 mbar to achieve a high homogeneity of the excimer laser beam.

A.2.4 LASCON Control

Access to information on and control of the LASCON server is provided by the "LASCON Control" panel (Fig. A.7(a)) and 4 data selection tabs: "LASCON Main" (Fig. A.7(b)), "LASCON Process data" (Fig. A.7(c)), "LASCON Pyrometer" (Fig. A.8(a)), and "LASCON Settings" (Fig. A.8(b)). The most important parameters can be monitored and controlled via the "LASCON Control" panel. The round indicator LED on the top left corner of the panel indicates the connection status of the software to the LASCON server: red: disconnected, green: connected. Note that a connection can be established via the "SetConnected Devices" button in the "Basic Motor Control" panel.

The status of the server core is displayed by the indicator "Core Status". The most common values are "READY" (core is idle) and "PROCESSING" (core is processing). The actual temperature measured by the built-in pyrometer is displayed in °C in "Actual Temperature (°C)". Moreover, the temperature measured by an additional pyrometer (equipped with a camera and mounted in such a fashion that the film side of the substrate can be monitored) is displayed in "Pyrometer Old Temperature" again in °C.

The current temperature set point in °C is shown in the input field "SetPoint (°C)". It is automatically updated if a process script changes this value. Moreover, the user can directly change the temperature set point by typing in the desired value into the input field and confirming with return. The current laser heater output is shown in bar graph "Power Heating Laser (%)". The values are ranging from 0% (no heater output) to 100% (maximum heater output). The user can directly input the value and confirm with return.

The number of the currently selected process script is displayed in "Active Process-script" and can be changed by the user. The buttons "Start Process" and "Stop Process"

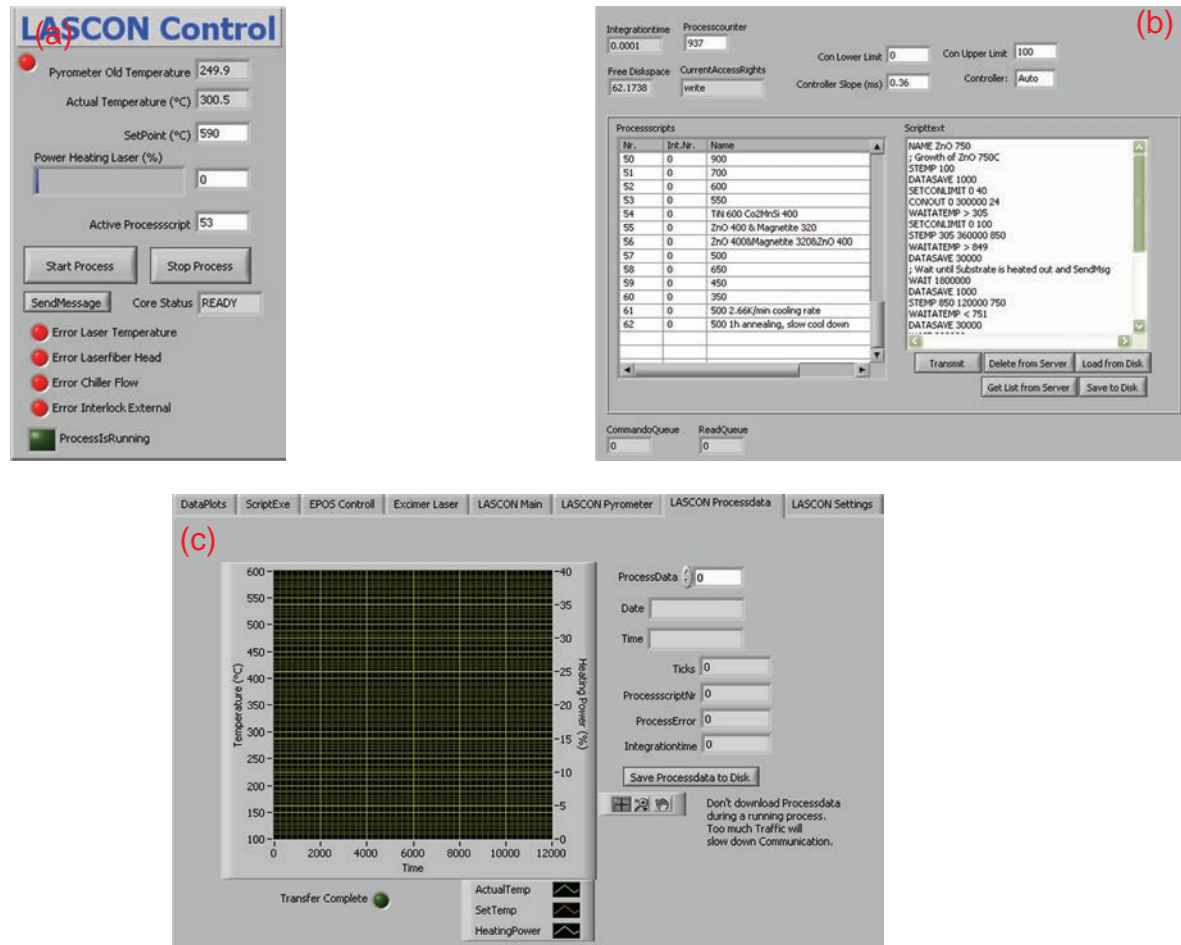


Figure A.7: (a) LASCON Control allows to directly control and monitor temperature set point, laser heater output and script process execution. (b) The LASCON Main Data tab allows to manipulate old and generate new scripts for the LASCON server to execute. (c) Process data of the LASCON server can be downloaded in the Process data tab.

start and stop the execution of the selected process script, respectively. The square LED indicator "ProcessIsRunning" at the bottom of the panel is bright green if a process is currently running.

The "SendMessage" button allows to send a message to the LASCON server. A popup appears, where the user has to type in the number of the message. This enables to communicate with the core during the execution of a process script and for example allows to continue the LASCON script execution if a "WAITMSG" is used in the script.

Critical errors are indicated by 4 round LEDs at the bottom of the panel. Please note that all 4 LEDs will be red after the start up of the LASCON Server as the measured temperature of the laser head is below the detection limit. After the heater output is above 0% this error display will be gone.

The process scripts executed by the LASCON core can be edited and viewed in the "Lascon Main" data selection tab.

A list of all process scripts stored on the LASCON server is displayed in the left list.

It is refreshed after a connection has been established between server and software. In addition, a manual refresh is achieved by clicking the "Get List From Server" button. In this list the process script number and name are displayed. Clicking one of the scripts on the list displays the script in the "Scripttext" box on the right. In this box the user can change and edit the script (for an introduction into the script language please consult the LASCON manuals). The displayed script can be saved and loaded from the local disk by clicking "Save to Disk" and "Load from Disk", respectively. To transmit the edited script to the server the user has to click the "Transmit" button. A pop up asks for the respective processscript number, to which the script should be saved to (a total number 1023 scripts can be stored on the LASCON server, when selecting an existing script number the old script will be replaced). Afterwards a popup informs the user if this process was successful. To delete a script from the server a click on the "Delete from Server" button is necessary. After clicking the button a pop up asks for the process script number to delete.

Apart from the editing and displaying of process scripts this data selection tab also informs the user about the available disk space on the LASCON server in "Free Diskspace". The LASCON server saves for each executed script the relevant parameters on its disk. If the disk is nearly full the auto delete function of the server will delete the oldest saved process data. To each process execution a unique number is assigned displayed in the "Processcounter" field. Using this number allows to download the process data from the server.

The download and display of process data is carried out in the "LASCON Processdata" data selection tab. *Please note that due to the large amount of traffic generated while downloading process data the download should be only executed while no script is running.* The data to display is selected by putting in the corresponding process script number into the "ProcessData" field. A graph on the left displays the data downloaded from the server. The button "Save Processdata to Disk" allows the user to store the downloaded process data in an ASCII encoded file.

The "LASCON Pyrometer" data selection tab displays relevant parameters of the built-in pyrometer of the LASCON system. The upper and lower detection limit of the current settings are displayed in "Upper Limit (°C)" and "Lower Limit (°C)", respectively. The pilot laser of the LASCON system can be switched on by clicking the round LED indicator "Pilot 2". Additionally, the intensity of the pilot laser can be tuned via the tuning knob right below or by typing a value into the input box (the integer intensity values range from 0 to 255, but are non linear. Be careful!).

The data selection tab "LASCON Settings" displays the currently active settings of the server. *Changes made in this tab influence the performance of the LASCON system and should therefore only be changed if you have first familiarized yourself with the LASCON manuals.* The user can select in the dropdown box "Current Setting" a setting and activate the setting by clicking the "Activate Setting" button. The settings itself can currently not be changed via the LabVIEW software, please use the LASCON client control software for changes.

A.2.5 Data Window

The "DataPlot" data selection tab (Fig. A.9) provides the user with data logs of the currently running process.

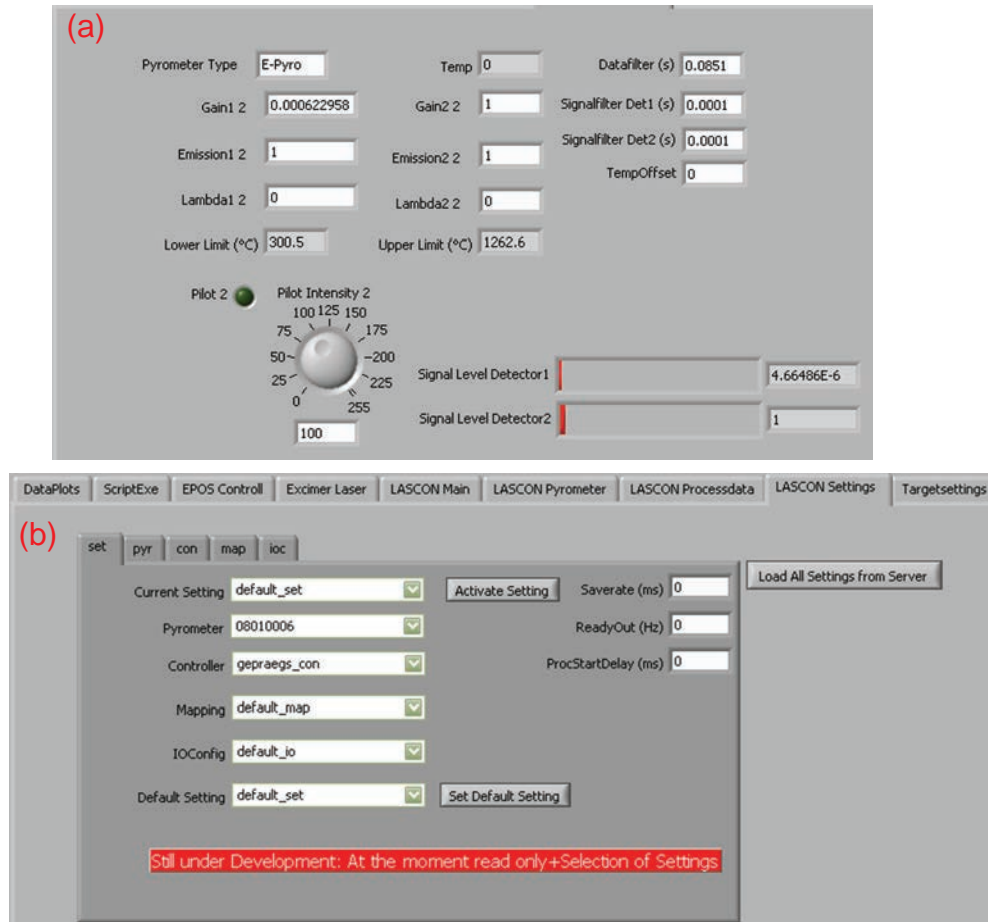


Figure A.8: (a) Information on the LASCON pyrometer are accessed in the LASCON Pyrometer data tab. (b) Advanced setting of the LASCON server can be read out using the LASCON Settings data tab.

This data selection tab provides two graphs that display relevant process information. The graph on the left side displays information on the substrate temperature: actual temperature (read from the LASCON server), temperature set point (LASCON server), additional temperature read from the second pyrometer, and heater output power. The graph on the right shows information regarding the excimer laser: pulse energy (measured internally in the excimer laser) and discharge voltage.

The "MessageReceived" indicator displays message numbers received from the LASCON Server. The "LASCONErrorMessage" indicator holds any error message sent from the LASCON server.

Please note that the software automatically updates every minute and generates a log file "D:\User\PLDlog.dat". This log file is ASCII encoded and contains all relevant parameters of the system. To increase the performance of the update process the size of the log file should be kept below 50 MB. If the file size is larger than this value, the user should stop the software and rename the file. On the next startup the software automatically generates a new log file.

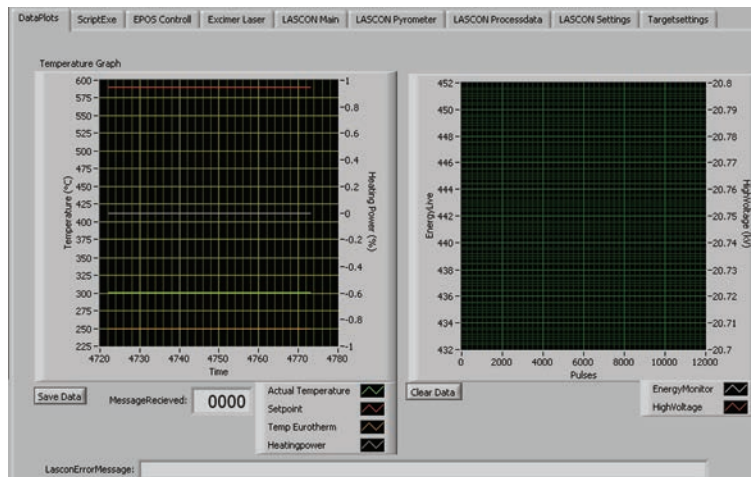


Figure A.9: The DataPlots data tab provides the user with information on the currently status of the substrate temperature and the excimer laser.

A.2.6 Target Control

A more convenient way of selecting the installed targets is realized with the "Targetsettings" data selection tab (Fig. A.10).

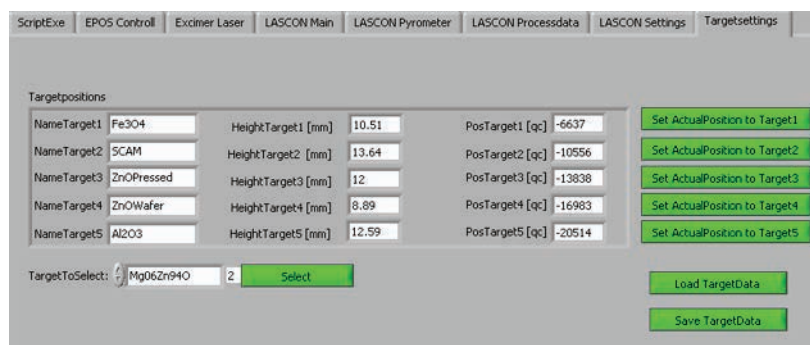


Figure A.10: The target data tab enables the user to store the positions and heights of the targets installed in the target carousel.

Within this tab the user can define the name of each target installed in the corresponding "Name Target" textboxes. Moreover, the target height is stored in units of mm in the "HeightTarget" textbox for each target. The position of the target is stored in the "PosTarget" textbox. To conveniently define this position the user can manually rotate the target carousel to the desired position and store the position for each target by clicking the corresponding "Set ActualPosition to Target" button. These parameters can be stored in an ASCII encoded file by clicking "Save TargetData" and loaded into the software by clicking "Load TargetData".

After the definition of all targets and positions the user can then use the drop down list "TargetToSelect" to select a target. The software then automatically sets the target height and rotates the target carousel to the right position.

A.2.7 Script Control

The "ScriptExe" data selection tab (Fig. A.11) allows the user to execute basic scripts that allow an automated execution of deposition processes. The script language is case

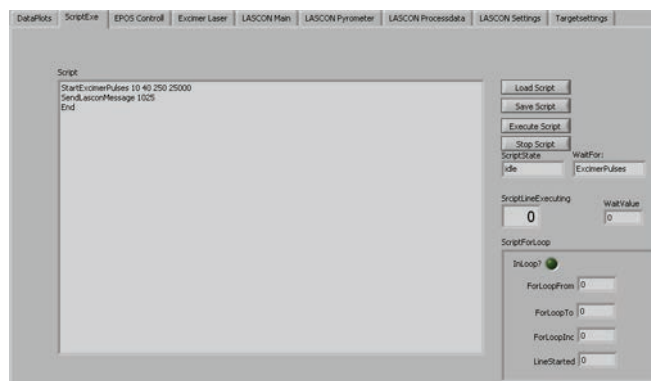


Figure A.11: The Script data tab allows to load and execute scripts in the laser-MBE software for the automation of certain tasks (e.g. repetition for multilayers, temperature ramping after deposition has finished).

sensitive. Each line of the script starts with a keyword, attached to this keyword are parameters. Keyword and parameters must be separated by a tabulator (ASCII-Code 9). Each line must end with a carriage return/line feed (ASCII-Code 13,10). The scripts can be created and edited with any standard text editor and must be ASCII encoded.

The following keywords are recognized by the software:

- **For** [**From**] [**To**] [**Inc**] These keywords define a loop that increases its count value from [**From**] to [**To**] by [**Inc**] for each execution. The end of the loop needs to be defined by a **DoEnd**. Please note that a nesting of loops is currently not possible.
- **DoEnd** encloses with **For** the part of the script that is looped.
- **ShowUserDialog** [**String**] displays an user dialog containing the [**String**].
- **End** stops the script executions. This keyword has to be used at the end of each script.
- **Wait** [**WaitFor**] [**WaitValue**] This keyword is used to put the script execution into the wait state. In this wait state it can wait for different events defined by the parameter [**WaitFor**]. Currently implemented are the following events: **Time**, sets the script to wait for the time in ms defined by the parameter [**WaitValue**]. **LasconMessage**, halts the script execution until a message from the LASCON server with the message number defined by the parameter [**WaitValue**] is received. **LensPositionsReady** pauses all script executions until the lens system is in the ready state. **TargetReady** waits until the selection of the target is finished. With the parameter **ExcimerPulses** script execution is stopped until the excimer puls packets are finished.

- **StartExcimerPulses** [Frequency] [#OfPackets] [#OfPulses] [Wait] starts the firing of excimer laser pulses in the packet state. *The excimer laser has to be in the "ON" state.* The parameter [Frequency] sets the repetition rate of the laser, [#OfPackets] the number of packets, [#OfPulses] the number of pulses per packet, and [Wait] the wait time in ms between packets. The script execution is automatically put into the wait "ExcimerPulses" state when encountering a **StartExcimerPulses** keyword.
- **SendLasconMessage** [LasconMessageNumber] sends a message to the LASCON server with the message number specified in the parameter [LasconMessageNumber]. This is used to synchronize script execution of the LASCON server and the LABVIEW software scripts.
- **VATSetPressure** [Pressure] [Unit] sets the set point of the variable pressure controller to [Pressure], where [Unit] defines the pressure unit, which is either mbar or μ bar. The state of the pressure controller is automatically set to "PRES".
- **SelectTarget** [Target#] selects the target from the target list. [Target#] specifies the target position ranging from 1 to 5. The script execution is automatically paused until the target is selected and the target height has been adjusted.
- **SetTargetRotation** [TargetRot] sets the target rotation speed to the value given with TargetRot.
- **SetEnergyDensity** [EnergyDensity] adjusts the lens positions to achieve an energy density defined by the parameter EnergyDensity. For the calculation the value in the field "Energy@target" is used. The script execution is automatically put into the wait state, and waits until the lenses have reached their new target positions.
- **VATSetPosition** [ValvePosition] puts the variable pressure controller into the "POS" state and sets the position set point to the value specified by the [ValvePosition] parameter.

Scripts can be loaded into the software by clicking the "Load Script" button and stored as an ASCII encoded file by clicking "Save Script". Clicking "Execute Script" starts the execution of the script. The script execution is stopped by clicking on the "Stop Script" button.

The script itself is shown in the script window, while the status of the script execution is displayed to the right side of the window.

A.3 Basic operation of laser-MBE

In this section we shortly outline the typical steps carried out during a deposition process. This is just an overview and does not contain all the relevant steps for a successful deposition process.

We begin at the point where the substrate holder is moved into the substrate manipulator. Switch on the laser heater, excimer laser and the additional pump for the RHEED, prior to transferring the substrate. (Laser protection goggles!). Establish a connection to

the LASCON server and the excimer laser using the control software on the laser-MBE PC. With the help of the pilot laser of the LASCON laser heater the substrate holder is positioned in the manipulator in such a way that the substrate is in the center of the pilot laser spot. After moving the robotic arm for the transfer process outside of the laser-MBE chamber, the slab gate valve connecting the transfer chamber to the laser-MBE chamber is closed and the filament of the pressure gauge is switched off.

As a next step the electron beam for the RHEED (Reflection High Energy Electron Diffraction) is switched on, and the substrate manipulator is used to adjust the substrate height (typically around 22-23), rotation and tilt to achieve a perfect RHEED pattern on the screen.

To introduce the growth atmosphere into the laser-MBE chamber the variable pressure controller is switched into the "POS" mode and the gate valve closed more than half (a position value of 400 is a good value). The gas bottle for the growth atmosphere and all relevant valves are opened. The corresponding flow controller is switched on and a fixed flow value is adjusted. Then the desired pressure can be set in the variable pressure controller via the LABVIEW software. Please note, that the achievable pressure range depends on the gas flow stabilized by the flow controller.

After the introduction of a growth atmosphere the substrate can be heated up. The keyswitch at the laser heater is turned to the "enable" position and, using the control software, the script to be executed is selected and started. (Check and record the RHEED pattern during heat up). When the substrate temperature approaches the deposition temperature the excimer laser can be put into the "On" state using the software. With the shutter closed a first series of 200 pulses needs to be fired to stabilize the excimer laser. After this warm up of the excimer laser an energy measurement has to be carried out using the software (the user should check that the shutter of the excimer is open and the mirror of the intelligent window is manually moved into position). After the energy measurement the desired energy density for the deposition process can be selected within the software.

The target for the deposition process can be selected manually or automatically with the help of the software. Please check if the correct height value and target carousel are selected in the software and target height and selection are in the "Enabled" state. Then start the rotation of the target via the software and manually move the shutter between target and substrate. After checking if the excimer laser hits the right spot of the target, a pre-ablation process can be carried out using the pulse control of the software (*the mirror of the intelligent window has to be in the retracted state, such that the excimer beam can pass into the laser-MBE chamber*). After the pre-ablation process the normal deposition process can start, and the RHEED pattern should be checked regularly for changes and intensity oscillations. When the process is finished a message can be sent to the LASCON server to start the substrate cool down. Moreover, the target can be released and rotated away to protect the target during the cool down. When the cool down process is finished, the growth atmosphere has to be removed from the laser-MBE chamber. This is achieved by first setting the variable pressure controller into the "POS" state via the control software to a position setting equal to the value during the pressure stabilization. Then the flow controller can be switched off and all relevant gas valves can be closed. Afterwards the pressure controller is switched into the open state and the substrate can be removed from the growth chamber after reaching the base pressure level.

The connection to the LASCON server and the excimer laser can then be disconnected and the laser heater and the excimer laser can be switched off.

This short description is by no way a full manual to the laser-MBE process, the versatility of our control software allows much more sophisticated deposition processes.

A.4 Operation of the RF atom source

Before we provide the basic steps for the operation of the RF atom source, we would like to point out that the operation of the atom source currently leads to an increase in noise for the pressure gauge used for the pressure stabilization and the pyroelectric measurement head. Therefore it is impossible to use pressure stabilization or energy measurement while the atom source is running

For the operation of the atom source first the cooling water for the source and all relevant devices need to be switched on (RF generator, Auto Tune controller, plasma controller, deflection unit.) The position of the pump gate valve should be set to some value below 400. Afterwards the RF-power to the source can be increased in steps of 50 W per minute to 200 W using the plasma controller in the manual mode, as explained in the atom source manual (check whether the reflected power is minimized by the auto tune function). Then using the needle valve the gas can be introduced into the source. By slowly increasing the amount of gas flowing into the source a plasma should strike signaling the correct operation of the RF atom source. After striking the plasma the RF power can be further increased and the gas flow tuned (typically reduced) until the desired deposition conditions are stabilized. A background gas can be introduced using the flow controller of the laser-MBE chamber. The plasma inside the discharge tube generates mainly atoms of the gas inside the tube (oxygen or nitrogen) and minimizes the generation of ions. The dissociated atoms thermally propagate through the aperture plate of the source towards the substrate.

The RF atom source is equipped with an optical view port that allows to couple out the light generated inside the discharge tube by the plasma. An optical line filter and an optical fibre are used to direct the light onto a photo detector. The signal of the detector is displayed on the plasma controller and can be used as a feedback for automatically stabilizing the plasma by tuning the RF power. For this automatic stabilization the plasma controller needs to be switched into the "Auto" mode. The line filter currently installed is suited for oxygen, an additional line filter suited for nitrogen is available.

After finishing the deposition process the RF power needs to be slowly reduced (1 W per second until the plasma is extinguished and then 20 W per minute) to minimize thermal strain in the discharge tube. After reducing the RF power to 0, the devices and the cooling water (after a 10 minutes wait) can be switched off.

In summary, the new extensions and improvements to our laser-MBE setup increase the versatility of our system and the stability of the deposition conditions. Thus, these additions are crucial for the reproducible fabrication of high quality thin films.

Appendix B

Extraction and simulation of temperature dependent Hall data

For the extraction of temperature dependent Hall data, we used square shaped ZnO samples with a film thickness t and placed an Al wire contact at each corner by wire wedge bonding. Using two different measurement geometries it is then possible to determine V_{long} (Fig. B.1(a)) and V_{trans} (Fig. B.1(d)) by applying a fixed current I to the sample. In both geometries we recorded up- and downsweep for an out-of-plane oriented magnetic field.

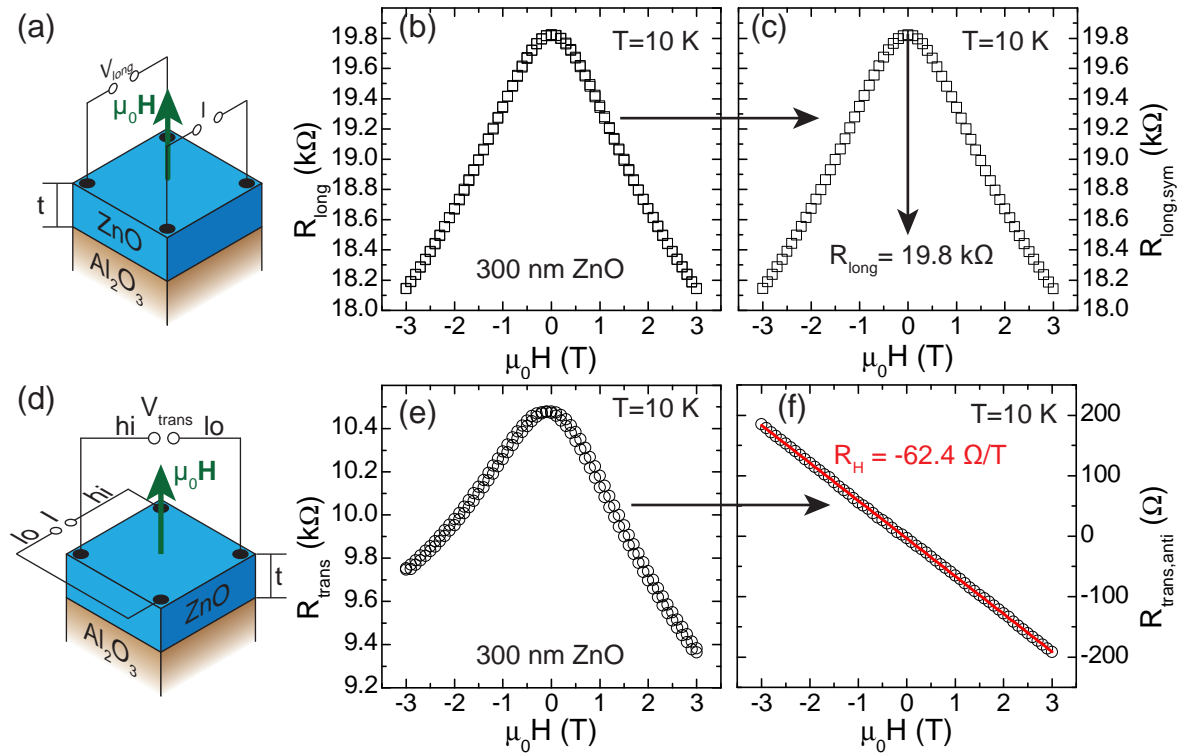


Figure B.1: (a) Illustration of the measurement geometry for extraction of R_{long} . (b) Magnetic field dependence of the longitudinal resistance at $T = 10$ K. The resistance shows a negative magnetoresistance. (c) Field dependent longitudinal resistance after symmetrization. (d) Illustration of the measurement geometry for extraction of R_{trans} . (e) Evolution of transverse resistance as a function of external magnetic field. (f) Magnetic field dependence of the transverse resistance after anti-symmetrization. A linear fit to the data is used to extract the Hall resistance (red line).

Using Ohms law we then calculated $R_{\text{long}}(H)$ and $R_{\text{trans}}(H)$ via

$$R_{\text{long}}(H) = \frac{V_{\text{long}}(H)}{I},$$

$$R_{\text{trans}}(H) = \frac{V_{\text{trans}}(H)}{I}.$$

In order to reduce the influence of spurious signals to $R_{\text{long}}(H)$ and $R_{\text{trans}}(H)$ we utilized the inherent field symmetry of both signals. The longitudinal resistance is symmetric to a magnetic field inversion, thus we can combine up- ($R_{\text{long,up}}(H)$) and downsweep ($R_{\text{long,down}}(H)$) of the data to obtain

$$R_{\text{long,sym}}(H) = \frac{R_{\text{long,down}}(H) + R_{\text{long,up}}(-H)}{2}.$$

In the same way, the transverse resistance is antisymmetric for a field inversion and we calculated with the up- ($R_{\text{trans,up}}(H)$) and downsweep ($R_{\text{trans,down}}(H)$) data

$$R_{\text{trans,anti}}(H) = \frac{R_{\text{trans,down}}(H) - R_{\text{trans,up}}(-H)}{2}.$$

We used the symmetrized longitudinal data, to determine R_{long} for $\mu_0 H = 0$ T, with this value we calculated the longitudinal resistivity ρ_{long} using the Van-der-Pauw formula [125]

$$\rho_{\text{long}} = R_{\text{long}} \times t \frac{\pi}{\ln(2)}.$$

With a linear fit to the field dependent anti-symmetrized transverse resistance, we determined the Hall resistance R_{H} as the slope of the linear fit and calculated the Hall carrier concentration using

$$n_{\text{Hall}} = \frac{1}{R_{\text{H}} t_{\text{film}} e}.$$

This procedure is illustrated for the longitudinal resistance in Fig. B.1(b) and (c), and for the transverse resistance in Fig. B.1(e) and (f).

In the following the MATHEMATICA code used for the Hall simulation is presented:

```
ClearAll["Global`*"];
h=6.62606957*10^(-34)
kb=1.3804*10^-23
e=1.60219177*10^-19
m0=9.10938291*10^-31
a0=0.529177*10^-10
eps0=8.859*10^-12
mn=0.3*m0
mStar=0.3m0
P=0.3
Eac=3.8*1.60217646*10^-19
cl=20.5*10^10
Tpo=837
clat=5.2042*10^-10
```

```

epsR=8.5
epsInf=4
Nd1=4.5*10^25
Na1=1*10^14
Ndis1=1*10^18
C1=2*10^-45
Nd2=7*10^22
Ed2=0.055*1.60217646*10^-19
Na2=2.2*10^16
Ndis2=3.5*10^13
Nn2=14*10^22
C2=4*10^-45
d=550*10^-9
d1=50*10^-9
d2=d-d1
hbar=h/(2*Pi)
muHall [T_]=(d1*mu1 [T]^2*n1 [T]+d2*mu2 [T]*mu2h [T]*n2 [T])
/(d1*mu1 [T]*n1 [T]+d2*mu2 [T]*n2 [T])
nHall [T_]=(d1*mu1 [T]*n1 [T]+d2*mu2 [T]*n2 [T])^2
/((d1+d2)*(d1*mu1 [T]^2*n1 [T]+d2*mu2 [T]*mu2h [T]*n2 [T]))
n1 [T_]=(Nd1-Na1)
n2 [T_]=0.5*(Phi [T]+Na2)*(Sqrt [1+(4*Phi [T]*(Nd2-Na2))/(Phi [T]+Na2)^2]-1)
Phi [T_]=(2*(2*Pi*m0*kb*T)^(3/2)/h^3)*(1/2)*(mn/m0)^(3/2)*Exp [-Ed2/(kb*T)]
y1 [x_, T_]=3^(1/3)*4*Pi^(8/3)*epsR*eps0*hbar^2*(Nd1-Na1)^(1/3)/(e^2*mStar)
tii1 [x_, T_]=(16*Sqrt [2]*Pi*(epsR*eps0)^2*mStar^0.5*(x*kb*T)^(3/2))
/((2*Na1+n1 [T])*e^4*(Log [1+y1 [x, T]]))
nPrime2 [T_]=n2 [T] (** (Nd2-Na2-n2 [T])*(Na2+n2 [T])/Nd2*)
y2 [x_, T_]=8*epsR*eps0*(kb*T)^2*x/(hbar^2*e^2*(nPrime2 [T]))
tii2 [x_, T_]=(16*Sqrt [2]*Pi*(epsR*eps0)^2*mStar^0.5*(x*kb*T)^(3/2))
/((2*Na2+n2 [T])*e^4*((Log [1+y2 [x, T]])-y2 [x, T]/(1+y2 [x, T])))
A1 [x_, T_]=35.2/Sqrt [x*kb*T/Ed2]*(1+Exp [-50*(x*kb*T/Ed2)])*
(1+80.6*(x*kb*T/Ed2)+23.7*(x*kb*T/Ed2)^2)/(1+41.3*(x*kb*T/Ed2)+
133*(x*kb*T/Ed2)^2*(1/(x*kb*T/Ed2)*Log [1+(x*kb*T/Ed2)]-(1+0.5
*(x*kb*T/Ed2)-(x*kb*T/Ed2)^2/6)/(1+x*kb*T/Ed2)^3)
tni2 [x_, T_]=mStar/(A1 [x, T]*Nn2*hbar*a0*epsR*m0/mStar)
tdis1 [x_, T_]=hbar^3*(epsR*eps0)^2*c1at^2*(1+4*(Pi^(1/6)*Sqrt [epsR*eps0]
*hbar/(3^(1/6)*2*Sqrt [mStar]*e*(Nd1-Na1)^(1/6)))^2*(2*mStar*x*kb*
T/hbar^2))^(3/2)/(Ndis1*mStar*e^4*(Pi^(1/6)*Sqrt [epsR*eps0]*hbar/
(3^(1/6)*2*Sqrt [mStar]*e*(Nd1-Na1)^(1/6)))^4)
tdis2 [x_, T_]=hbar^3*(epsR*eps0)^2*c1at^2*(1+4*(Sqrt [epsR*eps0*kb*T
/(e^2*n2 [T])])^2*(2*mStar*x*kb*T/hbar^2))^(3/2)/(Ndis2*mStar*e^4*
(Sqrt [epsR*eps0*kb*T/(e^2*nPrime2 [T])])^4)
tdp [x_, T_]=Pi*hbar^4*c1/(Sqrt [2]*Eac^2*mStar^(3/2)*kb*T*(x*kb*T)^(1/2))
tpz [x_, T_]=2*Sqrt [2]*Pi*hbar^2*epsR*eps0*(x*kb*T)^(1/2)/
(e^2*P^2*mStar^(1/2)*kb*T)
tpo [x_, T_]=2^1.5*Pi*hbar^2*eps0*(Exp [Tpo/T]-1)*(0.5446*
(x*kb*T)^0.5+0.58888*(kb*Tpo)^0.5-0.1683*(kb*Tpo)^-0.5*(x*kb*T))/

```

```

(e^2*kb*Tpo*mStar^0.5*(epsInf^-1-epsR^-1))
tstrain1[x_,T_]=C1/(x*kb*T)^1.5
tstrain2[x_,T_]=C2/(x*kb*T)^1.5
2^1.5*Pi*hbar^2*eps0/(e^2*kb*Tpo*mStar^0.5*(1/epsInf-1/epsR))
tLayer1[x_,T_]=(tdp[x,T]^-1+tpz[x,T]^-1+tpo[x,T]^-1
+tstrain1[x,T]^-1+tdis1[x,T]^-1+tii1[x,T]^-1)^-1
tLayer2[x_,T_]=(tdp[x,T]^-1+tpz[x,T]^-1+tpo[x,T]^-1
+tstrain2[x,T]^-1+tdis2[x,T]^-1+tii2[x,T]^-1+tni2[x,T]^-1)^-1
mu1[T_]=e*4/(3*Sqrt[Pi])*NIntegrate[x^1.5*tLayer1[x,T]
*Exp[-x],{x,0,20}]/mStar;
mu2[T_]=e*4/(3*Sqrt[Pi])*NIntegrate[x^1.5*tLayer2[x,T]
*Exp[-x],{x,0,20}]/mStar;
mu2h[T_]=e*4/(3*Sqrt[Pi])*NIntegrate[x^1.5*tLayer2[x,T]^2*
Exp[-x],{x,0,20}]/(NIntegrate[x^1.5
*tLayer2[x,T]*Exp[-x],{x,0,20}]*mStar);
nHall1Theo[T_]=(mu1[T]*n1[T])^2/(mu1[T]^2*n1[T]);
nHall2Theo[T_]=(mu2[T]*n2[T])^2/(mu2[T]*mu2h[T]*n2[T]);
muTheo={};
nTheo={};
mu1Theo={};
mu2Theo={};
n1Theo={};
n2Theo={};
For[i=10,i<=350,i++,
TM=N[i*1];
mutm=N[muHall[i*1]];
ntm=N[nHall[i*1]];
n1tm=N[nHall1Theo[i*1]];
n2tm=N[nHall2Theo[i*1]];
mu1tm=N[mu1[i*1]];
mu2tm=N[mu2h[i*1]];
AppendTo[muTheo,{TM,mutm}];
AppendTo[nTheo,{1/TM,ntm}];
AppendTo[n1Theo,{TM,n1tm}];
AppendTo[n2Theo,{TM,n2tm}];
AppendTo[mu1Theo,{TM,mu1tm}];
AppendTo[mu1Theo,{TM,mu1tm}];
AppendTo[mu2Theo,{TM,mu2tm}];
];
ListLogPlot[{muTheo,mu1Theo,mu2Theo},PlotRange->All]
ListLogPlot[nTheo,PlotRange->All]
Export["dataMuTheo.dat",muTheo,"Data"];
Export["dataMu1Theo.dat",mu1Theo,"Data"];
Export["dataMu2Theo.dat",mu2Theo,"Data"];
Export["dataNTheo.dat",nTheo,"Data"];
Export["dataN1Theo.dat",n1Theo,"Data"];
Export["dataN2Theo.dat",n2Theo,"Data"];

```

Appendix C

Calculation results and source code for GMR calculations

Based on the Valet Fert model presented in Section 2.5.2 we calculated the results for the nominator $N_{R.A}$

$$N_{R.A} = 4e^{-\frac{t_{FM1}}{2\lambda_{sf}^{FM1}} - \frac{t_{FM2}}{2\lambda_{sf}^{FM2}} + \frac{t_N}{\lambda_{sf}^N}} \lambda_{sf}^N \rho_N (\beta_{FM2} e^{\frac{t_{FM1}}{\lambda_{sf}^{FM1}}} \lambda_{sf}^{FM2} (\gamma r_b - \beta_{FM1} \lambda_{sf}^{FM1} \rho_{FM1}) \rho_{FM2} + e^{\frac{t_{FM2}}{\lambda_{sf}^{FM2}}} \times \\ \times (\beta_{FM1} \lambda_{sf}^{FM1} \rho_{FM1} + 2e^{\frac{t_{FM1}}{\lambda_{sf}^{FM1}}} (\gamma r_b - \beta_{FM1} \lambda_{sf}^{FM1} \rho_{FM1})) (\gamma r_b - \beta_{FM2} \lambda_{sf}^{FM2} \rho_{FM2})),$$

and for the denominator $D_{R.A}$

$$\begin{aligned}
D_{R.A} = & e^{\frac{1}{2} \left(\frac{t_{FM1}}{\lambda_{sf}^{FM1}} + \frac{t_{FM2}}{\lambda_{sf}^{FM2}} \right)} \left(-2(-1 + e^{\frac{2t_N}{\lambda_{sf}^N}})(-1 + \gamma^2)r_b^3 - ((\lambda_{sf}^{FM1} \rho_{FM1} - \lambda_{sf}^N \rho_N)(-\lambda_{sf}^{FM2} \rho_{FM2} + \right. \\
& + \lambda_{sf}^N \rho_N) + e^{\frac{2t_N}{\lambda_{sf}^N}} (\lambda_{sf}^{FM1} \rho_{FM1} + \lambda_{sf}^N \rho_N)(\lambda_{sf}^{FM2} \rho_{FM2} + \lambda_{sf}^N \rho_N))((-1 + \beta_{FM1}^2) \rho_{FM1} t_{FM1} + \\
& + (-1 + \beta_{FM2}^2) \rho_{FM2} t_{FM2} - \rho_N t_N) + r_b^2((-1 + e^{\frac{2t_N}{\lambda_{sf}^N}})(2 + (\beta_{FM1} - \gamma)\gamma) \lambda_{sf}^{FM1} \rho_{FM1} + \\
& + (-1 + e^{\frac{2t_N}{\lambda_{sf}^N}})(2 + (\beta_{FM2} - \gamma)\gamma) \lambda_{sf}^{FM2} \rho_{FM2} - 2(-2 + \gamma^2 + 2e^{\frac{t_N}{\lambda_{sf}^N}} \gamma^2 + e^{\frac{2t_N}{\lambda_{sf}^N}}(-2 + \gamma^2)) \times \\
& \times \lambda_{sf}^N \rho_N - (-1 + e^{\frac{2t_N}{\lambda_{sf}^N}})((-1 + \beta_{FM1}^2) \rho_{FM1} t_{FM1} + (-1 + \beta_{FM2}^2) \rho_{FM2} t_{FM2} - \rho_N t_N) + r_b \times \\
& \times (\lambda_{sf}^{FM1} \rho_{FM1}((-1 + e^{\frac{2t_N}{\lambda_{sf}^N}})(2 + (\beta_{FM1} + \beta_{FM2})\gamma) \lambda_{sf}^{FM2} \rho_{FM2} + (2 + \beta_{FM1} \gamma + 2\beta_{FM1} e^{\frac{t_N}{\lambda_{sf}^N}} \gamma + \\
& + e^{\frac{2t_N}{\lambda_{sf}^N}}(2 + \beta_{FM1} \gamma)) \lambda_{sf}^N \rho_N - (-1 + e^{\frac{2t_N}{\lambda_{sf}^N}})((-1 + \beta_{FM1}^2) \rho_{FM1} t_{FM1} + (-1 + \beta_{FM2}^2) \rho_{FM2} t_{FM2} - \\
& - \rho_N t_N)) + \lambda_{sf}^{FM2} \rho_{FM2}((2 + \beta_{FM2} \gamma + 2\beta_{FM2} e^{\frac{t_N}{\lambda_{sf}^N}} \gamma + e^{\frac{2t_N}{\lambda_{sf}^N}}(2 + \beta_{FM2} \gamma)) \lambda_{sf}^N \rho_N - (-1 + e^{\frac{2t_N}{\lambda_{sf}^N}}) \times \\
& \times ((-1 + \beta_{FM1}^2) \rho_{FM1} t_{FM1} + (-1 + \beta_{FM2}^2) \rho_{FM2} t_{FM2} - \rho_N t_N)) + 2\lambda_{sf}^N \rho_N((-1 + e^{\frac{2t_N}{\lambda_{sf}^N}}) \lambda_{sf}^N \rho_N - \\
& - (1 + e^{\frac{2t_N}{\lambda_{sf}^N}})((-1 + \beta_{FM1}^2) \rho_{FM1} t_{FM1} + (-1 + \beta_{FM2}^2) \rho_{FM2} t_{FM2} - \rho_N t_N))) + 4e^{\frac{t_N}{\lambda_{sf}^N}} \times \\
& \times (\beta_{FM1} e^{\frac{t_{FM2}}{2\lambda_{sf}^{FM2}}} \lambda_{sf}^{FM1} \rho_{FM1} \sinh\left(\frac{t_{FM1}}{2\lambda_{sf}^{FM1}}\right) (\lambda_{sf}^N (\gamma r_b - \beta_{FM2} \lambda_{sf}^{FM2} \rho_{FM2}) \rho_N + \lambda_{sf}^N \times \\
& \times (2\beta_{FM1} r_b + \gamma r_b + \beta_{FM1} \lambda_{sf}^{FM2} \rho_{FM2}) \rho_N \cosh\left(\frac{t_N}{\lambda_{sf}^N}\right) + ((\beta_{FM1} + \gamma) r_b (r_b + \lambda_{sf}^{FM2} \rho_{FM2}) + \\
& + \beta_{FM1} \lambda_{sf}^{N2} \rho_N^2) \sinh\left(\frac{t_N}{\lambda_{sf}^N}\right) + \beta_{FM2} e^{\frac{t_{FM1}}{2\lambda_{sf}^{FM1}}} \lambda_{sf}^{FM2} \rho_{FM2} \sinh\left(\frac{t_{FM2}}{2\lambda_{sf}^{FM2}}\right) (\lambda_{sf}^N (\gamma r_b - \\
& - \beta_{FM1} \lambda_{sf}^{FM1} \rho_{FM1}) \rho_N + \lambda_{sf}^N (2\beta_{FM2} r_b + \gamma r_b + \beta_{FM2} \lambda_{sf}^{FM1} \rho_{FM1}) \rho_N \cosh\left(\frac{t_N}{\lambda_{sf}^N}\right) + \\
& + ((\beta_{FM2} + \gamma) r_b (r_b + \lambda_{sf}^{FM1} \rho_{FM1}) + \beta_{FM2} \lambda_{sf}^{N2} \rho_N^2) \sinh\left(\frac{t_N}{\lambda_{sf}^N}\right))).
\end{aligned}$$

An exact calculation can be carried out by using the following MATHEMATICA code:

```

(*Parallel Alignment of ferromagnetic electrodes*)
ClearAll["Global`*"];
rFM1=rhoFM1*1SFFM1;
rFM2=rhoFM2*1SFFM2;
rN=rhoN*1SFN;
zI=-tN/2-tFM1/2;
zII=0;
zIII=tN/2+tFM2/2;
muupI[z_]=(1-beta1^2)*e*rhoFM1*J*(z-zI)+K1I+(1+beta1)*(K2I*Exp[(z-zI)/1SFFM1]+K3I*Exp[-(z-zI)/1SFFM1]);
mudownI[z_]=(1-beta1^2)*e*rhoFM1*J*(z-zI)+K1I-(1-beta1)*(K2I*Exp[(z-zI)/1SFFM1]+K3I*Exp[-(z-zI)/1SFFM1]);
JupI[z_]=1/2*(1-beta1)*J+1/(2*e*rFM1)*(K2I*Exp[(z-zI)/1SFFM1]-K3I*Exp[-(z-zI)/1SFFM1]);

```

```

JdownI[z_]=1/2*(1+beta1)*J-1/(2*e*rFM1)*(K2I*Exp[(z-zI)/lSFFM1]-K3I*
Exp[-(z-zI)/lSFFM1]);
FI[z_]=(1-beta1^2)*rhoFM1*J+beta1/(e*lSFFM1)*(K2I*Exp[(z-zI)/lSFFM1]-
K3I*Exp[-(z-zI)/lSFFM1]);
muupII[z_]=e*rhoN*J*z+K1II+(K2II*Exp[z/lSFN]+K3II*Exp[-z/lSFN]);
mudownII[z_]=e*rhoN*J*z+K1II-(K2II*Exp[z/lSFN]+K3II*Exp[-z/lSFN]);
JupII[z_]=1/2*J+1/(2*e*rN)*(K2II*Exp[z/lSFN]-K3II*Exp[-z/lSFN]);
JdownII[z_]=1/2*J-1/(2*e*rN)*(K2II*Exp[z/lSFN]-K3II*Exp[-z/lSFN]);
FII[z_]=rhoN*J;
muupIIIP[z_]=(1-beta2^2)*e*rhoFM2*J*(z-zIII)+K1III+(1+beta2)*(K2III*
Exp[(z-zIII)/lSFFM2]+K3III*Exp[-(z-zIII)/lSFFM2]);
mudownIIIP[z_]=(1-beta2^2)*e*rhoFM2*J*(z-zIII)+K1III-(1-beta2)*(K2III*
Exp[(z-zIII)/lSFFM2]+K3III*Exp[-(z-zIII)/lSFFM2]);
JupIIIP[z_]=1/2*(1-beta2)*J+1/(2*e*rFM2)*(K2III*Exp[(z-zIII)/lSFFM2]-
K3III*Exp[-(z-zIII)/lSFFM2]);
JdownIIIP[z_]=1/2*(1+beta2)*J-1/(2*e*rFM2)*(K2III*Exp[(z-zIII)/lSFFM2]-
K3III*Exp[-(z-zIII)/lSFFM2]);
FIII[z_]=(1-beta2^2)*rhoFM2*J+beta2/(e*lSFFM2)*(K2III*Exp[(z-zIII)/lSFFM2]-
K3III*Exp[-(z-zIII)/lSFFM2]);
Simplify[D[1/2*(muupIIIP[z]+mudownIIIP[z]),z]]
SolP=Simplify[Solve[{K3I==0,0==K2III,K1I==0,
muupII[-tN/2]-muupI[-tN/2]==2*e*rb*(1-gamma)*JupI[-tN/2],
mudownII[-tN/2]-mudownI[-tN/2]==2*e*rb*(1+gamma)*JdownI[-tN/2],
JupII[-tN/2]-JdownII[-tN/2]==JupI[-tN/2]-JdownI[-tN/2],
muupIIIP[tN/2]-muupII[tN/2]==2*e*rb*(1-gamma)*JupII[tN/2],
mudownIIIP[tN/2]-mudownII[tN/2]==2*e*rb*(1+gamma)*JdownII[tN/2],
JupIIIP[tN/2]-JdownIIIP[tN/2]==JupII[tN/2]-JdownII[tN/2]},
{K1I,K2I,K3I,K1II,K2II,K3II,K1III,K2III,K3III}]]
(*Antiparallel Aligemt, exchange muupIII with mudownIII and JupIII
with JdownIII and change 1-gamma to 1+gamma and vice versa for
second interface*)
SolAP=Simplify[Solve[{K3I==0,0==K2III,K1I==0,
muupII[-tN/2]-muupI[-tN/2]==2*e*rb*(1-gamma)*JupI[-tN/2],
mudownII[-tN/2]-mudownI[-tN/2]==2*e*rb*(1+gamma)*JdownI[-tN/2],
JupII[-tN/2]-JdownII[-tN/2]==JupI[-tN/2]-JdownI[-tN/2],
mudownIIIP[tN/2]-muupII[tN/2]==2*e*rb*(1+gamma)*JupII[tN/2],
muupIIIP[tN/2]-mudownII[tN/2]==2*e*rb*(1-gamma)*JdownII[tN/2],
JdownIIIP[tN/2]-JupIIIP[tN/2]==JupII[tN/2]-JdownII[tN/2]},
{K1I,K2I,K3I,K1II,K2II,K3II,K1III,K2III,K3III}]]
Simplify[(K2III-K2I)/.SolP]
Simplify[(K2I)/.SolP]
FullSimplify[(K2I)/.SolP]
FullSimplify[(K3III)/.SolP]
FullSimplify[(K2I)/.SolAP]
FullSimplify[(K3III)/.SolAP]
thickness=30*10^-9;
thicknessFM=15*10^-9;

```

```

Const={tN->thickness, rhoFM1->75*10^-9, beta1->-0.46, lSFFM1->60*10^-9,
tFM1->thicknessFM, rhoN->1.33*10^-1, lSFN->2*10^-8, gamma->0.5, rb->0,
rhoFM2->59*10^-9, lSFFM2->21*10^-9, tFM2->thicknessFM, beta2->-0.33,
J->1, e->-1};
Plot[{Piecewise[{{((JupI[z]-JdownI[z])/J)/.SolP/.Const, z<=-thickness/2},
{{((JupII[z]-JdownII[z])/J)/.SolP/.Const, thickness/2>=z>=-thickness/2},
{{((JupIIIP[z]-JdownIIIP[z])/J)/.SolP/.Const, thickness/2<=z}
}], {z, -thicknessFM-thickness, thicknessFM+thickness}, AxesOrigin->{0,0}]
Plot[{Piecewise[{{((muupI[z]-mudownI[z])/).SolP/.Const, z<=-thickness/2},
{{((muupII[z]-mudownII[z])/).SolP/.Const, thickness/2>=z>=-thickness/2},
{{((muupIIIP[z]-mudownIIIP[z])/).SolP/.Const, thickness/2<=z}
}], {z, -thicknessFM-thickness, thicknessFM+thickness}, PlotRange->Full]
Plot[{Piecewise[{{((JupI[z]-JdownI[z])/J)/.SolAP/.Const, z<=-thickness/2},
{{((JupII[z]-JdownII[z])/J)/.SolAP/.Const, thickness/2>=z>=-thickness/2},
{{((-JupIIIP[z]+JdownIIIP[z])/J)/.SolAP/.Const, thickness/2<=z}
}], {z, -thicknessFM-thickness, thicknessFM+thickness}, AxesOrigin->{0,0}]
Plot[{Piecewise[{{((muupI[z]-mudownI[z])/).SolAP/.Const, z<=-thickness/2},
{{((muupII[z]-mudownII[z])/).SolAP/.Const, thickness/2>=z>=-thickness/2},
{{((-muupIIIP[z]+mudownIIIP[z])/).SolAP/.Const, thickness/2<=z}
}], {z, -thicknessFM-thickness, thicknessFM+thickness}, PlotRange->Full]
muupP[z_]=Piecewise[{{(muupI[z])/.SolP/.Const, z<=-thickness/2},
{(muupII[z])/.SolP/.Const, thickness/2>=z>=-thickness/2},
{(muupIIIP[z])/.SolP/.Const, thickness/2<=z}
}];
mudownP[z_]=Piecewise[{{(mudownI[z])/.SolP/.Const, z<=-thickness/2},
{(mudownII[z])/.SolP/.Const, thickness/2>=z>=-thickness/2},
{(mudownIIIP[z])/.SolP/.Const, thickness/2<=z}
}];
muupAP[z_]=Piecewise[{{(muupI[z])/.SolAP/.Const, z<=-thickness/2},
{(muupII[z])/.SolAP/.Const, thickness/2>=z>=-thickness/2},
{(mudownIIIP[z])/.SolAP/.Const, thickness/2<=z}
}];
mudownAP[z_]=Piecewise[{{(mudownI[z])/.SolAP/.Const, z<=-thickness/2},
{(mudownII[z])/.SolAP/.Const, thickness/2>=z>=-thickness/2},
{(muupIIIP[z])/.SolAP/.Const, thickness/2<=z}
}];
SPP[z_]=Piecewise[{{((JupI[z]-JdownI[z])/J)/.SolP/.Const, z<=-thickness/2},
{{((JupII[z]-JdownII[z])/J)/.SolP/.Const, thickness/2>=z>=-thickness/2},
{{((JupIIIP[z]-JdownIIIP[z])/J)/.SolP/.Const, thickness/2<=z}
}];
DeltaMuP[z_]=Piecewise[{{((muupI[z]-mudownI[z])/).SolP
/.Const, z<=-thickness/2}, {{(muupII[z]-mudownII[z])/).SolP
/.Const, thickness/2>=z>=-thickness/2},
{{(muupIIIP[z]-mudownIIIP[z])/).SolP/.Const, thickness/2<=z}
}];
SPAP[z_]=Piecewise[{{((JupI[z]-JdownI[z])/J)/.SolAP
/.Const, z<=-thickness/2}, {{(JupII[z]-JdownII[z])/J)/.SolAP

```

```

/.Const,thickness/2>=z>=-thickness/2},
{((-JupIIIP[z]+JdownIIIP[z])/J)/.SolAP/.Const,thickness/2<=z}
}];
DeltaMuAP[z_]=Piecewise[{{((muupI[z]-mudownI[z]))/.SolAP
/.Const,z<=-thickness/2},{((muupII[z]-mudownII[z]))/.SolAP
/.Const,thickness/2>=z>=-thickness/2},
{((-muupIIIP[z]+mudownIIIP[z]))/.SolAP/.Const,thickness/2<=z}
}];
FP[z_]=Piecewise[{{((FI[z]))/.SolP/.Const,z<=-thickness/2},
{((FII[z]))/.SolP/.Const,thickness/2>=z>=-thickness/2},
{((FIII[z]))/.SolP/.Const,thickness/2<=z}
}];
FAP[z_]=Piecewise[{{((muupI[z]-mudownI[z]))/.SolAP
/.Const,z<=-thickness/2},{((muupII[z]-mudownII[z]))/.SolAP
/.Const,thickness/2>=z>=-thickness/2},
{((-muupIIIP[z]+mudownIIIP[z]))/.SolAP/.Const,thickness/2<=z}
}];
Plot[{muupP[z],mudownP[z]},{z,-thicknessFM,thicknessFM+thickness}]
Plot[{muupAP[z],mudownAP[z]},{z,-thicknessFM,thicknessFM+thickness}]
Plot[{FP[z]},{z,-thicknessFM-thickness,thicknessFM+thickness}]
Plot[{FAP[z]},{z,-thicknessFM-thickness,thicknessFM+thickness}]
dataSPP={};
dataDeltamuP={};
dataSPAP={};
dataDeltaMuAP={};
dataMuupP={};
dataMudownP={};
dataMuupAP={};
dataMudownAP={};
dataFP={};
dataFAP={};
For[i=0,i<=1000,i++,
x=N[-thicknessFM-thickness/2+(thickness+2*thicknessFM)/1000*i,20];
y1=N[SPP[x],20][[1]];
y2=N[DeltaMuP[x],20][[1]];
y3=N[SPAP[x],20][[1]];
y4=N[DeltaMuAP[x],20][[1]];
y5=N[muupP[x],20][[1]];
y6=N[mudownP[x],20][[1]];
y7=N[muupAP[x],20][[1]];
y8=N[mudownAP[x],20][[1]];
y9=N[FP[x],20][[1]];
y10=N[FAP[x],20][[1]];
AppendTo[dataSPP,{x,y1}];
AppendTo[dataDeltamuP,{x,y2}];
AppendTo[dataSPAP,{x,y3}];
AppendTo[dataDeltaMuAP,{x,y4}];

```

```

AppendTo[dataMuupP,{x,y5}];
AppendTo[dataMudownP,{x,y6}];
AppendTo[dataMuupAP,{x,y7}];
AppendTo[dataMudownAP,{x,y8}];
AppendTo[dataFP,{x,y9}];
AppendTo[dataFAP,{x,y10}];
]
Export["dataSPP.dat",dataSPP,"Data"];
Export["dataDeltamuP.dat",dataDeltamuP,"Data"];
Export["dataSPAP.dat",dataSPAP,"Data"];
Export["dataDeltaMuAP.dat",dataDeltaMuAP,"Data"];
Export["dataMuupP.dat",dataMuupP,"Data"];
Export["dataMudownP.dat",dataMudownP,"Data"];
Export["dataMuupAP.dat",dataMuupAP,"Data"];
Export["dataMudownAP.dat",dataMudownAP,"Data"];
Export["dataFP.dat",dataFP,"Data"];
Export["dataFAP.dat",dataFAP,"Data"];
FullSimplify[JupI[tN/2]-JdownI[tN/2]/.SolP]
RPara[tN_]=FullSimplify[(1-beta1^2)*rhoFM1*tFM1+rhoN*tN+(1-beta2^2)*
rhoFM2*tFM2+rb*(1-gamma/J*(JupI[-tN/2]-JdownI[-tN/2]))+rb*(1-gamma/J*
(JupIIIP[tN/2]-JdownIIIP[tN/2]))+2*beta1/(e*J)*(K2I-K3I)*Sinh[tFM1/
(2*1SFFM1)]+2*beta2/(e*J)*(K2III-K3III)*Sinh[tFM2/(2*1SFFM2)]]/.SolP]
RAntiPara[tN_]=FullSimplify[(1-beta1^2)*rhoFM1*tFM1+rhoN*tN+
(1-beta2^2)*rhoFM2*tFM2+rb*(1-gamma/J*(JupI[-tN/2]-JdownI[-tN/2]))+
rb*(1-gamma/J*(JupIIIP[tN/2]-JdownIIIP[tN/2]))+2*beta1/(e*J)*(K2I-K3I)*
Sinh[tFM1/(2*1SFFM1)]+2*beta2/(e*J)*(K2III-K3III)*
Sinh[tFM2/(2*1SFFM2)]]/.SolAP]
DeltaR[tN_]=FullSimplify[RAntiPara[tN]-RPara[tN]]

MR[tN_]=FullSimplify[DeltaR[tN]/RPara[tN]]
Const2={rhoFM1->75*10^-9,beta1->-0.46,1SFFM1->60*10^-9,
tFM1->thicknessFM,rhoN->1.33*10^-1,1SFN->4*10^-9,gamma->0.5,
rb->1*10^-10,rhoFM2->59*10^-9,1SFFM2->21*10^-9,tFM2->thicknessFM,
beta2->-0.33};
N[MR[20*10^-8]/.Const2]
LogPlot[{MR[tN]/.Const2},{tN,0,10^-8},PlotRange->Full]
dataMRofTN={};
dataMRofrb={};
dataMRofgamma{};
For[i=0,i<=1000,i++,
x1=N[0+0.1*10^-6/1000*i,20];
x2=N[1*10^-15+2*10^-15*Exp[i/20],20];
Const3={rhoFM1->75*10^-9,beta1->-0.46,1SFFM1->60*10^-9,
tFM1->thicknessFM,rhoN->1.33*10^-1,1SFN->4*10^-9,gamma->0.5,rb->x2,
rhoFM2->59*10^-9,1SFFM2->21*10^-9,tFM2->thicknessFM,beta2->-0.33};
y1=N[MR[x1]/.Const2,20][[1]];
y2=N[MR[30*10^-9]/.Const3,20][[1]];

```

```
AppendTo[dataMrofTN, {x1, y1}];  
AppendTo[dataMrofRB, {x2, y2}];  
]  
Export["dataMrofTN.dat", dataMrofTN, "Data"];  
Export["dataMrofRB.dat", dataMrofRB, "Data"];
```


Appendix D

Expansion coefficients in cubic and tetragonal symmetry

For the resistivity tensor we have the following relations

$$\begin{aligned}\rho^{(0)} &= \rho_{33}^{(0)}, \\ \rho^{(1)} &= \rho_{321}^{(1)}, \\ \rho^{(2,1)} &= \rho_{3322}^{(2)}, \\ \rho^{(2,2)} &= \rho_{3333}^{(2)} - \rho_{3322}^{(2)}, \\ \rho^{(2,3)} &= 2\rho_{3232}^{(2)}, \\ \rho^{(3,1)} &= 3\rho_{32331}^{(3)}, \\ \rho^{(3,2)} &= \rho_{32111}^{(3)} - 3\rho_{32331}^{(3)}, \\ \rho^{(4,1)} &= \rho_{332222}^{(4)}, \\ \rho^{(4,2)} &= 6\rho_{333322}^{(4)} - 2\rho_{332222}^{(4)}, \\ \rho^{(4,3)} &= 4\rho_{323332}^{(4)}, \\ \rho^{(4,4)} &= \rho_{333333}^{(4)} - 6\rho_{333322}^{(4)} + \rho_{332222}^{(4)}, \\ \rho^{(4,5)} &= 6\rho_{332211}^{(4)} - 2\rho_{332222}^{(4)}, \\ \rho^{(4,6)} &= 12\rho_{323211}^{(4)} - 4\rho_{323332}^{(4)}.\end{aligned}$$

For the Seebeck tensor in cubic symmetry

$$\begin{aligned}
\Sigma^{(0)} &= \Sigma_{33}^{(0)}, \\
\Sigma^{(1)} &= \Sigma_{321}^{(1)}, \\
\Sigma^{(2,1)} &= \Sigma_{3322}^{(2)}, \\
\Sigma^{(2,2)} &= \Sigma_{3333}^{(2)} - \Sigma_{3322}^{(2)}, \\
\Sigma^{(2,3)} &= 2\Sigma_{3232}^{(2)}, \\
\Sigma^{(3,1)} &= 3\Sigma_{32331}^{(3)}, \\
\Sigma^{(3,2)} &= \Sigma_{32111}^{(3)} - 3\Sigma_{32331}^{(3)}, \\
\Sigma^{(3,3)} &= 3\Sigma_{32221}^{(3)} - 3\Sigma_{32331}^{(3)}, \\
\Sigma^{(4,1)} &= \Sigma_{332222}^{(4)}, \\
\Sigma^{(4,2)} &= 6\Sigma_{333322}^{(4)} - 2\Sigma_{332222}^{(4)}, \\
\Sigma^{(4,3)} &= 4\Sigma_{323332}^{(4)}, \\
\Sigma^{(4,4)} &= \Sigma_{333333}^{(4)} - 6\Sigma_{333322}^{(4)} + \Sigma_{332222}^{(4)}, \\
\Sigma^{(4,5)} &= 6\Sigma_{332211}^{(4)} - 2\Sigma_{332222}^{(4)}, \\
\Sigma^{(4,6)} &= 12\Sigma_{323211}^{(4)} - 4\Sigma_{323332}^{(4)}, \\
\Sigma^{(4,7)} &= 4\Sigma_{323222}^{(4)} - 4\Sigma_{323332}^{(4)}.
\end{aligned}$$

For the resistivity tensor in tetragonal symmetry:

$$\begin{aligned}
\rho^{(0,a)} &= \rho_{22}^{(0)}, \\
\rho^{(0,c)} &= \rho_{33}^{(0)}, \\
\rho^{(1,a)} &= \rho_{213}^{(1)}, \\
\rho^{(1,c)} &= \rho_{321}^{(1)}, \\
\rho^{(2,1,a)} &= \rho_{2211}^{(2)}, \\
\rho^{(2,1,c)} &= \rho_{3322}^{(2)}, \\
\rho^{(2,2,a)} &= \rho_{2222}^{(2)} - \rho_{2211}^{(2)}, \\
\rho^{(2,2,c)} &= \rho_{3333}^{(2)} - \rho_{3322}^{(2)}, \\
\rho^{(2,3,a)} &= 2\rho_{2121}^{(2)}, \\
\rho^{(2,3,c)} &= 2\rho_{3232}^{(2)}, \\
\rho^{(2,4,a)} &= \rho_{2233}^{(2)} - \rho_{2211}^{(2)}, \\
\rho^{(3,1,a)} &= 3\rho_{21322}^{(3)}, \\
\rho^{(3,1,c)} &= 3\rho_{32221}^{(3)}, \\
\rho^{(3,2,a)} &= \rho_{21333}^{(3)} - 3\rho_{21322}^{(3)}, \\
\rho^{(3,2,c)} &= \rho_{32111}^{(3)} - 3\rho_{32221}^{(3)}, \\
\rho^{(3,3,c)} &= 3\rho_{32331}^{(3)}, \\
\rho^{(4,1,a)} &= \rho_{221111}^{(4)}, \\
\rho^{(4,1,c)} &= \rho_{332222}^{(4)}, \\
\rho^{(4,2,a)} &= 6\rho_{222211}^{(4)} - 2\rho_{221111}^{(4)}, \\
\rho^{(4,2,c)} &= 6\rho_{333322}^{(4)} - 2\rho_{332222}^{(4)}, \\
\rho^{(4,3,a)} &= 4\rho_{212221}^{(4)}, \\
\rho^{(4,3,c)} &= 4\rho_{323222}^{(4)}, \\
\rho^{(4,4,a)} &= 6\rho_{223322}^{(4)} - 6\rho_{222211}^{(4)}, \\
\rho^{(4,5,a)} &= \rho_{222222}^{(4)} - 6\rho_{222211}^{(4)} + \rho_{221111}^{(4)}, \\
\rho^{(4,5,c)} &= \rho_{333333}^{(4)} - 6\rho_{333322}^{(4)} + \rho_{332222}^{(4)}, \\
\rho^{(4,6,a)} &= 6\rho_{223311}^{(4)} + 6\rho_{222211}^{(4)} - 6\rho_{223322}^{(4)} - 2\rho_{221111}^{(4)}, \\
\rho^{(4,6,c)} &= 6\rho_{332211}^{(4)} - 2\rho_{332222}^{(4)}, \\
\rho^{(4,7,a)} &= 12\rho_{213321}^{(4)} - 4\rho_{212221}^{(4)}, \\
\rho^{(4,7,c)} &= 12\rho_{323211}^{(4)} - 4\rho_{323222}^{(4)}, \\
\rho^{(4,8,a)} &= 6\rho_{222211}^{(4)} - 6\rho_{223322}^{(4)} - \rho_{221111}^{(4)}, \\
\rho^{(4,9,c)} &= 4\rho_{323332}^{(4)} - 4\rho_{323222}^{(4)}.
\end{aligned}$$

Expansion coefficients for the Seebeck tensor in tetragonal symmetry

$$\begin{aligned}
\Sigma^{(0,a)} &= \Sigma_{22}^{(0)}, \\
\Sigma^{(0,c)} &= \Sigma_{33}^{(0)}, \\
\Sigma^{(1,a)} &= \Sigma_{213}^{(1)}, \\
\Sigma^{(1,c1)} &= -\Sigma_{231}^{(1)}, \\
\Sigma^{(1,c2)} &= \Sigma_{321}^{(1)}, \\
\Sigma^{(2,1,a)} &= \Sigma_{2211}^{(2)}, \\
\Sigma^{(2,1,c)} &= \Sigma_{3322}^{(2)}, \\
\Sigma^{(2,2,a)} &= \Sigma_{2222}^{(2)} - \Sigma_{2211}^{(2)}, \\
\Sigma^{(2,2,c)} &= \Sigma_{3333}^{(2)} - \Sigma_{3322}^{(2)}, \\
\Sigma^{(2,3,a)} &= 2\Sigma_{2121}^{(2)}, \\
\Sigma^{(2,3,c1)} &= 2\Sigma_{2332}^{(2)}, \\
\Sigma^{(2,3,c2)} &= 2\Sigma_{3232}^{(2)}, \\
\Sigma^{(2,4,a)} &= \Sigma_{2233}^{(2)} - \Sigma_{2211}^{(2)}, \\
\Sigma^{(3,1,a)} &= 3\Sigma_{21322}^{(3)}, \\
\Sigma^{(3,1,c1)} &= 3\Sigma_{23221}^{(3)}, \\
\Sigma^{(3,1,c2)} &= 3\Sigma_{32221}^{(3)}, \\
\Sigma^{(3,2,a)} &= \Sigma_{21333}^{(3)} - 3\Sigma_{21322}^{(3)}, \\
\Sigma^{(3,2,c1)} &= -\Sigma_{23111}^{(3)} + 3\Sigma_{23221}^{(3)}, \\
\Sigma^{(3,2,c2)} &= \Sigma_{32111}^{(3)} - 3\Sigma_{32221}^{(3)}, \\
\Sigma^{(3,3,a)} &= 3\Sigma_{21322}^{(3)} - 3\Sigma_{21311}^{(3)}, \\
\Sigma^{(3,3,c1)} &= -3\Sigma_{23331}^{(3)} + 3\Sigma_{23221}^{(3)}, \\
\Sigma^{(3,3,c2)} &= 3\Sigma_{32331}^{(3)} - 3\Sigma_{23221}^{(3)}, \\
\Sigma^{(3,4,a)} &= 6\Sigma_{22321}^{(3)}, \\
\Sigma^{(4,1,a)} &= \Sigma_{221111}^{(4)}, \\
\Sigma^{(4,1,c)} &= \Sigma_{332222}^{(4)}, \\
\Sigma^{(4,2,a)} &= 6\Sigma_{222211}^{(4)} - 2\Sigma_{221111}^{(4)}, \\
\Sigma^{(4,2,c)} &= 6\Sigma_{333322}^{(4)} - 2\Sigma_{332222}^{(4)}, \\
\Sigma^{(4,3,a)} &= 4\Sigma_{212221}^{(4)}, \\
\Sigma^{(4,3,c1)} &= 4\Sigma_{233222}^{(4)}, \\
\Sigma^{(4,3,c2)} &= 4\rho_{323222}^{(4)}, \\
\Sigma^{(4,4,a)} &= 6\Sigma_{223322}^{(4)} - 6\Sigma_{222211}^{(4)}, \\
\Sigma^{(4,5,a)} &= \Sigma_{222222}^{(4)} - 6\Sigma_{222211}^{(4)} + \Sigma_{221111}^{(4)}, \\
\Sigma^{(4,5,c)} &= \Sigma_{333333}^{(4)} - 6\Sigma_{333322}^{(4)} + \Sigma_{332222}^{(4)},
\end{aligned}$$

$$\begin{aligned}\Sigma^{(4,6,a)} &= 6\Sigma_{223311}^{(4)} + 6\Sigma_{222211}^{(4)} - 6\Sigma_{223322}^{(4)} - 2\Sigma_{221111}^{(4)}, \\ \Sigma^{(4,6,c)} &= 6\Sigma_{332211}^{(4)} - 2\Sigma_{332222}^{(4)}, \\ \Sigma^{(4,7,a)} &= 12\Sigma_{213321}^{(4)} - 4\Sigma_{212221}^{(4)}, \\ \Sigma^{(4,7,c1)} &= 12\Sigma_{233211}^{(4)} - 4\Sigma_{233222}^{(4)}, \\ \Sigma^{(4,7,c2)} &= 12\Sigma_{323211}^{(4)} - 4\Sigma_{323222}^{(4)}, \\ \Sigma^{(4,8,a)} &= 6\Sigma_{222211}^{(4)} - 6\Sigma_{223322}^{(4)} - \Sigma_{221111}^{(4)}, \\ \Sigma^{(4,9,a)} &= 4\Sigma_{212111}^{(4)} - 4\Sigma_{212221}^{(4)}, \\ \Sigma^{(4,9,c1)} &= 4\Sigma_{233332}^{(4)} - 4\Sigma_{233222}^{(4)}, \\ \Sigma^{(4,9,c2)} &= 4\Sigma_{323332}^{(4)} - 4\Sigma_{323222}^{(4)}.\end{aligned}$$

List of publications

- S. T. B. Goennenwein, M. Althammer, C. Bihler, A. Brandlmaier, S. Geprags, M. Opel, W. Schoch, W. Limmer, R. Gross, and M. S. Brandt, *Piezo-voltage control of magnetization orientation in a ferromagnetic semiconductor*, Physica Status Solidi-Rapid Research Letters **2**, 96 (2008).
- C. Bihler, M. Althammer, A. Brandlmaier, S. Geprags, M. Weiler, M. Opel, W. Schoch, W. Limmer, R. Gross, M. S. Brandt, and S. T. B. Goennenwein, *Ga_{1-x}Mn_xAs/piezoelectric actuator hybrids: A model system for magnetoelastic magnetization manipulation*, Physical Review B **78**, 045203 (2008).
- D. Venkateshvaran, W. Kaiser, A. Boger, M. Althammer, M. S. Ramachandra Rao, S. T. B. Goennenwein, M. Opel, R. Gross, *Anomalous Hall effect in magnetite: Universal scaling relation between Hall and longitudinal conductivity in low-conductivity ferromagnets*, Physical Review B **78**, 092405 (2008).
- A. Nielsen, A. Brandlmaier, M. Althammer, W. Kaiser, M. Opel, J. Simon, W. Mader, S. T. B. Goennenwein, R. Gross, *All oxide ferromagnet/semiconductor epitaxial heterostructures*, Applied Physics Letters **93**, 162510 (2008).
- M. Weiler, A. Brandlmaier, S. Geprags, M. Althammer, M. Opel, C. Bihler, H. Huebl, M. S. Brandt, R. Gross, and S. T. B. Goennenwein, *Voltage controlled inversion of magnetic anisotropy in a ferromagnetic thin film at room temperature*, New Journal of Physics **11**, 013021 (2009).
- D. Venkateshvaran, M. Althammer, A. Nielsen, S. Geprags, M. S. Ramachandra Rao, S. T. B. Goennenwein, M. Opel, R. Gross, *Epitaxial Zn_xFe_{3-x}O₄ thin films: A spintronic material with tunable electrical and magnetic properties*, Physical Review B **79**, 134405 (2009).
- T. A. Wassner, B. Laumer, M. Althammer, S. T. B. Goennenwein, M. Stutzmann, M. Eickhoff, M. S. Brandt, *Electron spin resonance of Zn_{1-x}Mg_xO thin films grown by plasma-assisted molecular beam epitaxy*, Applied Physics Letters **97**, 092102 (2010).
- F. D. Czeschka, L. Dreher, M. S. Brandt, M. Weiler, M. Althammer, I.-M. Imort, G. Reiss, A. Thomas, W. Schoch, W. Limmer, H. Huebl, R. Gross, and S. T. B. Goennenwein, *Scaling Behavior of the Spin Pumping Effect in Ferromagnet-Platinum Bilayers*, Physical Review Letters **107**, 046601 (2011).

- M. Opel, S. Geprägs, E. P. Menzel, A. Nielsen, D. Reisinger, K.-W. Nielsen, A. Brandlmaier, F. D. Czeschka, M. Althammer, M. Weiler, S. T. B. Goennenwein, J. Simon, M. Svete, W. Yu, S.-M. Hühne, W. Mader, and R. Gross, *Novel multifunctional materials based on oxide thin films and artificial heteroepitaxial multilayers*, *Physica Status Solidi A* **208**, 232 (2011).
- M. Weiler, M. Althammer, F. D. Czeschka, H. Huebl, M. S. Wagner, M. Opel, I.-M. Imort, G. Reiss, A. Thomas, R. Gross, and S. T. B. Goennenwein, *Local Charge and Spin Currents in Magnetothermal Landscapes*, *Physical Review Letters* **108**, 106602 (2012).
- M. Althammer, E.-M. Karrer-Müller, S. T. B. Goennenwein, M. Opel, and R. Gross, *Spin injection and spin transport in zinc oxide*, arxiv:1205.3666 submitted to *Applied Physics Letters* (2012).
- C. Schwark, M. Althammer, V. Klinke, C. Weier, M. Opel, R. Gross, G. Güntherot, M. S. Brandt, S. T. B. Goennenwein, and B. Beschoten, *Exciton enhancement of spin dephasing time in ZnO*, in preparation (2012).
- H. Nakayama, M. Althammer, Y. Chen, G. Bauer, S. T. B. Goennenwein, and E. Saitoh, *Nonequilibrium proximity in YIG—Pt introduced by the double spin Hall effect*, in preparation (2012).
- M. Althammer, H. Nakayama, M. Schreier, S. Meyer, M. Opel, S. Geprägs, Y. Chen, G. Bauer, R. Gross, E. Saitoh, and S. T. B. Goennenwein, *Spin current induced magnetoresistance*, in preparation (2012).

Bibliography

- [1] Y. Lin, C. Dimitrakopoulos, K. A. Jenkins, D. B. Farmer, H. Chiu, A. Grill, and P. Avouris, *Science* **327**, 662 (2010).
- [2] M. N. Baibich, J. M. Broto, A. Fert, F. N. Van Dau, F. Petroff, P. Eitenne, G. Creuzet, A. Friederich, and J. Chazelas, *Physical Review Letters* **61**, 2472 (1988).
- [3] G. Binasch, P. Grünberg, F. Saurenbach, and W. Zinn, *Physical Review B* **39**, 4828 (1989).
- [4] S. Murakami, N. Nagaosa, and S. Zhang, *Science* **301**, 1348 (2003).
- [5] Z. Qiu, Y. Kajiwara, K. Ando, Y. Fujikawa, K. Uchida, T. Tashiro, K. Harii, T. Yoshino, and E. Saitoh, *Applied Physics Letters* **100**, 022402 (2012).
- [6] E. Saitoh, M. Ueda, H. Miyajima, and G. Tatara, *Appl. Phys. Lett.* **88**, 182509 (2006).
- [7] K. Ando, M. Morikawa, T. Trypiniotis, Y. Fujikawa, C. H. W. Barnes, and E. Saitoh, *Journal of Applied Physics* **107**, 113902 (2010).
- [8] K. Ando, S. Takahashi, J. Ieda, H. Kurebayashi, T. Trypiniotis, C. H. W. Barnes, S. Maekawa, and E. Saitoh, *Nature Materials* **10**, 655 (2011).
- [9] K. Ando, M. Morikawa, T. Trypiniotis, Y. Fujikawa, C. H. W. Barnes, and E. Saitoh, *Applied Physics Letters* **96**, 082502 (2010).
- [10] K. Ando, S. Takahashi, J. Ieda, Y. Kajiwara, H. Nakayama, T. Yoshino, K. Harii, Y. Fujikawa, M. Matsuo, S. Maekawa, and E. Saitoh, *Journal of Applied Physics* **109**, 103913 (2011).
- [11] A. Hoffmann, *physica status solidi (c)* **4**, 4236 (2007).
- [12] K. Ando and E. Saitoh, *Nature Communications* **3**, 629 (2012).
- [13] F. D. Czeschka, L. Dreher, M. S. Brandt, M. Weiler, M. Althammer, I. Imort, G. Reiss, A. Thomas, W. Schoch, W. Limmer, H. Huebl, R. Gross, and S. T. B. Goennenwein, *Physical Review Letters* **107**, 046601 (2011).
- [14] K.-i. Uchida, T. An, Y. Kajiwara, M. Toda, and E. Saitoh, *Applied Physics Letters* **99**, 212501 (2011).
- [15] M. Weiler, H. Huebl, F. S. Goerg, F. D. Czeschka, R. Gross, and S. T. B. Goennenwein, *Physical Review Letters* **108**, 176601 (2012).

- [16] A. Brataas, Y. Tserkovnyak, G. E. W. Bauer, and B. I. Halperin, *Physical Review B* **66**, 060404 (2002).
- [17] K. Uchida, T. Ota, Y. Kajiwara, H. Umezawa, H. Kawai, and E. Saitoh, *Journal of Physics: Conference Series* **303**, 012096 (2011).
- [18] H. Adachi, J.-i. Ohe, S. Takahashi, and S. Maekawa, *Physical Review B* **83**, 094410 (2011).
- [19] H. Adachi, K.-i. Uchida, E. Saitoh, J.-i. Ohe, S. Takahashi, and S. Maekawa, *Applied Physics Letters* **97**, 252506 (2010).
- [20] K. Uchida, S. Takahashi, J. Ieda, K. Harii, K. Ikeda, W. Koshibae, S. Maekawa, and E. Saitoh, *Journal of Applied Physics* **105**, 07C908 (2009).
- [21] J. Xiao, G. E. W. Bauer, K.-c. Uchida, E. Saitoh, and S. Maekawa, *Physical Review B* **81**, 214418 (2010).
- [22] K.-i. Uchida, T. Nonaka, T. Ota, and E. Saitoh, *Applied Physics Letters* **97**, 262504 (2010).
- [23] K.-i. Uchida, H. Adachi, T. Ota, H. Nakayama, S. Maekawa, and E. Saitoh, *Applied Physics Letters* **97**, 172505 (2010).
- [24] K. Uchida, S. Takahashi, K. Harii, J. Ieda, W. Koshibae, K. Ando, S. Maekawa, and E. Saitoh, *Nature* **455**, 778 (2008).
- [25] C. M. Jaworski, J. Yang, S. Mack, D. D. Awschalom, J. P. Heremans, and R. C. Myers, *Nature Materials* **9**, 898 (2010).
- [26] K. Uchida, J. Xiao, H. Adachi, J. Ohe, S. Takahashi, J. Ieda, T. Ota, Y. Kajiwara, H. Umezawa, H. Kawai, G. E. W. Bauer, S. Maekawa, and E. Saitoh, *Nature Materials* **9**, 894 (2010).
- [27] C. M. Jaworski, J. Yang, S. Mack, D. D. Awschalom, R. C. Myers, and J. P. Heremans, *Physical Review Letters* **106**, 186601 (2011).
- [28] J. Le Breton, S. Sharma, H. Saito, S. Yuasa, and R. Jansen, *Nature* **475**, 82 (2011).
- [29] A. Slachter, F. L. Bakker, J. Adam, and B. J. van Wees, *Nature Physics* **6**, 879 (2010).
- [30] M. Weiler, M. Althammer, F. D. Czeschka, H. Huebl, M. S. Wagner, M. Opel, I. Imort, G. Reiss, A. Thomas, R. Gross, and S. T. B. Goennenwein, *Physical Review Letters* **108**, 106602 (2012).
- [31] G. Schmidt, D. Ferrand, L. W. Molenkamp, A. T. Filip, and B. J. van Wees, *Physical Review B* **62**, R4790 (2000).
- [32] U. Özgür, Y. I. Alivov, C. Liu, A. Teke, M. A. Reshchikov, S. Doğan, V. Avrutin, S. J. Cho, and H. Morkoç, *Journal of Applied Physics* **98**, 041301 (2005).

- [33] C. Jagadish, *Zinc oxide bulk, thin films and nanostructures : processing, properties and applications* (Elsevier, Amsterdam London, 2006).
- [34] R. Vispute, S. S. Hullavarad, D. Pugel, V. N. Kulkarni, S. Dhar, I. Takeuchi, and T. Venkatesan, in *Thin Films and Heterostructures for Oxide Electronics* (Springer-Verlag, New York) pp. 301–330.
- [35] D. Look, *Materials Science and Engineering: B* **80**, 383 (2001).
- [36] A. Janotti and C. G. Van de Walle, *Reports on Progress in Physics* **72**, 126501 (2009).
- [37] N. H. Nickel, *Zinc Oxide: A Material for Micro- and Optoelectronic Applications*, Vol. 194 (NATO Science Series, 2005).
- [38] V. Srikant and D. R. Clarke, *Journal of Applied Physics* **83**, 5447 (1998).
- [39] D. Thomas, *Journal of Physics and Chemistry of Solids* **15**, 86 (1960).
- [40] A. Mang, K. Reimann, and S. Rübenacke, *Solid State Communications* **94**, 251 (1995).
- [41] D. C. Reynolds, D. C. Look, B. Jogai, C. W. Litton, G. Cantwell, and W. C. Harsch, *Physical Review B* **60**, 2340 (1999).
- [42] Y. Chen, D. M. Bagnall, H.-j. Koh, K.-t. Park, K. Hiraga, Z. Zhu, and T. Yao, *Journal of Applied Physics* **84**, 3912 (1998).
- [43] D. M. Bagnall, Y. F. Chen, Z. Zhu, T. Yao, S. Koyama, M. Y. Shen, and T. Goto, *Applied Physics Letters* **70**, 2230 (1997).
- [44] D. Reynolds, D. Look, and B. Jogai, *Solid State Communications* **99**, 873 (1996).
- [45] H. Karzel, W. Potzel, M. Köfferlein, W. Schiessl, M. Steiner, U. Hiller, G. M. Kalvius, D. W. Mitchell, T. P. Das, P. Blaha, K. Schwarz, and M. P. Pasternak, *Physical Review B* **53**, 11425 (1996).
- [46] D. Klimm, S. Ganschow, D. Schulz, and R. Fornari, *Journal of Crystal Growth* **310**, 3009 (2008).
- [47] H. Tampo, K. Matsubara, A. Yamada, H. Shibata, P. Fons, M. Yamagata, H. Kanie, and S. Niki, *Journal of Crystal Growth* **301-302**, 358 (2007).
- [48] H. Tampo, H. Shibata, K. Matsubara, A. Yamada, P. Fons, S. Niki, M. Yamagata, and H. Kanie, *Applied Physics Letters* **89**, 132113 (2006).
- [49] H. Tampo, H. Shibata, K. Maejima, A. Yamada, K. Matsubara, P. Fons, S. Kashiwaya, S. Niki, Y. Chiba, T. Wakamatsu, and H. Kanie, *Applied Physics Letters* **93**, 202104 (2008).
- [50] A. Tsukazaki, A. Ohtomo, M. Kawasaki, S. Akasaka, H. Yuji, K. Tamura, K. Nakahara, T. Tanabe, A. Kamisawa, T. Gokmen, J. Shabani, and M. Shayegan, *Physical Review B* **78**, 233308 (2008).

- [51] J. D. Ye, S. Pannirselvam, S. T. Lim, J. F. Bi, X. W. Sun, G. Q. Lo, and K. L. Teo, *Applied Physics Letters* **97**, 111908 (2010).
- [52] M. Brandt, H. von Wenckstern, G. Benndorf, H. Hochmuth, M. Lorenz, and M. Grundmann, *Thin Solid Films* **518**, 1048 (2009).
- [53] K. v. Klitzing, G. Dorda, and M. Pepper, *Physical Review Letters* **45**, 494 (1980).
- [54] A. Tsukazaki, A. Ohtomo, T. Kita, Y. Ohno, H. Ohno, and M. Kawasaki, *Science* **315**, 1388 (2007).
- [55] D. C. Tsui, H. L. Stormer, and A. C. Gossard, *Physical Review Letters* **48**, 1559 (1982).
- [56] A. Tsukazaki, S. Akasaka, K. Nakahara, Y. Ohno, H. Ohno, D. Maryenko, A. Ohtomo, and M. Kawasaki, *Nat Mater* **9**, 889 (2010).
- [57] M. E. Brown, *ZnO Rediscovered*, edited by M. E. Brown (The New Jersey Zinc Company, New York, 1957).
- [58] M. Lannoo and J. Bourgoin, *Point Defects in Semiconductors: Theoretical aspects* (Springer, 1981).
- [59] M. Stavola, *Semiconductors and semimetals* (Academic Press, San Diego Calif. London, 1998).
- [60] S. E. Harrison, *Physical Review* **93**, 52 (1954).
- [61] A. R. Hutson, *Physical Review* **108**, 222 (1957).
- [62] K. Hoffmann and D. Hahn, *physica status solidi (a)* **24**, 637 (1974).
- [63] A. Hausmann, *Zeitschrift für Physik* **237**, 86 (1970).
- [64] L. S. Vlasenko and G. D. Watkins, *Physical Review B* **71**, 125210 (2005).
- [65] L. S. Vlasenko and G. D. Watkins, *Physical Review B* **72**, 035203 (2005).
- [66] A. F. Kohan, G. Ceder, D. Morgan, and C. G. Van de Walle, *Physical Review B* **61**, 15019 (2000).
- [67] V. d. W. Chris G., *Physica B: Condensed Matter* **308-310**, 899 (2001).
- [68] C. G. Van de Walle, *Physical Review Letters* **85**, 1012 (2000).
- [69] M. McCluskey and S. Jokela, *Physica B: Condensed Matter* **401-402**, 355 (2007).
- [70] M. Joseph, H. Tabata, and T. Kawai, *Japanese Journal of Applied Physics* **38**, L1205 (1999).
- [71] T. Aoki, Y. Hatanaka, and D. C. Look, *Applied Physics Letters* **76**, 3257 (2000).
- [72] K. Minegishi, Y. Koiwai, Y. Kikuchi, K. Yano, M. Kasuga, and A. Shimizu, *Japanese Journal of Applied Physics* **36**, L1453 (1997).

- [73] A. Tsukazaki, A. Ohtomo, T. Onuma, M. Ohtani, T. Makino, M. Sumiya, K. Ohtani, S. F. Chichibu, S. Fuke, Y. Segawa, H. Ohno, H. Koinuma, and M. Kawasaki, *Nat Mater* **4**, 42 (2005).
- [74] S. Chu, J. H. Lim, L. J. Mandalapu, Z. Yang, L. Li, and J. L. Liu, *Applied Physics Letters* **92**, 152103 (2008).
- [75] F. X. Xiu, Z. Yang, L. J. Mandalapu, D. T. Zhao, J. L. Liu, and W. P. Beyermann, *Applied Physics Letters* **87**, 152101 (2005).
- [76] Y. R. Ryu, T. S. Lee, and H. W. White, *Applied Physics Letters* **83**, 87 (2003).
- [77] Y. Ryu, S. Zhu, D. Look, J. Wrobel, H. Jeong, and H. White, *Journal of Crystal Growth* **216**, 330 (2000).
- [78] D. C. Look, D. C. Reynolds, C. W. Litton, R. L. Jones, D. B. Eason, and G. Cantwell, *Applied Physics Letters* **81**, 1830 (2002).
- [79] K. Kim, H. Kim, D. Hwang, J. Lim, and S. Park, *Applied Physics Letters* **83**, 63 (2003).
- [80] E. Senthil kumar, S. Venkatesh, and M. S. Ramachandra Rao, *Applied Physics Letters* **96**, 232504 (2010).
- [81] C. H. Park, S. B. Zhang, and S. Wei, *Physical Review B* **66**, 073202 (2002).
- [82] O. Bierwagen, T. Ive, C. G. Van de Walle, and J. S. Speck, *Applied Physics Letters* **93**, 242108 (2008).
- [83] T. Ohgaki, N. Ohashi, S. Sugimura, H. Ryoken, I. Sakaguchi, Y. Adachi, and H. Haneda, *Journal of Materials Research* **23**, 2293 (2008).
- [84] D. Look, *Surface Science* **601**, 5315 (2007).
- [85] O. Schmidt, A. Geis, P. Kiesel, C. G. Van de Walle, N. M. Johnson, A. Bakin, A. Waag, and G. H. Döhler, *Superlattices and Microstructures* **39**, 8 (2006).
- [86] O. Schmidt, P. Kiesel, C. G. Van de Walle, N. M. Johnson, J. Nause, and G. H. Döhler, *Japanese Journal of Applied Physics* **44**, 7271 (2005).
- [87] M. Sawicki, T. Dietl, J. Kossut, J. Igalson, T. Wojtowicz, and W. Plesiewicz, *Physical Review Letters* **56**, 508 (1986).
- [88] T. Dietl, F. Matsukura, and H. Ohno, *Physical Review B* **66**, 033203 (2002).
- [89] S. W. Jung, S. J. An, G. Yi, C. U. Jung, S. Lee, and S. Cho, *Applied Physics Letters* **80**, 4561 (2002).
- [90] M. Diaconu, H. Schmidt, H. Hochmuth, M. Lorenz, G. Benndorf, D. Spemann, A. Setzer, P. Esquinazi, A. Pöppel, H. von Wenckstern, K. Nielsen, R. Gross, H. Schmid, W. Mader, G. Wagner, and M. Grundmann, *Journal of Magnetism and Magnetic Materials* **307**, 212 (2006).

- [91] K. Ueda, H. Tabata, and T. Kawai, *Applied Physics Letters* **79**, 988 (2001).
- [92] T. Fukumura, Z. Jin, M. Kawasaki, T. Shono, T. Hasegawa, S. Koshihara, and H. Koinuma, *Applied Physics Letters* **78**, 958 (2001).
- [93] T. Fukumura, Z. Jin, A. Ohtomo, H. Koinuma, and M. Kawasaki, *Applied Physics Letters* **75**, 3366 (1999).
- [94] J. M. D. Coey, M. Venkatesan, and C. B. Fitzgerald, *Nat Mater* **4**, 173 (2005).
- [95] M. Opel, K. W. Nielsen, S. Bauer, S. T. B. Goennenwein, J. C. Cezar, D. Schmeisser, J. Simon, W. Mader, and R. Gross, *The European Physical Journal B* **63**, 437 (2008).
- [96] A. Ney, M. Opel, T. C. Kaspar, V. Ney, S. Ye, K. Ollefs, T. Kammermeier, S. Bauer, K. Nielsen, S. T. B. Goennenwein, M. H. Engelhard, S. Zhou, K. Potzger, J. Simon, W. Mader, S. M. Heald, J. C. Cezar, F. Wilhelm, A. Rogalev, R. Gross, and S. A. Chambers, *New Journal of Physics* **12**, 013020 (2010).
- [97] S. Ghosh, V. Sih, W. H. Lau, D. D. Awschalom, S. Bae, S. Wang, S. Vaidya, and G. Chapline, *Applied Physics Letters* **86**, 232507 (2005).
- [98] S. Ghosh, D. W. Steuerman, B. Maertz, K. Ohtani, H. Xu, H. Ohno, and D. D. Awschalom, *Applied Physics Letters* **92**, 162109 (2008).
- [99] N. J. Harmon, W. O. Putikka, and R. Joynt, *Physical Review B* **79**, 115204 (2009).
- [100] Y. Chen, M. Ren, G. Ji, J. Fang, J. Chen, S. Xiao, S. Xie, Y. Liu, and L. Mei, *Physics Letters A* **303**, 91 (2002).
- [101] J. Gang, Y. Shi-Shen, C. Yan-Xue, L. Guo-Lei, C. Qiang, and M. Liang-Mo, *Chinese Physics Letters* **23**, 446 (2006).
- [102] G. JI, Z. ZHANG, Y. CHEN, S. YAN, Y. LIU, and L. MEI, *Acta Metallurgica Sinica (English Letters)* **22**, 153 (2009).
- [103] K. Shimazawa, Y. Tsuchiya, T. Mizuno, S. Hara, T. Chou, D. Miyauchi, T. Machita, T. Ayukawa, T. Ichiki, and K. Noguchi, *IEEE Transactions on Magnetics* **46**, 1487 (2010).
- [104] R. J. Lad, *Journal of Vacuum Science and Technology* **17**, 808 (1980).
- [105] E. M. Kaidashev, M. Lorenz, H. von Wenckstern, A. Rahm, H. Semmelhack, K. Han, G. Benndorf, C. Bundesmann, H. Hochmuth, and M. Grundmann, *Applied Physics Letters* **82**, 3901 (2003).
- [106] Z. Chen, S. Yamamoto, A. Kawasuso, Y. Xu, and T. Sekiguchi, *Applied Surface Science* **244**, 377 (2005).
- [107] S. Heinze, A. Krtschil, J. Bläsing, T. Hempel, P. Veit, A. Dadgar, J. Christen, and A. Krost, *Journal of Crystal Growth* **308**, 170 (2007).

- [108] C. Neumann, S. Lautenschläger, S. Graubner, J. Sann, N. Volbers, B. K. Meyer, J. Bläsing, A. Krost, F. Bertram, and J. Christen, *Physica Status Solidi (B)* **244**, 1431 (2007).
- [109] T. A. Wassner, B. Laumer, M. Althammer, S. T. B. Goennenwein, M. Stutzmann, M. Eickhoff, and M. S. Brandt, *Applied Physics Letters* **97**, 092102 (2010).
- [110] T. Koyama, A. N. Fouda, N. Shibata, and S. F. Chichibu, *Journal of Applied Physics* **102**, 073505 (2007).
- [111] P. Fons, K. Iwata, S. Niki, A. Yamada, and K. Matsubara, *Journal of Crystal Growth* **201-202**, 627 (1999).
- [112] A. P. Ulyanenko, S. A. Stepanov, U. Pietsch, and R. Kohler, *Journal of Physics D: Applied Physics* **28**, 2522 (1995).
- [113] S. Akiyama, K. Minegishi, T. Tanaka, H. Ogawa, and M. Kasuga, *Japanese Journal of Applied Physics* **46**, 342 (2007).
- [114] M. Yoshimoto, T. Maeda, T. Ohnishi, H. Koinuma, O. Ishiyama, M. Shinohara, M. Kubo, R. Miura, and A. Miyamoto, *Applied Physics Letters* **67**, 2615 (1995).
- [115] K. Miyamoto, M. Sano, H. Kato, and T. Yao, *Japanese Journal of Applied Physics* **41**, L1203 (2002).
- [116] K. Nakahara, H. Takasu, P. Fons, K. Iwata, A. Yamada, K. Matsubara, R. Hunger, and S. Niki, *Journal of Crystal Growth* **227-228**, 923 (2001).
- [117] S. Sadofev, S. Blumstengel, J. Cui, J. Puls, S. Rogaschewski, P. Schäfer, Y. G. Sadofyev, and F. Henneberger, *Applied Physics Letters* **87**, 091903 (2005).
- [118] S. Choopun, R. D. Vispute, W. Noch, A. Balsamo, R. P. Sharma, T. Venkatesan, A. Iliadis, and D. C. Look, *Applied Physics Letters* **75**, 3947 (1999).
- [119] M. Lorenz, E. Kaidashev, H. von Wenckstern, V. Riede, C. Bundesmann, D. Spemann, G. Benndorf, H. Hochmuth, A. Rahm, H. Semmelhack, and M. Grundmann, *Solid-State Electronics* **47**, 2205 (2003).
- [120] V. Petukhov, J. Stoemenos, J. Rothman, A. Bakin, and A. Waag, *Applied Physics A* **102**, 161 (2010).
- [121] P. Fons, K. Iwata, A. Yamada, K. Matsubara, S. Niki, K. Nakahara, T. Tanabe, and H. Takasu, *Applied Physics Letters* **77**, 1801 (2000).
- [122] M. Sano, K. Miyamoto, H. Kato, and T. Yao, *Japanese Journal of Applied Physics* **42**, L1050 (2003).
- [123] J. Chauveau, M. Laügt, P. Vennegùès, M. Teisseire, B. Lo, C. Deparis, C. Morhain, and B. Vinter, *Semiconductor Science and Technology* **23**, 035005 (2008).
- [124] M. Liang, Y. Ho, W. Wang, C. Peng, and L. Chang, *Journal of Crystal Growth* **310**, 1847 (2008).

- [125] V. D. Pauw, Philips Research Reports **13**, 1 (1958).
- [126] S. M. Sze, *Semiconductor devices, physics and technology* (Wiley, 1985).
- [127] K. Maeda, M. Sato, I. Niikura, and T. Fukuda, Semiconductor Science and Technology **20**, S49 (2005).
- [128] H. von Wenckstern, M. Brandt, H. Schmidt, G. Biehne, R. Pickenhain, H. Hochmuth, M. Lorenz, and M. Grundmann, Applied Physics A **88**, 135 (2007).
- [129] D. C. Look, Journal of Applied Physics **104**, 063718 (2008).
- [130] B. K. Meyer, J. Sann, D. M. Hofmann, C. Neumann, and A. Zeuner, Semiconductor Science and Technology **20**, S62 (2005).
- [131] B. K. Meyer, H. Alves, D. M. Hofmann, W. Kriegseis, D. Forster, F. Bertram, J. Christen, A. Hoffmann, M. Straßburg, M. Dworzak, U. Haboek, and A. V. Rodina, Physica Status Solidi (B) **241**, 231 (2004).
- [132] D. Schulz, S. Ganschow, and D. Klimm, arXiv:0911.2318 (2009), in Zinc Oxide and Related Materials – 2009, edited by Steve Durbin, Martin Allen, and Holger von Wenckstern (Mater. Res. Soc. Symp. Proc. Volume 1201, Warrendale, PA, 2010), 1201-H06-10.
- [133] J. L. Birman, Physical Review **114**, 1490 (1959).
- [134] J. Stephens, J. Berezovsky, J. P. McGuire, L. J. Sham, A. C. Gossard, and D. D. Awschalom, Physical Review Letters **93**, 097602 (2004).
- [135] S. A. Crooker and D. L. Smith, Physical Review Letters **94**, 236601 (2005).
- [136] W. Hanle, Zeitschrift für Physik **30**, 93 (1924).
- [137] C. Weier, “Optische Untersuchung der Spindynamik und der elektrischen Spininjektion in Zinkoxid,” (2010).
- [138] O. Lopatiuk, L. Chernyak, A. Osinsky, and J. Q. Xie, Applied Physics Letters **87**, 214110 (2005).
- [139] T. Valet and A. Fert, Physical Review B **48**, 7099 (1993).
- [140] N. F. Mott, Proceedings of the Royal Society A: Mathematical, Physical and Engineering Sciences **156**, 368 (1936).
- [141] Y. Q. Jia, R. C. Shi, and S. Y. Chou, IEEE Transactions on Magnetics **32**, 4707 (1996).
- [142] M. Zhu, M. J. Wilson, B. L. Sheu, P. Mitra, P. Schiffer, and N. Samarth, Applied Physics Letters **91**, 192503 (2007).
- [143] H. J. Zhu, M. Ramsteiner, H. Kostial, M. Wassermeier, H. Schönherr, and K. H. Ploog, Physical Review Letters **87**, 016601 (2001).

- [144] D. Ning, T. Jian-Shi, Z. Lei, Z. Shu-Chao, and C. Pei-Yi, *Chinese Physics Letters* **27**, 098501 (2010).
- [145] R. E. Camley and J. Barnas, *Physical Review Letters* **63**, 664 (1989).
- [146] P. M. Levy, S. Zhang, and A. Fert, *Physical Review Letters* **65**, 1643 (1990).
- [147] S. Lee, W. Pratt Jr., Q. Yang, P. Holody, R. Loloee, P. Schroeder, and J. Bass, *Journal of Magnetism and Magnetic Materials* **118**, L1 (1993).
- [148] M. Johnson, *Physical Review Letters* **67**, 3594 (1991).
- [149] M. Johnson and R. H. Silsbee, *Physical Review B* **35**, 4959 (1987).
- [150] P. C. van Son, H. van Kempen, and P. Wyder, *Physical Review Letters* **58**, 2271 (1987).
- [151] A. Fert and H. Jaffres, *Physical Review B* **64**, 184420 (2001).
- [152] J. Bass and W. Pratt Jr., *Journal of Magnetism and Magnetic Materials* **200**, 274 (1999).
- [153] T. Sasaki, T. Oikawa, T. Suzuki, M. Shiraishi, Y. Suzuki, and K. Noguchi, *Applied Physics Letters* **96**, 122101 (2010).
- [154] A. M. Roy, D. E. Nikonov, and K. C. Saraswat, *Journal of Applied Physics* **107**, 064504 (2010).
- [155] A. Fert and L. Piraux, *Journal of Magnetism and Magnetic Materials* **200**, 338 (1999).
- [156] K. H. J. Buschow, *Handbook of Magnetic Materials* (Elsevier, 2009).
- [157] V. Talyansky, S. Choopun, M. Downes, R. P. Sharma, T. Venkatesan, Y. X. Li, L. G. Salamanca-Riba, M. C. Wood, R. T. Lareau, and K. A. Jones, *Journal of Materials Research* **14**, 3298 (1999).
- [158] W. Chen, Y. Lin, X. Guo, and S. Wu, *Japanese Journal of Applied Physics* **42**, 208 (2003).
- [159] H. Ago, Y. Ito, N. Mizuta, K. Yoshida, B. Hu, C. M. Orofeo, M. Tsuji, K.-i. Ikeda, and S. Mizuno, *ACS Nano* **4**, 7407 (2010).
- [160] G. Kästle, H. Boyen, B. Koslowski, A. Plettl, F. Weigl, and P. Ziemann, *Surface Science* **498**, 168 (2002).
- [161] R. C. O’Handley, *Modern Magnetic Materials: Principles and Applications* (Wiley-Interscience, 2000).
- [162] E.-M. Karrer-Müller, “Herstellung und Charakterisierung von Zinkoxid-Ferromagnet-Heterostrukturen zur Spininjektion,” (2011).
- [163] T. McGuire and R. Potter, *IEEE Trans. Magn.* **11**, 1018 (1975).

- [164] T. R. McGuire, AIP Conference Proceedings **24**, 435 (1975).
- [165] S. Chikazumi, *Physics of Ferromagnetism*, 2nd ed. (Oxford University Press, 1997).
- [166] W. Martienssen, *Springer Handbook of Condensed Matter and Materials Data*, 1st ed. (Springer Berlin Heidelberg, 2005).
- [167] L. Piraux, S. Dubois, A. Fert, and L. Belliard, The European Physical Journal B **4**, 413 (1998).
- [168] C. E. Moreau, I. C. Moraru, N. O. Birge, and W. P. Pratt, Applied Physics Letters **90**, 012101 (2007).
- [169] L. C. Lew Yan Voon, M. Willatzen, M. Cardona, and N. E. Christensen, Physical Review B **53**, 10703 (1996).
- [170] B. Heinrich, C. Burrowes, E. Montoya, B. Kardasz, E. Girt, Y. Song, Y. Sun, and M. Wu, Phys. Rev. Lett. **107**, 066604 (2011).
- [171] Y. Kajiwara, K. Harii, S. Takahashi, J. Ohe, K. Uchida, M. Mizuguchi, H. Umezawa, H. Kawai, K. Ando, K. Takanashi, S. Maekawa, and E. Saitoh, Nature **464**, 262 (2010).
- [172] F. Heusler, Verhandlungen der Deutschen Physikalischen Gesellschaft **5**, 219 (1903).
- [173] F. Heusler, Verhandlungen der Deutschen Physikalischen Gesellschaft **5**, 220 (1903).
- [174] H. H. Potter, Proceedings of the Physical Society **41**, 135 (1928).
- [175] G. Johnston and E. Hall, Journal of Physics and Chemistry of Solids **29**, 193 (1968).
- [176] P. J. Webster, Contemporary Physics **10**, 559 (1969).
- [177] H. Lin, L. A. Wray, Y. Xia, S. Xu, S. Jia, R. J. Cava, A. Bansil, and M. Z. Hasan, Nature Materials **9**, 546 (2010).
- [178] T. Graf, S. S. Parkin, and C. Felser, IEEE Transactions on Magnetics **47**, 367 (2011).
- [179] J. Winterlik, G. H. Fecher, C. Felser, M. Jourdan, K. Grube, F. Hardy, H. von Lohneysen, K. L. Holman, and R. J. Cava, Physical Review B **78**, 184506 (2008).
- [180] J. Winterlik, G. H. Fecher, A. Thomas, and C. Felser, Physical Review B **79**, 064508 (2009).
- [181] Y. Oner, O. Kamer, E. Alveroglu, M. Acet, and T. Krenke, Journal of Alloys and Compounds **429**, 64 (2007).
- [182] S. Trudel, O. Gaier, J. Hamrle, and B. Hillebrands, Journal of Physics D: Applied Physics **43**, 193001 (2010).
- [183] H. C. Kandpal, G. H. Fecher, and C. Felser, Journal of Physics D: Applied Physics **40**, 1507 (2007).

- [184] P. Webster, *Journal of Physics and Chemistry of Solids* **32**, 1221 (1971).
- [185] H. Schneider, E. Vilanova, B. Balke, C. Felser, and G. Jakob, *Journal of Physics D: Applied Physics* **42**, 084012 (2009).
- [186] O. Gaier, J. Hamrle, S. Trudel, B. Hillebrands, H. Schneider, and G. Jakob, *Journal of Physics D: Applied Physics* **42**, 232001 (2009).
- [187] M. R. Paudel, C. S. Wolfe, H. M. A. Patton, J. Simonson, I. Dubenko, N. Ali, and S. Stadler, *Journal of Applied Physics* **105**, 07E902 (2009).
- [188] W. H. Wang, M. Przybylski, W. Kuch, L. I. Chelaru, J. Wang, Y. F. Lu, J. Barthel, H. L. Meyerheim, and J. Kirschner, *Physical Review B* **71**, 144416 (2005).
- [189] E. Valerio, C. Grigorescu, S. Manea, F. Guinneton, W. Branford, and M. Autric, *Applied Surface Science* **247**, 151 (2005).
- [190] W. Wang, M. Przybylski, W. Kuch, L. Chelaru, J. Wang, Y. Lu, J. Barthel, and J. Kirschner, *Journal of Magnetism and Magnetic Materials* **286**, 336 (2005).
- [191] M. R. Paudel, C. S. Wolfe, N. Ali, S. Stadler, J. A. Christodoulides, D. L. Ederer, Y. Li, T. A. Callcott, and J. W. Freeland, *Journal of Applied Physics* **105**, 103907 (2009).
- [192] A. T. Krupp, "Growth and characterization of ferromagnetic Heusler compound thin films," (2010).
- [193] T. Graf, F. Casper, J. Winterlik, B. Balke, G. H. Fecher, and C. Felser, *Zeitschrift für anorganische und allgemeine Chemie* **635**, 976–981 (2009).
- [194] P. J. Brown, K. U. Neumann, P. J. Webster, and K. R. A. Ziebeck, *Journal of Physics: Condensed Matter* **12**, 1827 (2000).
- [195] M. Oogane, Y. Sakuraba, J. Nakata, H. Kubota, Y. Ando, A. Sakuma, and T. Miyazaki, *Journal of Physics D: Applied Physics* **39**, 834 (2006).
- [196] B. Balke, S. Ouardi, T. Graf, J. Barth, C. G. Blum, G. H. Fecher, A. Shkabko, A. Weidenkaff, and C. Felser, *Solid State Communications* **150**, 529 (2010).
- [197] W. Lu, W. Zhang, and L. Chen, *Journal of Alloys and Compounds* **484**, 812 (2009).
- [198] G. Winkler, *Magnetic garnets* (Vieweg, Braunschweig; Wiesbaden, 1981).
- [199] P. Hansen, K. Witter, and W. Tolksdorf, *Physical Review B* **27**, 6608 (1983).
- [200] M. A. Gilleo and S. Geller, *Physical Review* **110**, 73 (1958).
- [201] P. Hansen, P. Röschmann, and W. Tolksdorf, *Journal of Applied Physics* **45**, 2728 (1974).
- [202] Q. Yang, H. Zhang, Q. Wen, and Y. Liu, *Journal of Applied Physics* **108**, 073901 (2010).

- [203] S. Kück, K. Petermann, U. Pohlmann, U. Schönhoff, and G. Huber, *Applied Physics B Laser and Optics* **58**, 153 (1994).
- [204] S. Blank and J. Nielsen, *Journal of Crystal Growth* **17**, 302 (1972).
- [205] T. Aichele, A. Lorenz, R. Hergt, and P. Görnert, *Crystal Research and Technology* **38**, 575 (2003).
- [206] Y. Krockenberger, H. Matsui, T. Hasegawa, M. Kawasaki, and Y. Tokura, *Applied Physics Letters* **93**, 092505 (2008).
- [207] Y. Krockenberger, K. Yun, T. Hatano, S. Arisawa, M. Kawasaki, and Y. Tokura, *Journal of Applied Physics* **106**, 123911 (2009).
- [208] S. Kahl and A. M. Grishin, *Journal of Applied Physics* **93**, 6945 (2003).
- [209] S. A. Manuilov, R. Fors, S. I. Khartsev, and A. M. Grishin, *Journal of Applied Physics* **105**, 033917 (2009).
- [210] S. A. Manuilov and A. M. Grishin, *Journal of Applied Physics* **108**, 013902 (2010).
- [211] P. C. Dorsey, S. E. Bushnell, R. G. Seed, and C. Vittoria, *Journal of Applied Physics* **74**, 1242 (1993).
- [212] S. A. Manuilov, S. I. Khartsev, and A. M. Grishin, *Journal of Applied Physics* **106**, 123917 (2009).
- [213] J. M. D. Coey, *Magnetism and Magnetic Materials* (Cambridge University Press, 2010).
- [214] M. A. Gilileo and S. Geller, *Physical Review* **110**, 73 (1958).
- [215] S. Geller and M. A. Gilileo, *Acta Crystallographica* **10**, 239 (1957).
- [216] J. Helsing, *YIG resonators and filters* (Wiley, 1985).
- [217] A. Y. Elezzabi and M. R. Freeman, *Applied Physics Letters* **68**, 3546 (1996).
- [218] S. Geller and M. Gilileo, *Journal of Physics and Chemistry of Solids* **3**, 30 (1957).
- [219] E. E. Anderson, *Physical Review* **134**, A1581 (1964).
- [220] M. S. Wagner, *Epitaktisches Wachstum dünner, ferromagnetischer Schichten aus Y3Fe5O12 mittels gepulster Laserdeposition*, Master's thesis, Technische Universität München (2011).
- [221] B. Knörr and W. Tolksdorf, *Materials Research Bulletin* **19**, 1507 (1984).
- [222] R. W. G. Wyckoff, *Crystal Structures 1*, second edition ed. (Interscience Publishers, New York, 1963) pp. 7–83.
- [223] Y. Dumont, N. Keller, E. Popova, D. S. Schmool, S. Bhattacharya, B. Stahl, M. Tessier, and M. Guyot, *Journal of Applied Physics* **97**, 10G108 (2005).

- [224] E. Popova, N. Keller, F. Jomard, L. Thomas, M.-C. Brianso, F. Gendron, M. Guyot, and M. Tessier, *The European Physical Journal B - Condensed Matter and Complex Systems* **31**, 69 (2003).
- [225] M. Schwarz, "Aufbau und Charakterisierung eines FMR-Spektrometers für X- und K-Band," (2008).
- [226] C. Kittel, *Einführung in die Festkörperphysik*, 9th ed. (1991).
- [227] R. Birss, *Symmetry and magnetism*, Series of monographs on selected topics in solid state physics (North-Holland Pub. Co., 1966).
- [228] Y. C. Akgoz and G. A. Saunders, *Journal of Physics C: Solid State Physics* **8**, 2962 (1975).
- [229] Y. C. Akgoz and G. A. Saunders, *Journal of Physics C: Solid State Physics* **8**, 1387 (1975).
- [230] H. Grimmer, *Acta Crystallographica Section A Foundations of Crystallography* **49**, 763 (1993).
- [231] J. M. Ziman, *Electrons and phonons the theory of transport phenomena in solids* (Clarendon Press ; Oxford University Press, Oxford; New York, 2001).
- [232] M. Kohler, *Annalen der Physik* **441**, 18 (1950).
- [233] M. Kohler, *Annalen der Physik* **432**, 196 (1941).
- [234] H. Jones and C. Zener, *Proceedings of the Royal Society A: Mathematical, Physical and Engineering Sciences* **145**, 268 (1934).
- [235] W. Limmer, J. Daeubler, L. Dreher, M. Glunk, W. Schoch, S. Schwaiger, and R. Sauer, *Physical Review B* **77**, 205210 (2008).
- [236] W. Limmer, M. Glunk, J. Daeubler, T. Hummel, W. Schoch, R. Sauer, C. Bihler, H. Huebl, M. S. Brandt, and S. T. B. Goennenwein, *Physical Review B* **74**, 205205 (2006).
- [237] P. Muduli, K. Friedland, J. Herfort, H. Schönherr, and K. Ploog, *Physical Review B* **72**, 104430 (2005).
- [238] T. Dietl, H. Ohno, and F. Matsukura, *Physical Review B* **63**, 195205 (2001).
- [239] T. Jungwirth, J. Sinova, J. Mašek, J. Kučera, and A. H. MacDonald, *Reviews of Modern Physics* **78**, 809 (2006).
- [240] T. Dietl, H. Ohno, F. Matsukura, J. Cibert, and D. Ferrand, *Science* **287**, 1019 (2000).
- [241] P. Van Dorpe, Z. Liu, W. Van Roy, V. F. Motsnyi, M. Sawicki, G. Borghs, and J. De Boeck, *Applied Physics Letters* **84**, 3495 (2004).

- [242] Y. Ohno, D. K. Young, B. Beschoten, F. Matsukura, H. Ohno, and D. D. Awschalom, *Nature* **402**, 790 (1999).
- [243] C. Gould, C. Rüster, T. Jungwirth, E. Girgis, G. M. Schott, R. Giraud, K. Brunner, G. Schmidt, and L. W. Molenkamp, *Physical Review Letters* **93**, 117203 (2004).
- [244] C. Rüster, T. Borzenko, C. Gould, G. Schmidt, L. W. Molenkamp, X. Liu, T. J. Wojtowicz, J. K. Furdyna, Z. G. Yu, and M. E. Flatté, *Physical Review Letters* **91**, 216602 (2003).
- [245] T. Figielski, T. Wosinski, A. Morawski, A. Makosa, J. Wrobel, and J. Sadowski, *Applied Physics Letters* **90**, 052108 (2007).
- [246] K. Pappert, S. Humpfner, C. Gould, J. Wensch, K. Brunner, G. Schmidt, and L. W. Molenkamp, *Nat Phys* **3**, 573 (2007).
- [247] J. G. Braden, J. S. Parker, P. Xiong, S. H. Chun, and N. Samarth, *Physical Review Letters* **91**, 056602 (2003).
- [248] M. Tanaka and Y. Higo, *Physical Review Letters* **87**, 026602 (2001).
- [249] H. Ohno and F. Matsukura, *Solid State Communications* **117**, 179 (2001).
- [250] H. X. Tang, R. K. Kawakami, D. D. Awschalom, and M. L. Roukes, *Physical Review Letters* **90**, 107201 (2003).
- [251] C. Bihler, M. Althammer, A. Brandlmaier, S. Geprägs, M. Weiler, M. Opel, W. Schoch, W. Limmer, R. Gross, M. S. Brandt, and S. T. B. Goennenwein, *Physical Review B* **78**, 045203 (2008).
- [252] Y. Pu, E. Johnston-Halperin, D. D. Awschalom, and J. Shi, *Physical Review Letters* **97**, 036601 (2006).
- [253] Y. Pu, D. Chiba, F. Matsukura, H. Ohno, and J. Shi, *Physical Review Letters* **101**, 117208 (2008).
- [254] S. Meyer, “Magneto-thermo-galvanische Experimente an (Ga,Mn)As Dünnschichten,” (2012).
- [255] M. T. Elm, P. J. Klar, W. Heimbrod, U. Wurstbauer, M. Reinwald, and W. Wegscheider, *Journal of Applied Physics* **103**, 093710 (2008).
- [256] R. Kelekar and B. M. Clemens, *Journal of Applied Physics* **96**, 540 (2004).
- [257] P. K. Muduli, K. Friedland, J. Herfort, H. Schonherr, and K. H. Ploog, *Journal of Applied Physics* **105**, 07B104 (2009).
- [258] K. Friedland, M. Bowen, J. Herfort, H. P. Schonherr, and K. H. Ploog, *Journal of Physics: Condensed Matter* **18**, 2641 (2006).
- [259] H. Vinzelberg, J. Schumann, D. Elefant, E. Arushanov, and O. G. Schmidt, *Journal of Applied Physics* **104**, 093707 (2008).

- [260] D. Ebke, P. Thomas, O. Schebaum, M. Schäfers, D. Nissen, V. Drewello, A. Hütten, and A. Thomas, *Journal of Magnetism and Magnetic Materials* **322**, 996 (2010).
- [261] M. Obaida, K. Westerholt, and H. Zabel, *Physical Review B* **84**, 184416 (2011).
- [262] A. Husmann and L. J. Singh, *Physical Review B* **73**, 172417 (2006).
- [263] T. Ambrose, J. J. Krebs, and G. A. Prinz, *Applied Physics Letters* **76**, 3280 (2000).
- [264] Y. Tserkovnyak, A. Brataas, and G. E. W. Bauer, *Phys. Rev. Lett.* **88**, 117601 (2002).
- [265] F. Czeschka, *Spin Currents in Metallic Nanostructures*, Ph.D. thesis, TU München (2011).
- [266] X. Jia, K. Liu, K. Xia, and G. E. W. Bauer, arXiv:1103.3764 (2011).
- [267] Y. Tserkovnyak, A. Brataas, and G. E. W. Bauer, *Phys. Rev. B* **66**, 224403 (2002).
- [268] Y. Guan, W. Bailey, E. Vescovo, C. Kao, and D. Arena, *J. Magn. Magn. Mater.* **312**, 374 (2007).
- [269] K. Ando, T. Yoshino, and E. Saitoh, *Appl. Phys. Lett.* **94**, 152509 (2009).
- [270] O. Mosendz, J. E. Pearson, F. Y. Fradin, G. E. W. Bauer, S. D. Bader, and A. Hoffmann, *Phys. Rev. Lett.* **104**, 046601 (2010).
- [271] O. Mosendz, V. Vlaminck, J. E. Pearson, F. Y. Fradin, G. E. W. Bauer, S. D. Bader, and A. Hoffmann, *Phys. Rev. B* **82**, 214403 (2010).
- [272] S. Takahashi and S. Maekawa, *Science and Technology of Advanced Materials* **9**, 014105 (2008).
- [273] L. Vila, T. Kimura, and Y. Otani, *Phys. Rev. Lett.* **99**, 226604 (2007).
- [274] C. W. Sandweg, Y. Kajiwara, K. Ando, E. Saitoh, and B. Hillebrands, *Appl. Phys. Lett.* **97**, 252504 (2010).
- [275] Y. Tserkovnyak, A. Brataas, G. E. W. Bauer, and B. I. Halperin, *Reviews of Modern Physics* **77**, 1375 (2005).
- [276] M. D. Stiles and A. Zangwill, *Physical Review B* **66**, 014407 (2002).
- [277] D. Greig and D. Livesey, *Journal of Physics F: Metal Physics* **2**, 699 (1972).
- [278] N. Jaouen, F. Wilhelm, A. Rogalev, J. Tonnerre, T. Johal, and G. van der Laan, *IEEE Transactions on Magnetism* **41**, 3334 (2005).
- [279] F. Wilhelm, P. Pouloupoulos, G. Ceballos, H. Wende, K. Baberschke, P. Srivastava, D. Benea, H. Ebert, M. Angelakeris, N. K. Flevaris, D. Niarchos, A. Rogalev, and N. B. Brookes, *Physical Review Letters* **85**, 413 (2000).

- [280] P. Pouloupoulos, M. Angelakeris, E. T. Papaioannou, N. K. Flevaris, D. Niarchos, M. Nyvlt, V. Prosser, S. Visnovsky, C. Mueller, P. Fumagalli, F. Wilhelm, and A. Rogalev, *Journal of Applied Physics* **94**, 7662 (2003).
- [281] R. Henriquez, S. Oyarzun, M. Flores, M. A. Suarez, L. Moraga, G. Kremer, C. A. Gonzalez-Fuentes, M. Robles, and R. C. Munoz, *Journal of Applied Physics* **108**, 123704 (2010).
- [282] A. I. Schindler and E. M. Pugh, *Physical Review* **89**, 295 (1953).
- [283] B. Monemar, *Journal of Physics: Condensed Matter* **13**, 7011 (2001).
- [284] L. Gravier, S. Serrano-Guisan, F. Reuse, and J. Ansermet, *Physical Review B* **73**, 024419 (2006).
- [285] M. Weiler, *Magnon-phonon interactions in ferromagnetic thin films*, Ph.D. thesis, TU München (2012).
- [286] T. Mitsuyu, O. Yamazaki, K. Ohji, and K. Wasa, *Ferroelectrics* **42**, 233 (1982).
- [287] R. Sultan, A. D. Avery, G. Stiehl, and B. L. Zink, *Journal of Applied Physics* **105**, 043501 (2009).
- [288] E. Padrón-Hernández, A. Azevedo, and S. M. Rezende, *Applied Physics Letters* **99**, 192511 (2011).
- [289] Z. Wang, Y. Sun, M. Wu, V. Tiberkevich, and A. Slavin, *Physical Review Letters* **107**, 146602 (2011).
- [290] A. V. Chumak, A. A. Serga, M. B. Jungfleisch, R. Neb, D. A. Bozhko, V. S. Tiberkevich, and B. Hillebrands, *Applied Physics Letters* **100**, 082405 (2012).
- [291] G. Frank and H. Köstlin, *Applied Physics A: Materials Science & Processing* **27**, 197 (1982).

Acknowledgements

This thesis would not have been possible without the help and support of many people. In particular, I would like to thank:

- Prof. Dr. Rudolf Gross for giving me the opportunity to work at the Walther-Meißner-Institute and the freedom of choosing my own research focus. I will never forget his inexhaustible knowledge on all the physics in this world.
- Dr. Sebastian T. B. Goennenwein for all the great ideas, that sometimes did not work out as intended, for countless discussions on experiments and results, for being always in a good mood, and for showing me how to socially network on conferences using cocktails. “Audere est facere!”
- Dr. Matthias Opel for the support in the XRD, laser-MBE, SQUID lab and all computer related stuff, for the countless detailed corrections on written texts in a blink of an eye, and for the ability to keep a cheerful attitude in the middle of the worst case scenario. “It’s all about the details, details, details!”
- Dr. Hans Huebl for always asking the right questions, which kept me sometimes busy for endless weeks, for always having the right experimental equipment in his drawer, and for sharing his knowledge in avoiding experimental calamities. “Always keep smiling!”
- Dr. Stephan “Steve” Geprägs for always having some time available to discuss laser-MBE growth optimization and XRD results, fixing or helping to fix countless parts in the laser-MBE, XRD and SQUID lab. His long working hours during the installation of the new excimer laser beam path will never be forgotten.
- Dr. Mathias Weiler for sharing many of the bright and dark (Light induced Hall effect!) moments during my PhD thesis, for being the best roommate imaginable, for using my samples for his experiments, and for all the activities outside the institute. “Exitus acta probat.”
- Dr. Andreas Brandlmaier for the good times during our stays in Aachen, while measuring fancy piezoactuator hybrids and visiting the “Pontstraße” at night, for manually placing contacts on the tiniest samples in the world, and for all the discussions on physics and beyond.
- Dr. Franz D. Czeschka for all the ideas of how to reduce the noise in measurements, for measuring spin pumping with my samples, for helping to install the thank god it’s Friday beer event at the WMI and sharing a nightlife outside the WMI.
- Christoph Zollitsch for all the fun we had in the lab, while the experiments were working or stopped working, for the many free liquid helium refills on the weekend and for keeping a good spirit.

- Johannes Lotze for the spin pumping measurements on the YIG/Pt heterostructures and the FMR measurements on YIG samples, and for being always interested in discussing new measurement results.
- All my diploma students and bachelor students that contributed all in their own way to this thesis:
 - Michael Wagner, the first diploma student I had to supervise and who kept his good mood even as we arrived at the lengthy tensor calculations for his backup plan.
 - Alexander Krupp for his countless hours in the lab doing the ADMR experiments on Heusler compounds, optimizing the laser-MBE growth of CMS and for helping to start and understand the ADMTP experiments.
 - Georg Benka for trying to measure the Spin Seebeck effect in many different samples.
 - Martin Wagner for all his work related to the laser-MBE growth of YIG and the quick realization of my ideas.
 - Eva Karrer-Müller for always keeping within the schedule, for fabricating these nice and excellent zinc oxide based spin valve contacts and for always working with a smile on her face.
 - Sibylle Meyer for working hard on optimizing the ADMTP measurements on (Ga,Mn)As, for correcting all the tough tensor calculations, and for continuing as a PhD now the work on ADMR and ADMTP measurements at the WMI.
 - Michael Schreier for helping me to start the research on SMR and his contributions in developing a phenomenological model.
- Thomas “Tom” Brenninger for providing unlimited support to fix all the problems in the laser-MBE lab, for turning my fancy and wicked ideas into technical drawings that could even be realized, and for all the time spent in the Diplomandenwerkstatt to fabricate “quick” solutions. Especially, without his efforts during the installation and optimization of the new excimer laser beam path, finishing my thesis would have been impossible.
- My roommates at the WMI: Matthias Pernpeitner, Christoph Zollitsch, and Matthias Weiler for all the heated discussions, and for the remarkable moments we shared.
- Johannes Büttner and Elisabeth Hoffmann for all their support inside the institute, and for all the shared activities in the free time.
- Dr. Andreas Erb and Karen Helm-Knapp for fabricating many different laser-MBE targets, which always had the right stoichiometry.
- Inga-Mareen Imort, Dr. Andy Thomas and Prof. Dr. Günter Reiss from the Universität Bielefeld for preparing the excellent Cobalt-based Heusler samples.
- Wolfgang Limmer and Wladimir Schoch from the Universität Ulm for the high quality (Ga,Mn)As samples and the discussions on the ADMR experiments.

- Prof. Dr. Martin Brandt and Lukas “Luke” Dreher from the magnetism group of the WSI for all the stimulating discussions on experimental results and for all the free measurement time on their FMR machine. “Usus magister est optimus.”
- Dr. Thomas Wassner and Bernhard Laumer from the WSI for being partner in crime in the realm of zinc oxide, for sharing their knowledge on the buffer growth and PL measurements on ZnO, and for the PL measurements on my samples.
- Dr. Bernd Beschoten, Christoph Schwark, Vera Klinke, Christian Weier and all the others from the RWTH Aachen for the many detailed optical measurements on my zinc oxide samples and for the fun during my stays in Aachen.
- Dr. Georg Woltersdorf from the Universität Regensburg for the frequency dependent FMR measurements, and for all the discussions on physics in coffee bars during conferences.
- Dr. Arunava Gupta from the University of Alabama for the NFO samples.
- Deepak Venkateshvaran for sharing the workload in zinc oxide related topics during his stay at the WMI, and for the many conversations in English, that helped me to improve my language skills.
- All the other retired scientists, senior scientists, PhD students, diploma students, master students, and bachelor students inside and outside of the WMI, whom I didn’t mention, but still made working on my PhD a breeze and provided a lot of fun moments. Thank you!
- All the guys in our mechanical workshop, in particular Helmut Thies and Robert Müller, for making the impossible possible on such amazing short timescales.
- All the technical staff of the WMI that allowed me to focus on my thesis. Especially, the helium liquifier team as well as the administrative staff Emel Dönertas and Ludwig Osslander.
- Toni “The Helmet” Helm and Christoph “Dr. Wuff” Barkhausen for the great e-mail correspondence and for the middle day eating events.
- Holger Hochmuth and Christian Reiser, my handball team and all other friends for all the shared moments that are totally unrelated to physics.
- Sandra Paretzke, Sascha Wolff, and Anne Kaßbeckert-Schluck for always listening to my repair stories from the institute, for the shared activities outside the world of physics and Anne for doing my household duties, while I was busy with writing up my PhD.
- Everybody, that has made it through these 250 pages of my PhD thesis and survived. Congratulations!
- My family: Regina, my sister, Claudia, my mother, and Klaus, my father, for all their unlimited support given to me, and for all the memories we share.
- Last but not least, my sun and stars Annalena for forgiving me to always be late, and for sharing all the great moments in my life. I deeply love you!